CHEMICAL REVIEWS

pubs.acs.org/CR

Review

Bifunctional Electrocatalysts for Overall and Hybrid Water Splitting

Li Quan,[§] Hui Jiang,[§] Guoliang Mei,[§] Yujie Sun,* and Bo You*

Cite This: *Chem. Rev.* 2024, 124, 3694−3812

Read Online

ACCESS | Metrics & More | Article Recommendations

ABSTRACT: Electrocatalytic water splitting driven by renewable electricity has been recognized as a promising approach for green hydrogen production. Different from conventional strategies in developing electrocatalysts for the two half-reactions of water splitting (e.g., the hydrogen and oxygen evolution reactions, HER and OER) separately, there has been a growing interest in designing and developing bifunctional electrocatalysts, which are able to catalyze both the HER and OER. In addition, considering the high overpotentials required for OER while limited value of the produced oxygen, there is another rapidly growing interest in exploring alternative oxidation reactions to replace OER for hybrid water splitting toward energy-efficient hydrogen generation. This Review begins with an introduction on the fundamental aspects of water splitting, followed by a thorough discussion on various physicochemical characterization techniques that are frequently employed in probing the active sites, with an emphasis on the reconstruction of bifunctional electrocatalysts during redox electrolysis. The design, synthesis, and performance of diverse bifunctional electrocatalysts based on noble metals, nonprecious metals, and metal-free nanocarbons, for overall water splitting in acidic and alkaline electrolytes, are thoroughly summarized and compared. Next, their application toward hybrid water splitting is also presented, wherein the alternative anodic reactions include sacrificing agents oxidation, pollutants oxidative degradation, and organics oxidative upgrading. Finally, a concise statement on the current challenges and future opportunities of bifunctional electrocatalysts for both overall and hybrid water splitting is presented in the hope of guiding future endeavors in the quest for energy-efficient and sustainable green hydrogen production.

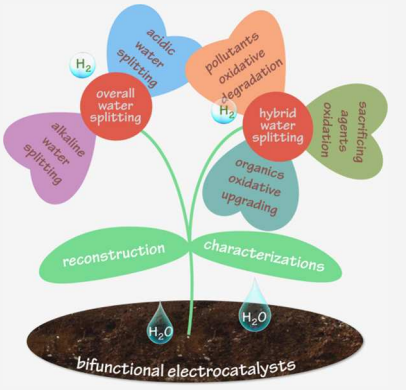

CONTENTS

Received: May 18, 2023
Revised: January 13, 2024
Accepted: February 8, 2024
Published: March 22, 2024

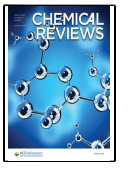

https://doi.org/10.1021/acs.chemrev.3c00332
Chem. Rev. 2024, 124, 3694−3812

1. INTRODUCTION

With the rapid development of global economy and the continuous growth of population, it has become evident that the limited reserves of nonrenewable fossil fuels will no longer be able to meet the ever-increasing energy demands of mankind.[1−5] Furthermore, the excessive utilization of these fossil fuels leads to significant emissions of pollutants and greenhouse gases, resulting in a range of environmental and societal issues.[6−9] These energy shortages and environmental problems pose significant obstacles to sustainable development of humanity. Therefore, there is an urgent need to develop low-cost, accessible, and environmentally friendly energy sources to reduce our excessive dependence on fossil fuels. Hydrogen, often referred to as 'the cleanest energy in the world', is gaining recognition due to its high combustion calorific value and zero-carbon emission. Currently, hydrogen is primarily used in petrochemical industry, ammonia production, metal smelting, and fuel desulfurization.[10−15] However, its application will extend to transportation, aviation, electronic industry, maritime operation, and food industry in the future. According to the Hydrogen Council, hydrogen production capacity is projected to exceed 10 million tons by 2030, with the demand for clean hydrogen reaching 75 million tons.[16−20] This emphasizes the need to develop efficient methods for hydrogen production, which will play a crucial role in our future energy portfolio (Figure 1a). At present, the prevailing methods of hydrogen production include steam-methane reforming, coal gasification, and water electrolysis.[21−25] Traditional strategies that rely on fossil fuels like coal and natural gas as raw materials are unsustainable and unsuitable for large-scale, centralized hydrogen generation from an environmental standpoint. In contrast, electrochemical water splitting, powered by renewable energy sources such as wind, solar, and tidal energy, offers a renewable solution with high-purity hydrogen as the product. As a result, it is widely regarded as the most promising environmentally friendly technology for future hydrogen supply (Figure 1a).[26−30]

Electrochemical water splitting involves two fundamental reactions: the hydrogen evolution reaction (HER) at the cathode and the oxygen evolution reaction (OER) at the anode. These reactions can occur in acidic, alkaline, or neutral electrolytes under ambient or high-temperature conditions. There are primarily three typical technologies for water splitting: alkaline water electrolysis (AWE), which was first introduced by Troostwijk and Diemann in 1789,[31] acidic proton exchange membrane water electrolysis (PEMWE), which utilizes solid polysulfonated membranes like Nafion, and solid oxide electrolysis (SOE). Currently, AWE is extensively implemented worldwide due to its low cost. It utilizes a 20−30 wt % KOH or NaOH solution as the electrolyte, Ni-based catalysts as the working electrodes, and asbestos as the diaphragm or separator.[32−34] When sufficient direct-current power is applied, water molecules (H_2O) are dissociated into H^+ and OH^- ions. H^+ ions gain electrons from the external circuit at the cathode to form H_2, while OH^- ions migrate across the diaphragm to the anode driven by the electric force and release electrons to generate O_2. However, AWE faces challenges such as the long distance between the cathode and the anode, high resistance for ion migration across the asbestos diaphragm, and modest electrocatalytic activities of Ni-based materials. These factors require additional voltage input, resulting in low energy conversion efficiency. Moreover, since the asbestos diaphragm cannot completely prevent gas crossover, electrolysis plant balancing becomes necessary, and both the current density (below 400 mA cm^{-2}) and hydrogen purity are not sufficiently high.[33] These issues can be partially addressed with the development of anion exchange membranes.

In comparison, PEMWE, first conceptualized by Grubb in 1966, overcomes many drawbacks of AWE. PEMWE benefits from high proton conductivity, low gas permeability, and thin thickness of the PEM,[31] offering advantages such as compact design, high current density (above 2000 mA cm^{-2}), high efficiency, fast response, small footprint, and high purity of hydrogen. In contrast to AWE, the catalysts-coated membrane electrodes in PEMWE are separated only by a PEM, and electrolyte is deionized water. In PEMWE, water molecules are oxidized at the anode to generate oxygen (O_2) and H^+ ions, and the resulting H^+ pass through the PEM to the cathode, acquiring electrons from the external circuit to form hydrogen (H_2).[12,35−42] The acidic environment necessitates high-cost, corrosion-resistant and active electrocatalysts.[43] The state-of-the-art electrocatalysts for PEMWE are based on noble metals such as Pt for cathodic HER and IrO_x/RuO_x for anodic OER, leading to excessive electrolyzer costs and limited large-scale

https://doi.org/10.1021/acs.chemrev.3c00332
Chem. Rev. 2024, 124, 3694−3812

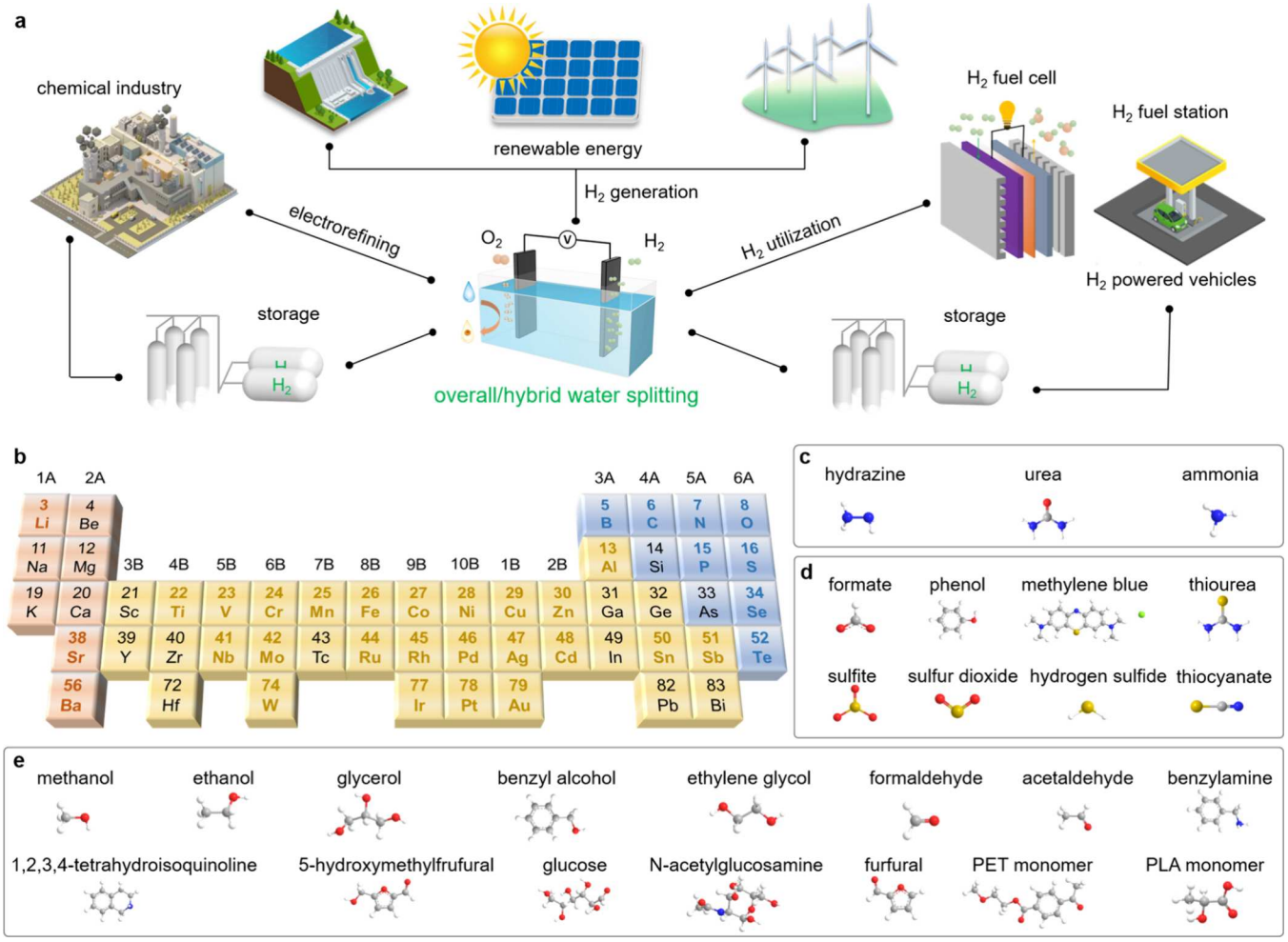

Figure 1. (a) Schematic diagram for green hydrogen cycling. (b) Element compositions of the involved bifunctional electrocatalysts highlighted by colored characters. Alternative oxidation of various substrates including (c) sacrificing agents, (d) pollutants, and (e) the organics that can generate value-added products in hybrid water splitting.

applications. Different from AEM and PEMWE, which operate at low temperatures (20−80 °C) with liquid electrolytes, SOE, first introduced by Donitz and Erdle in the 1980s, is an all-solid-state electrolytic cell that works at high temperatures (500−850 °C). It consists of a ceramic proton-conducting membrane, an anode (such as lanthanum manganate, lanthanum cobaltate, and their composites), and a cathode (metal, cermet, or mixed solid oxide).[31,44−46] During water electrolysis in SOE, water molecules are initially dissociated into H_2 and O^{2-} at the cathode. The O^{2-} ions are then transported to the anode through oxygen vacancies in the solid oxide lattice, resulting in the generation of oxygen (O_2). SOE can utilize industrial waste heat to improve energy conversion efficiency, and the ceramic membrane exhibits excellent airtightness, allowing the production of high-purity hydrogen. However, SOE is still relatively immature due to significant stability and degradation issues under harsh conditions, which currently limit its large-scale commercialization.[35,47,48] On the other hand, both AEM and PEMWE, operating at ambient conditions, offer promising and flexible feasibility for water splitting to produce hydrogen. Considering the sluggish kinetics of both HER and OER, different electrocatalysts at both cathode and anode, such as Pt for HER and IrO_2 for OER, are conventionally utilized. However, their single functionality necessitates different precursors, equipment, and/or procedures for separate synthesis, electrode assembly, and device fabrication, increasing the entire cost. Furthermore, in view of the harsh conditions during water splitting electrolysis (e.g., extreme pH, high potential, and long-term service), the reconstruction of electrocatalysts (e.g., leaching) is inevitable, which would result in severe cross-contamination between the two electrodes with different components. It is expected that such a cross-contamination issue can be alleviated if both HER and OER electrocatalysts are composed of the same materials. Accordingly, it has become an appealing strategy to develop highly active, stable, and cost-effective bifunctional electrocatalysts to drive both HER and OER for efficient overall water splitting (OWS).

From an energy perspective, the energy barrier of anodic OER, due to its multiple proton-coupled electron transfer nature, is much higher than that of HER, which predominantly determines the efficiency of hydrogen production from water splitting. Additionally, the generated O_2 is a low-value byproduct and may pose safety issues due to possible gas crossover and PEM degradation by the formed reactive oxygen species (ROS).[49,50] In response, a strategy called hybrid water splitting (HWS) has been proposed by us and other researchers, aiming to replace OER with alternative oxidation reactions that are thermodynamically more favorable and economically more attractive.[51−53] Currently, numerous

https://doi.org/10.1021/acs.chemrev.3c00332
Chem. Rev. 2024, 124, 3694−3812

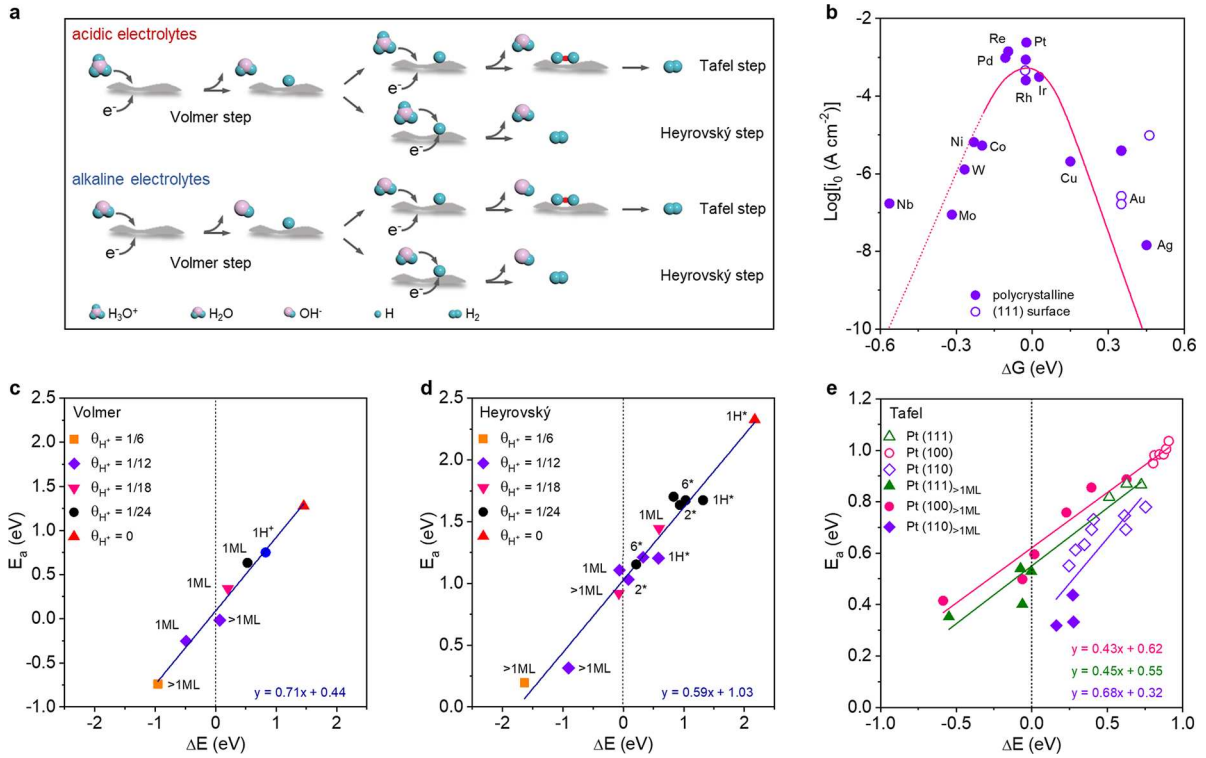

Figure 2. (a) Mechanisms of HER in acidic and alkaline electrolytes. Reproduced with permission from ref 65. Copyright 2020 John Wiley and Sons. (b) Free energy of hydrogen adsorption versus exchange current density. Circles represent experimental data, and the curve is a prediction by microkinetic models based on DFT calculations wherein the dash line indicates the metals which bind H stronger than 0.2 eV/H usually form oxides. (c–e) Scaling relation between reaction energy (ΔE) and activation barrier (E_a) for each elementary HER step. Reproduced with permission from ref 66. Copyright 2019 John Wiley and Sons.

oxidation reactions have been reported as alternatives to OER.[54−57] These alternative oxidation reactions can be divided into three categories based on the functionalities of the underlying substrates: sacrificing agents oxidation that consume relatively valuable substrates, pollutants oxidative degradation using environmental pollutants as oxidative substrates, and organics oxidative upgrading that obtain value-added products. All these oxidative reactions effectively reduce energy consumption for hydrogen production.

In this Review, we provide a comprehensive overview of recent advancements in overall and hybrid water splitting driven by bifunctional electrocatalysts. We begin by introducing the fundamental aspects of HER and OER based on microkinetics analysis and density functional theory (DFT) calculations, and discuss the principles of OWS and HWS. Next, we delve into the key reconstruction phenomenon of bifunctional electrocatalysts during both reduction (HER) and oxidation (e.g., OER and alternative oxidation reactions), highlighting the relevant physicochemical characterization techniques. Subsequently, we summarize the design and synthesis of diverse bifunctional electrocatalysts for overall water splitting in both acidic and alkaline solutions. These bifunctional electrocatalysts are based on noble metals, nonprecious metals, and metal-free nanocarbons (Figure 1b). Additionally, we elaborate on their applications for hybrid water splitting, where they effectively catalyze anodic reactions such as sacrificing agents oxidation (Figure 1c), pollutants oxidative degradation (Figure 1d), and organics oxidative upgrading (Figure 1e). Finally, we provide a concise conclusion and offer insights into future challenges pertaining to the development of advanced bifunctional electrocatalysts for overall and hybrid water splitting. We aim to provide a prognosis for the relevant research field.

2. FUNDAMENTALS OF WATER SPLITTING

2.1. Mechanism of HER

The hydrogen evolution reaction (HER) is a two-electron transfer process that occurs at the electrode/electrolyte interface of the cathode. The source of protons for HER varies depending on the pH of the electrolyte (Figure 2a). H_2 is generated through the reduction of H_3O^+ in acidic media or H_2O in alkaline media, both involving multiple steps. In acidic media, HER typically involves the following elementary pathways: Volmer–Tafel or Volmer–Heyrovský steps. First, an electron is transferred to the surface (∗) of the electrocatalyst via an external circuit, where it combines with a H_3O^+ to produce adsorbed hydrogen atom (H*). This process is known as the Volmer step or the discharge step. Subsequently, H* captures an electron and another H_3O^+ to form a molecular H_2, referred to as the Heyrovský step or electrochemical desorption step. Alternatively, two adjacent H* can combine to yield H_2, known as the Tafel step or chemical desorption step:

$$\text{Volmer step: } H_3O^+ + e^- + * \rightarrow H^* + H_2O$$

$$\text{Heyrovský step: } H_3O^+ + e^- + H^* \rightarrow H_2 + H_2O$$

$$\text{Tafel step: } H^* + H^* \rightarrow H_2 + 2^*$$

Similarly, the HER in alkaline media also involves the Volmer–Heyrovský or Volmer–Tafel steps, with the difference

https://doi.org/10.1021/acs.chemrev.3c00332
Chem. Rev. 2024, 124, 3694−3812

being the source of H* obtained through the dissociation of water molecules. Due to the absence of H^+, an H_2O accepts an electron to form H* and OH^- (Volmer step). Afterward, H* combines with another water molecule and an electron to produce H_2. This process is referred to as the Heyrovský step in alkaline solutions. On the other hand, the Tafel step remains the same as in acidic electrolytes:

$$\text{Volmer step: } H_2O + e^- + * \rightarrow H^* + OH^-$$

$$\text{Heyrovský step: } H_2O + e^- + H^* \rightarrow H_2 + OH^-$$

$$\text{Tafel step: } H^* + H^* \rightarrow H_2 + 2^*$$

These elementary steps highlight the crucial roles of electron transfer and hydrogen adsorption (H*) in HER, and it is evident that breaking the H−OH bond to obtain H* in alkaline solutions is more challenging than that in acidic media. In other words, acidic electrolytes are commonly more favorable for HER compared to alkaline electrolytes. To further determine which pathway is the rate-determining step (RDS) for HER over the underlying electrocatalyst, Tafel plot is usually drawn and the apparent value of Tafel slope serves as an indicator of RDS. Specifically, the values of approximately 118, 39, and 30 mV dec^{-1} imply the RDS role of the Volmer, Heyrovský, and Tafel steps, respectively.[58−65]

In view of the acidic HER pathways, H* on the surface of the electrocatalyst plays a vital role. Several electrochemistry pioneers experimentally found that the HER kinetics intensely relies on the interaction between electrode materials (mainly metals) and H*,[66−69] and a volcanic curve regarding the relationship between exchange current density and metal−hydrogen binding strength has been established (Figure 2b).[70] These findings indicate that an optimal H* sorption, that is neither too strong nor too weak, benefits to rapid HER kinetics, following to the Sabatier principle.[71] This experimental microkinetic analysis was subsequently confirmed by the theoretic calculations.

With the development of computational techniques, density functional theory (DFT) calculations have become a valuable tool to help us understand the details of various electrochemical processes at the atomic level. DFT calculations can provide computational energetics of elementary steps in a specific electrocatalytic process from the aspects of both thermodynamics and kinetics, allowing us to identify potential active centers and RDS. In terms of HER in acidic electrolytes, the Gibbs free energy of hydrogen adsorption (ΔG_{H^*}) is widely recognized as a crucial parameter to determine the HER activity of electrode materials. As shown in Figure 2b, the DFT predictions (curve) matches well with the experimental results for (111) single-crystal (open circles) and polycrystalline surfaces (filled circles). Additionally, the DFT calculations also exhibit scaling relations between the reaction energy (ΔE) and activation barrier of hydrogen gas formation (E_a), with regards to Volmer, Heyrovský, and Tafel elementary steps for Pt with different facets and hydrogen coverage (Figure 2c−e). For example, the weak hydrogen binding implies a high energy barrier for hydrogen generation and vice versa. Therefore, the most effective acidic HER electrocatalysts should bind with hydrogen neither too strong nor too weak.[72] As predicted, Pt is among the best for HER which is positioned at the apex of the volcano plot, in line with the experimental results. Although no consensus has so far been achieved for alkaline HER, the scaling relations are widely accepted and still effective.[64] Based on the above insights, the combination of theory and experiment is crucial for the development of advanced electrocatalysts and the in-depth study of electrocatalytic mechanisms for HER.[73]

2.2. Mechanism of OER

Compared to cathodic HER, anodic OER is a complex four-electron transfer process. In acidic electrolytes, H_2O undergoes oxidation to produce O_2 and H^+, whereas in neutral or alkaline electrolytes, OH^- is oxidized to form H_2O and O_2. Nowadays, various OER mechanisms over diverse electrocatalysts have been proposed. Matsumoto and Sato summarized some of these proposed OER pathways in 1986,[74] which were also included in recent Review articles (Table 1, Figure 3a−d).[37,75,76]

Table 1. Proposed Reaction Mechanisms of OER[a][37,76]

Acidic conditions	Alkaline conditions
Electrochemical oxide path	Electrochemical oxide path
$* + H_2O \rightarrow HO^* + H^+ + e^-$	$* + OH^- \rightarrow HO^* + e^-$
$HO^* \rightarrow O^* + H^+ + e^-$	$HO^* + OH^- \rightarrow O^* + H_2O + e^-$
$2\,O^* \rightarrow 2\,* + O_2$	$2\,O^* \rightarrow 2\,* + O_2$
Oxide path	Oxide path
$* + H_2O \rightarrow HO^* + H^+ + e^-$	$* + OH^- \rightarrow HO^* + e^-$
$2\,HO^* \rightarrow O^* + * + H_2O$	$2\,HO^* \rightarrow O^* + * + H_2O$
$2\,O^* \rightarrow 2\,* + O_2$	$2\,O^* \rightarrow 2\,* + O_2$
Krasil'shchkov path	Krasil'shchkov path
$* + H_2O \rightarrow HO^* + H^+ + e^-$	$* + OH^- \rightarrow HO^* + e^-$
$HO^* \rightarrow O^{-*} + H^+$	$HO^* + OH^- \rightarrow O^{-*} + H_2O$
$O^{-*} \rightarrow O^* + e^-$	$O^{-*} \rightarrow O^* + e^-$
$2\,O^* \rightarrow 2\,* + O_2$	$2\,O^* \rightarrow 2\,* + O_2$
Wade amd Hackerman's path	Yeager's path
$2\,* + 2\,H_2O \rightarrow O^* + H_2O^* + 2\,H^+ + 2\,e^-$	$* + OH^- \rightarrow HO^* + e^-$
$O^* + 2\,HO^{-*} \rightarrow 2\,* + H_2O^* + O_2 + 2\,e^-$	$HO^{z*} \rightarrow HO^{z+1*} + e^-$
	$2\,HO^{z+1*} + 2\,OH^- \rightarrow 2\,* + 2\,H_2O + O_2$
Electrochemical metal peroxide path	Bockris path
$* + H_2O \rightarrow HO^* + H^+ + e^-$	$* + OH^- \rightarrow HO^* + e^-$
$2\,HO^* \rightarrow O^* + * + H_2O$	$HO^* + OH^- \rightarrow H_2O_2^* + e^-$
$O^* + H_2O \rightarrow HOO^* + H^+ + e^-$	$H_2O_2^* + OH^- \rightarrow HOO^{-*} + H_2O$
$2\,HOO^* \rightarrow O^* + * + H_2O + O_2$	$H_2O_2^* + HOO^{-*} \rightarrow H_2O + OH^- + O_2$
DFT-predicted peroxide path	
$* + H_2O \rightarrow HO^* + H^+ + e^-$	
$HO^* \rightarrow O^* + H^+ + e^-$	
$O^* + H_2O \rightarrow HOO^* + H^+ + e^-$	
$HOO^* \rightarrow * + O_2 + H^+ + e^-$	

[a]* means an active site.

As shown in Table 1, except for the Wade and Hackerman's path, the initial step for all the other proposed OER involves the formation of HO*. Owing to the lack of free OH^- in acidic electrolytes, breaking the strong covalent HO−H bond in water is necessitated to initiate the first step, leading to sluggish reactive kinetics. In contrast, a large amount of free OH^- in alkaline conditions can be directly converted to HO* without water dissociation, and thus, relatively fast kinetics can be expected. Following the formation of HO*, subsequent elementary steps vary, implying multiple OER mechanisms.[74] Nonetheless, two categories of OER pathways are widely discussed including adsorbate evolution mechanism (AEM,

https://doi.org/10.1021/acs.chemrev.3c00332
Chem. Rev. 2024, 124, 3694−3812

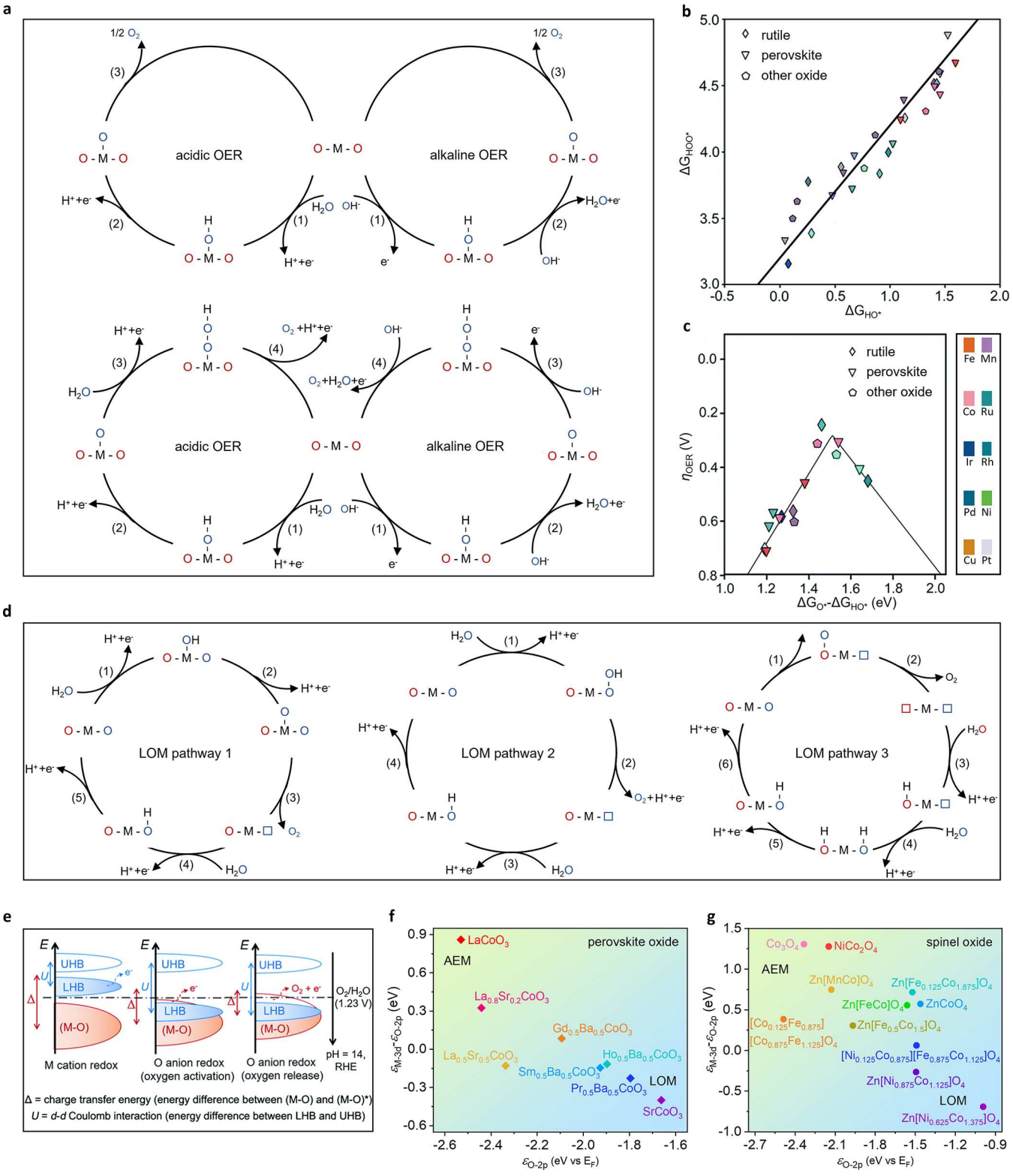

Figure 3. (a) Schematic of AEM mechanism for OER. Reproduced with permission from ref 87. Copyright 2022 John Wiley and Sons. (b) Scaling relation between the binding energies of HOO* and HO* on various TMOs. (c) OER volcano plot for various TMOs against the oxygen binding strength ($\Delta G_{O^*}-\Delta G_{HO^*}$). Reproduced with permission from ref 88. Copyright 2021 Royal Society of Chemistry. (d) Schematic of LOM mechanism for OER. Reproduced with permission from ref 87. Copyright 2022 John Wiley and Sons. (e) Schematic of cation/anion redox chemistry guided by d−d Coulomb interaction (U) and charge transfer energy (Δ), which manifest conventional metal cation oxidation (left), oxygen anion oxidation (middle) and direct oxygen anion release (right) for OER, respectively. Δ is the energy difference between bonding (M−O) and antibonding (M−O)* bands, and U is the energy difference between UHB and LHB, respectively. The band position can be determined by the related band center based on projected density of state (PDOS) diagrams, which are typically obtained by DFT calculations. (f,g) Relationship between the OER mechanism (AEM or LOM) and electronic descriptors for Co-based oxide electrocatalysts. Reproduced with permission from ref 88. Copyright 2021 Royal Society of Chemistry.

https://doi.org/10.1021/acs.chemrev.3c00332
Chem. Rev. 2024, 124, 3694−3812

Figure 3a) and lattice oxygen-mediated mechanism (LOM, Figure 3d).[77,78]

For AEM in acidic electrolytes:

$$H_2O + * \rightarrow HO^* + H^+ + e^-$$

$$HO^* \rightarrow O^* + H^+ + e^-$$

$$2O^* \rightarrow 2 * + O_2$$

$$\text{or } O^* + H_2O \rightarrow HOO^* + H^+ + e^-$$

$$HOO^* \rightarrow * + O_2 + H^+ + e^-$$

For AEM in alkaline electrolytes:

$$OH^- + * \rightarrow HO^* + e^-$$

$$HO^* + OH^- \rightarrow O^* + H_2O + e^-$$

$$2O^* \rightarrow 2 * + O_2$$

$$\text{or } O^* + OH^- \rightarrow HOO^* + e^-$$

$$HOO^* + OH^- \rightarrow * + O_2 + H_2O + e^-$$

Although the oxygen formation steps are different which can be generated from either coupling of O* intermediates or decomposition of HOO* derived from the reaction of O* with H_2O (in acidic media) or OH^- (in alkaline media), these AEM pathways typically involve three adsorbed intermediates on the catalyst surface (HO*, O*, and HOO*), as shown in Figure 3a. It is worth noting that the thermodynamic barrier for direct binding of two O* to produce oxygen is usually higher than that of stepwise generation of oxygen by O*.[79] The high energy barrier typically necessitates large overpotentials, and the corresponding elementary step is often regarded as the RDS from the perspective of kinetics. Bockris demonstrated that the observed Tafel slope in electrochemical measurements is determined by the RDS within five OER paths.[80] Therefore, the Tafel slope can be served as a key indicator for determining the RDS in OER process and elucidating the underlying mechanism.[81−84]

Apart from the above-mentioned microkinetic analysis, DFT calculations have been developed to study the OER mechanisms. Rossmeisl and coworkers conducted a theoretical description of the OER mechanism over (110) surfaces of rutile-type metal oxides based on DFT, and the following four electron−proton coupled pathways were employed as a model for OER.[85]

$$2H_2O + * \rightarrow H_2O + HO^* + H^+ + e^-$$

$$\Delta G_1 = \Delta G_{HO^*} - \Delta G_{H_2O} - eU + k_B T \ln[H^+]$$

$$H_2O + HO^* \rightarrow H_2O + O^* + H^+ + e^-$$

$$\Delta G_2 = \Delta G_{O^*} - \Delta G_{HO^*} - eU + k_B T \ln[H^+]$$

$$H_2O + O^* \rightarrow HOO^* + H^+ + e^-$$

$$\Delta G_3 = \Delta G_{HOO^*} - \Delta G_{O^*} - eU + k_B T \ln[H^+]$$

$$HOO^* \rightarrow * + O_2 + H^+ + e^-$$

$$\Delta G_4 = \Delta G_{O_2} - \Delta G_{HOO^*} - eU + k_B T \ln[H^+]$$

where ΔG_i (i = 1, 2, 3, 4) is the Gibbs free energy change of the corresponding elementary step, U is the electrode potential relative to the standard hydrogen electrode (SHE), and k_B is the Boltzmann constant. The step with the largest value among all ΔG_i was defined as the potential-determining step for OER (ΔG_{OER}). The relationship between ΔG_{OER} and the theoretical overpotential (η_{OER}) under standard conditions at U = 0 V vs SHE was given as

$$\eta = \max[\Delta G_1^0, \Delta G_2^0, \Delta G_3^0, \Delta G_4^0]/e - E^0$$

It is expected that the ideal value of ΔG_{OER} for each step is 1.23 eV, equivalent to the overpotential of zero (η_{OER} = 0).[82] In other words, the ideal OER electrocatalyst should have the same adsorption energies for all four elementary steps (1.23 eV at equilibrium conditions), while real electrocatalysts cannot fulfill this requirement and the scaling relations exist, which means that one ΔG changes, the others do too. An example is the linear relationship between the binding energies of HO* and HOO* on the surface of various oxides (e.g., rutile, perovskite, and others) with a constant difference of approximately 3.2 eV, as depicted in Figure 3b.[86] Considering the two-electron transfer between HO* and HOO* which indicates an ideal ΔG of 2.46 eV (2 × 1.23 eV), the minimum overpotential for OER can be calculated to be 0.37 V [(3.2−2.46) eV/2e]. Additionally, this scaling relation allows us to simplify DFT calculations, such that one parameter, the difference between ΔG_{O^*} and ΔG_{HO^*} can be employed as a universal descriptor to predict the OER activities of various electrocatalysts, and thus, a volcano plot regarding η_{OER} as a function of $\Delta G_{O^*} - \Delta G_{HO^*}$ can be constructed (Figure 3c), which provides valuable insights into the OER mechanism and facilitates the screening of OER electrocatalysts. Collectively, the ΔG_{OER} analysis based on DFT calculations can afford thermodynamic information on OER, complementary to the Tafel slope investigation that provides kinetic information.

Despite significant achievements guided by the AEM, several dilemmas still exist. For example, a plurality of reported OER electrocatalysts exhibit much lower onset potential than the AEM-predicted minimum (0.37 V).[88−90] Moreover, several experimental studies have revealed the dynamic surface reconstruction instead of a static platform for some OER electrocatalysts under high applied potentials. Alternatively, the LOM with lattice oxygen participated redox chemistry has been proposed to disentangle these mysteries.[88−90] As depicted in Figure 3d, three possible LOM pathways have been reported for acidic OER, differing mainly in the binding between the lattice oxygen and the intermediate species. Pathway 1 involves a direct combination of O* bound to the metal site with lattice oxygen to release O_2, leaving an oxygen vacancy on the electrocatalyst's surface. In Pathway 2, HO* binds to the lattice oxygen site rather than the metal site (M), generating HOO* which subsequently dissociates to produce O_2 as well as H^+. Pathway 3 includes the combination of two lattice oxygen atoms from Pathway 1 and Pathway 2 to generate O_2, resulting in the creation of two oxygen vacancies on the electrocatalyst's surface. All three LOM mechanisms for acidic OER include lattice oxygen participation via the nonelectrochemical route, and it is expected that activation of lattice oxygen would play a dominant role in the OER activity of underlying electrocatalysts following LOM pathway. Typically, for a transition metal (oxy)(hydr)oxide electrocatalyst, the metal nd orbital hybridizes with oxygen 2p to form bonding (M−O) and antibonding (M−O)* bands, along with energy level splitting.

https://doi.org/10.1021/acs.chemrev.3c00332
Chem. Rev. 2024, 124, 3694−3812

Their energy difference represents the charge transfer energy (Δ), which is determined by the electronegativity discrepancy ($\Delta\chi$) between metal and oxygen, and reflects the degree of hybridization.[88] The decreased value implies promoted hybridization with enhanced M−O covalency and vice versa. Moreover, the electrons localized in (M−O)* due to strong d−d Coulomb interaction can repel with each other, and further split (M−O)* to the empty upper Hubbard band (UHB) and the electron-filled lower Hubbard band (LHB). The energy difference between UHB and LHB is represented by a letter of *U*. These physical parameters determine the electronic structures of electrocatalysts and thus OER mechanisms. For example, typical transition metal (oxy)-(hydr)oxides exhibit large charge transfer energy and strong ionic properties of the M−O bond due to the large electronegativity of oxygen, wherein the M *n*d band locates above the O 2p with positive energy difference ($\varepsilon_{\text{M-3d}}-\varepsilon_{\text{O-2p}} > 0$, left of Figure 3e). Cationic redox is now thermodynamically more favorable and the metal site serves as an active center, allowing water oxidation to follow the AEM mechanism. When decreasing $\Delta\chi$ and enlarging *U*, the LHB can penetrate the O 2p band with negative energy difference ($\varepsilon_{\text{M-3d}}-\varepsilon_{\text{O-2p}} < 0$, middle of Figure 3e), making intramolecular electron transfer from oxygen ligand to metal cation feasible. Thus, the introduced ligand holes can be yielded for lattice oxygen activation. In this scenario, the M−O covalency and orbital hybridization are enhanced, which facilitate the sorption of OER-related species to decrease energy barrier and thus improve the OER activity, even the lattice oxygen cannot be directly released to form O_2. Further modulating the O 2p absolute energy level ($\varepsilon_{\text{O-2p}}$) above Fermi level ($E_F$) ensures the release of O_2 from the lattice matrix (Figure 3e, right). Collectively, it can be concluded that both the energy difference between M *n*d and O 2p orbitals ($\varepsilon_{\text{M-3d}}-\varepsilon_{\text{O-2p}}$) and the absolute energy level of $\varepsilon_{\text{O-2p}}$ significantly influence the OER mechanism.[88] As illustrated in Figure 3f and g, the computational results demonstrate that the perovskite and spinel electrocatalysts following the LOM mechanism generally exhibit relatively negative $\varepsilon_{\text{M-3d}}-\varepsilon_{\text{O-2p}}$ values and high $\varepsilon_{\text{O-2p}}$ values.

2.3. Overall Water Splitting

As previously discussed, overall water splitting (OWS) involves two half-reactions: the cathodic HER and the anodic OER. Irrespective of the specific pathways involved in both half-reactions, the thermodynamic voltage for the overall process is 1.23 V at standard conditions.[91]

$$\text{Overall reaction: } H_2O \rightarrow H_2 + \frac{1}{2}O_2 \ (E^0 = 1.23\ \text{V})$$

In acidic electrolytes:

$$\text{HER: } 2H^+ + 2e^- \rightarrow H_2$$

$$\text{OER: } H_2O \rightarrow 2H^+ + \frac{1}{2}O_2 + 2e^-$$

In neutral and alkaline electrolytes:

$$\text{HER: } 2H_2O + 2e^- \rightarrow H_2 + 2OH^-$$

$$\text{OER: } 2OH^- \rightarrow H_2O + \frac{1}{2}O_2 + 2e^-$$

However, driving the practical OWS always requires a voltage higher than the thermodynamic value. This additional voltage, known as the overpotential (η), is necessary to overcome inherent energy barriers at both the cathode (η_{HER}) and the anode (η_{OER}), as well as other resistances (η_{other}) such as solution and contact resistances. Consequently, the actual voltage required for OWS is given by[92]

$$E = 1.23\ \text{V} + \eta_{\text{HER}} + \eta_{\text{OER}} + \eta_{\text{other}}$$

Clearly, minimizing the applied voltage for OWS is crucial for efficient hydrogen generation. In addition to optimizing the cell configuration to reduce η_{other}, the use of efficient electrocatalysts for HER and OER is essential in reducing η_{HER} and η_{OER}, respectively. Therefore, the development of highly active and cost-effective electrocatalysts is highly desirable to make water splitting economically viable. Currently, Pt-based materials are widely used for HER, while Ru/Ir-based oxides are commonly employed for OER. However, it is important to note that these benchmark electrocatalysts typically exhibit high activity in either HER or OER, but not both simultaneously. Therefore, there is a need to develop efficient bifunctional electrocatalysts that offer high activity in both reactions while maintaining affordability. This approach would simplify the system and contribute to overall cost reduction.[92−96]

2.4. Hybrid Water Splitting

To address the challenges associated with OER in traditional water electrolysis, a new approach called hybrid water splitting (HWS) has emerged, which replaces OER with thermodynamically favorable oxidation reactions. HWS offers significant advantages over traditional water electrolysis. First, by replacing OER with these alternative oxidation reactions, the energy input is reduced. Second, the safety issues regarding H_2/O_2 mixing and reactive oxygen species (ROS) formation can be eliminated. Finally, by selecting suitable raw materials, it is possible to obtain value-added oxidative chemicals, maximizing the return on energy investment. Various alternative substrates have been explored in the context of hybrid water splitting, including alcohols,[97,98] aldehydes,[51,99] ammonia,[100,101] urea,[102,103] hydrazine,[104,105] sulfur compounds, organic dyes, biomass,[99] plastic wastes, and so on. These substrates can be classified into different types based on their functionalities in HWS, including sacrificing agents (Figure 1c), environmental pollutants (Figure 1d), and organics that can yield value-add oxidative products (Figure 1e), and the corresponding oxidation reactions are denoted as sacrificing agents oxidation, pollutants oxidative degradation, and organics oxidative upgrading.

The sacrificing reagents oxidation involves the oxidation of a valuable substrate to a less valuable product at the anode. In this case, the anode substrate is considered a sacrificing agent. Examples of such reactions include hydrazine oxidation[104,105] and ammonia oxidation,[100,101] where hydrazine and ammonia serve as hydrogen carriers in hydrogen storage systems and their oxidations produce low-value nitrogen (e.g., N_2). Although this type includes substrate downgrading which increases overall costs, the energy consumption for HWS toward H_2 can be significantly reduced due to the ultralow thermodynamically potentials relative to that of OER. In addition, the safety issues can be partly alleviated:

$$\text{hydrazine oxidation: } N_2H_4 + 4OH^- = N_2 + 4H_2O + 4e^- \ (E^0 = -0.33\ \text{V})$$

https://doi.org/10.1021/acs.chemrev.3c00332
Chem. Rev. 2024, 124, 3694−3812

Table 2. Examples of Reconstructed Electrocatalysts and the Newly Formed Active Species as Well as Associated Characterization Techniques

Electrocatalysts	Electrolytes	Active species	Characterization techniques	Ref
NiFe LDH	1.0 M KOH + 0.5 M NaCl	NiFe (oxy)hydroxide (OER) Ni_3Fe alloy (HER)	ex situ TEM/XAS	139
NiMoOS	1.0 M KOH	NiOOH (OER) Ni (HER)	ex situ TEM/XPS, in situ Raman	142
pyrite-type NiS_2	1.0 M KOH	Ni_3S_2 (HER)	ex situ TEM/XRD, in situ Raman, operando XAS	143
Cu-FeOOH/Fe_3O_4	1.0 M KOH	defective FeOOH (HER)	ex situ XRD/Raman/TEM/XPS/XAS	145
Co@CoFe-P	1.0 M KOH	P−Co−O−Co/Fe−P (HER) Co^{IV}−O−Fe^{IV} (OER)	operando XAS/Raman	147
CoF_2	1.0 M KOH	defective β-$Co(OH)_2$ (HER)	ex situ XRD/XPS, in situ Raman,	148
V_O-Co_3O_4	1.0 M NaOH	$(Co(II)O_x(OH)_y)$ (OER)	ex situ XPS, in situ XRD, operando Raman/TEM	150
$(NiCo)S_{1.33}$	1.0 M KOH	NiCo-O/OH (OER)	in situ TEM/EELS/FT-IR/DEMS	151
NiS_x/β-$Ni(OH)_2$	1.0 M KOH + 50 mM HMF	$Ni^{2+\delta}$ (HMFOR)	in situ Raman	152
$LaNiO_3$	1.0 M KOH	NiOOH (OER)	ex situ XPS, in situ Raman	153
$LiFe_{1-x}Co_x(H_2O)_2[BP_2O_2]\cdot H_2O$	1.0 M KOH	$Fe^{(4+)+}$ (OER)	ex situ TEM/XPS, Quasi-in situ XAS	154
CrMnFeCoNiZrNbMo HEAs	0.5 M H_2SO_4	Mn, Fe (HER) oxidized Fe/Co/Ni (OER)	quasi-in situ XPS	155
Cu_2S/CoFeCuOOH	1.0 M KOH	CoFeCuOOH (OER)	in situ Raman, operando UV−vis	156
$CoFe_2S_4$	1.0 M KOH	$Co(Fe)O_xH_y$ (OER)	ex situ TEM/EELS/XRD/XAS	157
V_{Co}-Co_3O_4	1.0 M KOH	bridge Co sites (OER)	ex situ TEM/XRD/SEM/XAS, in situ Raman	158
Ni_3S_2	0.1 M KOH	$Ni(O)_xS_y$ (OER)	ex situ TEM/SEM/TOF-SIMS/AES/XAS/XPS	159
NiOOH	1.0 M KOH + 10 μM Fe^{3+}	Fe-NiOOH (OER)	ex situ XFM/XAS	160
MnO_x	0.1 M borate buffer	birnessite (OER)	in situ RIXS/soft XAS	161
$CaMnO_3$	0.1 M PBS	Mn^V species (OER)	SI-SECM	162
β-$Co(OH)_2$	0.1 M KOH	Co^{3+} (β-CoOOH) (OER)	SECCM, EC-AFM, operando STXM-XAS/UV−vis	163

ammonia oxidation: $2NH_3 + 6OH^- = N_2 + 6H_2O + 6e^-$ ($E^0 = -0.77$ V)

By comparison, the pollutants oxidative degradation is more economical and environmentally friendly. The substrates at the anode for HWS are environmental pollutants and their electrochemical oxidation means oxidative degradation toward harmless products, like the waste treatment process. Typical reactions within this category include the oxidative degradation of organic dyes (e.g., methylene blue) in wastewater,[106] exhaust gas (e.g., H_2S) treatment,[107−109] and so on. These reactions are closely linked to our daily lives and industrial production so that coupling them with HER for hydrogen generation would gain both economic and ecological benefits:

hydrogen sulfide oxidation: $S^{2-} = S + 2e^-$ ($E^0 = -0.48$ V)

To maximize the return on energy investment in HWS, it is desirable to produce value-added products at the anode with applied potentials lower than that for OER. Therefore, organics oxidative upgrading has been proposed.[51,53,99,110] HWS based on this type involves the oxidation of a substrate at the anode to generate value-added products while generating hydrogen in an energy-saving manner. Typical reactions within this category include the upgrading of biomass derivatives like 5-hydroxymethyl furfural (HMF),[99,111] dehydrogenation of organics,[112,113] valorization of bio/plastics-waste, etc. We note that electrooxidation can be performed at ambient conditions (e.g., room temperature and atmospheric pressure) without additional chemical oxidant, offering several advantages over conventional industrial methods for oxidation upgrading. From an economic standpoint, the organics oxidative upgrading yields value-added products while requiring less energy input, making it highly promising among the three classes of alternative oxidation reactions:

$HMF + 6OH^- = FDCA + 4H_2O + 6e^-$ ($E^0 = -0.53$ V)

$CH_3OH + 5OH^- = HCOO^- + 4H_2O + 4e^-$ ($E^0 = 0.103$ V)

Benefiting from the advantages mentioned above, hybrid water splitting is currently garnering significant attention, and a wide range of bifunctional electrocatalysts have been employed to drive both HER and anodic alternative oxidation reactions as well.[51,53,99,114,115]

3. ELECTROCHEMICAL RECONSTRUCTION AND CHARACTERIZATIONS

The electrochemical reconstruction refers to changes of physicochemical properties (e.g., structure, composition, crystalline phase, interface, valence, etc.) of the electrocatalysts during electrocatalytic processes, which strongly correlate to their activity and stability, providing a new tool to design novel and high-performance electrocatalysts.[116−122] Thanks to the rapid development of various physiochemical characterization techniques, the electrochemical reconstruction process has been observed in many electrocatalysts during water splitting and alternative oxidations (Table 2),[123−125] which results in dramatically changed surface/interface properties and thus electrocatalytic performance.[126−132] Researchers have found that both HER and OER electrocatalysts undergo partial self-reduction/oxidation, components leaching/readsorption, ions doping, phase separation/transition, or even structure collapse under operating conditions.[133−135] The reconstruction rate and degree depend on both the intrinsic properties of pristine electrocatalysts (e.g., compositions, microstructures, valence

https://doi.org/10.1021/acs.chemrev.3c00332
Chem. Rev. 2024, 124, 3694−3812

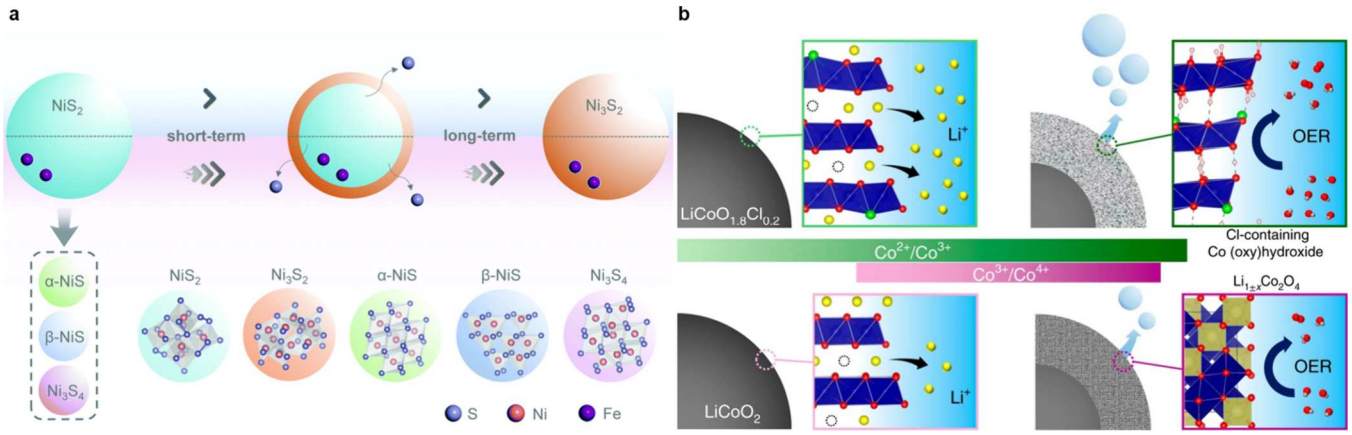

Figure 4. Schematic of the in situ electrochemical reconstruction of (a) multivalent nickel sulfide during HER and (b) $LiCoO_{2-x}Cl_x$ during OER. (a) Reproduced with permission from ref 143. Copyright 2022 Royal Society of Chemistry. (b) Reproduced from ref 184. Copyright 2021 Springer Nature.

states, defects level, etc.) and the actual reaction environments like applied potentials, pH, electrolytes, in situ-formed species, and so on.[133] Generally, appropriate reconstruction generates amorphous/low-crystalline, defects-rich active species and thus benefits to improved electrocatalytic activity.[133−135] Meanwhile, electrochemical reconstruction may bring some adverse effects. For example, low-crystallinity means relatively mediocre conductivity and abundant defects signify poor structural stability, which even lead to structure collapse.[136,137] In addition, the detached species during reconstruction may block the diaphragm and thus increase the internal resistance of the electrolyzer. It is therefore critical to monitor the electrochemical reconstruction process to unravel the activity origin and enrich the toolbox for electrocatalysts design toward efficient overall and hybrid water splitting.[133−163]

3.1. Reconstruction Phenomenon

As stated above, the electrochemical reconstruction of electrocatalysts usually occurs during electrocatalytic processes including both reduction (e.g., HER) and oxidation (e.g., OER), accompanied by their dynamic changes of structure, composition, crystalline phase, interface, valence, and so on.[138−149] For instance, Zhang's group discovered that the Mo in Ni_4Mo electrocatalysts can be oxidized to soluble MoO_4^{2-} and then readsorbed on Ni_4Mo surface during HER in 1.0 M KOH, beneficial for improved activity and durability.[138] Xie and colleagues reported that phosphorus (P) doping can trigger the structural transition of cubic $CoSe_2$ to the corresponding orthorhombic phase with poor stability for alkaline HER.[164] More recently, Zhang and coworkers observed phase and valence state evolution of pyrite-type NiS_2 for HER in 1.0 M KOH, assisted by multiple ex situ/operando characterization techniques (Figure 4a).[143] The dynamic reconstruction of NiS_2 was triggered by surface sulfur vacancy and propagated from surface to bulk with terminated Ni_3S_2 during long-term HER service. Apart from NiS_2, such a reduction (HER) reconstruction can be extendable to α-NiS, β-NiS, and Ni_3S_4, and can be accelerated by appropriate Fe doping. With the help of DFT calculations, the authors found that Fe substitution in NiS_2 raises S 3p band to Fermi level (E_F) for favorable formation of sulfur vacancies, and simultaneously expands the Ni 3d band to increase its overlap with S 3p band for facilitated sulfur release, collectively accountable for the reconstruction to Ni_3S_2.

In contrast, electrochemical oxidative (e.g., OER) reconstruction is even more common due to the harsh positive potentials and has received much more attention. In general, anodic polarization drives initial surface reconstruction of OER electrocatalysts (e.g., oxidation, phase/valence state transition, defect/vacancy level etc.), and local environments (e.g., pH, electrolyte, and temperature) can tune the reconstruction behavior as well.[154,165−175] Depending on these external factors, electrochemical oxidative reconstruction of an OER electrocatalyst can propagate to bulk from surface, especially under higher oxidative potential and harsher surroundings. The intrinsic properties of the electrocatalysts, of course, affect the reconstruction rate and degree as well.[150,176−183] For example, Lim and coworkers have achieved in situ reconstruction of layered $LiCoO_{2-x}Cl_x$ (x = 0, 0.1, and 0.2) by leaching of lithium ions, and they found that chlorine (Cl) doping lowers the triggered potential of cobalt oxidation and lithium leaching to facilitate the surface reconstruction to a self-terminated amorphous (oxy)hydroxide phase during OER (Figure 4b), in sharp contrast to the chlorine-free $LiCoO_2$ counterpart with higher triggered potential and reconstruction phase of spinel-type $Li_{1\pm x}Co_2O_4$.[184] Diverse physiochemical characterizations together with DFT calculations unveiled that introducing chlorine into $LiCoO_2$ makes the delithiation process from energetically unfavorable to favorable and thus prefers the formation of thermodynamically stable (oxy)hydroxide structure. Similarly, under OER oxidation potential, perovskites and spinel structures also undergo metal ion dissolution and lattice oxygen oxidation, restructuring to new phases.[133,185−194] Recently, Xu and coworkers observed that biased metal−oxygen covalency between MO_4 (tetrahedral units, M_T−O) and MO_6 (octahedral units, M_O−O) controls the reconstruction direction and degree of spinel $Li_xCo_{1-x}Co_2O_4$. Specifically, a stronger M_O−O covalency relative to M_T−O covalency benefits a more thorough reconstruction toward oxyhydroxides.[135]

Compared to transition metal oxides, metal nonoxides (e.g., chalcogenides, pnictides, carbides, etc.) possess more positive enthalpy values.[175,195] Therefore, their surface reconstruction toward (oxy)(hydr)oxide during electrocatalytic OER or alternative oxidation is more thermodynamically favorable.[196−203] Our group previously uncovered that both Ni_2P and Ni_3S_2 experience surface oxidative reconstruction to oxidized Ni species during OER and biomass oxidation.[51,99]

https://doi.org/10.1021/acs.chemrev.3c00332
Chem. Rev. 2024, 124, 3694−3812

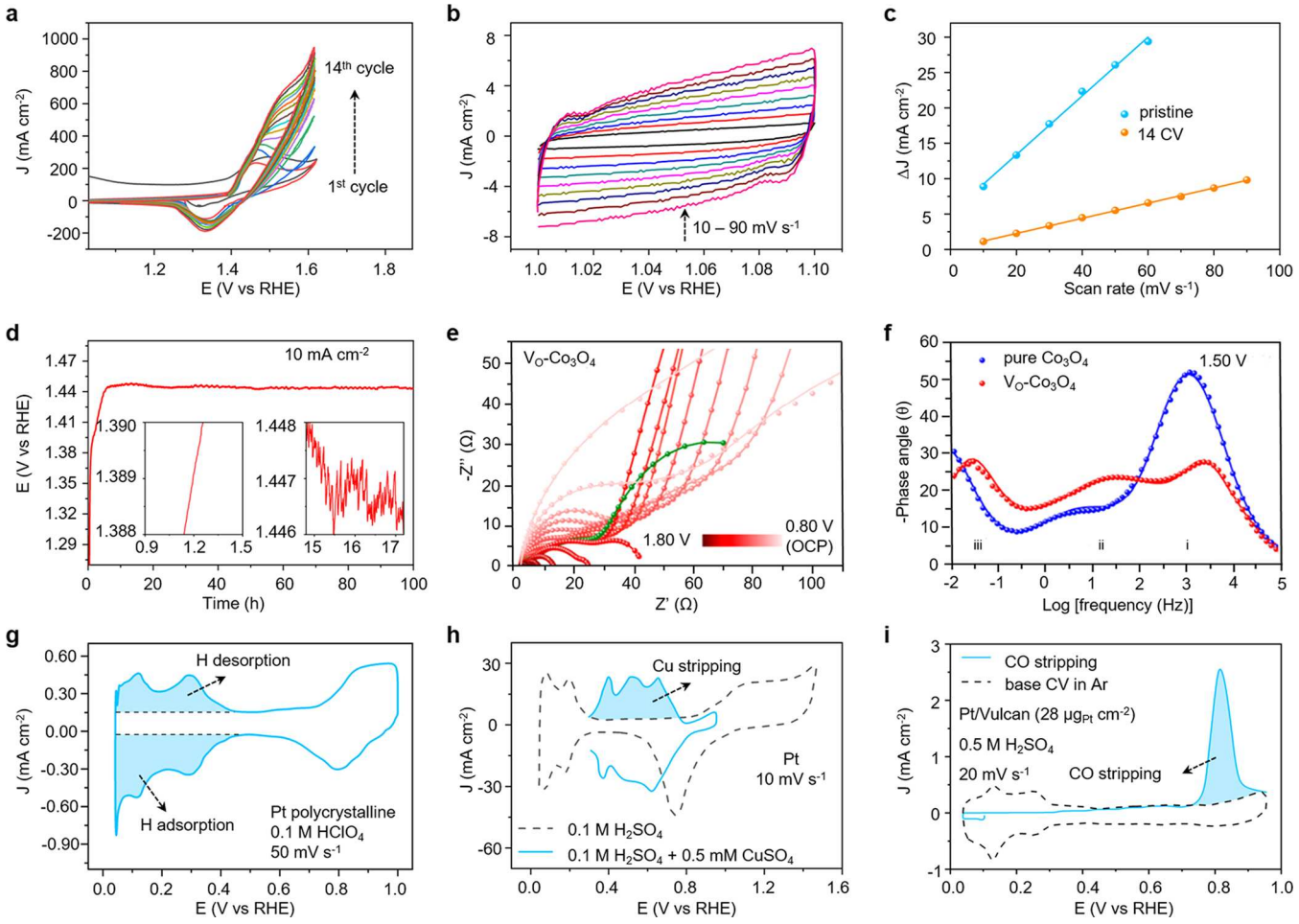

Figure 5. (a) CV curves of fresh h-NiS_x in 1.0 M KOH with cyclic potential scanning. (b) CV curves of h-NiS_x at different scan rates under non-Faradaic potential regions. (c) Scan rates dependence of current densities for h-NiS_x at 1.05 V vs RHE before and after 14 CV cycles. Reproduced with permission from ref 223. Copyright 2016 John Wiley and Sons. (d) CP curves of Ni_2P/Ni/NF at a current density of 10 mA cm^{-2} in 1.0 M KOH. Reproduced with permission from ref 227. Copyright 2016 American Chemical Society. (e) Operando EIS spectra for V_O-Co_3O_4 at potentials from OCP to 1.80 V vs RHE and (f) Bode phase plots of pure Co_3O_4 and V_O-Co_3O_4 at 1.50 V vs RHE in 1.0 M KOH. Reproduced with permission from ref 228. Copyright 2020 American Chemical Society. (g) CV curve of Pt at 50 mV s^{-1} in N_2-saturated 0.1 M $HClO_4$. Reproduced with permission from ref 229. Copyright 2012 American Chemical Society. (h) Cu UPD in 0.1 M H_2SO_4 with and without 0.5 mM $CuSO_4$ on Pt. Reproduced with permission from ref 230. Copyright 2002 American Chemical Society. (i) CO stripping of Pt/Vulcan at 20 mV s^{-1} in Ar-saturated 0.5 M H_2SO_4. Reproduced with permission from ref 231. Copyright 1998 IOP Publishing.

Interestingly, the electrochemical reconstruction is sometimes reversible. For example, Strasser and coworkers reported that the near-surface crystalline Co_3O_4 could be transformed into amorphous $CoO_x(OH)_y$ during OER process and the reconstructed components can be recrystallized back to stable crystalline state under rest conditions with applied potentials at non-OER region.[204] Lately, Wei and colleagues discovered potential-driven dynamic-coupling of oxygen on atomically dispersed heteronitrogen-configured Ir sites (AD-HN-Ir) during OER, wherein one oxygen atom can adsorb on Ir site to form a stable and highly active O-hetero-Ir-N_4 structure for OER, and this dynamically coupled oxygen would disappear after OER.[205]

In a word, electrochemical reconstruction is ubiquitous under either reduction (e.g., HER) or oxidation (e.g., OER and alternative oxidations) conditions, which would significantly modulate the electrocatalytic activity and stability of the underlying electrocatalysts toward overall and hybrid water splitting.[133,143,206−220] Consequently, exploring effective characterization techniques to monitor the dynamic reconstruction is of importance for understanding the structure−activity correlations and developing advanced electrocatalysts toward energy-efficient hydrogen generation from water.

3.2. Electrochemical Characterizations

3.2.1. Cyclic Voltammetry. The electrochemical reconstruction could tune local electronic structure of active centers, such as valence states, coordination environments, intermediates adsorption, and thus electrocatalytic activity, which can be reflected by electrochemical characterizations. Cyclic voltammetry (CV) is conducted by linear and cyclic scanning of potentials with a certain range, and the change caused by reconstruction could be signified by the recorded current responses or the shape of CV curves.[153,221,222] Zhang and coworkers revealed the atomic-scale evolution of NiS_2, α-NiS, β-NiS, and Ni_3S_4 during HER in 1.0 M KOH via CV and other operando characterization techniques.[143] Along with cyclic potential scanning, the reduction peaks for the three nickel sulfides gradually disappeared, indicative of their reduction reconstruction. Further, the more positive reduction potential of β-NiS relative to α-NiS and Ni_3S_4 implied the lower energy

https://doi.org/10.1021/acs.chemrev.3c00332
Chem. Rev. 2024, 124, 3694−3812

barrier to trigger this reconstruction. Besides, electrochemical oxidation (e.g., OER) reconstruction has also been reported via CV characterizations. As shown in Figure 5a, our group used CV tests to monitor the surface reconstruction of 3D hierarchically porous nickel sulfide superstructures (h-NiS_x) during OER.[223] The gradual increase of current density and dynamic redox peaks with ongoing 14 cycles of CV tests implied oxidative transformation of Ni species from low to high valence state in h-NiS_x. Additional characterization confirmed that the reconstructed h-NiS_x feature conductive NiS_x in inner layer and high-valence nickel species in outer layer. The same phenomenon was also observed by others, and the accompanied variation of electrocatalytic activity can be directly signified by linear sweep voltammetry (LSV) curves.[224,225] For instance, Xia and coworkers reported a homogeneous multimetal-site oxyhydroxide electrocatalyst derived from in situ electrochemically oxidative dealloying of a multimetal-site alloy ($FeNi_3$ and NiCu alloys). The anodic polarization curves showed gradually increased current density with increasing CV scans until to 3000 cycles, implying the reconstruction formation of M−OOH structure.[226]

Moreover, CV conducted at various scan rates under non-Faradaic potential regions can be used to obtain the electrochemical double layer capacitance (C_{dl}) of the underlying electrocatalyst, which reflects its active surface area and thus surface reconstruction. Our group measured the C_{dl} of h-NiS_x before and after 14 CV cycles by collecting CV curves in the non-Faradaic potential regions (Figure 5b). Linear fitting the scan rate dependence of the current density difference at middle potential resulted in the C_{dl} (Figure 5c).[223] The changed C_{dl} of h-NiS_x after CV cycling suggested the surface reconstruction.

3.2.2. Chronopotentiometry. In addition, chronopotentiometry (CP) could also be used to probe the electrochemical reconstruction, in which the current of the electrocatalyst-loaded working electrode is fixed and the recorded response is time-dependent potential curve. Electrochemical reconstruction and activation of 3D hierarchically porous urchin-like Ni_2P microsphere superstructures on nickel foam (Ni_2P/Ni/NF) were observed by us via CP measurement at 10 mA cm^{-2} for 100 h (Figure 5d).[227] During the initial 6 h, the gradual increase of potential and smooth CP curve suggested that no O_2 bubbles evolve, and thus, the passed charges account for the oxidation reconstruction of Ni_2P/Ni/NF. Further prolonging electrolysis time, the recorded potential remained relatively stable and the squiggles of the enlarged CP curve implied drastic formation and evolution of O_2 bubbles. Similarly, Subramanian and collaborators prepared a biphasic (spinel Co_3O_4 and CoO) thin film on FTO surface (Co_xO_y/FTO) through pulsed laser deposition.[232] The decreasing overpotential at a current density of 10 mA cm^{-2} over 16 h suggested the presence of reconstruction and activation during OER.

3.2.3. Electrochemical Impedance Spectroscopy. The variation of crystalline phase and electronic structure of underlying electrocatalysts during reconstruction would lead to changed electron transfer, which can be characterized by electrochemical impedance spectroscopy (EIS).[228,233] For instance, Wang and coworkers traced the evolution of oxygenated intermediates around Co sites in oxygen vacancy-rich Co_3O_4 (V_O-Co_3O_4) during OER by operando EIS.[228] Figure 5e showed the Nyquist plots of V_O-Co_3O_4 at different potentials from open circuit potential (OCP) to 1.80 V vs RHE in 1.0 M KOH, and the fitted equivalent circuit suggested the presence of charge transfer resistance (R_{CT}) and constant phase element (CPE_{CT}), representative of OH^- adsorption resistance and pseudocapacitance, respectively. The smaller R_{CT} and larger CPE_{CT} for V_O-Co_3O_4 relative to pure Co_3O_4 indicated the faster OH^- adsorption kinetics and accumulation, respectively. Both benefited surface reconstruction, as verified by the Bode phase plots at 1.50 V vs RHE (Figure 5f). As depicted Figure 5f, the phase peaks of i and ii in the corresponding high- and middle-frequency regions indicated the presence of surface oxidized species with the octahedral Co−O_6 and tetrahedral Co−O_4 sites. Moreover, the phase peak in low-frequency region (iii) suggested the faster deprotonation of Co−OOH intermediates. Zhao and collaborators employed operando EIS to study the surface reconstruction of V-doped Ni_2P for OER under different potentials. As expected, increasing applied potentials from 1.367 to 1.617 V vs RHE resulted in decreased charge transfer resistance due to faster OER kinetics, while the contact resistance of V-doped Ni_2P gradually increased along with positive scanning of potential, indicating the formation of metal oxyhydroxide with poor conductivity relative to metal phosphide due to self-oxidation reconstruction during OER.[233]

3.2.4. Underpotential Deposition. The reconstruction of an electrocatalyst would result in variations in electrochemically active surface area (ECSA); thus, the electrochemical reconstruction could be indirectly reflected by the evolution of ECSA.[234] Both hydrogen or metal underpotential deposition (UPD) are well-developed to measure the ECSA of metal-based materials. The hydrogen underpotential deposition (H UPD) relies on adsorption and desorption of H atom at a metal surface. As shown in Figure 5g, employing Pt polycrystalline as an example, the shaded regions between 0.05 and 0.4 V (vs RHE) represented the formation and desorption of H monolayer at Pt surface during potential scanning. Dividing the calculated average charges under shaded regions by a specific charge value for the formation of monolayer H atoms onto clean polycrystalline Pt (210 μC cm_{Pt}^{-2}) yielded the ECSA of the underlying Pt catalyst.[229] Similar to the H UPD, metal ions can be used as the probe of UPD as well. During the metal-based UPD process, the electrodeposition potential for the first monolayer is more positive than that for subsequent layers due to the more favorable interaction between depositing metal and substrate than that between themselves.[235] Using the UPD process of Cu ions (Cu UPD) on Pt as an example, Pt was first covered with a monolayer of Cu by electrodepositing at a specific potential for a required time in a mixed solution of H_2SO_4 and $CuSO_4$. After that, the anodic scan was performed starting from the deposition potential to the region where the deposited Cu can be thoroughly stripped off. Next, the baseline was collected by conducting similar CV scanning in H_2SO_4 solution without Cu ions. The charges of Cu stripping calculated in the shaded regions divided by the specific charge (420 μC cm_{Cu}^{-2}) gave the ECSA of Pt (Figure 5h).[230] Both the Cu UPD and the H UPD have been widely used to obtain the ECSAs of Pt-group metal-based materials.[236−238] However, the surface of metal compounds like oxides possess limited capability to specifically adsorb H or Cu species, and their ECSA measurements based on traditional UPD are difficult. Therefore, some special UPD methods have been developed. For example, Robinson's group reported a two-step route to

https://doi.org/10.1021/acs.chemrev.3c00332
Chem. Rev. 2024, 124, 3694−3812

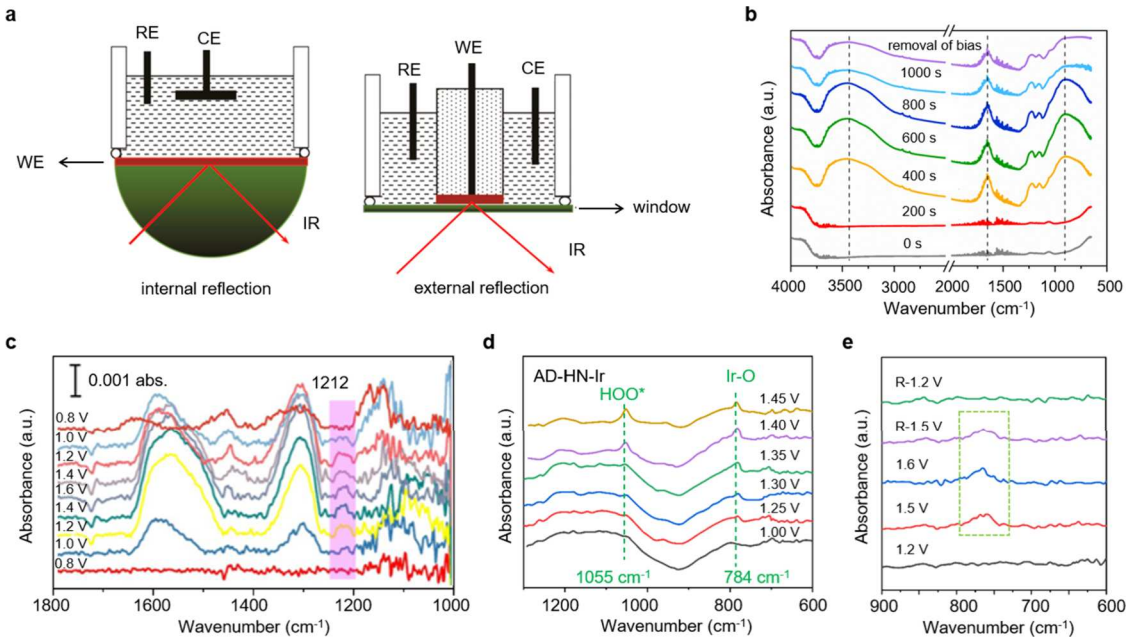

Figure 6. (a) Schematic of the in situ electrochemical ATR-FTIR setup. Reproduced with permission from ref 244. Copyright 2016, Elsevier. (b) In situ ATR-FTIR spectra of CoS_x at 1 mA in 1.0 M KOH for OER. Reproduced with permission from ref 245. Copyright 2019 American Chemical Society. (c) In situ ATR-FTIR spectra of Ru_1-Pt_3Cu recorded during the multipotential steps. Reproduced from ref 246. Copyright 2019 Springer Nature. (d) In situ SR-FTIR measurements under various potentials for AD-HN-Ir electrocatalyst during the acidic OER. Reproduced from ref 205 under the terms of the CC-BY 4.0 license. Copyright 2021 The Authors, published by Springer Nature. (e) Operando SR-FTIR spectroscopy measurements for Ru−N−C during the acidic OER. Reproduced from ref 247 under the terms of the CC-BY 4.0 license. Copyright 2019 The Authors, published by Springer Nature.

measure the ECSA of Co_3O_4 on the basis of sequential Ag electrodeposition and Pb UPD.[239]

3.2.5. CO Stripping. In analogy to UPD employing hydrogen or metal ions as the probe, the CO stripping utilizes CO as the probe molecule to quantify the ECSA by calculating the required charge to strip one monolayer CO from metal surface.[240−242] As shown in Figure 5i, the adsorption of CO monolayer was realized by immersing the Pt/Vulcan electrode into CO-saturated electrolyte with an applied potential of 0.1 V vs RHE for 3 min. Then Ar gas was purged into the electrolyte to remove the dissolved CO. Subsequently, the anodic scan was performed to strip the CO adsorbed on the surface of the Pt. After deducting the background obtained by similar CV scanning in Ar-saturated solution, the area for CO stripping can be integrated and then converted to ECSA of the underlying Pt by dividing a specific charge value of 420 μC cm_{Pt}^{-2}.[231,243] Similar with H UPD and metal-based UPD, CO stripping is generally applied for Pt-group metal-based catalysts which possess characteristic CO stripping peaks.

3.3. Optical Characterizations

Although the electrochemical characterizations can evidence the occurrence of electrochemical reconstruction, they usually provide ex situ and few information. The electrochemical reconstruction of electrocatalysts generally results in the formation of new chemical bonds, which can be detected by in situ/operando optical characterization techniques such as infrared spectroscopy, Raman spectroscopy, ultraviolet−visible spectroscopy (UV−vis), etc.

3.3.1. Infrared Spectroscopy. Fourier-transform infrared spectroscopy (FTIR) provides the energy level transition information on vibration/rotation of molecules or chemical bonds under infrared irradiation.[244] If the newly formed species during the reconstruction process are IR-active, the overall dynamic process under electrocatalytic conditions can be real-time monitored by the in situ/operando electrochemical FTIR techniques with internal or external reflection configuration (Figure 6a).[244] Yu and coworkers employed the in situ electrochemical attenuated total reflection (ATR) FTIR to probe the structural evolution of CoS_x for OER (at a constant current of 1 mA) with varying time (0−1000 s).[245] As shown in Figure 6b, the initially increased and then stabilized bands located at 3350 and 1630 cm^{-1} were ascribed to the stretching and bending vibration of hydrogen-bonded hydroxyl group, respectively, implying the enhanced adsorption of H_2O over the electrocatalyst. The increased band at 892 cm^{-1} along with prolonging time was originated from the bending vibrations of hydroxyls, implying the formation of hydroxide species on the surface of the electrocatalysts during OER. After removing the bias for OER, the remaining bands at 3350, 1630, and 892 cm^{-1} indicated the irreversible structural and composition transformation of CoS_x during OER. The further in-depth studies indicated that the amorphous CoS_x at the surface is initially transformed to the $Co(OH)_2$ intermediate, and eventually converted to crystalline CoOOH, which served as the real active sites for OER. Wu and coworkers used in situ electrochemical ATR-FTIR to track the structure evolution of the Pt_3Cu alloy-supported Ru single atoms electrocatalyst (Ru_1-Pt_3Cu) during acidic OER.[246] As shown in Figure 6c, the gradually apparent and then disappeared peak at nearly 1212 cm^{-1} along with cyclic potential scanning (from 0.8 to 1.6 and then back to 0.8 V vs RHE) was ascribed to the vibration of surface adsorbed superoxide, implying the AEM mechanism instead of LOM over Ru_1-Pt_3Cu. However, even potential was swept back to 0.8 V vs RHE, the newly formed peaks at round 1630, 1420, and 1300 cm^{-1} were still visible, implying the oxidative reconstruction of Ru_1-Pt_3Cu.

https://doi.org/10.1021/acs.chemrev.3c00332
Chem. Rev. 2024, 124, 3694−3812

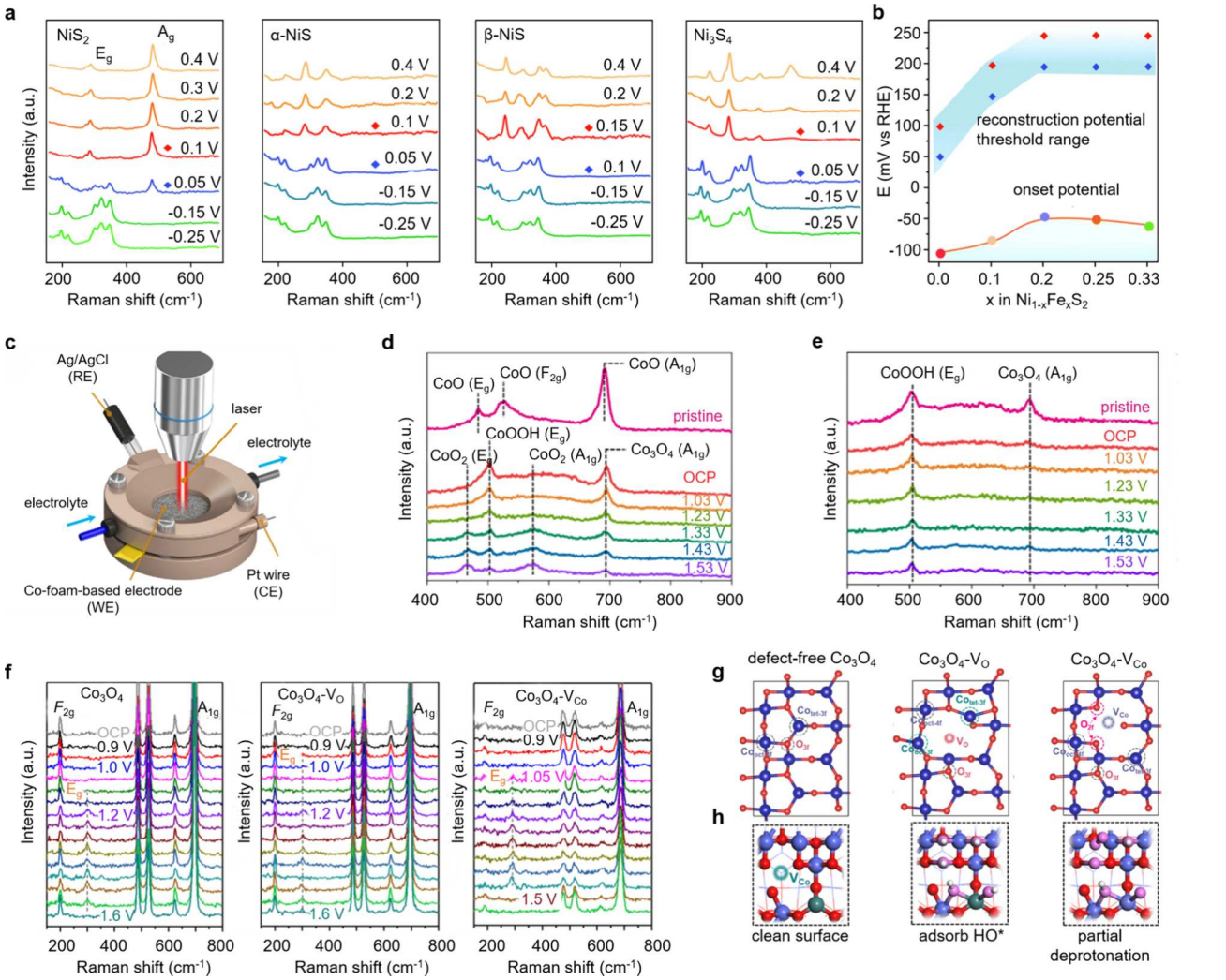

Figure 7. (a) In situ Raman spectra of nickel sulfides at the potentials of 0.4 to −0.25 V vs RHE in 1.0 M KOH for NiS_2, α-NiS, β-NiS, and Ni_3S_4. (b) Reconstruction potential threshold range for the $Ni_{1-x}Fe_xS_2$ ($x \approx 0-0.33$) samples, and the corresponding onset potentials of HER were plotted to show the dynamic correlation of structure−activity. Reproduced with permission from ref 143. Copyright 2022 Royal Society of Chemistry. (c) Schematic of the in situ/operando electrochemical Raman spectroscopy cell. In-situ/operando Raman spectra of (d) CF−O and (e) CF−FeSO. Reproduced from ref 254 under the terms of the CC-BY 4.0 license. Copyright 2022 The Authors, published by Springer Nature. (f) In situ Raman spectra of Co_3O_4, $Co_3O_4-V_O$, and $Co_3O_4-V_{Co}$ during OER under applied potentials from 0.9 to 1.55/1.60 V vs RHE with an increase step of 0.05 V. (g) Optimized structures of defect-free Co_3O_4, $Co_3O_4-V_O$, and $Co_3O_4-V_{Co}$. (h) Schematic of adsorption and deprotonation on (110) surface of $Co_3O_4-V_{Co}$. Reproduced with permission from ref 158. Copyright 2023 American Chemical Society.

To improve signal-to-noise ratio and spatial resolution, the high bright synchrotron-radiation-based FTIR (SR-FTIR) method has been applied. Wei and coworkers reported the direct observation of dynamic structural evolution of atomically dispersed heteronitrogen-configured Ir sites (AD-HN-Ir) during acidic OER using potential-dependent in situ SR-FTIR, as shown in Figure 6d.[205] A new absorption band at 784 cm^{-1} for AD-HN-Ir electrocatalyst appeared at the potential of 1.25 V vs RHE, indicating the formation of Ir−O during the acidic OER. This result suggested that the high-valence Ir site in AD-HN-Ir could adsorb oxygen to form O-hetero-Ir−N_4. Meanwhile, when the applied potential exceeded 1.35 V vs RHE, a new band of the HOO* intermediate at 1055 cm^{-1} could be observed. The vibration band intensity of the HOO* intermediate increased more obviously for AD-HN-Ir than Ir-NC with increasing applied potential, indicating that the O-hetero-Ir-N_4 moieties can accelerate the OER kinetics. The dynamically coupled oxygen disappeared after OER, confirming the reversible process of oxygen coupling with the change of applied potential. Analogy to the results of AD-HN-Ir electrocatalyst, a similar dynamic coupling process was also observed by Yao and coworkers in atomically dispersed Ru−N_4 site anchored on nitrogen−carbon (Ru-NC) electrocatalysts by operando SR-FTIR (Figure 6e).[247] When the applied potential exceeded 1.5 V vs RHE, a new absorption band corresponding to single adsorbed oxygen at 764 cm^{-1} confirmed the formation of O−Ru−N_4, which then disappeared when sweeping the potential back to 1.2 V vs RHE.

3.3.2. Raman Spectroscopy. Complementary to FTIR, Raman spectroscopy is also an optical technique, which detects vibration/rotation of molecules (or functional groups) upon inelastic scattering of monochromatic light (Raman effect). This inelastic scattering involves the energy transfer between the underlying molecules (or functional groups) and scattered photons, exhibiting either positive or negative photon energy shift (Raman shift). Investigation of these Raman shifts helps

https://doi.org/10.1021/acs.chemrev.3c00332
Chem. Rev. 2024, 124, 3694−3812

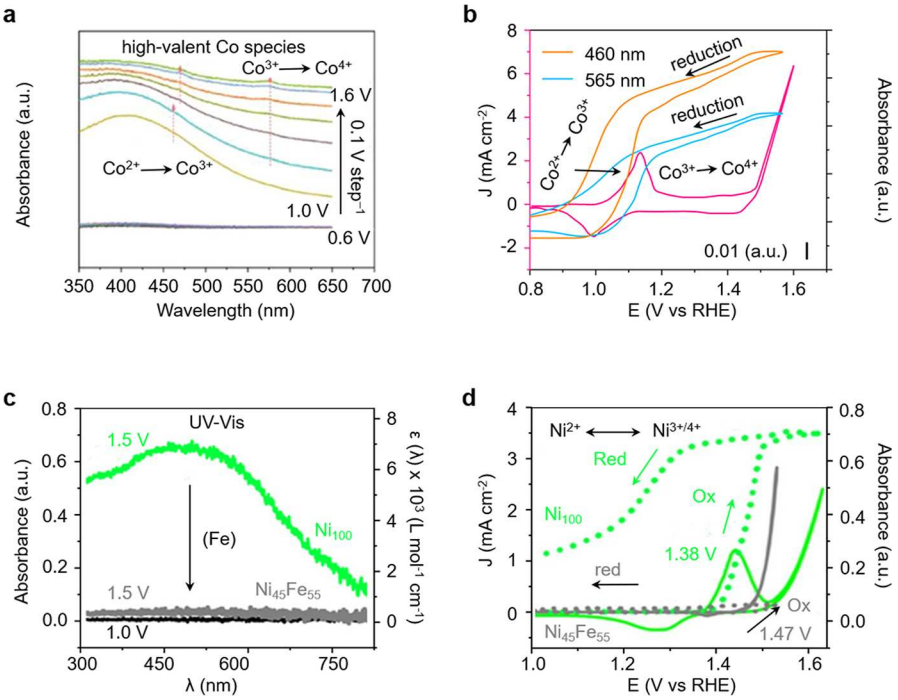

Figure 8. (a) Operando UV−vis spectra of Cu_2S/CoFe LDH from OCP to 1.6 V vs RHE with an increase step of 0.1 V. (b) UV−vis absorbance variation relative to potential and related CV curves of Cu_2S/CoFe LDH at 460 and 565 nm. Reproduced with permission from ref 156. Copyright 2023 John Wiley and Sons. (c) In situ UV−vis spectra of unsupported Ni(OOH) and $Ni_{45}Fe_{55}$(OOH) electrocatalysts at 1.5 V vs RHE in 0.1 M KOH. (d) In situ UV−vis spectra monitored at Abs_{450} ($\lambda_{450\ nm}$) during potential cycling of Ni(OOH) and $Ni_{45}Fe_{55}$(OOH) electrocatalysts in 0.1 M KOH. Reproduced with permission from ref 256. Copyright 2017 American Chemical Society.

to identify the fingerprints of surface species. The changes of chemical bonds on the surface of electrocatalysts can be reflected by in situ electrochemical Raman spectroscopy with high sensitivity.[152,248−253] For example, the dynamic reconstruction of HER electrocatalysts including NiS_2, α-NiS, β-NiS, and Ni_3S_4 in alkaline electrolyte was investigated by Zhang and coworkers via in situ Raman spectroscopy (Figure 7a,b).[143] As shown in Figure 7a, the E_g peak at 284.8 cm^{-1} and A_g peak at 479.3 cm^{-1} of NiS_2 were observable at the potential of 0.4 V vs RHE. As the potential increased cathodically from 0.4 to −0.25 V vs RHE, these characteristic peaks of NiS_2 gradually weakened until they disappeared, along with the emergence and growth of two A_1 (187.6 and 324.6 cm^{-1}) and four E (202.1, 223.6, 303.6, and 350.3 cm^{-1}) peaks for Ni_3S_2. This was interpreted by the phase reconstruction of NiS_2 during HER with threshold potential between 0.1 and 0.05 V vs RHE. The continuous redshift of A_g and E_g peaks of NiS_2 with applied potentials changed from 0.4 to 0.1 V vs RHE implied the softening of S−S bonds due to the generation and progressive accumulation of sulfur vacancies before alkaline HER-induced reconstruction. Besides NiS_2, other nickel sulfides like α-NiS, β-NiS, and Ni_3S_4 exhibited similar phase reconstruction to Ni_3S_2 during alkaline HER, with threshold potentials of 0.1−0.05 V, 0.15−0.1 V, and 0.1−0.05 V vs RHE, respectively, indicative of their different reconstruction energy barriers. Further studies indicated that moderate Fe doping (x < 0.2) into NiS_2 can decrease the reconstruction energy barrier, as revealed by the positive shift of threshold potential range (Figure 7b).

In addition, in situ/operando Raman spectroscopy was also employed to study the OER-induced reconstruction. For instance, Oh and coworkers tracked the electrochemical reconstruction and identified the actual alkaline OER active site of sulfur and iron treated cobalt foam (CF) electrode (CF-FeS) by using in situ/operando Raman spectroscopy (Figure 7c−e).[254] The CoO (E_g and F_{2g}) in CF after OER (CF−O) under OCP condition transformed into CoOOH (E_g) and Co_3O_4 (A_{1g}) in 1.0 M KOH solution. With the positive increase of applied potential, the reduced intensity of CoOOH and Co_3O_4 peaks, and the increased intensity of CoO_2 peak indicated the gradual oxidation of Co species from CoO, Co_3O_4, CoOOH to CoO_2 (Figure 7d). Different from CF−O, the peak of Co_3O_4 (A_{1g}) for reconstructed CF−FeS (CF−FeSO) disappeared under OCP and OER condition, and only the CoOOH (E_g) peak was detected under the whole potential range, demonstrating the presence and OER-active role of stable Fe-CoOOH phase in CF-FeSO (Figure 7e). Actually, the Co-based compounds, such as CoO, Co_3O_4, and $Co(OH)_2$, could undergo surface reconstruction during OER process to form CoO_xOH_y. The reconstruction process and final active species are highly dependent on the initial structure of the original electrocatalyst. Zou and coworkers employed Co_3O_4 with O vacancy (V_O) and Co vacancy (V_{Co}) to uncover the effects of defects in the reconstruction process via in situ Raman spectra (Figure 7f−h).[158] As shown in Figure 7f and g, for defect-free Co_3O_4, when the applied potential increased to 1.15 V vs RHE from OCP, a new peak at 290 cm^{-1} corresponding to E_g symmetrical vibration of amorphous $Co(OH)_2$ gradually emerged, representing the formation of chemical bonds between adsorbed HO* and the near-surface Co atoms in the edge-sharing octahedral [Co−$(OH)_6$]. The E_g peak gradually increased and subsequently disappeared with the potential increasing from 1.15 to 1.60 V vs RHE with 0.05 V step due to the partial deprotonation of amorphous [Co−$(OH)_6$] and the formation of amorphous Co−$O_{6-x}(OH)_x$ under high overpotential. For Co_3O_4−V_O, the E_g signal

https://doi.org/10.1021/acs.chemrev.3c00332
Chem. Rev. 2024, 124, 3694−3812

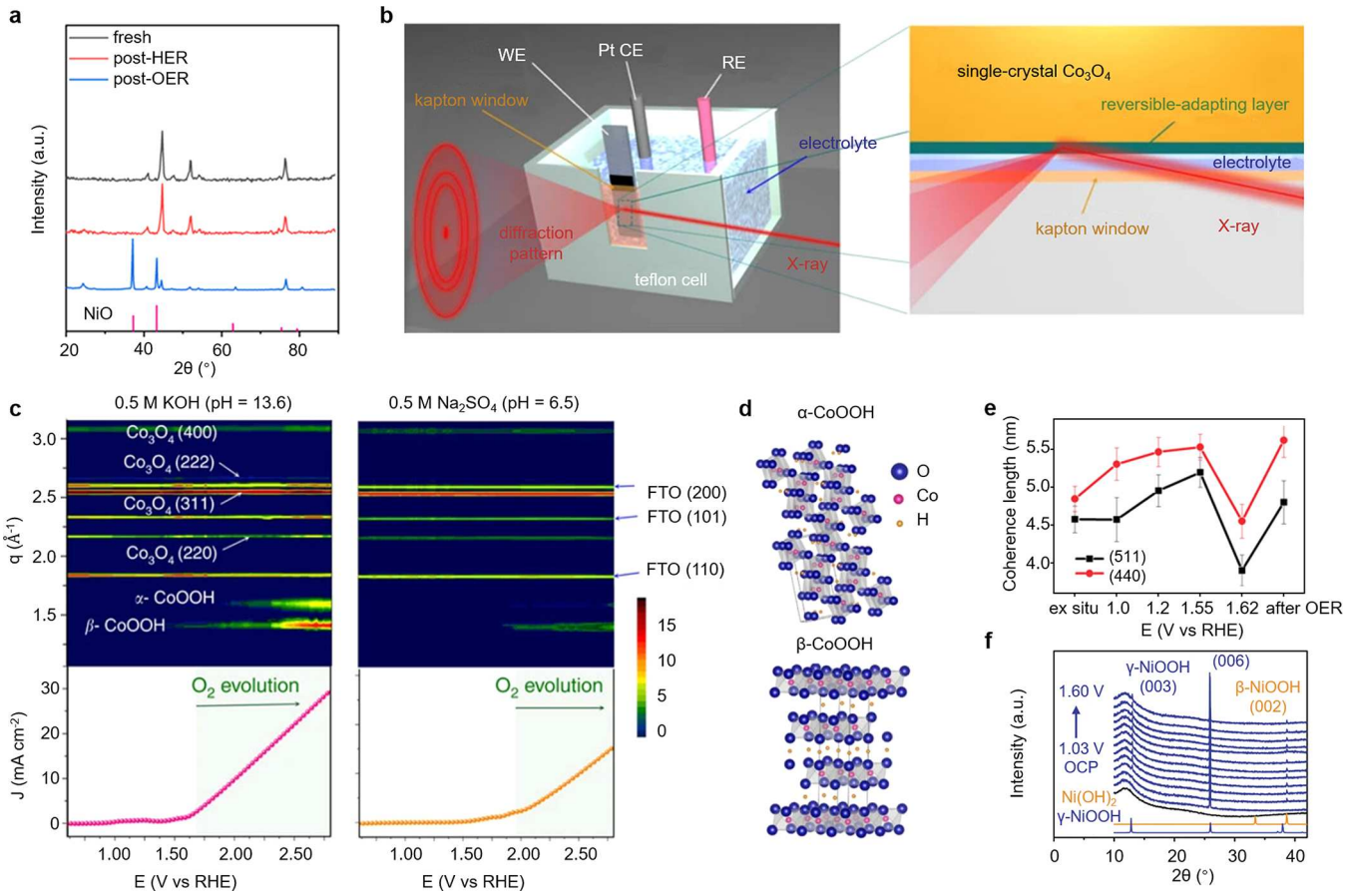

Figure 9. (a) Ex situ XRD patterns for fresh, post-HER, and post-OER Ni_2P/Ni/NF electrocatalysts. Reproduced with permission from ref 227. Copyright 2015 American Chemical Society. (b) Schematic of the in situ grazing-angle XRD apparatus. (c) Contour plots of in situ electrochemical grazing-angle XRD signals of a Co_3O_4@CoO SC in 0.5 M KOH (pH = 13.6) and 0.5 M Na_2SO_4 (pH = 6.5), along with LSV curves. (d) Schematic of the structures of β-CoOOH and α-CoOOH. Reproduced from ref 263 under the terms of the CC-BY 4.0 license. Copyright 2015 The Authors, published by Springer Nature. (e) Structural coherence length of Co_3O_4 electrocatalyst films. Reproduced from ref 204 under the terms of the CC-BY 4.0 license. Copyright 2015 The Authors, published by Springer Nature. (f) Operando XRD patterns of $Ni(OH)_2$/NF. Reproduced from ref 264 under the terms of the CC-BY 4.0 license. Copyright 2018 The Authors, published by Springer Nature.

appeared at relatively low potential (0.95 V vs RHE) and was still discernible at 1.60 V vs RHE, indicating the thermodynamic advantage for HO* adsorption and the high deprotonation energy barrier of Co sites. Moreover, the E_g signal of Co_3O_4–V_{Co} appeared at a potential of 0.95 V vs RHE and disappeared at a low potential of 1.50 V vs RHE, suggesting the improved adsorption of HO* and the accelerated deprotonation process. The peaks of A_{1g} (696 cm^{-1}) and F_{2g} (196 cm^{-1}) were assigned to trivalent octahedral cobalt (CoO_6, Co_{oct}) and divalent tetrahedral cobalt (CoO_4, Co_{tet}) of Co_3O_4, respectively. The results suggested that Co_3O_4 undergoes a two-step reconstruction during OER, from original structure to hydroxide and then to oxyhydroxide (Figure 7h). The stronger HO* adsorption but weaker deprotonation induced by O defects provided the driving force for reconstruction, while Co defects favored dehydrogenation and reduced the reconstruction rate. To further improve the sensitivity, surface-enhanced Raman spectroscopy (SERS) has been applied for the operando characterizations of electrocatalysts. By employing operando SERS, Hu and coworkers investigated the surface reconstruction of Co oxyhydroxide (CoOOH) during OER.[255] They found that under positive potentials above 1.35 V vs RHE, the primary CoOOH and residual Co^{2+} species are restructured to disordered CoO_2.

3.3.3. Ultraviolet–Visible Spectroscopy. Ultraviolet–visible spectroscopy (UV–vis) measures the absorbance of light in the ultraviolet–visible spectral region by matter, which causes the transitions between matter's electronic energy levels corresponding to the valence state changes. Hou and coworkers tracked the variation of metal oxidation states during reconstruction using operando UV–vis spectroscopy (Figure 8a,b).[156] The two peaks at 460 and 565 nm for Cu_2S/CoFe LDH were ascribed to the oxidation of Co^{2+} to Co^{3+} and Co^{3+} to Co^{4+}, respectively. The obvious increase of absorption at about 490 nm for Cu_2S/CoFe LDH appeared at 1.3 V vs RHE, assignable to the accumulation of high valence Co species. Both the UV–vis absorbance variation at 460 and 565 nm relative to potential and the corresponding CV curves showed the redox-transitions of Cu_2S/CoFe LDH (Figure 8b). They also found that the oxidation of Co species in Cu_2S/CoFe LDH appears at relatively lower potentials than those in CoFe LDH, indicating the easier oxidation of Co species in Cu_2S/CoFe LDH to high valent Co^{4+} during OER.

Analogous to the study, researchers also employed in situ UV–vis spectroscopy to explore the effect of doping on valence state during surface reconstruction. Strasser and

https://doi.org/10.1021/acs.chemrev.3c00332
Chem. Rev. 2024, 124, 3694–3812

collaborators tracked metal oxidation process in NiOOH and unsupported $Ni_{45}Fe_{55}OOH$ electrocatalysts using in situ UV−vis spectroscopy.[256] As shown in Figure 8c and d, applying OER catalytic potential (1.5 V vs RHE in 0.1 M KOH) induced the emergence of a broad spectral absorption band at 450 nm in NiOOH, indicating the Ni charge transfer process. The presence of Fe in $Ni_{45}Fe_{55}(OOH)$ suppressed this potential-induced absorption of the Ni almost entirely, with merely weak residual absorption. The extinction coefficients of NiOOH and $Ni_{45}Fe_{55}(OOH)$ at 1.5 V vs RHE were calculated to be 6500 and 200 L mol^{-1} cm^{-1}, respectively. These reduced absorption intensity after Fe incorporation confirmed the suppressed charge transfer of Ni^{2+} to $Ni^{3+/4+}$. Potential cycling revealed that the absorption band (at 450 nm) rising of the NiOOH locates after the onset of Ni^{2+}/Ni^{3+} redox wave, contrary to that for $Ni_{45}Fe_{55}OOH$ (Figure 8d). The authors concluded that Fe shifts the Ni oxidation closer to OER onset potential. Recently, Hu and coworkers used operando UV−vis spectroscopy to study Fe-induced changes in oxidation states of Co in CoFe (oxy)hydroxides ($CoFeO_xH_y$) during OER.[257] The results showed that increasing Fe content leads to higher oxidation state of Co^{4+}, and phase separation to form inactive FeOOH.

3.4. X-ray Characterizations

X-ray is an excellent probe to reveal the detailed structural information on substrates due to its comparable wavelength (10^{-8} cm) with the interatomic distances of materials. Over one hundred years of development, X-ray characterizations, such as X-ray diffraction (XRD), X-ray photoelectron spectroscopy (XPS), X-ray absorption spectroscopy (XAS), X-ray emission spectroscopy (XES), and X-ray fluorescence spectroscopy (XRF), have been widely applied for revealing the chemical composition, crystal structure, and electronic state of materials. Meanwhile, the developed in situ/operando X-ray characterizations techniques are effective to monitor the dynamic reconstruction evolution of active sites during electrocatalytic processes.

3.4.1. X-ray Diffraction. X-ray diffraction (XRD) utilizes the constructive interference between monochromatic X-rays and crystalline substances. By scanning the sample through 2θ angles, all possible directions of diffractions of the lattice can be obtained. XRD is thus an excellent technique to reveal the crystallographic information on materials, such as the cell parameters, strain, and microstructure, and can be employed to identify the crystalline phase evolution of the underlying electrocatalysts before and after the electrocatalytic processes.[258−260] For instance, our group detected the reconstruction of Ni_2P/Ni/NF bifunctional electrocatalyst after OER by ex situ XRD (Figure 9a).[227] Additional peaks assignable to NiO were observed for the post-OER sample, suggesting the electrochemical oxidation of Ni_2P/Ni/NF.

In contrast to the ex situ XRD which can only provide the crystal structure transformation of the material in initial and final states, in situ XRD could give the dynamic information during the electrocatalytic process in real-time, especially for the phase transformation and the structural evolution of electrocatalysts.[261,262] To obtain stable signal and monitor the surface states of electrocatalysts in liquid environment, Chen and coworkers customized a reaction cell and utilized the in situ synchrotron radiation grazing-angle XRD to investigate the structural evolution of Co_3O_4−CoO single-crystal cubes (Co_3O_4@CoO SC) during OER process in 0.5 M KOH and 0.5 M Na_2SO_4 (Figure 9b,c).[263] Before OER, main reflections corresponding to the fluorine-doped tin oxide (FTO) substrate and the spinel-type Co_3O_4 phases could be observed, and no CoO phase was detected due to its low content. At the onset of OER, the emergence of β-CoOOH on the surface of electrode in both alkaline and neutral condition confirmed that CoO layer is transformed into more active phase (Figure 9d). Further increasing the potential, a new phase, α-CoOOH, was observed, demonstrating that OER is strongly correlative with the formation of metal oxyhydroxide. In situ XRD characterizations under potential cycling between 2.0 and 0.1 V vs RHE showed that CoO layer could reversibly adapt to condition change during OER, consequently protecting the underlay electrocatalyst anodizing from applied potential.

Strasser and coworkers discovered the reversible amorphization of crystalline Co_3O_4 during OER by conducting in situ grazing-incident XRD.[204] The reflections from substrate and Co_3O_4 were only detectable crystalline phases during the entire testing process, while the broadening of selected Co_3O_4 reflections showed that the mean structural coherence length of the crystalline domains has changed (Figure 9e). The initial irreversible growth of Co_3O_4 crystallites caused by the Ostwald ripening and/or coalescence up to a potential of 1.2 V vs RHE resulted in the increase of coherence length. The largest structural coherence length was observed at the potential of 1.55 V vs RHE, just positive than that of Co redox features. When increasing the applied potential to 1.62 V vs RHE, the reversible structural transformation of crystalline Co_3O_4 to amorphous CoO_x shell resulted in the decrease of coherence length. Since the amorphous CoO_x shell could recrystallized to Co_3O_4 after OER, coherence length recovered to the value at 1.2 V vs RHE. Similar phase transformation during OER process was also observed in Ni-based electrocatalyst by Cheng and colleagues through an operando XRD (Figure 9f).[264] After shortly aging in 1.0 M KOH, the initially amorphous $Ni(OH)_2$ showed considerable crystallinity. When the applied potential exceeded 1.03 V vs RHE, the $Ni(OH)_2$ was mainly in γ-NiOOH phase with a small portion of β-$Ni(OH)_2$. Despite these achievements, we note that the XRD is not an effective technique for analyzing amorphous species during reconstruction of electrocatalysts.

3.4.2. X-ray Photoelectron Spectroscopy. X-ray photoelectron spectroscopy (XPS) gives the information on core−electron binding energy (BE) by measuring the kinetic energy of the emitted electrons from a sample's surface (typical penetration depth of <10 nm) bombarded by X-rays. It also provides insight into chemical shift since the BE depends not only on the shell of the electron, but also on the bonding environments. Thus, XPS can provide valuable surface information, including the element composition and chemical state.[265] Our group found that the h-NiS_x sample showed almost identical XRD patterns before and after OER test.[223] However, the high-resolution Ni $2P_{3/2}$ and S 2p XPS spectra of post-OER h-NiS_x showed decreased intensity of peaks corresponding to $Ni^{\delta+}$, S $2p_{3/2}$, and S $2p_{1/2}$, and increased intensity of peaks assigned to oxidized nickel and sulfur species. These results proved that the h-NiS_x is partially oxidized during OER. In addition, the ex situ XPS was also used to investigate the reconstruction of amorphous Co−P bifunctional electrocatalyst by us.[266] The emergence of the Co_3O_4 peaks and the disappearance of phosphide feature confirmed the partial oxidation of the original cobalt in the

https://doi.org/10.1021/acs.chemrev.3c00332
Chem. Rev. 2024, 124, 3694−3812

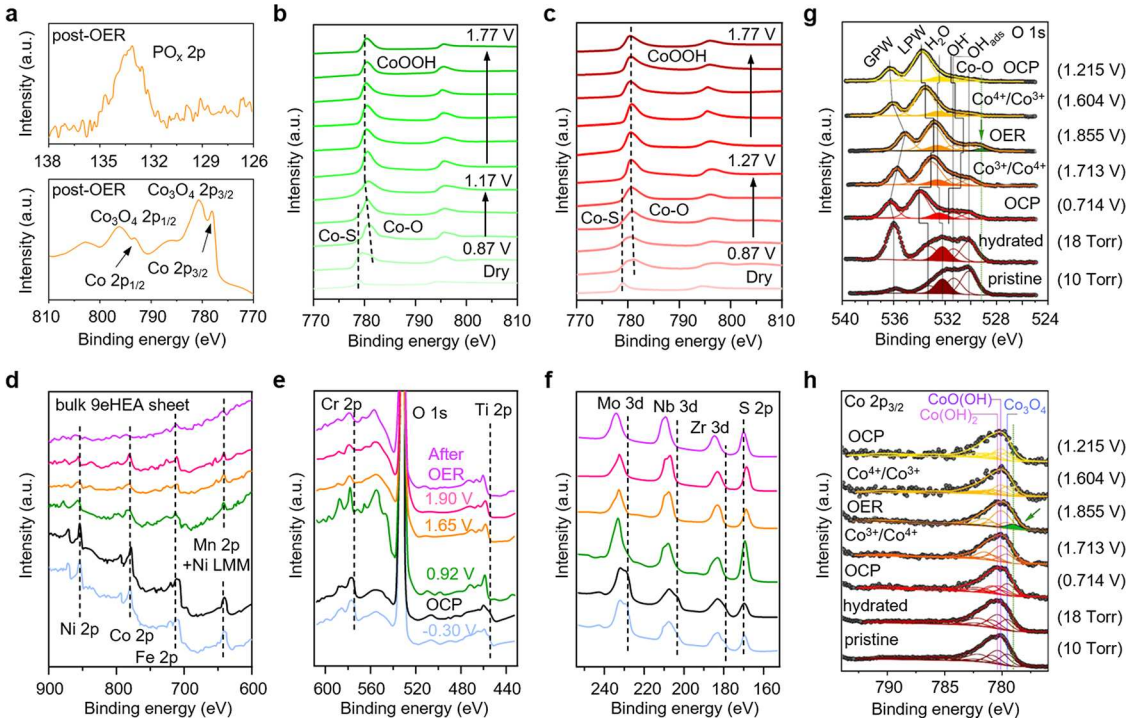

Figure 10. (a) Ex situ XPS spectra of P 2p and Co 2p for Co−P film. Reproduced with permission from ref 266. Copyright 2015 John Wiley and Sons. Quasi-operando Co 2p XPS spectra for (b) CeO_2−$CoS_{1.97}$ and (c) $CoS_{1.97}$-CeO_2 at specific potential from 0.87 V (OCP) to 1.77 V vs RHE. Reproduced with permission from ref 268. Copyright 2021 John Wiley and Sons. (d−f) EC-XPS spectra in the survey mode for 9eHEA at various applied potentials. Reproduced with permission from ref 155. Copyright 2022 John Wiley and Sons. Operando APXPS spectra evolution of (g) O 1s and (h) Co $2p_{3/2}$ of the biphasic CoO_x. Reproduced with permission from ref 269. Copyright 2017 American Chemical Society.

Co−P film to Co_3O_4 and cobalt phosphate during OER (Figure 10a).

Compared to the ex situ XPS characterization, (quasi-) in situ/operando XPS allows the direct probing of dynamic change of surface state during reconstruction. Generally, operation of XPS requires ultrahigh vacuum conditions to avoid photoelectron scattering from gas molecules. Therefore, quasi-in situ XPS is widely used, in which the specimens are treated inside the in situ chamber and then instantly subjected to XPS measurement.[267] For example, Xi and coworkers employed the quasi-operando XPS to investigate the role of spatial architectures of CeO_2-incorporation in reconstruction of $CoS_{1.97}$.[268] As shown in Figure 10b and c, when the sulfides were immersed into 1.0 M KOH, the appearance of Co−O bond indicated the preoxidation behaviors of sulfides. The higher intensity of Co−O bond for $CoS_{1.97}$−CeO_2 ($CoS_{1.97}$ decorated with CeO_2, Figure 10c) relative to CeO_2−$CoS_{1.97}$ (CeO_2 supported $CoS_{1.97}$, Figure 10b) at OCP suggested the spontaneous oxygen exchange and faster reconstruction of the former due to stronger adsorption of OH^- and higher oxygen ion conductivity at surface. Obvious phase transition can be observed as the potential increased. As expected, the transition potentials of CeO_2−$CoS_{1.97}$ and $CoS_{1.97}$-CeO_2 to CoOOH were different and both were lower than that for $CoS_{1.97}$, indicating spatial architecture-dependent surface reconstruction of $CoS_{1.97}$. For a multicomponent specimen, the quasi-in situ XPS characterization could monitor the changes of all involved elements, which is beneficial to identify their individual role. By conducting quasi-in situ electrochemical XPS (EC-XPS), Ito and coworkers investigated the surface states and corrosion behaviors of high-entropy alloys (9eHEA: Ti, Cr, Mn, Fe, Co, Ni, Zr, Nb, and Mo) during OER in acidic electrolyte.[155] As shown in Figure 10d−f, metallic Ti, Cr, Zr, Nb, and Mo were partially oxidized to (hydr)oxides at OCP and then further oxidized at 0.92 V vs RHE, while Mn, Fe, Co, and Ni started to be partially oxidized to (hydr)oxides at 0.92 V vs RHE despite their partial dissolution at OCP. As the potential further increased to 1.65 V vs RHE, Cr, Co, and Ni showed potential-dependent oxidation, converting hydroxides to oxides. All elements on the surface were completely oxidized at the potential of 1.90 V vs RHE, and the OCP was negatively shifted to 0.89 V vs RHE after OER, implying the irreversible reconstruction. Therefore, the role of nine metals was divided into three types: (i) passivation (Ti, Zr, Nb, and Mo), (ii) redox activity (Co, Ni, and Cr), and (iii) unassigned function (Mn and Fe).

One drawback of quasi-in situ/operando XPS is that the information obtained under ultrahigh vacuum conditions might not exactly correlate with the real surface states of the electrocatalyst under operation conditions.[267] The operando ambient-pressure XPS (AP-XPS) can overcome this issue. For instance, Sharp and coworkers investigated the structural evolution of a Co_3O_4/$Co(OH)_2$ biphasic electrocatalyst during OER in 1.0 M KOH by operando AP-XPS (Figure 10g,h).[269] The two highest BE components corresponded to oxygen in gas-phase water (GPW) and liquid-phase water (LPW). The results of spectral simulation and analysis confirmed that the biphasic electrocatalyst was composed of an interfacial Co_3O_4 spinel layer and a $Co(OH)_2$ outer layer, which was almost stable under hydrated conditions. The electrocatalyst underwent chemical−structural transformation as a function of the applied potential, with complete conversion of the $Co(OH)_2$ and partial conversion of the spinel Co_3O_4 phases to CoO(OH) when the potential increased above 1.713 V vs

https://doi.org/10.1021/acs.chemrev.3c00332
Chem. Rev. 2024, 124, 3694−3812

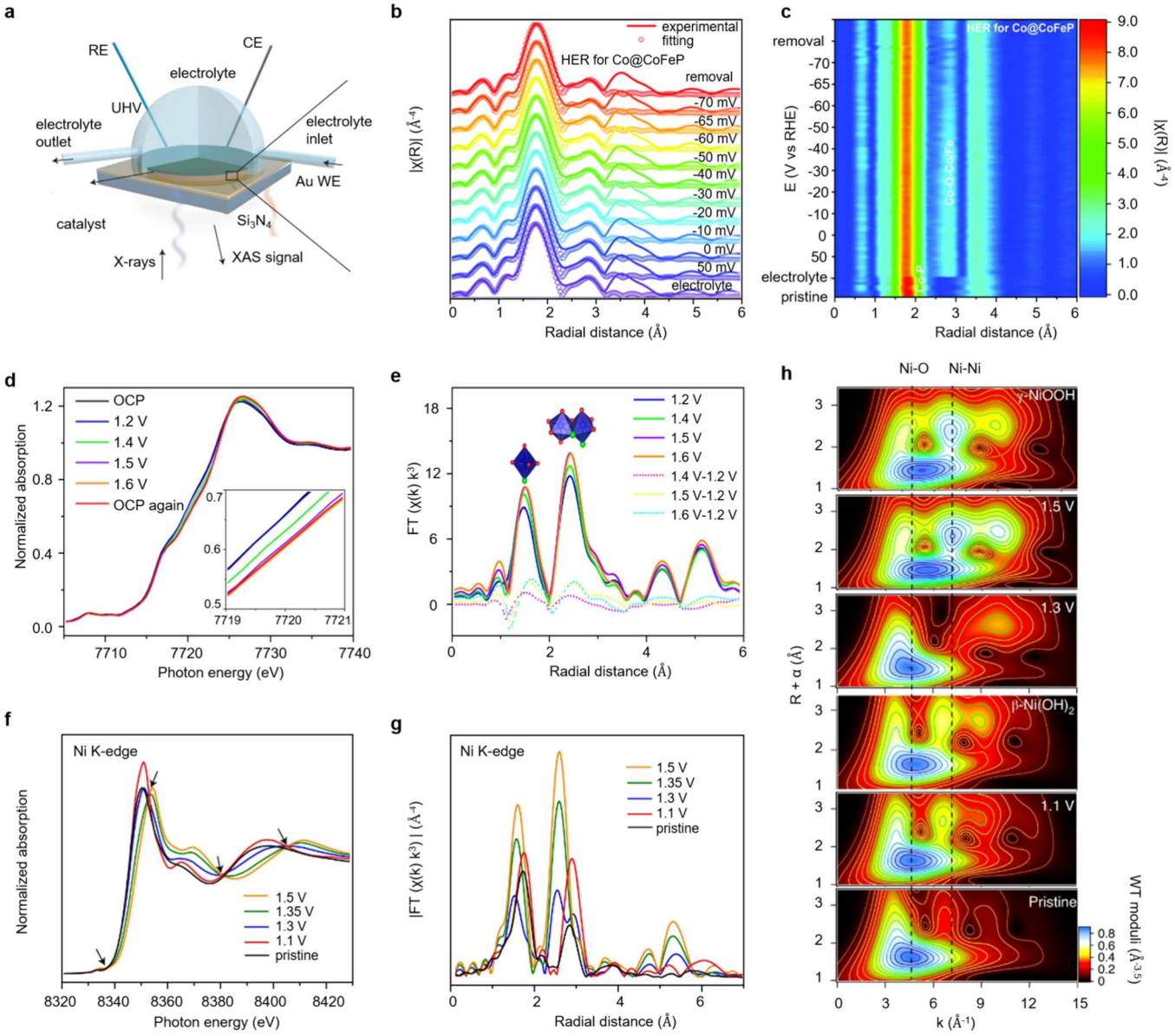

Figure 11. (a) Schematic of the in situ electrochemical flow cell-enabled operando XAS. Reproduced from ref 275. Copyright 2021 Springer Nature. (b) Fitting and (c) 2D contour plot of operando Co K-edge FT-EXAFS spectra of Co@CoFe-P at different applied potentials in 1.0 M KOH for HER. Reproduced from ref 147. Copyright 2022 Royal Society of Chemistry. (d) Co K-edge XANES spectra at different potentials for fresh $LiCoO_{1.8}Cl_{0.2}$ and (e) the corresponding k^3-weighted FT-EXAFS spectra. Reproduced from ref 184. Copyright 2021 Springer Nature. (f) Ni K-edge XANES spectra and (g) the corresponded k^3-weighted FT-EXAFS signals recorded at different potentials in 1.0 M KOH. (h) Comparison of Ni K-edge WT-EXAFS recorded for the pristine sample, standard references, and catalytic materials at 1.1, 1.3, and 1.5 V vs RHE. Reproduced from ref 276. Copyright 2020 Springer Nature.

RHE. Further increasing the potential up to OER catalytic range, new spectral features in both Co 2p and O 1s core-level regions emerged, corresponding to highly active Co^{4+} centers. Even at OCP after OER, the newly formed CoO(OH) still existed. These operando AP-XPS results confirmed that the relative phase stability of Co_3O_4 enables a durable substrate/catalyst interface, while the facile chemical transformation of $Co(OH)_2$ to CoO(OH) layered structure boosts high OER activity.

3.4.3. X-ray Absorption Spectroscopy. X-ray absorption spectroscopy (XAS), unlike XPS that deals with electrons emitted from the sample upon radiation by X-rays, studies the promotion of core electrons into higher energy unoccupied states of materials struck by synchrotron radiation X-rays.[270] It measures the transmission of a monochromatic X-ray scanned in small steps near the absorption edge of element of interest. XAS spectrum includes two main regions, namely the X-ray absorption near edge structure (XANES) and the extended X-ray absorption fine structure (EXAFS). XANES spectrum covers the X-ray energies nearest to the absorption edge and the position of the sharp absorption edge within this region gives insight into the local atomic information such as coordination environment and oxidation state.[271] EXAFS spectrum covers the region of ~30 eV after the absorption edge to ~1000 eV above the edge. The oscillatory features in this region are ascribed to the interactions of waves by ejected photoelectrons and neighbors of the absorbing atom, yielding information on surrounding atoms including number, type, and

https://doi.org/10.1021/acs.chemrev.3c00332
Chem. Rev. 2024, 124, 3694−3812

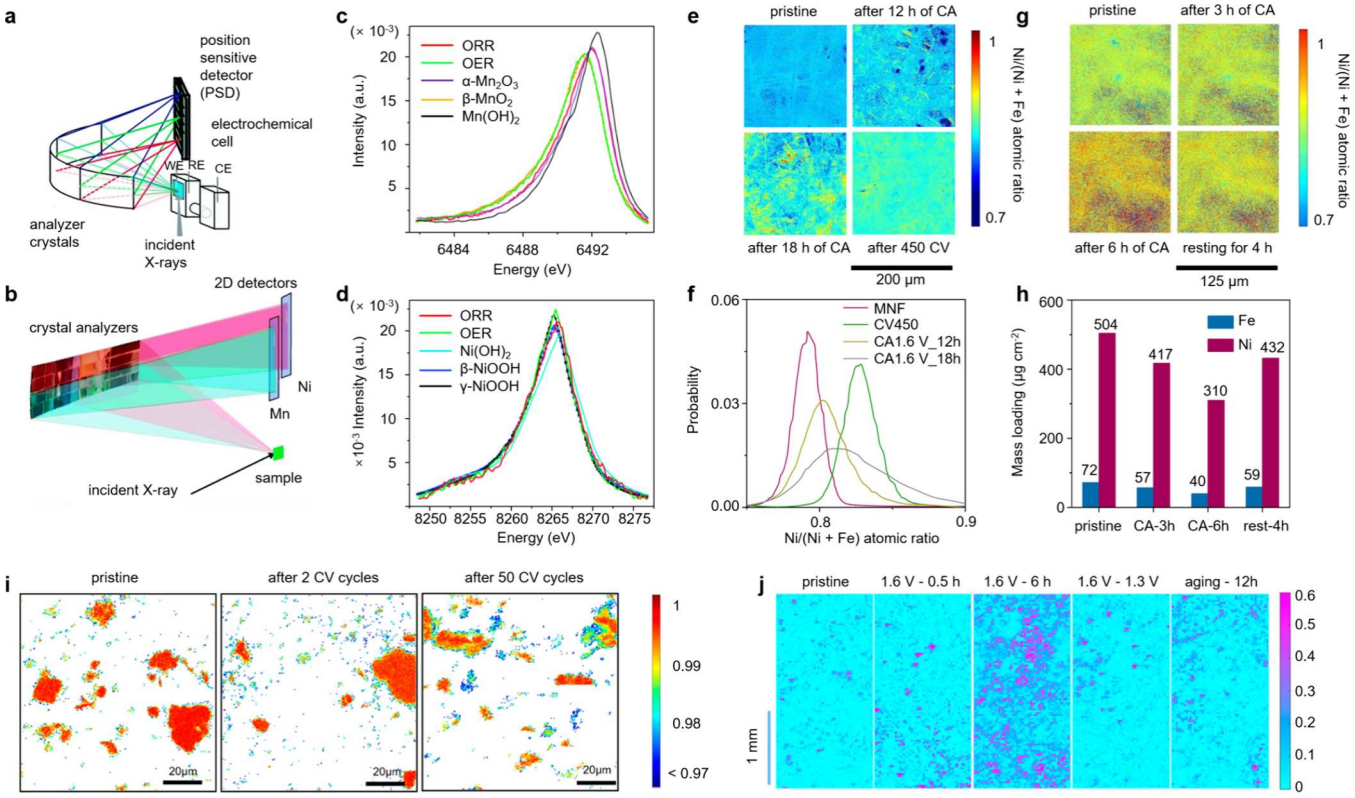

Figure 12. (a) Experimental setup for wavelength-dispersive XES with an in situ electrochemical cell. (b) Schematic of the setup for simultaneous detection of XES from two elements with the von Hamos spectrometer. (c) Comparison of the XES spectra of Mn oxide standards to the ORR phase and the OER phase of $MnNiO_x$. (d) Comparison of the XES spectra of Ni oxide standards to the ORR and OER phases of $MnNiO_x$. Reproduced with permission from ref 278. Copyright 2015 Royal Society of Chemistry. (e) Ni/(Ni+Fe) atomic ratio mapping images of pristine mixed Ni−Fe hydroxide (MNF), MNF after 12 h of chronoamperometry (CA) measurement at 1.6 V vs RHE, MNF after 18 h of CA measurement at 1.6 V vs RHE and MNF after 450 CV cycles in the range 1.2−1.8 V vs RHE. (f) Ni/(Ni+Fe) atomic ratio distribution of MNF before and after electrochemical measurement. (g) Ni/(Ni+Fe) atomic ratio mapping images of pristine MNF, thin MNF after 3 h of CA measurement at 1.6 V vs RHE, thin MNF after 6 h of CA measurement at 1.6 V vs RHE, thin MNF after 6 h of CA measurement at 1.6 V vs RHE and then resting in the electrolytic solution for 4 h. (h) Mass loading evolution of Ni and Fe before, during and after the OER, calculated based on XFM quantification. Reproduced from ref 280. Copyright 2020 Springer Nature. (i) Mapping image of the Ni/(Ni+Fe) atomic ratio of the pristine $Ni(OH)_2$, $Ni(OH)_2$ after 2 CV cycles, and $Ni(OH)_2$ after 50 CV cycles in 1.0 M KOH containing 10 μM Fe^{3+}. (j) Mapping images of the Fe/(Ni +Fe) atomic ratio of the pristine $Ni(OH)_2$, $Ni(OH)_2$ after 0.5 h CA measurement at 1.6 V, $Ni(OH)_2$ after 6 h CA measurement at 1.6 V, $Ni(OH)_2$ after 0.5 h CA measurement at 1.6 V and then another 0.5 h CA measurement at 1.3 V, and pristine $Ni(OH)_2$ aging for 12 h in 1.0 M KOH containing 10 μM Fe^{3+}. Reproduced with permission from ref 160. Copyright 2021 American Chemical Society.

distance. XANES and EXAFS give complementary structural information and are excellent tools to investigate the reconstruction of electrocatalysts during operation processes.[272−274] A typical in situ liquid cell XAS setup was schematically illustrated in Figure 11a.[275] Patzke and coworkers used operando XAS to track the dynamics of structural reconstruction of Fe-doped cobalt phosphide nanoboxes (Co@CoFe−P NBs) during HER.[147] As demonstrated in Figure 11b and c, the Co K-edge FT-EXAFS spectra (Figure 11b) and the corresponding 2D contour plots (Figure 11c) of Co@CoFe−P NBs revealed a distinctive second shell scattering at radial distance of 2.85 Å after immersing into the electrolyte (1.0 M KOH), indicating the formation of P−Co−O−Co/Fe−P. The intensity of this second shell scattering gradually decreased during negative potential scanning and increased after removal of the applied cathodic potential, suggesting the structural flexibility of P−Co−O−Co/Fe−P in Co@CoFe−P NBs during HER.

Furthermore, in situ/operando XAS was also employed to study the reconstruction during OER. Lim and collaborators explored the dynamic evolution of $LiCoO_{1.8}Cl_{0.2}$ during OER.[184] As shown in Figure 11d, the Co K-edge XANES spectra of $LiCoO_{1.8}Cl_{0.2}$ showed a positive shifts during the anodic polarization, implying elevated Co valence state. When the OER polarization ceased, the Co K-edge of $LiCoO_{1.8}Cl_{0.2}$ did not revert to the lower-energy position. The corresponding k^3-weighted FT-EXAFS spectra (Figure 11e) of $LiCoO_{1.8}Cl_{0.2}$ showed increased Co−O coordination number, confirming the elevated Co valence state during OER. The dynamic reconstruction of single atom electrocatalysts like Ru−N−C during OER was also investigated by Yao and collaborators using operando XAS.[247] Interestingly, Tang and coworkers recently observed a two-phase structural transition of $Ni_{0.5}Co_{0.5}$-MOF-74 nanocrystals at metal nodes with $Ni_{0.5}Co_{0.5}(OH)_2$ and $Ni_{0.5}Co_{0.5}OOH_{0.75}$ during OER, by operando XAS analysis (Figure 11f−h).[276] In the resting time from 1.1 to 1.2 V vs RHE (stage I), the increased intensity of the main XANES absorption peak at 8350 eV (Figure 11f) and the first two major peaks in FT-EXAFS spectra (Figure 11g) were discerned due to the Ni−M scattering and the formation of β-$Ni(OH)_2$, as confirmed by the corresponding wavelet transform (WT) analysis of EXAFS

https://doi.org/10.1021/acs.chemrev.3c00332
Chem. Rev. 2024, 124, 3694−3812

(Figure 11h). Meanwhile, the multiple-scattering peak at 5.98 Å in FT-EXAFS spectra suggested a collinear Ni−M−M arrangement, indicative of the formed denser packed [MO_x] polyhedral through edge-sharing in the resting state. Increasing the potential to precatalytic state (state II, 1.2 to 1.35 V vs RHE) and catalytic state (state III, 1.35 to 1.5 V vs RHE), the blueshift of Ni K-edge XANES peaks suggested the oxidation of Ni. Simultaneously, the appearance of four discrete isosbestic points (black arrows) implied the successive self-reconstruction process via a linear combination of two different Ni-based species, in consistent with the shorter radial distance shown in FT-EXAFS spectra. Furthermore, the disappearance of Ni−M scattering at 1.3 V vs RHE and its reemergence at 1.5 V vs RHE clearly demonstrated the formation of γ-NiOOH analogue. The results confirmed that $Ni_{0.5}Co_{0.5}$-MOF-74 underwent a dynamic two-step reconstruction during OER, from pristine structure to hydroxide analogue and then to oxyhydroxide analogue. Interestingly, the self-healing phenomenon of $Ni_{0.5}Co_{0.5}$-MOF-74 can be observed after being placed in air for 15 days, in which the $Ni_{0.5}Co_{0.5}$-MOF-74 gradually reversed to the pristine structure.

3.4.4. X-ray Emission Spectroscopy. X-ray emission spectroscopy (XES) serves as a complementary analytical technique to XAS. By probing the decay process of electron from excited states to core orbitals, the XES analyzes the energy difference between electronic levels and provides unique information about electronic structure such as charge/spin state, ligand properties, and symmetry. Based on the origin of transitions to the core K-shell, the emission lines can be divided into K-, L-, and M-edge spectral signals. For nonresonant XES, the incident X-ray excitation energy is sufficiently far above the core ionization energy to excite the core electron to the continuum.[277] The probed X-ray contains various X-ray emission lines, for example, K$\beta_{1,3}$ and Kβ' transitions correspond to 3p to 1s decays, and the peak positions reflect the number of unpaired electrons through the 3p/3d exchange interaction. Yano and coworkers employed the in situ electrochemical wavelength-dispersive XES to identify the changes in structure and oxidation state of $MnNiO_x$ during both oxygen reduction reaction (ORR) and OER.[278] As shown in Figure 12a and b, the angle between the incident and emitted X-rays (scattering angle) was set to 90° to minimize the contribution of the elastic scattering from the sample. The Mn K$\beta_{1,3}$ peak of $MnNiO_x$ at about 6491 eV can be attributed to the emission process of Mn 3p to 1s transition with constructive spin configuration. At the applied potential of 1.8 V vs RHE, the overlapped Mn K$\beta_{1,3}$ peaks of $MnNiO_x$ and β-MnO_2 suggested an oxidation state of +4 for Mn (Figure 12c). In contrast, at 0.6 V vs RHE, the Mn spectrum of $MnNiO_x$ was similar to that of α-Mn_2O_3 with an oxidation state of Mn between +3 and +4. Meanwhile, the Ni XES spectra of $MnNiO_x$ also revealed a higher oxidation state of Ni at 1.8 V vs RHE compared to that under 0.6 V vs RHE (Figure 12d).

Furthermore, tuning the excitation energy around a specific narrow energy range or absorption edge gives rise to resonant inelastic X-ray scattering (RIXS) and high-energy-resolution fluorescence-detected XAS (HERFD-XAS).[267] The corresponding techniques are known as resonant XES.[277] These two methods afford high spectral resolution and detailed element-specific electronic structure information, thus making it possible to measure highly dilute specimens, which is challenging for conventional XAS measurements.[161,277,279]

3.4.5. X-ray Fluorescence Spectroscopy. X-ray fluorescence spectroscopy (XRF) is a nondestructive analytical technique based on atomic emission. Namely, a primary X-ray first irradiates on the sample and knocks out electrons from inner orbitals within atoms to form holes. Then electrons from outer orbitals fall into the holes to restore equilibrium and meantime releasing excess energy in the form of fluorescent X-rays (secondary X-rays). The discrete energies of the emitted X-rays provide insightful information on transition between electron orbitals of the probed element. Lin and coworkers reported a phase segregation reversibility in mixed Ni−Fe hydroxide (MNF) OER electrocatalysts by synchrotron X-ray fluorescence microscopy (XFM).[280] As shown in Figure 12e and f, after 18 h of chronoamperometry (CA) measurement at 1.63 V vs RHE, phase segregation of MNF gradually became visible, in sharp contrast to that without obvious phase segregation in CV measurements (1.2−1.8 V vs RHE) even after 450 cycles. The increased Ni concentration with prolonging CA time indicated the preferential dissolution of Fe into the electrolyte. The higher Ni concentration and narrower Ni distribution after 450 CV cycles compared to that observed in the CA measurement suggested that CV cycling may induce more severe Fe depletion, but more homogeneous Ni−Fe distribution. Additionally, they conducted XFM analysis under operando conditions to monitor the evolution of metal species (Figure 12g,h). The Ni/(Ni+Fe) ratio gradually increased due to the depletion of Fe in MNF and the mass loading of both Ni and Fe decreased as prolonged CA measurements. After resting for 4 h, the average atomic ratio and mass loading recovered to some extent, and the distribution became narrower again. Subsequently, the same group revealed the dynamics of Fe incorporation in Ni hydroxide during OER process.[160] As shown in Figure 12i, the XFM mapping revealed an increased Fe concentration at the edge sites as the CV cycling increased to 50 cycles in Fe-containing electrolyte. More obvious changes of the Ni/(Ni+Fe) ratio were observed after CA measurement at 1.6 V compared to that after CV cycling conducted at 1.03−1.73 V vs RHE. This result implied that the Fe incorporation mainly occurs at OER reactive potential, with drastic transformation of the electrochemical interface.

3.5. Electron Microscopy Characterizations

The electrochemical reconstruction of an electrocatalyst is generally companied by the change of surface properties, such as the morphology, composition, and roughness, which can be detected using electron microscopy, including scanning electron microscopy (SEM) and transition electron microscopy (TEM).

3.5.1. Scanning Electron Microscopy. Scanning electron microscopy (SEM) is conducted by scanning the surface of sample with a focused beam of electrons. The interaction between electrons and atoms in the sample produces various signals that contain the surface topography, along with compositions of the sample. The reconstruction can be observed by analyzing the SEM images before and after electrocatalytic processes. For instance, Yang and coworkers used SEM to observe the HER-induced surface reconstruction of a Cu−Fe_3O_4 electrocatalyst.[145] As shown in Figure 13a, the as-prepared Cu−Fe_3O_4 exhibited a nanosheets-assembled morphology with an average thickness of about 1 μm. After electrochemical activation at −0.12 V vs RHE in 1.0 M KOH for 20 h, the resulting Cu−Fe_3O_4-20 featured a newborn

https://doi.org/10.1021/acs.chemrev.3c00332
Chem. Rev. 2024, 124, 3694−3812

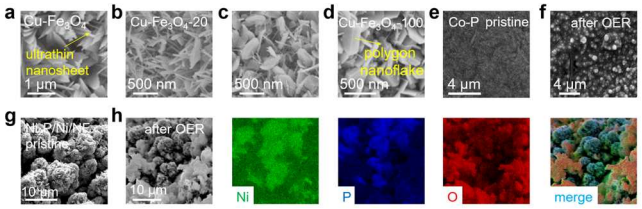

Figure 13. SEM images of (a) pristine Cu−Fe_3O_4, (b) Cu−Fe_3O_4-20, (c) Cu−FeOOH−Fe_3O_4, and (d) Cu−Fe_3O_4-100. Reproduced with permission from ref 145. Copyright 2022 Wiley-VCH. SEM images of Co−P film (e) before and (f) after OER. Reproduced with permission from ref 266. Copyright 2015 John Wiley and Sons. SEM images of Ni_2P/Ni/NF (g) before and (g) after OER along with the corresponding elemental mapping images. Reproduced with permission from ref 227. Copyright 2016 American Chemical Society.

polygon nanoflakes morphology with dwindled nanosheets (Figure 13b). These polygon nanoflakes were identified as Cu-FeOOH/Fe_3O_4, which subsequently became the main one accomplished with gradual disappearance of original nanosheets after 50 h activation (Figure 13c). Further prolonging the activation time to 100 h, the microstructure of the resulting Cu−Fe_3O_4-100 remained almost unchanged (Figure 13d).

Compared to the HER-induced reconstruction discussed above, the OER-triggered counterpart is more common and it was discovered by SEM earlier. We previously explored the morphologic change of Co−P and Ni_2P/Ni/NF bifunctional electrocatalysts before and after long-term OER process.[227,266] As shown in Figure 13e and f, the pristine Co−P demonstrated a homogeneous and smooth surface, in stark contrast to the large nanoparticle-aggregated microstructure of the post-OER sample.[266] Similarly, we found that the urchin-like microparticle superstructures with numerous nanosheets (Figure 13g) of pristine Ni_2P/Ni/NF are partially converted to featureless monoliths (Figure 13h) after a 20 h OER test at 10 mA cm^{-2} (post-OER Ni_2P/Ni/NF).[227] Moreover, elemental mapping results (Figure 13h) uncovered the large concentrations of O over these featureless monoliths, suggesting the oxidative reconstruction of Ni_2P/Ni/NF during OER.

3.5.2. Transmission Electron Microscopy. Transmission electron microscope (TEM) forms the images by transmitting accelerated and focused electron beam crossing the specimen. In comparison to SEM technique, TEM is capable to detect the surface evolution and inner structure.[157,281] For instance, Hu's group used ex situ high-resolution TEM (HRTEM) to probe the surface reconstruction of Ni_2P after OER in alkaline electrolyte (1.0 M KOH) at 1.5 V vs RHE for 1 h.[282] As depicted in Figure 14a, the HRTEM image of post-OER Ni_2P exhibited the appearance of numerous small nanoparticles in the outer layer with an average size of 2−3 nm and low crystallinity. The lattice spacings of the outer and inner layers were ascribed to nickel oxides/hydroxides species and Ni_2P, respectively. This core−shell Ni_2P/NiO_x structure was further confirmed by the elemental mapping images, at which surface-rich oxygen was observed (Figure 14b).

In order to reveal the dynamically structural and composition transformation of $(NiCo)S_{1.33}$ particles, Xi and coworkers employed in situ electrochemical TEM to directly observe the sulfur−oxygen exchange.[151] As shown in Figure 14c and d, when the potential of 0.9 V (vs Pt pseudoreference) was applied for 21 s in 0.1 M KOH, the hydroxide intercalation induced the formation of a new shell on the surface of the particles, resulting in a 14 nm increase in diameter. The average thickness of the hydroxide shell increased from 27.75 to 57.00 nm in two seconds (24−26 s) accompanied by the increase of overall diameter from 582.6 to 597.3 nm, indicating the gradually intensified reconstruction during OER. As prolonging the time, the reconstruction continued until to 32 s to reach a stable state with a shell thickness of 127.1 nm. In addition, the authors also revealed a more detailed insight into the surface reconstruction of $(NiCo)S_{1.33}$ by conducting in situ

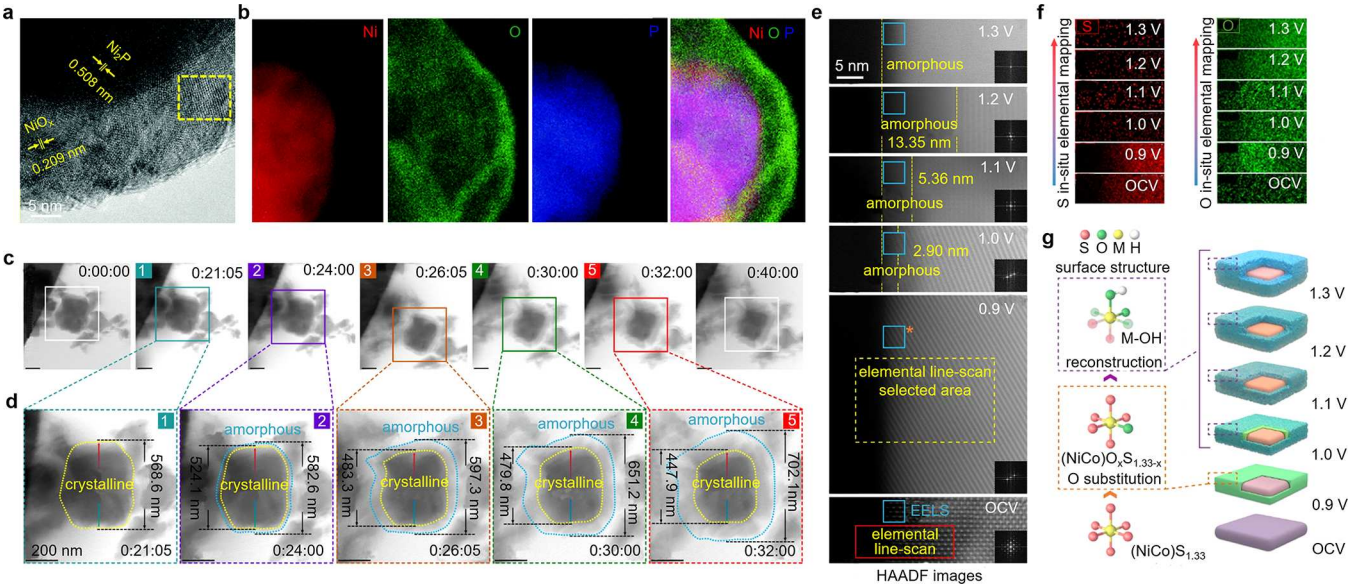

Figure 14. (a) HRTEM image of post-OER Ni_2P and (b) corresponding elemental mapping images. Reproduced from ref 282. Copyright 2015 Royal Society of Chemistry. (c, d) In situ TEM images of $(NiCo)S_{1.33}$ under 0.9 V. (e) In situ atomic HAADF images of $(NiCo)S_{1.33}$ after constantly applying different potentials for 20 s. (f) In situ elemental mapping images of S and O under different applied potentials. (g) Schematic diagram of lattice sulfur−oxygen substitution process. Reproduced from ref 151 under the terms of the CC-BY 4.0 license. Copyright 2023 The Authors, published by Springer Nature.

https://doi.org/10.1021/acs.chemrev.3c00332
Chem. Rev. 2024, 124, 3694−3812

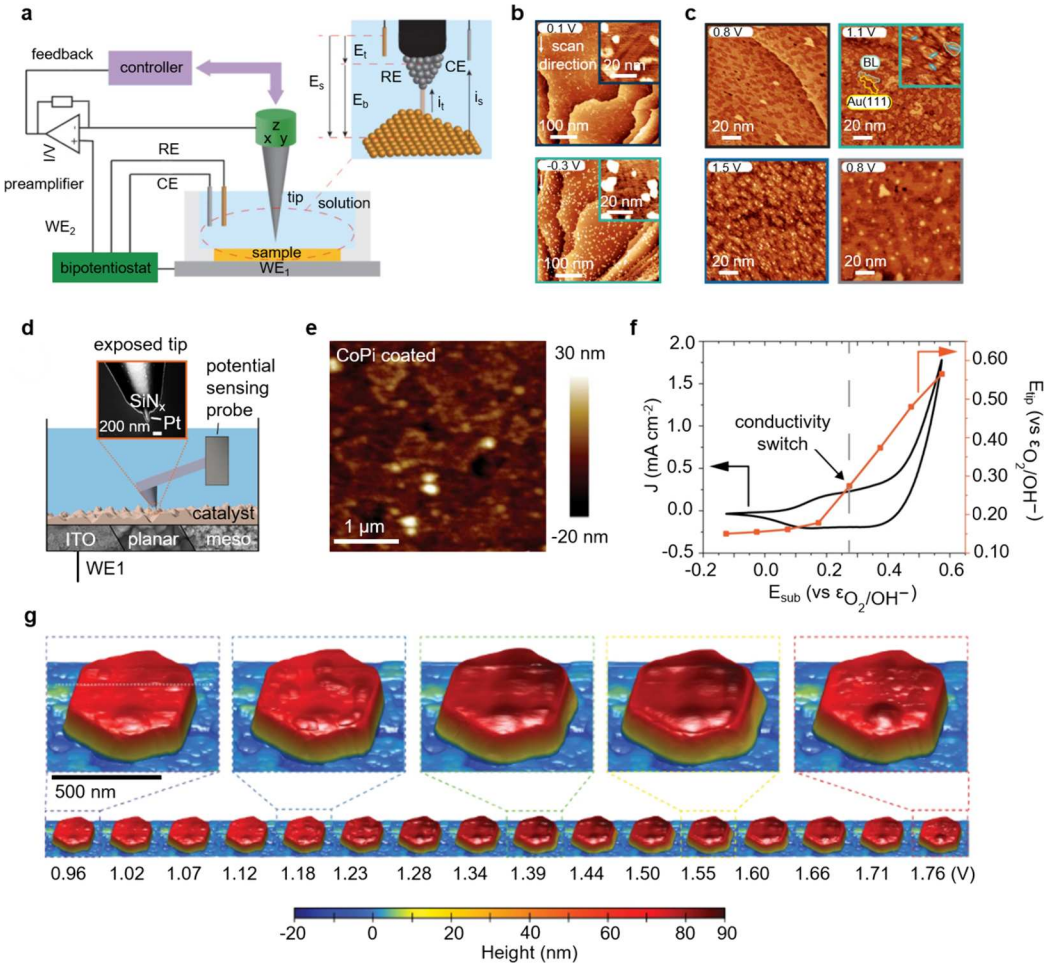

Figure 15. (a) Schematic of EC-STM. Reproduced from ref 286. Copyright 2023 Elsevier. (b) EC-STM images of cobalt oxide NIs measured at 0.1 V and −0.3 V vs RHE. (c) EC-STM images of cobalt oxide NIs measured at 0.8 V, 1.1 V, 1.5 and 0.8 V vs RHE. Reproduced from ref 287. Copyright 2021 John Wiley and Sons. (d) Potential-sensing electrochemical AFM setup with the cantilever, fully electrically insulated except for the exposed nanotip, serving as a potential probe. (e) AFM topographic image of CoPi-coated ITO surface. (f) Potential-step experiments performed in 0.1 M aqueous potassium phosphate. Reproduced from ref 291. Copyright 2017 Springer Nature. (g) EC-STM topography of a β-Co(OH)$_2$ particle in 0.1 M KOH at different applied potentials. Reproduced from ref 163. Copyright 2021 Springer Nature.

atomic HAADF imaging. After constantly applying different potentials (0.9−1.3 V vs Pt pseudoreference) for 20 s, the in situ HAADF images (Figure 14e) of (NiCo)$S_{1.33}$ showed intensified surface reconstruction (amorphous regions) with increasing potential anodically. The corresponding elemental mapping along with extracted elemental distribution curves (Figure 14f,g) at 0.9 V revealed the progressive replacement of S by O to form the S−O coexisting phase in the sulfide lattice. Combined with electron energy loss spectroscopy (EELS) based on the inelastic scattering between incident electrons with specimens,[283] a more detailed analysis of atomic electronic environment of oxygen could be obtained to expound the lattice sulfur−oxygen exchange process (Figure 14g). Under 0.9 V where (NiCo)$S_{1.33}$ particle maintained the crystal structure without any reconstruction behavior, three peaks of the in situ EELS of O K-edge can be assigned to the hybridization of O 2p with Co 3d, Ni 3d, and Co 4sp orbitals, respectively, confirming the substitution of O for S in (NiCo)$S_{1.33}$ and the formation of ionic bonds between O and Co/Ni atoms. As the surface reconstruction proceeded, the dissociation of the surface crystal structure induced the bond breaking of Co−O and Ni−O, as evidenced by the presence of peak assignable to the characteristic oxygen in an amorphous structure.

3.6. Scanning Probe Microscopy

In situ/operando scanning probe microscopy (SPM) that utilizes the interaction between a scanning tip and surface can obtain local surface/interface structure information at atomic scale under real conditions with high spatial resolution and temporal sensitivity, making it powerful to study the dynamic electrochemical reconstruction.[284,285] SPM represents a family of techniques; it typically includes scanning tunneling microscopy (STM), atomic force microscopy (AFM), scanning electrochemical microscopy (SECM), and scanning electrochemical cell microscopy (SECCM).

3.6.1. Scanning Tunneling Microscopy. Electrochemical STM (EC-STM) uses a sharp metallic tip as the probe to scan over a conducting sample and the corresponding tunneling current (i_t) is detected for positional feedback (Figure 15a), providing local structural properties at the electrified solid−liquid interface with high-resolution.[284−286] Generally, EC-STM is operated using the constant current mode at which E_b is fixed, and E_t and E_s are changed simultaneously. When the slightly polarized tip is scanned close to the underlying

https://doi.org/10.1021/acs.chemrev.3c00332
Chem. Rev. 2024, 124, 3694−3812

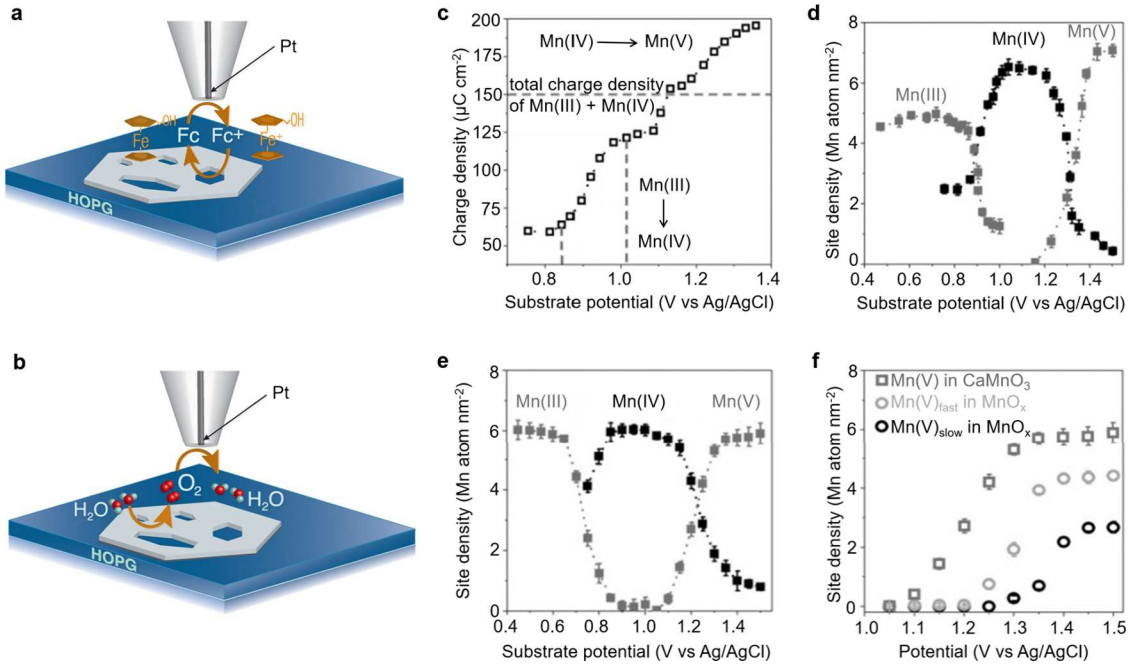

Figure 16. Schematic of SECM with (a) positive feedback produced by oxidation/reduction of ferrocenemethanol (Fc) and (b) substrate generation/tip collection of dioxygen at NiO nanosheet. Reproduced with permission from ref 293. Copyright 2019 PNAS. Surface interrogation-SECM measured (c, e) integrated charge density plotted against substrate potential for (c) MnO_x and (e) $CaMnO_3$, and (d) plots of site density of Mn(III), Mn(IV), and Mn(V) for MnO_x, as well as (f) plots of site density of Mn^V in $CaMnO_3$, Mn^V_{fast} in MnO_x, and Mn^V_{slow} in MnO_x. Reproduced with permission from ref 162. Copyright 2020 John Wiley and Sons.

conductive sample with a distance in the atomic range, the i_t is initiated. Then the vertical distance (z) between the tip and sample is dynamically adjusted using the feedback loop to keep i_t constant at each lateral point (x, y) of the conductive sample. The insulation layer of the tip is used to deconvolute the tunneling current from the Faradaic process.

In this way, Brummel and coworker investigated the structural dynamics of cobalt oxide nanoislands (NIs) during both HER and OER by EC-STM.[287] In the potential region of HER, a coated PtIr tip was employed, and the tip was kept constant at 0.5 V vs RHE with a tunneling current of 0.8 nA. At 0.1 V vs RHE, numerous bilayers (BL) NIs were presented on the surface (Figure 15b). Small aggregates with an apparent height of 3.0 Å corresponding to double-bilayer (DL) NIs then formed at the potential of 0.0 V vs RHE. Further decreasing the potential to −0.3 V vs RHE, an additional type of island formed with an apparent height of 5.6 Å, corresponding to 3 atomic layers of metallic cobalt (Figure 15b). When scanning the potential back to 0.2 and 0.8 V vs RHE, the islands of both metallic cobalt and DL dissolved, with only few residues of BL NIs on the surface. These results suggested that cobalt oxide NIs are highly dynamic at the onset of reduction of Co^{3+} to Co^{2+} and below, wherein restructuring, dissolution, and redeposition processes occurred during HER. In the potential region from OCP to OER, the W-tip was kept constant at 0.35 V vs RHE with a tunneling current of 0.1 nA (Figure 15c). At 1.1 V vs RHE, the striped features oriented in hexagonal symmetry on the top of the DL NIs were observed and the apparent height was calculated to be 3.1 Å. Further increasing potential to 1.5 V vs RHE, round features distributed over the whole surface appeared. After keeping at 1.8 V vs RHE for 20 min and switching back to 0.8 V vs RHE, additional small islands with an apparent width of 2 to 5 nm and an apparent height of 2.4 Å can be observed, in stark contrast to that at the same potential before positive potential scanning. The surface morphology reconstruction was ascribed to the oxidation of cobalt and gold species during OER.

Recently, Zhang and coworkers directly observed the dynamic reversible reconstruction of $LaNiO_3$ (LNO) during OER process by EC-STM.[288] The EC-STM images revealed that the surface reconstruction-induced potential-dependent and revisible change of the mean height (0.76 → 2.71 → 0.79 nm) for Ni-rich terminated LNO was ascribed to the redox reaction of the Ni component (β-$Ni(OH)_2$ ↔ NiOOH).[288]

3.6.2. Atomic Force Microscopy. One limit of EC-STM is that only conductive samples can be analyzed. In contrast, the electrochemical atomic force microscopy (EC-AFM) utilizes tip−sample force interactions instead of their tunneling current, so that a wider variety of samples including insulators can be studied.[289,290] Boettcher and collaborators demonstrated a contact-based potential-sensing EC-AFM for operando measurement of the surface electrochemical potential in heterogeneous electrochemical system during OER.[291] In their experiment, the force feedback was applied to control tip−substrate interaction through cantilever deflection, allowing a stable electrical connection between the substrate and the potential-sensing tip of AFM nanoelectrode (Figure 15d). When the tip was brought to contact with the cobalt (oxyhydroxide) phosphate (CoPi) deposited ITO substrate, the corresponding surface can be mapped (Figure 15e). At the substrate potential (E_{sub}) of below 0.2 V vs the OER thermodynamic potential (ε_{O_2/OH^-}), the measured catalyst potential (E_{tip}) was almost unaffected (Figure 15f). By contrast, increasing the E_{sub} to 0.27 V vs ε_{O_2/OH^-} or more, the measured E_{tip} began closely tracking E_{sub}, consistent with the increase in conductivity due to oxidation of CoPi to Co (oxy)hydroxide (Figure 15f).

https://doi.org/10.1021/acs.chemrev.3c00332
Chem. Rev. 2024, 124, 3694−3812

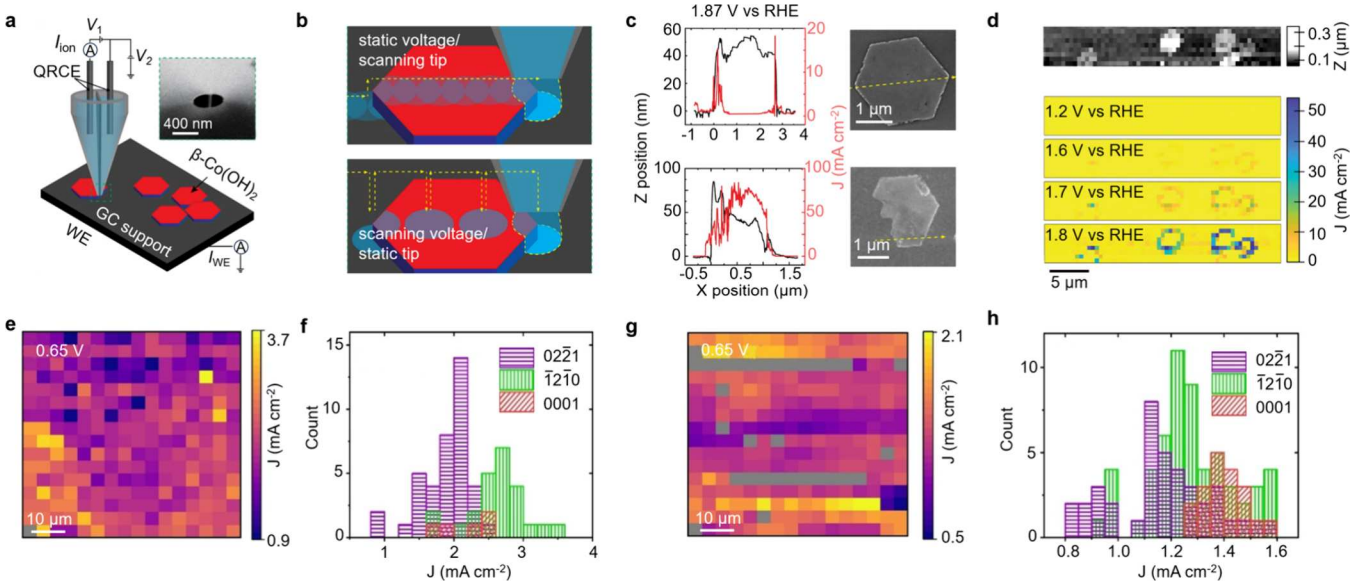

Figure 17. (a) Schematic of the SECCM technique. (b) Scanning-mode and hopping-mode SECCM. (c) Tip current density as a function of position in scanning constant height mode for β-$Co(OH)_2$ particles shown in the SEM images on the right. The scan direction was indicated by the dotted yellow arrows and the interrogation width was calculated to be approximately 400 nm. (d) Topography and local current density mapping images at different potentials. Reproduced with permission from ref 163. Copyright 2021 Springer Nature. (e) SECCM mapping image and (f) current density histogram of the 100-cycle microelectrode measured at 0.65 V vs Pt QRCE. (g) SECCM mapping image and (h) current density histogram of the as-polished Co microelectrode, plotted from the 2nd CV cycle. Reproduced with permission from ref 296 under the terms of a CC-BY 4.0 license. Copyright 2023 The Authors, published by John Wiley and Sons.

Similarly, Chueh and coworkers investigated the changes in particle morphology of β-$Co(OH)_2$ during OER by EC-AFM (Figure 15g).[163] The particle height increased by approximately 10% on average at 1.2 V vs RHE, similar to previously reported EC-AFM results for single-layer CoO_xH_y after cycling. This change in height was correlated with the lateral expansion of the particle and reached a maximum at the potential of 1.39 V vs RHE. Subsequently, the particle started contraction at ~1.58 V vs RHE and reached its initial dimension gradually.

3.6.3. Scanning Electrochemical Microscopy. Compared with EC-STM and EC-AFM, scanning electrochemical microscopy (SECM) can resolve the electrochemical reactivity at nanoscale, which uses an ultramicroelectrode tip as a working electrode in a cell equipped with counter and reference electrodes to scan the substrate surface. The electrochemical reactions at the tip, substrate, or both can be detected. Although SECM is developed based on STM, its operating principle depends on Faradaic current between the tip−substrate interaction.[284,285,292] Figure 16a and b showed two main operational modes of SECM, the feedback (FB) mode and generation/collection (G-C) mode.[293] In the FB mode, a reversible redox mediator is, for example, oxidized at the tip under positive potential. When the tip moves closes to a conductive substrate, the oxidized species generated at the tip can diffuse and be reduced back, leading to additional mediator flux to the tip and thus positive feedback (Figure 16a). In the G-C mode (Figure 16b), the generated electroactive species at a biased substrate/tip are detected and collected electrochemically at tip/substrate.

Bard's group employed surface interrogation SECM to analyze the surface kinetics of Ni^{4+} and Fe^{4+} in NiFe-based oxyhydroxides in an alkaline environment using Fe-based triethanolamine (TEA) complex as the redox mediator.[294] The unusually high densities of surface catalytic sites in these NiFe-based oxyhydroxides indicated that many bulk atoms are involved for OER via fast interlayer hole transfer. They also found that Ni^{4+} is indeed OER-inactive, while the dispersed Fe^{4+} in a NiOOH matrix is the highly active site for OER in $Ni_{1-x}Fe_xOOH$. After that, the same group also investigated the manganese oxidation state in amorphous MnO_x and perovskite $CaMnO_3$ during the OER by surface interrogation SECM (Figure 16c−f).[162] A current rise with increasing substrate potential from 0.8 to 1.0 V vs Ag/AgCl indicated the transformation of Mn^{3+} to Mn^{4+} (Figure 16c), while Mn^{4+} trace showed the increase of the tip current due to the reduction of Mn^{4+} intermediates. When pulsing the substrate potential to 1.16 V vs Ag/AgCl, the second rise of the charge density was larger than the total original charge density of Mn^{3+} and Mn^{4+}, implying the formation of Mn^{5+} during OER (Figure 16d). Similarly, the oxidation state of Mn in $CaMnO_3$ was also examined. As depicted in Figure 16e, the Mn^{5+} in $CaMnO_3$ can be generated above 1.1 V vs Ag/AgCl associated with OER, lower than that for amorphous MnO_x. Based on the time-delay titration of Mn^{5+} (Figure 16f), they found that the MnO_x possess two different sites with different reaction rate (1.21 and 0.24 s^{-1}), while the $CaMnO_3$ display only one kinetic behavior with a faster reaction rate (1.72 s^{-1}).

3.6.4. Scanning Electrochemical Cell Microscopy. Scanning electrochemical cell microscopy (SECCM) is a pipet-based tip technique to image surface with a lateral resolution at nanometer ranges.[295] In SECCM, the electrochemical cell is confined in a droplet (pipet), which combines with one or two back-inserted quasi-reference counter electrode(s) (QRCE) as the probe.[284,285] As shown in Figure 17a, the feedback signal is originated from the ionic current induced by applying a bias between the QRCEs and can be used to obtain height profile. Chueh and coworkers used SECCM to directly map the OER current and bulk redox transformations of β-$Co(OH)_2$ particles.[163] Both the scanning and hopping modes (Figure 17b) were used to collect

https://doi.org/10.1021/acs.chemrev.3c00332
Chem. Rev. 2024, 124, 3694−3812

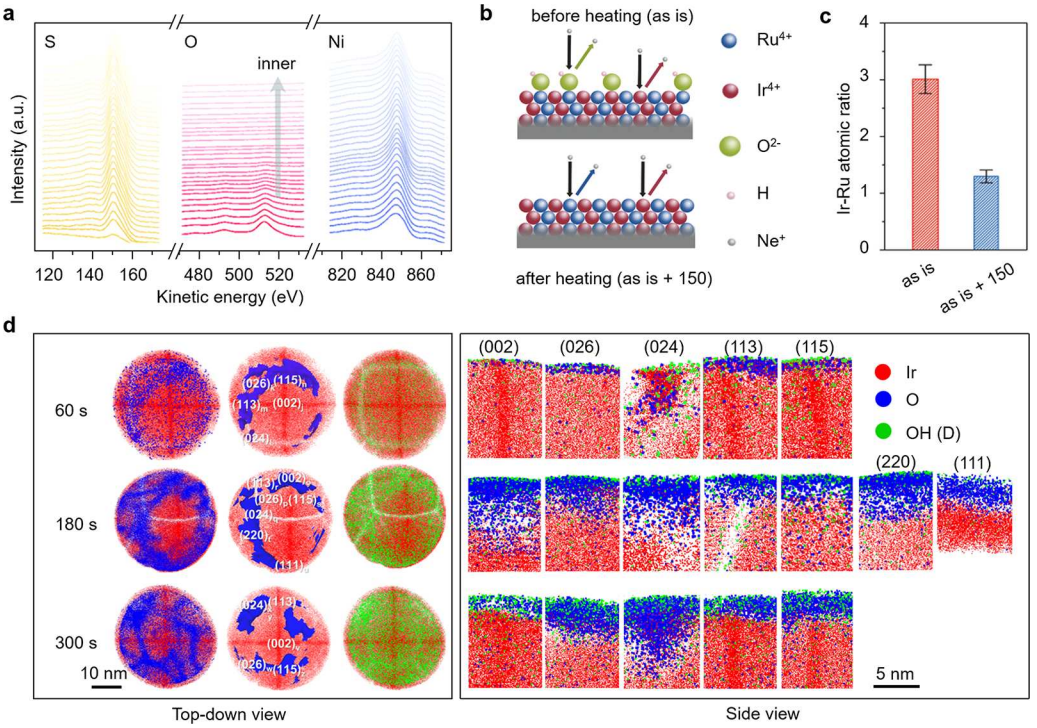

Figure 18. (a) Depth-profiling sulfur, oxygen, and nickel AES spectra of the Ni_3S_2 after OER. Reproduced with permission from ref 159. Copyright 2022 Royal Society of Chemistry. (b) Schematic of LEIS on probing the elemental compositions at the topmost surface of $Ru_xIr_yO_2$. (c) Ir/Ru atomic ratios of $Ru_xIr_yO_2$ ("as is") and after in situ heating at 150 °C in vacuum ("as is +150"), respectively. Reproduced with permission from ref 297. Copyright 2020 Science China Press and Springer-Verlag GmbH Germany, part of Springer Nature. (d) Top-down view and cross-sectional side view of APT reconstruction after anodic oxidation at 1.55 V vs RHE for 60, 180, and 300 s. Reproduced with permission from ref 298. Copyright 2023 John Wiley and Sons.

complementary information on the connection between local OER activity and bulk oxidation. The chronoamperometry at 1.87 V vs RHE was employed in the scanning mode, and the pipet was moved over the particles with a lateral translation rate of 30 nm s^{-1}. As shown in Figure 17c, the current was observed only at the edge of the particles, implying that the particle edge facets dominate the electrochemical reactivity of the system. In the hopping-mode at which electrolyte contact with the surface was broken and re-established during each step, the pipet was scanned across the particles and linear sweep voltammetry was performed at a scan rate of 1.0 V s^{-1} at each step. Simultaneous topographical (top) and voltammetric mapping (bottom) of the electrochemical response (Figure 17d) across the particles revealed the high electrochemical activity of particle edge facets relative to the basal planes again. The activity sites for OER were expected to be the oxidized phase of CoO_xH_y. In the progressive oxidation of layered β-$Co(OH)_2$, ion (de)intercalation was facilitated at the edge facets featuring adequate contact with electrolyte. By contrast, the restricted ion movement in the <0001> direction of the CoO_2 slabs prevented bulk redox transformation reactions from forming more conductive CoO_xH_y species.

Recently, Li and coworkers combined SECCM and electron backscatter diffraction (EBSD) to reveal the trend in OER activity across various facets of Co (oxy)hydroxides, along with reconstruction.[296] The SECCM mapping image of 100-cycle Co microelectrode (Figure 17e) was obtained by conducting chronoamperometry measurement at a fixed potential of 0.65 V vs a Pt QRCE during OER, and a distinct current difference can be observed for different facets. For instance, the (oxy)hydroxide formed on the $[\bar{1}2\bar{1}0]$-oriented Co facet exhibited higher current response than that from $[02\bar{2}1]$-oriented Co (Figure 17f). Additionally, the correlative EBSD-SECM measurements on the as-polished Co microelectrode showed that [0001]-oriented Co facet features higher currents than $[02\bar{2}1]$-orientated Co facet after one cycle of SECCM test (Figure 17g,h).

3.7. Other Characterizations

In addition to the above characterization techniques, several other methods could also be used to identify the electrochemical reconstruction during water splitting. These advanced techniques include Auger electron spectroscopy, ion scattering spectroscopy, atom probe tomography, Mössbauer spectroscopy, and mass spectrometry.

Similar to XPS, Auger electron spectroscopy (AES) is another sensitive surface-analysis technique and can be used to identify the specific element. The incident electron or X-ray interacts with sample and excites an electron in the inner layer to form a hole. The energy release during the transition of the outer electron at higher energy level to inner hole excites another electron to form free electron named as the Auger electron, and the kinetic energy of Auger electron is independence of the incident radiation/electron.[265] Zhang and coworkers conducted AES depth-profiling to analyze the surface oxidative reconstruction of Ni_3S_2 after OER (Figure 18a).[159] With increasing surface etching, the sulfur content gradually increased from 6.1 to 23.2 at% and became stable, while the O content reduced from 49.8 to 0 at%, collectively confirming the core−shell structural elemental distribution and the formation of the surface oxysulfide.

https://doi.org/10.1021/acs.chemrev.3c00332
Chem. Rev. 2024, 124, 3694−3812

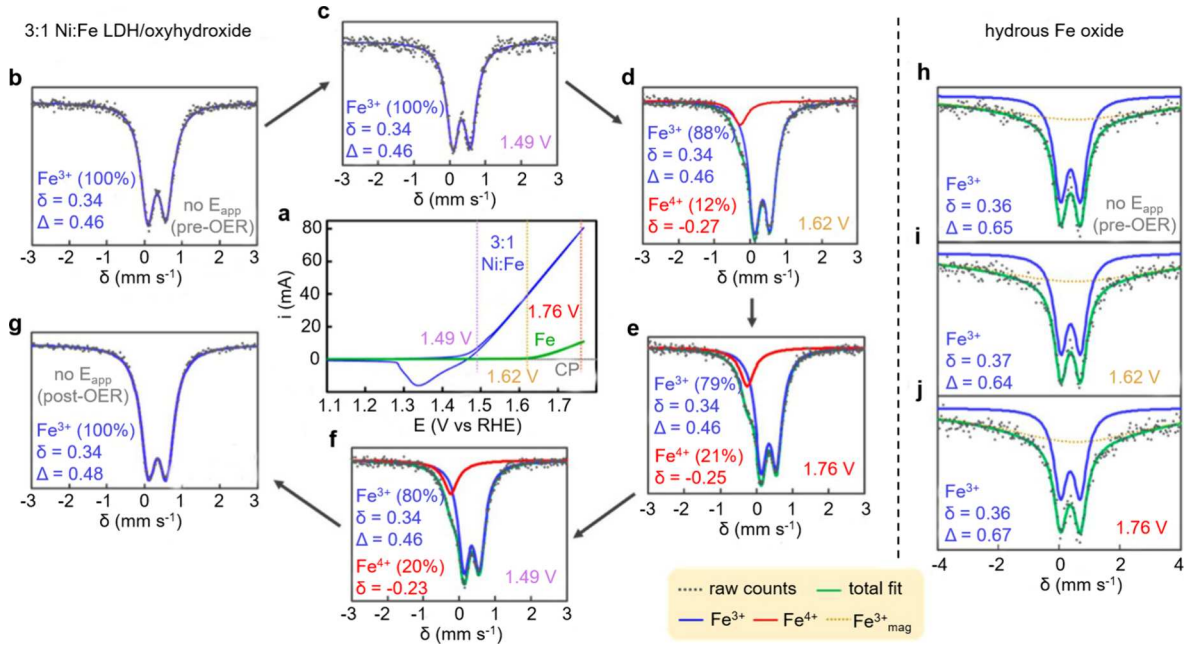

Figure 19. (a) CV curves of 3:1 Ni:Fe LDH/oxyhydroxide (blue), hydrous Fe oxide (green), and carbon paper (CP). Operando Mössbauer spectra of 3:1 Ni:Fe LDH/oxyhydroxide collected at potentials cycling from (b) open circuit, (c) 1.49 V, and (d) 1.62 V, to (e) 1.76 V, and then back to (f) 1.49 V and (g) open circuit vs RHE. Operando Mössbauer spectra of hydrous Fe oxide collected at potentials from (h) open circuit to (i) 1.62 and (j) 1.76 V vs RHE. Reproduced with permission from ref 301. Copyright 2015 American Chemical Society.

Ion scattering spectroscopy, also known as low-energy ion scattering (LEIS) is also a powerful technique to analyze the elemental composition of the outermost atomic layer of a material. Peng and collaborators, for example, conducted the LEIS measurement to quantify the adsorbed oxygen species on the surface Ru or Ir sites of $Ru_xIr_yO_2$ for OER on the basis of the variations in Ru and Ir signal intensities (Figure 18b,c).[297] After in situ heating at 150 °C in vacuum, Ir/Ru atomic ratio at topmost atomic layers of $Ru_xIr_yO_2$ decreased from 3.01 to 1.30, different from the unchanged Ir/Ru ratio in bulk. This result suggested the higher amount of oxygen species released from the surface Ru sites than from the surface Ir sites.

Atom probe tomography (APT) relies on ionization and subsequent field evaporation of individual atoms/clusters from a specimen surface. It is a nanoscale analysis technique that can provide three-dimensional spatial imaging with high sensitivity. To examine the effect of surface orientations on the formation of oxide species of Ir electrode during OER, Li and coworkers prepared the Ir APT sample by electropolishing of Ir wire and conducted the APT analysis (Figure 18d).[298] After anodic oxidation at 1.55 V vs RHE for 60 s, the oxides with high coverage on (024), (026), (113), and (115) planes as indicated by the O iso-concentration surfaces (blue) were observed (top-down view), along with the formation of uniform hydroxy groups (green) on the Ir tip surface (top-down view). The corresponding cross-sectional side view images revealed thin oxides layers on (002), (026), (113), and (115) planes (2−6 atoms) and a relatively thick oxide layer (6 nm) on (024) plane. As the time prolonged to 180 s, more oxides were selectively grown on (026), (024), (220), and (111) planes as well as step edges of the (002) plane (top-down view), along with increased layer thickness (side view). Further increasing the time to 300 s, the tip surface of Ir was fully oxidized with most obvious growth on the (026), (024), (113), and (115) planes. Remarkably, the thickness of the oxides on (113) and (115) planes was still thin (2−3 nm, side view), in contrast to that on (024) and (026) planes (6−10 nm). These results clearly demonstrated the surface orientation-dependent oxidative reconstruction of Ir during OER. Recently, Li and coworkers also employed APT analysis to investigate the structure−activity relationships of various faceted β-CoOOH formed on a Co microelectrode under OER conditions.[296]

Mössbauer spectroscopy is based on the recoilless nuclear resonance emission and absorption of γ- rays by specific nuclei and is a powerful technique to investigate the evolution of coordination symmetry, oxidation state, electron spin state, and magnetic information on active sites, of which ^{57}Fe centers are the most widely explored in various elements.[299,300] Three primary parameters related to Mössbauer spectroscopy, the isomer shift (δ), the quadrupole splitting (Δ), and the magnetic hyperfine field (B), depict the valence/spin state, electronic symmetry, and magnetic structure of the atomic nuclei, respectively. Stahl and coworkers conducted operando Mössbauer measurements to analyze the role of Fe in NiFe layered oxyhydroxide (^{57}Fe-enriched hydrous Fe oxide and 3:1 Ni:Fe LDH/oxyhydroxide).[301] As shown in Figure 19a, CV curves were collected in the operando cell prior to Mössbauer tests. The initial Mössbauer spectroscopy (Figure 19b) of 3:1 Ni:Fe LDH/oxyhydroxide under OCP showed a doublet with a δ of 0.34 mm s^{-1} and a Δ of 0.46 mm s^{-1}, corresponding to the high-spin and Jahn−Teller-distorted Fe^{3+} species. No change was observed at the potential of 1.49 V vs RHE (Figure 19c). Upon applying a potential of 1.62 V vs RHE (significant OER), a shoulder emerged at $\delta = -0.27$ mm s^{-1} was identified as Fe^{4+} species, and the intensity reflected that approximately 12% of Fe^{3+} is oxidized to Fe^{4+}(Figure 19d). The content of Fe^{4+} increased to 21% when the potential increased to 1.76 V vs RHE (Figure 19e) and maintained at 20% even when the potential dropped back to 1.49 V vs RHE (Figure 19f). The oxidized Fe peak finally disappeared after keeping the post-OER sample for 48 h in the absence of applied potential

https://doi.org/10.1021/acs.chemrev.3c00332
Chem. Rev. 2024, 124, 3694−3812

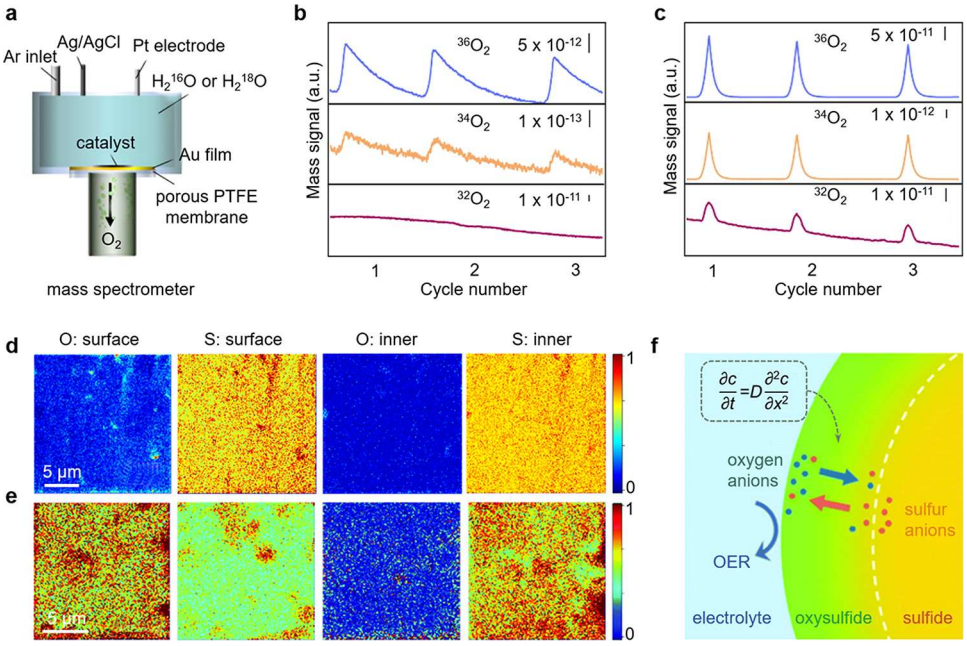

Figure 20. (a) Schematic of the operando DEMS. DEMS signals of O_2 products for (b) 4Ru/MnO_2 and (c) 12Ru/MnO_2 in the electrolyte using $H_2{}^{18}O$ as the solvent during three times of LSV in the potential range of 1.17−1.72 V vs RHE. Reproduced from ref 307. Copyright 2021 Springer Nature. TOF-SIMS mapping images of sulfur and oxygen on the surface (left) and on the inner layer (right) of the Ni_3S_2 electrocatalyst (d) before and (e) after OER. (f) Schematic of structural reconstruction of the Ni_3S_2 during OER process. Reproduced with permission from ref 159. Copyright 2022 Royal Society of Chemistry.

(Figure 19g). By comparison, the Mössbauer spectroscopy of ^{57}Fe-labeled hydrous Fe oxide did not signify the formation of Fe^{4+} species (Figure 19h−j), reflecting the influence of the second-coordination-sphere metal ions. Additionally, the larger quadrupole splitting suggested the Fe sites have a more-distorted geometry in the Fe-only electrocatalyst. These data provided the direct evidence of OER reconstruction and the formation of Fe^{4+} for 3:1 Ni:Fe LDH/oxyhydroxide.

Differential electrochemical mass spectrometry (DEMS) shows a unique superiority in the qualitative and quantitative analysis of products during electrocatalysis process and the dissolved ions of electrocatalysts (if any), which can be used to indirectly identify the electrochemical reconstruction.[302−306] Lee and coworkers demonstrated the dynamic cation exchange of Ru-atom-array patches supported on α-MnO_2 with Ru mass loading of 11.6 wt % (12Ru/MnO_2) during OER following the oxide path mechanism (OPM) by operando isotope labeling DEMS (Figure 20a−c).[307] The DEMS signals of produced O_2 for 4Ru/MnO_2 (Ru single atoms) and 12Ru/MnO_2 were collected in the $H_2{}^{18}O$ electrolyte during three times of LSV (1.17−1.72 V vs RHE). The 4Ru/MnO_2 produced only $^{34}O_2$ and $^{36}O_2$ (Figure 20b), while the 12Ru/MnO_2 steadily produced $^{32}O_2$, $^{34}O_2$ and $^{36}O_2$ (Figure 20c). The presence of $^{32}O_2$ implied the direct coupling of $^{16}O_{ads}$ (surface oxygen adsorbates) on neighboring Ru sites and thus the OPM over 12Ru/MnO_2 for OER. After washing with abundant $H_2{}^{16}O$, the $^{36}O_2$ products can be also detected during 12Ru/MnO_2-catalyzed OER in the $H_2{}^{16}O$-contained electrolyte, confirming the OPM pathway again. Similarly, Hou and coworkers used the in situ DEMS to observe an irreversible reconstruction behavior accompanied by copper dynamic evolution for Cu_2S/CoFe LDH during OER and they verified the oxygen-vacancy-site mechanism (OVSM) pathway.[156] Additionally, secondary ion mass spectroscopy (SIMS), as a sensitive surface-analysis technique, is also employed to determine electrochemical reconstruction. Typically, SIMS is conducted by sputtering of a specimen with an ion beam and the ejected secondary ions are analyzed subsequently by MS. To prove the sulfide-oxysulfide core−shell structure after surface reconstruction of Ni_3S_2 during OER, Zhang and collaborators selected time-of-flight SIMS (TOF-SIMS) to characterize the element depth-profiling.[159] As shown in Figure 20d, the pristine Ni_3S_2 demonstrated similar sulfur-rich and oxygen-free element composition on both the surface and the inner layer. By contrast, the post-OER Ni_3S_2 exhibited decreased oxygen signal and increased sulfur signal after depth etching (Figure 20e), confirming the OER-triggered surface oxidative reconstruction of Ni_3S_2 toward the unique sulfide-oxysulfide core−shell structure (Figure 20f). At the end, we have summarized the working principle and capability of the relevant characterization techniques in Table 3.

4. BIFUNCTIONAL ELECTROCATALYSTS FOR OVERALL WATER SPLITTING

Water splitting proceeds through two half-reactions with a thermodynamic potential of 1.23 V: the hydrogen evolution reaction (HER) and the oxygen evolution reaction (OER).[32,308] In order to improve the energy conversion efficiency for hydrogen generation, electrocatalytic water splitting is usually conducted in either acidic or alkaline solution to reduce solution resistance, and advanced electrocatalysts like Pt-based materials for HER and Ru/Ir-based oxides for OER are used to accelerate the reaction kinetics.[309] Generally, OER with four-electron transfer needs higher overpotentials than two-electron HER even catalyzed by commercial RuO_2 and IrO_2 benchmarks,[43,310] accountable for the main electricity consumption. Based on the Nernst equation, alkaline conditions are favorable to OER and acidic

https://doi.org/10.1021/acs.chemrev.3c00332
Chem. Rev. 2024, 124, 3694−3812

Table 3. Summary of Working Principle, Signal Acquisition, and Capability of the Relevant Characterization Techniques

Techniques	Working principle	Signal acquisition	Capability
FTIR	absorption of incident infrared photons by samples	transmission or reflection infrared photons	chemical bonds and groups
Raman	inelastic scattering of incident photons with samples	scattered photons (transmission or reflection)	chemical bonds and groups
UV−vis	absorption of UV and visible light by molecules or ions of substances	transmission UV and visible lights photons	composition, content, and structure
XRD	elastic scattering of incident X-ray and interfering of secondary X-ray with each other to produce specific diffraction	scattered and interfered X-rays	phase structure and crystal size
XPS	inelastic scattering of incident X-ray photons with samples	photoelectrons	elemental composition and chemical valence states
XAS	absorption of incident X-ray photons by samples	secondary electrons, fluorescence, transmission photons	electronic state/coordination environment
XES	emission of secondary X-ray photons excitated by incident X-rays	emitted X-ray photons	charge/spin state, ligand properties, and symmetry
XRF	excitation of elemental characteristic X-ray photons by incident monochromatic X-rays	fluorescence X-ray photons	composition, distribution, and chemical state
SEM	interaction between incident electron beam and specimen	backscattered electrons, secondary electrons	surface morphology
TEM	interaction between incident electron beam and specimen	transmission electrons	surface morphology and hyperfine structure
STM	detecting the tunneling current between the probe and sample surface for positional feedback	tunneling current	imaging topography and electronic structure, in situ/operando investigating interfacial evolution, quantifying local activity
AFM	detecting the interactive forces between the tip and sample	physical or chemical force	mapping topography and local work function, in situ/operando investigating interfacial evolution
SECM	detecting Faradaic current of a redox mediator between the tip and substrate	Faradaiccurrent	quantitatively detecting reaction products and studying reaction kinetics, mapping surface reactivity
SECCM	detecting the feedback signal (ionic current/Faradaic current) induced by applying a bias between the QRCEs	ionic current, Faradaic current	mapping local reactivity
Mössbauer Spectroscopy	the recoilless nuclear resonance emission and absorption of γ-rays by specific nuclei	transmission and backscattered γ-rays	oxidation state, electron spin configuration, symmetry and magnetic information
DEMS	deflection of moving ions by electric and magnetic fields	mass-to-charge ratio	qualitative and quantitative detection of volatile products or intermediates
SIMS	detecting secondary ions produced from the incident primary ions with specimen	secondary ions	surface element and structure makeup
AES	Auger effect	Auger electrons	surface element and structure makeup
LEIS	elastic collision of noble gas ions with the outmost atomic layers of a sample	backscattered ions	surface element and structure makeup

electrolytes are conducive to HER. Consequently, most of the early research focuses on developing high-performance HER or OER electrocatalysts in acidic or alkaline electrolytes, respectively,[311−315] while such a difference of electrolytes is not suitable for practical water electrolysis, wherein the same electrolyte at both cathode and anode is preferred. Although recent studies have developed alkaline HER electrocatalysts[316−318] or acidic OER electrocatalysts to couple with counter electrodes for overall water splitting (OWS),[90,319] different precursors, equipment, and/or procedures are needed to separately synthesize and assemble them due to their single functionality. In this regard, developing bifunctional electrocatalysts with both HER and OER activities in the same electrolyte are particularly desirable for practical applications, as it would simplify the electrocatalysts synthesis, electrodes fabrication and thus reduce the overall cost.[320] Moreover, bifunctional electrocatalysts with the same composites would alleviate the cross-contamination issue due to the electrochemical reconstruction of electrocatalysts during long-term operation.

Currently, the bifunctional electrocatalysts for acidic OWS with decent activity and stability are still limited to noble metal Ru and Ir. Their high price and scarcity significantly prohibit the large-scale commercialization.[321,322] The prevailing strategies in this field is disentangling the activity-cost trade-off. On the other hand, for the alkaline OWS, numerous nonprecious metal-based materials have been explored as bifunctional electrocatalysts.[32,33] In this section, we review the relevant progress on synthesis of various bifunctional electrocatalysts for OWS in acidic and alkaline electrolytes based on noble metals, nonprecious metals, and metal-free nanocarbons.

4.1. Overall Water Splitting in Acidic Electrolytes

With compact design, fast response, ultrahigh hydrogen purity, and superior stability toward loading-cycling and shutdowns,[75] acidic water electrolysis based on PEM has received much attention. One of the most challenges in this field is how to develop high performance and cost-effective bifunctional electrocatalysts.

4.1.1. Ru-Based Electrocatalysts. Ruthenium (Ru) has garnered considerable attention compared to other platinum group metals due to its relative cost-effectiveness, moderate binding with reactive intermediates, and decent corrosion resistance.[323−325] To improve the atomic utilization, Ru-based nanoparticles are usually employed.[326] To further improve their electrocatalytic HER and OER activities, as well as inhibit the peroxidation during OER,[75,327−329] various nanostructuring strategies have been reported.

Zhang and coworkers employed the interfacial engineering to prepare a heterostructure of oxygen vacancy-rich subnanometer RuO_2 skin integrated with interconnected Ru clusters on a carbon hybrid microsheet (Ru@V-RuO_2/C HMS) through controlled thermal treatment of Ru/C microsheet (Figure 21a).[330] HRTEM and aberration corrected HAADF-

https://doi.org/10.1021/acs.chemrev.3c00332
Chem. Rev. 2024, 124, 3694−3812

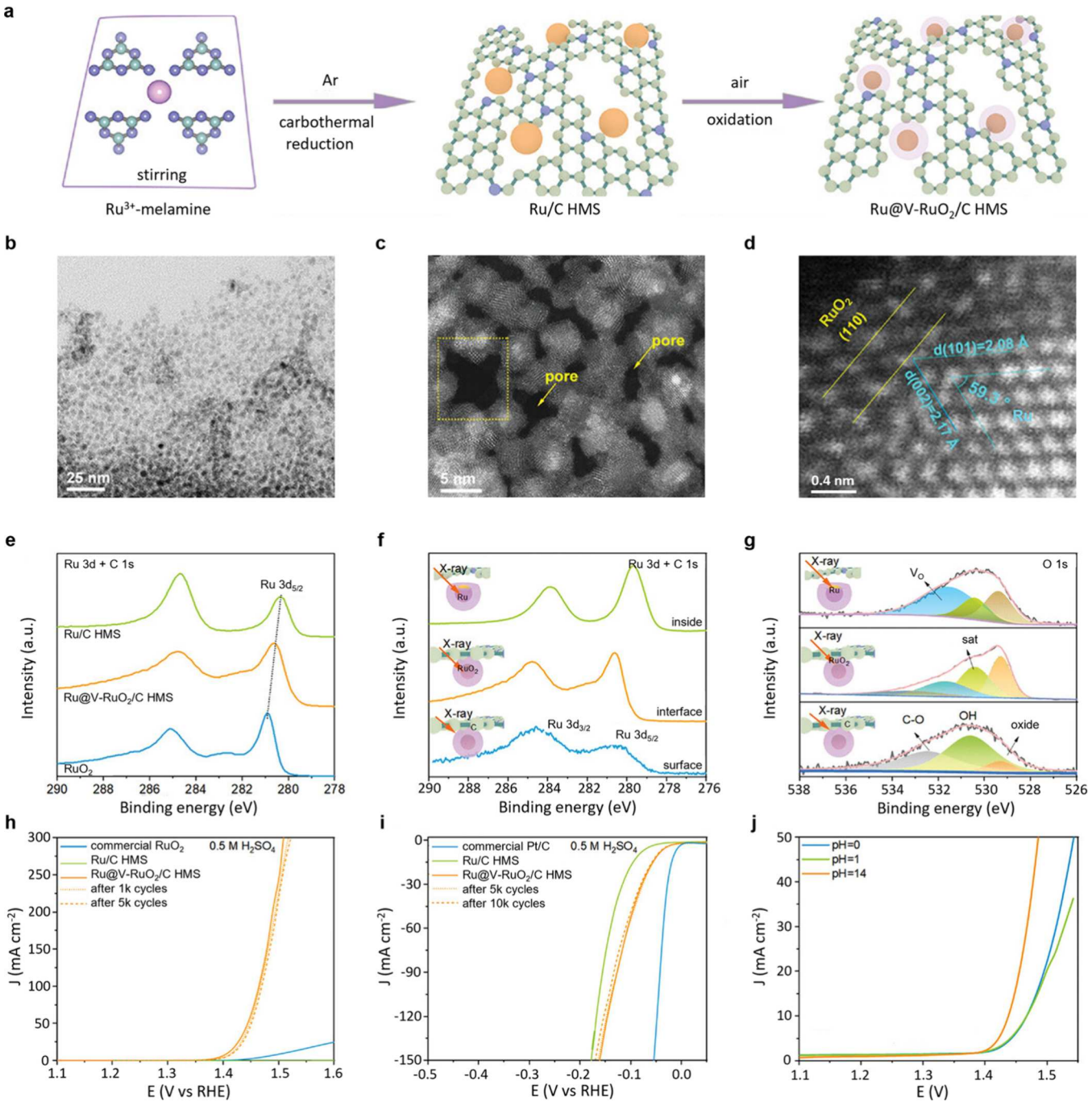

Figure 21. (a) Schematic of the formation of Ru@V-RuO_2/C HMS. (b) HRTEM and (c, d) aberration-corrected HAADF-STEM images of Ru@V-RuO_2/C HMS. (e) High-resolution Ru 3d + C 1s XPS spectra of Ru/C HMS, Ru@V-RuO_2/C HMS, and RuO_2. High-resolution (f) Ru 3d + C 1s and (g) O 1s XPS spectra of Ru@V-RuO_2/C HMS at different depths. LSV curves of Ru@V-RuO_2/C HMS before and after cycles, and controls for (h) OER and (i) HER. (j) LSV curves of Ru@V-RuO_2/C HMS couple for OWS. Reproduced with permission from ref 330. Copyright 2022 John Wiley and Sons.

TEM images of Ru@V-RuO_2/C HMS revealed that the core−shell clusters with Ru core covered by several atomic layers of RuO_2 shells are widely distributed within porous microsheets (Figure 21b−d). Geometric phase analysis (GPA) showcased the presence of asymmetrical strain distribution at the Ru/RuO_2 interface. Analysis of the Ru 3d XPS spectra (Figure 21e) indicated that the valence of Ru in Ru@V-RuO_2/C HMS is less than 4+ and between those for Ru/C HMS and RuO_2, indicative of the suppressed peroxidation of Ru^{4+}. To confirm the core−shell structure of Ru@V-RuO_2/C HMS, the authors conducted XPS depth profile analysis (Figure 21f). From surface to interface and then to inside, the Ru 3d peaks gradually enhanced with negative shift toward low binding energy, indicating the inhomogeneity of metallic Ru and the metal@metal oxide heterostructure. Additionally, the depth high-resolution O 1s XPS spectra (Figure 21g) confirmed the presence of oxygen vacancies (V_O) at the interface between Ru and RuO_2, as revealed by their increased peak intensity. The authors speculated that the unique core−shell heterostructure with asymmetrical strain and plentiful V_O not only prevents

https://doi.org/10.1021/acs.chemrev.3c00332
Chem. Rev. 2024, 124, 3694−3812

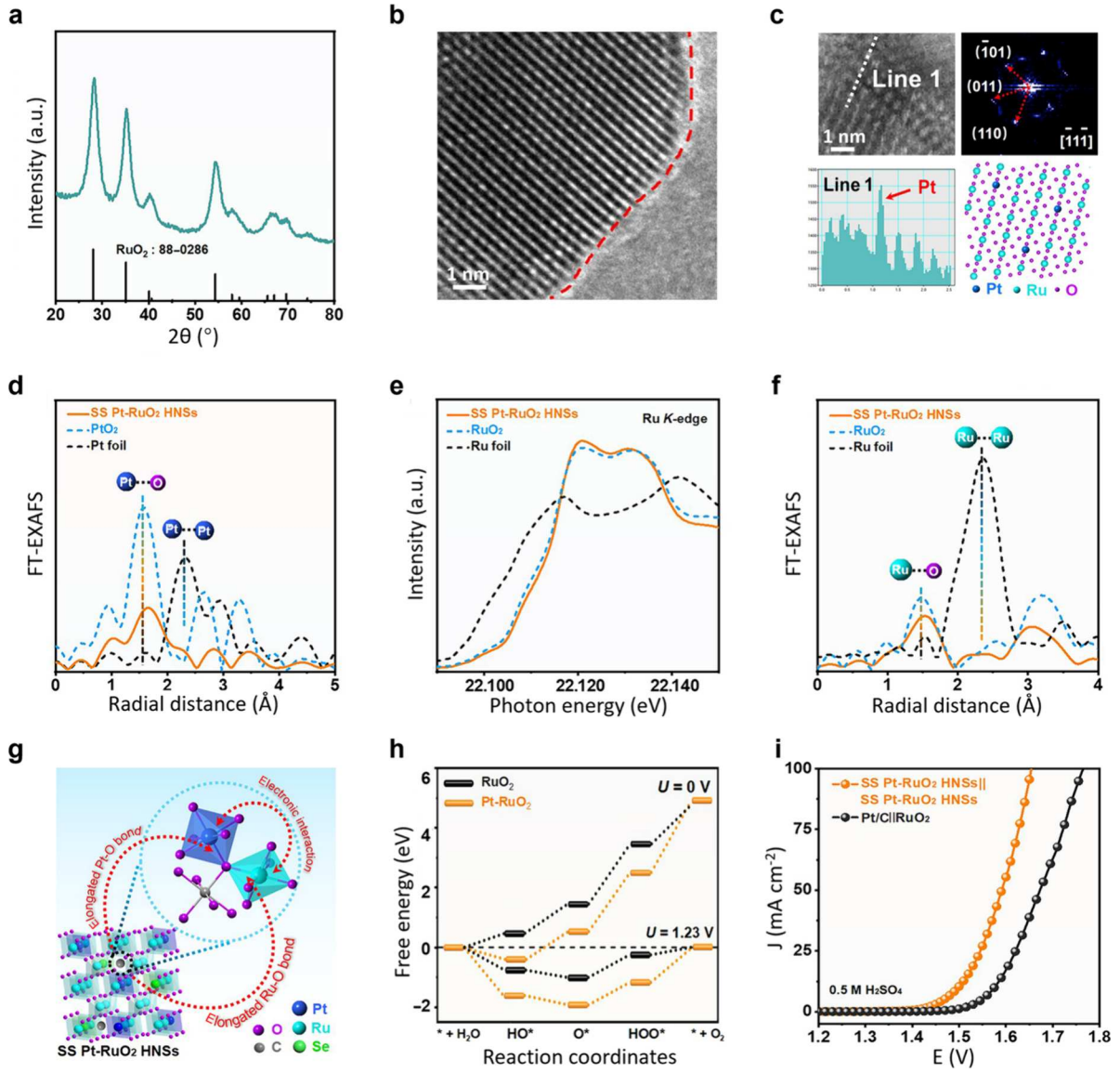

Figure 22. (a) XRD pattern, (b) HRTEM image, and (c) HAADF-STEM image (upper left), FFT pattern (upper right), line-scanning intensity profile obtained from the white line 1 (lower left), and crystal structure model (lower right) of SS Pt-RuO_2 HNSs. (d) Pt L_3-edge FT-EXAFS spectra of SS Pt-RuO_2 HNSs, PtO_2, and Pt foil. (e) Ru K-edge XANES and (f) Ru K-edge FT-EXAFS spectra of SS Pt-RuO_2 HNSs, commercial RuO_2, and Ru foil. (g) Structural illustration of SS Pt-RuO_2 HNSs. (h) Free energy profiles of OER process on RuO_2 and SS Pt-RuO_2 HNSs. (i) LSV curves of SS Pt-RuO_2 HNSs couple and commercial Pt/C||RuO_2 couple in 0.5 M H_2SO_4. Reproduced with permission from ref 5 under the terms of a CC-BY 4.0 license. Copyright 2022 The Authors, published by American Association for the Advancement of Science.

peroxidation of RuO_2 but also optimizes kinetics, collectively accelerating the electrocatalytic HER/OER kinetics. Electrochemical tests demonstrated that the Ru@V-RuO_2/C HMS exhibits excellent electrocatalytic activity and stability for both HER and OER in acidic solution (0.5 M H_2SO_4) with respective overpotentials of 47 and 176 mV at 10 mA cm^{-2} (Figure 21h,i), lower than those of Ru/C HMS (>80 mV for HER) and commercial RuO_2 (277 mV for OER). The almost overlapped LSV curves of Ru@V-RuO_2/C HMS for both HER and OER before and after 5k or 10k cycles evidenced its robust stability. Moreover, the Ru@V-RuO_2/C HMS couple showcased extraordinary activity for OWS in 0.5 M H_2SO_4, with a requirement of only 1.467 V to achieve 10 mA cm^{-2} (Figure 21j).

Doping exotic metals is another powerful route to tailor the electronic structure of the underlying RuO_2 electrocatalyst for enhanced activity and stability. Huang and coworkers reported the synthesis of single-site Pt-doped RuO_2 hollow nanospheres (SS Pt-RuO_2 HNSs) with interstitial carbon (C) using a hydrothermal followed by high-temperature annealing method.[5] XRD pattern of the SS Pt-RuO_2 HNSs (Figure 22a) showed characteristic diffraction peaks attributed to RuO_2 and the absence of metallic Pt peaks indicated the well-dispersion of Pt atoms on RuO_2 surface. Moreover, the absence of carbon shells in HRTEM image (Figure 22b) confirmed the incorporation of C into RuO_2 lattice. Spherical aberration-corrected HAADF-STEM with atomic line profile and fast Fourier transform (FFT) images (Figure 22c) revealed a tetragonal structural arrangement ($P_{42/mnm}$) of Ru and O atoms, with isolated Pt atoms occupying the Ru positions. Additionally, X-ray absorption spectroscopy (Figure 22d–f) including XANES and FT-EXAFS spectra of SS Pt-RuO_2

https://doi.org/10.1021/acs.chemrev.3c00332
Chem. Rev. 2024, 124, 3694–3812

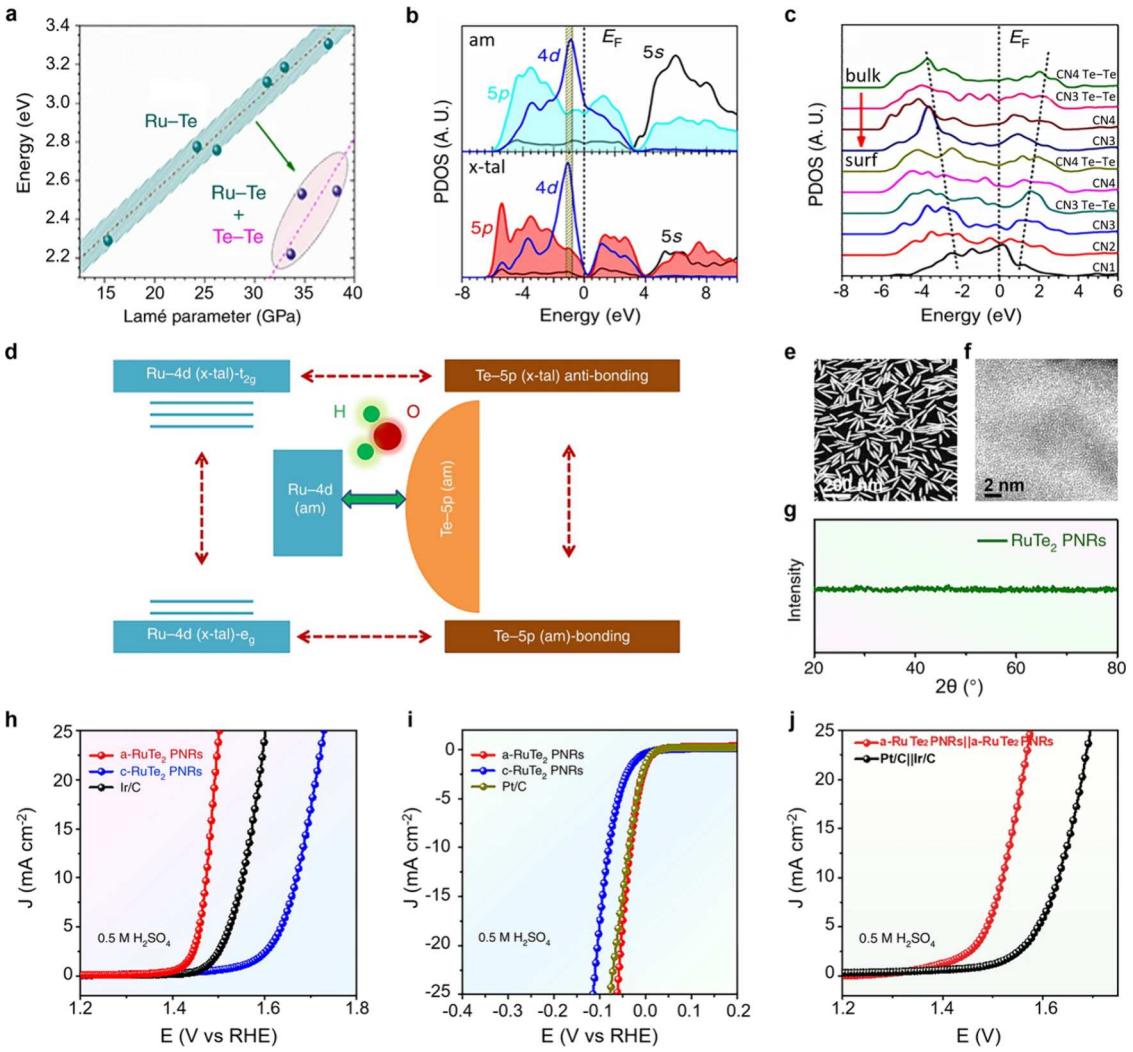

Figure 23. (a) Structural formation energy variation trend with related to the Lamé parameters for describing the bulk lattice distortion induced strain effect, and the Te−Te bond formation. (b) PDOSs comparison between amorphous and crystalline $RuTe_2$. (c) Site-dependent PDOSs variation of Te-5p band. (d) Schematic for the illustration of the amorphous $RuTe_2$ boosting OER performance via highly efficient electron-transfer site-independently. (e, f) HAADF-STEM images and (g) XRD pattern of a-$RuTe_2$ PNRs. LSV curves of a-$RuTe_2$ PNRs, c-$RuTe_2$ PNRs, and controls for (h) OER and (i) HER in 0.5 M H_2SO_4. (j) LSV curves of a-$RuTe_2$ PNRs couple and Ir/C||Pt/C in 0.5 M H_2SO_4. Reproduced with permission from ref 333 under the terms of a CC-BY 4.0 license. Copyright 2019 The Authors, published by Springer Nature.

HNSs indicated the absence of Pt−Pt coordination (Figure 22d), obvious electron transfer between Pt and RuO_2 (Figure 22e) and an expanded interatomic distance between Pt−O and Ru−O bonds due to the insertion of carbon atoms (interstitial atoms) into the gap (Figure 22f,g). The strong interaction between the single-site Pt and RuO_2 significantly changed the electronic properties of the SS Pt-RuO_2 HNSs, leading to improved electrocatalytic performance. DFT calculations (Figure 22h) demonstrated that RuO_2 with single-site Pt exhibits a reduced energy barrier of RDS relative to bare RuO_2 for OER under both zero and equilibrium potential. As a result, the SS Pt-RuO_2 HNSs couple required a cell voltage of only 1.49 V to afford 10 mA cm^{-2} in 0.5 M H_2SO_4 for OWS (Figure 22i), lower than that of commercial Pt/C and RuO_2 benchmark couple (1.56 V).

To maximize the utilization of noble Ru atoms, Xin and coworkers synthesized single-atom Ru sites anchored on $Ti_3C_2T_x$ MXene nanosheets (Ru-SA/$Ti_3C_2T_x$).[331] The isolated Ru−O_2 sites in Ru-SA/$Ti_3C_2T_x$ effectively optimized reactants/intermediates adsorption and thus reduced the energy barrier during HER and OER for accelerated OWS kinetics. Consequently, a low cell voltage of 1.56 V was needed for Ru-SA/$Ti_3C_2T_x$ couple to achieve a current density of 10 mA cm^{-2} in 0.1 M $HClO_4$ solution.

Besides metals/RuO_2-based bifunctional electrocatalysts, Mu and collaborators recently found that the laminar Ru/RuS_2 is also active for acidic HER and OER due to interfacial charge rearrangement and boosted electron conduction.[332] Such effects balanced the sorption of key intermediates over electron-deficient Ru atoms, leading to reduced energy barriers. Notably, the Ru/RuS_2 couple demonstrated a significantly low cell voltage of 1.501 V at 10 mA cm^{-2} in 0.5 M H_2SO_4.

It is worth noting that most reported water splitting electrocatalysts are crystalline materials, amorphous counterparts have been overlooked. It is believed that the amorphous materials with disordered structures possess numerous dangling bonds and defects, providing a wealth of highly active sites which are beneficial for electrocatalytic applications. Furthermore, their anisotropy imparts high corrosion resist-

https://doi.org/10.1021/acs.chemrev.3c00332
Chem. Rev. 2024, 124, 3694−3812

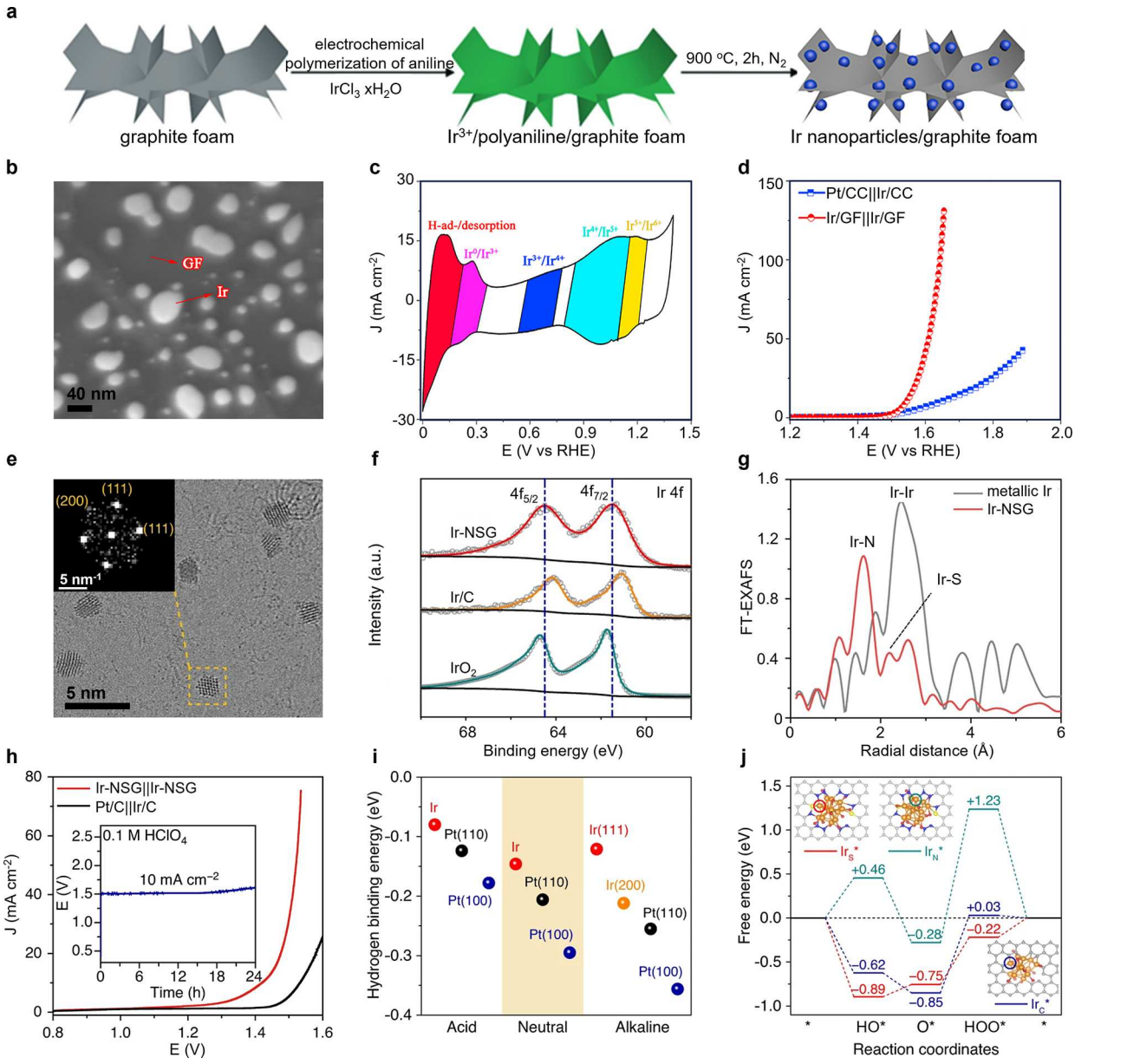

Figure 24. (a) Schematic for the preparation of Ir/GF. (b) SEM image of the Ir/GF. (c) CV curve of the Ir/GF. (d) LSV curves of Ir/GF couple and Pt/CC||Ir/CC couple. Reproduced with permission from ref 344. Copyright 2017 Elsevier. (e) Bright-field HRSTEM image and the corresponding FFT of the selected area in the yellow square (inset). (f) High-resolution XPS Ir 4f spectra. (g) The k^3-weighted FT-EXAFS spectra of Ir-NSG and metallic Ir. (h) LSV curves of Ir-NSG|| Ir-NSG and Pt/C||Ir/C couple. Inset shows the corresponding chronopotentiometric curves at 10 mA cm^{-2}. (i) Comparison of HBE for Ir-NSG and Pt/C in a full range of pH. (j) DFT calculation of the predicted free-energy diagrams for OER at U = 1.23 V on Ir_S*, Ir_N*, and Ir_C* sites. The balls in gray, blue, yellow, pink, red, orange, and cyan represent C, N, S, H, O, Ir, and Pt atoms, respectively. Reproduced with permission from ref 348 under the terms of a CC-BY 4.0 license. Copyright 2020 The Authors, published by Springer Nature.

ance.[333] In this respect, Huang and coworkers designed and synthesized bullet-like amorphous $RuTe_2$ porous nanorods (a-$RuTe_2$ PNRs) for enhanced acidic OWS, harnessing the intrinsically high activity of amorphous structures.[333] In order to investigate the intrinsic activity of a-$RuTe_2$ PNRs from a theoretical perspective, the authors first conducted DFT calculations (Figure 23a–d). Figure 23a exhibited the structural formation energy as a function of Lamé parameter and it revealed that the formation of Te–Te homopolar bond facilitates wider-range relaxations toward higher stabilities, confirming the critical effect of p–π coupling on both energetic performance and electronic activities. Meanwhile, the projected partial density of states (PDOSs) revealed the enhanced inter-d-orbital electron-transfer ability among Ru sites induced by distorted Ru–Te lattice. Also, the Te-5p occupied from the energy (E_V) of −4.5 eV to E_F showed more overlapping with Ru-4d for amorphous $RuTe_2$ relative to crystalline counterpart, indicative of the enhanced p–d coupled electron-exchange and thus antioxidation for the former (Figure 23b). Furthermore, site-dependent PDOSs analysis of Te-5p band suggested that the decreased bonding and antibonding splitting of Te-5p band in the surface region with lower coordination number results in gradually active and more overlapped with Ru-4d (Figure 23c). Such effects were

https://doi.org/10.1021/acs.chemrev.3c00332
Chem. Rev. 2024, 124, 3694–3812

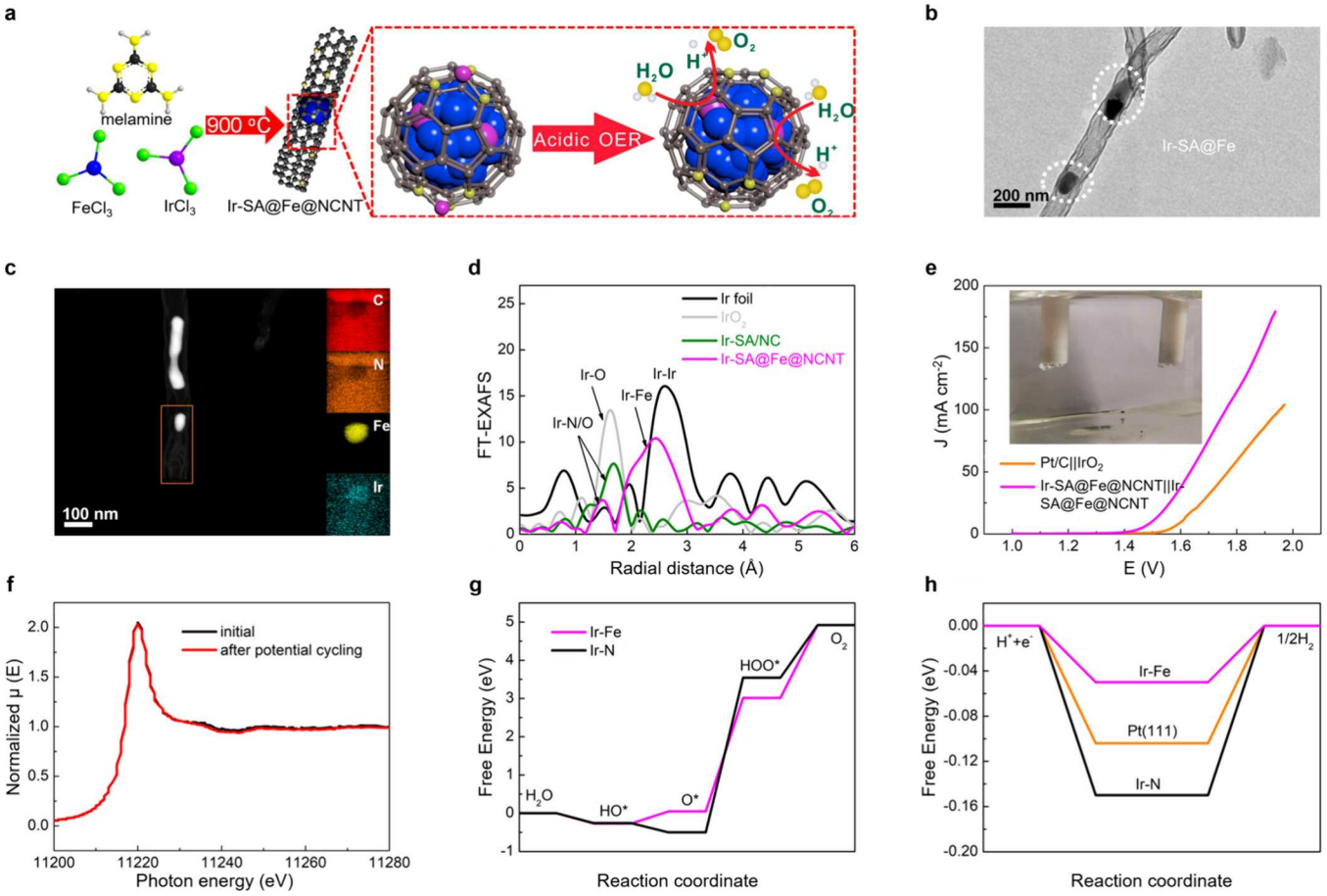

Figure 25. (a) Schematic of the preparation of Ir-SA@Fe@NCNT. (b) TEM image and (c) HAADF-STEM and the related elemental mapping images of Ir-SA@Fe@NCNT. (d) k^3-weighted Ir-L_3 edge FT-EXAFS spectra of Ir foil, IrO_2, Ir-SA/NC, and Ir-SA@Fe@NCNT. (e) LSV curves of Ir-SA@Fe@NCNT couple and Pt/C||IrO_2 for OWS in 0.5 M H_2SO_4. (f) Ir-L_3 edge XANES spectra of Ir-SA@Fe@NCNT at the initial state and after potential cycling. Free energy diagrams of (g) OER and (h) HER processes over Fe−Ir and Ir−N models. Reproduced with permission from ref 353. Copyright 2020 American Chemical Society.

believed to facilitate the overlapping between p−π orbital of H_2O and Te-5p band and thus a strong p−π coupling to activate the H_2O molecule for efficient splitting. Subsequently, the authors calculated the free energies of acidic OER pathways on the amorphous $RuTe_2$ surface and found the facilitated water splitting and secondary dehydrogenation, favoring the critical HOO* formation step. Specifically, as shown in Figure 23d, the surface distortion-strain effect of amorphous $RuTe_2$ sensitized the Te−pπ coupling and annihilated the crystal-field splitting effect of Ru for highly active intra- and interorbital electron transfer, collectively leading to improved OER activity. To experimentally confirm these theoretical predictions, the a-$RuTe_2$ PNRs were synthesized via a hydrothermal method, and the amorphous nature was confirmed by the XRD pattern and atomic-resolution HAADF-STEM image (Figure 23e−g). Importantly, electrochemical tests demonstrated the excellent OER and HER activities of a-$RuTe_2$ PNRs with respective overpotentials of 245 mV (Figure 23h) and 33 mV (Figure 23i) at 10 mA cm^{-2} in 0.5 M H_2SO_4, much lower than those of highly crystalline counterpart (c-$RuTe_2$ PNRs). Additionally, the a-$RuTe_2$ PNRs couple exhibited superior activity for OWS with a low cell voltage of 1.52 V to achieve 10 mA cm^{-2}, lower than that of commercial Pt/C and Ir/C couple (Figure 23j).

4.1.2. Ir-Based Electrocatalysts. Compared to Ru-based materials like RuO_2, Ir-based electrocatalysts (e.g., IrO_2) usually possess higher stability in acidic electrolytes,[96,334] and have been explored for acidic OER.[335,336] Additionally, experimental measurements and theoretical calculations based on the Sabatier principle indicate that Ir is positioned near the apex of the volcano relationship for acidic HER,[7] making it suitable as a bifunctional electrocatalyst for both HER and OER toward OWS. Note that albeit with higher stability of Ir-based electrocatalysts relative to Ru-based counterparts, their OER activity is relatively lower,[337−340] and the issue of deactivation still exists especially in harsh operating conditions.[335,341−343] Therefore, rational design of durable and highly active Ir-based bifunctional electrocatalysts is crucial for the commercialization of PEMWE. Currently, a variety of synthetic strategies such as heteroatom doping, defect engineering, morphology controlling, and heterostructure constructing have been implemented to obtain various Ir-based electrocatalysts, including metallic Ir (nanoparticles, nanoclusters, single atoms,), Ir alloys (bimetallic and polymetallic), and Ir-based oxides or other compounds for OWS in acidic solutions.

One common and straightforward approach to enhance the specific catalytic activity is reducing the particle size. Feng and coworkers successfully synthesized the low-content Ir nano-

https://doi.org/10.1021/acs.chemrev.3c00332
Chem. Rev. 2024, 124, 3694−3812

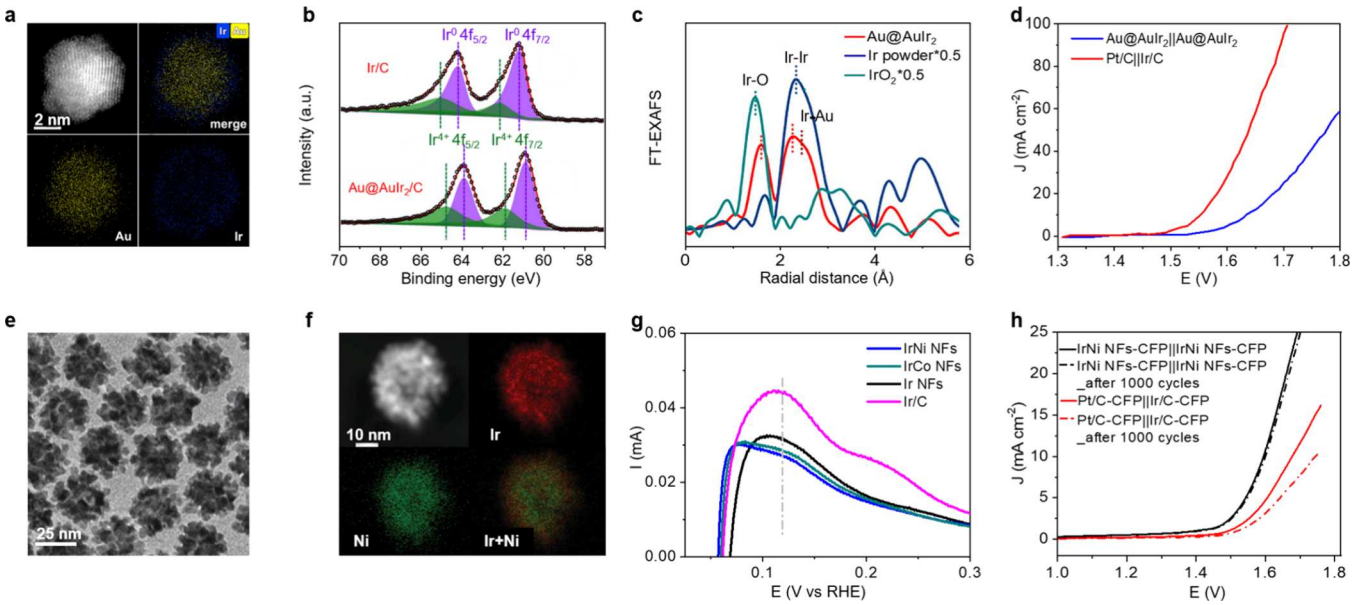

Figure 26. (a) HAADF-STEM and elemental mapping images of Au@AuIr$_2$/C. (b) High-resolution Ir 4f XPS spectra of Au@AuIr$_2$/C and Ir/C. (c) k^3-weighted Ir L$_3$-edge FT-EXAFS spectra of Au@AuIr$_2$/C and controls. (d) LSV curves of Au@AuIr$_2$/C couple and Pt/C||Ir/C couple for OWS in 0.5 M H_2SO_4. Reproduced with permission from ref 354. Copyright 2021 American Chemical Society. (e) TEM and (f) elemental mapping images of IrNi NFs. (g) H desorption peaks of IrNi NFs, IrCo NFs, Ir NFs, and Ir/C in 0.1 M $HClO_4$. (h) LSV curves of IrNi NFs, Ir/C, and Pt/C on CFP couples for OWS in 0.5 M H_2SO_4 before and after 1000 cycles. Reproduced with permission from ref 355. Copyright 2019 John Wiley and Sons.

particles (5.91 wt %) supported on three-dimensional porous graphite foam (Ir/GF) through high-temperature annealing of an Ir^{3+}/polyaniline complex on GF (Figure 24a).[344] SEM image (Figure 24b) corroborated the successful formation of Ir nanoparticles with sizes of 10−56 nm homogeneously anchored on the surface of GF. CV measurements shown in Figure 24c revealed multiple redox pairs originated from the transition of various valence states of Ir species, which functioned as active sites for acidic OWS. Moreover, the GF served as the current collector, providing good conductivity and excellent resistance against oxidative corrosion. Consequently, the resulting Ir/GF (Figure 24d) exhibited outstanding activity, with low overpotentials of approximately 7 and 290 mV for HER and OER at 10 mA cm^{-2} in acidic solution, respectively. Furthermore, a cell voltage of only 1.55 V was needed for the Ir/GF couple to afford 10 mA cm^{-2} toward OWS.

In comparison to nanoparticles, nanoclusters with higher specific surface areas as well as remarkable quantum/surface geometry effect and unique electronic properties are also promising for electrocatalytic applications.[345−347] Liu and colleagues reported a bifunctional water splitting electrocatalyst named as uniformly dispersed Ir nanoclusters embedded on N,S-doped graphene (Ir-NSG) obtained through facile pyrolysis of a mixture of melamine, L-cysteine, and iridium(III) chloride.[348] HRSTEM image along with FFT pattern (Figure 24e) clearly demonstrated the nanoscale crystal structure of Ir nanoclusters uniformly distributed on the graphene substrate. High-resolution Ir 4f XPS spectra (Figure 24f) revealed that the full width at half-maximum of Ir-NSG is significantly broader than that of IrO_2 and Ir/C, indicating the presence of various valence states of Ir. FT-EXAFS spectra (Figure 24g) indicated a core−shell-like structure of the Ir nanoclusters, with the core layer of Ir atoms bonded through Ir−Ir metal bonds, and the shell layer of Ir atoms bonded with adjacent N/S atoms. This unique structure endowed the Ir-NSG exceptional activity and stability for acidic OWS (Figure 24h). For example, the Ir-NSG couple exhibited a low cell voltage of 1.42 V to reach 10 mA cm^{-2}, outperforming the commercial Pt/C and Ir/C benchmark couple. DFT calculations manifested that the enhanced HER activity of Ir-NSG can be attributed to the neutral hydrogen binding energy (HBE) (Figure 24i) and its excellent OER activity originates from the favorable binding of HO* and HOO* intermediates with N and S atoms-coordinated Ir sites (Figure 24j).

Relative to nanoparticles and nanoclusters, single-atom electrocatalysts feature ultimate atomic utilization efficiency and distinctive electronic structure due to unique confinement within atomic level, exhibiting appealing performance for OWS.[349−352] Cai and collaborators successfully dispersed Ir single atoms (Ir-SA) in/onto Fe nanoparticles and encapsulated the resulting IrFe into nitrogen-doped carbon nanotubes (Ir-SA@Fe@NCNT) via a pyrolysis process (Figure 25a).[353] Close observation from the TEM image of Ir-SA@Fe@NCNT revealed the confinement of nanoparticles into NCNT (Figure 25b). Elemental mapping images (Figure 25c) of Ir-SA@Fe@NCNT revealed the enrichment of Ir-SA within the Fe nanoparticles and confirmed the confinement configuration of Ir-SA@Fe. The k^3-weighted Ir L$_3$-edge FT-EXAFS spectra (Figure 25d) excluded the Ir−Ir bonding and suggested the atomic dispersion of Ir atoms in Ir-SA@Fe@NCNT. Electrochemical experiments showed that a cell voltage of only 1.51 V is needed to achieve 10 mA cm^{-2} for Ir-SA@Fe@NCNT couple in 0.5 M H_2SO_4 toward OWS, lower than that of commercial Pt/C and RuO_2 couple (Figure 25e). The almost overlapping of Ir-L$_3$ XANES spectra for Ir-SA@Fe@NCNT before and after potential cycling (Figure 25f) confirmed its high durability, suggestive of the maintained oxidation state and coordination environment of Ir-SA. DFT calculations

https://doi.org/10.1021/acs.chemrev.3c00332
Chem. Rev. 2024, 124, 3694−3812

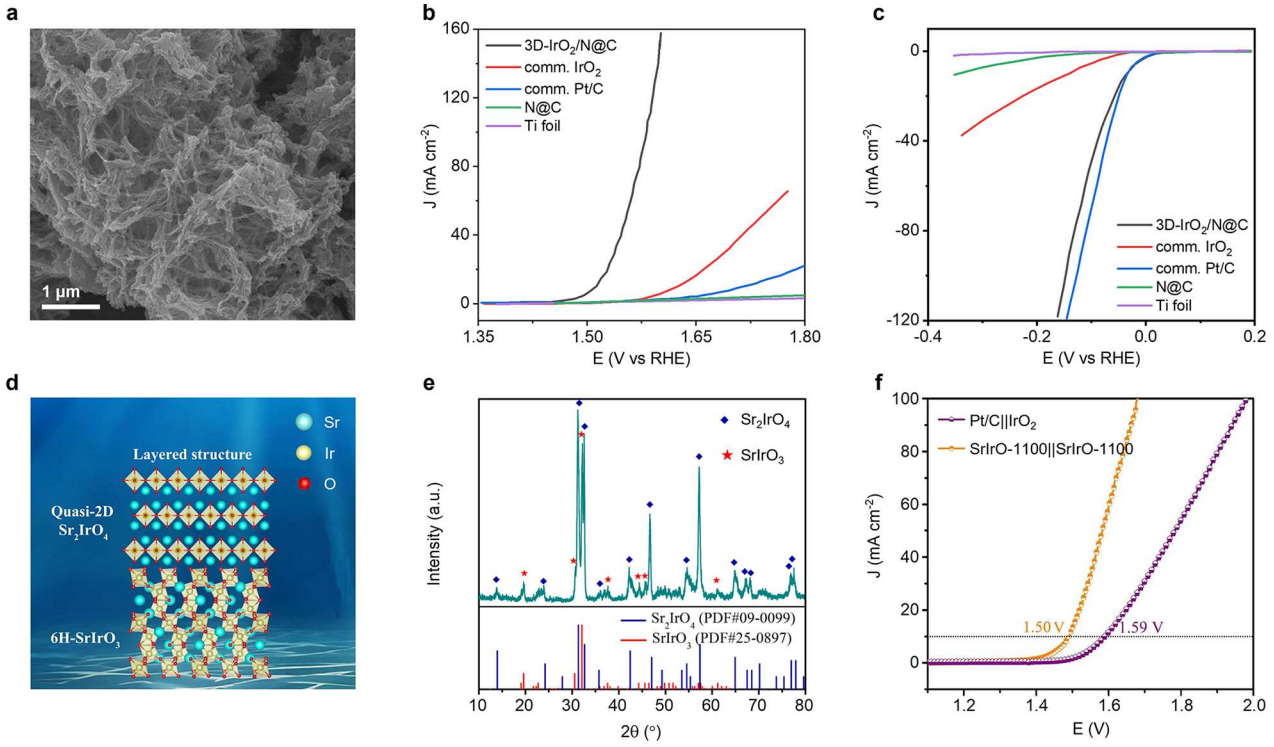

Figure 27. (a) SEM image of 3D-IrO_2/N@C. LSV curves of 3D-IrO_2/N@C, comm. IrO_2, comm. Pt/C, N@C, and Ti foil for (b) OER and (c) HER in 0.5 M $HClO_4$. Reproduced with permission from ref 357. Copyright 2020 Elsevier. (d) Structure schematic of quasi-2D Sr_2IrO_4 and 3D $SrIrO_3$. (e) XRD pattern of SrIrO-1100. (f) LSV curves for SrIrO-1100 couple and Pt/C||IrO_2 couple in 0.5 M H_2SO_4. Reproduced with permission from ref 361. Copyright 2021 Elsevier.

(Figure 25g) revealed that the Ir−Fe sites lower the energy barrier of RDS (HOO* formation) in OER (2.96 eV) relative to Ir−N (4.04 eV). Additionally, the ΔG_{H^*} over Ir−Fe sites (−0.05 eV) was calculated to be closer to the ideal value for acidic HER (0 eV) than those over Ir−N (−0.15 eV) and Pt (−0.10 eV) as shown in Figure 25h, implying a more moderate hydrogen sorption and thus improved HER. These DFT calculations matched well with their electrochemical results.

Besides downsizing Ir metals, alloying them with relatively cheap metals is also effective to reduce the cost, plus tuning the electronic structure of the resulting materials with improved electrocatalytic activity. With this consideration, Cao and coworkers synthesized a core−shell Au@$AuIr_2$ nanoparticles with Au as the core and $AuIr_2$ alloy as the shell using a one-pot method.[354] HAADF-STEM and the corresponding elemental mapping images of Au@$AuIr_2$ (Figure 26a) clearly indicated the core−shell structure with Au in the core region and Ir in the shell layer. High-resolution Ir 4f XPS spectra (Figure 26b) revealed the presence of metallic Ir and IrO_x in Au@$AuIr_2$, and the redshift of Ir peaks relative to Ir/C, suggesting electron transfer from Au to Ir. The k^3-weighted Ir L_3-edge FT-EXAFS spectra of Au@$AuIr_2$ (Figure 26c) showed the existence of Ir−O, Ir−Ir, and Ir−Au, indicative of strong electronic coupling between Au and Ir again. Benefiting from the above unique structure, the Au@$AuIr_2$ couple achieved 10 mA cm^{-2} at a significantly low voltage of 1.55 V for OWS in 0.5 M H_2SO_4, 80 mV lower than that of commercial Pt/C and Ir/C couple (Figure 26d). Similarly, Guo and collaborators alloyed nonprecious Ni and Co metals into Ir to obtain 3D nanoflower-like IrNi and IrCo alloys (IrNi and IrCo NFs).[355] For example, TEM (Figure 26e) and elemental mapping images (Figure 26f) of IrNi NFs collectively certified the nanoflower-like alloy structures with uniform distribution of Ir and Ni. Considering the key role of hydrogen binding energy (HBE), the authors conducted CV to detect the position of under potential deposited H for IrNi NFs, IrCo NFs, Ir NFs, and Ir/C control. As shown in Figure 26g, the potentials of H desorption peaks for the electrocatalysts followed the order of Ir/C ≈ Ir NFs > IrCo NFs > IrNi NFs, suggesting the gradually weakened H binding on Ir, which was expected to improve the HER activity in acidic media. To achieve 10 mA cm^{-2} for acidic OWS (0.5 M H_2SO_4), the couple of IrNi NFs deposited on carbon fiber paper (IrNi NFs-CFP) required a low cell voltage of 1.60 V (Figure 26h), much lower than that of commercial Pt/C and Ir/C couple (1.68 V). Besides Ir-based binary alloys, multicomponent high-entropy alloy of nanoporous AlNiCoIrMo with low Ir content was also reported by Qiu and coworkers, which required a cell voltage of only 1.505 V to reach 10 mA cm^{-2}.[356]

In addition to designing metallic Ir-based bifunctional electrocatalysts, numerous studies have explored iridium oxide-based materials for acidic OWS as well. For instance, Barman's group successfully synthesized a 3D hierarchically porous iridium oxide/nitrogen-doped carbon hybrid (3D-IrO_2/N@C), with remarkable bifunctional activities for both HER and OER in acidic solution.[357] SEM image (Figure 27a) of 3D-IrO_2/N@C clearly demonstrated the porous structure and well-dispersion of IrO_2 nanoparticles within the 3D porous N@C network. The resulting 3D-IrO_2/N@C bifunctional electrocatalyst exhibited excellent OER and HER activities in 0.5 M $HClO_4$ (Figure 27b,c), with overpotentials of 280 and 35 mV to reach 10 mA cm^{-2}, respectively. Such outstanding activity of 3D-IrO_2/N@C was attributed to the unique hierarchical porosity for facilitated mass transfer, the large

https://doi.org/10.1021/acs.chemrev.3c00332
Chem. Rev. 2024, 124, 3694−3812

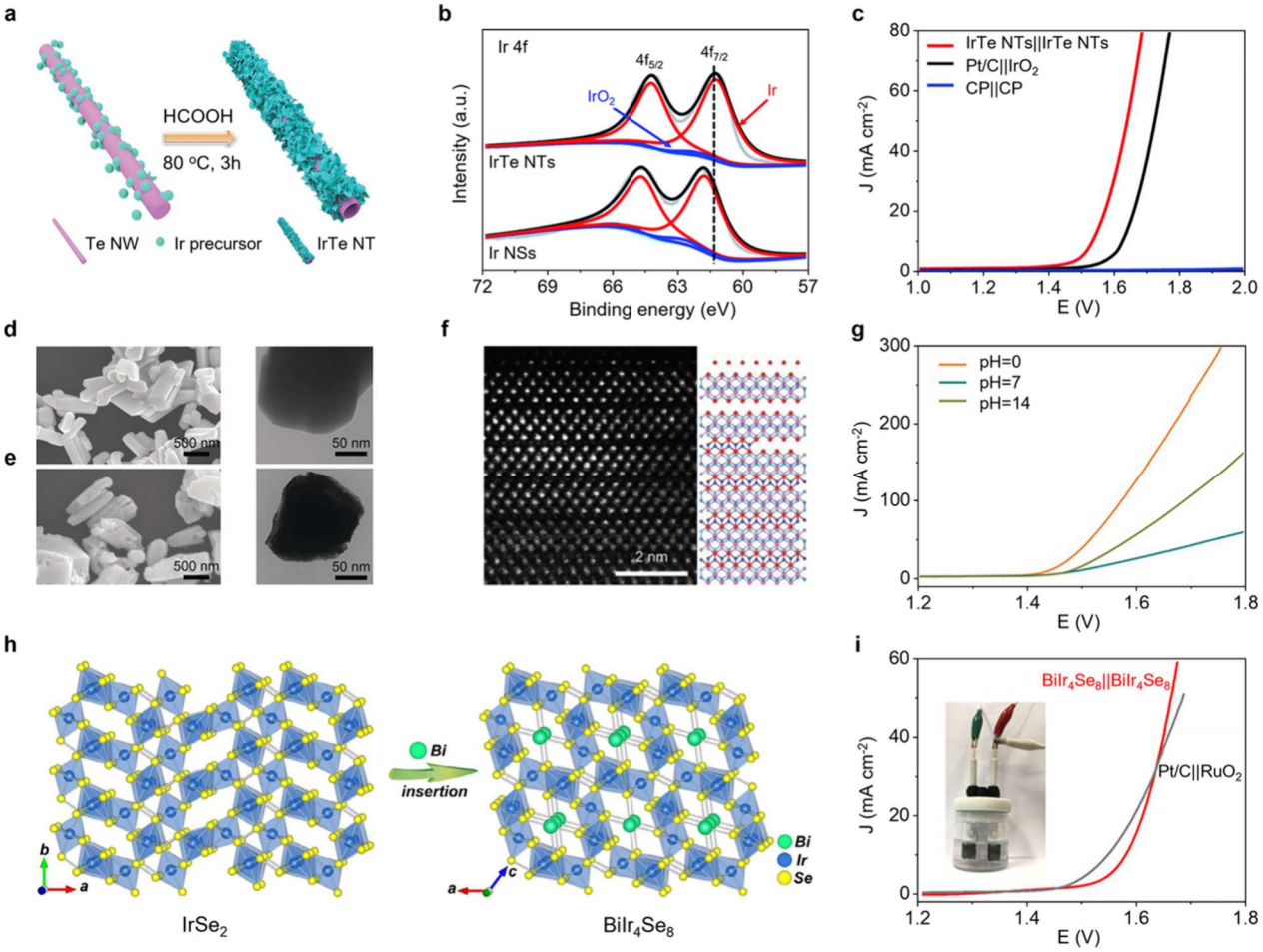

Figure 28. (a) Schematic of the preparation of IrTe NTs. (b) High-resolution Ir 4f XPS spectra of IrTe NTs and Ir NSs. (c) LSV curves of IrTe NTs couple and Pt/C||IrO_2 couple for OWS in 0.5 M H_2SO_4. Reproduced with permission from ref 362. Copyright 2021 Royal Society of Chemistry. SEM and TEM images of (d) $IrSe_2$ and (e) Li-$IrSe_2$. (f) HAADF-STEM image and corresponding structure of Li-$IrSe_2$. (g) LSV curves of Li-$IrSe_2$ couple for OWS. Reproduced with permission from ref 363. Copyright 2019 John Wiley and Sons. (h) Schematic single-crystal structure of $IrSe_2$ and $BiIr_4Se_8$. (i) LSV curves of $BiIr_4Se_8$ couple and Pt/C||RuO_2 couple for OWS in 0.5 M H_2SO_4. The inset showed the symmetrical electrolyzer. Reproduced with permission from ref 364 under the terms of a CC-BY 4.0 license. Copyright 2021 The Authors, published by John Wiley and Sons.

active surface area for enhanced interaction between active sites and reactants, and the synergistic effect between IrO_2 and N-doped carbon. Moreover, multimetal mixed oxides with even higher activity compared to individual metal Ir or IrO_2 have been reported recently.[358−360] For instance, Cho and collaborators prepared a novel Ir-based electrocatalyst of laminar Sr_2IrO_4-modified 6H phase $SrIrO_3$ (SrIrO-1100), as depicted in Figure 27d.[361] XRD pattern (Figure 27e) confirmed the copresence of both quasi-2D Sr_2IrO_4 and 3D 6H-$SrIrO_3$ phases, indicating the combination of quasi-2D and 3D Ir-based perovskites. The authors found that the 2D lamellar structure allows Sr leaching during electrocatalytic processes without deconstructing the structural integrity of the in-plane IrO_6 framework, and the corner/face-shared IrO_6 octahedral dimers in 3D 6H-$SrIrO_3$ phase serve as active centers. Consequently, the SrIrO-1100 couple demonstrated a low cell voltage of 1.50 V at 10 mA cm^{-2} (Figure 27f), in sharp contrast to that of Pt/C and IrO_2 couple (1.59 V).

Apart from single metallic Ir, Ir alloys, and Ir oxides, Ir nonoxides have garnered significant research interest in the field of water electrolysis. Wang and coworkers prepared hierarchical IrTe nanotubes (NTs) with assembled nanosheets through a substitution reaction between Te nanowires and Ir precursors (Figure 28a).[362] High-resolution Ir 4f XPS spectra (Figure 28b) of IrTe NTs showed a negative shift of binding energy due to the introduction of Te elements, suggesting strong electronic coupling between Ir and Te. Benefiting from the unique hollow structure and nanosheet assemblies as well as electronic effects, the resulting IrTe NTs can act as bifunctional electrocatalysts for both OER and HER in 0.5 M H_2SO_4, requiring a cell voltage of 1.53 V to drive 10 mA cm^{-2} (Figure 28c). Zeng and coworkers developed a lithium-intercalated iridium diselenide (Li-$IrSe_2$) through chemical intercalation, demonstrating exceptional OWS activity under acidic conditions.[363] SEM and TEM images (Figure 28d,e) revealed that the Li-$IrSe_2$ (Figure 28e) maintains the particle morphology of pristine $IrSe_2$ (Figure 28d) while it exhibits a rough and cracked surface. HAADF-STEM image of Li-$IrSe_2$ (Figure 28f) along the [010] zone axis indicated the absence of a portion of Se anion on the near surface owing to the lithium intercalation. Thanks to the high porosity, large surface area, and Se vacancies, the Li-$IrSe_2$ required a low voltage of 1.44 V to achieve 10 mA cm^{-2} in 0.5 M H_2SO_4 (Figure 28g). Similar investigations were conducted by Huang and coworkers: a

https://doi.org/10.1021/acs.chemrev.3c00332
Chem. Rev. 2024, 124, 3694−3812

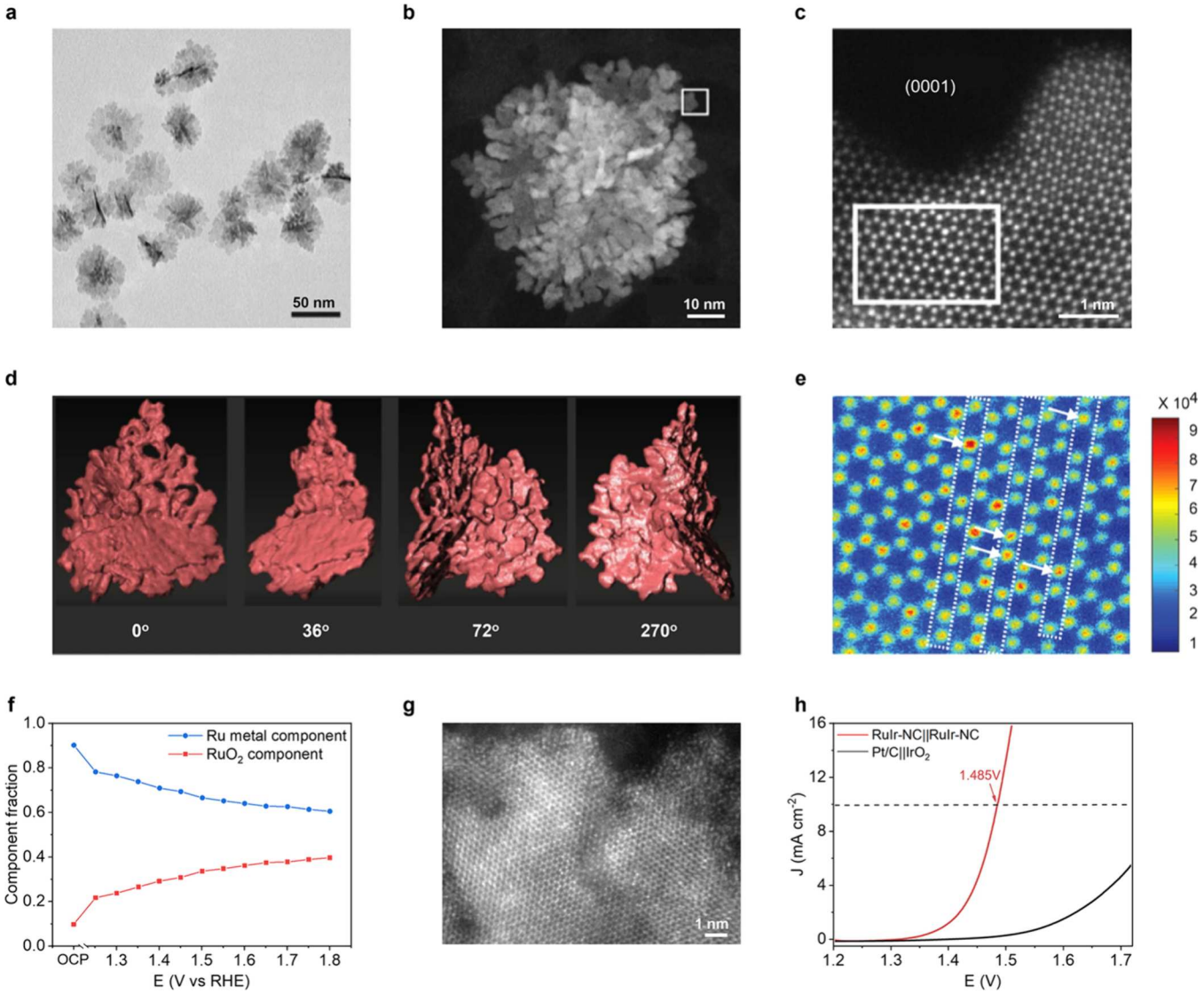

Figure 29. (a) TEM and (b) HAADF-STEM images of RuIr-NC. (c) Atomic-resolution HAADF-STEM image from the selected area in (b) showing the extended (0001) plane. (d) 3D tomographic reconstruction of RuIr-NC. (e) Magnified image of the selected area in (c), where the color bar represented the Gaussian intensity of the electron diffraction located at the column position. (f) Linear composition fitting (LCF) results using two components, Ru metal and RuO_2 in the XANES spectra of RuIr-NC collected by operando tests. (g) HAADF-STEM image of RuIr-NC under 1.80 V vs RHE in 0.05 M H_2SO_4. (h) LSV curves of the RuIr-NC couple and Pt/C||IrO_2 couple for OWS in 0.05 M H_2SO_4. Reproduced with permission from ref 371 under the terms of a CC-BY 4.0 license. Copyright 2021 The Authors, published by Springer Nature.

novel bismuth-inserted iridium-based selenide ($BiIr_4Se_8$) was synthesized by them via solid-phase reactions (Figure 28h).[364] The unique crystal structure of $BiIr_4Se_8$, featuring a smaller band gap and faster electron transport, enabled its high bifunctional activity for OWS in 0.5 M H_2SO_4 with cell voltages lower than those of commercial Pt/C and IrO_2 couple at current densities exceeding 35 mA cm^{-2} (Figure 28i).

4.1.3. RuIr-Based Electrocatalysts. As discussed above, numerous approaches have been reported to synthesize diverse bifunctional electrocatalysts based on Ru or Ir for acidic overall water splitting (OWS), with remarkably improved electrocatalytic performance relative to commercial benchmarks. It is agreed that Ru-based electrocatalysts commonly show high activity while mediocre stability under high anodic potential in acidic conditions,[37,323,365,366] Ir-based materials exhibit relatively good corrosion resistance and stability, but low activity.[367−369] Consequently, it is expected to combine Ru and Ir together to realize high activity and long-term stability simultaneously for acidic OWS.[327,370]

Kitagawa and coworkers synthesized a solid-solution Ru−Ir bifunctional electrocatalyst with a unique nanoscale coral structure (RuIr-NC).[371] TEM image (Figure 29a) showed the nanosized-coral structure of RuIr-NC with a particle size of 57 ± 7 nm and numerous nanosheets. HAADF-STEM images (Figure 29b,c) further revealed that the lamellar fragments of RuIr-NC expose a hexagonal atomic arrangement contributed to (0001) hexagonal closed-packed (*hcp*) crystal planes. The coral-like structure with 2D nanosheets assemblies of RuIr-NC was also verified by the 3D tomographic reconstruction (Figure 29d). Quantitative analysis (Figure 29e) of the selected area in Figure 29c indicated that each atomic column contains approximately 6 to 9 atoms including 1 or 2 Ir atoms (the arrows), corresponding to a thickness of approximately 3 nm. The unique structure of RuIr-NC contributed to its excellent OER performance in 0.05 M H_2SO_4, with an

https://doi.org/10.1021/acs.chemrev.3c00332
Chem. Rev. 2024, 124, 3694−3812

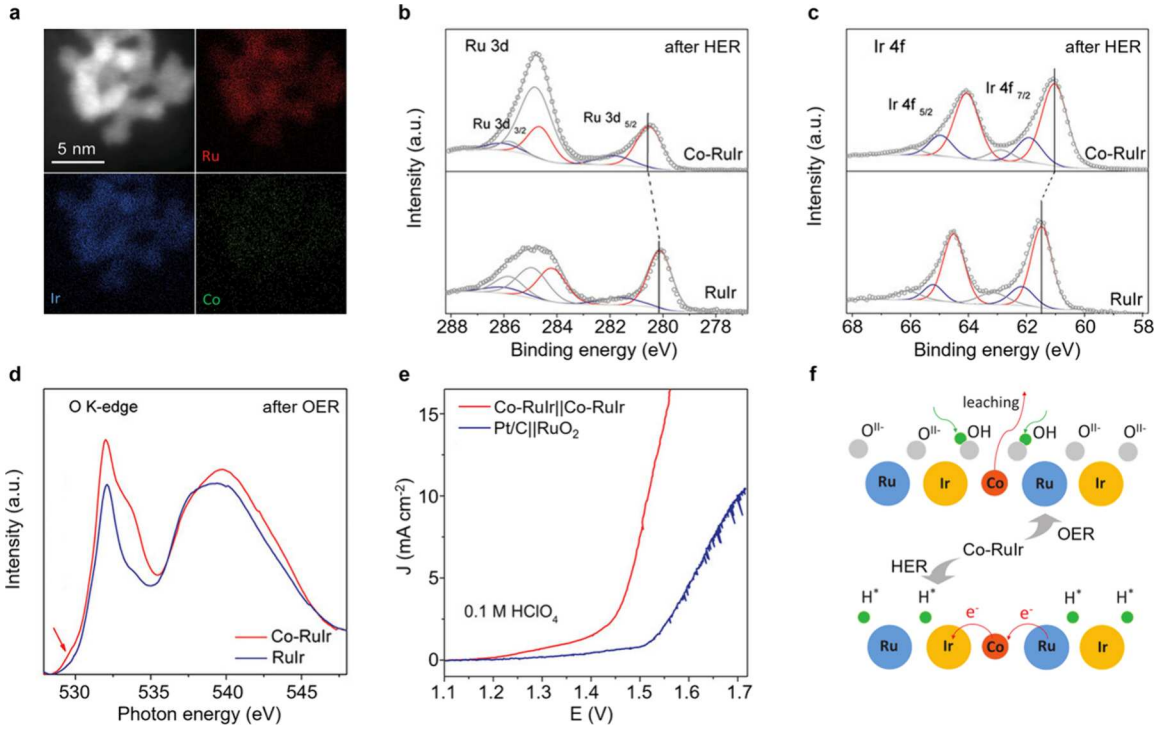

Figure 30. (a) HAADF-STEM and elemental mapping images of Co-RuIr. High-resolution (b) Ru 3d and (c) Ir 4f XPS spectra of Co-RuIr and RuIr electrocatalysts after HER tests. (d) O K-edge XANES spectra of Co-RuIr and RuIr after OER tests. (e) LSV curves of Co-RuIr couple and Pt/C||RuO_2 couple for OWS in 0.1 M $HClO_4$. (f) Schematic of OER and HER mechanisms on Co-RuIr bifunctional electrocatalyst in acidic media. Reproduced with permission from ref 373. Copyright 2019 John Wiley and Sons.

overpotential of only 165 mV to afford 10 mA cm^{-2} and robust stability. Operando XANES analysis suggested the oxidation of Ru to RuO_2 in RuIr-NC with increasing potentials. To quantitatively evaluate the proportions of the two components, the authors performed linear combination fitting (LCF), as shown in Figure 29f. Along with the increased potential, the oxidation of RuIr-NC was slow with 60% maintenance of metallic component at 1.80 V vs RHE, in contrast to that for nanospherical RuIr-NS control (25% maintenance). HAADF-STEM image (Figure 29g) of RuIr-NC under 1.80 V vs RHE revealed the preservation of the crystal structure. These results jointly confirmed the excellent durability of RuIr-NC. Besides exceptional OER performance, the RuIr-NC also exhibited comparable HER activity to commercial Pt/C. When served as a bifunctional electrocatalyst for acidic OWS, the RuIr-NC couple needed a low cell voltage of 1.485 V to achieve 10 mA cm^{-2} (Figure 29h), outperforming the combination of commercial Pt/C and IrO_2. Recently, He and coworkers successfully synthesized unsupported $Ru_{0.5}Ir_{0.5}$ alloy nanoparticles (NPs) using a room temperature reduction method.[372] TEM and elemental mapping images confirmed the uniform distribution of Ru and Ir atoms within the $Ru_{0.5}Ir_{0.5}$ NPs with an average particle size of 4 nm. XPS analysis revealed that the strong electron transfer from Ir to Ru in $Ru_{0.5}Ir_{0.5}$ NPs inhibits peroxidation of Ru, accountable for the improved acidic OWS performance. Electrochemical tests displayed that $Ru_{0.5}Ir_{0.5}$ NPs couple requires only a cell voltage of 1.44 V to achieve 10 mA cm^{-2} and maintains robust stability for 400 h in 0.5 M H_2SO_4.

To further reduce the usage of noble Ru and Ir, and modulate the electronic structure for boosted acidic OWS, doping RuIr alloys with nonprecious metals has been reported. For instance, Qiao and coworkers introduced a Co-doped RuIr alloy electrocatalyst (Co-RuIr) with improved bifunctionality for OWS.[373] HAADF-STEM and the corresponding elemental mapping images (Figure 30a) of Co-RuIr demonstrated an ultrasmall diameter of 2.1 ± 0.1 nm, along with uniform distribution of Co, Ru, and Ir. In view of the key role of surface chemical and valence states in electrocatalysis, XPS and XANES measurements were conducted. Figure 30b and c showed the high-resolution Ru 3d and Ir 4f XPS spectra of Co-RuIr and RuIr counterparts after HER. Clearly, Co doping induced the formation of higher-valence Ru and lower-valence Ir sites, leading to optimal hydrogen binding toward boosted HER. Additionally, the O K-edge XANES spectra of Co-RuIr after OER (Figure 30d) displayed the presence of O^{I-} species, beneficial to nucleophilic attack by water for promoted OER. Electrocatalytic OWS experiments utilizing Co-RuIr as both cathode and anode demonstrated excellent activity, with a low cell voltage of 1.52 V at 10 mA cm^{-2} (Figure 30e). The favorable HER and OER performance of Co-RuIr was explained by the dual effects of Co doping (Figure 30f). For HER, the charge transfer induced by Co dopant modified the surface valence state, facilitating appropriate hydrogen adsorption. For OER, the inevitable leaching of Co led to a significant increase in O^{I-} species, thereby enhancing OER activity.

Moreover, extensive investigations into RuIr-based oxides besides alloys for acidic OER have revealed their potential as bifunctional electrocatalysts for acidic overall water splitting.[310,358,374,375] Li and coworkers successfully obtained nanosized hollow $RuIrO_x$ ($x > 0$) nanonetcages using the dispersing-etching-holing strategy (Figure 31a).[376] HAADF-STEM images (Figure 31b,c) at different magnifications illustrated that the $RuIrO_x$ nanonetcages comprise interconnected ultrathin nanowires with a substantial number of holes,

https://doi.org/10.1021/acs.chemrev.3c00332
Chem. Rev. 2024, 124, 3694−3812

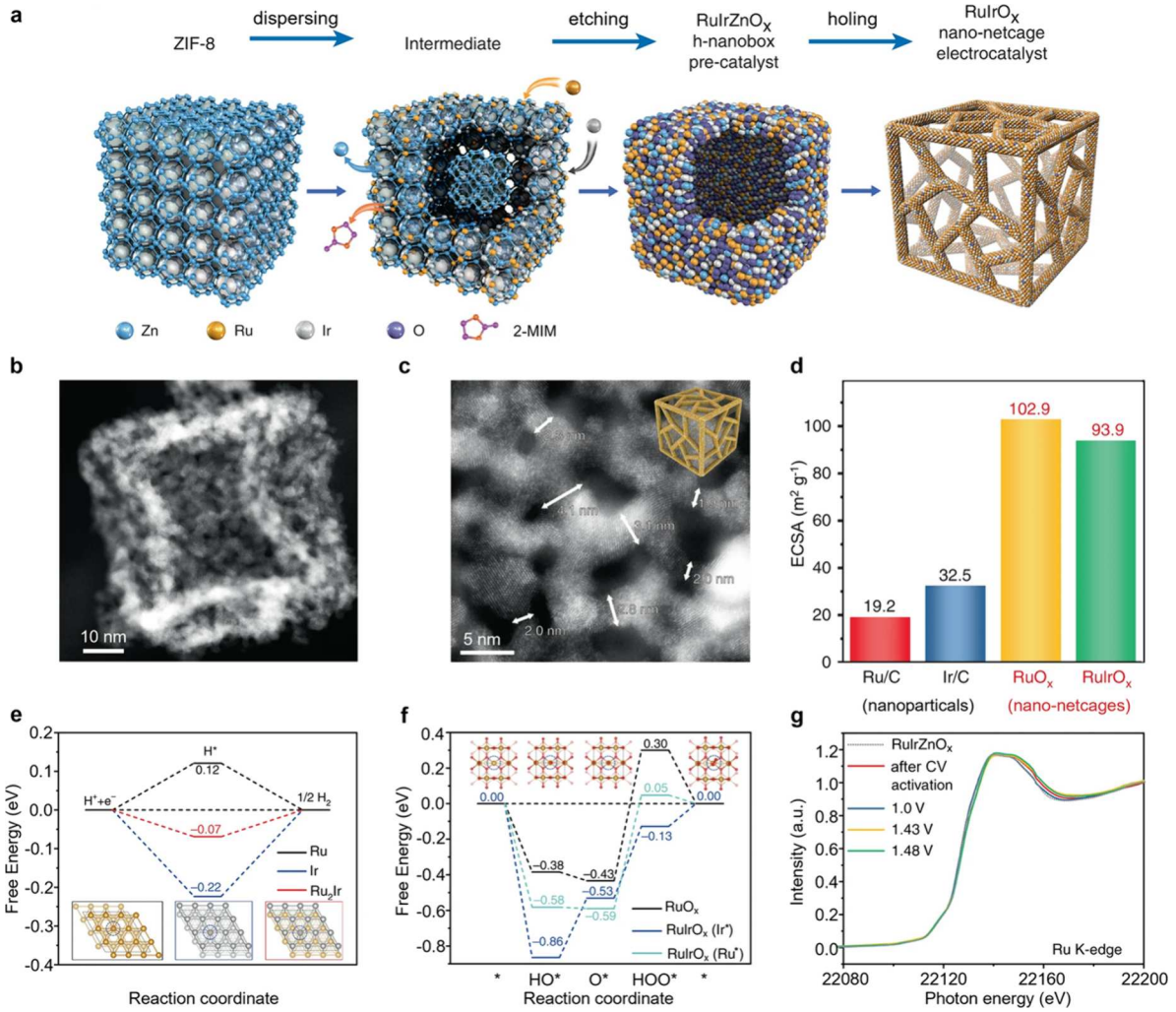

Figure 31. (a) Schematic of the synthesis of $RuIrO_x$ nanonetcages. (b, c) HAADF-STEM images of $RuIrO_x$ nanonetcages at different magnifications. (d) Calculated ECSAs of $RuIrO_x$, and RuO_x nanonetcages, as well as commercial Ru/C, and Ir/C nanoparticles. Free energy profiles for (e) HER on Ru(0001) (black line), Ir(111) (blue line) and $Ru_2Ir(111)$ (red line) surfaces at U = 0 eV, and for (f) OER on $RuO_2(110)$ surface (black line), $RuIrO_x(110)$ surfaces with Ir (blue line) and Ru (cyan line) as active sites at U = 1.23 eV. The colors of pink, red, gray, and gold represented H, O, Ir, and Ru atoms. (g) Ru K-edge XANES spectra of $RuIrO_x$ nanonetcages measured at different potentials during the OER process under acidic conditions. Reproduced with permission from ref 376 under the terms of a CC-BY 4.0 license. Copyright 2019 The Authors, published by Springer Nature.

beneficial to atomic utilization of Ru and Ir, as confirmed by the ECSA tests. As shown in Figure 31d, the ECSAs of both RuO_x and $RuIrO_x$ nanonetcages were calculated to be significantly larger than those of Ru/C and Ir/C nanoparticles, suggestive of increased accessibility of active sites. DFT calculations unraveled that incorporation of Ir into RuO_x optimizes the hydrogen adsorption over Ru_2Ir active sites for boosted HER (Figure 31e), and reduces the energy barriers of RDS for improved OER (Figure 31f). Additionally, Ru K-edge XANES spectra (Figure 31g) of $RuIrO_x$ nanonetcages under different positive potentials indicated that introduction of Ir prevents peroxidation of Ru and thus enhances the stability under acidic conditions. Consequently, the cell voltage required for $RuIrO_x$ nanonetcages couple to drive acidic OWS was as low as 1.45 V at 10 mA cm^{-2} in 0.5 M H_2SO_4, surpassing those for most previously reported bifunctional electrocatalysts.

Lately, ruthenium−iridium tellurides have been investigated for acidic OWS as well. Wang and coworkers conducted a successive galvanic replacement of Te nanowires route to synthesize ternary RuIrTe nanotubes (NTs), as schematically shown in Figure 32a.[377] TEM image (Figure 32b) of the resulting RuIrTe NTs revealed a tube-like structure with a diameter of approximately 20 nm consisting of numerous surface nanoparticles aggregates. High-resolution Te 3d XPS spectra (Figure 32c) of RuIrTe NTs demonstrated that the peaks of Te^0 at binding energies of 572.4 and 582.8 eV gradually diminish upon the sequential introduction of Ru and Ir, implying the successful galvanic replacement between Te nanowires and Ru/Ir as well as strong electronic coupling. Moreover, the redshift of the TeO_x peak indicated electron enrichment within TeO_x due to the addition of Ru and Ir atoms. Compared to RuTe NTs and IrTe NTs controls, introducing both Ru and Ir resulted in the averaging of binding energies of Ir and Ru in RuIrTe NTs (Figure 32d,e), highlighting the strong electronic interactions between Ru and Ir. These electronic couplings optimized intermediates binding and benefitted both HER and OER in 0.5 M H_2SO_4. For example, to reach a current density of 10 mA cm^{-2}, the RuIrTe NTs required overpotentials of 29 mV for HER

https://doi.org/10.1021/acs.chemrev.3c00332
Chem. Rev. 2024, 124, 3694−3812

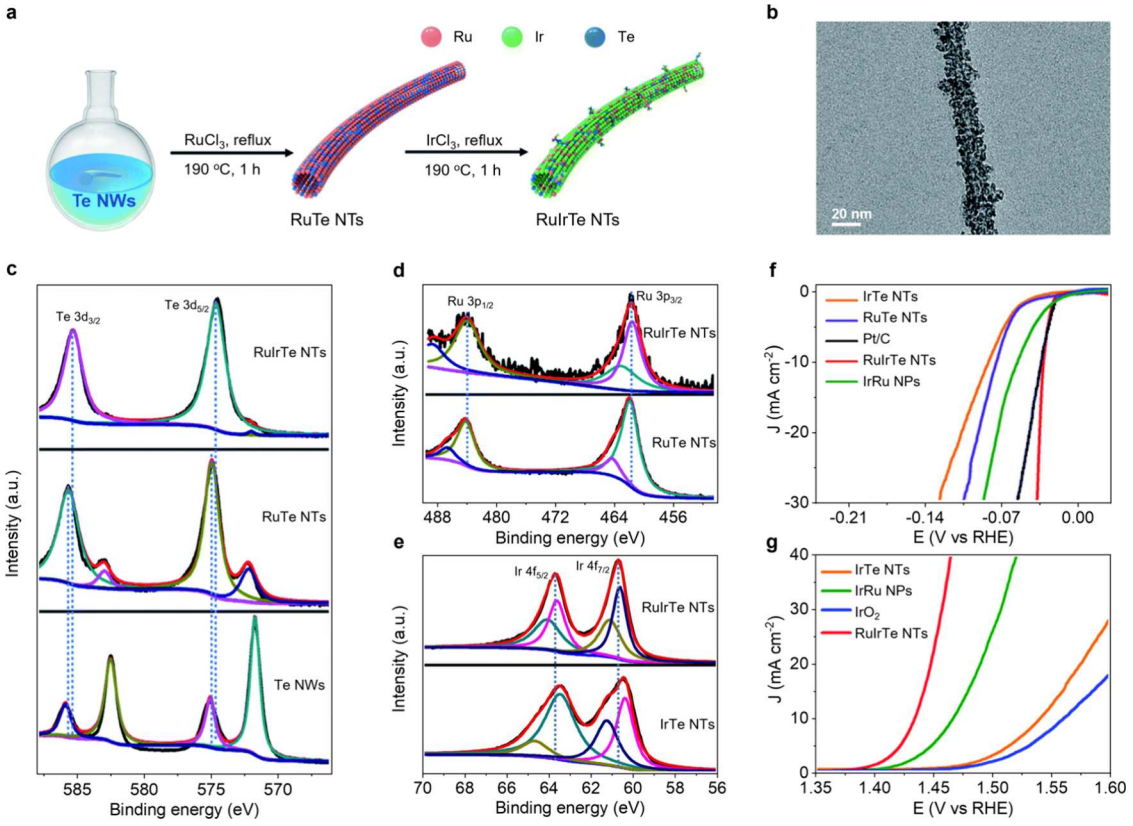

Figure 32. (a) Schematic of the preparation of RuIrTe NTs. (b) TEM image of RuIrTe NTs. (c) High-resolution Te 3d XPS spectra of Te NWs, RuTe NTs, and RuIrTe NTs. (d) High-resolution Ru 3p XPS spectra of RuTe NTs and RuIrTe NTs. (e) High-resolution Ir 4f XPS spectra of IrTe NTs and RuIrTe NTs. LSV curves of RuIrTe NTs and controls for (f) HER and (g) OER in 0.5 M H_2SO_4. Reproduced with permission from ref 377. Copyright 2022 Royal Society of Chemistry.

(Figure 32f) and 205 mV for OER (Figure 32g), both of which were lower than those of control samples.

4.1.4. Noble-Metal-Free Electrocatalysts. Compared to reducing the amounts of noble metals for OWS, it is more appealing to develop advanced electrocatalysts based on earth-abundant transition metals or even metal-free materials.[37,378] However, nonprecious electrocatalysts usually exhibit worse electrocatalytic activity and stability relative to Ru/Ir-based materials.[319,379−381] Consequently, the search for high active, cost-effective and durable nonprecious electrocatalysts for OWS in acidic media remains a significant challenge. Presently, only a few of noble-metal-free materials, such as nonprecious-metal sulfides, phosphides, nitrides, borates, etc., have been investigated for acidic OWS.

Owing to the relatively low cost, 2D layer structure and unique electronic properties, transition metal disulfides have triggered extensive interest in electrochemical applications.[382] Among them, MoS_2, as a typical 2D sulfide, has been explored for acidic HER,[383−385] while its OER activity is extremely poor.[386,387] To address this problem, it is desirable to dope exotic metals into MoS_2. In view of the excellent HER and OER performance of cobalt-based compounds,[388,389] introducing cobalt species into MoS_2 is expected to improve its HER and OER activity under acidic conditions. Lee and collaborators synthesized a bifunctional electrocatalyst for acidic OWS by growing single-atom cobalt-modified MoS_2 nanosheets on 3D titanium nitride (TiN) nanorod arrays (CoSAs-MoS_2/TiN NRs, Figure 33a).[390] Combined SEM and TEM images of CoSAs-MoS_2/TiN NRs revealed the formation of a unique hierarchical core/shell nanostructure with TiN nanorods as the core and ultrathin CoSAs-MoS_2 nanosheets as the shell (Figure 33b,c). EDX pattern inserted in Figure 33b certified the successful Co doping into MoS_2. Close observation of the shell revealed interlayer distances of 0.65 and 0.274 nm assignable to (002) and (100) planes of MoS_2, respectively (Figure 33d,e). Also, many dark dots contributable to Co SAs were observed (Figure 33e), confirming the Co doping again. High-resolution Mo 3d (Figure 33f) and S 2p (Figure 33g) XPS spectra of CoSAs-MoS_2/TiN NRs exhibited the redshift of binding energies compared to MoS_2/TiN NRs, indicating remarkable electron transfer from CoSAs to MoS_2. These electronic synergies were believed to not only improve the catalytic behavior through modulation of the electronic structure but also facilitate efficient electron transport between the core−shell components. Consequently, the CoSAs-MoS_2/TiN NRs couple demonstrated decent OWS activity and stability in 0.5 M H_2SO_4 (Figure 33h), achieving 10 mA cm^{-2} at a cell voltage of 1.7 V and retaining 96.9% of the initial current after a 30 h chronoamperometry test. Similarly, Zhao and coworkers prepared vertically aligned Co-doped MoS_2 nanosheets on carbon cloth (Co-MoS_2@CC) via a facile one-step hydrothermal method.[391] the Co-MoS_2@CC required a cell voltage of 1.55 V to reach 10 mA cm^{-2} in 0.5 M H_2SO_4. The authors ascribed the exceptional performance of Co-MoS_2@CC to the expansion of MoS_2 layer spacing through Co doping which ensured the exposure of more active sites and accelerated charge transfer during both HER and OER processes.

https://doi.org/10.1021/acs.chemrev.3c00332
Chem. Rev. 2024, 124, 3694−3812

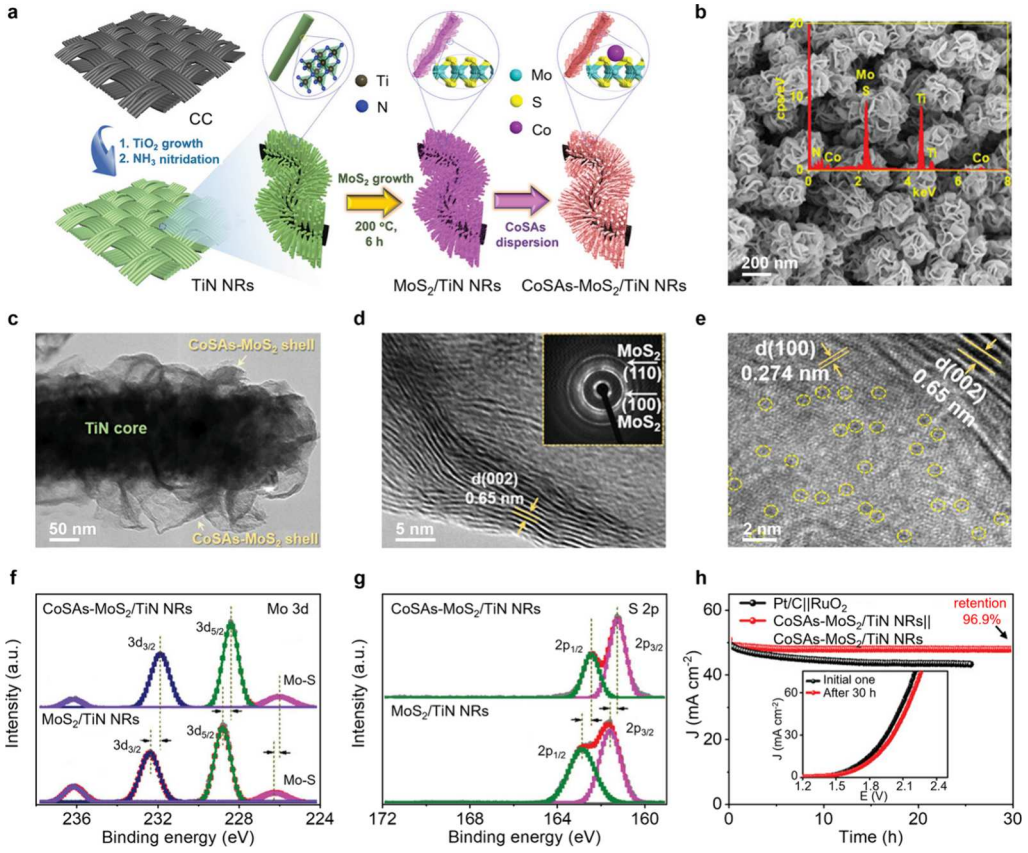

Figure 33. (a) Schematic of the fabrication of CoSAs-MoS_2/TiN NRs. (b) SEM and (c) TEM images with EDX pattern of CoSAs-MoS_2/TiN NRs. (d) HRTEM image of the outer CoSAs-MoS_2 nanosheet. Inset in (d): SAED pattern. (e) Atomic-resolution TEM image of the outer CoSAs-MoS_2 nanosheet (CoSAs were highlighted by yellow circles). High-resolution (f) Mo 3d and (g) S 2p XPS spectra of CoSAs-MoS_2/TiN NRs and MoS_2/TiN NRs. (h) Chronoamperometric curves of CoSAs-MoS_2/TiN NRs couple and Pt/C||RuO_2 couple in 0.5 M H_2SO_4. Inset in (h): LSV curves of CoSAs-MoS_2/TiN NRs couple before and after the chronoamperometric test. Reproduced with permission from ref 390. Copyright 2021 John Wiley and Sons.

Given the satisfactory OER activity of CoS_x and NiS_x, Kanatzidis and coworkers developed a CoMoNiS-NF-31 bifunctional electrocatalyst consisting of hierarchically coassembled MoS_2 and Co_9S_8 nanosheets on nickel foam-supported Ni_3S_2 nanorods arrays through a one-pot hydrothermal method (Figure 34a).[314] SEM image of CoMoNiS-NF-31 revealed that Co_9S_8 and MoS_2 nanosheets grow directly on the Ni_3S_2 nanorods without any redundant nanosheets aggregates (Figure 34b). HRTEM images depicted in Figure 34c clearly exhibited the presence of lattices fringes corresponding to Co_9S_8, MoS_2, and Ni_3S_2. In comparison to the high-resolution Co 2p XPS spectra of Co_9S_8/Ni_3S_2/NF control (Figure 34f) and Mo 3d of MoS_2/Ni_3S_2/NF (Figure 34g), the corresponding high-resolution XPS spectra of CoMoNiS-NF-31 (Figure 34d,e) demonstrated a blueshift of Co 2p peaks and a redshift of Mo 3d peaks, indicating a strong interaction between Co_9S_8 and MoS_2. The authors claimed that the unique hierarchical structure of CoMoNiS-NF-31 can expose a greater number of active sites, and the interaction between Co_9S_8 and MoS_2 modifies the adsorption of intermediates involved in HER and OER toward lowered energy barriers. Therefore, the CoMoNiS-NF-31 exhibited improved HER and OER activities relative to the control samples including Co_9S_8/Ni_3S_2/NF, MoS_2/Ni_3S_2/NF, and Ni_3S_2/NF in 0.5 M H_2SO_4, with overpotentials of only 103 (Figure 34h) and 228 mV (Figure 34i) to afford 10 mA cm^{-2}, respectively. Moreover, a cell voltage of 1.45 V was acquired at 10 mA cm^{-2} for OWS, while the stability needed to be further improved.

Analogues to sulfides, transition metal phosphides have been developed as potential electrocatalysts for acidic OWS. Liu and coworkers developed a 3D metal-vacancy $NiAl_\delta P$ nanowall arrays through a combination of selective alkali etching and phosphorization route.[392] The unique 3D structure of $NiAl_\delta P$ exhibited excellent conductivity and large specific surface area, facilitating efficient electrolyte contact, and charge/mass transport. Moreover, the alkali etching process resulted in the formation of dense surface metal defects, providing desirable unsaturated coordination sites as catalytic active centers. Consequently, the resulting $NiAl_\delta P$ couple achieved 10 mA cm^{-2} at a cell voltage of 1.52 V in 0.5 M H_2SO_4 for OWS. Recently, Fu's group fabricated vanadium-doped CoP_2 nanowire arrays tightly grown on carbon cloth (V-CoP_2/CC) via hydrothermal followed by phosphorization method (Figure 35a).[393] The porous structure and lattice expansion of CoP_2 after V doping were confirmed by N_2 sorption analysis (Figure 35b) and HRTEM images (Figure 35c,d), respectively. Furthermore, the introduction of V promoted the formation of a thicker Co-oxide layer via surface reconstruction of CoP_2 during OER (Figure 35e), which enhanced both OER activity and corrosion resistance in acidic conditions. DFT calculations (Figure 35f) demonstrated that V doping induces lattice expansion of CoP_2 and thus shifts its d-band center up to E_F for increased hydrogen adsorption at P site, leading to

https://doi.org/10.1021/acs.chemrev.3c00332
Chem. Rev. 2024, 124, 3694−3812

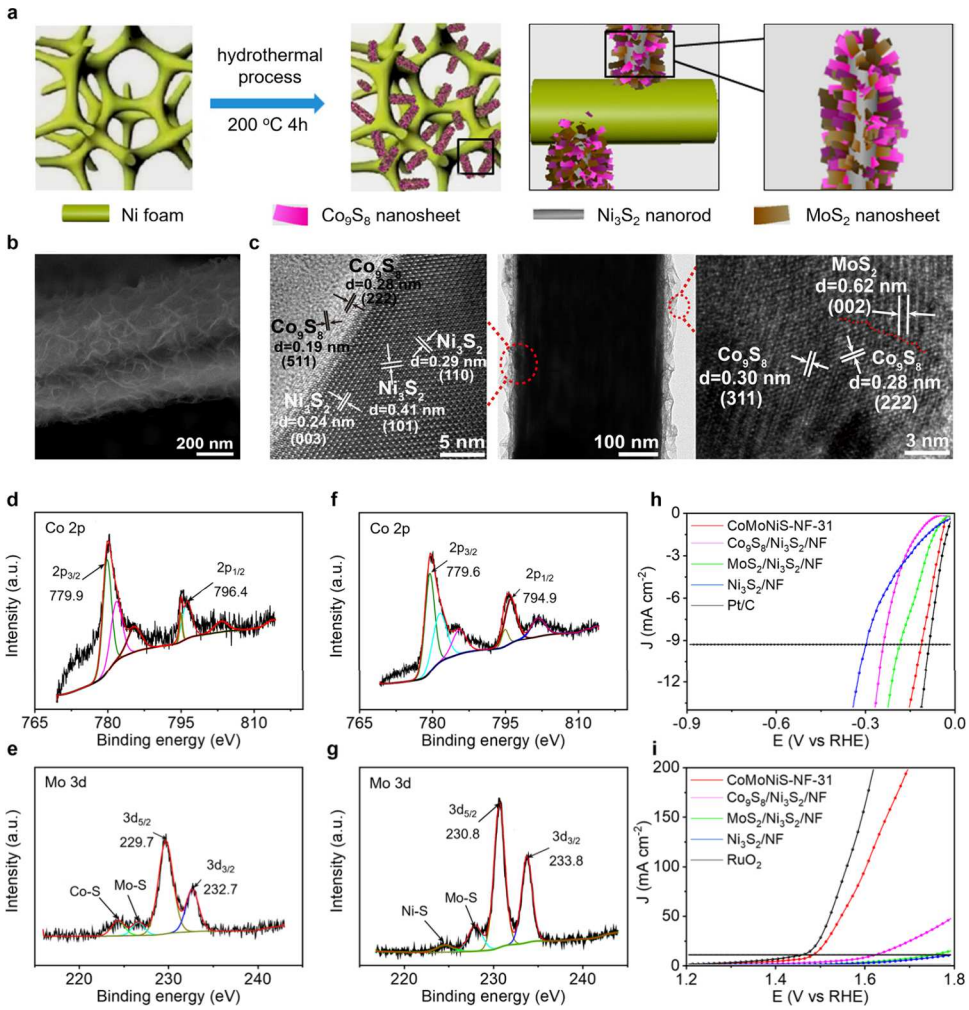

Figure 34. (a) Schematic of the synthesis and growth of hierarchical CoMoNiS-NF-31. (b) SEM and (c) HRTEM images of CoMoNiS-NF-31. High-resolution (d) Co 2p, and (e) Mo 3d XPS spectra of CoMoNiS-NF-31. High-resolution (f) Co 2p XPS spectra of Co_9S_8/Ni_3S_2/NF control, and (g) Mo 3d XPS spectra of MoS_2/Ni_3S_2/NF control. LSV curves of CoMoNiS-NF-31 and controls for (h) HER and (i) OER in 0.5 M H_2SO_4. Reproduced with permission from ref 314. Copyright 2019 American Chemical Society.

enhanced HER activity. Based on these advantages, the V-CoP_2/CC couple required only 1.47 V to achieve a current density of 10 mA cm^{-2} for OWS in 0.5 M H_2SO_4 (Figure 35g).

In addition, transition metal carbides, borides, and nitrides were also examined as bifunctional electrocatalysts for acidic OWS due to their good electrical conductivity, decent acid resistance, and promising electrocatalytic activity.[394,395] Sun and collaborators fabricated a superaerophobic N-doped WC (N-WC) nanoarray for efficient OWS in 0.5 M H_2SO_4.[396] The N-WC nanoarray was prepared by hydrothermal and subsequent chemical vapor deposition techniques (Figure 36a). DFT calculations (Figure 36b) revealed that the d-band center of W atoms in N-WC(001) is more closer to Pt(111) compared to that in WC(001), resulting in weaker hydrogen adsorption on N-WC surface for boosted HER. The adhesion force (AF) analysis of bubbles and catalyst surfaces (Figure 36c) demonstrated that both the nanostructure and N doping decrease the AF from 19 μN for non-nanostructured WC, to 12 μN for non-nanostructured N-WC, and 5 μN for WC nanoarray to <1.2 μN for N-WC nanoarray, indicative of facilitated bubbles detachment and thus efficient HER. Notably, despite its limited stability for acidic OER, N-WC nanoarray exhibited impressive OER catalytic activity with an onset potential of only 1.35 V vs RHE in 0.5 M H_2SO_4, even lower than those of commercial IrO_2 and Ir/C. Surprisingly, the N-WC couple initiated acidic OWS at approximately 1.4 V.

Transition metal borides have been discovered with eminent electrocatalytic activity for acidic HER and alkaline OER,[328,397−399] which makes them promising for acidic OWS. Jiang and collaborators developed a bifunctional electrocatalyst of FeCoNiB@B-VG by electroless deposition of FeCoNiB alloy nanoparticles on B-doped vertically aligned graphene array for acidic HER and OER (Figure 36d).[400] The high conductivity of B-VG and the synergistic effect between FeCoNiB and B-VG collectively improved electrocatalytic activity of FeCoNiB@B-VG toward both HER and OER in 0.5 M H_2SO_4. Specifically, the FeCoNiB@B-VG afforded low overpotentials of 148 mV and 635 mV at 10 mA cm^{-2} for HER and OER, respectively, along with decent stability of about 10 h at 10 mA cm^{-2} for OWS.

Likewise, in view of the superior HER under all pH and alkaline OER activity of transition metal nitrides,[401,402] several researchers have studied their acidic OWS performance. For instance, Wang and coworkers synthesized ultrafine Co_4N nanodots anchored on a nitrogen-doped carbon framework (Co_4N@NC) using a space-restricted strategy.[403] The

https://doi.org/10.1021/acs.chemrev.3c00332
Chem. Rev. 2024, 124, 3694−3812

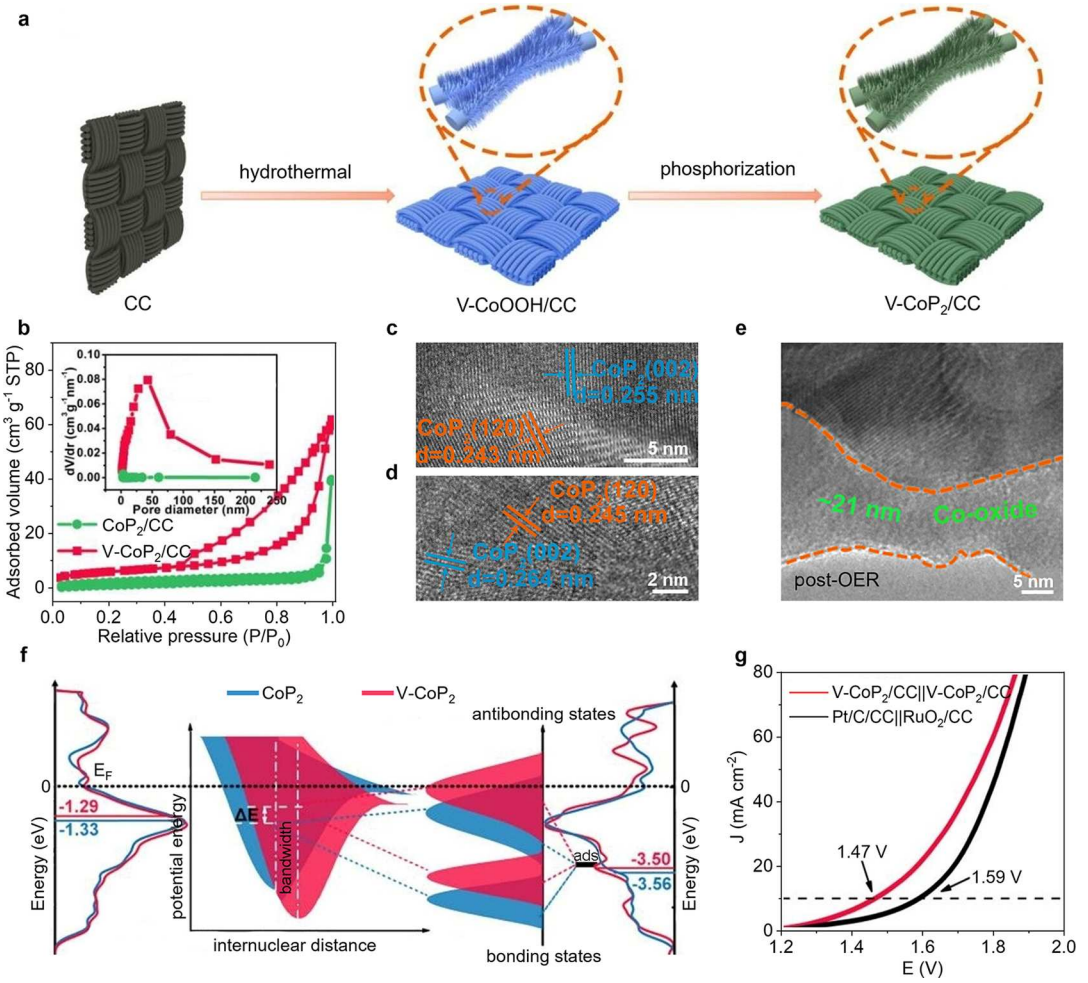

Figure 35. (a) Schematic of the synthesis of V-CoP_2/CC. (b) N_2 sorption isotherms of V-CoP_2/CC and CoP_2/CC as well as the pore size distribution (inset). HRTEM images of (c) CoP_2/CC and (d) V-CoP_2/CC. (e) TEM image of V-CoP_2/CC after OER electrocatalysis. (f) DOS of CoP_2 and V-CoP_2 with/without hydrogen adsorption and the schematic of the relation between narrowed bandwidth and hydrogen adsorption strength. (g) LSV curves of V-CoP_2/CC couple and Pt/C/CC||RuO_2/CC couple in 0.5 M H_2SO_4 for OWS. Reproduced with permission from ref 393. Copyright 2022 John Wiley and Sons.

generated Co−C bonding species at the interface of Co_4N@NC accelerated electron transfer and optimized adsorption/desorption of the intermediates during acidic OWS. As a result, the Co_4N@NC couple exhibited remarkable electrocatalytic OWS activity in 0.5 M H_2SO_4 with a cell voltage of only 1.47 V to achieve 10 mA cm^{-2}. While the stability can be further improved, as revealed by the chronoamperometry measurements for only 5 h.

4.1.5. Metal-Free Electrocatalysts. As discussed above, noble metal-based bifunctional electrocatalysts feature excellent activity and stability toward acidic OWS, while their high cost and limited availability hinder the large-scale commercialization of PEMWE.[404,405] The bifunctional electrocatalysts based on nonprecious metals mostly exhibit unsatisfactory stability in acidic media, even with relatively low cost.[406,407] In contrast, carbon-based metal-free materials have triggered tremendous research interest in energy storage and conversion over the past decade, by virtue of their unique electronic structure, high conductivity, superior chemical/mechanical stability, and sustainability.[408−410] Lately, Dai and collaborators explored a class of new metal-free bifunctional HER/OER electrocatalysts by adsorbing C_{60} onto single-walled carbon nanotubes (C_{60}-SWCNT), as schematically shown in Figure 37a.[411] The binding energy of C 1s XPS peak of C_{60}-SWCNT (Figure 37b) exhibited a gradual redshift with increasing C_{60} adsorption time, indicating charge transfer between SWCNT and C_{60}. This charge transfer mechanism led to excellent electrocatalytic OWS activity in 0.5 M H_2SO_4, with overpotentials of 320 and 400 mV to afford 10 mA cm^{-2} for HER and OER, respectively.

Additionally, Li and coworkers developed 3D porous fluorographdiyne networks (p-FGDY/CC) on carbon cloth as an efficient metal-free bifunctional electrocatalyst (Figure 37c).[412] SEM image (Figure 37d) and contact angle tests (Figure 37e) confirmed the formation of 3D porous networks with superhydrophilicity in p-FGDY/CC. The high intensity of D band in the Raman spectrum (Figure 37f) indicated a high density of defects, beneficial to increase conductivity and facilitate mass and charge transfer. Moreover, DFT calculations (Figure 37g) revealed that the strong C−F bonding in FGDY induces charge polarization and enhances electron localization near the C_2 site, ensuring higher selectivity for adsorption/desorption of various O/H-related species (i.e., H_2O, O, OOH, and O_2). All these unique morphology and electronic structures collectively led to improved electrocatalytic activity of p-FGDY/CC for both HER and OER, with a low cell

https://doi.org/10.1021/acs.chemrev.3c00332
Chem. Rev. 2024, 124, 3694−3812

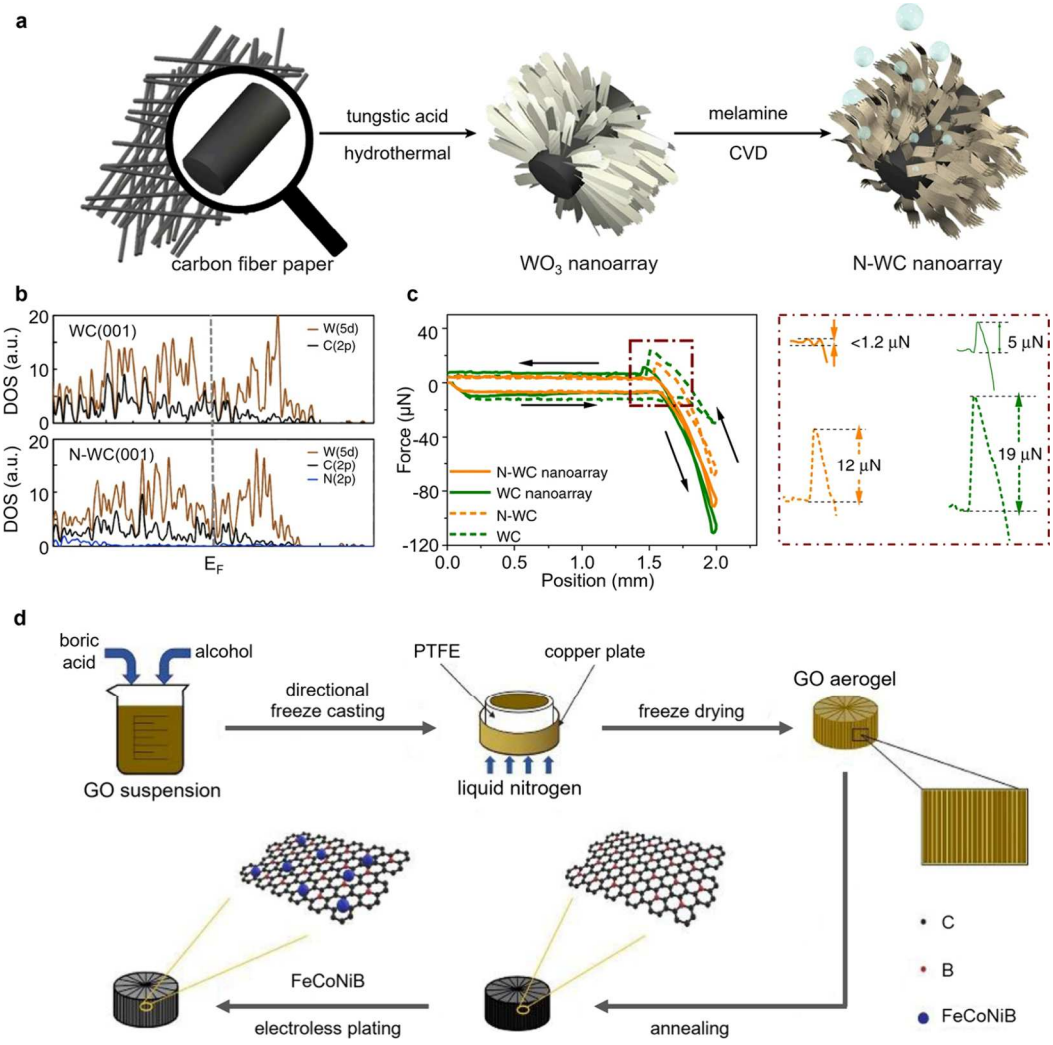

Figure 36. (a) Schematic of the synthesis of N-WC nanoarray. (b) DOS of WC(001) and N-WC(001). (c) Bubble adhesion forces on different electrodes of WC, WC nanoarray, N-WC, and N-WC nanoarray. Reproduced with permission from ref 396 under the terms of a CC-BY 4.0 license. Copyright 2018 The Authors, published by Springer Nature. (d) Schematic of the preparation of FeCoNiB@B-VG. Reproduced with permission from ref 400. Copyright 2021 Elsevier.

voltage of 1.8 V to achieve 10 mA cm^{-2} in 0.5 M H_2SO_4. Besides the single heteroatom doping, codoping two elements with higher or lower electronegativity than that of C (χ = 2.55) including B (χ = 2.04) and N (χ = 3.04) can introduce synergistic coupling effect to further enhance the activity of underlying carbon-based electrocatalysts.[413] Song and coworkers reported the synthesis of B, N codoped carbon nanosheets (B5/GCS), achieving a cell voltage of 1.45 V at 10 mA cm^{-2} in 0.5 M H_2SO_4.[414] The excellent electrocatalytic performance was attributed to the synergistic effect of B, N codoping and the formation of fragmented nanosheets through cation-embedded exfoliation. These properties collectively optimized intermediates adsorption and catalytic kinetics. Table 4 summarizes the electrocatalytic overall water splitting (OWS) activities of various bifunctional electrocatalysts in acidic electrolytes.

4.2. Overall Water Splitting in Alkaline Electrolytes

Compared to PEMWE, the alkaline water electrolysis (AWE) enables the usage of nonprecious and earth-abundant electrocatalysts with longer lifetime and lower cost, while the energy conversion efficiency for hydrogen generation needs to be further improved due to the mediocre activities of the underlying nonprecious electrocatalysts. Therefore, various nanostructuring strategies have been developed to design and synthesize high-performance bifunctional electrocatalysts for alkaline OWS.

4.2.1. Fe-Based Electrocatalysts. Iron, as one of the most abundant elements on Earth, exhibits diverse redox states and a rich coordination chemistry.[438,439] These properties make it a promising candidate for electrocatalysis application. Reisner's group introduced a bifunctional iron-only material for water electrolysis, capable of functioning as both an anode and a cathode in an alkaline electrolyzer. This material maintained a stable cell voltage of 2.0 V at a current density of 10 mA cm^{-2}.[439] The bifunctional activity of the iron-only electrode originated from an oxide-supported Fe(0) phase with HER activity, and an iron oxide-hydroxide (FeO_x) phase featuring OER activity. Remarkably, the active species on the electrode surface underwent reconstruction transformation between these phases and regenerated during the switching of the anode and cathode. This feature enhanced the stability and longevity of the alkaline electrolyzer system.

https://doi.org/10.1021/acs.chemrev.3c00332
Chem. Rev. 2024, 124, 3694−3812

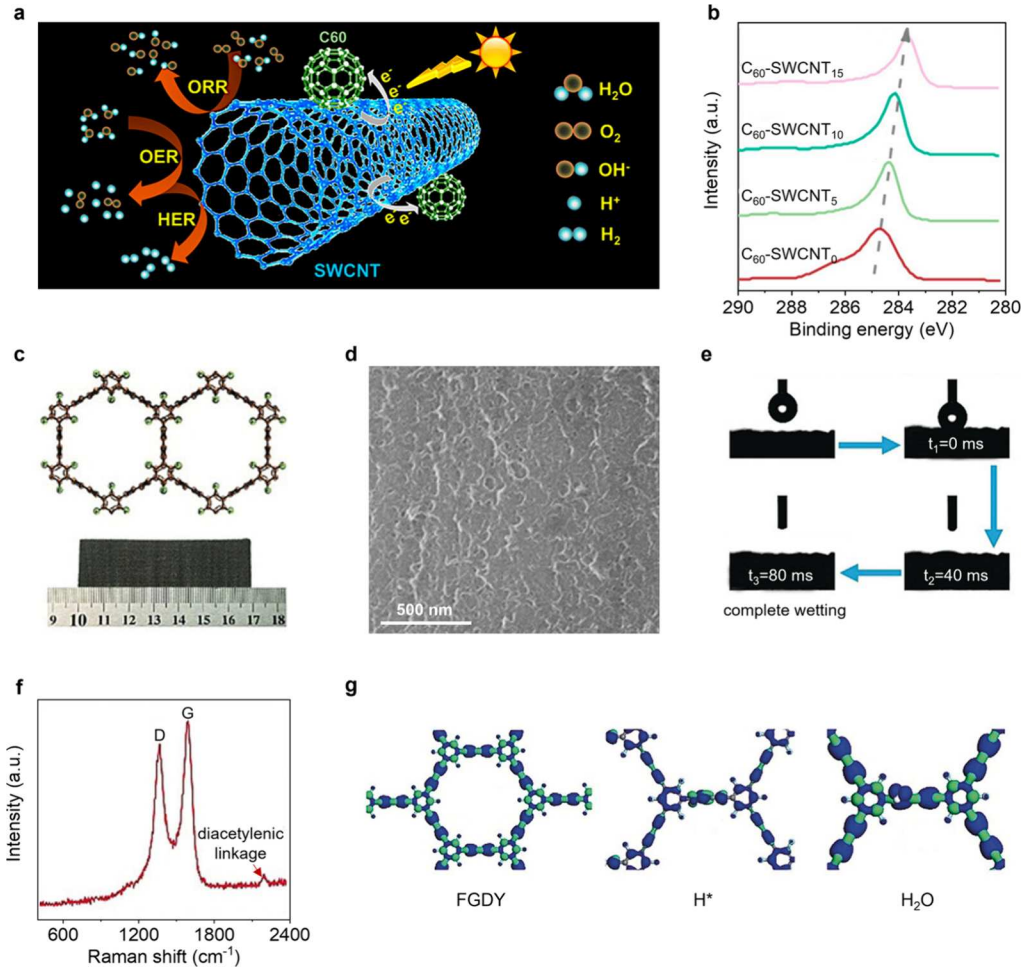

Figure 37. (a) Illustration of charge-transfer process and OER/HER on C_{60}-SWCNTs. (b) High-resolution C 1s XPS spectra of C_{60}-SWCNT$_n$ (n = 0, 5, 10, and 15 min). Reproduced with permission from ref 411. Copyright 2019 American Chemical Society. (c) Structural schematic of FGDY and photograph of the p-FGDY/CC material. (d) SEM image of p-FGDY/CC. (e) Contact angle measurements of p-FGDY/CC. (f) Raman spectrum of p-FGDY/CC. (g) Real spatial contour plots of bonding and antibonding orbitals near E_F of pristine FGDY, hydrogen adsorption on FGDY, and initial H_2O adsorption on FGDY. Reproduced with permission from ref 412. Copyright 2019 John Wiley and Sons.

Furthermore, extensive research has been dedicated to exploring iron-based inorganic compounds, such as hydroxides, sulfides, phosphides, carbides, and others, as bifunctional electrocatalysts for alkaline OWS. Zhang and coworkers presented a wet chemical method to grow ultrathin iron–oxygen hydrate nanosheets with abundant iron vacancies on nickel foam (δ-FeOOH NSs/NF).[440] Low-magnified SEM image (Figure 38a) illustrated the dense networked architecture of δ-FeOOH NSs uniformly grown on NF, benefiting the exposure of catalytic active sites and enhancing mechanical stability. HRTEM image (Figure 38b) revealed the presence of defects and lattice distortions in δ-FeOOH NSs/NF, beneficial to accelerated mass and charge transfer. Moreover, in a two-electrode system, δ-FeOOH NSs/NF couple exhibited remarkable performance for OWS in 1.0 M KOH, achieving a low cell voltage of only 1.62 V at a current density of 10 mA cm^{-2} with negligible activity decay over 60 h continuous electrolysis at an overpotential of 500 mV (Figure 38c). DFT calculations (Figure 38d–f) conducted by the authors indicated that the abundant Fe vacancies (V_{Fe}) activate their second neighbored Fe atoms (Fe2) with optimal hydrogen adsorption for improved HER (Figure 38d) and enhance the binding with O* intermediates with reduced theoretical OER overpotential of 0.46 V relative to that of bare δ-FeOOH NSs (0.57 V) for boosted OER (Figure 38e,f). The authors also noted that the activation of Fe sites next to V_{Fe} (denoted as Fe1) is not as good as that for Fe2.

During electrocatalytic OWS, especially in the OER, the transformation of an electrocatalyst to form new active species known as electrochemical reconstruction is a common phenomenon, as discussed in the Section 3. Zhang and collaborators synthesized mackinawite FeS nanosheets grown on iron foam (FeS/IF) as an efficient bifunctional pre-electrocatalyst for alkaline OWS (Figure 39a).[441] In the HER tests, the surface FeS nanosheets (Figure 39b) of inactive FeS/IF were transformed to catalytically active Fe@FeO$_x$S$_y$ nanoparticles in situ (Figure 39c). By contrast, during the OER test, the FeS nanosheets were entirely converted to porous and amorphous FeO$_x$ films (Figure 39d). When utilized as cathode and anode in a two-electrode system for OWS, this unique material exhibited superior activity (1.65 V at 10 mA cm^{-2} in 1.0 M KOH) compared to commercial Pt/C and IrO$_2$ benchmark couple, due to the synergistic effect of the binary nonmetallic materials and the effective modulation of the OER by the anode film.

Furthermore, iron-based phosphides have garnered significant attention in electrocatalytic water splitting due to their unique electronic properties.[28,442] Driess and colleagues

https://doi.org/10.1021/acs.chemrev.3c00332
Chem. Rev. 2024, 124, 3694–3812

Table 4. Summary of Bifunctional Electrocatalysts for Overall Water Splitting (OWS) in Acidic Electrolytes

Electrocatalysts	Electrolyte	Application	η_{10} and E_{10}	Ref
SS Pt-RuO_2 HNSs	0.5 M H_2SO_4	HER	26 mV	5
		OER	228 mV	
		OWS	1.49 V	
$MoS_2/Co_9S_8/Ni_3S_2$/Ni	0.5 M H_2SO_4	HER	103 mV	314
		OER	228 mV	
		OWS	1.45 V	
Ru@V-RuO_2/C HMS	0.5 M H_2SO_4	HER	47 mV	330
		OER	176 mV	
		OWS	1.467 V	
Ru-SA/$Ti_3C_2T_x$	0.1 M $HClO_4$	HER	70 mV	331
		OER	290 mV	
		OWS	1.56 V	
Ru/RuS_2 heterostructure	0.5 M H_2SO_4	HER	45 mV	332
		OER	201 mV	
		OWS	1.501 V	
a-$RuTe_2$ PNRs	0.5 M H_2SO_4	HER	33 mV	333
		OER	245 mV	
		OWS	1.52 V	
Ir/GF	0.5 M H_2SO_4	HER	7 mV	344
		OER	290 mV	
		OWS	1.55 V	
Ir-NSG	0.1 M $HClO_4$	HER	17 mV	348
		OER	265 mV	
		OWS	1.42 V	
Ir-SA@Fe@NCNT	0.5 M H_2SO_4	HER	26 mV	353
		OER	250 mV	
		OWS	1.51 V	
Au@$AuIr_2$	0.5 M H_2SO_4	HER	29 mV	354
		OER	261 mV	
		OWS	1.55 V	
IrNi NFs	0.1 M $HClO_4$	HER	25 mV	355
		OER	293 mV	
		OWS	1.6 V	
AlNiCoIrMo np-HEA	0.5 M H_2SO_4	HER	18.5 mV	356
		OER	233 mV	
		OWS	1.505 V	
3D-IrO_2/N@C	0.5 M $HClO_4$	HER	35 mV	357
		OER	280 mV	
		OWS	1.55 V	
SrIrO	0.5 M H_2SO_4	HER	18.2 mV	361
		OER	245 mV	
		OWS	1.50 V	
IrTe NTs	0.5 M H_2SO_4	HER	36 mV	362
		OER	271 mV	
		OWS	1.53 V	
Li-$IrSe_2$	0.5 M H_2SO_4	HER	55 mV	363
		OER	180 mV	
		OWS	1.44 V	
$BiIr_4Se_8$	0.5 M H_2SO_4	HER	85 mV	364
		OER	379 mV	
		OWS	1.56 V	
RuIr-NC	0.05 M H_2SO_4	HER	46 mV	371
		OER	165 mV	
		OWS	1.485 V	
$Ru_{0.5}Ir_{0.5}$ NPs	0.5 M H_2SO_4	HER	4 mV	372
		OER	160 mV	
		OWS	1.44 V	
Co-RuIr	0.1 M $HClO_4$	HER	14 mV	373
		OER	235 mV	
		OWS	1.52 V	
$RuIrO_x$	0.5 M H_2SO_4	HER	12 mV	376
		OER	233 mV	
		OWS	1.45 V	
RuIrTe NTs	0.5 M H_2SO_4	HER	29 mV	377
		OER	205 mV	
		OWS	1.511 V	
CoSAs-MoS_2/TiN NRs	0.5 M H_2SO_4	HER	187.5 mV	390
		OER	454.9 mV	
		OWS	1.7 V	
Co-MoS_2@CC	0.5 M H_2SO_4	HER	130 mV	391
		OER	201 mV	
		OWS	1.55 V	
$NiAl_\delta P$	0.5 M H_2SO_4	HER	35 mV	392
		OER	256 mV	
		OWS	1.52 V	
V-CoP_2	0.5 M H_2SO_4	HER	50 mV	393
		OER	91 mV	
		OWS	1.47 V	
FeCoNiB@B-VG	0.5 M H_2SO_4	HER	148 mV	400
		OER	635 mV	
Co_4N@NC	0.5 M H_2SO_4	HER	55 mV	403
		OER	110 mV	
		OWS	1.47 V	
C_{60}-SWCNT	0.5 M H_2SO_4	HER	320 mV	411
		OER	400 mV	
p-FGDY/CC	0.5 M H_2SO_4	HER	92 mV	412
		OER	570 mV	
		OWS	1.8 V	
B5/GCS	0.5 M H_2SO_4	HER	52 mV	414
		OER	170 mV	
		OWS	1.45 V	
RuCu NSs/C	0.5 M H_2SO_4	HER	19 mV	415
		OER	236 mV	
		OWS	1.49 V	
$Ru_{0.85}Zn_{0.15}O_{2-\delta}$	0.5 M H_2SO_4	HER	33 mV	416
		OER	190 mV	
		OWS	1.50 V	
RuO_2/Co_3O_4-RuCo@NC	0.5 M H_2SO_4	HER	141 mV	417
		OER	247 mV	
		OWS	1.66 V	
NiRu@MWCNTs	0.5 M H_2SO_4	HER	61 mV	418
		OER	430 mV	
		OWS	1.56 V	
RuCo@CDs	0.5 M H_2SO_4	HER	51 mV	419
		OER	190 mV	
		OWS	1.49 V	
RuB_2	0.5 M H_2SO_4	HER	52 mV	420
		OER	223 mV	
		OWS	1.525 V	
hollow Pt/NiO/RuO_2	0.1 M $HClO_4$	HER	29.6 mV	421
		OER	239 mV	
		OWS	1.524 V	
Mn-Ru/RuO_2@CNT	0.5 M H_2SO_4	HER	30 mV	422
		OER	177 mV	
		OWS	1.43 V	
La-RuO_2	0.5 M H_2SO_4	HER	71 mV	423
		OER	208 mV	
		OWS	1.53 V	
Ru@$MoO(S)_3$	0.5 M H_2SO_4	HER	63 mV	424
		OER	226 mV	
		OWS	1.522 V	
Ru-30 aerogel	0.5 M H_2SO_4	HER	24 mV	425

https://doi.org/10.1021/acs.chemrev.3c00332
Chem. Rev. 2024, 124, 3694−3812

Table 4. continued

Electrocatalysts	Electrolyte	Application	η_{10} and E_{10}	Ref
		OER	181 mV	
		OWS	1.468 V	
5%Pt-Ru ONAs	0.5 M H_2SO_4	HER	31 mV	426
		OER	227 mV	
		OWS	1.486 V	
Ru-RuO_2-NC	0.5 M H_2SO_4	HER	112 mV	427
		OER	176 mV	
		OWS	1.55 V	
Ru/Mo_2C	0.5 M H_2SO_4	HER	40 mV	428
		OER	215 mV	
		OWS	1.51 V	
Ir-NCT/CC	0.1 M $HClO_4$	HER	9 mV	429
		OER	202 mV	
		OWS	1.469 V	
Ir@Ni-NDC	0.5 M H_2SO_4	HER	41 mV	430
		OER	219 mV	
		OWS	1.54 V	
PdCu/Ir	0.1 M $HClO_4$	HER	20 mV	431
		OER	283 mV	
		OWS	1.583 V	
Ir-modified BP	0.5 M H_2SO_4	HER	25 mV	432
		OER	290 mV	
		OWS	1.54 V	
Mo-Ni-P	0.5 M H_2SO_4	HER	58 mV	433
		OER	291 mV	
Mo-Co_9S_8@C	0.5 M H_2SO_4	HER	98 mV	434
		OER	370 mV	
		OWS	1.68 V	
Mn-FeP/$Co_3(PO_4)_2$	0.5 M H_2SO_4	HER	27 mV	435
		OER	390 mV	
		OWS	1.75 V	
Co_3S_4@MoS_2@20TiP-CP	0.5 M H_2SO_4	HER	110 mV	436
		OER	247 mV	
		OWS	1.41 V	
CoMnP/Ni_2P/NF	0.5 M H_2SO_4	HER	84 mV	437
		OER	165 mV	
		OWS	1.43 V	

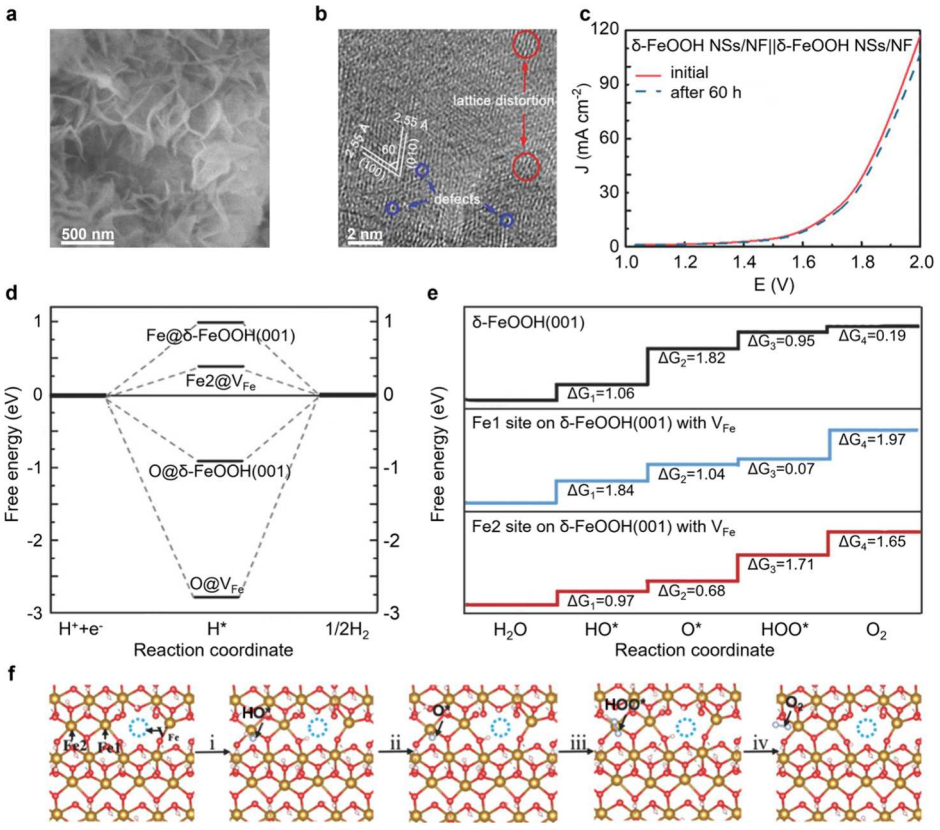

Figure 38. (a) SEM and (b) HRTEM images of δ-FeOOH NSs/NF. (c) LSV curves of δ-FeOOH NSs/NF couple for OWS in 1.0 M KOH before and after stability test for 60 h. (d) Free energy diagrams of the HER process on the O and Fe in δ-FeOOH NSs without V_{Fe} (marked as δ-FeOOH(001)) and the O neighboring to V_{Fe} and the second neighboring Fe to V_{Fe} (Fe2) in δ-FeOOH NSs with V_{Fe} (marked as V_{Fe}). (e) Free energy diagram of the OER processes on the δ-FeOOH(001), and Fe1 and Fe2 sites on δ-FeOOH(001) NSs with V_{Fe}. Fe1 indicated the first neighboring Fe to V_{Fe}. (f) Primitive steps of the OER process on the surface of δ-FeOOH NSs with V_{Fe} (top view). The Roman numerals represented (i) adsorption step, (ii, iii) dissociation steps, and (iv) desorption step during the OER process. Brown: Fe; red: O. Reproduced with permission from ref 440. Copyright 2018 John Wiley and Sons.

successfully transformed molecular iron phosphide precursors (Figure 39e) to monodispersed, ultrasmall, and highly active iron phosphide (FeP) nanoparticles for alkaline OWS.[443] By converting a diiron triphosphide complex to FeP nanoparticles under oleylamine thermal injection conditions, the FeP nanocrystals were obtained with an orthorhombic space group $Pna2_1$ and stacked along [100], as depicted in Figure 39f. Selected area electron diffraction (SAED) pattern (Figure

https://doi.org/10.1021/acs.chemrev.3c00332
Chem. Rev. 2024, 124, 3694−3812

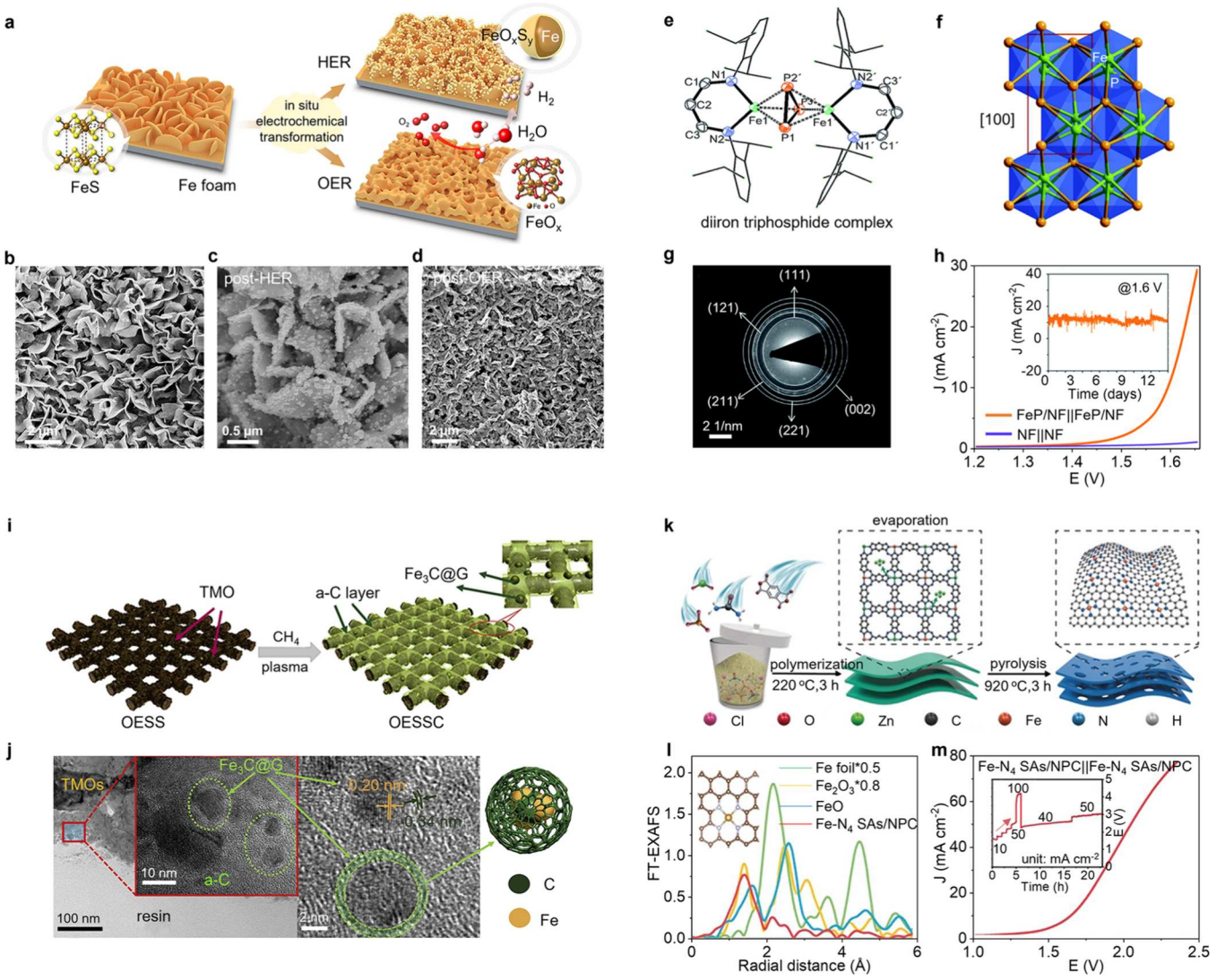

Figure 39. (a) Schematic of a FeS/IF pre-electrocatalyst for generating active electrocatalysts toward both HER and OER. SEM images of (b) fresh FeS/IF, (c) post-HER FeS/IF, and (d) post-OER FeS/IF. Reproduced with permission from ref 441. Copyright 2018 Elsevier. (e) Structure of molecular iron phosphide precursors. Hydrogen atoms were omitted for clarity. (f) Crystal structure of FeP with the orthorhombic space group $Pna2_1$ (shown along [100]; the unit cell is shown in red). (g) SAED pattern of FeP. (h) LSV curves of FeP and NF couples for OWS in 1.0 M KOH. Inset: the stability tests of FeP couple at 1.6 V. Reproduced with permission from ref 443 under the terms of a CC-BY 4.0 license. Copyright 2018 The Authors, published by Royal Society of Chemistry. (i) Schematic of the fabrication of OESSC. (j) TEM images of OESSC at low (left) and high magnifications (middle), and schematic of Fe_3C@G (right). Reproduced with permission from ref 444. Copyright 2019 Elsevier. (k) Schematic of the synthesis of Fe−N_4 SAs/NPC. (l) k^3-weighted Fe K-edge FT-EXAFS spectra of Fe−N_4 SAs/NPC and controls. Inset: Fe atomic structure model; C gold, N silver, and Fe orange. (m) LSV curve of the Fe−N_4 SAs/NPC couple for OWS in 1.0 M KOH. Inset: chronopotentiometric curve at different current densities. Reproduced with permission from ref 445. Copyright 2018 John Wiley and Sons.

39g) from the corresponding TEM image exhibited characteristic rings of phase-purified FeP. Electrocatalytic OWS measurements employing FeP as a bifunctional electrocatalyst in 1.0 M KOH, demonstrated a low cell voltage of merely 1.59 V at 10 mA cm^{-2} along with long-term stability at 1.6 V for 14 days (Figure 39h). The exceptional OER activity of FeP was attributed to in situ formed anionic vacancies and amorphous Fe-rich shells ($Fe(OH)_2$/FeOOH species) over ultrasmall and monodispersed FeP nanocrystals through the oxidation process, and its superior HER activity stemmed from the electronegativity of the phosphorus (P) atom, which reduced the electron density of iron (Fe) and created active sites. Moreover, the metallic nature of FeP was believed to facilitate efficient charge transfer during electrocatalysis processes.

From a commercial standpoint, the direct utilization of stainless steel (SS) can effectively reduce costs. Wang and coworkers treated the oxidized and etched SS surface with CH_4 plasma (OESSC), resulting in the formation of amorphous carbon layers and graphene-coated Fe_3C nanoparticles (Figure 39i).[444] As observed in the TEM images at different magnifications (Figure 39j), the OESSC surface exhibited numerous Fe_3C nanoparticles encapsulated by carbons, with lattice spacings of about 0.20 and 0.34 nm, respectively. When employed as bifunctional electrocatalysts for alkaline OWS in 1.0 M KOH, the OESSC couple exhibited a cell voltage of 1.74 V at 10 mA cm^{-2}, surpassing the SS couple. This superior performance was ascribed to the defect-rich amorphous carbon layers and carbides (Fe_3C) obtained through CH_4 plasma

https://doi.org/10.1021/acs.chemrev.3c00332
Chem. Rev. 2024, 124, 3694−3812

treatment, which resulted in the increase of active sites and tailored electronic structure.

To improve the metal utilization, nitrogen-coordinated single atom Fe electrocatalysts have been developed and explored for alkaline OWS. Chen and coworkers reported a polymerization-pyrolysis-evaporation (PPE) strategy to synthesize N-doped porous carbon-anchored Fe−N_4 active sites with atomic dispersion (Fe−N_4 SAs/NPC), as schematically depicted in Figure 39k.[445] The k^3-weighted FT-EXAFS analysis of Fe−N_4 SAs/NPC (Figure 39l) revealed the presence of Fe−N bonding with a coordination number of 4, and without the Fe−Fe coordination, confirming the atomic dispersion of Fe−N_4 active sites. Thanks to the synergistic effect between the atomic Fe−N_4 sites and porous conductive carbon network, the resulting Fe−N_4 SAs/NPC couple exhibited remarkable OWS activity and stability in 1.0 M KOH, as confirmed by a low cell voltage of only 1.67 V at 10 mA cm^{-2} and stable voltage outputs at various current densities for 23 h (Figure 39m).

4.2.2. Co-Based Electrocatalysts. Cobalt-based materials have emerged as promising alternatives to precious metals, owing to their abundant sources, low cost, and high catalytic activity.[446,447] To date, significant research efforts have been dedicated to the advancement of cobalt-based inorganic compounds, encompassing oxides, sulfides, phosphides, nitrides, etc., as bifunctional electrocatalysts for alkaline OWS.

Based on previous studies, cobalt oxides have demonstrated high electrocatalytic activity for OER in alkaline solutions.[448,449] Moreover, cobalt-based materials with low energy barriers for hydrogen (H) adsorption have shown great potential for HER.[450] Wang's group developed cobalt−cobalt oxide/N-doped carbon hybrids (CoO_x@CN) composed of Co^0, CoO, and Co_3O_4 using a one-pot annealing method for alkaline OWS in 1.0 M KOH.[451] The exceptional HER performance of CoO_x@CN was attributed to the high electrical conductivity of carbon, the synergistic effect between metallic cobalt and cobalt oxide, the stability provided by carbon-encapsulated cobalt nanoparticles, and the introduction of electron-rich nitrogen. Additionally, the enhanced electrocatalytic activity of R-CoO_x@CN (CoO_x@CN after 30 min of HER) for OER was attributed to the increased Co^{2+} content compared to CoO_x@CN. When employed in OWS, the CoO_x@CN couple achieved a current density of 20 mA cm^{-2} at 1.55 V. Furthermore, easily obtainable cobalt hydroxide has garnered significant attention due to its layered structure, which provides a large surface area to facilitate the accessibility of active sites.[452,453] Liu and coworkers fabricated ultrathin α-$Co(OH)_2$ nanosheets on a combined substrate of N-doped carbon nanotubes (NCNT) and nickel foam ($Co(OH)_2$@NCNTs@NF) using chemical vapor deposition and electrodeposition techniques.[454] The unique structure of $Co(OH)_2$@NCNTs@NF enhanced the accessibility of active sites, facilitated mass and charge transfer, and prevented nanosheet agglomeration. Consequently, the $Co(OH)_2$@NCNTs@NF exhibited overpotentials of 170 mV for HER and 270 mV for OER at 10 mA cm^{-2} in 1.0 M KOH. Moreover, a low cell voltage of 1.72 V was enough to achieve 10 mA cm^{-2} for OWS.

Moreover, cobalt sulfides have garnered significant attention as well for various electrocatalysis applications.[455] Luo and collaborators utilized a gas phase growth method to transform a self-sacrificing template into a well-aligned metal−organic framework (MOF) and subsequently obtained the Co_3S_4/EC-MOF hybrid with echinops-like morphology (Figure 40a).[456]

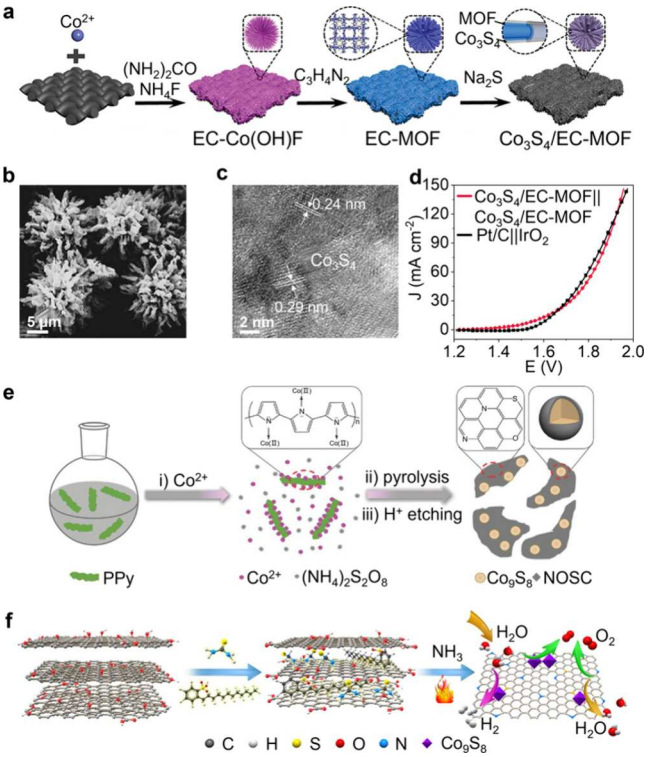

Figure 40. (a) Schematic of the preparation of Co_3S_4/EC-MOF. (b) SEM and (c) HRTEM images of Co_3S_4/EC-MOF. (d) LSV curves of Co_3S_4/EC-MOF couple and Pt/C||IrO_2 couple for OWS in 1.0 M KOH. Reproduced with permission from ref 456. Copyright 2018 John Wiley and Sons. (e) Schematic of the synthetic procedures of Co_9S_8@NOSC. Reproduced with permission from ref 457. Copyright 2016 John Wiley and Sons. (f) Schematic of the preparation of NS/rGO-Co. Reproduced with permission from ref 458. Copyright 2017 John Wiley and Sons.

SEM and HRTEM images (Figure 40b,c) of Co_3S_4/EC-MOF confirmed the successful formation of echinops-like structures and Co_3S_4. The highly divergent structure of well-aligned hollow nanorod arrays was expected to facilitate the exposure of active sites and mass/charge transfer. Moreover, the generation of Co_3S_4 species not only improved the low conductivity of the MOF but also provided additional active centers. As a result, the Co_3S_4/EC-MOF exhibited remarkable performance for HER and OER, achieving 10 mA cm^{-2} for OWS with a cell voltage of only 1.55 V in 1.0 M KOH (Figure 40d). In another study, Wu and colleagues synthesized N-, O-, and S-tridoped carbon-encapsulated Co_9S_8 (Co_9S_8@NOSC) by pyrolyzing solid precursors containing sulfur and Co(II)-containing polypyrrole (Figure 40e).[457] Benefiting from the synergistic effect between the heteroatom-doped carbon layer and the Co_9S_8 core, the resulting Co_9S_8@NOSC couple achieved a current density of 10 mA cm^{-2} at 1.60 V for OWS in 1.0 M KOH. Similarly, Chen and coworkers reported the synthesis of nitrogen and sulfur codoped reduced graphene oxide composites with Co_9S_8 (NS/rGO-Co) by annealing the graphene oxide (GO) nanosheets containing $Co(NO_3)_2$ and thiourea in NH_3 (Figure 40f).[458] The synergistic effect between N,S codoped rGO and Co_9S_8 nanoparticles resulted in excellent activity of NS/rGO-Co for OWS under alkaline conditions (1.0 M KOH).

Transition metal phosphides are a significant class of compounds known for their high conductivity and chemical

https://doi.org/10.1021/acs.chemrev.3c00332
Chem. Rev. 2024, 124, 3694−3812

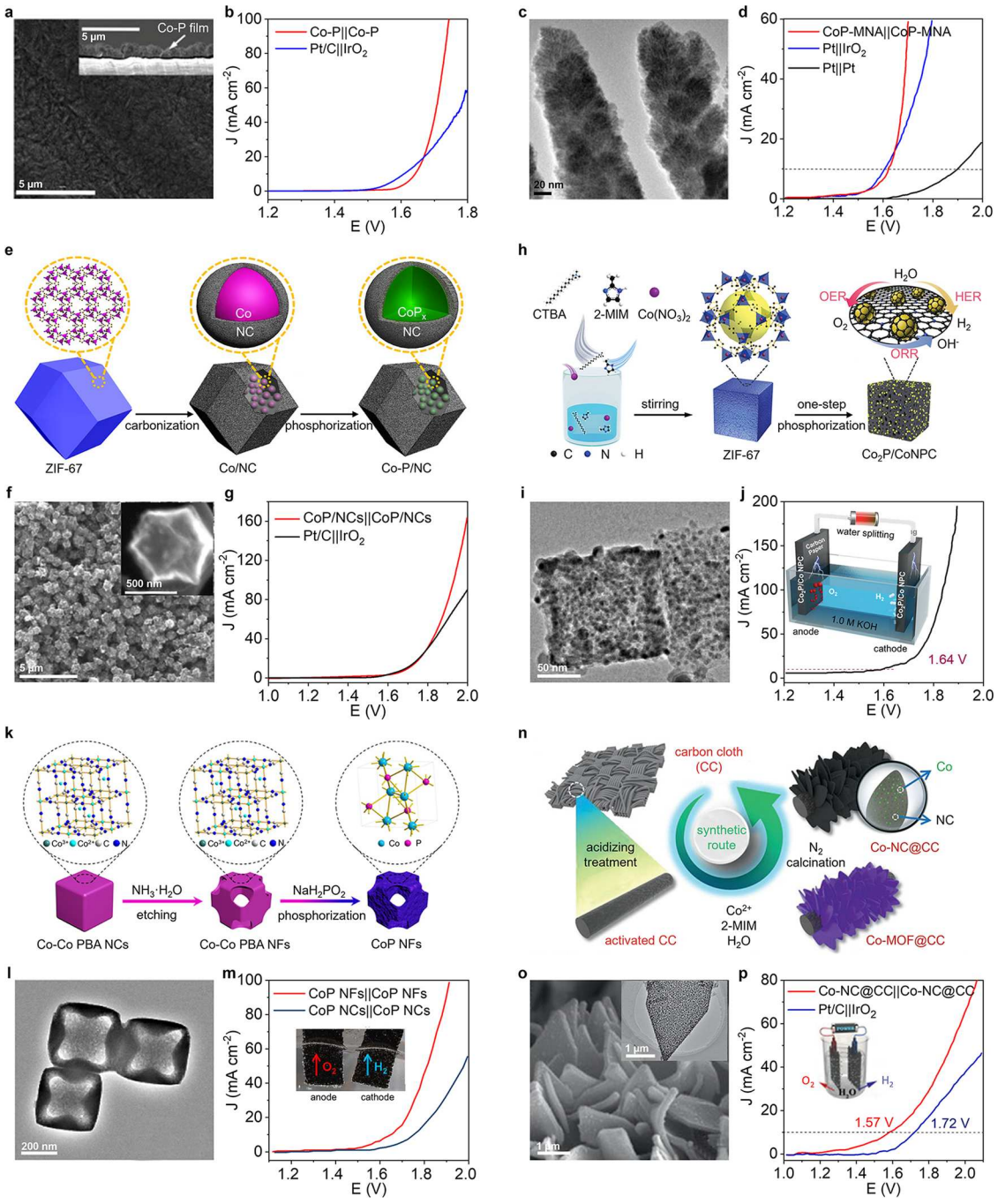

Figure 41. (a) SEM image of the as-prepared Co−P film. (b) LSV curves of Co−P couple and Pt/C||IrO_2 couple for OWS in 1.0 M KOH. Reproduced with permission from ref 266. Copyright 2015 John Wiley and Sons. (c) TEM image of CoP-MNA. (d) LSV curves of CoP-MNA couple, Pt||Pt couple and Pt||IrO_2 couple for OWS in 1.0 M KOH. Reproduced with permission from ref 461. Copyright 2015 John Wiley and Sons. (e) Schematic of the synthesis of Co−P/NC. (f) SEM images of Co−P/NC. (g) LSV curves of Co−P/NC couple and Pt/C||IrO_2 for OWS in 1.0 M KOH. Reproduced with permission from ref 464. Copyright 2015 American Chemical Society. (h) Schematic of the synthesis of Co_2P/CoNPC. (i) TEM image of Co_2P/CoNPC. (j) LSV curve of Co_2P/CoNPC couple for OWS in 1.0 M KOH and the corresponding scheme of electrolyzer. Reproduced with permission from ref 465. Copyright 2020 John Wiley and Sons. (k) Scheme for the synthesis of CoP NFs. (l) TEM image of CoP NFs. (m) LSV curves of CoP NFs couple and CoP NCs||CoP NCs couple for OWS in 1.0 M KOH. Reproduced with permission from ref 466. Copyright 2020 American Chemical Society. (n) Schematic for the synthesis of Co-NC@CC. (o) SEM and TEM images of Co-NC@CC. (p) LSV curves of Co-NC@CC couple and Pt/C||IrO_2 couple for OWS in 1.0 M KOH. Reproduced with permission from ref 467. Copyright 2020 John Wiley and Sons.

stability. Among them, cobalt phosphide has emerged as an extensively studied bifunctional electrocatalyst for OWS.[459,460] Our group has reported the use of electrodeposited Co−P film on copper foil as a bifunctional electrocatalyst for alkaline OWS (Figure 41a).[266] Notably, the Co−P film exhibited a cell voltage of 1.744 V to afford 100 mA cm^{-2} for OWS in 1.0 M KOH (Figure 41b), lower than that for the couple of Pt/C and IrO_2 benchmark. Similarly, Yuan and coworkers fabricated CoP mesoporous nanorod arrays on conductive nickel foam (CoP-MNA) via electrodeposition.[461] TEM image of CoP-

https://doi.org/10.1021/acs.chemrev.3c00332
Chem. Rev. 2024, 124, 3694−3812

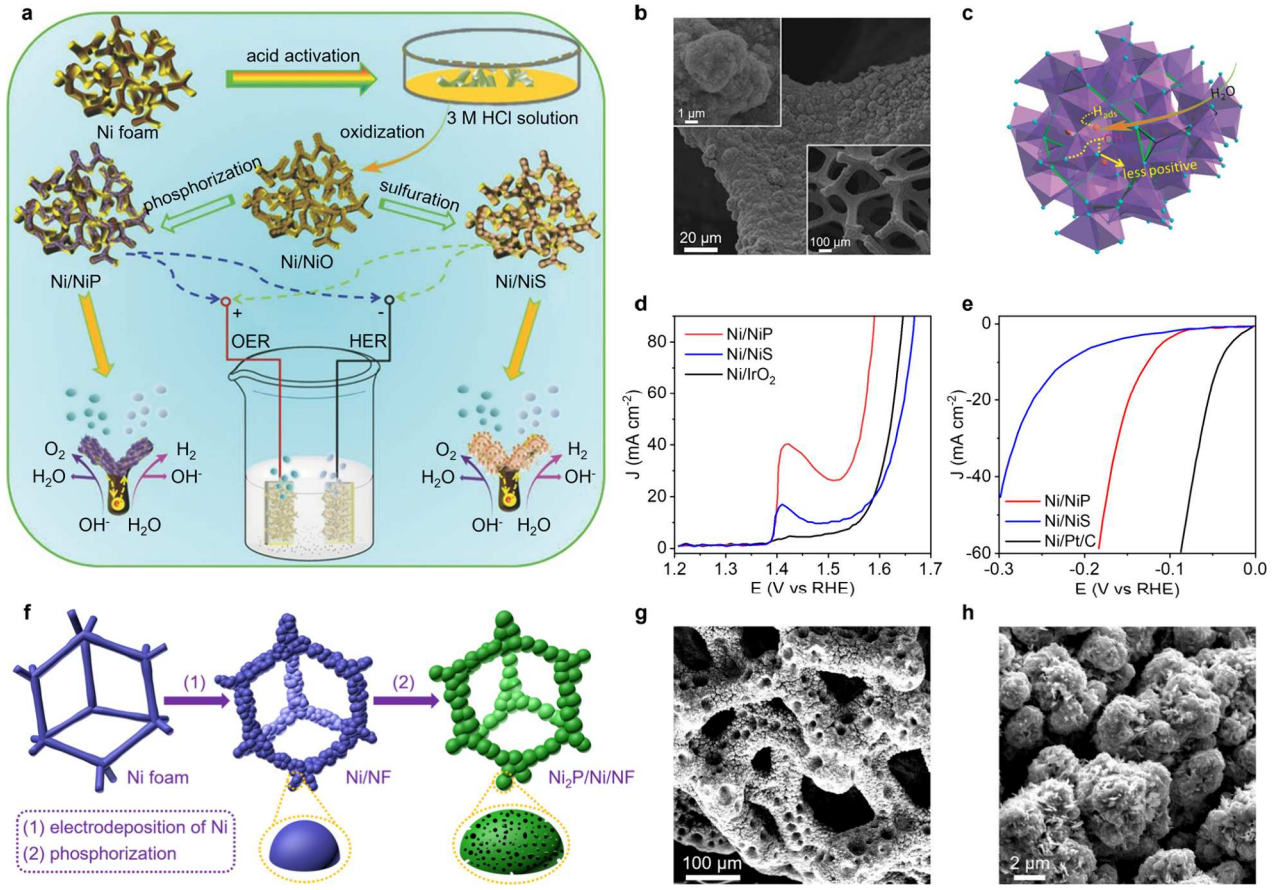

Figure 42. (a) Schematic illustration of the synthesis of 3D Ni/Ni_xM_y (M = P, S) electrocatalytic electrodes. (b) SEM images of Ni/NiS. (c) Schematic of the Volmer step in a unit cell of orthorhombic Ni_9S_8. LSV curves of Ni/NiS and controls for (d) OER and (e) HER in 1.0 M KOH. Reproduced with permission from ref 475. Copyright 2015 John Wiley and Sons. (f) Scheme of the preparation of Ni_2P/Ni/NF. (g,h) SEM images of Ni_2P/Ni/NF. Reproduced with permission from ref 315. Copyright 2018 American Chemical Society.

MNA (Figure 41c) demonstrated a uniformly covered nickel foam surface with vertically aligned nanorod arrays containing mesopores. This unique structure enhanced mass and charge transfer, and improved the electrical conductivity, allowing CoP-MNA to function as both cathode and anode with an overpotential of only 390 mV to achieve 10 mA cm^{-2} (Figure 41d).

Despite significant progress, further improvement of electrocatalytic performance is hindered by challenges such as low specific surface area and nanoparticle agglomeration.[462] Metal−organic frameworks (MOFs) offer a promising alternative for the synthesis of advanced electrocatalysts as they possess periodic and tunable pore structures, and large specific surface areas.[463] Our group synthesized porous Co−P/NC nanopolyhedrons composed of CoP_x (a mixture of CoP and Co_2P) nanoparticles embedded in N-doped carbon matrices through a facile two-step method (Figure 41e).[464] SEM images of Co−P/NC (Figure 41f) indicated the retention of the polyhedron-like morphology of zeolitic imidazolate framework-67 (ZIF-67). Consequently, the Co−P/NC exhibited promising performance for OWS in 1.0 M KOH, with 165 mA cm^{-2} at a cell voltage of 2.0 V (Figure 41g). In another study, Xu and coworkers synthesized a bifunctional electrocatalyst consisting of Co_2P embedded in Co, N, and P multidoped carbon (Co_2P/CoNPC) using ZIF-67 as a precursor (Figure 41h).[465] TEM analysis (Figure 41i) revealed that Co_2P/CoNPC inherits the ultrahigh porosity and large specific surface area of ZIF-67, with Co_2P nanoparticles uniformly anchored to the carbon backbone. The synergistic effect between Co_2P and the multiheteroatom-doped carbon substrate, along with the unique structural advantage of MOF derivatives, enabled Co_2P/CoNPC to achieve a current density of 10 mA cm^{-2} at a cell voltage of only 1.64 V in 1.0 M KOH (Figure 41j). Furthermore, hollow MOFs exhibit remarkable characteristics such as large surface area and high atom utilization efficiency, suitable for fabrication of highly active electrocatalysts. Chen and coworkers synthesized CoP nanoframes (CoP NFs) using a strategy involving precipitation, chemical etching, and low-temperature phosphorization steps (Figure 41k).[466] During the phosphorization treatment, transition metal ions, and cyano ligands were transformed into CoP nanoparticles within an N-doped carbon substrate, while the carbon backbone inhibited excessive growth of CoP nanoparticles. TEM analysis (Figure 41l) revealed the unique cavity structure of CoP NFs. Such a unique nanostructure provided highly dispersed CoP active sites, and facilitated electrolyte permeation and gas emission. Consequently, the resulting CoP NFs couple enabled efficient OWS with a cell voltage of 1.65 V at 10 mA cm^{-2} in 1.0 M KOH, superior to the couple of CoP nanocubes (CoP NCs) counterpart (Figure 41m).

Furthermore, the MOF-derived Co−N−C materials has been extensively explored for alkaline OWS as well. Li and coworkers successfully obtained Co nanoparticles immobilized

https://doi.org/10.1021/acs.chemrev.3c00332
Chem. Rev. 2024, 124, 3694−3812

within N-doped carbon microarrays (Co-NC@CC) by growing 2D micron-sized Co-based MOF (Co-MOF@CC) on carbon cloth fibers and subsequently carbonization (Figure 41n).[467] SEM and TEM images (Figure 41o) revealed the rough angular morphology of Co-NC@CC, with uniformly dispersed Co nanoparticles. The resulting Co-NC@CC exhibited abundant and dispersed active sites and a porous structure, both of which facilitated reaction kinetics and accelerated mass transport. The protection of well-dispersed Co nanoparticles by the N-doped carbon ensured excellent conductivity and stability. Consequently, the two-electrode system based on Co-NC@CC couple achieved a current density of 10 mA cm^{-2} at a low cell voltage of 1.57 V (Figure 41p). Additionally, Wu and coworkers synthesized oriented 2D ZIF-67 nanosheets grafted with 3D ZIF-67 polyhedral structures on the carbon cloth (CC) surface.[468] Subsequent low-temperature pyrolysis transformed these precursors into hybrid composites (Co@N-CS/N-HCP@CC). The Co@N-CS/N-HCP@CC consisted of ultrafine cobalt nanoparticles embedded within 2D N-doped carbon nanosheets and 3D N-doped hollow carbon polyhedra. This unique structure offered several advantages: the CC substrate suppressed the aggregation of nanosheets/nanoparticles and enhanced conductivity/mechanical flexibility, the ultrathin 2D nanosheets exposed abundant active sites and accelerated charge transfer, and the porous 3D hollow polyhedra ensured superior mass transfer capability/high structural stability. As a result, the Co@N-CS/N-HCP@CC served as a bifunctional electrocatalysts for OWS (in 1.0 M KOH) required a cell voltage as low as 1.545 V to achieve 10 mA cm^{-2}.

4.2.3. Ni-Based Electrocatalysts. To date, Ni-based composites have garnered significant attention due to their abundant reserves and electrochemical activity. Various Ni-based materials, including oxides/hydroxides, sulfides, phosphides, nitrides, and others, have been reported and demonstrated potential in alkaline OWS. To further enhance the electrocatalytic activity of Ni-based catalysts, several approaches have been employed, such as microstructural modification, heterostructures construction, and nanocarbons hybridization.[469,470]

Drawing inspiration from the unique physicochemical properties of heterogeneous structural materials, Zhang and coworkers synthesized ultrathin Ni(0) embedded $Ni(OH)_2$ heterostructured nanosheets (Ni/$Ni(OH)_2$ nanosheets) through a partial reduction strategy.[471] By utilizing these Ni/$Ni(OH)_2$ nanosheets as cathode and anode electrocatalysts in a two-electrode water electrolysis system, a current density of 10 mA cm^{-2} was achieved with a cell voltage of 1.59 V in 1.0 M KOH, highlighting the promising performance for alkaline OWS.

Nickel sulfides are desirable materials for various electrocatalysis due to their low cost, high electrical conductivity, and easy availability.[472,473] Wang and coworkers introduced a novel approach using a deep eutectic solvent (DES) as a precursor to synthesize 2D NiS/graphene (NiS/G) heterostructured composites through a pyrolysis-assisted sulfidation process.[474] The utilization of DES as a homogeneous system enabled sufficient contact between the components, facilitating the growth and coupling of NiS and graphene. Additionally, graphene effectively enhanced conductivity and provided corrosion protection for the NiS nanosheets. Consequently, the 2D NiS/G heterostructure exhibited efficient HER and OER activities. Apart from synthesis of 2D nickel sulfides-based electrocatalysts, Qiao and collaborators developed a straightforward method to prepare 3D porous Ni/Ni_9S_8 (denoted as Ni/NiS) a bifunctional electrocatalyst via acid activation and oxidation of commercial nickel foam followed by sulfidation (Figure 42a).[475] The resulting Ni/NiS displayed 3D nanoparticles-stacked morphology (Figure 42b). The electron transfer from Ni to S revealed by XPS facilitated the destabilization of H_2O for improved alkaline HER (Figure 42c), and the reconstructed oxidized Ni species accounted for enhanced OER. For example, the low overpotentials of 230 mV at 10 mA cm^{-2} and 340 mV at 30 mA cm^{-2} can be obtained over Ni/NiS in 1.0 M KOH for HER and OER, respectively (Figure 42d,e).

Similarly, nickel phosphides have also been studied for alkaline OWS. Our group successfully obtained 3D hierarchical porous Ni_2P superstructures on nickel foam (Ni_2P/Ni/NF) by template-free electrodeposition of porous metal Ni microsphere arrays on NF, followed by phosphorization (Figure 42f).[227,315] SEM images (Figure 42g,h) revealed the hierarchical macroporosity and urchin-like morphology of Ni_2P/Ni/NF, where the hierarchical macroporous structure not only enhanced the accessibility of active sites but also facilitated ion transport and gas diffusion by buffering the electrolyte. As a result, the Ni_2P/Ni/NF-based electrolyzer needed a low cell voltage of only 1.49 V to afford 10 mA cm^{-2} in 1.0 M KOH for OWS. Phosphorization of the acid activated and oxidized NF resulted in the 3D nanoflocs Ni/Ni_8P_3 (denoted as Ni/NiP), as reported by Qiao and coworkers (Figure 42a).[475] The resulting Ni/NiP exhibited superior HER and OER activities (Figure 42d,e), and a low cell voltage of 1.61 V at 10 mA cm^{-2} in 1.0 M KOH for OWS. Liu and coworkers prepared the CP@Ni−P self-supporting electrode through electrodeposition of Ni on functionalized carbon fiber paper (CP) followed by phosphorization.[476] The CP@Ni−P self-supporting electrode also exhibited excellent activity and stability when utilized as both cathode and anode for alkaline OWS. In-depth investigations were conducted by Driess and coworkers to explore the electrocatalytic OWS of nickel phosphides with different phases.[477] $Ni_{12}P_5$ and Ni_2P were synthesized using hydrothermal methods, and their surface reconstruction during OER and HER were examined under alkaline conditions to gain insights into the structure−activity relationships. Generally, the OER activity originated from the NiOOH/$Ni(OH)_2$ species formed on the catalyst surface during the reaction. The higher Ni content in $Ni_{12}P_5$ preferred to produce more catalytically active NiOOH/$Ni(OH)_2$ species compared to Ni_2P. Regarding HER, the higher concentration of P on the surface of Ni_2P significantly enhanced the catalytic activity because the surface P atoms with a small negative charge can trap protons and facilitate hydrogen removal from the surface.

Nickel borides represent a relatively rare class of electrocatalysts that have shown promise in HER and OER. Wu and coworkers conducted a transformation of Ni-ZIF nanorods into ultrathin Ni-ZIF/Ni−B nanosheets with abundant crystalline−amorphous phase boundaries through room temperature boronization (Figure 43a,b).[478] The morphology evolution of the Ni-ZIF@NF during boronization in a $NaBH_4$ solution was evidenced in the SEM images (Figure 43c−e). Initially, the rod-like Ni-ZIF structures were uniformly stacked on the NF for the Ni-ZIF@NF precursor. However, with prolonged reaction time in $NaBH_4$, the morphology underwent significant changes, transitioning into a 2D sheet structure.

https://doi.org/10.1021/acs.chemrev.3c00332
Chem. Rev. 2024, 124, 3694−3812

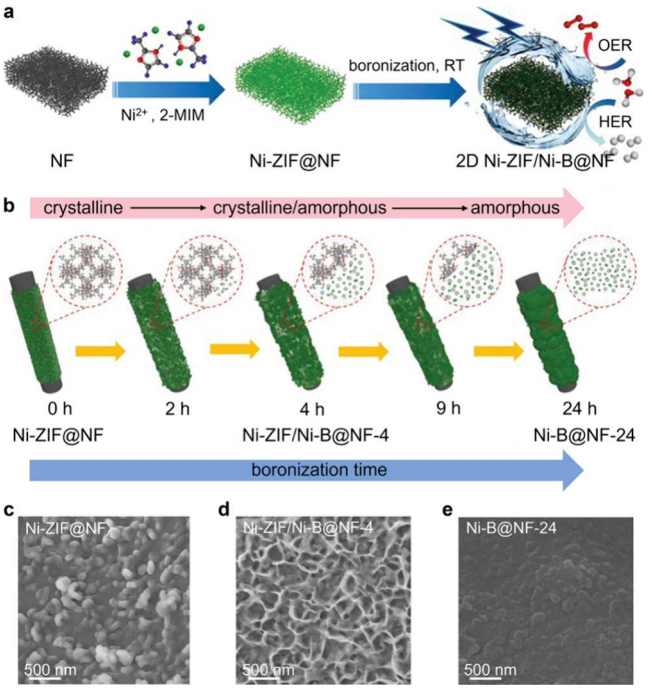

Figure 43. (a, b) Schematic of the synthesis of Ni-ZIF/Ni−B@NF. SEM images of (c) Ni-ZIF@NF, (d) Ni-ZIF/Ni−B@NF-4, and (e) Ni−B@NF-24. Reproduced with permission from ref 478. Copyright 2020 John Wiley and Sons.

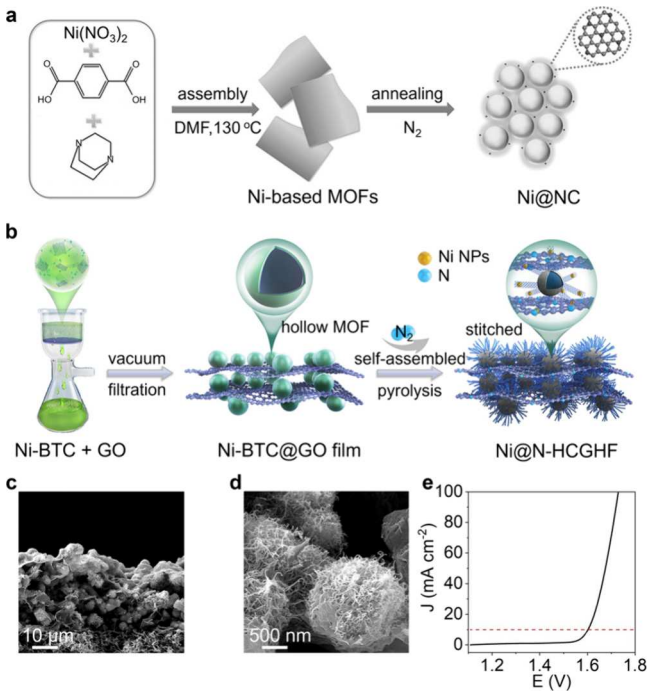

Figure 44. (a) Schematic of the preparation of Ni@NC. Reproduced with permission from ref 480. Copyright 2017 John Wiley and Sons. (b) Schematic of the preparation of Ni@N-HCGHF. (c, d) Cross-sectional SEM images of Ni@N-HCGHF. (e) LSV curves of Ni@N-HCGHF couple for OWS in 1.0 M KOH. Reproduced with permission from ref 481. Copyright 2020 John Wiley and Sons.

After 4 h of boronization, the nanosheets became thinner and more unfolded, resulting in the formation of Ni-ZIF/Ni−B@NF-4. Further extending the boronization time, the nanosheets collapsed, eventually forming worm-like Ni−B structures densely covered on the NF surface (known as Ni−B@NF-24). Remarkably, the Ni-ZIF/Ni−B@NF-4 exhibited excellent HER and OER activities, achieving a current density of 10 mA cm^{-2} at an ultralow cell voltage of 1.54 V when utilized as the cathode and anode in an alkaline OWS electrolyzer. This remarkable electrocatalytic performance was attributed to the presence of ultrathin nanosheets and rich crystalline−amorphous boundaries, which provided a large active surface area, facilitated mass and charge transfer, and offered suitable adsorption energy for reaction intermediates.

Furthermore, extensive research has been conducted on nickel-based carbon nanocomposites for various electrocatalysis processes including alkaline OWS, owing to their favorable electrical conductivity, large specific surface area, and corrosion resistance.[479] Xu and coworkers developed a method to prepare Ni nanoparticles (Ni NPs) encapsulated in few-layer nitrogen-doped graphene (Ni@NC) through high-temperature annealing of Ni-MOF (Figure 44a).[480] The synergistic effect between the Ni NP cores and the N-doped thin graphene shells imparted excellent activity to Ni@NC in alkaline OWS (1.0 M KOH), achieving a current density of 10 mA cm^{-2} at 1.60 V. Similarly, Wang and coworkers obtained self-supported 3D heterojunction thin film materials (Ni@N-HCGHF) by pyrolyzing Ni-MOF/graphene oxide compounds (Figure 44b).[481] SEM images (Figure 44c,d) at different magnifications revealed the hierarchical structure of Ni@N-HCGHF, consisting of a uniform arrangement of N-doped carbon nanotube-assembled hollow-microsphere (HM) and reduced graphene oxide (rGO). The MOF-derived CNT-HM structure prevented the aggregation of rGO and provided a large surface area to expose more active sites. With the high specific surface area, hierarchical porosity, controllable dopants, and conductive CNT@rGO heterostructures, the Ni@N-HCGHF coupe demonstrated remarkable performance. In a two-electrode system, it required only 1.60 V to achieve 10 mA cm^{-2} for OWS in 1.0 M KOH (Figure 44e).

4.2.4. Other Monometal-Based Electrocatalysts. In addition to Fe-, Co-, and Ni-based nonprecious bifunctional electrocatalysts, monometallic Mo- and Cu-based electrocatalysts have also been explored for alkaline OWS. For instance, Cui and coworkers synthesized porous MoO_2 nanosheets grown on NF through a wet chemistry followed by annealing method (Figure 45a).[482] SEM images (Figure 45b,c) revealed that the entire surface of NF is covered by porous MoO_2 nanosheets. The porous structure of MoO_2 allowed for efficient electrolyte storage, facilitating fast ion supply and reducing ion diffusion distance. As a result, the porous MoO_2 exhibited remarkable performance for alkaline OWS in 1.0 M KOH, requiring a cell voltage of only 1.53 V to achieve a current density of 10 mA cm^{-2} (Figure 45d). Notably, the alkaline OWS can be driven by a single 1.5 V battery (Figure 45e).

As mentioned earlier, molybdenum sulfide has demonstrated excellent catalytic performance for HER. Its catalytic activity for OER can be further improved through integration with multiple compounds. Zhang and collaborators employed a two-step sequential chemical vapor deposition (CVD) method to synthesize three-dimensional (3D) mesoporous van der Waals (vdW) heterostructures of graphene and N-doped MoS_2 (G@N-MoS_2, Figure 45f).[483] HAADF-STEM and HRTEM images (Figure 45g,h) revealed the uniform distribution of N-MoS_2 with a hexagonal appearance on mesoporous graphene

https://doi.org/10.1021/acs.chemrev.3c00332
Chem. Rev. 2024, 124, 3694−3812

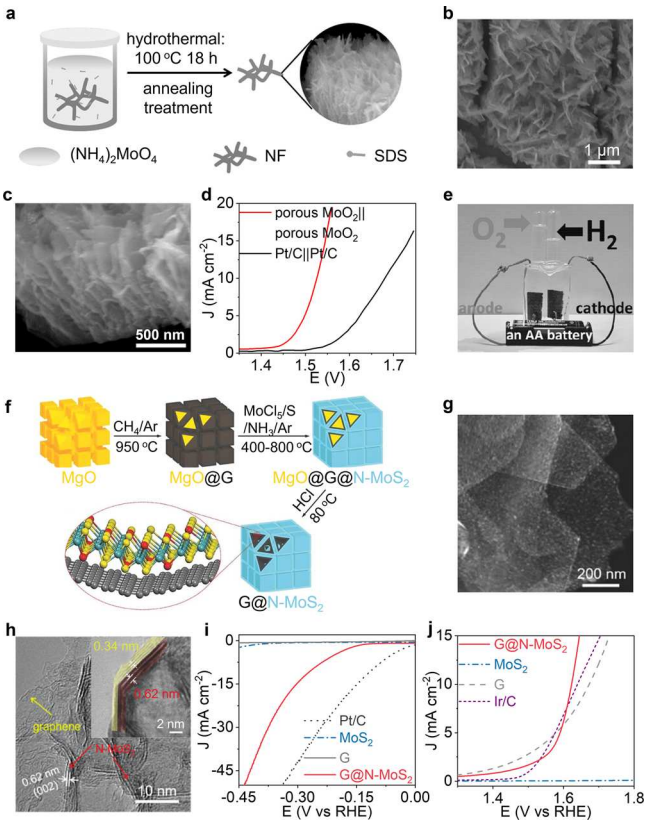

Figure 45. (a) Schematic of the synthesis of porous MoO_2 nanosheets on NF directly. (b,c) SEM top-view and side-view images of porous MoO_2 nanosheets. (d) LSV curves of porous MoO_2 couple and Pt/C couple for OWS in 1.0 M KOH. (e) Demonstration of porous MoO_2 couple-driven OWS device powered by a single 1.5 V battery. Reproduced with permission from ref 482. Copyright 2016 John Wiley and Sons. (f) Schematic of the synthesis of 3D mesoporous G@N-MoS_2. (g) HAADF-STEM image and (h) HRTEM images of G@N-MoS_2. LSV curves of G@N-MoS_2 and controls for (i) HER and (j) OER in 0.1 M KOH. Reproduced with permission from ref 483. Copyright 2018 John Wiley and Sons.

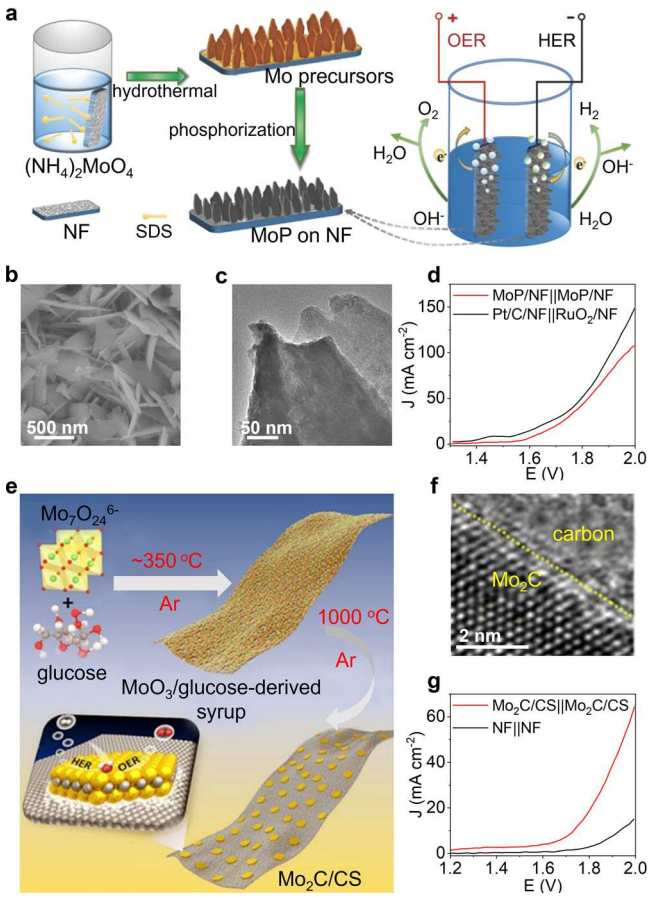

Figure 46. (a) Scheme of the synthesis of porous MoP nanosheet arrays on nickel foam (MoP/NF). (b) SEM and (c) TEM images of MoP/NF. (d) LSV curves of MoP/NF couple and Pt/C/NF||IrO_2/NF couple for OWS in 1.0 M KOH. Reproduced with permission from ref 485. Copyright 2018 John Wiley and Sons. (e) Schematic illustration of the synthetic process of Mo_2C/CS. (f) HRTEM image of Mo_2C/CS. (g) LSV curves for OWS on Mo_2C/CS couple and control. Reproduced with permission from ref 486. Copyright 2017 John Wiley and Sons.

framework. The interface between graphene and N-MoS_2 was clearly observed on thick graphene sheets, indicating the layer-by-layer stacking of vdW heterostructures. The integration of 3D mesoporous graphene and N-MoS_2 provided improved conductivity, enhanced accessibility of active sites, and optimized adsorption of reaction intermediates, leading to significantly enhanced electrocatalytic HER and OER activities in 0.1 M KOH (Figure 45i,j). Furthermore, Mu and coworkers reported a bifunctional electrocatalyst consisting of vertically aligned MoS_2 nanosheets encapsulated Mo−N/C framework with interfacial Mo−N coupling centers (Mo−N/C@MoS_2).[484] The distinct chemical composition, unique three-phase active sites and synergistic effect of the hierarchical porous structure enabled Mo−N/C@MoS_2 to exhibit superior HER and OER activities in KOH electrolytes, with respective overpotentials of 117 and 390 mV at 10 mA cm^{-2}.

Remarkably, molybdenum phosphide (MoP) also exhibits outstanding electrocatalytic activity for alkaline OWS. Shen and coworkers successfully synthesized a self-supported porous MoP nanoflakes on Ni foam (MoP/NF) via phosphorization of MoO_2 nanoflakes grown on NF (Figure 46a).[485] SEM and TEM images (Figure 46b,c) revealed the presence of vertically immobilized porous MoP nanoflakes with 200−500 nm in width and >500 nm in depth on NF. The unique nanoflake array structure and the reduced size of MoP enabled the exposure of active sites and promoted efficient gas diffusion and mass transfer. As a result, the MoP/NF self-supported electrode achieved a current density of 10 mA cm^{-2} at a cell voltage of 1.62 V for OWS in 1.0 M KOH (Figure 46d), comparable to Pt/C/NF and IrO_2/NF couple.

Furthermore, Mo_2C has been recognized as an excellent catalyst for HER due to its Pt-like electronic structure and suitable hydrogen adsorption capacity,[486−489] Recently, it was investigated as a bifunctional electrocatalyst for OWS. Gao and coworkers synthesized highly crystalline Mo_2C nanoparticles loaded on carbon sheets (Mo_2C/CS) using a one-pot method (Figure 46e).[486] HRTEM image (Figure 46f) clearly demonstrated that the hexagonal Mo_2C is strongly coupled with carbon sheets. With the highly active catalytic properties of Mo_2C, the high surface area of carbon sheets, and efficient charge transfer in the strongly coupled composite, Mo_2C/CS exhibited a bifunctional electrocatalytic performance in 1.0 M KOH for OWS, requiring a cell voltage of 1.73 V to achieve 10 mA cm^{-2} (Figure 46g).

https://doi.org/10.1021/acs.chemrev.3c00332
Chem. Rev. 2024, 124, 3694−3812

Due to their high abundance, low cost, and favorable electrical conductivity, Cu-based materials have emerged as potential bifunctional electrocatalysts for alkaline OWS. Among them, copper chalcogenides and pnictides have been extensively explored and showed promising activity. For instance, Zheng and colleagues developed self-supported sulfur-doped copper oxide ($Cu_2O_xS_{1-x}$) with a nanoporous structure using a three-step approach, with the electrochemical cycling potential reconstruction of Cu_2S being a key step (Figure 47a).[490] SEM images showed the transformation of 1D nanowires (Figure 47b) of Cu_2S into nanoporous films (Figure 47c) of $Cu_2O_xS_{1-x}$ after electrochemical reconstruction. This specific nanoporous structure exposed more active sites, and the heteroatom doping tailored the electronic structure of the electrocatalyst. As a result, the $Cu_2O_xS_{1-x}$ couple exhibited excellent OWS activity in 1.0 M KOH, better than Pt/C and IrO_2 couple (Figure 47d).

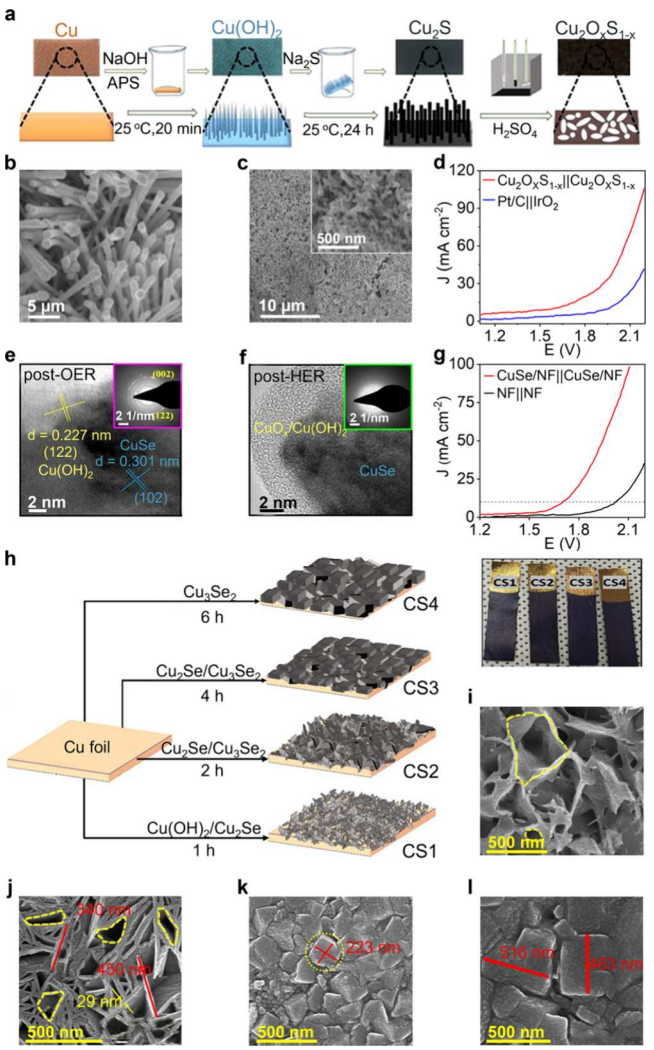

Figure 47. (a) Schematic of the fabrication process of $Cu_2O_xS_{1-x}$/Cu. SEM images of (b) Cu_2S/Cu and (c) $Cu_2O_xS_{1-x}$/Cu. (d) LSV curves of $Cu_2O_xS_{1-x}$/Cu couple and Pt/C||IrO_2 couple for OWS in 1.0 M KOH. Reproduced with permission from ref 490. Copyright 2018 American Chemical Society. HRTEM images of the CuSe/NF (e) after OER and (f) after HER tests. (g) LSV curve of CuSe/NF couple and control for OWS in 1.0 M KOH. Reproduced with permission from ref 491 under the terms of a CC-BY 4.0 license. Copyright 2020 John Wiley and Sons. (h) Schematic of chemical bath deposition for the synthesis of Cu_3Se_2 films on Cu substrate and films evolution with time. The inset image showed a photograph of four copper selenide films. SEM images of (i) CS1, (j) CS2, (k) CS3, and (l) CS4. Reproduced with permission from ref 492. Copyright 2023 John Wiley and Sons.

Furthermore, copper selenides were used as bifunctional OWS electrocatalysts due to the unique adsorption of reactive intermediates containing oxygen and hydrogen. Driess and coworkers successfully obtained pure-phase and highly crystalline klockmannite CuSe on NF using an electrophoretic deposition (EPD) method.[491] Remarkably, during OER, the surface CuSe was converted to highly active crystalline $Cu(OH)_2$ due to electrochemically oxidative reconstruction (Figure 47e), while during HER, it formed amorphous $Cu(OH)_2/CuO_x$ active surfaces (Figure 47f), thereby enhancing both OER and HER performance. Consequently, the CuSe couple exhibited excellent OWS under 1.0 M KOH (Figure 47g). Another example involves the work of Lokhande and coworkers, who prepared self-supported copper selenide electrocatalysts using a self-growth method with varying immersion times (Figure 47h).[492] SEM images (Figure 47i–l) illustrated the morphological transformation at different time intervals (1, 2, 4, and 6 h). Initially, the surface of copper selenide with an immersion time of 1h (CS1) was composed of vertically aligned sheets of $Cu(OH)_2$ and Cu_2Se, displaying large cage-like structures. As the immersion time increased to 2 h, the resulting CS_2 films exhibited an increase in the number and size of $Cu(OH)_2$ sheets, with further transformation into Cu_3Se_2 and Cu_2Se. With an immersion time of 4 h (CS3), more Cu was converted to copper selenide, resulting in a cube-like microstructure. Further increasing the soaking time to 6 h, the cuboidal structure was transformed into horizontally extended sheets (CS4). These structural transformations led to changes in the catalyst's surface porosity, and the microflake morphology of CS2 maximized the number of catalytic active sites, resulting in superior OER, HER, and OWS activities in 1.0 M KOH.

In recent studies, copper phosphide nanostructures have emerged as highly effective electrocatalysts for both OER and HER. Cui and collaborators successfully obtained a three-dimensional self-supported Cu_3P nanobush grown on a copper mesh (Cu_3P/Cu) through one-step phosphorization (Figure 48a).[493] SEM image (Figure 48b) revealed the presence of uniform 3D nanowires in the Cu_3P/Cu, providing a large number of active sites and promoting gas production and bubble release. Additionally, the Cu_3P/Cu exhibited good electrical conductivity, facilitating charge transfer. Consequently, the Cu_3P/Cu couple achieved a current density of 10 mA cm^{-2} at 1.85 V (Figure 48c) and maintained decent stability for over 12 h in 1.0 M KOH (Figure 48d). In another study, Du's group synthesized crystalline Cu_3P nanosheets on conductive nickel foam (Cu_3P@NF) by phosphorization of $Cu(OH)_xF$/NF obtained through a hydrothermal process (Figure 48e).[494] SEM image (Figure 48f) demonstrated the uniform coverage of Cu_3P nanosheets on the surface of a nickel foam substrate. The resulting Cu_3P@NF electrode exhibited remarkable bifunctional catalytic activity for OWS, reaching 10 mA cm^{-2} with only 1.67 V in 1.0 M KOH. The unique structure of metal–organic frameworks (MOFs) makes them excellent precursors for the preparation of porous nanocatalysts.[495] In this regard, Zhang and coworkers prepared porous Cu_3P@C by low-temperature phosphorization of sea urchin-like Cu-BDC (Figure 48g).[496] The resulting Cu_3P@C

https://doi.org/10.1021/acs.chemrev.3c00332
Chem. Rev. 2024, 124, 3694–3812

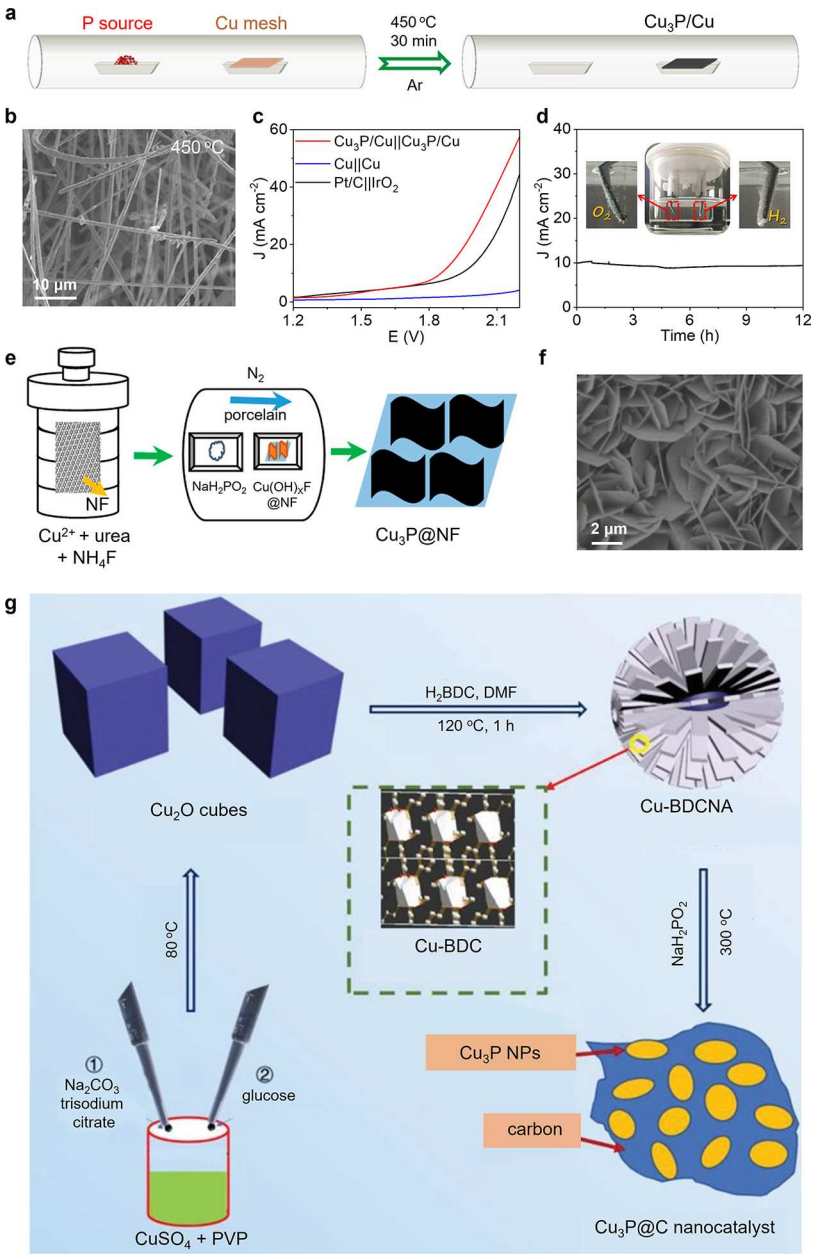

Figure 48. (a) Schematic of the preparation of Cu_3P/Cu. (b) SEM image of Cu_3P/Cu. (c) LSV curves of Cu_3P/Cu couple and control couples for OWS in 1.0 M KOH. (d) Chronoamperometric curve of Cu_3P NB/Cu couple at 1.88 V for OWS and the corresponding photograph. Reproduced with permission from ref 493. Copyright 2016 American Chemical Society. (e) Schematic of the preparation of Cu_3P@NF. (f) SEM image of Cu_3P@NF. Reproduced with permission from ref 494. Copyright 2017 American Chemical Society. (g) Schematic of the preparation of Cu_3P@C. Reproduced with permission from ref 496. Copyright 2019 John Wiley and Sons.

maintained the sea urchin-like structure with high porosity and uniform dispersion of Cu_3P nanoparticles, making it promising for alkaline OWS.

The excellent conductivity and other properties of metal nitrides renders them exceptional performance as electrode materials.[402,497] Driess and collaborators synthesized nanoscale Cu_3N by nitriding copper acetate and subsequently deposited Cu_3N on NF (Cu_3N/NF) via electrophoretic deposition (Figure 49a).[498] Remarkably, the resulting Cu_3N/NF exhibited a propensity to form Cu-oxygen/hydroxide reactive species rich in defects under oxidizing conditions, while reducing conditions resulted in the formation of highly conductive Cu and CuO. Consequently, the Cu_3N/NF demonstrated remarkably low overpotentials for both OER and HER, along with excellent activity and durability for OWS. In addition, heteroatom-doped carbon-based materials have garnered significant attention due to their high surface area, excellent conductivity and chemical stability.[499,500] Li and collaborators prepared a porous carbon-based electrocatalyst doped with Cu, N, and S (Cu−N−SC-1100) through high-temperature treatment of oxidized polyphenylene sulfide (PPS) and Cu foil in an NH_3 atmosphere (Figure 49b).[501] SEM analysis (Figure 49c) revealed the spongy nature of Cu−N−SC-1100, with rough surface and porous structure. The abundance of defects and the porosity enhanced the exposure of active sites and facilitated electron transfer. Moreover, the unique coordination among Cu, N, S, and C endowed Cu−N−SC-1100 with distinctive electronic properties. As a result, the as-

https://doi.org/10.1021/acs.chemrev.3c00332
Chem. Rev. 2024, 124, 3694−3812

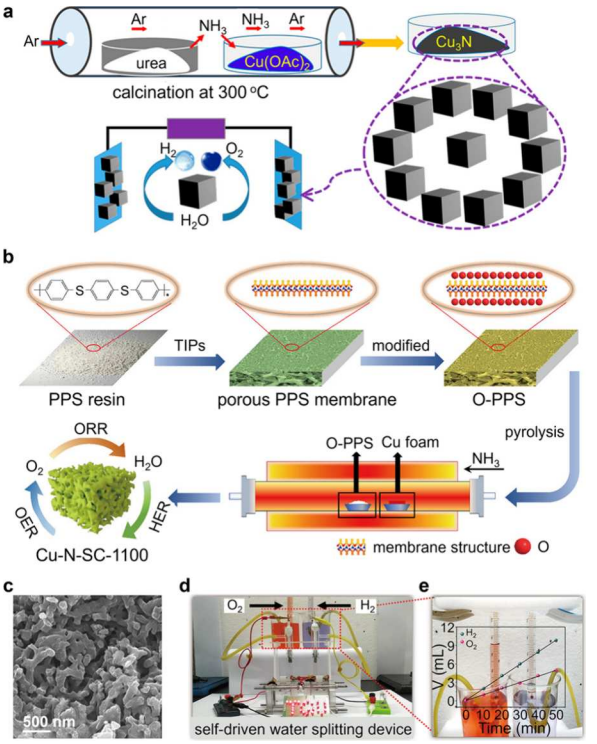

Figure 49. (a) Schematic of the fabrication of Cu_3N/NF. Reproduced with permission from ref 498. Copyright 2019 American Chemical Society. (b) Schematic of the preparation of Cu−N−SC-1100. (c) SEM image of Cu−N−SC-1100. (d) Photograph of the self-driven water-splitting device based on Cu−N−SC-1100, and the corresponding (e) photograph of gas collected and quantification by the drainage method. Reproduced with permission from ref 501. Copyright 2021 American Chemical Society.

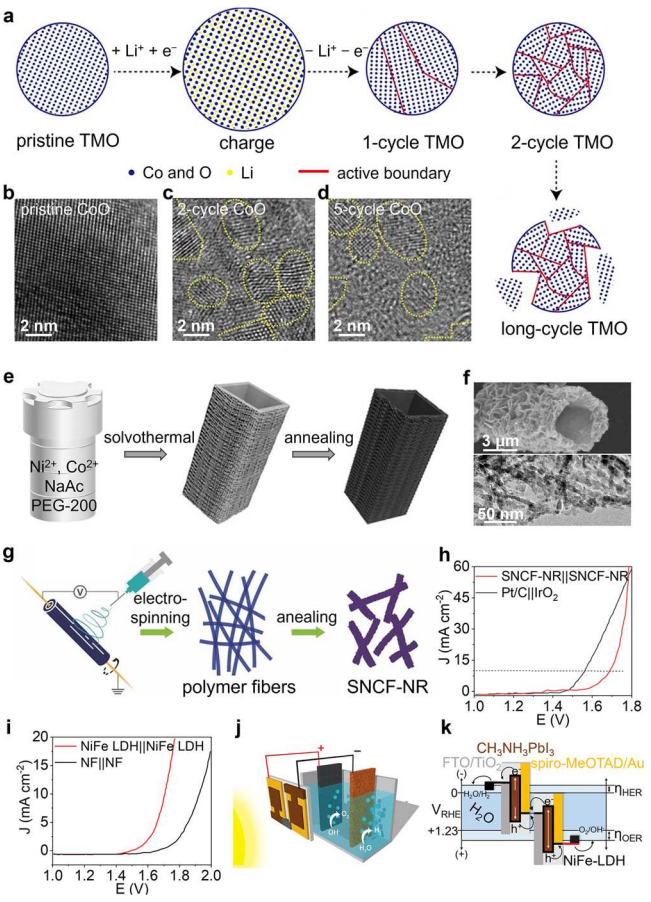

Figure 50. (a) Schematic of Li-induced transformation of TMO particles from single crystalline to ultrasmall interconnected crystalline NPs. TEM images of (b) pristine CoO/CNF, (c) 2-cycle CoO/CNF, and (d) 5-cycle CoO/CNF. Reproduced with permission from ref 504 under the terms of a CC-BY 4.0 license. Copyright 2015 The Authors, published by Springer Nature. (e) Schematic of the formation of hierarchical $NiCo_2O_4$ HMCs. (f) SEM and TEM images of $NiCo_2O_4$ HMCs. Reproduced with permission from ref 505. Copyright 2016 John Wiley and Sons. (g) Schematic of the preparation of SNCF-NR. (h) LSV curves of SNCF-NR couple and Pt/C||IrO_2 couple for OWS in 1.0 M KOH. Reproduced with permission from ref 507. Copyright 2017 John Wiley and Sons. (i) LSV curves of NiFe LDH couple and NF||NF couple for OWS in 1.0 M NaOH. (j) Schematic of the perovskite solar cell-powered water-splitting device. (k) Energy schematic of the perovskite tandem cell for OWS. Reproduced with permission from ref 510. Copyright 2014 American Association for the Advancement of Science.

prepared Cu−N−SC-1100 exhibited excellent activity for alkaline OWS, achieving a current density of 10 mA cm^{-2} with a remarkably low voltage of only 1.64 V, thereby enabling rapid production of H_2 and O_2 (Figure 49d,e).

4.2.5. Multimetal-Based Electrocatalysts. In the above subsection, we examined the overall water splitting performance of monometallic electrocatalysts in alkaline solutions. However, it is worth noting that multimetallic materials often exhibit enhanced electrocatalytic activity due to their synergistic interactions.[502] Various transition metal oxides, sulfides, selenides, phosphides, nitrides, carbides, and alloys are exemplary multimetallic electrocatalysts currently investigated for alkaline OWS.

Multimetal oxides have been explored as highly active and durable electrocatalysts for water splitting, owing to their inherent properties.[503] Cui's group achieved the transformation of transition metal oxide nanoparticles (Fe, Co, Ni oxides, and their mixed oxides) into ultrasmall nanoparticles (2−5 nm) through a Li-induced transformation reaction (Figure 50a).[504] TEM images (Figure 50b−d) revealed the gradually increase of interconnected ultrasmall nanoparticles with abundant grain boundaries along with galvanostatic lithiation/delithiation cycling. These numerous grain boundaries were believed to be active for OWS. For example, the Li-induced ultrasmall $NiFeO_x$ nanoparticles exhibited remarkable activity and stability for OWS in 1.0 M KOH, requiring only 1.51 V to achieve 10 mA cm^{-2} and maintaining stability over 200 h. In a different study, Lin and coworkers synthesized hierarchical $NiCo_2O_4$ hollow microcuboids (HMCs) through a thermally driven conversion process (Figure 50e).[505] SEM and TEM images (Figure 50f) clearly displayed the hollow microcuboids structure composed of one-dimensional nanowires, with numerous mesopores distributed throughout the shell. The 1D nanowire meshwork and hollow structure provided a large active surface area, facilitating electrochemical reactions, electrolyte penetration, and gas release. Consequently, the $NiCo_2O_4$ HMCs couple demonstrated excellent activity for OWS in 1.0 M NaOH. Furthermore, Wang and collaborators synthesized a series of $NiCo_2O_4$ with different crystalline planes using a hydrothermal method to achieve efficient OWS in 1.0 M KOH.[506] The authors found that the $NiCo_2O_4$ nanosheets exposing [110] facets exhibit higher HER and OER activities than $NiCo_2O_4$ octahedron exposing [111]

https://doi.org/10.1021/acs.chemrev.3c00332
Chem. Rev. 2024, 124, 3694−3812

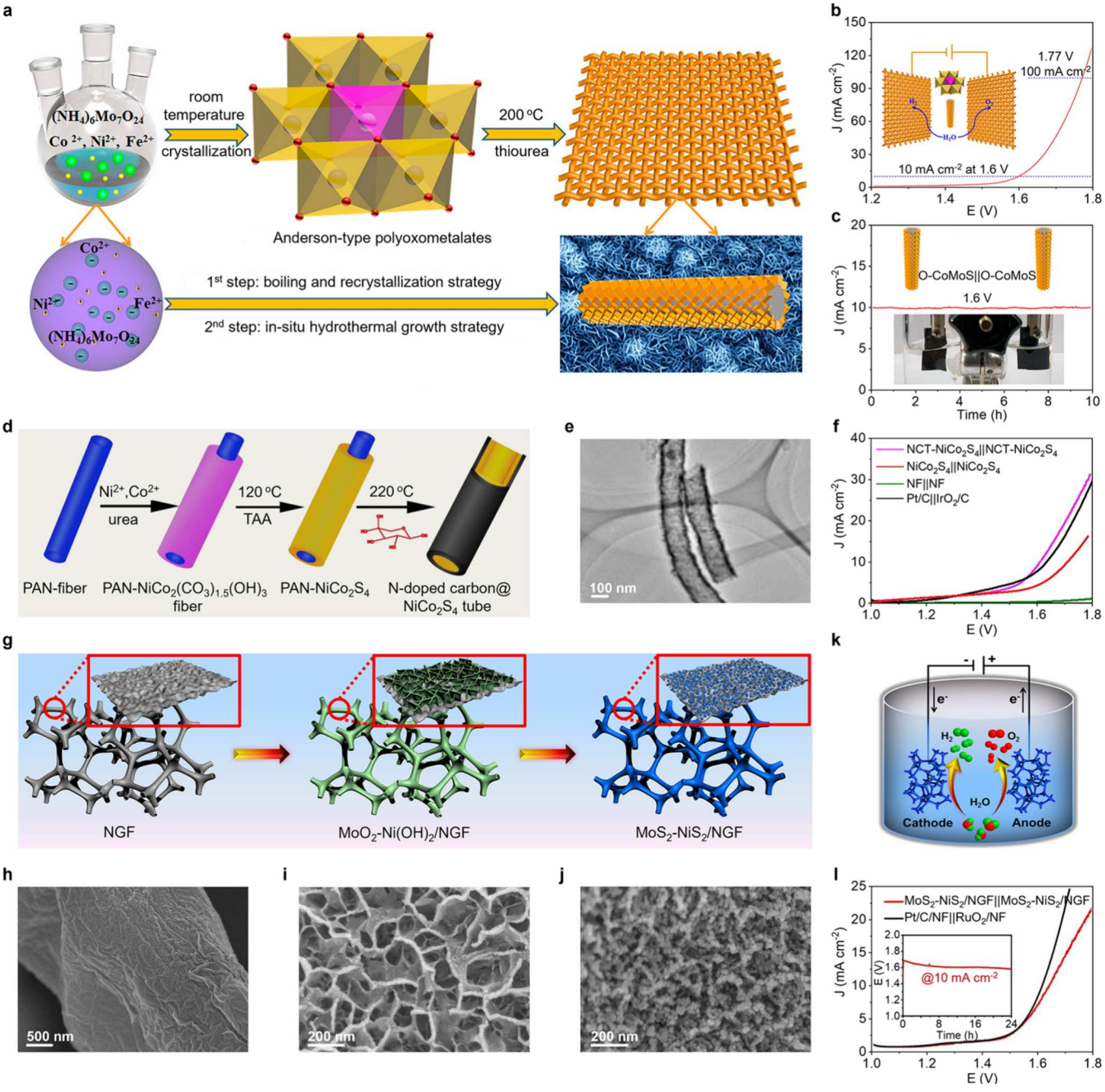

Figure 51. (a) Schematic of the synthesis of O-CoMoS heteronanosheet arrays. (b) LSV curves and (c) chronoamperometric curve of O-CoMoS couple for OWS in 1.0 M KOH. Reproduced with permission from ref 512. Copyright 2018 American Chemical Society. (d) Schematic of the formation of NCT-$NiCo_2S_4$. (e) TEM image of NCT-$NiCo_2S_4$. (f) LSV curves of NCT-$NiCo_2S_4$ couple and control couples for OWS in 1.0 M KOH. Reproduced with permission from ref 513. Copyright 2019 Elsevier. (g) Schematic for the synthesis of MoS_2−NiS_2/NGF. SEM images of (h) NGF, (i) MoO_2−$Ni(OH)_2$/NGF, and (j) MoS_2−NiS_2/NGF. (k) Schematic of the two-electrode water electrolysis device. (l) LSV and chronopotentiometric curves of MoS_2−NiS_2/NGF couple for OWS in 1.0 M KOH. Reproduced with permission from ref 514. Copyright 2019 Elsevier.

facets and $NiCo_2O_4$ truncated octahedron exposing [111] and [100] facets.

Perovskite materials have garnered significant attention as a promising class of electrocatalysts as well. Shao and coworkers employed the electrospinning method followed by annealing to prepare the $SrNb_{0.1}Co_{0.7}Fe_{0.2}O_{3-\delta}$ perovskite nanorod (SNCF-NR) (Figure 50g).[507] Leveraging the catalytic properties and unique structural features of perovskites, the SNCF-NR couple achieved a current density of 10 mA cm^{-2} at an impressively low cell voltage of 1.68 V (Figure 50h). Another noteworthy example is the work of Ciucci and coworkers, who synthesized $NdBaMn_2O_{5.5}$, a double perovskite layered oxide, as a bifunctional electrode material for alkaline OWS.[508] Analogous to transition metal oxides, transition metal hydroxides/(oxy)hydroxides have also been explored as efficient bifunctional OWS electrocatalysts.[509] Grätzel and coworkers obtained NiFe layered double hydroxides (NiFe-LDH) on NF through a hydrothermal method, which exhibited high

https://doi.org/10.1021/acs.chemrev.3c00332
Chem. Rev. 2024, 124, 3694−3812

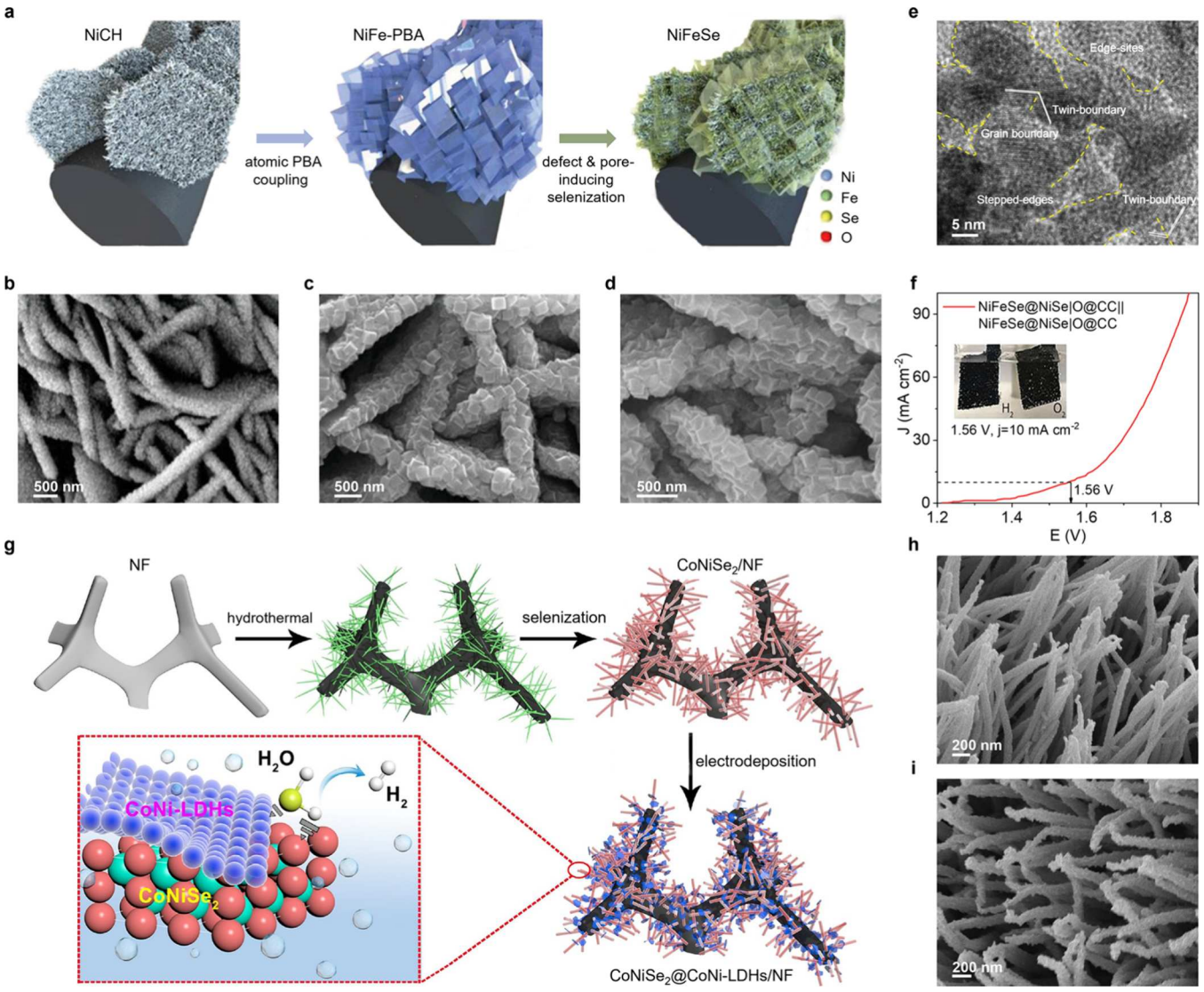

Figure 52. (a) Schematic of the synthesis of NiFeSe@NiSe|O@CC. SEM images of (b) NiCH@CC, (c) NiFe-PBA@NiCH@CC, and (d) NiFeSe@NiSe|O@CC. (e) HRTEM image of NiFeSe@NiSe|O@CC. (f) LSV curves of NiFeSe@NiSe|O@CC couple for alkaline OWS in 1.0 M KOH. Reproduced with permission from ref 516. Copyright 2019 John Wiley and Sons. (g) Schematic of the synthesis of $CoNiSe_2$@CoNi-LDHs/NF. SEM images of (h) $CoNiSe_2$/NF and (i) $CoNiSe_2$@CoNi-LDHs/NF. Reproduced with permission from ref 517. Copyright 2019 Elsevier.

activity for both OER and HER in 1.0 M NaOH.[510] Furthermore, the NiFe-LDH was employed as both cathode and anode in a perovskite solar cell-powered water-splitting device (Figure 50i–k), capable of achieving a current of 10 mA cm^{-2} at only 1.7 V (Figure 50i).

Multimetal sulfides have garnered significant attention as electrocatalysts for OWS as well.[511] Sun and coworkers developed vertically aligned oxygen-containing CoS_2–MoS_2 (O-CoMoS) heteronanosheets grown on carbon fiber cloth by the use of a polyoxometalate as precursor (Figure 51a).[512] The unique nanosheet structure of O-CoMoS facilitated the exposure of active heterogeneous interfaces, the synergistic effects of heterostructures created abundant active sites, and the 2D conductive networks enhanced charge transfer. Consequently, the resulting O-CoMoS achieved 10 mA cm^{-2} at a low cell voltage of only 1.6 V for OWS in 1.0 M KOH (Figure 51b) and sustained continuous electrolysis at 10 mA cm^{-2} with negligible voltage fluctuations for 10 h (Figure 51c). In another study, Lv and collaborators utilized polyacrylonitrile (PAN) nanofibers as template and nitrogen source to synthesize N-doped carbon/$NiCo_2S_4$ hollow nanotubes (NCT-$NiCo_2S_4$) through a one-pot method (Figure 51d).[513] TEM image confirmed the hollow nature of NCT-$NiCo_2S_4$ (Figure 51e). The carbon-encapsulated hollow nanotube structure promoted accessibility of active sites and mass transfer, and alleviated electrolyte corrosion, resulting in enhanced activity and stability for alkaline OWS. The resulting NCT-$NiCo_2S_4$ exhibited low overpotentials of 295 and 330 mV for HER and OER to afford 100 mA cm^{-2} in 1.0 M KOH, respectively. When applied as both cathode and anode in an electrolyzer, it required only 1.6 V to afford 10 mA cm^{-2}, lower than those of control couples (Figure 51f). Additionally, Fan and coworkers fabricated bimetallic sulfide anchored 3D nitrogen-doped graphene foam (MoS_2–NiS_2/NGF) hybrids via hydrothermal growth of MoO_2–$Ni(OH)_2$ nanowalls followed by sulfurization, as schematically shown in Figure 51g.[514] SEM image (Figure 51h) of nitrogen-doped graphene foam (NGF) revealed a highly wrinkled surface, beneficial to the homogeneous nucleation and growth of MoO_2–$Ni(OH)_2$ nanowalls with a hierarchical 2D/3D hybrid structure (Figure

https://doi.org/10.1021/acs.chemrev.3c00332
Chem. Rev. 2024, 124, 3694–3812

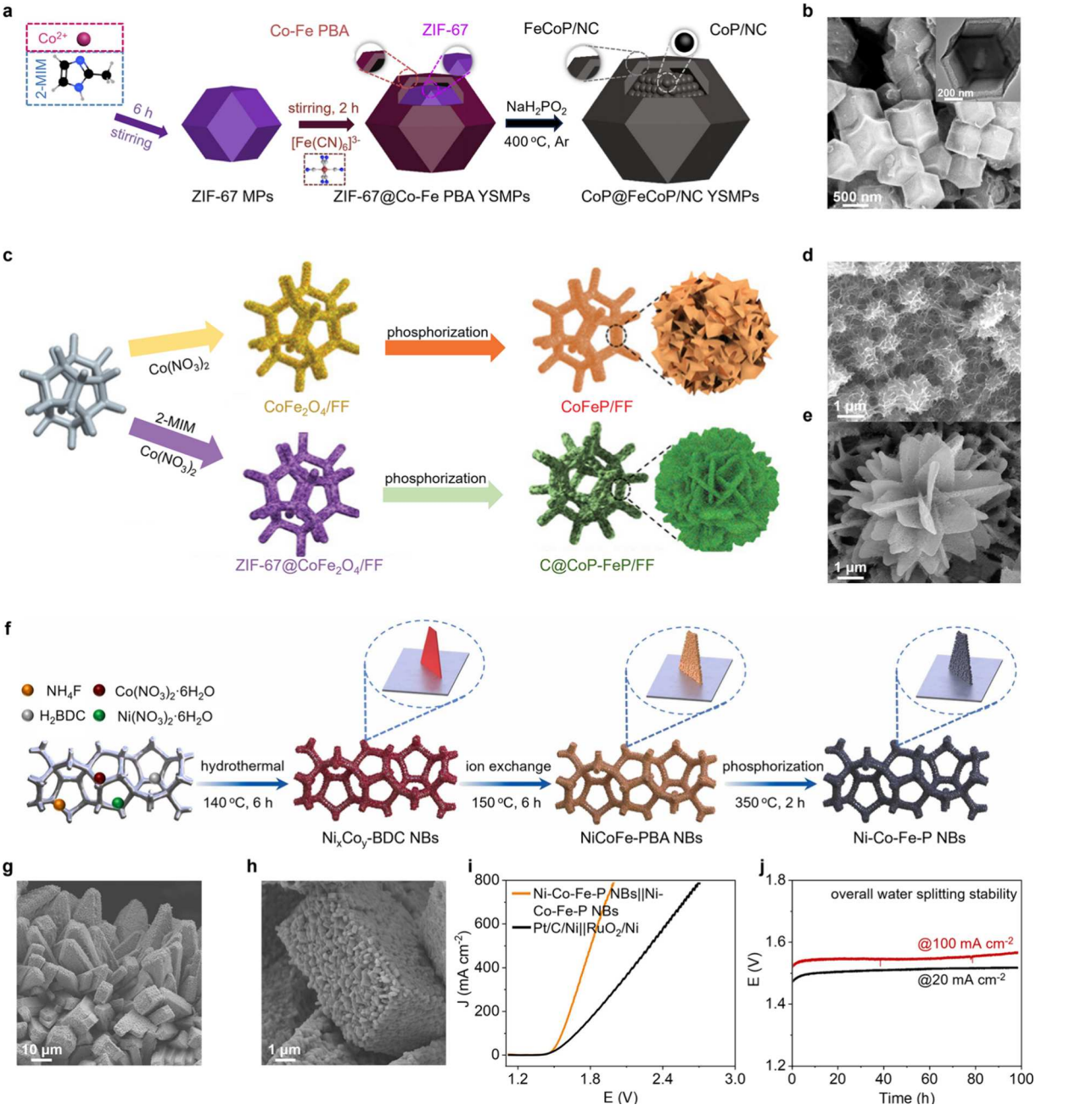

Figure 53. (a) Schematic of the formation of CoP@FeCoP/NC YSMPs. (b) SEM and TEM images of ZIF-67@Co−Fe PBA YSMPs. Reproduced with permission from ref 519. Copyright 2021 Elsevier. (c) Schematic of the preparation of CoFeP/FF and C@CoP-FeP/FF. SEM images of (d) CoFeP/FF and (e) C@CoP-FeP/FF. Reproduced with permission from ref 520. Copyright 2023 John Wiley and Sons. (f) Schematic of the preparation of Ni−Co−Fe−P NBs. (g, h) SEM images of Ni−Co−Fe−P NBs. (i) LSV curves of Ni−Co−Fe−P NBs couple and Pt/C/Ni||RuO_2/Ni couple for OWS in 1.0 M KOH. (j) Chronopotentiometric curves of Ni−Co−Fe−P NBs couple for OWS at different current densities. Reproduced with permission from ref 521. Copyright 2022 Elsevier.

51i). Notably, the MoO_2−$Ni(OH)_2$ nanowalls can be converted into MoS_2−NiS_2 nanoparticles while maintaining the 3D interconnected tubular structure of NGF (Figure 51j). The heterointerfaces between NGF and MoS_2−NiS_2 enabled the exposure of abundant active sites and efficient mass/charge transfer. As a result, the two-electrode system of MoS_2−NiS_2/NGF couple (Figure 51k) achieved a current density of 10 mA cm^{-2} at 1.64 V in 1.0 M KOH (Figure 51l).

Besides, multimetal selenides have also been explored, offering excellent activity, durability, and cost-effectiveness.[515] Ho's group employed a coordinative self-templating method to convert nickel−iron Prussian blue analog (NiFe-PBA) and nickel hydroxide carbonate (NiCH) templates into porous and defect-rich nickel−iron selenide hybrids on carbon cloth (NiFeSe@NiSeIO@CC) (Figure 52a).[516] SEM images illustrated the morphological evolution during synthesis (Figure 52b−d). Initially, hexagonal nanosheet structures of NiCH@CC self-templates were obtained via a hydrothermal method (Figure 52b). Subsequently, NiFe-PBA was grown on the NiCH@CC template at room temperature, with the nanosheets being surrounded by uniformly crystallized NiFe-PBA nanocubes (Figure 52c). Finally, selenization of the resulting

https://doi.org/10.1021/acs.chemrev.3c00332
Chem. Rev. 2024, 124, 3694−3812

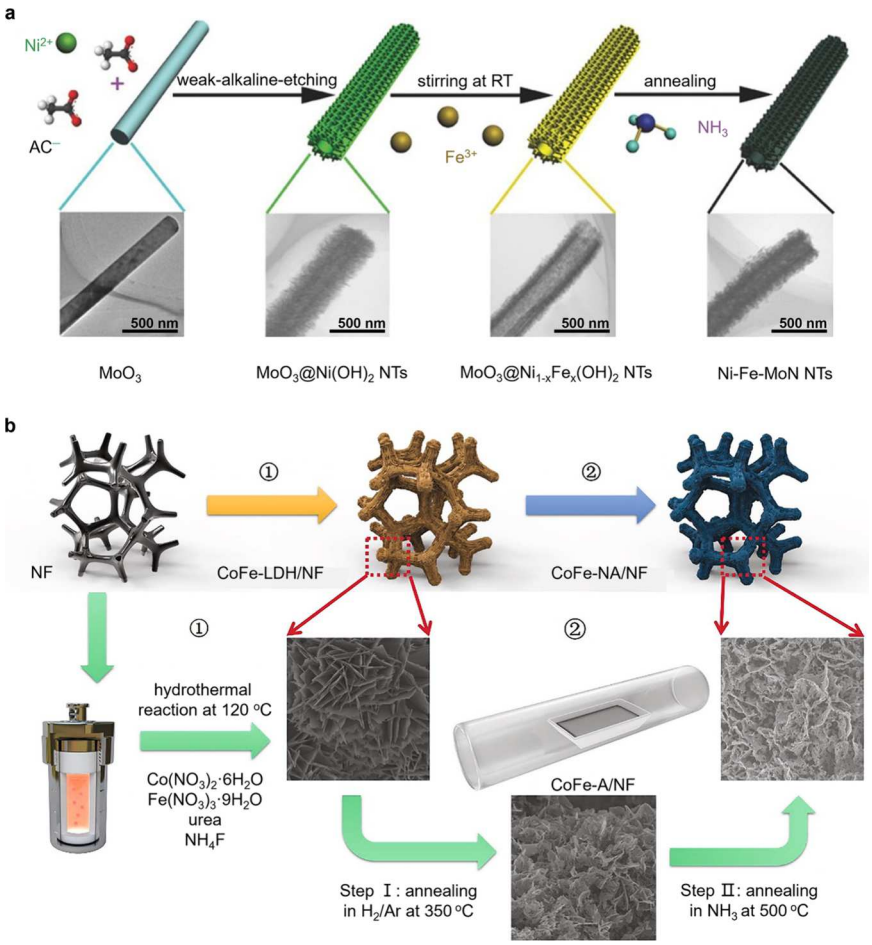

Figure 54. (a) Schematic of the synthesis of Ni−Fe−MoN NTs. Reproduced with permission from ref 524. Copyright 2018 John Wiley and Sons. (b) Schematic of the synthesis of CoFe-NA/NF electrodes. Reproduced with permission from ref 525. Copyright 2022 Elsevier.

PBA@NiCH@CC resulted in NiFeSe@NiSeIO@CC (Figure 52d). HRTEM image revealed the abundance of unsaturated sites and defects in the NiFeSe@NiSeIO@CC (Figure 52e). This unique structure, with increased reactive sites and improved conductivity, contributed to the excellent electrocatalytic performance of NiFeSe@NiSeIO@CC for OWS in 1.0 M KOH (Figure 52f). In another study, Gao and collaborators designed $CoNiSe_2$ heterogeneous nanorods decorated with LDH nanosheets on Ni foam ($CoNiSe_2$@CoNi-LDHs/NF).[517] As shown in Figure 52g, the $CoNiSe_2$/NF with nanorod structure were first vertically attached to a NF substrate via hydrothermal and selenization of 1D Co−Ni precursors, as revealed by the SEM image (Figure 52h). Subsequently, nanorod structures decorated with ultrathin nanosheets were achieved through electrodeposition of CoNi-LDHs (Figure 52i). The unique interfaces enhanced adsorption of H_2O to facilitate its dissociation for boosted HER, as confirmed by both DFT and in situ Raman analysis. As a result, the resulting $CoNiSe_2$@CoNi-LDHs/NF couple required an ultralow cell voltage of only 1.44 V to reach 10 mA cm^{-2} under alkaline conditions (1.0 M KOH), outperforming the $CoNiSe_2$/NF and CoNi-LDHs/NF control couples.

Due to their excellent electrical conductivity, metallic properties, and proton trapping capabilities at the P site,[518] multimetal phosphides have been investigated for alkaline OWS. Lu and coworkers synthesized nitrogen-doped carbon-decorated CoP@FeCoP yolk−shell micropolyhedras (CoP@FeCoP/NC YSMPs) through the phosphorization of ZIF-67@Co−Fe Prussian blue analogue YSMPs (Figure 53a).[519] SEM and TEM images (Figure 53b) showcased the unique yolk−shell structure of ZIF-67@Co−Fe PBA YSMPs, featuring a thin shell and a thick core. Such a structure can be maintained after phosphorization for CoP@FeCoP/NC YSMPs, and the resulting nitrogen-doped carbon substrate can effectively mitigate the agglomeration of CoP, leading to increased specific surface area for exposure of active sites. The synergistic effect between the yolk−shell structure and the nitrogen-doped carbon substrate optimized the electronic structure and enhanced the electrocatalytic activity of CoP@FeCoP/NC YSMPs. When utilized for alkaline OWS in 1.0 M KOH, the CoP@FeCoP/NC YSMPs couple required a low cell voltage of only 1.68 V to achieve 10 mA cm^{-2}, with excellent stability over 20 h. Additionally, Wang and coworkers prepared a self-supported bifunctional electrocatalyst of carbon-encapsulated bimetallic phosphides on Fe foam (C@CoP-FeP/FF) via a simple two-step process (Figure 53c).[520] SEM images showcased the critical role of ZIF-67 protective layer (Figure 53d,e). Obviously, the CoFeP/FF control featured curved nanosheets with cross-link structures (Figure 53d). In contrast, the C@CoP-FeP/FF presented nanosheet array morphology with abundant pores due to the introduction of N-doped carbon from ZIF-67 (Figure 53e). The abundant heterogeneous interface and the porous N-doped carbon layer favored the exposure of active sites, and mass/charge transfer.

https://doi.org/10.1021/acs.chemrev.3c00332
Chem. Rev. 2024, 124, 3694−3812

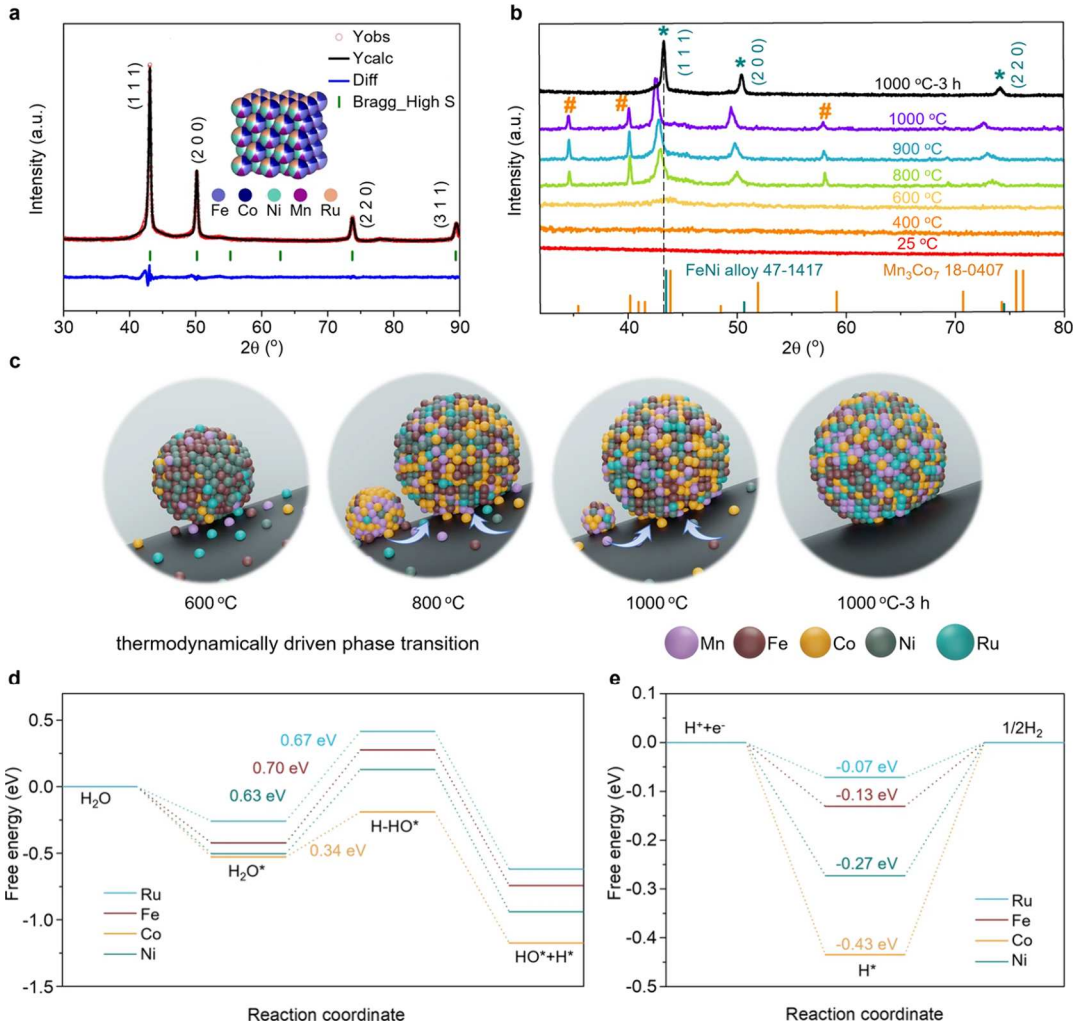

Figure 55. (a) XRD patterns of FeCoNiMnRu/CNFs with detailed Rietveld refinements. (b) Real-time in situ XRD patterns for FeCoNiMnRu/CNFs with temperatures ranging from 25 to 1000 °C. (c) Schematic of thermodynamically driven phase transition of FeCoNiMnRu NPs in CNF nanofiber reactors. (d) Gibbs free energy profiles for water dissociation on various catalytic sites of the FeCoNiMnRu HEA surface. (e) Gibbs free energy profiles on various catalytic sites of the FeCoNiMnRu HEA surface. Reproduced with permission from ref 528 under the terms of a CC-BY 4.0 license. Copyright 2022 The Authors, published by Springer Nature.

Consequently, the C@CoP-FeP/FF couple required only 1.73 V to achieve a current density of 100 mA cm^{-2} in a simulated seawater electrolyte (1.0 M KOH + 0.5 M NaCl). Wei and collaborators synthesized porous Ni−Co−Fe trimetallic phosphide nanobricks with precisely tunable composition and morphology using Ni−Co MOF precursors (Figure 53f).[521] First, Ni_xCo_y-BDC NBs were prepared through a one-pot hydrothermal reaction, which were then converted into porous NiCo Prussian blue (NiCoFe-PBA NBs) through an ion-exchange reaction in a $K_3Fe(CN)_6$ solution. Finally, the porous Ni−Co−Fe−P NBs were obtained by phosphorization of the resulting NiCoFe-PBA, as depicted in the SEM images (Figure 53g,h). The unique structure of Ni−Co−Fe−P NBs enabled them to achieve a low cell voltage of 1.46 V to reach 10 mA cm^{-2} for OWS in 1.0 M KOH, along with robust durability at both low and high current densities (Figure 53i,j).

Additionally, multimetal nitrides have also shown great potential in alkaline OWS due to the multicomponent synergy.[522,523] Chou and coworkers developed a multistep synthetic strategy to fabricate layered Ni−Fe−Mo trimetallic nitride nanotubes (Ni−Fe−MoN NTs) through Fe doping at room temperature followed by NH_3 heat treatment of hierarchical core−shell MoO_3@$Ni(OH)_2$ NTs (Figure 54a).[524] TEM images revealed that the outer wall of Ni−Fe−MoN NTs consists of porous sheet-like nanostructures. Optimized Ni−Fe−Mo trimetallic nitride nanotubes exhibited excellent electrocatalytic activity for both HER and OER in 1.0 M KOH, with respective overpotentials of 55 and 228 mV at 10 mA cm^{-2}. When used as a bifunctional electrocatalyst for OWS in 1.0 M KOH, the optimized Ni−Fe−MoN NTs couple needed a cell voltage of 1.513 V at 10 mA cm^{-2}. In another example, Pan and collaborators constructed cobalt−iron nitride/alloy nanosheets on nickel foam (CoFe-NA/NF) using a three-step strategy (Figure 54b).[525] Initially, CoFe-LDH hierarchical nanosheets (CoFe-LDH/NF) were uniformly grown on the NF through hydrothermal reaction. After annealing at 350 °C under an Ar/H_2 atmosphere, porous and interconnected structures of CoFe-A/NF were formed. Subsequently, the CoFe-A/NF was nitrided by annealing in NH_3 at 500 °C to obtain the final product of CoFe-NA/NF. SEM images of CoFe-NA nanosheets demonstrated numerous nanoparticles with abundant mesopores and macropores on the surface, forming a porous 3D network structure. The porous surface provided a large active surface area. Thus, the

https://doi.org/10.1021/acs.chemrev.3c00332
Chem. Rev. 2024, 124, 3694−3812

Table 5. Summary of Bifunctional Electrocatalysts for Overall Water Splitting (OWS) in 1.0 M KOH

Electrocatalysts	Current density ($mA\ cm^{-2}$)	Cell voltage (V)	Ref
Ni_2P/Ni/NF	10	1.49	227
Co-P film	100	1.744	266
δ-FeOOH NSs/NF	10	1.62	440
FeS/IF	10	1.65	441
FeP	10	1.59	443
OESSC	10	1.74	444
Fe-N_4 SAs/NPC	10	1.67	445
CoO_x@CN	20	1.55	451
$Co(OH)_2$@NCNTs@NF	10	1.72	454
Co_3S_4/EC-MOF	10	1.55	456
Co_9S_8@NOSC	20	1.74	457
NS/rGO-Co	10	1.72	458
Co-P/NC	165	2.0	464
Co_2P/CoNPC	10	1.64	465
CoP NFs	10	1.65	466
Co-NC@CC	10	1.57	467
Co@N-CS/N-HCP@CC	10	1.545	468
Ni/$Ni(OH)_2$	10	1.59	471
NiS/G	10	1.54	474
Ni/Ni_8P_3	10	1.61	475
Ni_2P	10	1.58	477
Ni-ZIF/Ni-B@NF	10	1.54	478
Ni@NC	10	1.6	480
Ni@N-HCGHF	10	1.6	481
porous MoO_2	10	1.53	482
MoP/NF	10	1.62	485
Mo_2C@CS	10	1.73	486
$Cu_2O_xS_{1-x}$	10	1.56	490
CuSe/NF	10	1.68	491
CS2	100	2.08	492
Cu_3P/Cu	10	1.85	493
Cu_3P@NF	10	1.67	494
Cu_3N/NF	10	1.6	498
Cu-N-SC-1100	10	1.64	501
$NiFeO_x$ NPs	10	1.51	504
$NiCo_2O_4$ HMCs/NF[a]	10	1.65	505
(110)$NiCo_2O_4$NSs/NF	10	1.59	506
SNCF-NRs	10	1.68	507
$NdBaMn_2O_{5.5}$	10	1.67	508
NiFe-LDH[a]	10	1.7	510
O-CoMoS	10	1.6	512
$NiCo_2S_4$	10	1.6	513
MoS_2-NiS_2	10	1.64	514
NiFeSe@NiSeIO@CC	10	1.56	516
$CoNiSe_2$@CoNi-LDH/NF	10	1.44	517
CoP@FeCoP	10	1.68	519
C@CoP-FeP/FF	100	1.74	520
Ni-Co-Fe-P NBs	10	1.46	521
Ni-Fe-MoN NTs	10	1.513	524
CoFe-NA/NF	10	1.564	525
$CoSn_2$	10	1.55	527
FeCoNiMnRu/CNFs	100	1.65	528
Co_3O_4-MTA	10	1.63	529
ceria/Ni-TMO	10	1.58	530
MoS_2/NiS_2	10	1.59	531
MoS_2/NiS	10	1.61	532
La-NMS@NF	100	1.72	533
$CoMoS_x$/NF	500	1.89	534
Ni_2P-Ni_3S_2	10	1.5	535
N-CoS_2/NF	10	1.5	536
N-$NiMoO_4$/NiS_2	10	1.6	537
Ni_3S_2/MnO_2	10	1.52	538
CoS_x-Ni_3S_2	100	1.63	539
Co_9S_8/Ni_3S_2	10	1.64	540
Se-MnS/NiS	10	1.47	541
Cu@Cu_2S	20	1.61	542
$CuCo_2S_4$/CC	10	1.58	543
P-$CoNi_2S_4$ YSSs	10	1.544	544
Co-Ni_3S_2	10	1.54	545
Ni-Mo-S	100	2	546
NiFe/$(Ni,Fe)_3S_2$	400	1.9	547
Co_3Se_4/CF	10	1.59	548
p-$CoSe_2$/CC	10	1.62	549
$NiSe_2Ni_2P$/NF	10	1.5	550
two-tiered NiSe	10	1.69	551
CoFe PBA@CoP	10	1.542	552
(Fe-Co)Se_2	10	1.59	553
Cu-14-Co_3Se_4	10	1.62	554
$(Ni,Co)_{0.85}Se$	10	1.65	555
$NiCo_2Se_4$	10	1.68	556
CoNiSe/C/NF	10	1.6	557
CeO_2-NiCoP	500	1.82	558
Ni_5P_4	10	1.7	559
Ni-P film	10	1.67	560
Ni_1Mo_1P NSs@MCNTs	10	1.601	561
NiCoP/rGO	10	1.59	562
Mo-CoP	10	1.56	563
Co_2P/Mo_2C/Mo_3Co_3C@C	10	1.74	564
CoP@PNC	10	1.52	565
CoPS@NPS-C	10	1.62	566
$Co_{0.17}Fe_{0.79}P$/NC	10	1.66	567
Co/CoP-HNC	10	1.68	568
FeNiP/NC	10	1.54	569
Co_4Ni_1P	10	1.59	570
CoP/NCNHP	10	1.64	571
CoP/rGO-400	10	1.7	572
Ni_2P/rGO	10	1.61	573
Co-Mo-P@NCNS	10	1.58	574
NiFe-P@GNS	10	1.578	575
Fe-Ni_2P/C	500	1.66	576
Mn-NiCoP	100	1.69	577
$Fe_{0.27}Co_{0.73}P$	10	1.68	578
Ni_2P	10	1.52	579
Co-P@PC	10	1.6	580
H-CoP@NC	10	1.72	581
CoPO	10	1.52	582
Ni-Fe-P@C NRs	10	1.52	583
CoP NS/CC	10	1.67	584
Co_4N-$VN_{1-x}O_x$/CC	10	1.64	585
TiN@Ni_3N	10	1.64	586
Ni_3FeN/r-GO-20	10	1.6	587
Co_4Mo_2@NC/Ti	10	1.74	588
Fe-Co films	10	1.68	589

[a] 1.0 M NaOH.

https://doi.org/10.1021/acs.chemrev.3c00332
Chem. Rev. 2024, 124, 3694−3812

two-electrode system assembled with CoFe-NA/NF couple achieved 10 mA cm^{-2} at a cell voltage of 1.564 V and maintained excellent stability for over 50 h in 1.0 M KOH.

Multimetal alloys exhibit unique crystallographic and electronic properties, leading to unexpected electrocatalytic behavior.[526] Driess and coworkers employed solution chemistry for the controlled synthesis of $CoSn_2$ nanocrystals.[527] Under basic conditions, the loss of Sn from the lattice and oxidation of Co led to the formation of highly disordered amorphous active $CoO_x(H)$ as OER active species. The Co^0 atom in $CoSn_2$ then acted as the active site for HER, and the presence of Sn ensures excellent conductivity. As a result, the as-prepared $CoSn_2$/NF couple exhibited high activity, achieving 10 mA cm^{-2} with a cell voltage of only 1.55 V. Recently, Zhu and coworkers developed a FeCoNiMnRu high-entropy alloy (HEA) system on carbon nanofibers (FeCoNiMnRu/CNFs) with diverse active sites to overcome the limitations of single-element catalysts.[528] XRD analysis of FeCoNiMnRu/CNFs (Figure 55a) revealed no peaks corresponding to Fe, Co, Ni, Mn, Ru, or metal oxides, indicating the presence of a single face-centered cubic (*fcc*) phase of the HEA alloy. Temperature-dependent in situ XRD patterns (Figure 55b) demonstrated that at 600 °C, only the FeNi alloy phase is observed; while at 800 and 1000 °C, the Mn_3Co_7 phase coexists with the HEA *fcc* phase, which is transformed entirely into the HEA *fcc* phase with increasing temperature and prolonged heat treatment. The authors concluded that the combination of high temperature and extended heat treatment facilitates the complete mixing of multiple metal atoms, as illustrated in Figure 55c. Subsequently, an alkaline OWS electrolyzer was fabricated using FeCoNiMnRu/CNFs as the bifunctional electrocatalyst, and the FeCoNiMnRu/CNFs couple required only 1.65 V at 100 mA cm^{-2}. DFT calculations (Figure 55d,e) revealed that the electronegativity difference among the mixed elements in the HEA induces significant charge redistribution, resulting in highly active Co and Ru sites with optimized adsorption to simultaneously stabilize HO* and H* intermediates. This enhanced the efficiency of water dissociation under alkaline conditions. The electrocatalytic OWS activities of diverse bifunctional electrocatalysts in alkaline solutions are summarized in Table 5.

5. BIFUNCTIONAL ELECTROCATALYSTS FOR HYBRID WATER SPLITTING

Although developing bifunctional electrocatalysts for overall water splitting can avoid the requirement for separate synthesis of single functional HER and OER electrocatalysts and thus reduce the overall cost, OER still couples with HER in traditional OWS, leading to several challenges: (1) low energy conversion efficiency, the OER is thermodynamically sluggish due to the four-electron transfer process, requiring much higher overpotentials than HER with two-electron transfer and usually consuming ~90% electrical energy;[51,590−593] (2) safety issues, OER and HER occur simultaneously during water splitting and hence explosive H_2/O_2 gas mixtures may form arising from possible gas crossover;[594−600] (3) low economic benefit and high cost, O_2 is not only regarded as a byproduct because of its low economic value but also may lead to membrane degradation due to the formation of reactive oxygen species (ROS).[99,598,601,602]

In light of this, a concept of hybrid water splitting (HWS) has been proposed to replace OER.[51,99,315] Electro-oxidation of carefully selective substrates with favorable kinetics relative to OER can dramatically reduce anodic potentials and at the same time, produce value-added chemicals for food, pharmaceutical and chemical industries, as well as sustainable alternatives to fossil fuels.[103,317,318,603−612] These alternative substrates include hydrazine, ammonia, urea, alcohols, aldehydes, amines, biomass derivatives, bio/plastic wastes and so on.[609,613−620] Therefore, hybrid water splitting (HWS) would be more economically feasible. In this section, we summarize the bifunctional electrocatalysts-driven hybrid water splitting (HWS) that use alternative oxidation reactions to replace OER. Based on the substrates' functionalities and properties, these alternative oxidation reactions can be divided into three categories, including sacrificing agents oxidation, pollutants oxidative degradation, and organics oxidative upgrading.

5.1. Hybridizing with Sacrificing Agents Oxidation

If a small-molecule is electro-oxidized to degraded or worthless product(s), it can be regarded as a sacrificing agent. In this respect, hybridizing with sacrificing agents oxidation (SAO) will increase the overall cost of HWS. However, benefiting from its extremely low oxidative potential, the SAO-coupled hybrid water splitting can obtain a cell voltage much lower than that of overall water splitting (OWS), which substantially reduces the energy input for hydrogen generation. Typical small molecules that fall into this category include hydrazine,[104,621,622] ammonia,[623,624] and urea.[625−627]

5.1.1. Hydrazine Oxidation. Hydrazine (N_2H_4), as an industrial raw material in agriculture, pharmaceutical, and chemical industries, is well soluble in water with more favorable oxidation than water.[628−634] The typical hydrazine oxidation reactions (HzOR) in alkaline and acidic solution are given below:

$$N_2H_4 + 4OH^- = N_2 + 4H_2O + 4e^-$$

$$NH_2NH_3^+ = N_2 + 4e^- + 5H^+$$

The thermodynamic potential of HzOR is only −0.33 V.[606,609] More importantly, there is no greenhouse gas releasing during HzOR with nitrogen being the main product.

Sun and coworkers reported an impressive work on coupling HzOR with HER for hybrid water splitting. In their work, the Ni_2P on Ni foam nanoarrays (Ni_2P/NF) prepared by high-temperature phosphorization of $Ni(OH)_2$/NF was used as a high-performance bifunctional electrocatalyst for both HzOR and HER.[609] Remarkably, the resulting Ni_2P/NF showed an early and sharp rise of anodic current in the presence of hydrazine, indicative of greatly enhanced HzOR activity. It required a potential of only −25 mV vs RHE to drive 50 mA cm^{-2} in 1.0 M KOH containing 0.5 M N_2H_4. Moreover, the Ni_2P/NF couple achieved 500 mA cm^{-2} at a cell voltage of only 1.0 V with a Faradaic efficiency (FE) of 100% for H_2 evolution, in contrast to that of 1.6 V at 20 mA cm^{-2} for OWS. Additionally, this hybrid electrolyzer can remain stable for 10 h at 100 mA cm^{-2}. Subsequently, many other bifunctional and noble-metal-free electrocatalysts with single-component like tubular $CoSe_2$ were designed, which achieved 10 mA cm^{-2} at a cell voltage of only 0.164 V in 1.0 M KOH with 0.5 M N_2H_4.[619]

Besides, multicomponent bifunctional electrocatalysts with tunable electronic structures and multiple active centers were also developed. For example, Xie and coworkers investigated the role of heterointerfaces in HWS. The hierarchical porous nanosheet array with abundant Ni_3N−Co_3N heterointerfaces

https://doi.org/10.1021/acs.chemrev.3c00332
Chem. Rev. 2024, 124, 3694−3812

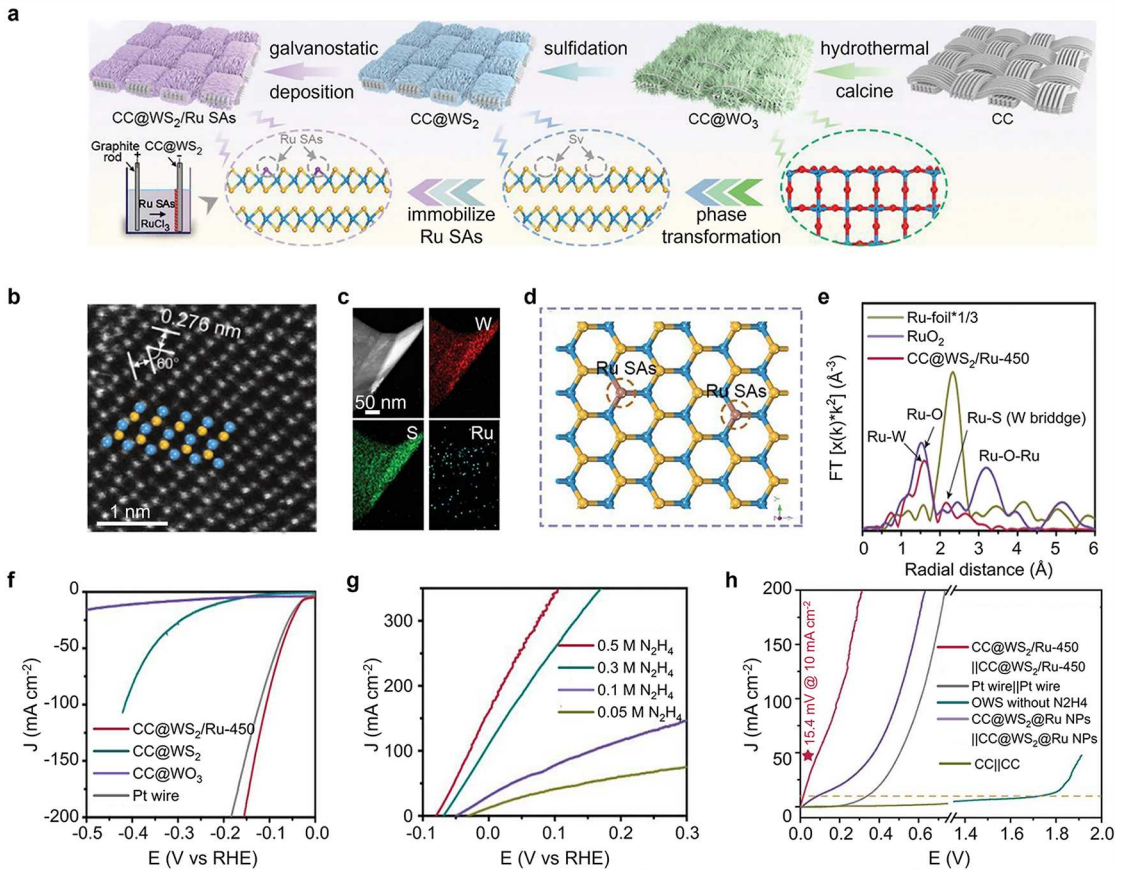

Figure 56. (a) Schematic for the preparation of CC@WS_2/Ru SAs and crystal transformation from WO_3 to WS_2/Ru SAs. (b) HAADF STEM and (c) elemental mapping images of CC@WS_2/Ru-450. (d) Crystal structure of 2H phase of WS_2 with several Ru SAs isolated in V_S. (e) Ru K-edge FT-EXAFS spectra of CC@WS_2/Ru-450, Ru foil, and RuO_2. (f) LSV curves of CC@WO_3, CC@WS_2, CC@WS_2/Ru-450, and Pt wire for HER. (g) LSV curves of the CC@WS_2/Ru-450 with variable N_2H_4 concentrations in 1.0 M KOH for HzOR. (h) LSV curves of two-electrode couples for CC@WS_2/Ru-450 with or without 0.5 M N_2H_4, as well as Pt wire couple, CC@WS_2@Ru NPs couple, and CC couple in 1.0 M KOH with 0.5 M N_2H_4. Reproduced with permission from ref 637. Copyright 2022 John Wiley and Sons.

was obtained as a highly active nonprecious electrocatalyst for HER and HzOR in alkaline media (1.0 M KOH).[635] Applied potentials of only −43 and −88 mV vs RHE were required to afford 10 mA cm^{-2} for HER and HzOR, respectively, both of which were lower than those for single Ni_3N and Co_3N. This comparison underscored the positive synergy between Ni_3N and Co_3N. Note that the Ni_3N−Co_3N heterointerfaces can achieve 1000 mA cm^{-2} at a potential of only 0.2 V vs RHE for HzOR, significantly lower than the thermodynamic potential of OER (1.23 V vs RHE). Moreover, this bifunctional Ni_3N−Co_3N heterointerfaces-derived two-electrode system delivered 10 and 400 mA cm^{-2} at cell voltages of only 0.071 and 0.76 V, respectively. DFT calculations unraveled the critical role of heterointerfaces between Ni_3N and Co_3N, wherein the Gibbs free energy of adsorbed hydrogen (ΔG_H) and stepwise hydrazine dehydrogenation can be optimized, accountable for improved HER and HzOR, respectively. Recently, the same group constructed dual nanoislands on Ni/C hybrid nanosheet array (Ni−C HNSA) by pyrolysis of Ni-based MOF in N_2, in which Ni-decorated carbon shell and exposed Ni atoms were regarded as active sites for HER and HzOR, respectively.[636] As a result, the Ni−C HNSA displayed applied potentials of −37 mV vs RHE for HER and −20 mV vs RHE for HzOR at 10 mA cm^{-2}. More importantly, the two-electrode electrolyzer exhibited superb activity achieving 50 mA cm^{-2} at a low cell voltage of 0.14 V in 1.0 M KOH with 0.1 M N_2H_4. Similarly, a bifunctional copper−nickel nitride (Cu_1Ni_2−N) with rich Cu_4N/Ni_3N interface was synthesized for HzOR-coupled hybrid water splitting as well, which delivered 10 mA cm^{-2} at a cell voltage of 0.24 V with excellent stability over 75 h.[611]

Heteroatom doping is also powerful to tune the electronic state of the underlying catalysts. Ma and coworkers recently designed and prepared the Ru single atoms anchored on S vacancies of WS_2 over conductive carbon cloths (CC@WS_2/Ru SAs) bifunctional electrocatalyst by sulfidation of hydrothermal WO_3 on CC followed by facile galvanostatic deposition strategy, as shown in Figure 56a.[637] Specifically, the WO_3 nanowires were grown on CC by hydrothermal and calcining process first. Then the WO_3 were converted to WS_2 by high-temperature sulfidation under sulfur vapor atmosphere and sulfur-vacancies (V_S) were introduced. Finally, Ru SAs were immobilized onto the V_S of WS_2 by galvanostatic deposition for 450 s. As shown in Figure 56b, the spherical aberration correction (AC) HAADF-STEM image of the as-prepared CC@WS_2/Ru SAs-450 showed a hexagonal structure where the yellow and blue spheres represented S and W atoms, respectively. Furthermore, elemental mapping images in Figure 56c revealed the homogeneous and individual distribution of Ru atoms, suggestive of their atomic dispersion. Figure 56d showed the schematic crystal structure of 2H WS_2 with several Ru SAs isolated in V_S, which was further confirmed by the FT-EXAFS analysis at Ru K-edge. As shown in Figure 56e, the

https://doi.org/10.1021/acs.chemrev.3c00332
Chem. Rev. 2024, 124, 3694−3812

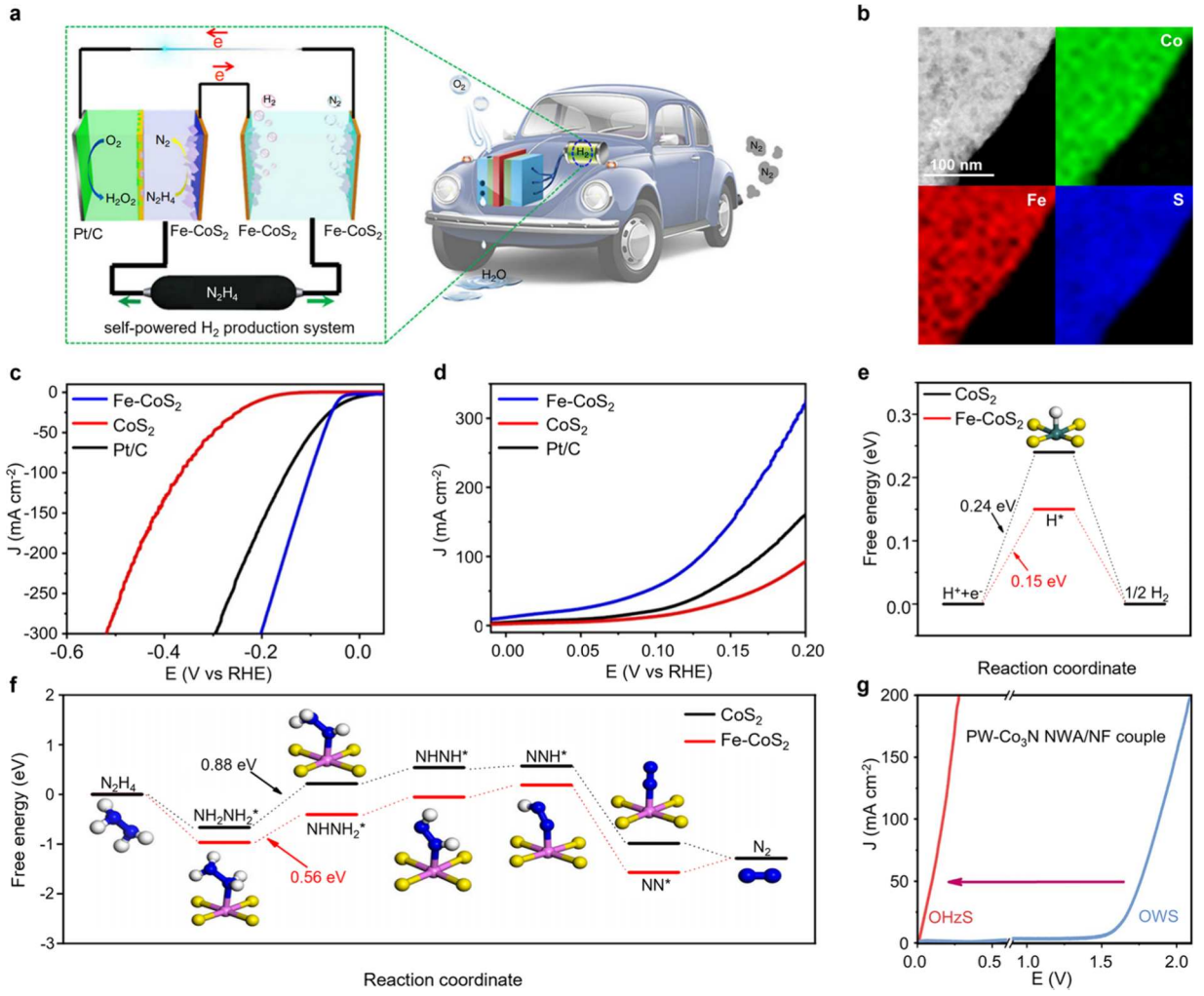

Figure 57. (a) Schematic illustration of a self-powered hydrogen production system. (b) HAADF STEM and the corresponding elemental mapping images of Fe-CoS_2. (c) LSV curves for HER on 20 wt % Pt/C, pristine CoS_2 nanosheets and Fe-CoS_2 in 1.0 M KOH. (d) LSV curves for HzOR on 20 wt % Pt/C, pristine CoS_2 nanosheets and Fe-CoS_2 in 1.0 M KOH with 0.1 M N_2H_4. (e) Free energy profiles of alkaline HER on CoS_2(001) and Fe-CoS_2(001) surfaces at 0 V vs RHE. The inset in (e) is the most stable configuration of the intermediate (H*) adsorbed on the surface of CoS_2. (f) Free energy profiles of HzOR on the CoS_2(001) and the Fe-CoS_2(001) surfaces at 0 V vs RHE. Reproduced with permission from ref 616 under the terms of a CC-BY 4.0 license. Copyright 2018 The Authors, published by Springer Nature. (g) LSV curves of PW-Co_3N NWA/NF couple for HzOR-assisted HWS in 1.0 M KOH with and without 0.1 M N_2H_4. Reproduced with permission from ref 639 under the terms of a CC-BY 4.0 license. Copyright 2020 The Authors, published by Springer Nature.

peaks at 1.63 and 2.2 Å can be attributed to Ru−W and Ru−S, respectively, ruling out the existence of metallic Ru−Ru and Ru−O. The HER and HzOR activities of the resulting CC@WS_2/Ru SAs-450 were then examined by linear sweep voltammetry (LSV) in 1.0 M KOH with and without N_2H_4. The LSV curve implied a low potential of merely −32.1 mV vs RHE for HER at 10 mA cm^{-2} for CC@WS_2/Ru SAs-450, comparable to that for commercial Pt/C and much lower than those for controls of CC@WS_2 and CC@WO_3 (Figure 56f). Such comparisons clearly emphasized the improved role of both sulfidation and Ru SAs doping. Additionally, the CC@WS_2/Ru SAs-450 showcased promising HzOR activity in the same electrolyte after adding N_2H_4 with different concentrations. For instance, with 0.5 M N_2H_4 in 1.0 M KOH, an ultralow potential of only −74 mV vs RHE was needed to reach 10 mA cm^{-2} (Figure 56g). With the superior HER and HzOR performance of CC@WS_2/Ru SAs-450 in hand, the authors then fabricated a two-electrode electrolyzer for HzOR-assisted HWS (Figure 56h). As depicted in Figure 56h, an ultrasmall cell voltage of only 0.0154 V was required to approach 10 mA cm^{-2} for CC@WS_2/Ru SAs-450 couple, much lower than those for CC@WS_2/Ru NPs and Pt wire couples. In sharp contrast, the cell voltage of the same couple (CC@WS_2/Ru SAs-450) for OWS to achieve the same current density was high to 1.72 V (Figure 56h), indicating a 1.7 V voltage saving after introducing 0.5 M N_2H_4. To unravel the effects of Ru SAs and WS_2 sites on both alkaline HER and HzOR, DFT calculations were conducted and the results indicated that Ru sites facilitate water dissociation and the strong metal−support interaction induces local structural polarization to favor hydrogen adsorption on S sites, synergistically resulting in enhanced alkaline HER. Furthermore, the Ru sites also promoted the rate-determining step (RDS) of dehydrogenation from $*N_2H_4$ to $*N_2H_3$ for accelerated HzOR.

In addition to noble metal doping, Zhang and coworkers reported that doping nonprecious metals can enhance both the HER and HzOR as well.[638] They constructed the Mo doped

https://doi.org/10.1021/acs.chemrev.3c00332
Chem. Rev. 2024, 124, 3694−3812

Table 6. Summary of Bifunctional Electrocatalysts for HzOR-Assisted Hybrid Water Splitting (HWS)

Electrocatalysts	Electrolytes (x M KOH + y M N_2H_4)	Current density(mA cm^{-2})	Cell voltage (V)	Ref
Ni_2P/NF	1.0 + 0.5	500	1.0	609
Cu_1Ni_2-N	1.0 + 0.5	10	0.24	611
Fe-CoS_2 NSs	1.0 + 0.1	500	0.95	616
$CoSe_2$	1.0 + 0.5	10	0.164	619
RhIr MNs	1.0 + 0.5	10	0.13	622
		100	0.604	
Ni_3N-Co_3N	1.0 + 0.1	10	0.071	635
		400	0.76	
Ni-C HNSA	1.0 + 0.1	50	0.14	636
		100	0.25	
		150	0.34	
		200	0.40	
WS_2/Ru SAs	1.0 + 0.5	10	0.0154	637
Mo-Ni_3N/Ni/NF	1.0 + 0.1	10	0.055	638
		300	0.423	
PW-Co_3N NWA/NF	1.0 + 0.1	10	0.358	639
		50	0.428	
		100	0.501	
		200	0.607	
$RhRu_{0.5}$-alloy	1.0 + 1.0	10	−0.048	642
		100	0.054	
		853	0.6	
Ni NCNAs	1.0 + 0.3	10	0.023	643
		892	0.485	
Ni_2P/Zn-Ni-P	1.0 + 0.1	10	0.165	644
		100	0.358	
		400	0.532	
NiCo-$MoNi_4$ HMNAs/NF	1.0 + 0.1	250	0.63	645
Cu_3P/CF	1.0 + 0.5	100	0.72	646
Mn-SA/BNC	1.0 + 0.5	10	0.41	647
Ni(Cu)/NF	1.0 + 0.5	100	0.41	648
Rh/RhO_x NSs	1.0 + 0.5	10	0.068	649
		100	0.279	
Rh/N-CBs	1.0 + 0.5	10	0.18	650
		20	0.2	
Au@Rh ultra-NWs	1.0 + 0.1	10	0.18	651
RuP_2/C	1.0 + 0.3	10	0.023	652

Ni_3N/Ni heterostructure porous nanosheets grown on Ni foam (Mo−Ni_3N/Ni/NF). Benefiting from the synergy of Mo substitution and abundant Ni_3N/Ni interface, the as-prepared Mo−Ni_3N/Ni/NF revealed low potentials of −45 and −0.3 mV vs RHE at 10 mA cm^{-2} for HER and HzOR, respectively. Also, the Mo−Ni_3N/Ni/NF couple can deliver 10 mA cm^{-2} at a cell voltage of only 0.055 V for the HzOR-assisted HWS, along with remarkable long-term durability. DFT calculations deciphered that the Mo substitution and Ni_3N/Ni interface, corporately optimize ΔG_H toward HER and dehydrogenation process for HzOR. Likewise, doping Fe into CoS_2 nanosheets (Fe-CoS_2) also resulted in improved HER and HzOR, as reported by Ding and coworkers.[616] They also assembled a self-powered H_2 production system by integrating a direct hydrazine fuel cell and a HzOR-mediated HWS unit (Figure 57a). Elemental mapping images suggested the successful and homogeneous Fe doping over the entire CoS_2 nanosheets (Figure 57b). Electrochemical measurements showed that the Fe-CoS_2 endows outstanding bifunctional electrocatalytic performance for both HER and HzOR in alkaline electrolyte, better than Pt/C and CoS_2 controls (Figure 57c,d),[616] as confirmed by the extremely low applied potentials at given current densities. For example, the required potentials at 100 mA cm^{-2} for Fe-CoS_2 in 1.0 M KOH were only −129 and 129 mV vs RHE for HER and HzOR (0.1 M N_2H_4), respectively. By contrast, the Pt/C needed the relevant potentials of −170 and 170 mV vs RHE, and much higher overpotentials were needed for pure CoS_2 to reach the same current density (>350 mV and 205 mV vs RHE for HER and HzOR), suggesting the beneficial role of Fe doping. As a result, the Fe-CoS_2 couple achieved 500 mA cm^{-2} at a low cell voltage of 0.95 V. Additionally, the resulting self-powered H_2 production system exhibited high H_2 evolution rate of 9.95 mmol h^{-1} with FE of 98% for 20 h. DFT calculations demonstrated that Fe doping leads to a more thermoneutral value for hydrogen adsorption over Fe-CoS_2(001) (ΔG_H = 0.15 eV) compared to that for bare CoS_2(001) without doping (ΔG_H = 0.24 eV), suggestive of the favorable HER (Figure 57e). For HzOR, the theory computations revealed that Fe doping into CoS_2(001) enhances N_2H_4 adsorption and favors the following dehydrogenation with reduced ΔG from 0.88 to 0.56 eV, owing to a lower electronegativity of Fe atoms compared to Co atoms which resulted in a stronger interaction between Fe and negatively charged N atoms (Figure 57f). Besides single cation

https://doi.org/10.1021/acs.chemrev.3c00332
Chem. Rev. 2024, 124, 3694−3812

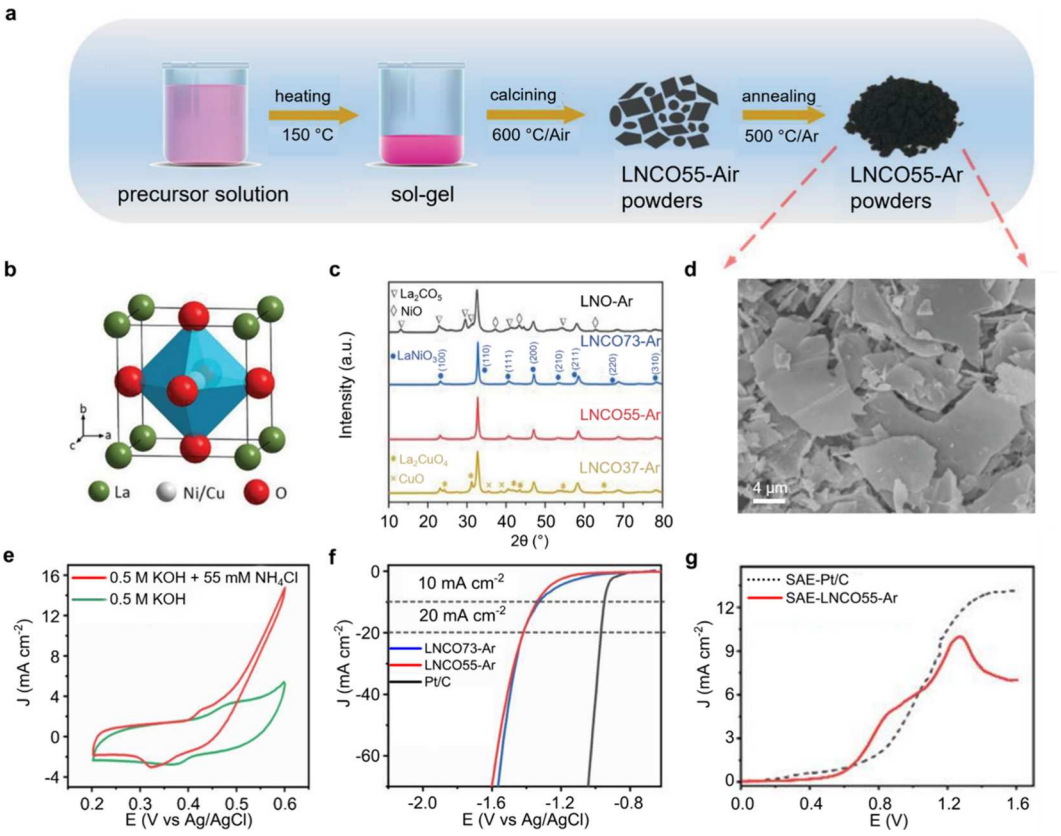

Figure 58. (a) Schematic illustration of the preparation process of LNCO55-Ar. (b) Perovskite structure. (c) XRD patterns of as-synthesized LNO-Ar, LNCO73-Ar, LNCO55-Ar, and LNCO37-Ar. (d) SEM image of LNCO55-Ar. (e) CV curves of LNCO55-Ar electrode in 0.5 M KOH with and without 55 mM NH_4Cl. (f) LSV curves of LNCO73-Ar, LNCO55-Ar, and Pt/C for HER in Ar-saturated 0.5 M KOH solution at a scan rate of 10 mV s^{-1}. (g) LSV curves of symmetric ammonia electrolyzer based on LNCO55-Ar (SAE-LNCO55-Ar) and SAE-Pt/C in 0.5 M KOH with 2210 ppm of NH_4Cl. Reproduced with permission from ref 658 under the terms of a CC-BY 4.0 license. Copyright 2021 The Authors, published by John Wiley and Sons.

doping, introducing single anion or anion/cation codopants is also beneficial for improved electrocatalytic applications.[639,640] For example, Zhang and coworkers recently reported an anion/cation dual-doping strategy to fabricate bifunctional P, W codoped Co_3N nanowire arrays on Ni foam (PW-Co_3N NWA/NF).[639] Because of the optimized hydrogen adsorption/desorption and dehydrogenation kinetics after dual-doping, the PW-Co_3N NWA/NF displayed improved electrocatalytic activities for HER, HzOR, and HzOR-assisted HWS. The PW-Co_3N NWA/NF required potentials of only −41 and −55 mV vs RHE to afford 10 mA cm^{-2} for HER and HzOR (0.1 M) in 1.0 M KOH, respectively. Also, a low cell voltage of only 0.028 V was needed for PW-Co_3N NWA/NF couple-driven two-electrode system for H_2 generation assisted by HzOR (Figure 57g).

In view of the involvement of harmful species during synthesis of metal compounds like NH_3, PH_3 and so on, directly developing metals or their alloys-based bifunctional electrocatalysts without the need of these harmful species is desirable. Guay's group used rotating disk electrode (RDE) voltammetry to explore a number of metals, including first-row transition metals (Co, Ni), coinage metals (Ag, Au), and Pt group metals (Ru, Rh, Pd, Ir, Pt) for HzOR in 1.0 M NaOH.[641] The results demonstrated that both Ru and Rh exhibit the lowest half-wave potentials among them, hinting their priority role as HzOR electrocatalysts irrespective of the cost. Duan and coworkers reported that alloying Ru with Rh can bring synergistic benefits to lower the overpotential and inhibit side reaction for HzOR as well as promote HER.[642] By using a facile solvothermal method, they synthesized ultrathin $RhRu_{0.5}$-alloy wavy nanowires as a bifunctional electrocatalyst for both HzOR and HER in 1.0 M KOH. Compared with Rh wavy nanowires-based anode and cathode, the $RhRu_{0.5}$-alloy wavy nanowires couple showed improved performance of hydrazine-assisted HWS with ultralow cell voltages of 0.054 and 0.6 V to afford 100 and 853 mA cm^{-2}, respectively. DFT calculations revealed that the d-band center of surface Rh atoms is downshifted relative to the Fermi level (E_F) by 0.26 eV in comparison with Rh after alloying, leading to weakened interaction with adsorbates and facilitated N_2 desorption for enhanced HzOR. Additionally, alloying also optimized the adsorption of H with a value of −0.23 eV, more favorable than the Rh counterpart. Examples about bifunctional electrocatalysts for hydrazine-assisted hybrid water splitting can be seen in Table 6.

5.1.2. Ammonia Oxidation. Liquid ammonia is a potentially nontoxic medium for hydrogen storage, which is more common and more readily obtainable compared with hydrazine.[653,654] Moreover, the oxidation of ammonia with a thermodynamic potential of −0.77 V is also thermodynamically more favorable than OER. Ammonia oxidation reaction (AOR) is as follows:[655,656]

$$2NH_3 + 6OH^- = N_2 + 6H_2O + 6e^-$$

https://doi.org/10.1021/acs.chemrev.3c00332
Chem. Rev. 2024, 124, 3694−3812

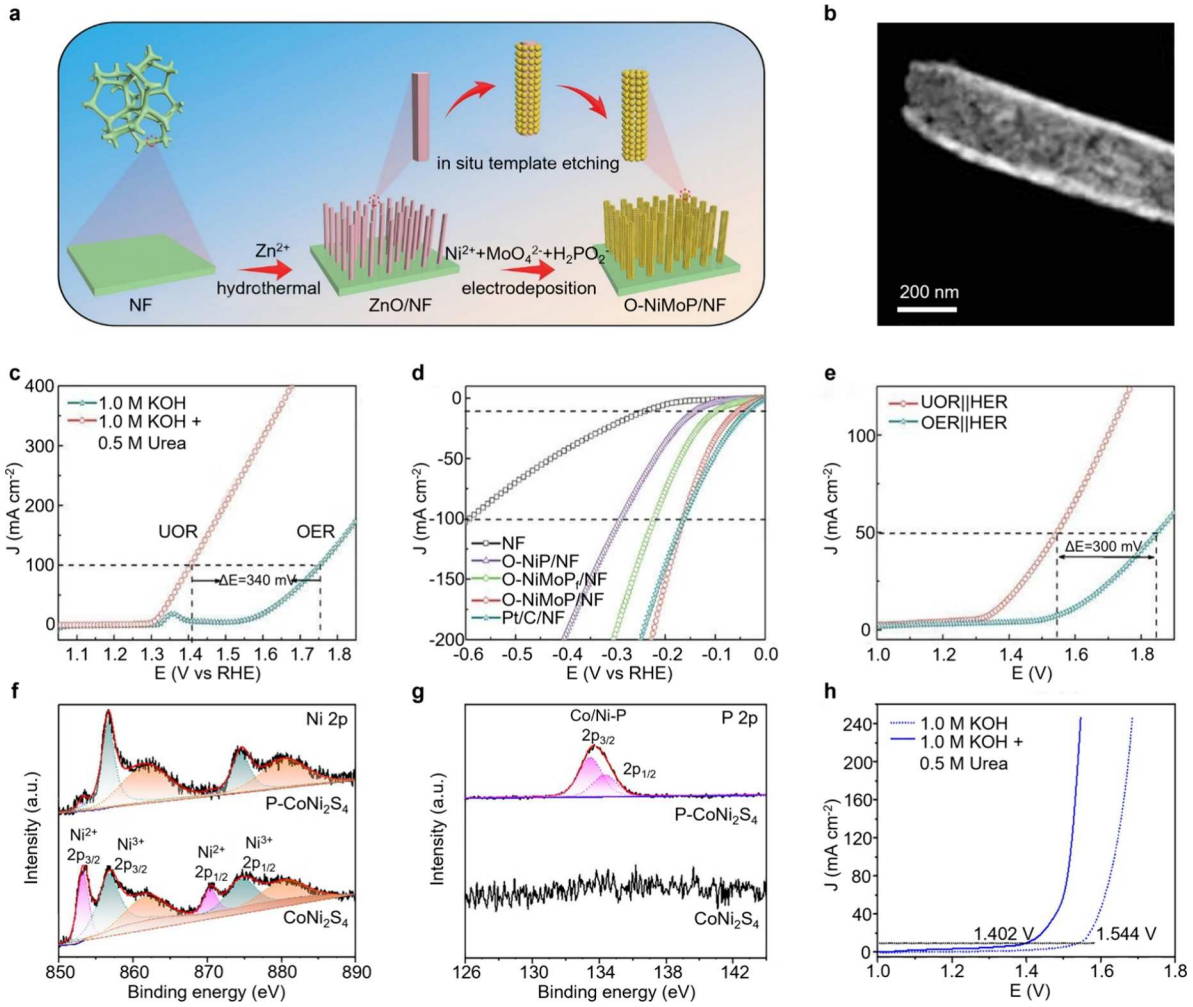

Figure 59. (a) Schematic for the preparation of O-NiMoP/NF. (b) STEM image of O-NiMoP nanotube. (c) LSV curves of O-NiMoP/NF for UOR and OER in 1.0 M KOH with and without 0.5 M urea. (d) LSV curves of NF, O-NiP/NF, O-NiMoP$_f$/NF, O-NiMoP/NF, and Pt/C/NF in 1.0 M KOH for HER. (e) LSV curves of O-NiMoP/NF couple for UOR-assisted HWS and OWS. Reproduced with permission from ref 670. Copyright 2021 John Wiley and Sons. High-resolution (f) Ni 2p XPS and (g) P 2p spectra of $CoNi_2S_4$ YSSs and P-$CoNi_2S_4$ YSSs. (h) LSV curves of P-$CoNi_2S_4$ YSSs couple toward OWS and UOR-assisted HWS. Reproduced with permission from ref 544. Copyright 2021 John Wiley and Sons.

To improve the kinetics of AOR, Mei and coworkers prepared a bifunctional electrocatalyst of N-doped NiZnCu-LDH with reduced graphene oxide grown on Ni foam (N-NiZnCu LDH/rGO) by hydrothermal and calcination procedures.[657] The multiple active sites in N-NiZnCu LDH/rGO modulated adsorption and desorption of H, and collectively resulted in enhanced AOR performance. For example, low potentials of −183 mV and 621 mV vs RHE were required over N-NiZnCu LDH/rGO to afford 100 mA cm^{-2} for HER and AOR in 1.0 M KOH with 0.3 M NH_4Cl, respectively. Also, the N-NiZnCu LDH/rGO-based two-electrode electrolyzer required a cell voltage of 0.489 V at 10 mA cm^{-2} for AOR-coupled HWS, along with excellent stability. Tao and coworkers demonstrated that a perovskite oxide of $LaNi_{0.5}Cu_{0.5}O_{3-\delta}$ annealed in Ar (LNCO55-Ar) has superior bifunctional activities toward both HER and AOR.[658] As schematically shown in Figure 58a, the LNCO55-Ar was synthesized via a sol−gel annealing method followed by a reduction process. The LNCO55-Ar perovskite had super physicochemical stability due to the presence of stable BO_6 octahedron, sharing corners to form a 3D network (Figure 58b). XRD pattern (Figure 58c) demonstrated that annealing in Ar does not vary the crystal structures of perovskite and confirmed the identity of LNCO55-Ar with $LaNiO_3$, different from the mixed phases for other control samples. SEM image showed a flake-like morphology for the resulting LNCO55-Ar (Figure 58d). After introducing 55 mM NH_4Cl into 0.5 M KOH, the CV curves of LNCO55-Ar displayed a remarkable increase of anodic current density with an onset potential of 0.42 V vs Ag/AgCl, suggesting its good current response to AOR (Figure 58e). For HER, the potential required to deliver 10 mA cm^{-2} for LNCO55-Ar was −1.34 V vs Ag/AgCl, slightly higher than that of commercial Pt/C (Figure 58f). The symmetric ammonia electrolyzer (SAE) based on bifunctional LNCO55-Ar was subsequently fabricated for AOR-assisted HWS, and it exhibited a small onset voltage (∼0.48 V) in 0.5 M KOH with 2210 ppm of NH_4Cl (Figure 58g), comparable to Pt/C-based couple. Chronopotentiometry test demonstrated that the ammonia conversion efficiency is about 100% after operating for 100 h. DFT calculations revealed that incorporation of Cu into the perovskite facilitates the adsorption of ammonia on the Ni-site, leading to superior AOR activity. Besides metal oxides/hydroxides, transition-metal nitrides were also reported as bifunctional electro-

https://doi.org/10.1021/acs.chemrev.3c00332
Chem. Rev. 2024, 124, 3694−3812

catalysts for AOR and HER. Liu and coworkers synthesized 1D nanoneedle nickel−cobalt bimetallic nitride ($NiCo_2N$).[659] The coexistence of Ni and Co substantiated an optimal electronic structure of $NiCo_2N$ and thus promoted AOR and HER.[659] A symmetric ammonia electrolyzer constructed with $NiCo_2N$ couple required only 0.71 V at 100 mA cm^{-2} in the 1.0 M KOH with 1.0 M $NH_3{\cdot}H_2O$.

To further reduce the cell voltage of AOR-coupled HWS, noble metals with higher activities were introduced. Chen and coworkers designed and synthesized high-quality platinum nanocubes (Pt-NCs) with (100) facets.[655] The resulting Pt-NCs displayed outstanding activity and stability for AOR and HER, so that a symmetric ammonia electrolyzer based on Pt-NCs couple required only 0.68 V to afford 5 mA cm^{-2} for hydrogen generation in 1 M KOH with 0.1 M NH_4OH. Similarly, Tao and coworkers developed Pt-SnO_x-based nanoparticles by a simple layer-by-layer method, which maintained high electrocatalytic performance in terms of activity and stability for AOR toward efficient hydrogen generation.[660] Combined electrochemical and physiochemical characterizations revealed that Pt-SnO_x is a trifunctional electrocatalyst with facilitated ammonia adsorption on SnO_x, hydrogen (H) adsorption on Pt-SnO_x, and hydrogen (H) transfer along the −Sn−OH bond. Chen and coworkers incorporated Ru into Pt to obtain high-quality Pt_xRu nanocubes (Pt_xRu-NCs) with adjustable composition and exposed (100) planes.[656] For AOR, the Pt_6Ru-NCs showed a mass activity of 192 mA mg_{Pt}^{-1} and a specific activity of 1.02 mA cm^{-2}, higher than those of other Pt_xRu-NCs, Pt-NCs, and commercial Pt. For HER, the resulting Pt_6Ru-NCs also showed the smallest overpotential of 37.6 mV at 10 mA cm^{-2}, relative to control samples. Moreover, a Pt_6Ru-NCs couple-based ammonia electrolyzer reached 10 $mAcm^{-2}$ at a low cell voltage of 0.72 V for hydrogen generation. DFT calculations demonstrated that the $Pt_6Ru(100)$ plane owns the stronger binding of $*NH_2$ and *NH, more energetically favorable for AOR. This activity enhancement also reduced the HER overpotential. In other words, the high bifunctional activity of Pt_6Ru-NCs can be attributed to the crystal effect and Pt−Ru bimetallic synergy.

5.1.3. Urea Oxidation. In addition to hydrazine and ammonia, urea is another sacrificing reagent and the urea oxidation reaction (UOR) is thermodynamically more favorable than OER as well.[103,661−665] Typically, UOR produces N_2, CO_2, and H_2O in alkaline media as shown in the following equation, with a theoretically thermodynamic potential of about 0.37 V:[626]

$$CO(NH_2)_2 + 6OH^- = N_2 + 5H_2O + CO_2 + 6e^-$$

To further accelerate its sluggish kinetics due to six-electron-transfer process,[666−668] advanced electrocatalysts are necessary. Sun and coworkers designed 3D nickel phosphide nanoarrays on carbon cloth (Ni_2P NF/CC) as a bifunctional electrocatalyst toward urea-assisted energy-saving hydrogen production.[669] Owing to the decent activity, high chemical stability, and good conductivity, the resulting Ni_2P NF/CC featured high performance for both UOR and HER, and thus its two-electrode alkaline electrolyzer for HWS can attain 50 mA cm^{-2} at a cell voltage of only 1.35 V.[669]

Recently, bimetallic nickel-based phosphides have been obtained to simultaneously catalyze UOR and HER as well. Zhang and collaborators employed combined electrodeposition and in situ template etching strategy to yield oxygen-incorporated nickel molybdenum phosphide nanotube arrays on nickel foam (O-NiMoP/NF), as shown in Figure 59a.[670] STEM image demonstrated the formation of nanotubes with porous walls (Figure 59b). The electrocatalytic UOR activity of the resulting O-NiMoP/NF was then evaluated in 1.0 M KOH with 0.5 M urea. As presented in Figure 59c, a current density of 100 mA cm^{-2} for UOR was achieved at only 1.41 V vs RHE, 340 mV lower than that for OER at the same current density. Such a superior UOR activity of O-NiMoP/NF was also better than those of oxygen-incorporated nickel phosphide nanotube arrays (O-NiP/NF) and oxygen-incorporated nickel molybdenum phosphide nanoparticle film (O-$NiMoP_f$/NF), underscoring the promotion role of bimetal synergy and morphology of porous nanotube arrays. HER measurements as depicted in Figure 59d showed that the O-NiMoP/NF needs an overpotential of 54 mV to obtain 10 mA cm^{-2}, comparable to Pt/C and better than O-NiP/NF and O-$NiMoP_f$/NF. Remarkably, when used as both anode and cathode simultaneously, the O-NiMoP/NF couple required a cell voltage of merely 1.55 V to reach 50 mA cm^{-2} (Figure 59e), 300 mV lower than that for overall water splitting (OWS). PDOS analysis revealed that the Mo 4d orbital with a broad range protects the robust valence of Ni sites and promotes the Ni 3d orbital to a position close to E_F for facilitated intermediates adsorption, collectively leading to improved electrocatalytic activity. In addition, the energy levels of both P 3p and O 2p orbitals were away from E_F, indicating their electron-rich features which can suppress the overbinding by Ni−H and Ni−O. All these beneficial effects collectively resulted in the enhanced UOR and HER performance, which was further confirmed by DFT calculations.

Besides phosphides, transition-metal sulfides have the advantages of unique d-electron configuration and good electrical conductivity, thus gaining attention for UOR-coupled HWS.[671] Doping heteroatoms can generate more interfaces and active sites, and induce atomic distortions or interior defects to further enhance the intrinsic activity and stability of metal sulfides. Liu and coworkers constructed a NiS_2 doped with Co and V (NCVS-3) by a two-step hydrothermal method.[102] Thanks to the ternary synergism of Co, V, and Ni, the optimal NCVS-3 featured with excellent UOR activity with a potential of 1.5 V vs RHE to afford 77 mA cm^{-2}, and rapid hydrogen production rate of 143 L min^{-1} g_{cat}^{-1} at 1.8 V vs RHE. Based on the electrochemical experiments, in situ electrochemical Raman spectroscopy/isotope-labeled mass spectrometry, and DFT calculations, the roles of Ni, Co, and V elements were clearly revealed. The authors revealed that introduction of V atoms reduces the electron density of Ni and Co, and energy barrier of urea dehydrogenation and meanwhile promotes overlap between S 3p and Ni 3d to enhance their electron transmission. Moreover, they found that the coexistence of Co and V atoms also boosts CO fragments oxidation during UOR, and the presence of S facilitates CO_3^{2-} decomposition.

Anion doping is also effective to tune the electronic configuration of transition metal sulfides for improved UOR and HER. Lou and coworkers synthesized porous phosphorus-substituted $CoNi_2S_4$ yolk−shell spheres (P-$CoNi_2S_4$ YSSs) via a facial hydrothermal sulfidation followed by gas-phase phosphorization.[544] High-resolution Ni 2p XPS spectra of P-$CoNi_2S_4$ YSSs shown in Figure 59f revealed higher ratios of Ni^{3+}/Ni^{2+} calculated by integrating the corresponding peak areas. High-resolution P 2p XPS spectra (Figure 59g) revealed

https://doi.org/10.1021/acs.chemrev.3c00332
Chem. Rev. 2024, 124, 3694−3812

Table 7. Summary of Bifunctional Electrocatalysts for UOR-Assisted Hybrid Water Splitting (HWS)

Electrocatalysts	Electrolytes (x M KOH + y M urea)	Current density (mA cm^{-2})	Cell voltage (V)	Ref
P-$CoNi_2S_4$ YSSs	1.0 + 0.5	10	1.402	544
Ni@NCNT-3	1.0 + 0.5	10	1.56	663
Ni_2P NF/CC	1.0 + 0.5	50	1.35	669
O-NiMoP/NF	1.0 + 0.5	50	1.55	670
F-NiO/Ni@C	1.0 + 0.3	10	1.37	672
F-P-Co_3O_4/NF	1.0 + 0.5	10	1.427	676
Ni-S-Se/NF	1.0 + 0.5	10	1.47	677
Ni-Mo	1.0 + 0.1	10	1.43	678
$CoMn/CoMn_2O_4$	1.0 + 0.5	10	1.51	679
W-NiS_2/MoO_2@CC	1.0 + 0.33	10	1.372	680
$Ni_2P/Ni_{0.96}S$/NF	1.0 + 0.5	100	1.453	681
NiF_3/Ni_2P	1.0 + 0.33	50	1.83	682
N-WS_2/Co_3N	1.0 + 0.5	500	1.72	683
N-Co_9S_8/Ni_3S_2/NF	1.0 + 0.5	10	1.40	684
Ni/MoC/Ti_3C_2Tx@C	1.0 + 0.3	10	1.56	685
P-mAuRh film/NF	1.0 + 0.33	100	1.47	686
CoS_x/Co-MOF	1.0 + 0.5	10	1.48	687
Co_3O_4/Ti_3C_2 MXene	1.0 + 0.5	50	1.49	688
Ni_3N/Mo_2N	1.0 + 0.33	10	1.36	689
$Zn_{0.08}Co_{0.92}$P/TM	1.0 + 0.5	10	1.38	690
$Ni(OH)_2$-$NiMoO_x$/NF	1.0 + 0.5	10	1.42	691
Fe-Ni_3S_2	1.0 + 0.5	100	1.57	692
$NiCoP_x$@NiFeCo-MOF	1.0 + 0.5	100	1.54	693
Ni_9S_8/CuS/Cu_2O/NF	1.0 + 0.33	10	1.47	694
$Cu_2S@Ni_3Se_2$	1.0 + 0.5	10	1.48	695
V-$FeNi_3N/Ni_3N$	1.0 + 0.33	10	1.46	696
Mo-Co-S-Se/CC	1.0 + 0.5	10	1.40	697
P-CoS_2/Ti	1.0 + 0.3	10	1.375	698
NiCoB@C	1.0 + 0.33	10	1.34	699
$Co_{0.26}$-$Ni(OH)_2$ NPs/CF	1.0 + 0.5	10	1.42	700
$NiCo_2S_4$/CC	1.0 + 0.33	10	1.45	701
N-NiS/NiS_2	1.0 + 0.33	10	1.62	702
$NiSe_2$	1.0 + 0.33	10	1.39	703
Ni_3N/rGO@NF	1.0 + 0.5	100	1.51	704
Ni_3N NA/CC	1.0 + 0.33	10	1.44	705

the P-bonded Co/Ni in P-$CoNi_2S_4$. Benefiting from the advantages of enriched Ni^{3+} induced by phosphorization, the P-$CoNi_2S_4$ YSSs exhibited excellent activity toward HER and UOR, affording low potentials of −0.135 and 1.306 V vs RHE at 10 mA cm^{-2}, respectively. Particularly, in a symmetrical electrolyzer, a cell voltage of 1.402 V was obtained at 10 mA cm^{-2}, lower than that for OWS (Figure 59h). Wang and coworkers increased electron delocalization of NiO/Ni@C by F-doping, which not only provided ready-to-use F-NiO active sites but also allowed F-NiO/Ni@C to achieve optimum H* adsorption for HER and a lower energy barrier for UOR.[672] The as-configured F-NiO/Ni@C couple cell required a low cell voltage of 1.37 V to achieve 10 mA cm^{-2} in alkaline media (with 0.3 M urea) due to the interphase synergy. Additionally, binary-nonmetal modification has been reported to show synergism as well,[673−675] similar to that in bimetal electrocatalysts. For example, Du and coworkers synthesized F, P codoped Co_3O_4 nanosheet array on nickel foam (F−P−Co_3O_4/NF) as a bifunctional electrocatalyst for UOR-paired HWS in 1.0 M KOH containing 0.5 M urea, with a low cell voltage of 1.427 V to achieve 10 mA cm^{-2}.[676] DFT calculations revealed that codoping of F and P optimizes the electronic structure and hydrogen adsorption, jointly promoting the electrocatalytic activities. Cao and coworkers reported amorphous Ni−S−Se/NF with high bifunctional electrocatalytic activities for UOR and HER.[677] The full urea-coupled HWS driven by Ni−S−Se/NF couple delivered 10 mA cm^{-2} at a cell voltage of 1.47 V in 1.0 M KOH with 0.5 M urea. The introduction of S in Ni−S−Se improved water adsorption ability, and amorphous oxyhydroxides were regarded as active species for UOR.

Besides metal compounds, metal alloys were also explored for UOR-assisted HWS. Xia and coworkers reported a bifunctional Ni−Mo alloy nanotube, with ultralow potentials of −44 mV and 1.36 V vs RHE to deliver 10 mA cm^{-2} for HER and UOR, respectively.[678] The UOR-assisted HWS delivered 10 mA cm^{-2} at a low voltage of 1.43 V for hydrogen production. DFT calculations revealed that the Mo center plays the role of active site for chemisorption and O−H bond cleavage of H_2O, while the hydrogen-evolving site is Ni center. Wang and coworkers recently coupled CoMn alloy with $CoMn_2O_4$ to construct $CoMn/CoMn_2O_4$ with Schottky heterojunction structure which can facilitate the adsorption of reactant molecules and the fracture of chemical bonds, giving rise to low potentials of −0.069 and 1.32 V vs RHE at 10 mA cm^{-2} for HER and UOR, respectively. Also, a low cell voltage of only 1.51 V was needed to achieve 10 mA cm^{-2} for the UOR-coupled HWS.[679] More examples of bifunctional

https://doi.org/10.1021/acs.chemrev.3c00332
Chem. Rev. 2024, 124, 3694−3812

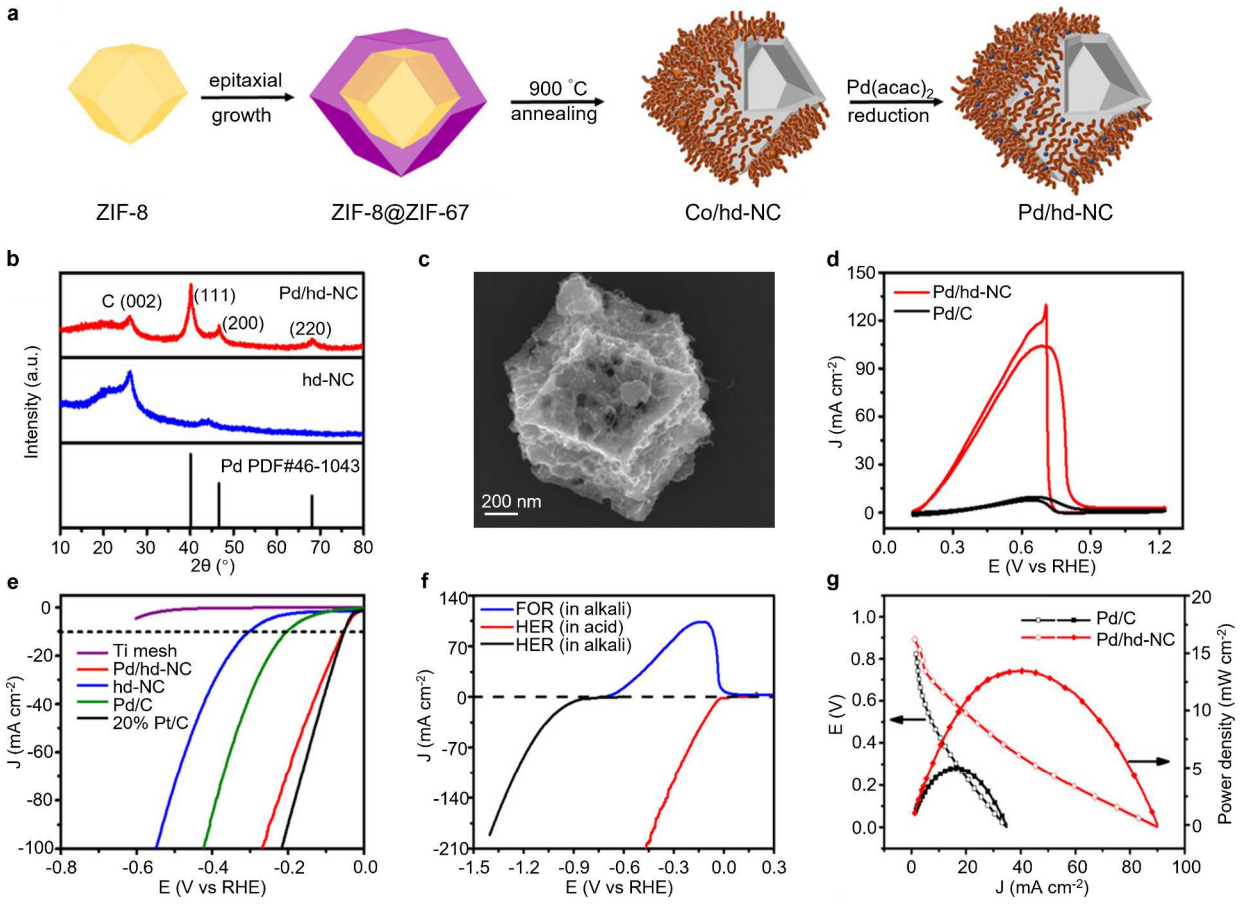

Figure 60. (a) Schematic illustration of the synthesis of Pd/hd-NC. (b) XRD patterns of Pd/hd-NC and hd-NC. (c) SEM image of Pd/hd-NC. (d) CV curves of Pd/hd-NC and Pd/C in 1.0 M KOH with 0.5 M $HCOO^-$. (e) LSV curves of different electrocatalysts for HER in Ar-saturated 0.5 M H_2SO_4. (f) LSV curves for FOR in alkaline and HER in acid and alkaline solutions. (g) LSV curves and the recorded power densities for the alkaline/acid cells with Pd/hd-NC or Pd/C couples. Reproduced with permission from ref 731. Copyright 2021 John Wiley and Sons.

electrocatalysts for UOR-assisted hybrid water splitting can be seen in Table 7.

5.2. Hybridizing with Pollutants Oxidative Degradation

In the past decades, water pollution has become an urgent problem worldwide.[706] Various technologies including photodegradation and catalytic oxidation have been applied to degrade pollutants in wastewater.[707−709] Among them, electrochemistry-based technologies show the advantages of high efficiency, mild working conditions, easy automation, strong universality, and low cost.[710−713] More importantly, when the oxidative degradation of pollutants is coupled with hydrogen production, the energy efficiency and return can be further boosted.

5.2.1. Formic Acid/Formate Oxidation. Formic acid/formate is common in wastewater discharged from chemical industries of dye production and fabric printing. Fortunately, the electrochemical technology based on formic acid/formate electro-oxidation reaction (FAOR/FOR) offers a green and effective treatment for their removal.[714,715] The FAOR has different expressions depending on the reaction conditions.

In acidic solution:

$$HCOOH = CO_2 + 2H^+ + 2e^-$$

In alkaline solution:

$$HCOO^- + 3OH^- = CO_3^{2-} + 2H_2O + 2e^-$$

Pt- and Pd-based nanostructures are the most active electrocatalysts for FAOR,[640,716−721] and Pt is also the most efficient electrocatalysts for HER.[722−728] Thus, Pt-based electrocatalysts have been extensively explored as bifunctional electrocatalysts for FAOR-assisted HWS for hydrogen generation. Chen and coworkers synthesized ultrafine Au core-PtAu alloy shell nanowires (Au@Pt_xAu UFNWs) by one-pot route to improve Pt utilization and electrocatalytic performance.[729] The as-prepared Au@$Pt_{0.077}$Au UFNWs required potentials of −22.6 mV and 290 mV vs RHE to afford a current density of 10 mA cm^{-2} for HER and FAOR in 0.5 M H_2SO_4 with 1.0 M HCOOH, respectively. A hybrid acid cell was then developed by them using Au@$Pt_{0.077}$Au UFNWs as both anode and cathode electrocatalysts for FAOR and HER, and a low cell voltage of 0.51 V was required to afford 10 mA cm^{-2}. DFT calculations revealed that the Au-rich PtAu alloy nanostructure can optimize adsorption configuration and strength of reactive species on Pt, promoting the relevant reactive kinetics. More recently, Chen and coworkers improved the electrocatalytic FAOR-coupled HWS performance of Pt by both structure and interface engineering.[730] They first synthesized high-quality holey platinum nanotubes (Pt−H−NTs) through facile pyrolysis using Pt^{II}-phenanthroline coordination compound as a self-template and self-reduction precursor. After up-bottom postmodification, the polyallylamine (PA) modified Pt−H−NTs (Pt−H−NTs@PA) can be obtained. PA modification sharply promoted the electro-

https://doi.org/10.1021/acs.chemrev.3c00332
Chem. Rev. 2024, 124, 3694−3812

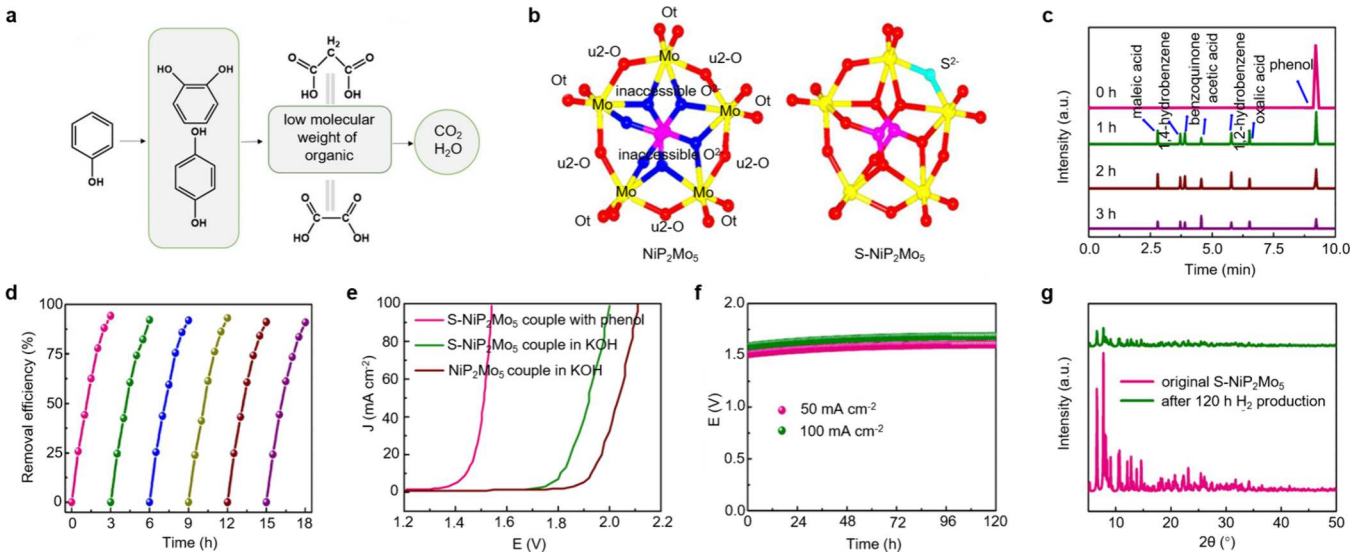

Figure 61. (a) Schematic of the phenol oxidation pathway. Reproduced with permission from ref 739. Copyright 2021 American Chemical Society. (b) O^{2-} in the $[(HO_2C_3H_4PO_3)_2Mo_5O_{15}]^{4-}$cluster of NiP_2Mo_5 and S-NiP_2Mo_5.The $[Ni(bipy)_2(H_2O)]^{2+}$ units are omitted for clarity. (c) Chromatograms of products during phenol degradation at 20 mA cm^{-2} over S-NiP_2Mo_5. (d) Six-cycle phenol degradation test over S-NiP_2Mo_5. (e) LSV curves of NiP_2Mo_5 and S-NiP_2Mo_5 couples for POR-coupled HWS and OWS in 1.0 M KOH with and without 0.4 M phenol. (f) Chronopotentiometric curves of S-NiP_2Mo_5 couple at 50 and 200 mA cm^{-2} for POR-coupled HWS. (g) XRD patterns of S-NiP_2Mo_5 couple before and after 120 h stability test for POR-coupled HWS. Reproduced with permission from ref 740. Copyright 2020 American Chemical Society.

catalytic activity of Pt−H−NTs for FAOR by changing reaction pathway, and for HER by proton enrichment at electrolyte/electrode interface. The FAOR-boosted HWS system required an operational voltage of only 0.47 V to reach 10 mA cm^{-2}.

Wen and coworkers developed uniformly dispersed Pd nanoparticles on a hollow dodecahedron N-doped carbon network (Pd/hd-NC) as a bifunctional electrocatalyst for FOR and HER as depicted in Figure 60a.[731] XRD patterns in Figure 60b revealed three new diffraction peaks after the introduction of Pd for Pd/hd-NC, corresponding well to the (110), (200), and (220) facets of Pd. The SEM image in Figure 60c revealed a dodecahedron morphology of Pd/hd-NC, inheriting from its precursor of ZIF-8. The CV curves of Pd/hd-NC obtained in 1.0 M KOH solution with 0.5 M formate ($HCOO^-$) demonstrated superior electrocatalytic activity for FOR than that of Pd/C, with current densities of 104 mA cm^{-2} and 9.5 mA cm^{-2} at 0.68 V, respectively (Figure 60d). The LSV curve of Pd/hd-NC in 0.5 M H_2SO_4 solution shown in Figure 60e demonstrated a much better HER performance compared to that of commercial Pd/C, with a small overpotential of 54 mV at 10 mA cm^{-2}. Such a low overpotential was comparable to that of 20% Pt/C. Moreover, the acidic HER catalyzed by Pd/hd-NC occurred at a potential more positive than that for alkaline FOR as shown in Figure 60f, demonstrating the feasibility of hybrid alkali/acid self-powered system to achieve the formate-assisted HER. Figure 60g showed the LSV curves of the hybrid alkali/acid cell using Pd/hd-NC or Pd/C control as bifunctional electrodes. With the voltage decreasing from the open-circuit voltage to 0 V, the current density for Pd/hd-NC increased to 90 mA cm^{-2}, higher than that for Pd/C couple (35 mA cm^{-2}). Also, the Pd/hd-NC couple achieved a maximum power density of 13.5 mW cm^{-2}, 3-times higher than that of Pd/C couple.

Strain engineering is powerful to optimize the catalytic activity of electrocatalysts. Wang's group designed the tensile-strained PdNi bimetallene as a bifunctional electrocatalyst for HER and FOR by a CO-confined growth method.[732] PdNi bimetallene had sufficient active sites and modulated the adsorption/dissociation of intermediates arising from the introduction of Ni and ultrathin curved geometry. The bifunctional PdNi bimetallene-based FOR-HER system achieved a current density of 20 mA cm^{-2} at a low cell voltage of 0.51 V.

5.2.2. Phenol Oxidation. Phenol is a typical organic pollutant with high concentration in industrial wastewater from chemical engineering, petroleum refining, coal processing, biopharmaceuticals, and so on,[733−736] which poses serious threat to human health. It is thus of importance to seek green and efficient methods to degrade the phenol in wastewater.[737,738]

Figure 61a displayed the oxidation pathway of phenol over nickel foam supported $NiMoO_4$ electrocatalyst reported by Mao and coworkers.[739] Clearly, the phenol can be degraded to p-phenol, o-phenol, malonic acid, oxalic acid intermediates, and eventually CO_2 and H_2O. The combination of phenol electro-oxidation (POR) and HER is a promising strategy for simultaneous hydrogen generation and pollution degradation.[739,740] Xu's group synthesized the vulcanized polyoxometalate of $[Ni(bipy)_2(H_2O)]_2[(HO_2C_3H_4PO_3)_2Mo_5O_{15}]\cdot 10H_2O$ (NiP_2Mo_5, bipy = 2,2′-bipyridine; $HO_2C_3H_4PO_3$ = 3-phosphonopropionic acid) via replacing one O^{2-} of NiP_2Mo_5 by S^{2-} (S-NiP_2Mo_5) as a bifunctional electrocatalyst for POR and HER in alkaline solution (Figure 61b).[740] To test the POR performance of S-NiP_2Mo_5, the authors conducted chronopotentiometric electrolysis at 20 mA cm^{-2} in 1.0 M KOH containing 20 mg L^{-1} phenol for 3 h. With prolonging electrolysis time, the phenol was gradually oxidized to 1,4-hydrobenzene, 1,2-hydrobenzene, benzoquinone, maleic acid, oxalic acid, and acetic acid, as confirmed by the high-performance liquid chromatography analysis (Figure 61c). A phenol-removal efficiency of 94.2% can be obtained for S-NiP_2Mo_5, higher than that of NiP_2Mo_5 (72.1%). Besides high POR activity, the S-NiP_2Mo_5 also featured robust stability, as

https://doi.org/10.1021/acs.chemrev.3c00332
Chem. Rev. 2024, 124, 3694−3812

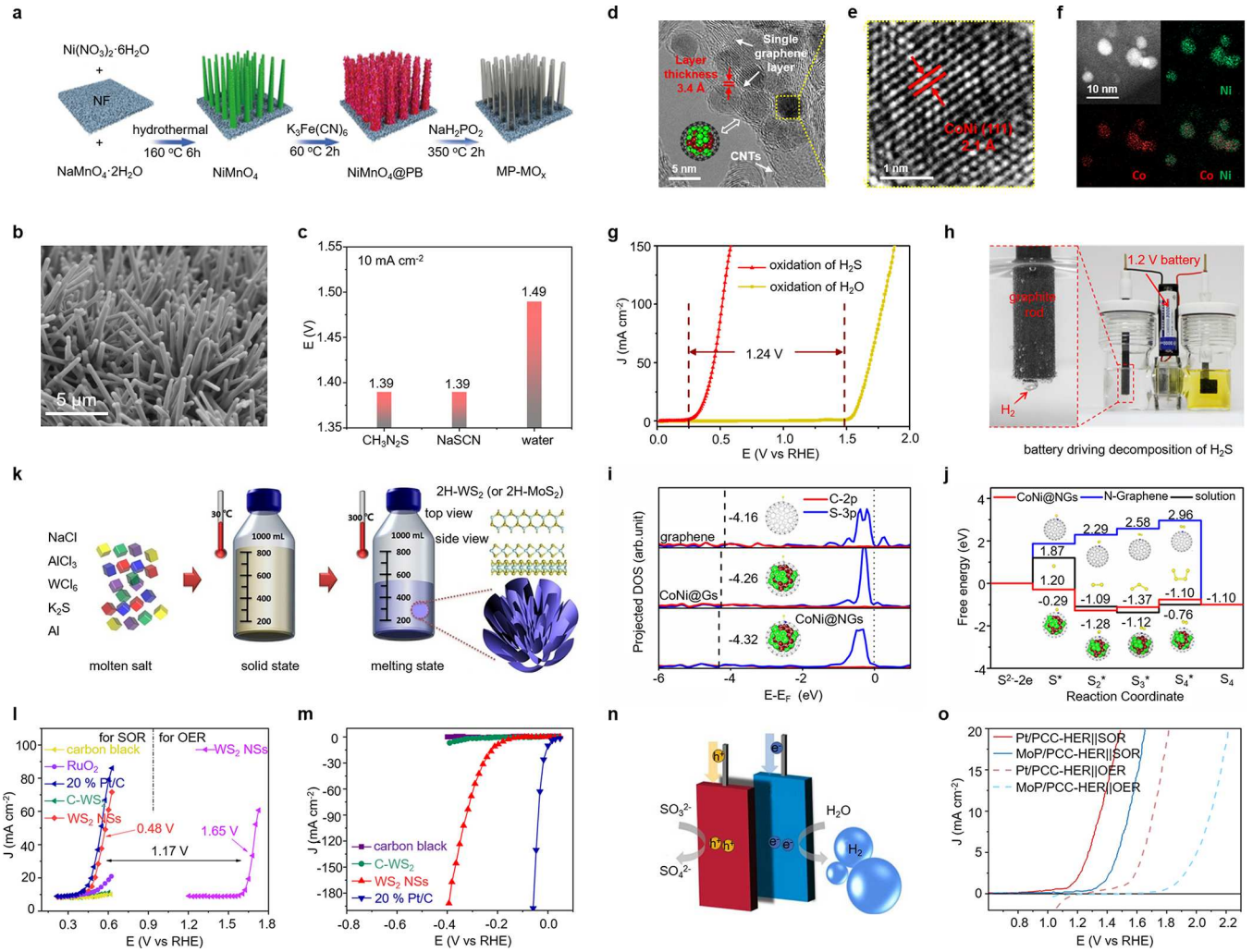

Figure 62. (a) Scheme for the synthesis of MP-MO_x. (b) SEM image of MP-MO_x. (c) Comparison of the cell voltage of MP-MO_x couple for TOR or STOR-assisted HWS and OWS in 1.0 M KOH at 10 mA cm^{-2}. Reproduced with permission from ref 748. Copyright 2020 Elsevier. (d) TEM, (e) HRTEM, and (f) elemental mapping images of CoNi@NGs. (g) Comparison of LSV curves for SOR and OER on CoNi@NGs. (h) Photograph of a device with a 1.2 V commercial battery directly driving the decomposition of H_2S. (i) Comparison of the projected DOS of S 3p and its bonded C 2p when S is adsorbed on the surface of pristine graphene, CoNi@Gs, and CoNi@NGs. (j) Free energy profiles of the formation of polysulfides (S_x*) in the aqueous solution on the surface of N-graphene or CoNi@NGs. Reproduced with permission from ref 108. Copyright 2020 Royal Society of Chemistry. (k) Schematic of molten salts assisted synthesis of WS_2 NSs in a 1000 mL blue cap bottle. (l) LSV curves for SOR on WS_2 NSs and controls, and for OER on WS_2 NSs. (m) LSV curves for HER on WS_2 NSs, carbon black, 20% Pt/C, and C-WS_2. Reproduced with permission from ref 109. Copyright 2022 John Wiley and Sons. (n) Conceptual diagram of SOR-coupled HWS. (o) LSV curves of MoP/PCC and Pt/PCC couples for SOR-assisted HWS and OWS. Reproduced with permission from ref 759. Copyright 2022 Elsevier.

revealed by the slight decay of degradation efficiency after six cycles (Figure 61d). LSV curves illustrated that the S-NiP_2Mo_5 requires 1.38 V vs RHE to reach 100 mA cm^{-2} in 1.0 M KOH with 0.4 M phenol, suggestive of 360 mV potential saving relative to that for OER. Combined physiochemical characterizations suggested that the $[Ni(bipy)_2(H_2O)]^{2+}$ units of S-NiP_2Mo_5 function as active sites for POR. Moreover, the S-NiP_2Mo_5 also exhibited superior HER activity relative to NiP_2Mo_5 in the same electrolyte, with overpotentials of 55 and 94 mV to achieve 10 and 100 mA cm^{-2}, respectively. DFT calculations rationalized that the optimal adsorption free energy of H* over S-NiP_2Mo_5 (ΔG = 0.183 eV) relative to NiP_2Mo_5 (ΔG = −0.819 eV) accounts for its good HER activity. Owing to the outstanding POR and HER activity of S-NiP_2Mo_5, they then fabricated a S-NiP_2Mo_5 couple-based two-electrode electrolyzer to achieve POR-assisted HWS toward efficient hydrogen generation (Figure 61e). As depicted in Figure 61e, to afford 100 mA cm^{-2}, the NiP_2Mo_5 control couple needed a cell voltage of 2.11 V for OWS, which can be reduced to 1.99 V for S-NiP_2Mo_5 couple. After introducing phenol into electrolyte, the cell voltage can be further reduced to 1.54 V for S-NiP_2Mo_5 couple. These results highlighted the positive effect of both vulcanization on NiP_2Mo_5 and POR replacing on improved hydrogen production. After 120 h electrolysis at 50 and 200 mA cm^{-2}, the S-NiP_2Mo_5 exhibited excellent durability, as revealed by the similar XRD patterns (Figure 61g).

5.2.3. Sulfur Compounds Oxidation. As one of the sulfur-containing compounds, thiourea (CH_4N_2S) is an important industrial material that is usually used as an additive for reductive bleaching.[741,742] It has been found that thiourea and its metabolic intermediates have great impact on the environment and animals.[743−745] Another industrial raw material, thiocyanate like sodium thiocyanate (NaSCN), is

https://doi.org/10.1021/acs.chemrev.3c00332
Chem. Rev. 2024, 124, 3694−3812

widely used in petrochemical, textile, electroplating, and other industries. The SCN^- in wastewater can react with oxidants to generate highly toxic cyanide chloride or cyanide, posing safety issues.[746,747] Thus, exploring efficient electrochemical oxidation degradation of these sulfur-containing compounds to couple with HER is beneficial for both energy and safety concerns.

Wei and coworkers[748] reported a MP-MO_x (M = Ni, Fe, and Mo) bifunctional electrocatalyst that can combine HER with thiourea or sodium thiocyanate electro-oxidation reaction (TOR or STOR). Figure 62a displayed the schematic synthesis of MP-MO_x via hydrothermal growth of $NiMoO_4$ nanowire arrays on nickel foam (NF) followed by Prussian blue (PB) coating and low-temperature phosphorization. SEM image of MP-MO_x revealed the uniform growth on NF and the successful formation of nanowires with a diameter of about 400 nm (Figure 62b). High-magnified TEM image revealed a thin shell with an average thickness of ∼10 nm coated on the hollow nanowire, and XRD patterns confirmed the existence of Fe_2P and Ni_2P in MP-MO_x. Electrochemical measurements suggested the outstanding HER activity of MP-MO_x in 1.0 M KOH with a low overpotential of 26 mV at 10 mA cm^{-2}, comparable to that of Pt/C. More importantly, the resulting MP-MO_x also processed superior TOR or STOR activity in 1.0 M KOH electrolyte with 0.05 M CH_4N_2S or NaSCN. Specifically, it needed potentials of 1.30 V vs RHE for TOR and 1.31 V vs RHE for STOR to achieve 10 mA cm^{-2}, approximately 120 mV lower than that for OER. For integrating HER with TOR or STOR (Figure 62c), the MP-MO_x couple required a voltage of only 1.39 V to deliver a current density of 10 mA cm^{-2}, suggesting a potential saving of 120 mV compared to that for OWS (1.49 V). Also, this MP-MO_x couple-driven HWS exhibited remarkable stability at 20 mA cm^{-2} for at least 10 h.

In addition to the above-mentioned sulfur-containing organics, inorganic sulfides like sulfion (S^{2-}), hydrogen sulfide (H_2S, HS^-), sulfite (SO_3^{2-}) and so on are usually toxic, corrosive, or smelly in sewage from tannery, paper mill, and petrochemical plants.[109,749−752] Efficient desulfurization via sulfides electro-oxidation reaction (SOR) is crucial to environment protection and human health. In view of the more favorable thermodynamics of SOR like sulfion ($S^{2-} \rightarrow S + 2e^-$, −0.48 V vs RHE) than OER, it is attractive to couple SOR with HER for energy-saving hydrogen production, and simultaneous conversion of harmful sulfion to valuable sulfur powder.

Deng and coworkers coupled H_2S oxidation with HER electrocatalyzed by a bifunctional N-doped graphene encapsulated CoNi alloy (CoNi@NGs).[108] HRTEM image of CoNi@NGs showed the presence of metal nanoparticles with an average diameter of 4−6 nm completely encapsulated by single-layer graphene layers with a thickness of 3.4 Å (Figure 62d). Also, the lattice fringe of 2.1 Å matched well with the (111) plane of CoNi alloy (Figure 62e). Elemental mapping images further confirmed the homogeneous distributions of Co and Ni in CoNi@NGs (Figure 62f). The electrocatalytic SOR performance of CoNi@NGs was evaluated in 1.0 M NaOH with 1.0 M Na_2S solutions. As shown in Figure 62g, the LSV curves for SOR over CoNi@NGs suggested a low onset potential of only 0.25 V vs RHE at 1 mA cm^{-2}, 1.24 V lower than that of OER. Such a low oxidation potential enabled a commercial 1.2 V battery to directly drive the SOR and HER even on a graphite rod cathode for simultaneous H_2S decomposition and hydrogen bubbles generation (Figure 62h). The SOR activity of CoNi@NGs was superior to those of control samples including $CoNiO_x$-CNTs, N-carbon, and 40% Pt/C. Detailed physiochemical characterizations including online gas chromatography (GC) and in situ electrochemical UV−vis spectroscopy revealed a FE of 98% for hydrogen production, and the formation of polysulfides due to SOR. To rationalize the excellent SOR activity of CoNi@NGs, DFT calculations were conducted. Considering the steps of initial S^{2-} adsorption followed by electrochemical oxidation to S* intermediates and then to S product during SOR, the authors believed that the binding strength of S* is critical, which should be neither too strong nor too weak. The ΔG of S* adsorption on CoNi@NGs was calculated to be −0.29 eV (ΔG_{S^*} = −0.29 eV), closest to the ideal value (0 eV) than those of N-doped graphene (1.87 eV), Co@NGs (0.84 eV), Ni@NGs (0.66 eV), and CoNi (−1.76 eV). The calculated projected density of states (DOS) in Figure 62i showed a downshifted band center for the C−S bond occupation on CoNi@NGs relative to CoNi@Gs and graphene, suggesting the enhanced sulfur adsorption. Electronic state analysis further revealed that the enriched charge density of the carbon atoms near the CoNi cluster and nitrogen dopants account for the improved sulfur adsorption and thus stabilization of the S* intermediate. Figure 62j displayed Gibbs free energy profiles of SOR reaction paths containing different adsorbed S species from initial S* to S_4*. The calculated ΔG of all the sulfur intermediates on CoNi@NGs were lower than those in solution and on graphene, indicative of favorable polysulfide formation for CoNi@NGs.

Recently, Wen and coworkers fabricated WS_2 nanosheets (WS_2 NSs) through a low-temperature molten-salt-assisted route (Figure 62k).[109] The resulting WS_2 NSs exhibited a flaky morphology as shown in the corresponding TEM image. LSV curves of the WS_2 NSs in 1.0 M NaOH with 1.0 M Na_2S indicated that the potential of SOR at 10 mA cm^{-2} (0.48 V vs RHE) is significantly low than that for OER (1.65 V vs RHE), demonstrating the preference of the former (Figure 62l). Notably, the SOR activity of WS_2 NSs was also better than that of RuO_2 and comparable to that of 20% Pt/C. Additionally, the WS_2 NSs exhibited high HER activity in 0.5 M H_2SO_4, with a low overpotential of 214 mV to reach 10 mA cm^{-2} (Figure 62m). DFT calculations revealed that the rich edge sites of WS_2 NSs contribute to the outstanding electrocatalytic performance toward alkaline SOR and acidic HER. A three-chamber flow cell using the bifunctional WS_2 NSs as alkaline anode and acidic cathode was then assembled, wherein deionized water was flowed through the middle chamber to separate anolyte and catholyte. The assembled electrolyzer showed self-powered capability with a current density of 8.54 mA cm^{-2} at a bias-free voltage for both SOR and HER, with an average hydrogen production rate of 336.3 L h^{-1} m^{-2} and a FE of 99.22%.

Other transition-metal sulfides like cobalt-based sulfides have gained great interest owing to their outstanding stability, excellent adsorption ability of S^{2-} ions, and high conversion efficiency of polysulfides,[753−755] making them promising for SOR. Yang and coworkers[756] synthesized Co_3S_4 nanowires grown on nickel foam as a bifunctional electrocatalyst for SOR-assisted HWS in seawater, wherein high current densities of 100 and 300 mA cm^{-2} can be obtained at cell voltages of only 0.496 and 0.608 V, respectively. DFT calculations proved that the Co_3S_4 reduces energy barriers of the rate-determining

https://doi.org/10.1021/acs.chemrev.3c00332
Chem. Rev. 2024, 124, 3694−3812

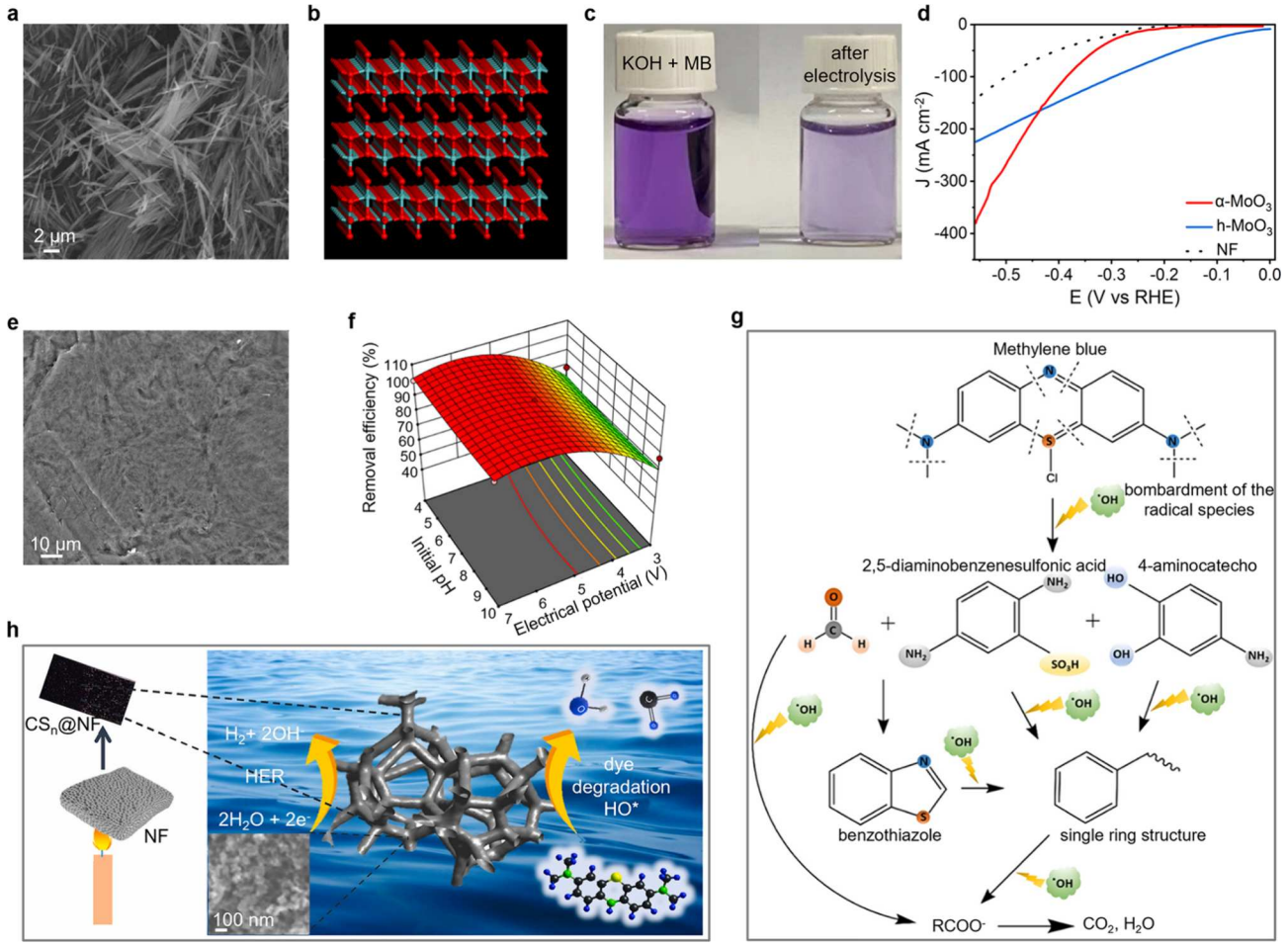

Figure 63. (a) SEM image of α-MoO_3. (b) Crystal structure of α-MoO_3. (c) Color change of the MB solution before and after electrolysis. (d) LSV curves of α-MoO_3 and h-MoO_3 for HER. Reproduced with permission from ref 760. Copyright 2021 Elsevier. (e) SEM of commercial graphite electrode. (f) 3D response surface graphs for the influence of pH and potential on MB removal efficiency. (g) Possible MB degradation pathways. Reproduced with permission from ref 761. Copyright 2022 American Chemical Society. (h) Conceptual diagram of the usage of $CS_{2.5}$@NF for simultaneous wastewater treatment and hydrogen generation. Reproduced with permission from ref 762. Copyright 2023 Elsevier.

SO_3^{2-} to SO_4^{2-} oxidation step, and S_8 desorption step. Zhong and coworkers reported a Cu_2S microflake supported on nickel foam (Cu_2S/NF) bifunctional electrocatalyst, exhibiting excellent activity and stability for both SOR (0.26 V vs RHE) and HER (−0.18 V vs RHE) at 10 mA cm^{-2}.[757] By coupling the SOR and HER on Cu_2S/NF, a current density of 100 mA cm^{-2} was obtained at a cell voltage of only 0.64 V, saving over 74% energy consumption for hydrogen generation compared to the corresponding OWS.

Sulfur dioxide (SO_2) generated from fossil fuel power plants, is a sulfur-containing gas that can induce irrecoverable climate change and atmospheric pollution.[758] Conventional method for removal of SO_2 is to use NaOH solution as adsorbent to form Na_2SO_3 followed by further oxidization toward valuable Na_2SO_4 with purged air, which is energy-intensive. Therefore, Moon and coworkers coupled the electrochemical sulfite oxidation with HER (Figure 62n).[759] The MoP/porous carbon cloth (MoP/PCC) was synthesized by low-temperature phosphorization of MoO_2/PCC. TEM image of MoP/PCC indicated an average size of 40−50 nm. The MoP/PCC required an applied potential of 1.25 V vs RHE to reach 10 mA cm^{-2} for SOR and its HER performance was insusceptible to SO_3^{2-}. Based on the above results, a hybrid cell was developed using MoP/PCC as the bifunctional electrocatalyst for concurrent SOR and HER. A low cell voltage of 1.34 V was achieved at 10 mA cm^{-2} (Figure 62o), lower than those for OWS based on MoP/PCC and even Pt/PCC couples.

5.2.4. Organic Dyes Oxidation. Another typical pollutant in wastewater from textile, cosmetic, paper, and leather industries is organic dye,[760−762] which is generally carcinogenic and mutagenic to organisms. Integrating electrochemical oxidative decomposition of these organic dyes with preferred kinetics and HER to achieve simultaneous hydrogen evolution and dye degradation would gain both economic and ecological benefits. Using methylene blue (MB) as a model organic dye, Teng and coworkers demonstrated the feasibility of MB decomposition and concurrent hydrogen generation in alkaline solution (1.0 M KOH with 10 mg L^{-1} MB) using α-MoO_3 with a orthorhombic phase as the bifunctional electrocatalyst.[760] The α-MoO_3 was prepared by a simple hydrothermal method. To highlight the phase-dependent electrocatalytic activity, a control sample of h-MoO_3 with a hexagonal phase was also included for comparison. XRD patterns confirmed the successful synthesis of both phase-pure α-MoO_3 and h-MoO_3. SEM image revealed the nanowire-like morphology of α-MoO_3 with a diameter of 200−300 nm and a length of 5−10 μm (Figure 63a), in contrast to hexagonal microrods of h-MoO_3 with 2−5 μm in diameter and 20−30

https://doi.org/10.1021/acs.chemrev.3c00332
Chem. Rev. 2024, 124, 3694−3812

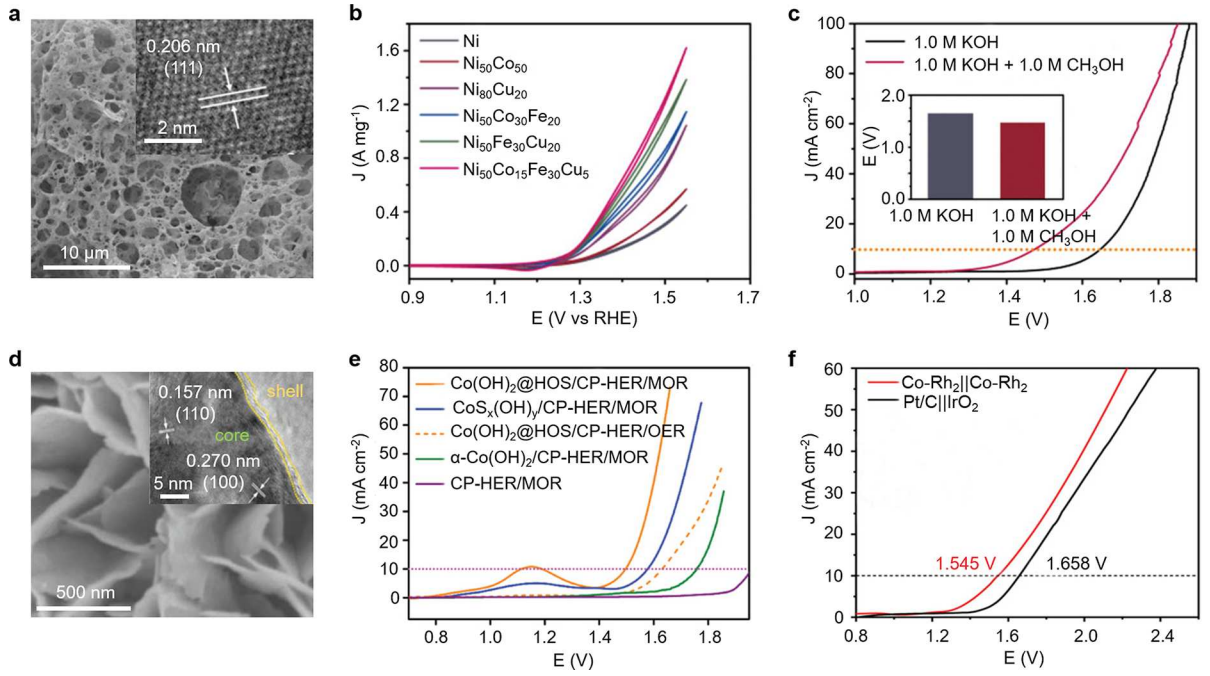

Figure 64. (a) SEM and HRTEM images of $Ni_{50}Co_{15}Fe_{30}Cu_5$ MEAAs. (b) CV curves of different aerogel electrocatalysts for MOR. (c) LSV curves of OWS and MOR-coupled HWS for $Ni_{50}Co_{15}Fe_{30}Cu_5$ MEAAs couple. Reproduced with permission from ref 763. Copyright 2022 John Wiley and Sons. (d) SEM and HRTEM images of $Co(OH)_2$@HOS. (e) LSV curves of $Co(OH)_2$@HOS/CP in 1.0 M KOH with and without methanol in a two-electrode system. Reproduced with permission from ref 617. Copyright 2020 John Wiley and Sons. (f) LSV curves of Co−Rh_2 couple (Co−Rh_2||Co−Rh_2) and Pt/C||IrO_2 couple for MOR-assisted HWS. Reproduced with permission from ref 773 under the terms of a CC-BY 4.0 license. Copyright 2020 John Wiley and Sons.

mm in length. Combining physiochemical characterizations and electrochemical experiments, the authors found that the interlayers of α-MoO_3 (Figure 63b) can facilitate intercalation reaction of ions and the obvious Jahn−Teller distortion of MoO_6 octahedron in α-MoO_3 favors the generation of Lewis acid sites which benefit adsorption and activation of reactants, collectively improving the MB oxidation and HER at large current density. As depicted in Figure 63c, the color of 1.0 M KOH with 15 mg L^{-1} MB solution changed from dark purple to light purple after electrolysis at 1.6 V vs RHE for 2 h, consistent with the gradual decrease of absorption peaks at 610 and 640 nm. These results proved the MB degradation during electrooxidation. Notably, the anode potential after introducing MB at 20 mA cm^{-2} was reduced by about 240 mV. Moreover, the α-MoO_3 showcased excellent HER activity in 1.0 M KOH (Figure 63d). At an overpotential of 550 mV, the α-MoO_3 afforded a current density of 358 mA cm^{-2}, much higher than those of h-MoO_3 (218 mA cm^{-2}) and NF (<150 mA cm^{-2}). The smaller Tafel slope of α-MoO_3 (117 mV dec^{-1}) relative to h-MoO_3 (184 mV dec^{-1}) further confirmed the fast HER kinetics of the former.

Besides metal-based materials, Okten's group recently found that commercially available flexible graphite, which is low-cost, highly conductive, and environmentally benign, can serve as a bifunctional electrode for MB oxidative degradation coupled with HER.[761] SEM image shown in Figure 63e revealed a rough and undulating surface of the flexible graphite. By systemically varying the operating conditions such as MB concentration, solution pH, electrolyte dose, applied potential, and operating time, along with Box-Behnken experimental design, the degradation performance of MB was optimized with minimal tests. For example, Figure 63f demonstrated the influence of both applied potential and pH on the removal efficiency of MB, and suggested that the MB removal efficiency is primarily affected by applied potential rather than pH. Increasing applied potential resulted in improved effectiveness of MB removal. According to p- and F-values, they concluded that the applied potential relative to other parameters has a greater influence on MB removal. The proposed MB electrooxidation degradation pathway was depicted in Figure 63g, wherein the formed OH radicals by water oxidation at anode facilitated MB degradation.

To further increase active surface area, Devi and coworkers used porous nickel foam (NF) as substrate and candle soot as the precursor to fabricate NF-supported candle soot-derived carbon with a mass loading of 2.5 mg cm^{-2} ($CS_{2.5}$@NF).[762] The $CS_{2.5}$@NF was prepared by one-step flame combustion of NF above the flame tip (Figure 63h). Raman and FT-IR spectra of $CS_{2.5}$@NF jointly revealed the formation of defective carbon with plentiful C−O/C=O, C=C, and −OH functional groups. High-magnification SEM image indicated the existence of nanoparticles' aggregate with an average size of about 40−50 nm for $CS_{2.5}$@NF (Figure 63h inset). UV−vis spectra underscored that around 62% MB (5 ppm in 0.5 M H_2SO_4) can be degraded over $CS_{2.5}$@NF within 90 min. In addition, the $CS_{2.5}$@NF exhibited decent HER activity in the same electrolyte with an overpotential of 117 mV to afford 10 mA cm^{-2}. ECSA and EIS measurements revealed that the superior MB oxidative degradation and HER performance of $CS_{2.5}$@NF are ascribed to its low contact/charge transfer resistances and large active surface area.

5.3. Hybridizing with Organics Oxidative Upgrading

An ideal hybrid electrolysis system should couple HER with oxidative upgrading reactions which are thermodynamically more favorable than OER, as it not only decreases overall

https://doi.org/10.1021/acs.chemrev.3c00332
Chem. Rev. 2024, 124, 3694−3812

Table 8. Summary of Bifunctional Electrocatalysts for MOR-Assisted Hybrid Water Splitting (HWS)

Electrocatalysts	Electrolytes (x M KOH + y M methanol)	Current density (mA cm^{-2})	Cell voltage (V)	Ref
$Co(OH)_2$@HOS/CP	1.0 + 3.0	10	1.497	617
$Ni_{50}Co_{15}Fe_{30}Cu_5$ MEAAs	1.0 + 1.0	10	1.476	763
mPtRh NSs	3.0 + 1.0	10	0.51	769
Co-Rh_2	1.0 + 1.0	10	1.545	773
Ru&Fe-WO_x	1.0 + 3.0	10	1.38	774
		100	1.50	
		500	1.62	
NiIr-MOF/NF	1.0 + 4.0	10	1.39	775
$Ni_{0.33}Co_{0.67}(OH)_2$/NF	1.0 + 0.5	10	1.50	776
		20	1.56	
		50	1.65	
		100	1.75	
V_P-Ni_2P−Pt/CC	1.0 + 2.0	50	1.1	777
Mo-Co_4N	1.0 + 3.0	10	1.427	778
CNFs@NiSe/CC	1.0 + 1.0	100	1.43	779
Au@PdRu RNs	1.0 + 1.0	10	0.88	780
Pt-CoTe/NC	0.5[a] + 1.0	10	0.68	781[a]
$NiFe_xP$@NiCo-LDH	1.0 + 0.5	50	1.42	782
Pt-CoSe/NC	0.5[a] + 1.0	10	0.67	783[a]
Cu_2O-Cu@Ni_2P/NF	1.0 + 1.0	10	1.40	784
Co_xP@NiCo-LDH/NF	1.0 + 0.5	10	1.43	785
NiSe/$MoSe_2$/CC	1.0 + 1.0	10	1.50	786
PdRh bimetallene	1.0 + 1.0	10	0.657	787
$NiFe_2O_4$/NF	1.0 + 0.5	100	1.74	788
		800	2.00	
NiCo	1.0 + 2.0	20	1.47	789
NiCu@Cu	1.0 + 2.0	10	1.45	790

[a]H_2SO_4.

energy inputs but also maximizes the return of the electrolyzer. Desirable reactions that can meet the above criteria include alcohols oxidation, aldehydes oxidation, amines oxidation, biomass oxidation, and plastic wastes oxidation.

5.3.1. Alcohols Oxidation. Electrochemical oxidation of various alcohols has aroused widespread attention due to their low toxicity and great promise for carbon neutrality. Besides, the electrochemical oxidation of alcohols can produce value-added aldehyde and carboxylic acid as well.[763]

5.3.1.1. Methanol Oxidation. Methanol (CH_3OH) is a kind of small molecule alcohols with easy availability, low cost, abundance, and high hydrogen density (12.6 wt %), which can be obtained from renewable biomass resources.[764] Electrochemical methanol oxidation reaction (MOR) can generate valuable formate, and the theoretical thermodynamic potential is about 0.10 V,[765−767] significantly lower than that of OER (1.23 V).

Medium-entropy alloys (MEAs) have the advantages (adjustable composition, complex surface, high tolerance, etc.) of high-entropy alloys (HEAs), and can provide clearer catalytically active sites than HEAs due to fewer components.[768] However, it is still a challenge to achieve single-phase MEA aerogels (MEAAs) limited by the immiscible behavior of different metals. Guo and collaborators successfully addressed the synthetic challenge via a general combined autocombustion and subsequent low-temperature reduction strategy, to obtain 3D $Ni_{50}Co_{15}Fe_{30}Cu_5$ MEAAs with the lowest density among the reported metal materials.[763] SEM image of the resulting $Ni_{50}Co_{15}Fe_{30}Cu_5$ MEAAs demonstrated a porous structure (Figure 64a), with the Brunauer−Emmett−Teller (BET) specific surface area of 8.1 m^2 g^{-1} as determined by N_2 sorption experiments. HRTEM image showed a well-resolved lattice spacing of 0.206 nm, corresponding to the (111) facet of MEAAs (Figure 64a inset). The MOR activities of $Ni_{50}Co_{15}Fe_{30}Cu_5$ MEAAs and other low-entropy controls with fewer components were tested in 1.0 M KOH containing 1.0 M CH_3OH by cyclic voltammetry (CV). As shown in Figure 64b, the quaternary $Ni_{50}Co_{15}Fe_{30}Cu_5$ MEAAs exhibited the lowest onset potential and the mass activity (MA) can go up to 1.62 A mg^{-1} with a specific activity of 132.24 mA cm^{-2} for MOR at 1.65 V vs RHE. The MOR activity order was calculated to be $Ni_{50}Co_{15}Fe_{30}Cu_5$ > $Ni_{50}Fe_{30}Cu_{20}$ > $Ni_{50}Co_{30}Fe_{20}$ > $Ni_{80}Cu_{20}$ > $Ni_{50}Co_{50}$ > Ni, underscoring the positive role of multicomponent synergy. Importantly, as depicted in Figure 64c, the MOR-assisted HWS based on $Ni_{50}Co_{15}Fe_{30}Cu_5$ MEAAs couple attained a low cell voltage of 1.476 V at 10 mA cm^{-2}, much lower than that of OWS at the same current density (1.649 V). Also, the cogeneration of value-added formate instead of oxygen at the anode, and hydrogen at the cathode can be achieved.

Apart from metallic materials, oxidized metals-based nanocomposites were also explored. Fu and coworkers recently synthesized a core−shell cobalt hydroxide@hydroxysulfide nanosheets grown on carbon paper ($Co(OH)_2$@HOS/CP) as a bifunctional electrocatalyst via electrodeposition followed by rapid room temperature sulfurization with 10 s.[617] High-magnification SEM image confirmed the nanosheet-assembled morphology of $Co(OH)_2$@HOS/CP (Figure 64d). HRTEM demonstrated the lattice fringes of 0.157 and 0.270 nm corresponding to (110) and (100) planes of $Co(OH)_2$, respectively (Figure 64d inset). The peripheral thin layer with a thickness of 2−2.5 nm corresponded to amorphous

https://doi.org/10.1021/acs.chemrev.3c00332
Chem. Rev. 2024, 124, 3694−3812

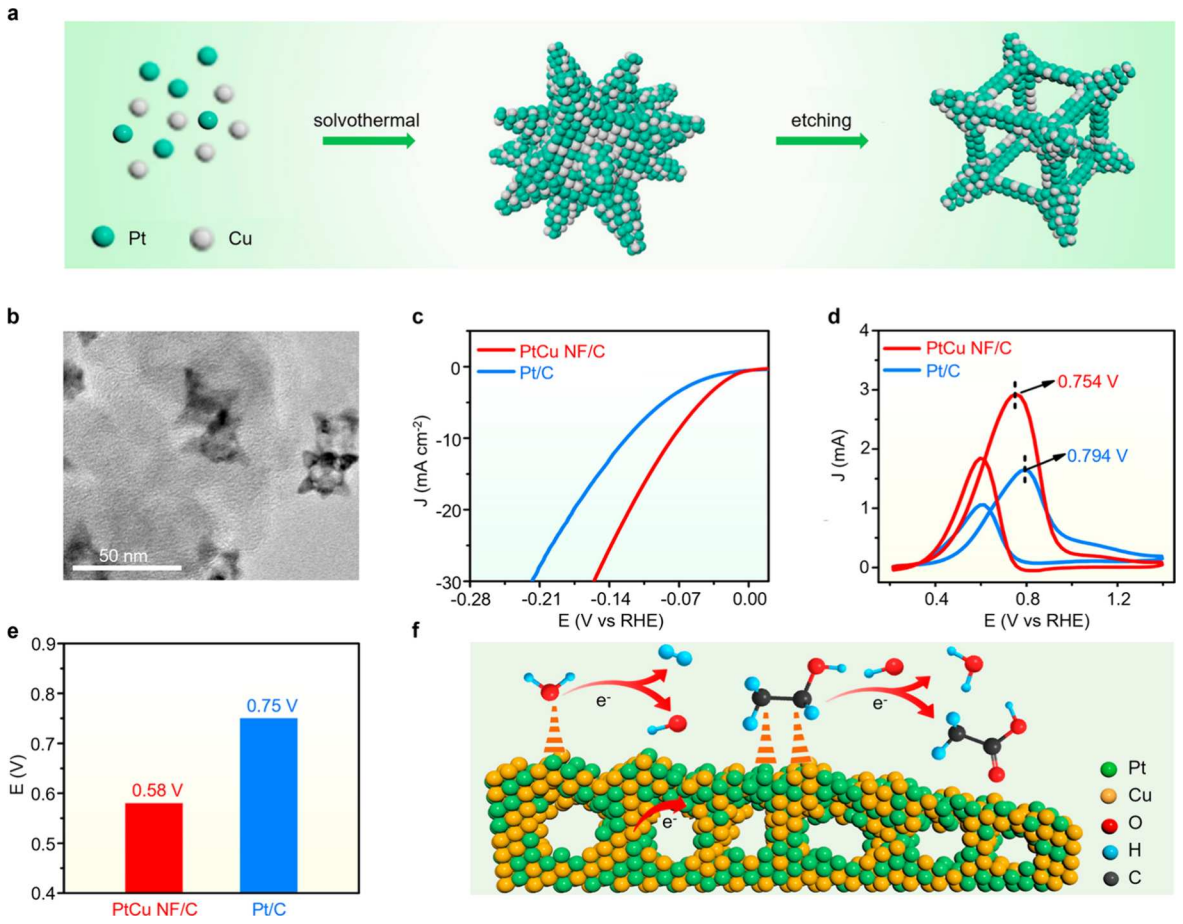

Figure 65. (a) Schematic for the synthesis of PtCu NF. (b) TEM image of PtCu NF/C. (c) LSV curves of PtCu NF/C and commercial Pt/C in 1.0 M KOH for HER. (d) CV curves of PtCu NF/C and commercial Pt/C for EOR. (e) Cell voltages needed at 10 mA cm^{-2} for the bifunctional electrocatalysts toward EOR-coupled HWS. (f) Schematic illustration of the mechanism for EOR and HER on PtCu NF/C. Reproduced with permission from ref 796. Copyright 2022 American Chemical Society.

hydroxysulfide. The cell voltage to achieve 10 mA cm^{-2} based on $Co(OH)_2$@HOS/CP couple was only 1.497 V for MOR-assisted HWS in 1.0 M KOH with 1.0 M CH_3OH (Figure 64e), lower than that of OWS (1.631 V). Moreover, benefiting from the unique properties of core−shell structure with partial surface sulfurization such as abundant active sites, regulated electronic structure, and strongly coupled heterointerface, the HWS activity of $Co(OH)_2$@HOS/CP couple also exceeded those of control bifunctional electrocatalysts including $CoS_x(OH)_y$/CP and α-$Co(OH)_2$/CP.

Relative to non-noble metal-based materials, noble metals like Rh, Ru, Ir, Pd, and Pt-based nanocatalysts have exhibited enhanced performance for HER and/or MOR.[617,769] Considering the high cost and limited reserve of noble metals, it is highly desirable to reduce their usage as well as improving their catalytic activity. As one of the most promising strategies, the introduction of second nonnoble metals (e.g., Fe, Co, Ni, etc.) into noble metal-based catalysts has been studied.[770−775] Yang and coworkers synthesized the Co-doped Rh nanoparticles on carbon black using ultrathin Co nanosheets as the bridge to modulate Rh nucleation and growth.[773] The Co-doped Rh nanoparticles with a size of about 1.94 nm (Co−Rh_2) exhibited lower overpotential of merely 2 mV at 10 mA cm^{-2} than Rh/C and Pt/C. Furthermore, a high mass activity of 889 mA mg^{-1} at the peak potential for MOR in alkaline media (1.0 M KOH with 1.0 M CH_3OH) can be achieved as well, about 5-fold greater than that of Rh/C. The bifunctional two-electrode cell needed a cell voltage of 1.545 V at 10 mA cm^{-2} for MOR-coupled HWS, even lower than that of commercial Pt/C and IrO_2 couple (Figure 64f). As revealed by DFT calculations, Co-doping downshifted the d-band center of Rh, which optimized adsorption of intermediates in HER to reduce the energy barriers of Volmer step and accelerated the conversion of *CO to *COOH during MOR. Feng and collaborators synthesized a ternary electrocatalyst of Ru&Fe-WO_x for anodic MOR and cathodic HER in 1.0 M KOH with 3 M CH_3OH, delivering 100 mA cm^{-2} at a cell voltage of only 1.50 V with good stability and high FEs of nearly 100% and >90% for hydrogen and formate, respectively.[774] By combining experiments and DFT computations, the authors verified that WO_x host and Ru- and Fe-based dopants synergistically result in optimized H* adsorption on lattice oxygen for HER and enhanced HOOC* desorption on Ru site for MOR. Recently, the introduction of Ni into Ir to obtain NiIr-based metal−organic framework (MOF) nanosheet arrays (NiIr-MOF/NF) was reported as the bifunctional electrocatalyst for MOR and HER,[775] which can deliver a current density of 10 mA cm^{-2} at 1.39 V. More examples of bifunctional electrocatalysts for MOR-assisted hybrid water splitting (HWS) can be seen in Table 8.

5.3.1.2. Ethanol Oxidation. Ethanol (EtOH) contains 13.0 wt % hydrogen with the advantages of easy availability and

https://doi.org/10.1021/acs.chemrev.3c00332
Chem. Rev. 2024, 124, 3694−3812

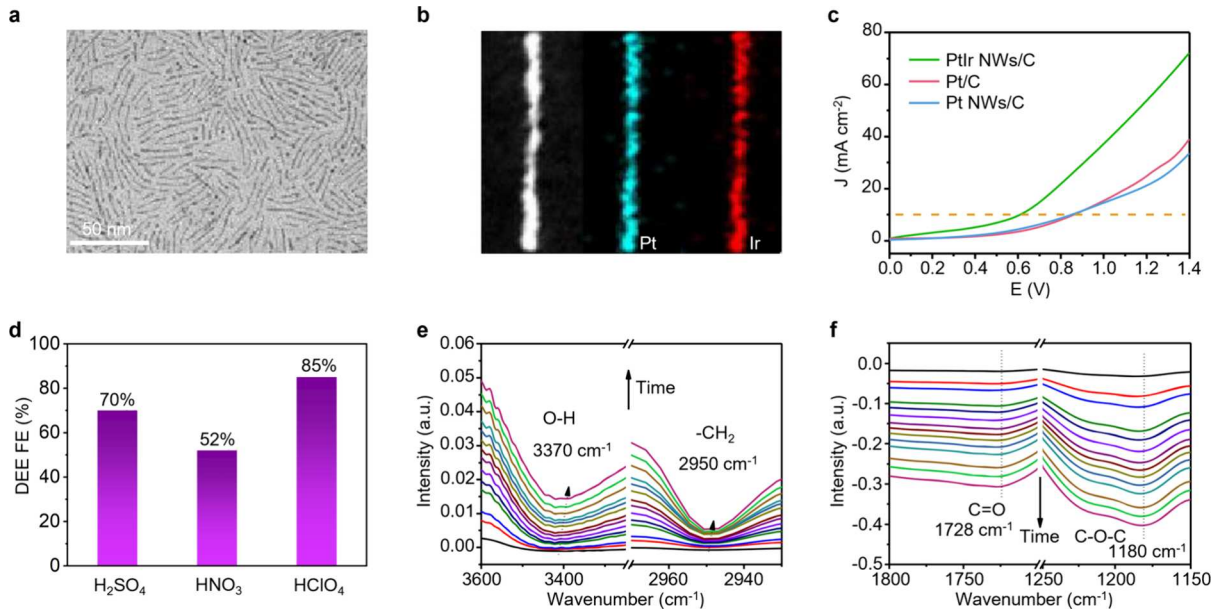

Figure 66. (a) TEM image of PtIr NWs, (b) HADDF-STEM and elemental mapping images of PtIr NWs. (c) LSV curves of PtIr NWs/C couple, Pt NWs/C couple, and Pt/C couple in 0.5 M H_2SO_4-contained EtOH solution at a scan rate of 5 mV s^{-1}. (d) The FEs of DEE in different acids at 10 mA cm^{-2}. (e, f) In situ FTIR spectra of the electrocatalytic DEE production over PtIr NWs/C. Reproduced with permission from ref 800. Copyright 2021 American Chemical Society.

storage. It is thus an ideal substrate for oxidation upgrading to replace OER toward value-added chemicals and hydrogen coproduction.[791]

Our group previously reported that the hierarchically porous Ni_3S_2 on nickel foam (Ni_3S_2/NF) prepared by direct low-temperature sulfurization of commercial NF at 280 °C for 10 min can function as a bifunctional electrocatalyst for both ethanol oxidation reaction (EOR) and HER and in alkaline solution.[99] After introducing 10 mM EtOH in 1.0 M KOH, the onset potential of Ni_3S_2/NF shifted from ∼1.50 to ∼1.35 V vs RHE and rapid current rise was observed within 1.40 V vs RHE, suggestive of more favorable EOR with respect to OER. To achieve a benchmark current density of 100 mA cm^{-2}, the oxidative potential for EOR on Ni_3S_2/NF was ∼190 mV smaller than that of OER. ^{1}H NMR analysis revealed a near unity FE for acetate production, and systematic physiochemical characterizations including SEM and XPS unveiled in situ surface oxidation restructuring of Ni_3S_2/NF. Besides the prominent EOR performance, the Ni_3S_2/NF also exhibited good HER activity in 1.0 M KOH, requiring an overpotential of only 116 mV to reach 10 mA cm^{-2}. Further phosphorization of transition-metal sulfides like CoS_2 would lead to improved EOR activity, as reported by Cao and coworkers.[792] They prepared P-doped CoS_2 nanosheet arrays on carbon cloth (Co−S−P/CC) and found that the EOR activity of CoS_2/CC in 1.0 M KOH with 1.0 M EtOH is enhanced by P-doping, with the decreased Tafel slope from 133 to 112 mV dec^{-1}.

By comparison, noble-metal-based electrocatalysts can further accelerate the EOR-coupled HWS albeit with higher cost. For example, Pt-based materials have displayed excellent performance toward HER and/or various small-molecules oxidation reactions.[793,794] Usually, single Pt has mediocre or even poor selectivity for EOR due to the weak substrates' adsorption (EtOH and H_2O) and C−H bond dissociation capacities.[795] Introducing other elements to form Pt-based alloy materials is a promising method to improve their EOR and HER activities. Liu and collaborators designed a three-dimensional (3D) PtCu nanoframe (NF) with high-index facets and multichannels through solvothermal treatment and subsequent etching (Figure 65a).[796] TEM image of PtCu NF confirmed the successful etching of PtCu nanodendrites (NDs) toward the 3D open structure (Figure 65b). HRTEM images further revealed the presence of plentiful high-index (331) facet in PtCu NF. The PtCu NF was then loaded on Vulcan XC-72R carbon assisted by sonication, and the resulting PtCu NF/C was used as a bifunctional HER and EOR electrocatalyst. As demonstrated in Figure 65c, the PtCu NF/C possessed more exceptional electrocatalytic HER activity in 1.0 M KOH than commercial Pt/C. For instance, the overpotential of PtCu NF/C at 10 mA cm^{-2} was calculated to be only 76 mV, 46 mV lower than that of Pt/C. Moreover, the mass activity at 10 mA cm^{-2} for PtCu NF/C (0.98 A mg_{Pt}^{-1}) was higher than that for Pt/C as well (0.39 A mg_{Pt}^{-1}). Then the EOR-to-acetate performance of PtCu NF/C was further tested in 1.0 M KOH solution containing 0.5 M EtOH. The CV curves shown in Figure 65d demonstrated that the PtCu NF/C has a lower ethanol oxidation potential than commercial Pt/C (0.754 vs 0.794 V vs RHE). The EOR-assisted HWS based on PtCu NF/C couple required a voltage of 0.58 V to reach 10 mA cm^{-2} (Figure 65e), lower than that for Pt/C control couple (0.75 V). Besides higher activity, the PtCu NF/C also showed better stability than Pt/C. The authors ascribed these enhanced HER and EOR performance of PtCu NF/C to the combination of open 3D structure, Cu introduction, and high-index facet, which optimized the adsorption of ethanol and H_2O, and improved C−H bond dissociation of EtOH (Figure 65f). Additionally, alloying Cu with Pd can lead to improved EOR performance. Zhen and coworkers reported self-supported 3D PdCu alloy nanosheets (NSs) as a bifunctional electrode for EOR and HER.[797] For EOR, the onset potential of 3D PdCu alloy NSs was calculated to be 330 mV vs RHE, lower than that of Pd NSs control (370 mV vs RHE). For HER, the 3D PdCu alloy NSs achieved 10 mA cm^{-2} at an overpotential of 106 mV, lower than that of Pd

https://doi.org/10.1021/acs.chemrev.3c00332
Chem. Rev. 2024, 124, 3694−3812

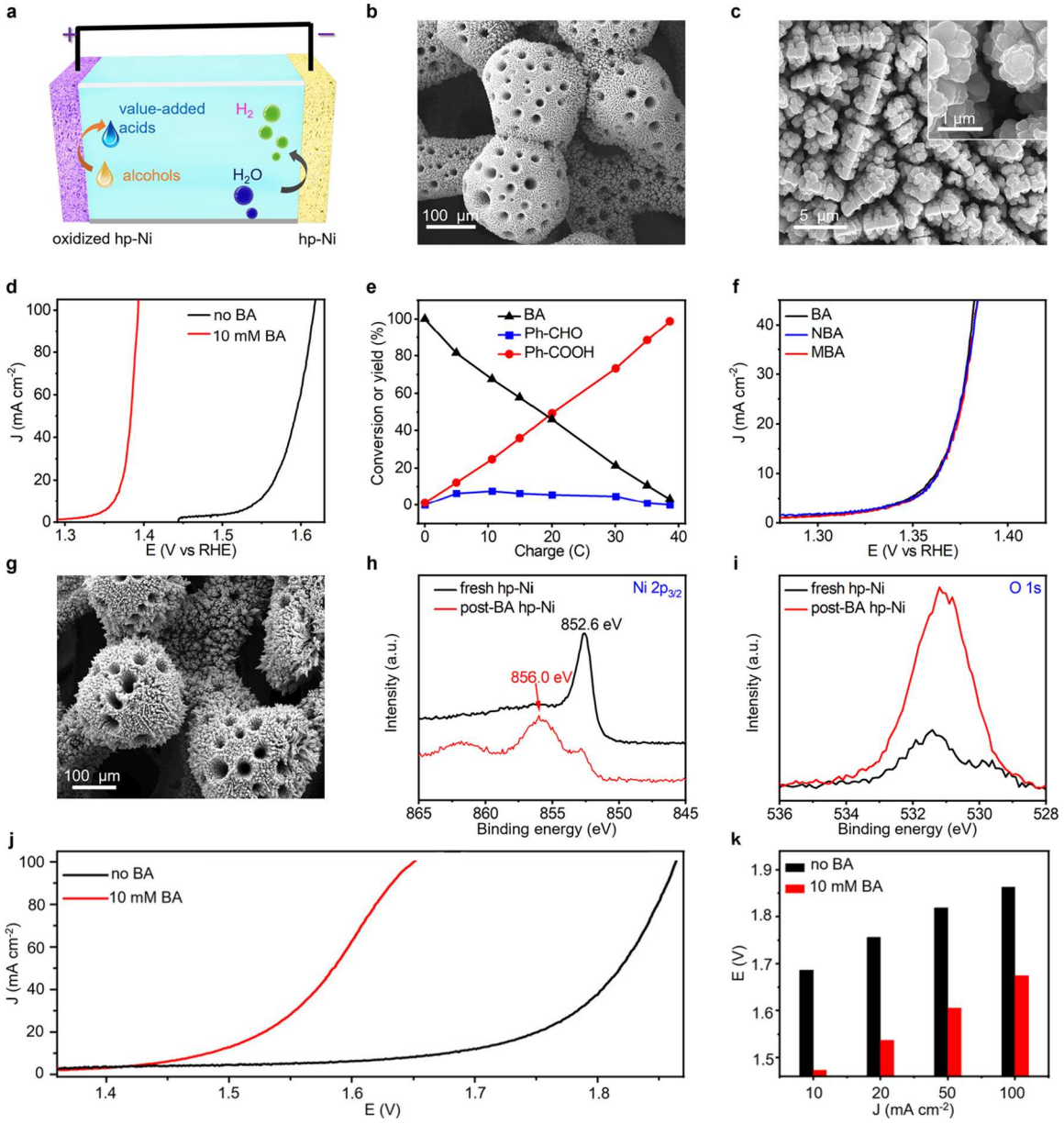

Figure 67. (a) Schematic of alcohols oxidation-couped HWS over the hp-Ni bifunctional electrocatalyst. (b, c) SEM images of hp-Ni at different magnifications. (d) LSV curves of hp-Ni at 2 mV s^{-1} in 1.0 M KOH with or without 10 mM benzyl alcohol (BA). (e) Conversion or yield (%) dependence of BA and its oxidation products on passed charges during electrochemical oxidation at 1.423 V vs RHE in 10 mL of 1.0 M KOH solution containing 10 mM BA (Ph−CHO: benzyl aldehyde; Ph−COOH: benzoic acid). (f) LSV curves of hp-Ni at 2 mV s^{-1} in 1.0 M KOH solution containing 10 mM BA, 4-methylbenzyl alcohol (MBA), or 4-nitrobenzyl alcohol (NBA). (g) SEM image of post-BA hp-Ni. High-resolution XPS spectra of (h) Ni $2p_{3/2}$ and (i) O 1s for the fresh and post-BA hp-Ni electrocatalysts. (j) LSV curves and (k) comparison of cell voltages at various current densities utilizing the hp-Ni couple in 1.0 M KOH solution containing 0 mM and 10 mM BA. Reproduced with permission from ref 111. Copyright 2017 American Chemical Society.

NSs (235 mV). These enhanced EOR and HER performances were ascribed to the ultrathin 3D structure and synergistic effect between Pd and Cu. Apart from introducing exotic metals, Wang and coworkers synthesized S, P-codoped Pd metallene (PdSP metallene) as the bifunctional electrocatalyst for EOR-assisted HWS,[798] delivering a current density of 10 mA cm^{-2} at 0.88 V.

Beyond alloying or doping, shape engineering has been explored as well. For example, 3D palladium nanonetwork (PdNN) was reported as a bifunctional electrocatalyst for EOR and HER,[799] which can achieve 2.6-fold higher mass activity with significantly lower CO_2 production for EOR and afford 10 mA cm^{-2} at a low overpotential of 110 mV for HER. The nanonetwork structure was proved to be beneficial to the exposure of active sites and electron transport.

In addition to producing acetate from EOR, oxidative coupling of EtOH can yield valuable 1,1-diethoxyethane (DEE) fine chemicals.[800,801] It is of great significance to control the selectivity of EOR to DEE coupled with hydrogen production. Guo and collaborators reported PtIr alloy nanowires (NWs) as the bifunctional electrocatalyst for simultaneous generation of DEE and hydrogen from EtOH and water.[800] TEM image (Figure 66a) of PtIr NWs presented ultrafine 1D morphology with a diameter of 1.0 nm and an

https://doi.org/10.1021/acs.chemrev.3c00332
Chem. Rev. 2024, 124, 3694−3812

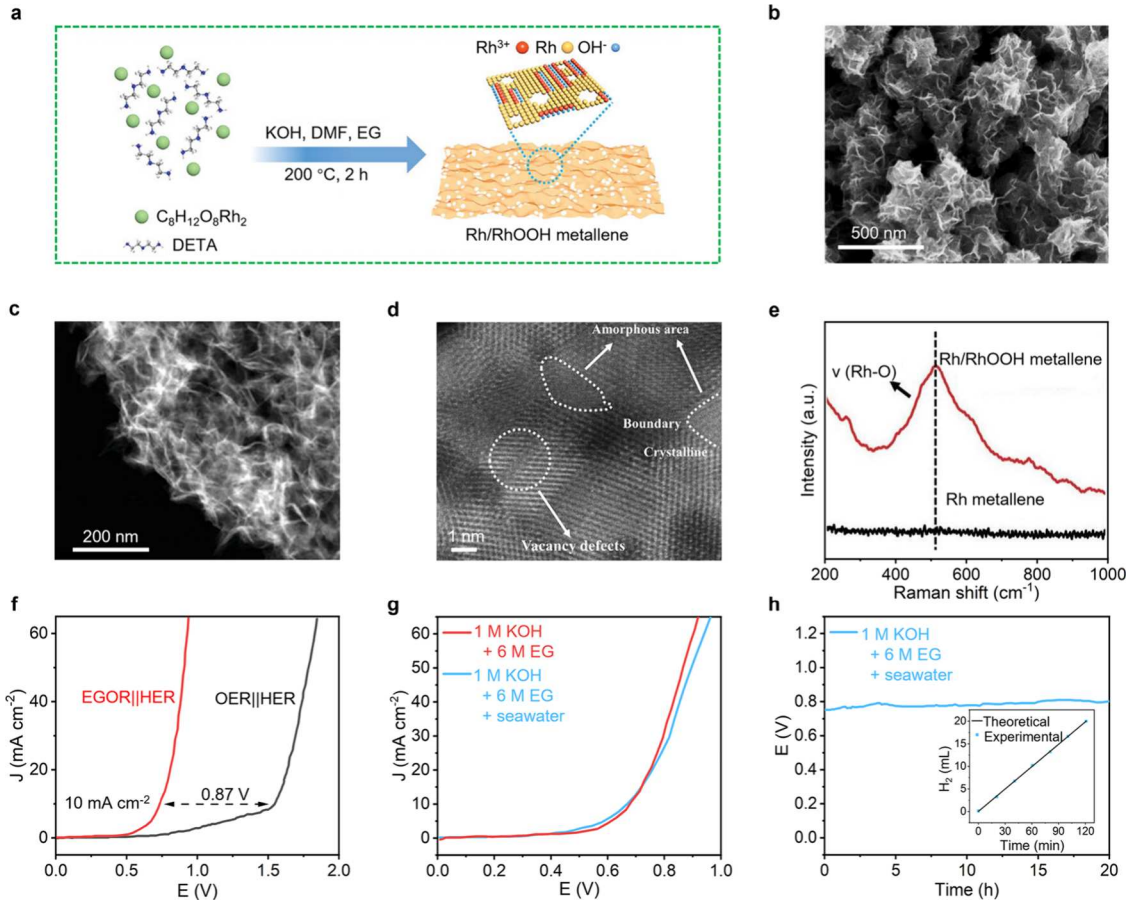

Figure 68. (a) Schematic for the synthesis of Rh/RhOOH metallene. (b) SEM and (c, d) HAADF-STEM images of Rh/RhOOH metallene. (e) Raman spectra of Rh/RhOOH metallene and Rh metallene. (f) LSV curves of Rh/RhOOH metallene couple in 1.0 M KOH with and without 6.0 M EG solutions. (g) LSV curves of Rh/RhOOH metallene couple in 1.0 M KOH with 6.0 M EG and 1 M KOH with 6 M EG and seawater solutions. (h) Chronopotentiometry curves of Rh/RhOOH metallene couple at 10 mA cm^{-2} in 1 M KOH with 6 M EG and seawater solutions for 20 h. The inset in (h) illustrates the measured H_2 quantity and theoretical values at cathode. Reproduced with permission from ref 805. Copyright 2022 John Wiley and Sons.

average length of 30 nm. HADDF-STEM and element mapping images (Figure 66b) confirmed the homogeneous distribution of Pt and Ir along the PtIr nanowire. Before electrochemical tests in 0.5 M H_2SO_4-EtOH electrolyte, the PtIr NWs were loaded on commercial carbon supports followed by acetic acid and potential cycling pretreatments. For the EOR toward DEE, the resulting PtIr NWs/C only required a potential of 0.45 V vs SCE at 10 mA cm^{-2}, lower than those of Pt NWs/C (~ 0.92 V vs SCE) and commercial Pt/C (~ 0.93 V vs SCE). Besides the prominent EOR performance, the PtIr NWs/C showed a high HER activity at −0.15 V vs SCE to achieve 10 mA cm^{-2}, in sharp contrast to those for Pt NWs/C (−0.28 V vs SCE) and Pt/C (−0.30 V vs SCE). As a result, the PtIr NWs/C couple required a cell voltage of 0.61 V for HER and EOR at 10 mA cm^{-2}, much lower than that of 0.86 V for the commercial Pt/C couple (Figure 66c). Moreover, the PtIr NWs/C couple can achieve a FE of 85% for DEE in 0.5 M $HClO_4$-EtOH solution, much higher than those in 0.5 M H_2SO_4- (70%) or HNO_3 (52%)-contained EtOH (Figure 66d). The difference of FEs in diverse acids was attributed to their acidity which affected the acetalation rate and extent. To understand the mechanism of the DEE formation from EOR, in situ FTIR spectroscopy studies were implemented and the results revealed an interaction between adsorbed EtOH and PtIr NWs, as revealed by the redshifts of O−H and $-CH_2$ vibration peaks of EtOH (Figure 66e). In addition, the two gradually enhanced negative peaks ascribed to C=O and C−O−C bonds uncovered the formation of acetaldehyde intermediate and DEE (Figure 66f).

5.3.1.3. Benzyl Alcohol Oxidation. Electrocatalytic benzyl alcohol oxidation reaction (BAOR) is another ideal alternative to OER, and its oxidation products are benzaldehyde and benzoic acid, both of them are widely used as important and versatile intermediates in pharmaceuticals and fine chemicals.[111,802]

Our group reported a bifunctional 3D hierarchically porous nickel framework (hp-Ni) electrocatalyst for BAOR-assisted HWS (Figure 67a),[111] which was synthesized via a facile and environmentally friendly dynamic bubbles-templated electrodeposition route.[8] SEM images (Figure 67b,c) of hp-Ni revealed the presence of interconnected macropore walls with abundant smaller macropores (approximately 10 μm). The hierarchical porosity is conducive to mass transport and gas diffusion for accelerated BAOR and HER. Figure 67d showed the LSV curves of hp-Ni at 2 mV s^{-1} in 1.0 M KOH containing 0 mM or 10 mM benzyl alcohol (BA), revealing an onset potential shift from 1.51 to 1.35 V vs RHE after BA addition. Particularly, the high FE and conversion rate for benzoic acid were achieved (Figure 67e). Additionally, 4-nitrobenzyl alcohol (NBA) and 4-methylbenzyl alcohol (MBA) were

https://doi.org/10.1021/acs.chemrev.3c00332
Chem. Rev. 2024, 124, 3694−3812

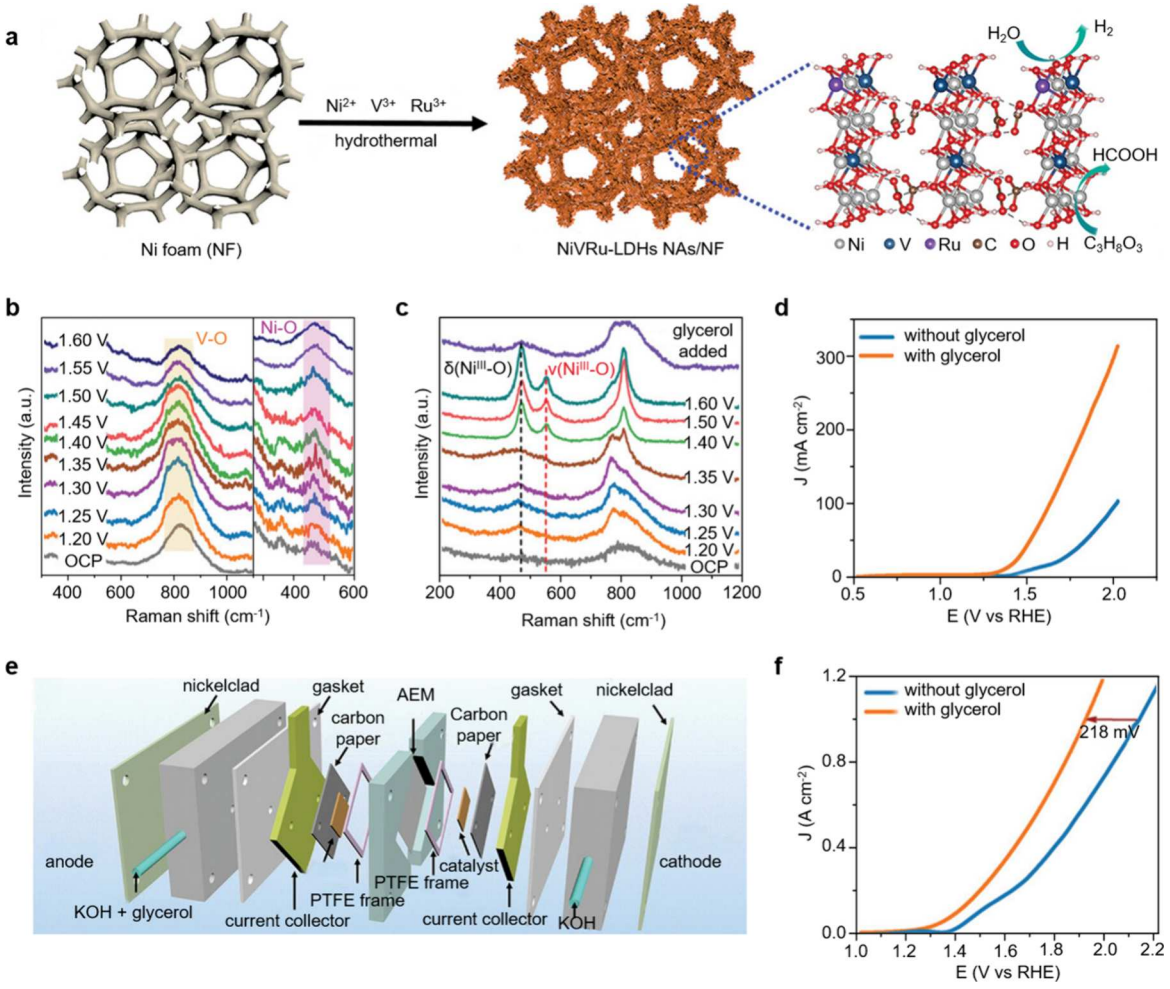

Figure 69. (a) Scheme for the synthesis of NiVRu-LDHs NAs/NF. Potential-dependent operando Raman spectra of the NiVRu-LDHs NAs/NF anode collected in (b) 1.0 M KOH with 0.1 M glycerol and (c) 1.0 M KOH. (d) LSV curves of NiVRu-LDHs NAs/NF couple for GLOR-paired HWS and OWS in 1.0 M KOH with and without glycerol. (e) Schematic illustration of the two-electrode flow cell configuration. (f) LSV curves for GLOR-paired HWS and OWS over NiVRu-LDHs NAs/NF couple using the flow cell. Reproduced with permission from ref 815. Copyright 2023 John Wiley and Sons.

subjected to similar electrocatalytic oxidation, with similar onset potential in comparison to BA (Figure 67f). This result indicated that the catalytic onset potentials of these three alcohol oxidations are predominantly determined by the desirable oxidation state of the underlying electrocatalyst instead of their intrinsic thermodynamics. After the stability tests of the hp-Ni electrocatalyst (denoted as post-BA hp-Ni), the electrocatalyst can maintain 3D hierarchical porous morphology (Figure 67g). XPS spectra of post-BA hp-Ni relative to the fresh counterpart revealed a decreased peak at 852.6 eV ascribed to metallic Ni, an increased peak at 856.0 eV attributed to oxidized Ni species, and enhanced peak intensity of O 1s, indicative of the partial oxidation reconstruction of metallic Ni (Figure 67h,i). Furthermore, the BAOR-coupled HWS electrolyzer based on hp-Ni can afford 10, 20, 50, and 100 mA cm^{-2} at the cell voltages of 1.50, 1.54, 1.60, and 1.66 V, respectively, significantly smaller than those of OWS (Figure 67j,k). In addition, the FEs of benzoic acid and H_2 can be attained as high as 97% and nearly 100%, respectively. As expected, the hp-Ni exhibited promising HER activity in 1.0 M KOH as well, with an overpotential of approximately 219 mV at a current density of 50 mA cm^{-2}.

In addition to metallic Ni, we reported that the Ni_3S_2/NF is also bifunctionally active for both BAOR and HER in alkaline solution, with ∼190 mV voltage saving at 100 mA cm^{-2} relative to OWS.[99] Later, Wang and collaborators reported that CuCo nitride can catalyze BAOR and HER as well.[802] By employing combined hydrothermal, carbon coating and NH_3 calcination, they obtained a self-supported hierarchical porous nitrogen-doped carbon-coated $CuCo_2N_x$ on carbon fiber (NC@$CuCo_2N_x$/CF). The NC@$CuCo_2N_x$/CF only required a cell voltage of 1.55 V for BAOR-coupled HWS at 10 mA cm^{-2} in 1.0 M KOH containing 15 mM BA, much smaller than that of OWS based on Pt/C and IrO_2 couple. DFT calculations revealed that the modulation of key species adsorption owing to the synergistic effect between CoN and CuN benefits the electrocatalytic activities.

5.3.1.4. Ethylene Glycol Oxidation. Ethylene glycol (EG) is the simplest diatomic alcohol, with many advantages of low toxicity, low cost, and convenient storage.[803] One of its oxidative products, glycolic acid, has been widely used in diverse fields, such as adhesives, metal cleaning, leather processing, textiles, and healthcare products. More importantly, the thermodynamic potential of ethylene glycol

https://doi.org/10.1021/acs.chemrev.3c00332
Chem. Rev. 2024, 124, 3694−3812

oxidation reaction (EGOR) toward glycolic acid is only 0.57 V vs RHE, much lower than that of OER.[804]

Two-dimensional (2D) metallene with large surface area, atomic-level thickness, and outstanding electron transport property has been employed as high-performance electrocatalysts in various electrocatalytic fields.[805−809] Wang's group synthesized the partially hydroxylated Rh metallene (Rh/RhOOH metallene) using hydrothermal method for EGOR-assisted seawater electrolysis (Figure 68a).[805] SEM and HAADF-STEM images of Rh/RhOOH metallene showed a typical ultrathin nanosheet morphology (Figure 68b,c). Notably, the Rh/RhOOH metallene featured a defect-rich structure (Figure 68d). Raman spectra showed a typical peak at ∼515 cm^{-1} ascribed to Rh−O vibration (Figure 68e), indicative of the formation of surface RhOOH species contributing to the stabilization of 2D ultrathin Rh/RhOOH metallene. The Rh/RhOOH metallene required a low overpotential (29 mV) to attain 10 mA cm^{-2} for HER. Moreover, for a two-electrode EGOR-assisted HWS, a current density of 10 mA cm^{-2} can be obtained at a cell voltage of only 0.678 V, much lower than that for OWS (1.548 V), as depicted in Figure 68f. Such superior bifunctional activity can be maintained in alkaline seawater (Figure 68g). Moreover, the Rh/RhOOH metallene couple presented remarkable stability at 10 mA cm^{-2} for 20 h during EGOR-assisted hydrogen generation with ∼100% FE (Figure 68h).

Subsequently, Wang and coworkers synthesized PtRh nanowires with Rh atom modification ($PtRh_{0.02}$@Rh NWs) as the advanced bifunctional electrocatalyst for EGOR-coupled HWS system.[810] Due to the regulated electronic structure, the introduction of heteroatom active centers, and the lattice strain, the $PtRh_{0.02}$@Rh NWs exhibited excellent HER and EGOR activities. The $PtRh_{0.02}$@Rh NWs obtained low overpotentials of 30.6 and 45.8 mV to reach a current density of 10 mA cm^{-2} for HER in alkaline and seawater electrolytes, respectively. Additionally, the $PtRh_{0.02}$@Rh NWs-based HER-EGOR two-electrode system can deliver 10 mA cm^{-2} at a cell voltage of 0.66 V in 0.1 M KOH solution containing 0.5 M EG, much smaller than that of OWS (1.57 V). In situ FTIR spectroscopy showed that $PtRh_{0.02}$@Rh NWs promote the formation of C_2 intermediates, contributable to the production of high-value glycolic acid.

5.3.1.5. Glycerol Oxidation. Glycerol ($C_3H_8O_3$) is a low-value-added byproduct during the production of biodiesel, which is used in pharmaceutical industry.[811] Electrocatalytic glycerol oxidation reaction (GLOR) can selectively produce various products and intermediates with higher economic value, such as dihydroxyacetone (DHA), glyceraldehyde (GALD), glyceric acid (GLA), formic acid (FA) and so on.[812] More importantly, the thermodynamic potential of GLOR toward FA is 0.69 V, making it possible to replace OER.

Several non-noble metal-based HER electrocatalysts have been proved to be active for GLOR, showing promise in GLOR-coupled HWS.[813] For instance, Shi's group synthesized the nickel−molybdenum−nitride nanoplates loaded on carbon fiber cloth (Ni−Mo−N/CFC) and its GLOR performance was tested in 1.0 M KOH containing 0.1 M glycerol.[813] The Ni−Mo−N/CFC showed an excellent GLOR activity with a potential of 1.30 V vs RHE to reach 10 mA cm^{-2}, much lower than that of OER (1.57 V vs RHE). In addition, the overpotential of Ni−Mo−N/CFC at 10 mA cm^{-2} for HER was only 40 mV. Therefore, the bifunctional Ni−Mo−N/CFC couple-based electrolyzer required a cell voltage as low as 1.36 V to achieve 10 mA cm^{-2}, with high FEs of 99.7% for hydrogen evolution and 95.0% for formate production. Furthermore, they confirmed that the formed formate comes from both the primary and secondary carbons of glycerol by using ^{13}C-labeled glycerol as a reactant.

Considering the critical role of hydroxyl adsorption on the catalyst surface for GLOR,[814] exploring (oxy)(hydr)oxides such as layered double hydroxides (LDHs) nanomaterials featuring high oxophilicity is desirable. Xie and coworkers designed ternary NiVRu-LDHs nanosheet arrays grown on nickel foam (NiVRu-LDHs NAs/NF).[815] Figure 69a schematically showed the synthetic process, in which NiVRu-LDHs nanosheet arrays with a thin thickness of 7∼8 nm were vertically grown on the NF substrate through a facile hydrothermal method. For GLOR, the NiVRu-LDHs NAs/NF needed low potentials of only 1.24 and 1.41 V vs RHE to deliver 10 and 300 mA cm^{-2} in 1.0 M KOH with 0.1 M glycerol, respectively, more negative than that for OER (>1.5 V vs RHE). In addition, the NiVRu-LDHs NAs/NF afforded 10 mA cm^{-2} with a low overpotential of 35 mV for HER, comparable to that of Pt/C. To understand the electrocatalytic GLOR mechanism, operando Raman spectroscopy analysis was conducted. As shown in Figure 69b, the characteristic peaks of the NiVRu-LDHs NAs/NF were basically stable for GLOR under the applied potential region (Figure 69b), while during OER process, two peaks at 476 and 555 cm^{-1} attributed to the $\delta(Ni^{III}-O)$ and $\nu(Ni^{III}-O)$ vibrations of Ni-OOH can be observed and these signals completely disappeared upon the addition of glycerol (Figure 69c). They believed that glycerol is oxidized by Ni^{III} with the participation of hydroxyl group and thus the Ni^{III} is reduced into Ni^{II}, accountable for the disappearance of the typical peaks of $Ni^{III}-OOH$. The authors also evaluated the bifunctional performance of NiVRu-LDHs NAs/NF for GLOR-coupled HWS. As shown in Figures 69d, the two-electrode glycerol electrolyzer afforded 10 and 100 mA cm^{-2} at voltages of 1.35 and 1.62 V, respectively, smaller than those of OWS (1.50 and 1.99 V). To further assess the potential for practical application, a flow cell utilizing the NiVRu-LDHs NAs/NF as bipolar electrodes was assembled (Figures 69e), and the device yielded an industry-level current density of 1 A cm^{-2} at the voltage of 1.933 V, saving 218 mV compared to that of OWS (Figures 69f). Also, DFT calculations showed that doping Ru optimizes Gibbs free energy of hydrogen adsorption, and facilitates the oxidation of Ni^{II} to Ni^{III} and C−C bond cleavage.

Similarly, Johnsson and coworkers introduced Pt nanoparticles at oxygen vacancies of MoO_x nanosheets, yielding the advanced MoO_x/Pt bifunctional electrocatalyst for both GLOR and HER in 1.0 M KOH with or without 0.1 M glycerol.[816] Combined electrochemistry experiments and DFT calculations revealed that the MoO_x nanosheets strongly coupled with Pt optimize the adsorption of glycerol molecules in GLOR and the dissociation of water molecules in HER, significantly enhancing the specific mass activity of Pt and the kinetics for both reactions. A 0.90 V voltage saving at 10 mA cm^{-2} can be obtained after adding 0.1 M glycerol.

5.3.2. Aldehydes Oxidation. Highly efficient production of hydrogen and simultaneous upgrading of aldehydes into value-added products like carboxylic acids are meaningful and attractive. Typical aldehydes include formaldehyde,[817−819] and acetaldehyde.[820] The formyl group-containing biomass-derivatives such as 5-hydroxymethylfurfural, furfural, and glucose will be discussed in the section of biomass oxidation (Section

https://doi.org/10.1021/acs.chemrev.3c00332
Chem. Rev. 2024, 124, 3694−3812

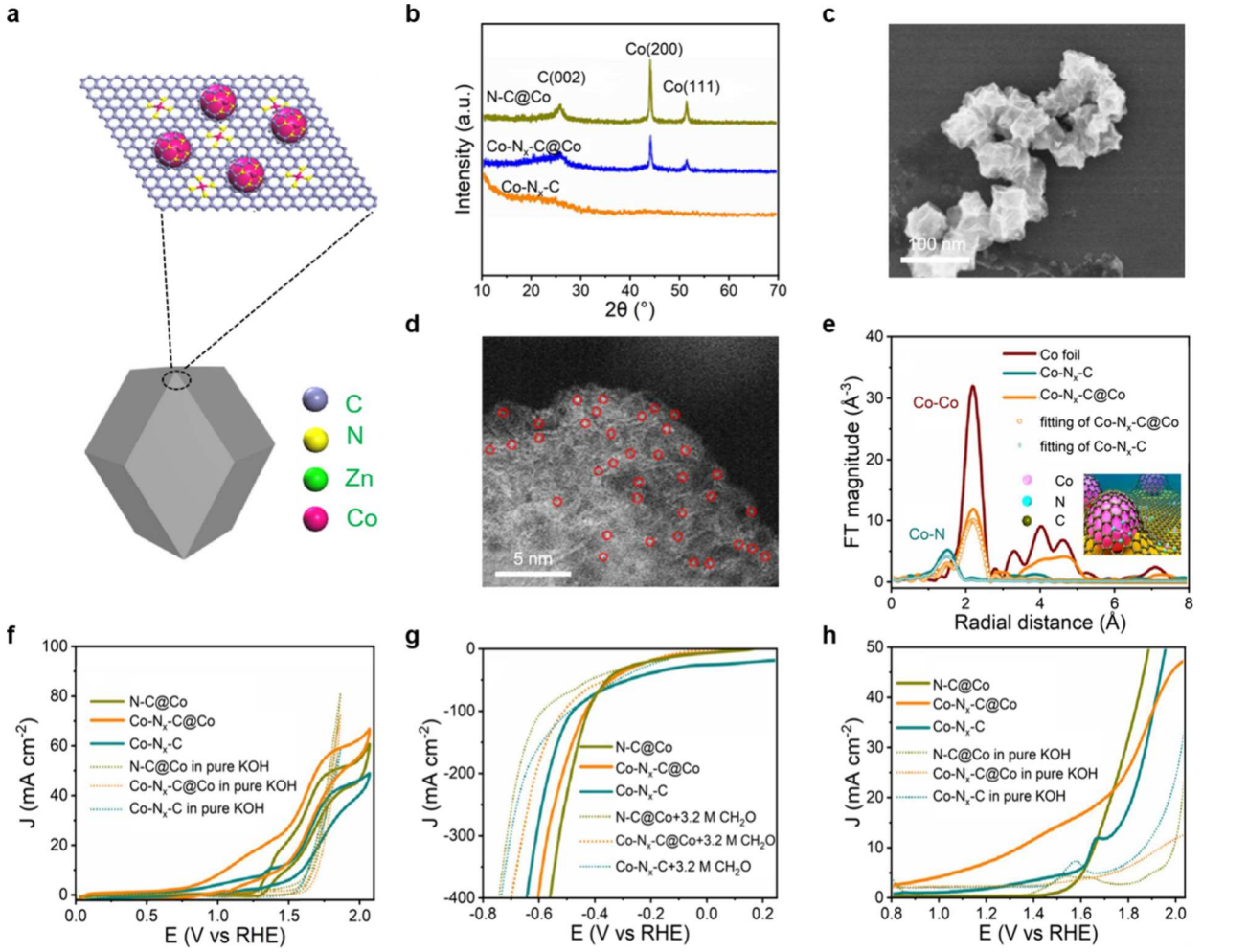

Figure 70. (a) Schematic of Co−N_x−C@Co. (b) XRD patterns of N−C@Co, Co−N_x−C@Co, and Co−N_x−C. (c) SEM image of Co−N_x−C@Co. (d) HAADF-STEM image of Co−N_x−C@Co. (e) FT-EXAFS spectra of Co−N_x−C@Co, Co−N_x−C, and Co foil. (f) CV curves of N−C@Co, Co−N_x−C@Co, and Co−Ni−C anodes in a divided cell containing 1.0 M KOH electrolyte with and without 3.2 M formaldehyde addition in the anode chamber. (g) LSV curves of N−C@Co, Co−N_x−C@Co, and Co−N_x−C for HER in 1.0 M KOH electrolyte with and without formaldehyde addition. (h) LSV curves of N−C@Co, Co−N_x−C@Co, and Co−N_x−C couples in 1.0 M KOH electrolyte with and without formaldehyde in a divided cell. Reproduced with permission from ref 822. Copyright 2021 American Chemical Society.

5.3.4). In light of lower price of formaldehyde (HCHO) relative to acetaldehyde, electrocatalytic formaldehyde oxidation reaction (FaOR) was routinely used to replace OER for hydrogen production from water, and its oxidative product, carbon monoxide, is a vital C_1 feedstock to produce hydrocarbons in chemical industry.[821] Although noble metal-based electrocatalysts have excellent performance in HER, they are easily poisoned due to the strong adsorption of CO produced from anodic FaOR. Therefore, advanced nonprecious metal-based electrocatalysts, such as Ni/Co-based nanomaterials, were explored for FaOR-assisted HWS.

With maximum atomic utilization, well-defined active centers and unique electronic properties, single-atom catalysts (SACs) have excelled as a rising star in the field of materials and catalysis.[9] Fan and coworkers fabricated Co−N_x−C@Co containing abundant atomically dispersed Co−N_4 sites and Co nanoparticles as a bifunctional electrocatalyst for HER and FOR, via pyrolysis of the Zn/Co bimetal ZIF (Figure 70a).[822] As shown in Figure 70b, three distinct diffraction peaks at 2θ = 23.6°, 43.0°, and 51.5° were indexed to C(002), and Co(111) and Co(200) of metallic Co, respectively, manifesting the formation of Co nanoparticles in Co−N_x−C@Co. SEM image showed polyhedral morphology of Co−N_x−C@Co with inward collapsed walls arising from pyrolysis of the organic ligand toward N-doped carbon (Figure 70c). The high-resolution HAADF-STEM image of Co−N_x−C@Co showed a few cobalt single atom sites marked with red circles (Figure 70d). FT-EXAFS spectra of Co−N_x−C@Co showed the coexistence of Co−Co bond at about 2.21 Å, and Co−N coordination with a relatively lower broad peak at around 1.47 Å (Figure 70e). For FaOR, after addition of 3.2 M HCHO into 1.0 M KOH, the potential to achieve 10 mA cm^{-2} decreased significantly from around 1.73 to 1.00 V vs RHE (Figure 70f). Such a potential for FaOR toward CO was lower than those of Co−N_x−C and N−C@Co (>1.25 V vs RHE). Also, the potential to afford 50 mA cm^{-2} for HER over Co−N_x−C@Co was smaller than those over Co−N_x−C and N−C@Co (Figure 70g). These results emphasized the synergistic effect of Co−N_4 sites and Co nanoparticles. As displayed in Figure 70h, the Co−N_x−C@Co couple based three-electrode electrolyzer for FaOR-assisted HWS required a potential of only 1.43 V vs RHE to achieve 10 mA cm^{-2}, 450 mV lower than that for OWS. To better understand the catalytical properties of Co−N_x−C@Co, DFT calculations were carried out by them and

https://doi.org/10.1021/acs.chemrev.3c00332
Chem. Rev. 2024, 124, 3694−3812

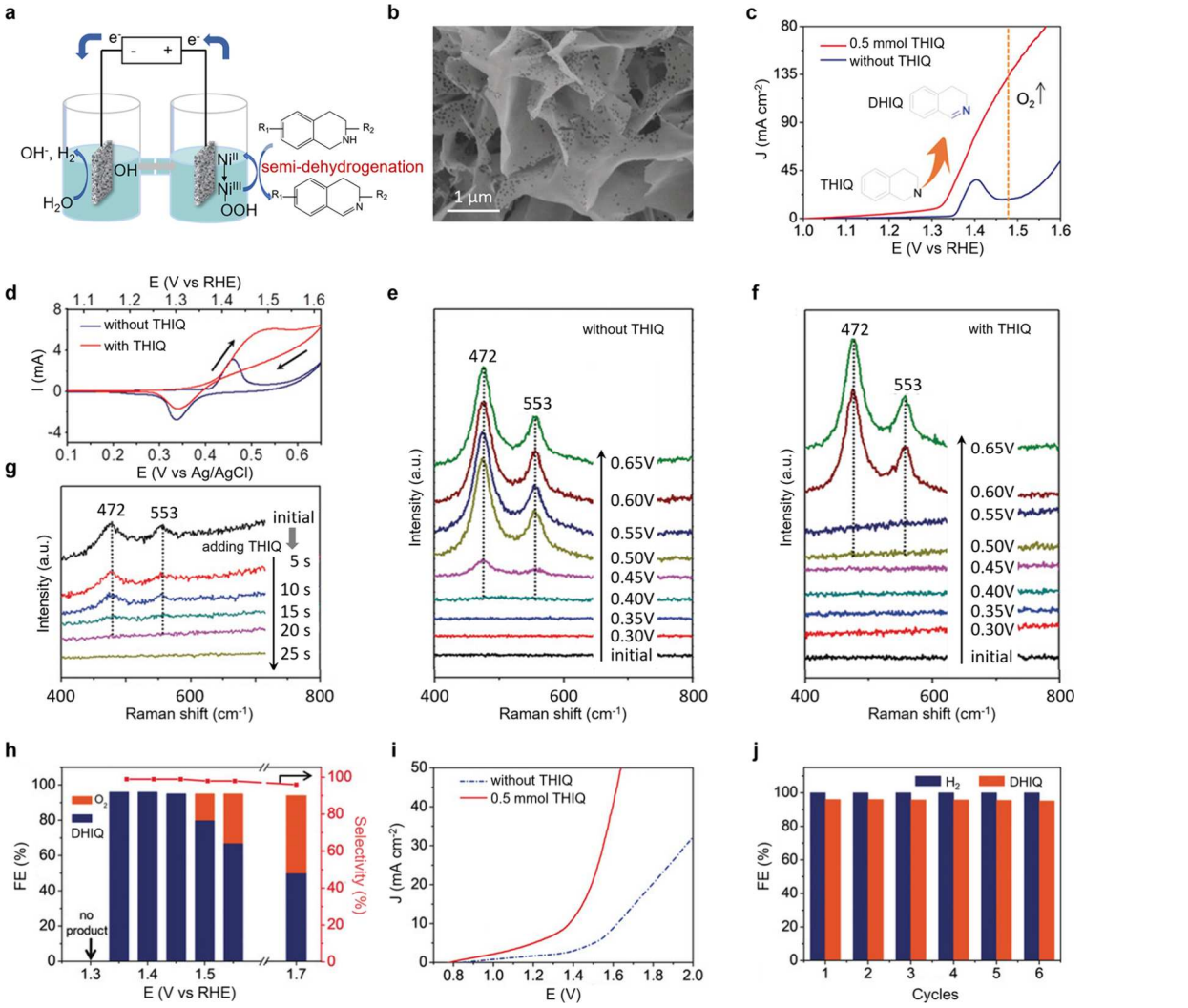

Figure 71. (a) Scheme of electrocatalytic semidehydrogenation of 1,2,3,4-tetrahydroisoquinoline (THIQ) coupled with HER in water. (b) SEM image of the bifunctional Ni_2P nanosheet electrode. (c) LSV curves of the Ni_2P anode at a scan rate of 5 mV s^{-1} in 40 mL 1.0 M KOH with and without 0.5 mmol THIQ. (d) CV curves of the Ni_2P anode in 0.1 M KOH with and without THIQ. (e, f) Potential-dependent in situ Raman spectra of the Ni_2P anode in the electrolyte without and with THIQ. (g) In situ Raman spectra collected under chronoamperometry test at 0.5 V vs Ag/AgCl in 0.1 M KOH solution without THIQ (initial) and after the addition of THIQ. (h) FEs and selectivities of dihydroisoquinolines (DHIQ) production at different potentials. (i) LSV curves of the Ni_2P couple-based electrolyzer in 1.0 M KOH with and without 0.5 mmol THIQ. (j) Cycle-dependent FEs of a Ni_2P couple-based electrolyzer for both H_2 and DHIQ production in 1.0 M KOH solution with 0.5 mmol THIQ. Reproduced with permission from ref 112. Copyright 2019 John Wiley and Sons.

the results revealed that Co−N_4 sites and Co nanoparticles with the lowest energy barrier promote the production of CO and hydrogen.

Zhou and collaborators synthesized the NiCo−NiCoP nanoparticles embedded P-doped carbon nanotubes on carbon cloth (NiCo−NiCoP@PCT/CC), with superior electrocatalytic activities for both HER and FaOR. It achieved 10 mA cm^{-2} at a low overpotential of 135 mV for HER and an ultralow potential of 1.18 V vs RHE for FaOR.[823] Accordingly, the NiCo−NiCoP@PCT/CC couple required a cell voltage of only 1.76 V for FaOR-coupled HWS at 50 mA cm^{-2}, 320 mV lower than that of OWS under the same conditions.

5.3.3. Amines Oxidation. With favorable oxidation relative to OER, amines oxidation reaction (AmOR) can produce various common precursors of fine chemicals such as pharmaceuticals, natural products and pesticides.[824−827] The main substrates of AmOR discussed in this section include 1,2,3,4-tetrahydroisoquinoline (THIQ) and primary amine like benzylamine (BAm). The corresponding reactions are THIQ semidehydrogenation (THIQ-SDH) and BAm oxidation reaction (BAmOR).

Electrocatalytic THIQ semidehydrogenation (THIQ-SDH) can generate the valuable chemical of dihydroisoquinoline (DHIQ), which demonstrates potential applications in pharmaceutical industry for the development of drugs in antitumor, antifungal, vasodilation, and monoamine oxidase inhibition.[828,829] Zhang and coworkers reported that SDH of THIQs with diverse substituent groups can replace OER to boost hydrogen evolution in water using a bifunctional Ni_2P nanosheet electrode (Figure 71a).[112] SEM image (Figure 71b) showed the porous nanosheet-assembled morphology of Ni_2P with open network. The THIQ-SDH catalyzed by Ni_2P was carried out in 1.0 M KOH containing 0.5 mM THIQ. As shown in Figure 71c, the current density increased dramatically at the potential beyond 1.32 V vs RHE and oxygen bubbles did not appear until the potential reached about 1.48 V vs RHE.

https://doi.org/10.1021/acs.chemrev.3c00332
Chem. Rev. 2024, 124, 3694−3812

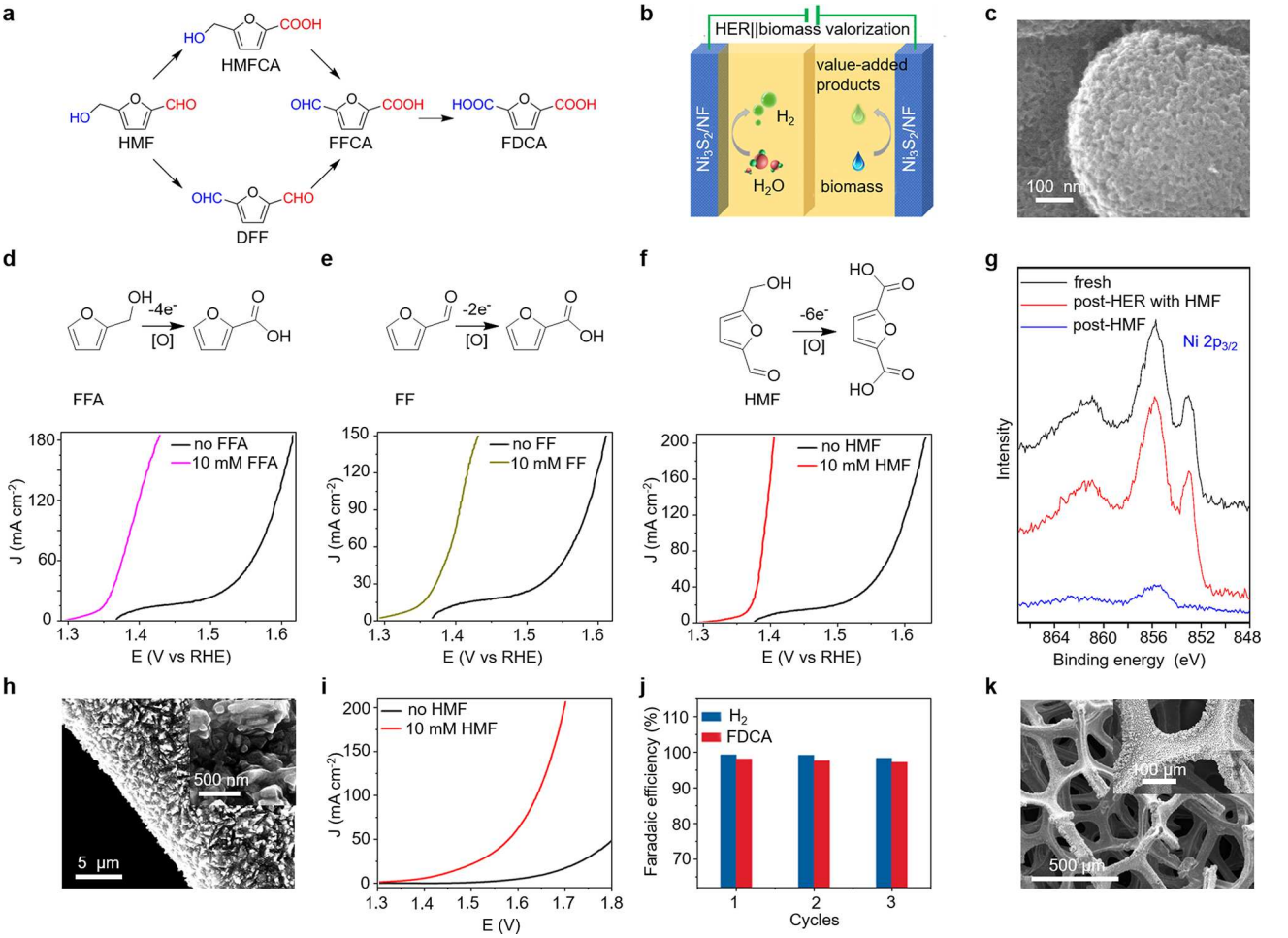

Figure 72. (a) Two possible pathways of HMF oxidation to FDCA. (b) Schematic of biomass oxidation-coupled HER over the bifunctional Ni_3S_2/NF electrocatalyst. (c) SEM image of as-prepared Ni_3S_2/NF. (d–f) Oxidation of selected organics to value-added products and the corresponding LSV curves over Ni_3S_2/NF at a scan rate of 2 mV s^{-1} in 1.0 M KOH with and without 10 mM organic substrates (FFA: furfuryl alcohol; FF: furfural; HMF: 5-hydroxymethylfurfural). (g) High-resolution XPS spectra of Ni $2p_{3/2}$ for the fresh, post-HER with HMF, and post-HMF Ni_3S_2/NF samples. Reproduced with permission from ref 99. Copyright 2016 American Chemical Society. (h) SEM images of Ni_2P NPA/NF. (i) LSV curves for a Ni_2P NPA/NF couple in 1.0 M KOH with and without 10 mM HMF. (j) FEs of Ni_2P NPA/NF couple for simultaneous H_2 and FDCA generation in 1.0 M KOH with 10 mM HMF for three successive electrolysis cycles. Reproduced with permission from ref 51. Copyright 2016 John Wiley and Sons. (k) SEM images of bifunctional Co–P/CF. Reproduced with permission from ref 591. Copyright 2016 American Chemical Society.

To gain insight into the mechanism for THIQ-SDH over Ni_2P anode, CVs and in situ Raman spectra at different applied potentials were collected and displayed in Figure 71d–f. The CV curves clearly showed the oxidation peak (0.4–0.5 V vs Ag/AgCl) of Ni^{II}/Ni^{III} without THIQ (Figure 71d) and meanwhile, two peaks at 472 and 553 cm^{-1} attributed to Ni–O vibrations of NiOOH started to appear (Figure 71e). Introducing THIQ into the electrolyte resulted in increased current density, as observed from the CV curve (Figure 71d). While the NiOOH peaks did not appear until the potential reached 0.6 V vs Ag/AgCl (Figure 71f). In addition, the NiOOH peaks disappeared gradually after adding THIQ (Figure 71g). These results gave an evidence that Ni^{III}–OOH first forms on the surface of Ni_2P under positive potential, and then quickly goes back to Ni^{II} after capturing the electron from THIQ toward DHIQ, so that the peaks of NiOOH cannot be observed from in situ Raman spectra during the THIQ-SDH process. By carefully controlling oxidative potentials, high FE of 96% and selectivity of 99% for DHIQ can be achieved (Figure 71h). Given the excellent HER activity of Ni_2P electrode (a low overpotential of 95 mV at 10 mA cm^{-2}), the authors constructed a Ni_2P couple-based two-electrode electrolyzer for both HER and THIQ-SDH with higher energy efficiency relative to OWS. As shown in Figure 71i, the cell voltage at 20 mA cm^{-2} for the assembled electrolyzer was 300 mV smaller than that of OWS. Long-term electrolysis at a cell voltage of 1.50 V demonstrated high FEs of about 100% and 96% for hydrogen and DHIQ, respectively (Figure 71j).

Benzonitrile, produced from BAmOR, is a useful precursor for the synthesis of various pharmaceuticals, natural products, and pesticides.[830] Chen and coworkers successfully synthesized the ultrathin Ni_2P nanomeshes with 1.9 nm thickness on NF (Ni_2P-UNMs/NF) for electrocatalytic BAmOR and HER toward energy-saving benzonitrile and hydrogen coproduction.[831] Particularly, the Ni_2P-UNMs/NF couple needed a cell voltage of 1.41 V to achieve 10 mA cm^{-2} in 1.0 M KOH containing 0.125 M benzylamine. The FEs of benzonitrile and hydrogen were calculated to be around 98% and 100%, respectively.

https://doi.org/10.1021/acs.chemrev.3c00332
Chem. Rev. 2024, 124, 3694–3812

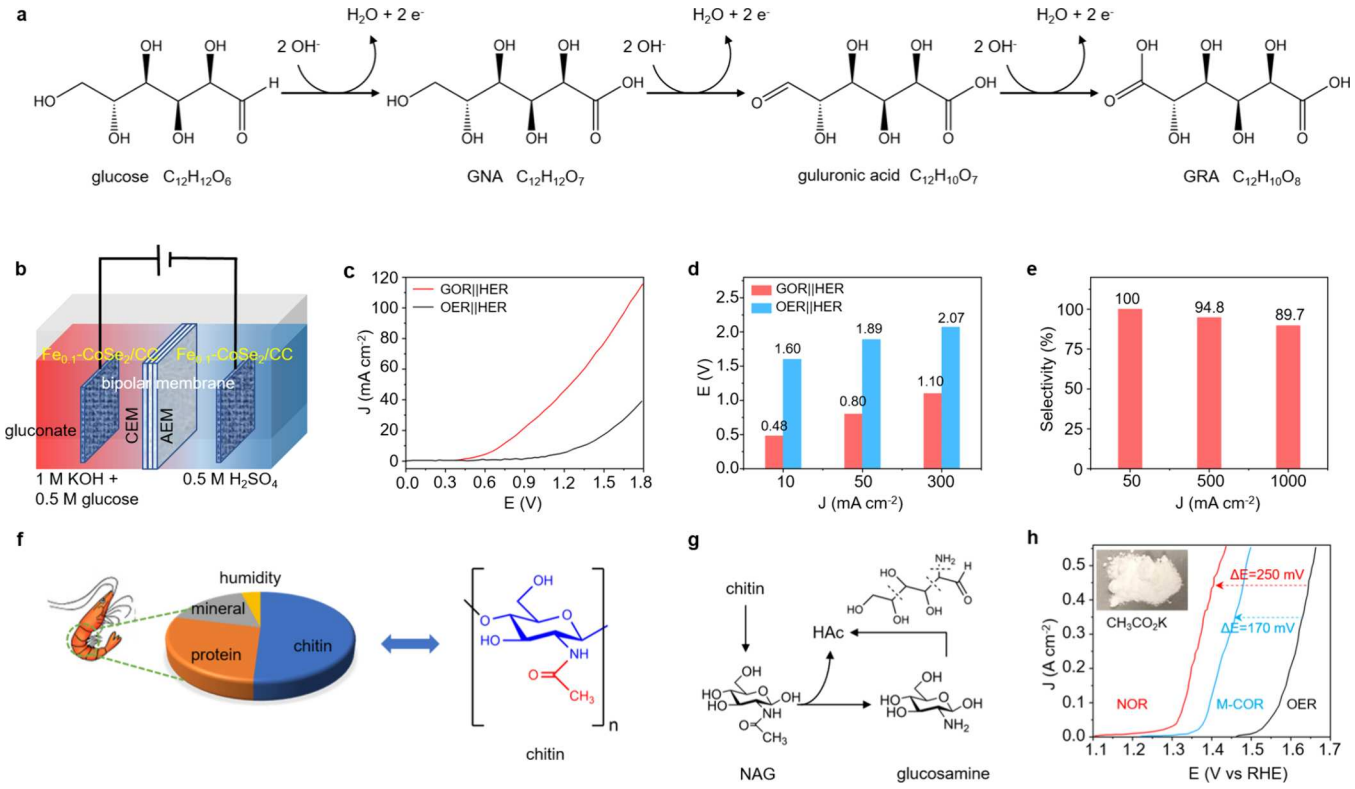

Figure 73. (a) Schematic of the possible pathway for electrochemical oxidation of glucose to GNA and GRA. Reproduced with permission from ref 846 under the terms of a CC-BY 4.0 license. Copyright 2020 The Authors, published by Springer Nature. (b) Schematic of asymmetric-electrolyte electrolyzer for GOR-assisted HWS. (c) LSV curves for the GOR-assisted HWS and OWS over $Fe_{0.1}$-$CoSe_2$/CC with ΔpH = 14. Reproduced with permission from ref 847. Copyright 2020 Elsevier. (d) Cell voltages of GOR-coupled HWS and OWS over Fe_3O_4/Au/CoFe-LDH couple at different current densities. (e) Selectivity of GOR over Fe_3O_4/Au/CoFe-LDH couple at different current densities. Reproduced with permission from ref 848. Copyright 2021 John Wiley and Sons. (f) Schematic of abundant biopolymer chitin existed in the exoskeleton of insects and crustaceans. (g) Main reaction pathway for selective electroreforming of chitin to acetic acid (HAc). (h) LSV curves of oxidative reactions in 1.0 M KOH (OER; black curve) and 1.0 M KOH containing 2.2 g L^{-1} N-acetyl glucosamine (red curve labeled with NOR) or 3.5 g L^{-1} milled chitin (blue curve labeled with M-COR). The arrow indicates the shift of potential after adding the corresponding biomass. Inset: a picture of 436 mg of oxidation product, potassium acetate (CH_3COOK). Reproduced with permission from ref 835 under the terms of a CC-BY 4.0 license. Copyright 2021 The Authors, published by Springer Nature.

5.3.4. Biomass Oxidation. Biomass is the only accessible and renewable carbon source with tremendous annual production and wide distribution, and bioeconomy is regarded as an alternative to petroleum refining without altering our current ecosystem.[832−835] Oxidative reforming of raw biomass holds great potential to produce alternatives to petrochemical industry-based platform chemicals. Particularly, electrocatalytic biomass oxidation represents a green process relative to traditional industrial approaches, and it is possible to couple selectively favorable biomass oxidation with HER for energy-efficient chemicals and hydrogen coproduction.

5.3.4.1. Furans Oxidation. Furanic compounds like 5-hydroxymethylfrufural (HMF, $C_6H_6O_3$) and furfural ($C_5H_4O_2$), as representative top biomass-derived building block chemicals, are dehydration products of the corresponding carbohydrates and can be used as versatile precursors for the production of plastics, polymers, and fuels.[836−838] For example, 2,5-furandicarboxylic acid (FDCA) obtained from HMF oxidation reaction (HMFOR) is a value-added alternative to terephthalic acid for the synthesis of polyamides, polyesters, and polyurethanes (Figure 72a).[839] Our group reported a series of bifunctional electrocatalysts including Co−P/CF,[591] 3D Ni_2P nanoparticle arrays on nickel foam (Ni_2P NPA/NF),[51] Ni_3S_2/NF,[99] and hp-Ni[111] for HWS coupled with oxidation of various biomass like furfuryl alcohol (FFA), furfural (FF) and HMF (Figure 72b). For instance, the hierarchically porous Ni_3S_2/NF was prepared by direct sulfurization of NF and the SEM image showed a morphology of stacked nanoparticles with numerous mesopores (Figure 72c). The LSV curves showed that high current density can be achieved at lower potentials after adding 10 mM FFA (Figure 72d), FF (Figure 72e), or HMF (Figure 72f), exhibiting preferable furans oxidation-assisted HWS relative to OWS. Using HMF oxidation reaction (HMFOR) as a model, we found that although the overall 3D hierarchically porous configuration of Ni_3S_2/NF can be maintained after stability test, the surface reconstruction happened indeed, different from that for HER. As shown in Figure 72g, high-resolution Ni $2p_{3/2}$ XPS spectra demonstrated the appearance of oxidized Ni species with increased intensity ratio relative to those of fresh and post-HER controls, which were believed to be real active species for HMFOR. We also proved the negligible effect of HMF on Ni_3S_2/NF-catalyzed HER, as revealed by the almost overlapped LSV curves and small change of Tafel slope (from 128 to 136 mV dec^{-1}) in 1.0 M KOH after adding 10 mM HMF. The Ni_3S_2/NF couple-based HWS electrolyzer can achieve 100 mV cm^{-2} at a cell voltage of only 1.64 V, 200 mV smaller than that for OWS. Additionally, the generated

https://doi.org/10.1021/acs.chemrev.3c00332
Chem. Rev. 2024, 124, 3694−3812

hydrogen at cathode and FDCA at anode featured high FEs of 100 and 98%, respectively.

Similarly, direct phosphorization of nickel foam (NF) can obtain the Ni_2P NPA/NF bifunctional electrocatalyst.[51] SEM images of Ni_2P NPA/NF showed a rough and porous morphology composed of Ni_2P nanoparticles (Figure 72h). Electrochemical measurements indicated that introducing 10 mM HMF in 1.0 M KOH electrolyte leads to obviously decreased onset potential from 1.50 to 1.35 V vs RHE for Ni_2P NPA/NF, confirming the favorable HMFOR relative to OER. Also, the cell voltage for integrated HER and HMFOR over Ni_2P NPA/NF couple was reduced from 1.80 to 1.58 V at 50 mA cm^{-2} (Figure 72i). As shown in Figure 72j, the high FEs for hydrogen (100%) and FDCA (98%) can be obtained via product quantification of the generated gas and liquids after long-term electrocatalysis at 1.5 V with charge passing 59 C. By employing a facile potentiodynamic deposition, we prepared the bifunctional Co−P on copper foam (Co−P/CF) electrocatalyst. SEM images at different magnifications displayed a porous morphology containing numerous Co−P particles on copper foam (Figure 72k). For the HMFOR-assisted HWS, the Co−P/CF couple can afford 20 mA cm^{-2} at a cell voltage of only 1.44 V in 50 mM HMF-contained 1.0 M KOH.[591]

Choi's group recently used similar electrodeposition to prepare nanocrystalline Cu foam (NCF) as a bifunctional electrode for HMFOR/HER in 0.1 M KOH containing 5 mM HMF, with high FEs of 95.3% and 100% for FDCA and hydrogen, respectively.[840] More recently, Fu and coworkers constructed a robust bifunctional electrocatalyst (MoO_2−FeP@C) with improved HER and HMFOR performance due to the mutual promotion role of the two components.[620] The resulting MoO_2−FeP@C featuring a novel porous nanospindle morphology composed of a carbon-encapsulated MoO_2−FeP heterojunction was fabricated by self-sacrificial templating followed by low temperature phosphorization. The spindle-like structure with numerous pores of MoO_2−FeP@C increased the accessible surface areas, enabling adequate contact between active sites and reactants. Consequently, the MoO_2−FeP@C couple-based electrolyzer required a low cell voltage of 1.486 V at 10 mA cm^{-2} with 99.4% HMF conversion, 98.6% FDCA selectivity, and 97.8% FE for FDCA, higher than those for FeP@C and MoO_2@C counterparts.

Other advanced bifunctional electrocatalysts such as carbon-coupled Ni_3N nanosheet (Ni_3N@C),[841] Co_3O_4 nanowires on NF (CoNW/NF),[842] 3D N-doped MoO_2/Ni_3S_2 core−shell nanoarray,[843] and NiSe@NiO_x core−shell nanowires[844] were also reported for the HMFOR-coupled HWS with desirable electrocatalytic performance.

5.3.4.2. Carbohydrates Oxidation. Carbohydrates are probably the most abundant and widespread organic substances in nature. Glucose is a widely distributed and important monosaccharide with advantages in low cost, nontoxicity, and easy accessibility from biomass.[845] Glucose oxidation reaction (GOR) can produce value-added gluconic acid (GNA), glucaric acid (GRA), gluconate, and so on (Figure 73a), endowing it with high potential to couple with HER for hybrid water splitting.[846]

Wen and coworkers designed and fabricated a bifunctional electrode of Fe-doped $CoSe_2$ nanowires on carbon cloth ($Fe_{0.1}$-$CoSe_2$/CC).[847] The resulting electrocatalyst can afford 100 mA cm^{-2} for HER at a small overpotential of 270 mV in 0.5 M H_2SO_4. Besides, the excellent electrocatalytic performance toward GOR was also achieved, as revealed by the low onset potential of 1.12 V vs RHE in 1.0 M KOH electrolyte containing 0.5 M glucose. The $Fe_{0.1}$-$CoSe_2$/CC couple-based electrolyzer required a reduced cell voltage of 0.72 V at 10 mA cm^{-2} for HWS relative to OWS toward hydrogen and gluconate coproduction (Figure 73b,c), indicative of significant decrease of energy consumption assisted by GOR. To gain insight into the eminent activities of $Fe_{0.1}$-$CoSe_2$/CC for both HER and GOR, the authors conducted DFT calculations. The model for $Fe_{0.1}$-$CoSe_2$/CC was first optimized via Metropolis Monte Carlo simulation, which identified the position of dilute Fe. They then used the "detective pin" method to confirm the active role of "Co" in $Fe_{0.1}$-$CoSe_2$. With these results in hand, the authors calculated Gibbs free energy changes (ΔG) of the steps in both HER and GOR. The results showed that the ΔG of adsorbed hydrogen (ΔG_{H^*}) on $Fe_{0.1}$-$CoSe_2$ is more neutral relative to $CoSe_2$ and $FeSe_2$, suggestive of its preferable HER activity. On the other hand, the energy barrier of RDS for GOR (first step) over $Fe_{0.1}$-$CoSe_2$ is ∼0.04 eV lower than that over $CoSe_2$, accountable for its improved GOR activity.

Introducing a small amount of noble metals into the nonprecious electrocatalysts would lead to improved activities for both HER and GOR. Zhang and coworkers synthesized the Fe_3O_4/Au/CoFe-LDH with a sandwich structure via spontaneous galvanic displacement due to the thermodynamic potential difference between $AuCl_4^-$/Au (+1.002 V), Fe$(OH)_2$/Fe$(OH)_3$ (+0.56 V), and Co$(OH)_2$/Co$(OH)_3$ (−0.17 V).[848] Combined structural and electrochemical characterizations revealed that Fe_3O_4 serves as active site and stabilizer for HER, CoFe-LDH acts as substrate and Fe precursor of Fe_3O_4, and the metallic Au at interlayer is active for GOR and accelerate the electron transfer between Fe_3O_4 and CoFe-LDH basal plane due to its metallic conductivity. The resulting Fe_3O_4/Au/CoFe-LDH therefore achieved the current densities of 10, 50, and 300 mA cm^{-2} at respective cell voltages of 0.48, 0.80, and 1.10 V for GOR-coupled HWS, in stark contrast to those for OWS (Figure 73d). Besides, the Fe_3O_4/Au/CoFe-LDH couple exhibited high selectivity of GOR relative to OER, even at a large current density of 1000 mA cm^{-2} (Figure 73e). Likewise, Yang and coworkers integrated Ru nanoparticles with nickel boride grown on nickel foam (Ru@Ni−B/NF).[849] The as-prepared Ru@Ni−B/NF was also active for GOR-assisted HWS, with small cell voltages of 1.24 and 1.36 V to deliver 10 and 50 mA cm^{-2}, respectively.

In addition to glucose, chitin, composed of β-(1,4)-linked N-acetyl-β-D-glucosamine, is another abundant natural carbohydrate in insect skeletons and crustacean shells (Figure 73f). Depolymerizing it leads to N-acetylglucosamine (NAG) which can be further oxidized to acetic acid (HAc) or deacetylated to glucosamine. Further, opening the pyranose ring of glucosamine can also produce HAc (Figure 73g).[835] We and collaborators coupled chitin oxidation reaction (COR) to HER for cogeneration of acetate (with over 90% yield) and hydrogen, with reduced energy inputs due to the favorable kinetics of COR relative to OER.[835] To increase the solubility of chitin, ball-milling pretreatment was conducted, and the hp-Ni was used as an electrocatalyst. As shown in Figure 73h, about 170 mV potential saving can be obtained by replacing OER with milled chitin oxidation reaction (M-COR) over hp-Ni in 1.0 M KOH with 3.5 g L^{-1} milled chitin. Notably, the potential requirement can be further reduced by 250 mV through introducing the NAG (2.2 g L^{-1}) at anode, and precipitation extraction of the resulting anolyte can gain potassium acetate powder (Figure 73h inset). DFT calcu-

https://doi.org/10.1021/acs.chemrev.3c00332
Chem. Rev. 2024, 124, 3694−3812

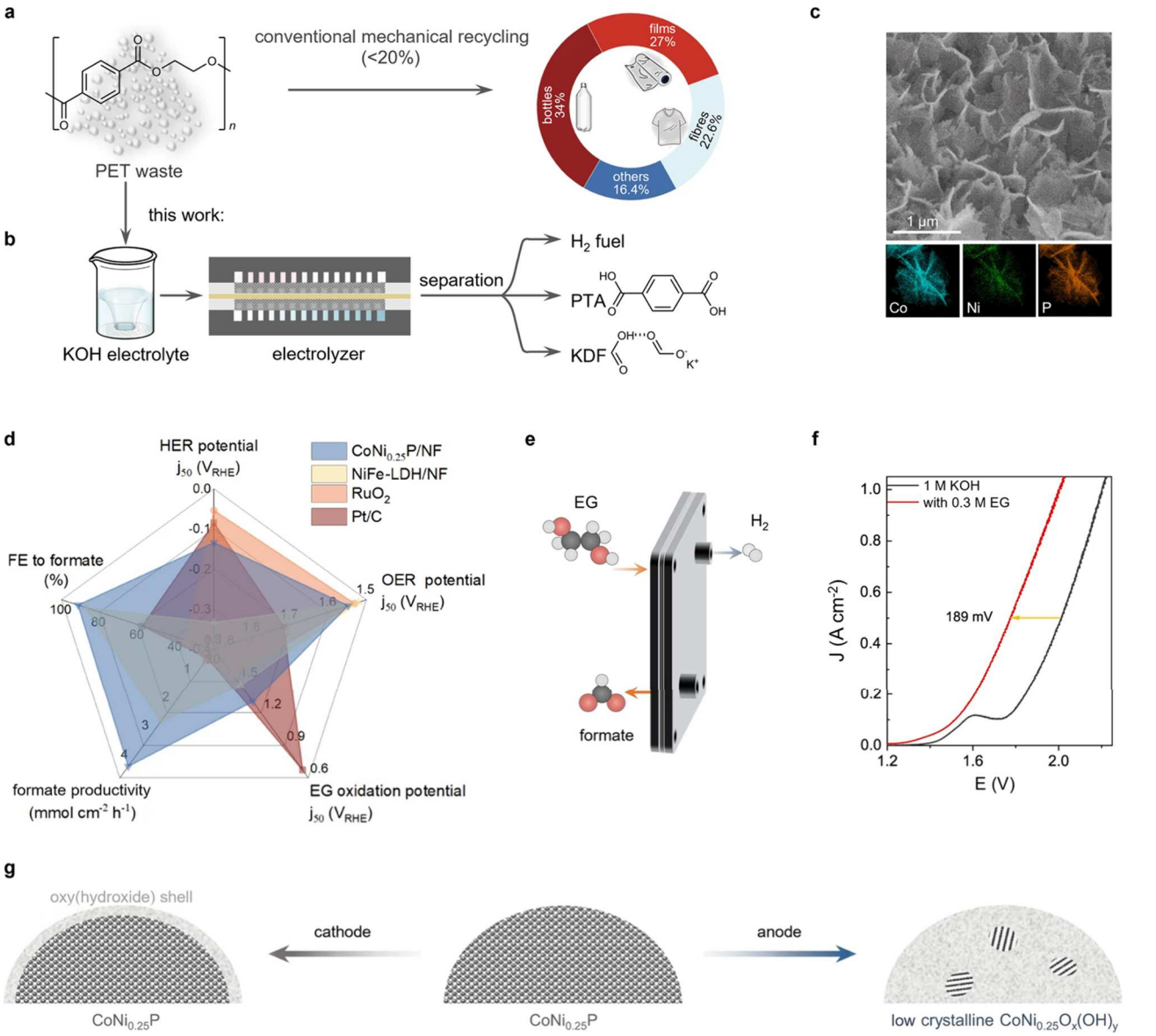

Figure 74. (a) Conventional route for PET recycling. (b) Scheme of electrocatalytic PET upcycling to commodity chemicals and hydrogen. (c) SEM and elemental mapping images of $CoNi_{0.25}P$/NF. (d) Comparison of the electrocatalytic performance of $CoNi_{0.25}P$/NF and known electrocatalysts. (e) MEA setup for EGOR-paired HWS. (f) LSV curves for OWS and EGOR-paired HWS in the MEA flow reactor at a scan rate of 10 mV s^{-1}. (g) Schematic illustration of the structural evolution of $CoNi_{0.25}P$ electrocatalyst under reaction conditions. Reproduced with permission from ref 803 under the terms of a CC-BY 4.0 license. Copyright 2021 The Authors, published by Springer Nature.

lations disclosed that the energy barriers needed for opening pyranose-ring and breaking glycosidic bond are much lower than that of OER, consistent with the electrochemical results.

5.3.5. Plastic Wastes Oxidation. Plastic wastes with environmental and biological threats are a largely untapped resource for manufacturing chemicals and fuels. Nowadays, 79% of the produced plastics are discarded and accumulated in landfills or aquatic systems, which have caused severe environmental and biological threat.[850−853] In this respect, upcycling the plastic wastes into value-added products is essential for our sustainable development.

Polyethylene terephthalate (PET) is produced ~70 million tons annually and only a small fraction (<20%) of them are recycled via the mechanical route (Figure 74a).[803,852] Considering the readily digestion of PET into its monomers including ethylene glycol (EG) and terephthalic acid (PTA),[414] Duan and coworkers developed an electrocatalytic route for oxidative upcycling of PET waste paired with HER in KOH electrolyte (Figure 74b).[803] The resulting EG from KOH-pretreated PEG was subjected to C−C cleavage toward formate through bifunctional $CoNi_{0.25}P$-driven anodic electrooxidation, along with hydrogen generation. The bifunctional nickel-modified cobalt phosphide on NF ($CoNi_{0.25}P$/NF) electrocatalyst was prepared by a facile tandem electrodeposition and subsequent phosphorization. SEM and elemental mapping images of $CoNi_{0.25}P$/NF showed the morphology of nanosheets-stacked arrays with homogeneous distribution of Co, Ni, and P on matrix (Figure 74c). HRTEM further demonstrated the presence of CoP-Ni_2P heterojunctions in $CoNi_{0.25}P$. Electrochemical measurements in 1.0 M KOH revealed the superior HER, OER, and EG (0.3 M) oxidation performance of $CoNi_{0.25}P$/NF, comparable to Pt/C, RuO_2, and NiFe-LDH/NF counterparts (Figure 74d). Specifically, adding 0.3 M EG into electrolyte negatively

https://doi.org/10.1021/acs.chemrev.3c00332
Chem. Rev. 2024, 124, 3694−3812

shifted the potential at 50 mA cm^{-2} from >1.50 V vs RHE for OER to <0.70 V vs RHE for EG oxidation reaction (EGOR) over $CoNi_{0.25}P$/NF, indicative of more favorable EGOR than OER. Additionally, the $CoNi_{0.25}P$/NF displayed the highest FE for formate (91.3%) with excellent productivity of 4.01 mmol cm^{-2} h^{-1} at 1.7 V vs RHE, along with good HER activity (Figure 74d). Subsequently, the authors fabricated a two-electrode zero-gap membrane-electrode assembly (MEA) flow reactor catalyzed by the bifunctional $CoNi_{0.25}P$/NF couple for energy-saving formate and hydrogen coproduction (Figure 74e). Compared with the traditional H-type electrolyzer, the MEA possesses reduced Ohmic resistance, thus industrial-grade current density can be gained.[854,855] The MEA reactor afforded a significantly higher current density (500 mA cm^{-2}) at a low cell voltage (<1.8 V), in contrast to that in H-cell (<150 mA cm^{-2}). Moreover, the cell voltage at 500 mA cm^{-2} for EGOR-assisted HWS was 189 mV smaller than that for OWS, as shown in Figure 74f. To understand the evolution of $CoNi_{0.25}P$ active species during HER and EGOR, a range of physiochemical characterizations including HRTEM, Raman spectroscopy, and XAS were employed. TEM image showed the fresh $CoNi_{0.25}P$ species undergo complete reconstruction after EGOR to a low-crystalline metal oxy(hydroxide) analogue. Raman spectra revealed the peaks at 410−720 cm^{-1} attributed to $CoO_x(OH)_y$ after EGOR and OER. Co K-edge FT-EXAFS spectra also confirmed this oxidative restructuring of fresh $CoNi_{0.25}P$. In comparison, the main structure of $CoNi_{0.25}P$ during HER can be maintained, with slight oxidation and dissolution toward an amorphous metal oxy(hydroxide) shell (Figure 74g). In other words, the fresh $CoNi_{0.25}P$ evolved into a $CoNi_{0.25}P/CoNi_{0.25}O_x(OH)_y$ core−shell structure at cathode, while it was drastically oxidized and reconstructed into low-crystalline $CoNi_{0.25}O_x(OH)_y$ at anode.

Zhu and coworkers synthesized an atomic Ni-doped CoP with ordered macroporous superstructure (OMS−Ni_1−CoP) as a bifunctional electrocatalyst for energy-saving HWS via coupling HER and EGOR in PET plastic hydrolysate.[856] A low voltage of 1.57 V was required to afford 10 mA cm^{-2}. Huang and coworkers synthesized the Ni_3N/W_5N_4 Janus nanostructure with barrier-free heterointerface.[857] Thanks to the interface synergy, superhydrophilicity and unique Janus structure, the as-prepared Ni_3N/W_5N_4 displayed Pt-like HER performance and high activity toward PET electroreforming, with a low voltage of 1.47 at 50 mA cm^{-2}, 230 mV lower than that for OWS (1.70 V). In addition, the FE for formate at anode was high to ∼85%, and a high solar-to-hydrogen (STH) conversion efficiency of 16.04% under 1 sun illumination can be achieved.

Polylactic acid (PLA) plastic with good thermoplasticity is widely applied to fabricate disposable goods. The theoretical thermodynamic potential of PLA electro-oxidation reaction (PAOR) toward HAc is much lower than that of OER, which can boost the energy conversion efficiency of hydrogen generation. Gao and collaborators fabricated cobalt selenide nanosheets on nickel foam ($CoSe_2$/NF) as a bifunctional electrocatalyst for PAOR-assisted HWS in 1.0 M KOH with a cell voltage of only 1.37 V to reach 10 mA cm^{-2}, in contrast to that for OWS (1.63 V).[858] Also, the high conversion rate of 87% for HAc from PLA was yielded at anode.

6. CONCLUSION AND PERSPECTIVE

This Review focuses on the advancements in exploring bifunctional electrocatalysts for overall and hybrid water splitting for energy-efficient hydrogen generation. With the flourish of synthetic methodologies of nanomaterials like shape/composition-controlled synthesis, defect engineering, heteroatom doping, surface modification, interface hybridizing, etc., various bifunctional electrocatalysts consisting of noble metals (e.g., Ru and Ir), nonprecious metals (e.g., Fe, Co, Ni, Mo, Cu, Mn, etc.), and metal-free nanocarbons have been reported with promising activities for potentially large-scale employment. In particular, the dynamic electrochemical reconstruction which endows them with bifunctionality and modulated electrocatalytic performance for both reduction and oxidation reactions has been highlighted through advanced characterization techniques based on electrochemistry (cycle voltammetry, chronopotentiometry, electrochemical impedance spectroscopy, underpotential deposition, and CO stripping), optics (FTIR, Raman and UV−vis spectroscopy), X-rays (XRD, XPS, XAS, XES, and XRF), electron microscopy (SEM and TEM), scanning probe microscopy (STM, AFM, SECM, and SECCM), auger electron, ion scattering, atom probe tomography, Mössbauer spectroscopy, and mass spectrometry. To further address the issues associated with OER like sluggish kinetics, low value of O_2, possible H_2/O_2 mixing and formation of ROS, alternative oxidation reactions driven by bifunctional electrocatalysts have been introduced to replace OER for hybrid water splitting. Based on the functionalities of the substrates, these alternative oxidation reactions can be divided into sacrificing agents oxidation that consumes valuable substrates (hydrazine, ammonia and urea), pollutants oxidative degradation using environmental pollutants as oxidative substrates (formic acid/formate, phenol, sulfur compounds and organic dyes), and oxidative upgrading of selected organics (alcohols, aldehydes, amines, biomass, and plastic wastes). All these oxidative reactions exhibit favorable kinetics relative to OER and therefore effectively reduce energy consumption for hydrogen production, and in some case produce value-added chemicals for food, pharmacy, and chemical industries toward maximum return on energy investment. Although great progress has been made, we are still facing several challenges and there is a long way ahead for the efficient synthesis, characterization, understanding, and large-scale implementation of bifunctional electrocatalysts-driven overall and hybrid water splitting toward affordable hydrogen generation in a sustainable manner (Figure 75).

First, although various synthetic strategies including hydrothermal/solvothermal growth, electrodeposition, soft/hard templating, elevated-temperature annealing, photochemistry, and so on, are effective to prepare diverse bifunctional electrocatalysts, they usually produce catalytic materials at small-scale in laboratory. Such perfect synthetic configurations are suitable for electrocatalytic research, the attempt to simplify scale up synthesis for practical membrane electrode assemblies or even reactor stack fabrication would fail due to the variations in mass/heat transfer, operability, and cost at large scale. Moreover, many synthetic methods involve toxic gases like NH_3, PH_3, S, etc., and tedious procedures, making them neither economical nor environmentally benign. Thus, developing green, affordable, and rapid methodologies for large-scale synthesis of bifunctional electrocatalysts is urgent and of great practical importance. In this regard, recently developed heating methods based on nonthermal radiation such as microwave, joule heat, plasma, and laser, along with electroshock and 3D-printing deserve to be introduced. Novel containers like multichannel flow reactors are worth being

https://doi.org/10.1021/acs.chemrev.3c00332
Chem. Rev. 2024, 124, 3694−3812

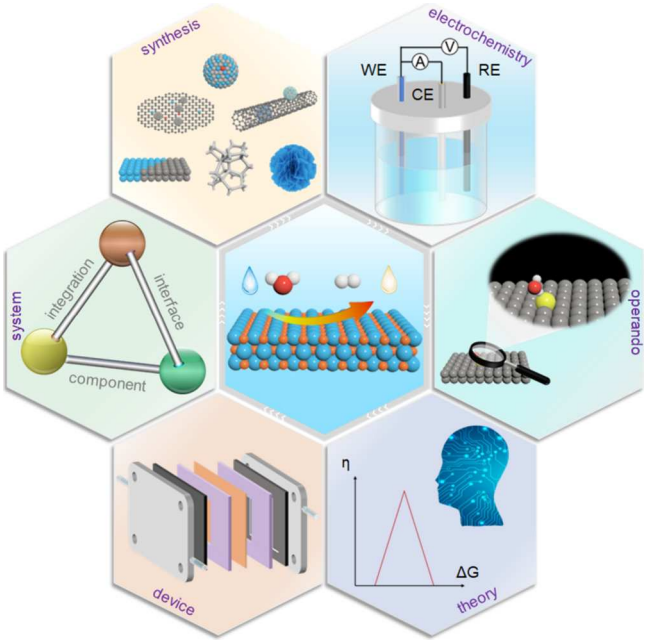

Figure 75. Perspective of system materials engineering for bifunctional electrocatalysts toward overall and hybrid water splitting.

explored as well for large-scale synthesis due to the improved mass/heat transport via continuously circulating the precursors' solutions and products. Given the triphase interface properties of water splitting reaction with sluggish kinetics, precisely designing the bifunctional electrocatalysts with 3D hierarchically open porous architectures, plentiful defects, and strong interface/electronic coupling would improve both the accessibility and the activity of active sites. For hybrid water splitting, the introduced substrates like biomass or relevant reactive intermediates at anode compartment would diffuse to the cathode compartment due to crossover effect, and then specifically adsorb on the surface of bifunctional electrocatalysts, which may block, deactivate or even poison the underlying active sites during both HER and oxidation reactions. Additionally, for selective oxidation of alternative substrates, the electrocatalytic interface is also critical. Accordingly, accurately tailoring the surface or adjusting the local microenvironment of bifunctional electrocatalysts, such as surface coating of charged polymer, porous membrane, and inorganic Lewis acid/base layer, or introducing external field (e.g., magnetic field) is welcome to suppress the specific adsorption and improve the products selectivity.

Second, electrochemical reconstruction during overall and hybrid water splitting that form amorphous/low-crystalline and defects-rich active species provides a new tool to design advanced bifunctional electrocatalysts, while full understanding of the whole reconstruction is still not yet achieved due to the complex convolution of chemical reactions, mass transport, and catalytic interfaces which involve multiple processes like electrocatalysts restructuring/reactants or intermediates conversion at the triphase interface, bubble formation/release, electrolytes diffusion, along with dynamic changes of surface forces, wetting properties, electric field, and so on. Although a suite of in situ/operando characterization techniques have been adopted to track the dynamic evolution of electrochemical reconstruction, the limited time/space resolution is insufficient to accurately judge the instantaneous reconstruction processes. For example, numerous electrochemical reconstructions like electrooxidation occur on the order of picoseconds to nanoseconds,[118] such a time interval is too short to acquire data for many characterization technologies like FTIR, Raman, XAS, XPS, SPM, etc. Additionally, the prevailing characterization techniques, in many cases, can only provide the average or bulk information on reconstruction instead of precise local changes. Given that the electrochemical reconstruction usually involves multicomponent evolution at the local electrolyte-electrode interface with low content and crystallinity (e.g., amorphous phases), one or few in situ/operando characterization techniques cannot give us a full picture of what happens for the entire process due to their own limitations in terms of detection range and resolution. Consequently, developing correlative characterizations and innovative techniques with high spatiotemporal resolution and broad detection range as well as massive data analysis system such as machine learning is strongly recommended to monitor the comprehensive reconstruction in real-time. Note that electrochemical reconstruction is usually accompanied by compositions detaching or even structures deterioration. These detached species may dissolve in electrolytes, attach on the surface of electrocatalysts, or interact with reactants/intermediates, inevitably changing the catalytic interface and complicating the study of activity−structure correlation. Intentionally introducing exotic analogs to electrolytes to mimic the real electrocatalytic interfaces can offer some insightful information.

Third, theoretical simulations like DFT, combined with in situ/operando characterizations, have shown great success in understanding the mechanisms for both HER and OER. With recent achievements in computing power, algorithms, and big data availability from experiment and computation, computer-guided machine learning has emerged as a salient tool to predict structure−activity relationships at the previously impossible scales, and then to promote the discovery of advanced bifunctional electrocatalysts, while current DFT calculations are still based on simplified models, which are far from real-world electrocatalysis processes. The influence of electric field, electrochemical double-layer, solvation, dissolved ions, strain, and so forth is suggested to be thoroughly considered in the future. In view of the complexity and importance of electrochemical reconstruction, DFT calculations are encouraged to simulate this dynamic process, while little attention has been paid presently. In addition, the alternative oxidations of exotic substrates (e.g., biomass, chitin, plastic wastes, and so on) for hybrid water splitting usually involve multiple electron transfers/intermediates/adsorption sites, such that experimentally identifying the precise stereoconfiguration of catalytic interface and measuring the binding energies of intermediates are often challenging. Thus, extending DFT modeling to these oxidation reactions beyond HER and OER is urgent and necessary.

Fourth, in terms of hybrid water splitting, the selection of alternative oxidation reactions has been broad, with the main emphasis on reducing the overall energy input for hydrogen generation from water. Future efforts should be more focused on the production of value-added oxidation products. Given the impressive scale of green hydrogen demand in the future, it seems more appealing to explore the oxidative upgrading of commodity chemicals featuring high solubility. Furthermore, to ensure the high purity of hydrogen generated at cathode or avoid gaseous mixtures separation, the gas-free oxidation

https://doi.org/10.1021/acs.chemrev.3c00332
Chem. Rev. 2024, 124, 3694−3812

reactions or PEM-based hybrid water splitting are exactly what we need. While for long-term operation, the benign neutral condition is desirable. It is therefore imperative to perform the technoeconomic analysis first when deciding on an alternative oxidation reaction to replace OER.

Fifth, the high activity of bifunctional electrocatalysts evaluated in the laboratory cannot guarantee their prominent performance in final systems, due to the new challenges in scaling up like water/heat management, reactants/products transfer, and device assembly. It means that separate investigation of individual components following the established paradigms is insufficient for real integrated systems. It is still a long way from basic research to industrial application and extending the performance evaluation of bifunctional electrocatalysts in working conditions deserves further studies.

Overall, significant advancements have been made in the field of overall and hybrid water splitting using bifunctional electrocatalysts over the past decade. These remarkable achievements have paved the way for sustainable hydrogen production, facilitating the transition toward a clean energy economy. Besides exploring advanced synthetic methods, cutting-edge characterization techniques, high-throughput computation/screening models, and compatible oxidation reactions (Figure 75), it is also increasingly important to conduct the relevant studies at the system level, which not only investigate the aspects of individual components but also emphasize their interactions within an integrated system.

AUTHOR INFORMATION

Corresponding Authors

Yujie Sun − *Department of Chemistry, University of Cincinnati, Cincinnati, Ohio 45221, United States;* orcid.org/0000-0002-4122-6255; Email: yujie.sun@uc.edu

Bo You − *Key Laboratory of Material Chemistry for Energy Conversion and Storage Ministry of Education, Hubei Key Laboratory of Material Chemistry and Service Failure, School of Chemistry and Chemical Engineering, Huazhong University of Science and Technology, Wuhan, Hubei 430074, China;* orcid.org/0000-0003-1849-0418; Email: youbo@hust.edu.cn

Authors

Li Quan − *Key Laboratory of Material Chemistry for Energy Conversion and Storage Ministry of Education, Hubei Key Laboratory of Material Chemistry and Service Failure, School of Chemistry and Chemical Engineering, Huazhong University of Science and Technology, Wuhan, Hubei 430074, China*

Hui Jiang − *Key Laboratory of Material Chemistry for Energy Conversion and Storage Ministry of Education, Hubei Key Laboratory of Material Chemistry and Service Failure, School of Chemistry and Chemical Engineering, Huazhong University of Science and Technology, Wuhan, Hubei 430074, China*

Guoliang Mei − *Key Laboratory of Material Chemistry for Energy Conversion and Storage Ministry of Education, Hubei Key Laboratory of Material Chemistry and Service Failure, School of Chemistry and Chemical Engineering, Huazhong University of Science and Technology, Wuhan, Hubei 430074, China*

Complete contact information is available at: https://pubs.acs.org/10.1021/acs.chemrev.3c00332

Author Contributions

[§]L.Q., H.J., and G.M. contributed equally to this work. CRediT: **Li Quan** writing-original draft, writing-review & editing; **Hui Jiang** writing-original draft, writing-review & editing; **Guoliang Mei** writing-original draft, writing-review & editing; **Yujie Sun** conceptualization, funding acquisition, project administration, resources, supervision, writing-original draft, writing-review & editing; **Bo You** conceptualization, funding acquisition, project administration, resources, supervision, writing-original draft, writing-review & editing.

Notes

The authors declare no competing financial interest.

Biographies

Li Quan is a Ph.D. candidate at Huazhong University of Science and Technology. Her research interest focuses on the development of highly active electrocatalysts for overall/hybrid water splitting.

Hui Jiang is a Ph.D. candidate at Huazhong University of Science and Technology. His research interests include the synthesis of inorganic nanomaterials for energy catalysis.

Guoliang Mei is a Master candidate at Huazhong University of Science and Technology. His research interest is electrochemical CO_2 reduction.

Yujie Sun received a B.S. degree in Chemistry from Fudan University in 2005 and a Ph.D. degree in Inorganic Chemistry at The Ohio State University in 2010. After a postdoctoral stint at the University of California, Berkeley and Lawrence Berkeley National Laboratory, Yujie started his independent career in 2013 and now is a Professor of Chemistry at the University of Cincinnati. His group is interested in developing and understanding novel materials and molecules for catalysis and biomedical applications.

Bo You received his Ph.D. degree in 2014 under the supervision of Prof. Zhaoxiang Deng at University of Science and Technology of China. He then joined Prof. Yujie Sun's group at Utah State University, Prof. Hong Li's group at Nanyang Technological University, and Prof. Shi Zhang Qiao's group at The University of Adelaide from 2014 to 2019 as a postdoctoral researcher. Currently, he is a full professor at Huazhong University of Science and Technology. His research focuses on integration-designed electro-activation (IDEA) for renewable energy.

ACKNOWLEDGMENTS

This work is supported by The National Key Research and Development Program of China (2021YFA1600800), the Program for HUST Academic Frontier Youth Team, and The Innovation and Talent Recruitment Base of New Energy Chemistry and Device (B21003). Y.S. acknowledges the support of the US National Science Foundation (CHE-2328176 and CHE-2102220) and the ACS Petroleum Research Fund (66635-ND3).

REFERENCES

(1) Chu, S.; Majumdar, A. Opportunities and Challenges for a Sustainable Energy Future. *Nature* **2012**, *488*, 294−303.

(2) Lewis, N. S. Research Opportunities to Advance Solar Energy Utilization. *Science* **2016**, *351*, aad1920.

(3) Dotan, H.; Landman, A.; Sheehan, S. W.; Malviya, K. D.; Shter, G. E.; Grave, D. A.; Arzi, Z.; Yehudai, N.; Halabi, M.; Gal, N.; Hadari, N.; Cohen, C.; Rothschild, A.; Grader, G. S. Decoupled Hydrogen

and Oxygen Evolution by a Two-Step Electrochemical-Chemical Cycle for Efficient Overall Water Splitting. *Nat. Energy* **2019**, *4*, 786−795.
(4) Muhich, C. L.; Evanko, B. W.; Weston, K. C.; Lichty, P.; Liang, X.; Martinek, J.; Musgrave, C. B.; Weimer, A. W. Efficient Generation of H_2 by Splitting Water with an Isothermal Redox Cycle. *Science* **2013**, *341*, 540−542.
(5) Wang, J.; Yang, H.; Li, F.; Li, L.; Wu, J.; Liu, S.; Cheng, T.; Xu, Y.; Shao, Q.; Huang, X. Single-Site Pt-Doped RuO_2 Hollow Nanospheres With Interstitial C for High-Performance Acidic Overall Water Splitting. *Sci. Adv.* **2022**, *8*, eabl9271.
(6) Turner, J. A. Sustainable Hydrogen Production. *Science* **2004**, *305*, 972−974.
(7) Jaramillo, T. F.; Jorgensen, K. P.; Bonde, J.; Nielsen, J. H.; Horch, S.; Chorkendorff, I. Identification of Active Edge Sites for Electrochemical H_2 Evolution from MoS_2 Nanocatalysts. *Science* **2007**, *317*, 100−102.
(8) Jiang, H.; Sun, Y.; You, B. Dynamic Electrodeposition on Bubbles: An Effective Strategy toward Porous Electrocatalysts for Green Hydrogen Cycling. *Acc. Chem. Res.* **2023**, *56*, 1421−1432.
(9) Zhao, X.; He, D.; Xia, B. Y.; Sun, Y.; You, B. Ambient Electrosynthesis toward Single-Atom Sites for Electrocatalytic Green Hydrogen Cycling. *Adv. Mater.* **2023**, *35*, 2210703.
(10) Lubitz, W.; Tumas, W. Hydrogen: An Overview. *Chem. Rev.* **2007**, *107*, 3900−3903.
(11) Kovac, A.; Paranos, M.; Marcius, D. Hydrogen in Energy Transition: A Review. *Int. J. Hydrogen Energy* **2021**, *46*, 10016−10035.
(12) Barbir, F. PEM Electrolysis for Production of Hydrogen from Renewable Energy Sources. *Sol. Energy* **2005**, *78*, 661−669.
(13) Dodds, P. E.; Staffell, L.; Hawkes, A. D.; Li, F.; Grunewald, P.; Mcdowall, W.; Ekins, P. Hydrogen and Fuel Cell Technologies for Heating: A Review. *Int. J. Hydrogen Energy* **2015**, *40*, 2065−2083.
(14) Moradi, R.; Groth, K. M. Hydrogen Storage and Delivery: Review of the State of the Art Technologies and Risk and Reliability Analysis. *Int. J. Hydrogen Energy* **2019**, *44*, 12254−12269.
(15) Wang, M.; Wang, Z.; Gong, X.; Guo, Z. The Intensification Technologies to Water Electrolysis for Hydrogen Production - A Review. *Renew. Sust. Energy Rev.* **2014**, *29*, 573−588.
(16) Luo, M.; Yi, Y.; Wang, S.; Wang, Z.; Du, M.; Pan, J.; Wang, Q. Review of Hydrogen Production Using Chemical-Looping Technology. *Renew. Sust. Energy Rev.* **2018**, *81*, 3186−3214.
(17) Parra, D.; Valverde, L.; Pino, F. J.; Patel, M. K. A Review On The Role, Cost and Value of Hydrogen Energy Systems for Deep Decarbonisation. *Renew. Sust. Energy Rev.* **2019**, *101*, 279−294.
(18) Acar, C.; Dincer, I. The Potential Role of Hydrogen as a Sustainable Transportation Fuel to Combat Global Warming. *Int. J. Hydrogen Energy* **2020**, *45*, 3396−3406.
(19) Elam, C. C.; Padró, C. E. G.; Sandrock, G.; Luzzi, A.; Lindblad, P.; Hagen, E. F. Realizing the Hydrogen Future: The International Energy Agency's Efforts to Advance Hydrogen Energy Technologies. *Int. J. Hydrogen Energy* **2003**, *28*, 601−607.
(20) Najjar, Y. S. H. Hydrogen Safety: The Road Toward Green Technology. *Int. J. Hydrogen Energy* **2013**, *38*, 10716−10728.
(21) Posso, F.; Pulido, A.; Acevedo-Páez, J. C. Towards the Hydrogen Economy: Estimation of Green Hydrogen Production Potential and the Impact of Its Uses in Ecuador as a Case Study. *Int. J. Hydrogen Energy* **2023**, *48*, 11922−11942.
(22) Wu, T.; Wang, J. Reliability Evaluation for Integrated Electricity-Gas Systems Considering Hydrogen. *IEEE Trans. Sustain. Energy* **2023**, *14*, 920−934.
(23) Mueller-Langer, F.; Tzimas, E.; Kaltschmitt, M.; Peteves, S. Techno-Economic Assessment of Hydrogen Production Processes for The Hydrogen Economy for the Short and Medium Term. *Int. J. Hydrogen Energy* **2007**, *32*, 3797−3810.
(24) Barreto, L.; Makihira, A.; Riahi, K. The Hydrogen Economy in the 21st Century: A Sustainable Development Scenario. *Int. J. Hydrogen Energy* **2003**, *28*, 267−284.
(25) Marbán, G.; Valdás-Solís, T. Towards the Hydrogen Economy? *Int. J. Hydrogen Energy* **2007**, *32*, 1625−1637.
(26) Schmidt, O.; Gambhir, A.; Staffell, I.; Hawkes, A.; Nelson, J.; Few, S. Future Cost and Performance of Water Electrolysis: An Expert Elicitation Study. *Int. J. Hydrogen Energy* **2017**, *42*, 30470−30492.
(27) De Luna, P.; Hahn, C.; Higgins, D.; Jaffer, S. A.; Jaramillo, T. F.; Sargent, E. H. What Would It Take for Renewably Powered Electrosynthesis to Displace Petrochemical Processes? *Science* **2019**, *364*, eaav3506.
(28) Shi, Y.; Zhang, B. Recent Advances in Transition Metal Phosphide Nanomaterials: Synthesis and Applications in Hydrogen Evolution Reaction. *Chem. Soc. Rev.* **2016**, *45*, 1529−1541.
(29) Abbasi, T.; Abbasi, S. A. 'Renewable' Hydrogen: Prospects and Challenges. *Renew. Sust. Energy Rev.* **2011**, *15*, 3034−3040.
(30) Quan, L.; Chen, X.; Liu, J.; Fan, S.; Xia, B. Y.; You, B. Atomic Pt-N_4 Sites in Porous N-Doped Nanocarbons for Enhanced On-Site Chlorination Coupled with H_2 Evolution in Acidic Water. *Adv. Funct. Mater.* **2023**, *33*, 2307643.
(31) Shiva Kumar, S.; Himabindu, V. Hydrogen Production by PEM Water Electrolysis - A Review. *Mater. Sci. Energy Technol.* **2019**, *2*, 442−454.
(32) Wan, L.; Xu, Z.; Xu, Q.; Pang, M.; Lin, D.; Liu, J.; Wang, B. Key Components and Design Strategy of the Membrane Electrode Assembly for Alkaline Water Electrolysis. *Energy Environ. Sci.* **2023**, *16*, 1384−1430.
(33) Yu, Z.-Y.; Duan, Y.; Feng, X.-Y.; Yu, X.; Gao, M.-R.; Yu, S.-H. Clean and Affordable Hydrogen Fuel from Alkaline Water Splitting: Past, Recent Progress, and Future Prospects. *Adv. Mater.* **2021**, *33*, 2007100.
(34) Zeng, K.; Zhang, D. Recent Progress in Alkaline Water Electrolysis for Hydrogen Production and Applications. *Prog. Energy Combust. Sci.* **2010**, *36*, 307−326.
(35) Chen, Z.; Guo, L.; Pan, L.; Yan, T.; He, Z.; Li, Y.; Shi, C.; Huang, Z.-F.; Zhang, X.; Zou, J.-J. Advances in Oxygen Evolution Electrocatalysts for Proton Exchange Membrane Water Electrolyzers. *Adv. Energy Mater.* **2022**, *12*, 2103670.
(36) Herring, A. M. Inorganic-Polymer Composite Membranes for Proton Exchange Membrane Fuel Cells. *Polym. Rev.* **2006**, *46*, 245−296.
(37) Li, L.; Wang, P.; Shao, Q.; Huang, X. Recent Progress in Advanced Electrocatalyst Design for Acidic Oxygen Evolution Reaction. *Adv. Mater.* **2021**, *33*, 2004243.
(38) Liu, R.-T.; Xu, Z.-L.; Li, F.-M.; Chen, F. Y.; Yu, J.-Y.; Yan, Y.; Chen, Y.; Xia, B. Y. Recent Advances in Proton Exchange Membrane Water Electrolysis. *Chem. Soc. Rev.* **2023**, *52*, 5652−5683.
(39) Abbasi, R.; Setzler, B. P.; Lin, S.; Wang, J.; Zhao, Y.; Xu, H.; Pivovar, B.; Tian, B.; Chen, X.; Wu, G.; Yan, Y. A Roadmap to Low-Cost Hydrogen with Hydroxide Exchange Membrane Electrolyzers. *Adv. Mater.* **2019**, *31*, 1805876.
(40) Goni-Urtiaga, A.; Presvytes, D.; Scott, K. Solid Acids as Electrolyte Materials for Proton Exchange Membrane (PEM) Electrolysis: Review. *Int. J. Hydrogen Energy* **2012**, *37*, 3358−3372.
(41) Lindquist, G. A.; Xu, Q.; Oener, S. Z.; Boettcher, S. W. Membrane Electrolyzers for Impure-Water Splitting. *Joule* **2020**, *4*, 2549−2561.
(42) Santoro, C.; Lavacchi, A.; Mustarelli, P.; Di Noto, V.; Elbaz, L.; Dekel, D. R.; Jaouen, F. What is Next in Anion-Exchange Membrane Water Electrolyzers? Bottlenecks, Benefits, and Future. *ChemSushem* **2022**, *15*, e202200027.
(43) Mccrory, C. C. L.; Jung, S.; Peters, J. C.; Jaramillo, T. F. Benchmarking Heterogeneous Electrocatalysts for the Oxygen Evolution Reaction. *J. Am. Chem. Soc.* **2013**, *135*, 16977−16987.
(44) Biswas, S.; Kulkarni, A. P.; Giddey, S.; Bhattacharya, S. A Review on Synthesis of Methane as a Pathway for Renewable Energy Storage with a Focus on Solid Oxide Electrolytic Cell-Based Processes. *Front. Energy Res.* **2020**, *8*, 570112.
(45) Hua, B.; Li, M.; Sun, Y.-F.; Li, J.-H.; Luo, J.-L. Enhancing Perovskite Electrocatalysis of Solid Oxide Cells through Controlled Exsolution of Nanoparticles. *ChemSusChem* **2017**, *10*, 3333−3341.

https://doi.org/10.1021/acs.chemrev.3c00332
Chem. Rev. 2024, 124, 3694−3812

(46) Tucker, M. C. Progress in Metal-Supported Solid Oxide Electrolysis Cells: A Review. *Int. J. Hydrogen Energy* **2020**, *45*, 24203−24218.
(47) Hauch, A.; Küngas, R.; Blennow, P.; Hansen, A. B.; Hansen, J. B.; Mathiesen, B. V.; Mogensen, M. B. Recent Advances in Solid Oxide Cell Technology for Electrolysis. *Science* **2020**, *370*, eaba6118.
(48) Laguna-Bercero, M. A. Recent Advances in High Temperature Electrolysis Using Solid Oxide Fuel Cells: A Review. *J. Power Sources* **2012**, *203*, 4−16.
(49) Zhang, Z.; Li, X.; Zhong, C.; Zhao, N.; Deng, Y.; Han, X.; Hu, W. Spontaneous Synthesis of Silver-Nanoparticle-Decorated Transition-Metal Hydroxides for Enhanced Oxygen Evolution Reaction. *Angew. Chem., Int. Ed.* **2020**, *59*, 7245−7250.
(50) Du, J.; Li, F.; Sun, L. Metal-Organic Frameworks and Their Derivatives as Electrocatalysts for the Oxygen Evolution Reaction. *Chem. Soc. Rev.* **2021**, *50*, 2663−2695.
(51) You, B.; Jiang, N.; Liu, X.; Sun, Y. Simultaneous H_2 Generation and Biomass Upgrading in Water by an Efficient Noble-Metal-Free Bifunctional Electrocatalyst. *Angew. Chem., Int. Ed.* **2016**, *55*, 9913−9917.
(52) Du, L.; Sun, Y.; You, B. Hybrid Water Electrolysis: Replacing Oxygen Evolution Reaction for Energy-Efficient Hydrogen Production and Beyond. *Mater. Rep. Energy* **2021**, *1*, 100004.
(53) Chen, Y. X.; Lavacchi, A.; Miller, H. A.; Bevilacqua, M.; Filippi, J.; Innocenti, M.; Marchionni, A.; Oberhauser, W.; Wang, L.; Vizza, F. Nanotechnology Makes Biomass Electrolysis More Energy Efficient than Water Electrolysis. *Nat. Commun.* **2014**, *5*, 4036.
(54) Liu, X.; Han, Y.; Guo, Y.; Zhao, X.; Pan, D.; Li, K.; Wen, Z. Electrochemical Hydrogen Generation by Oxygen Evolution Reaction-Alternative Anodic Oxidation Reactions. *Adv. Energy Sustainability Res.* **2022**, *3*, 2200005.
(55) Li, Y.; Wei, X.; Chen, L.; Shi, J. Electrocatalytic Hydrogen Production Trilogy. *Angew. Chem., Int. Ed.* **2021**, *60*, 19550−19571.
(56) Arshad, F.; Ul Haq, T.; Hussain, I.; Sher, F. Recent Advances in Electrocatalysts toward Alcohol-Assisted, Energy-Saving Hydrogen Production. *ACS Appl. Energy Mater.* **2021**, *4*, 8685−8701.
(57) Lee, K.-M.; Lee, H.-J.; Seo, J.; Lee, T.; Yoon, J.; Kim, C.; Lee, C. Electrochemical Oxidation Processes for the Treatment of Organic Pollutants in Water: Performance Evaluation Using Different Figures of Merit. *ACS EST Engg.* **2022**, *2*, 1797−1824.
(58) Tian, X.; Zhao, P.; Sheng, W. Hydrogen Evolution and Oxidation: Mechanistic Studies and Material Advances. *Adv. Mater.* **2019**, *31*, 1808066.
(59) Zhu, J.; Hu, L.; Zhao, P.; Lee, L. Y. S.; Wong, K.-Y. Recent Advances in Electrocatalytic Hydrogen Evolution Using Nanoparticles. *Chem. Rev.* **2020**, *120*, 851−918.
(60) Mahmood, N.; Yao, Y.; Zhang, J.-W.; Pan, L.; Zhang, X.; Zou, J.-J. Electrocatalysts for Hydrogen Evolution in Alkaline Electrolytes: Mechanisms, Challenges, and Prospective Solutions. *Adv. Sci.* **2018**, *5*, 1700464.
(61) Cheng, T.; Wang, L.; Merinov, B. V.; Goddard, W. A. Explanation of Dramatic pH-Dependence of Hydrogen Binding on Noble Metal Electrode: Greatly Weakened Water Adsorption at High pH. *J. Am. Chem. Soc.* **2018**, *140*, 7787−7790.
(62) Giles, S. A.; Wilson, J. C.; Nash, J.; Xu, B.; Vlachos, D. G.; Yan, Y. Recent Advances in Understanding the pH Dependence of the Hydrogen Oxidation and Evolution Reactions. *J. Catal.* **2018**, *367*, 328−331.
(63) Ledezma-Yanez, I.; Wallace, W. D. Z.; Sebastian-Pascual, P.; Climent, V.; Feliu, J. M.; Koper, M. T. M. Interfacial Water Reorganization as a pH-Dependent Descriptor of the Hydrogen Evolution Rate on Platinum Electrodes. *Nat. Energy* **2017**, *2*, 17031.
(64) Strmcnik, D.; Lopes, P. P.; Genorio, B.; Stamenkovic, V. R.; Markovic, N. M. Design Principles for Hydrogen Evolution Reaction Catalyst Materials. *Nano Energy* **2016**, *29*, 29−36.
(65) Weng, C.-C.; Ren, J.-T.; Yuan, Z.-Y. Transition Metal Phosphide-Based Materials for Efficient Electrochemical Hydrogen Evolution: A Critical Review. *ChemSusChem* **2020**, *13*, 3357−3375.
(66) You, B.; Tang, M. T.; Tsai, C.; Abild-Pedersen, F.; Zheng, X.; Li, H. Enhancing Electrocatalytic Water Splitting by Strain Engineering. *Adv. Mater.* **2019**, *31*, 1807001.
(67) Quaino, P.; Juarez, F.; Santos, E.; Schmickler, W. Volcano Plots in Hydrogen Electrocatalysis-Uses and Abuses. *Beilstein J. Nanotechnol.* **2014**, *5*, 846−854.
(68) Parsons, R. The Rate of Electrolytic Hydrogen Evolution and the Heat of Adsorption of Hydrogen. *Trans. Faraday Soc.* **1958**, *54*, 1053−1063.
(69) Bockris, J. O'M. Electrolytic Polarisation-I. The Overpotential of Hydrogen on Some Less Common Metals at High Current Densities. Influence of Current Density and Time. *Trans. Faraday Soc.* **1947**, *43*, 417−429.
(70) Trasatti, S. Work Function, Electronegativity, and Electrochemical Behaviour of Metals: III. Electrolytic Hydrogen Evolution in Acid Solutions. *J. Electroanal. Chem. Interfacial Electrochem.* **1972**, *39*, 163−184.
(71) Jin, H.; Zhao, R.; Cui, P.; Liu, X.; Yan, J.; Yu, X.; Ma, D.; Song, W.; Cao, C. Sabatier Phenomenon in Hydrogenation Reactions Induced by Single-Atom Density. *J. Am. Chem. Soc.* **2023**, *145*, 12023−12032.
(72) Nørskov, J. K.; Bligaard, T.; Logadottir, A.; Kitchin, J. R.; Chen, J. G.; Pandelov, S.; Stimming, U. Trends in the Exchange Current for Hydrogen Evolution. *J. Electrochem. Soc.* **2005**, *152*, J23.
(73) Skulason, E.; Tripkovic, V.; Bjorketun, M. E.; Gudmundsdottir, S.; Karlberg, G.; Rossmeisl, J.; Bligaard, T.; Jonsson, H.; Nørskov, J. K. Modeling the Electrochemical Hydrogen Oxidation and Evolution Reactions on the Basis of Density Functional Theory Calculations. *J. Phys. Chem. C* **2010**, *114*, 18182−18197.
(74) Matsumoto, Y.; Sato, E. Electrocatalytic Properties of Transition Metal Oxides for Oxygen Evolution Reaction. *Mater. Chem. Phys.* **1986**, *14*, 397−426.
(75) Reier, T.; Nong, H. N.; Teschner, D.; Schloegl, R.; Strasser, P. Electrocatalytic Oxygen Evolution Reaction in Acidic Environments-Reaction Mechanisms and Catalysts. *Adv. Energy Mater.* **2017**, *7*, 1601275.
(76) Joo, J.; Kim, T.; Lee, J.; Choi, S.-I.; Lee, K. Morphology-Controlled Metal Sulfides and Phosphides for Electrochemical Water Splitting. *Adv. Mater.* **2019**, *31*, 1806682.
(77) Tahir, M.; Pan, L.; Idrees, F.; Zhang, X.; Wang, L.; Zou, J.-J.; Wang, Z. L. Electrocatalytic Oxygen Evolution Reaction for Energy Conversion and Storage: A Comprehensive Review. *Nano Energy* **2017**, *37*, 136−157.
(78) Kim, J. S.; Kim, B.; Kim, H.; Kang, K. Recent Progress On Multimetal Oxide Catalysts for the Oxygen Evolution Reaction. *Adv. Energy Mater.* **2018**, *8*, 1702774.
(79) Li, S.; Hao, X.; Abudula, A.; Guan, G. Nanostructured Co-Based Bifunctional Electrocatalysts for Energy Conversion and Storage: Current Status and Perspectives. *J. Mater. Chem. A* **2019**, *7*, 18674−18707.
(80) Bockris, J. O. Kinetics of Activation Controlled Consecutive Electrochemical Reactions: Anodic Evolution of Oxygen. *J. Chem. Phys.* **1956**, *24*, 817−827.
(81) Iqbal, B.; Saleem, M.; Arshad, S. N.; Rashid, J.; Hussain, N.; Zaheer, M. One-Pot Synthesis of Heterobimetallic Metal-Organic Frameworks (MOFs) for Multifunctional Catalysis. *Chem. Eur. J.* **2019**, *25*, 10490−10498.
(82) Xu, H.; Cheng, D.; Cao, D.; Zeng, X. C. A Universal Principle for a Rational Design of Single-Atom Electrocatalysts. *Nat. Catal.* **2018**, *1*, 339−348.
(83) Rossmeisl, J.; Dimitrievski, K.; Siegbahn, P.; Nørskov, J. K. Comparing Electrochemical and Biological Water Splitting. *J. Phys. Chem. C* **2007**, *111*, 18821−18823.
(84) Zhang, J.; Yang, H. B.; Zhou, D.; Liu, B. Adsorption Energy in Oxygen Electrocatalysis. *Chem. Rev.* **2022**, *122*, 17028−17072.
(85) Rossmeisl, J.; Qu, Z. W.; Zhu, H.; Kroes, G. J.; Nørskov, J. K. Electrolysis of Water on Oxide Surfaces. *J. Electroanal. Chem.* **2007**, *607*, 83−89.

https://doi.org/10.1021/acs.chemrev.3c00332
Chem. Rev. 2024, 124, 3694−3812

(86) Man, I. C.; Su, H.-Y.; Calle-Vallejo, F.; Hansen, H. A.; Martinez, J. I.; Inoglu, N. G.; Kitchin, J.; Jaramillo, T. F.; Nørskov, J. K.; Rossmeisl, J. Universality in Oxygen Evolution Electrocatalysis on Oxide Surfaces. *ChemCatChem.* **2011**, *3*, 1159−1165.
(87) Zhou, B.; Gao, R.; Zou, J.-J.; Yang, H. Surface Design Strategy of Catalysts for Water Electrolysis. *Small* **2022**, *18*, 2202336.
(88) Zhang, N.; Chai, Y. Lattice Oxygen Redox Chemistry in Solid-State Electrocatalysts for Water Oxidation. *Energy Environ. Sci.* **2021**, *14*, 4647−4671.
(89) Lei, Z.; Wang, T.; Zhao, B.; Cai, W.; Liu, Y.; Jiao, S.; Li, Q.; Cao, R.; Liu, M. Recent Progress in Electrocatalysts for Acidic Water Oxidation. *Adv. Energy Mater.* **2020**, *10*, 2000478.
(90) Lin, Y.; Dong, Y.; Wang, X.; Chen, L. Electrocatalysts for the Oxygen Evolution Reaction in Acidic Media. *Adv. Mater.* **2023**, *35*, 2210565.
(91) Roger, I.; Shipman, M.; Symes, M. Earth-Abundant Catalysts for Electrochemical and Photoelectrochemical Water Splitting. *Nat. Rev. Chem.* **2017**, *1*, 0003.
(92) Zou, X.; Zhang, Y. Noble Metal-Free Hydrogen Evolution Catalysts for Water Splitting. *Chem. Soc. Rev.* **2015**, *44*, 5148−5180.
(93) Seh, Z. W.; Kibsgaard, J.; Dickens, C. F.; Chorkendorff, I. B.; Nørskov, J. K.; Jaramillo, T. F. Combining Theory and Experiment in Electrocatalysis: Insights into Materials Design. *Science* **2017**, *355*, eaad4998.
(94) Vij, V.; Sultan, S.; Harzandi, A. M.; Meena, A.; Tiwari, J. N.; Lee, W.-G.; Yoon, T.; Kim, K. S. Nickel-Based Electrocatalysts for Energy-Related Applications: Oxygen Reduction, Oxygen Evolution, and Hydrogen Evolution Reactions. *ACS Catal.* **2017**, *7*, 7196−7225.
(95) Wang, J.; Xu, F.; Jin, H.; Chen, Y.; Wang, Y. Non-Noble Metal-Based Carbon Composites in Hydrogen Evolution Reaction: Fundamentals to Applications. *Adv. Mater.* **2017**, *29*, 1605838.
(96) Suen, N.-T.; Hung, S.-F.; Quan, Q.; Zhang, N.; Xu, Y.-J.; Chen, H. M. Electrocatalysis for the Oxygen Evolution Reaction: Recent Development and Future Perspectives. *Chem. Soc. Rev.* **2017**, *46*, 337−365.
(97) Zhou, X.; Ma, Y.; Ge, Y.; Zhu, S.; Cui, Y.; Chen, B.; Liao, L.; Yun, Q.; He, Z.; Long, H.; et al. Preparation of Au@Pd Core-Shell Nanorods with Fcc-2H-Fcc Heterophase for Highly Efficient Electrocatalytic Alcohol Oxidation. *J. Am. Chem. Soc.* **2022**, *144*, 547−555.
(98) Zhou, M.; Liu, J.; Ling, C.; Ge, Y.; Chen, B.; Tan, C.; Fan, Z.; Huang, J.; Chen, J.; Liu, Z.; et al. Synthesis of Pd_3Sn and PdCuSn Nanorods with $L1_2$ Phase for Highly Efficient Electrocatalytic Ethanol Oxidation. *Adv. Mater.* **2022**, *34*, 2106115.
(99) You, B.; Liu, X.; Jiang, N.; Sun, Y. A General Strategy for Decoupled Hydrogen Production from Water Splitting by Integrating Oxidative Biomass Valorization. *J. Am. Chem. Soc.* **2016**, *138*, 13639−13646.
(100) Trenerry, M. J.; Wallen, C. M.; Brown, T. R.; Park, S. V.; Berry, J. F. Spontaneous N_2 Formation by a Diruthenium Complex Enables Electrocatalytic and Aerobic Oxidation of Ammonia. *Nat. Chem.* **2021**, *13*, 1221−1227.
(101) Chan, Y. T.; Siddharth, K.; Shao, M. Investigation of Cubic Pt Alloys for Ammonia Oxidation Reaction. *Nano Res.* **2020**, *13*, 1920−1927.
(102) Ji, Z.; Song, Y.; Zhao, S.; Li, Y.; Liu, J.; Hu, W. Pathway Manipulation via Ni, Co, and V Ternary Synergism to Realize High Efficiency for Urea Electrocatalytic Oxidation. *ACS Catal.* **2022**, *12*, 569−579.
(103) Chen, W.; Xu, L.; Zhu, X.; Huang, Y.-C.; Zhou, W.; Wang, D.; Zhou, Y.; Du, S.; Li, Q.; Xie, C.; et al. Unveiling the Electrooxidation of Urea: Intramolecular Coupling of the N-N Bond. *Angew. Chem., Int. Ed.* **2021**, *60*, 7297−7307.
(104) Katiyar, N. K.; Dhakar, S.; Parui, A.; Gakhad, P.; Singh, A. K.; Biswas, K.; Tiwary, C. S.; Sharma, S. Electrooxidation of Hydrazine Utilizing High-Entropy Alloys: Assisting the Oxygen Evolution Reaction at the Thermodynamic Voltage. *ACS Catal.* **2021**, *11*, 14000−14007.
(105) Miao, R.; Shao, L.; Compton, R. G. Single Entity Electrochemistry and the Electron Transfer Kinetics of Hydrazine Oxidation. *Nano Res.* **2021**, *14*, 4132−4139.
(106) Dong, G.; Lang, K.; Gao, Y.; Zhang, W.; Guo, D.; Li, J.; Chai, D.-F.; Jing, L.; Zhang, Z.; Wang, Y. A Novel Composite Anode via Immobilizing of Ce-Doped PbO_2 on $CoTiO_3$ for Efficiently Electrocatalytic Degradation of Dye. *J. Colloid Interface Sci.* **2022**, *608*, 2921−2931.
(107) Zhang, L.; Wang, Z.; Qiu, J. Energy-Saving Hydrogen Production by Seawater Electrolysis Coupling Sulfion Degradation. *Adv. Mater.* **2022**, *34*, 2109321.
(108) Zhang, M.; Guan, J.; Tu, Y.; Chen, S.; Wang, Y.; Wang, S.; Yu, L.; Ma, C.; Deng, D.; Bao, X. Highly Efficient H_2 Production from H_2S via a Robust Graphene-Encapsulated Metal Catalyst. *Energy Environ. Sci.* **2020**, *13*, 119−126.
(109) Yi, L.; Ji, Y.; Shao, P.; Chen, J.; Li, J.; Li, H.; Chen, K.; Peng, X.; Wen, Z. Scalable Synthesis of Tungsten Disulfide Nanosheets for Alkali-Acid Electrocatalytic Sulfion Recycling and H_2 Generation. *Angew. Chem., Int. Ed.* **2021**, *60*, 21550−21557.
(110) You, B.; Han, G.; Sun, Y. Electrocatalytic and Photocatalytic Hydrogen Evolution Integrated with Organic Oxidation. *Chem. Commun.* **2018**, *54*, 5943−5955.
(111) You, B.; Liu, X.; Liu, X.; Sun, Y. Efficient H_2 Evolution Coupled with Oxidative Refining of Alcohols via a Hierarchically Porous Nickel Bifunctional Electrocatalyst. *ACS Catal.* **2017**, *7*, 4564−4570.
(112) Huang, C.; Huang, Y.; Liu, C.; Yu, Y.; Zhang, B. Integrating Hydrogen Production with Aqueous Selective Semi-Dehydrogenation of Tetrahydroisoquinolines over a Ni_2P Bifunctional Electrode. *Angew. Chem., Int. Ed.* **2019**, *58*, 12014−12017.
(113) Mondal, B.; Karjule, N.; Singh, C.; Shimoni, R.; Volokh, M.; Hod, I.; Shalom, M. Unraveling the Mechanisms of Electrocatalytic Oxygenation and Dehydrogenation of Organic Molecules to Value-Added Chemicals over a Ni-Fe Oxide Catalyst. *Adv. Energy Mater.* **2021**, *11*, 2101858.
(114) Chen, G.; Li, X.; Feng, X. Upgrading Organic Compounds through the Coupling of Electrooxidation with Hydrogen Evolution. *Angew. Chem., Int. Ed.* **2022**, *61*, e202209014.
(115) Xu, Y.; Zhang, B. Recent Advances in Electrochemical Hydrogen Production from Water Assisted by Alternative Oxidation Reactions. *ChemElectroChem.* **2019**, *6*, 3214−3226.
(116) Zhou, H.; Li, Z.; Xu, S.-M.; Lu, L.; Xu, M.; Ji, K.; Ge, R.; Yan, Y.; Ma, L.; Kong, X.; Zheng, L.; Duan, H. Selectively Upgrading Lignin Derivatives to Carboxylates through Electrochemical Oxidative C(OH)-C Bond Cleavage by a Mn-Doped Cobalt Oxyhydroxide Catalyst. *Angew. Chem., Int. Ed.* **2021**, *60*, 8976−8982.
(117) Zhao, S.; Yang, Y.; Tang, Z. Insight into Structural Evolution, Active Sites, and Stability of Heterogeneous Electrocatalysts. *Angew. Chem., Int. Ed.* **2022**, *61*, e202110186.
(118) Singh, B.; Mannu, P.; Huang, Y. C.; Prakash, R.; Shen, S.; Dong, C. L.; Indra, A. Deciphering Ligand Controlled Structural Evolution of Prussian Blue Analogues and Their Electrochemical Activation during Alkaline Water Oxidation. *Angew. Chem., Int. Ed.* **2022**, *61*, e202211585.
(119) Liu, L.; Corma, A. Structural Transformations of Solid Electrocatalysts and Photocatalysts. *Nat. Rev. Chem.* **2021**, *5*, 256−276.
(120) Guo, T.; Li, L.; Wang, Z. Recent Development and Future Perspectives of Amorphous Transition Metal-Based Electrocatalysts for Oxygen Evolution Reaction. *Adv. Energy Mater.* **2022**, *12*, 2200827.
(121) Liu, X.; Guo, R.; Huang, W.; Zhu, J.; Wen, B.; Mai, L. Advances in Understanding the Electrocatalytic Reconstruction Chemistry of Coordination Compounds. *Small* **2021**, *17*, 2100629.
(122) Ding, H.; Liu, H.; Chu, W.; Wu, C.; Xie, Y. Structural Transformation of Heterogeneous Materials for Electrocatalytic Oxygen Evolution Reaction. *Chem. Rev.* **2021**, *121*, 13174−13212.
(123) Zhong, H.; Wang, X.; Sun, G.; Tang, Y.; Tan, S.; He, Q.; Zhang, J.; Xiong, T.; Diao, C.; Yu, Z.; Xi, S.; Lee, W. S. V.; Xue, J.

https://doi.org/10.1021/acs.chemrev.3c00332
Chem. Rev. 2024, 124, 3694−3812

Optimization of Oxygen Evolution Activity by Tuning e^*_g Band Broadening in Nickel Oxyhydroxide. *Energy Environ. Sci.* **2023**, *16*, 641−652.
(124) Hong, Q.; Wang, Y.; Wang, R.; Chen, Z.; Yang, H.; Yu, K.; Liu, Y.; Huang, H.; Kang, Z.; Menezes, P. W. In Situ Coupling of Carbon Dots with Co-ZIF Nanoarrays Enabling Highly Efficient Oxygen Evolution Electrocatalysis. *Small* **2023**, *19*, 2206723.
(125) Li, G. L.; Qiao, X. Y.; Miao, Y. Y.; Wang, T. Y.; Deng, F. Synergistic Effect of N-$NiMoO_4$ /Ni Heterogeneous Interface with Oxygen Vacancies in N-$NiMoO_4$/Ni/CNTS for Superior Overall Water Splitting. *Small* **2023**, *19*, 2207196.
(126) Wang, S.; Jiang, Q.; Ju, S.; Hsu, C. S.; Chen, H. M.; Zhang, D.; Song, F. Identifying the Geometric Catalytic Active Sites of Crystalline Cobalt Oxyhydroxides for Oxygen Evolution Reaction. *Nat. Commun.* **2022**, *13*, 6650.
(127) Zhang, L.; Wang, J.; Jiang, K.; Xiao, Z.; Gao, Y.; Lin, S.; Chen, B. Self-Reconstructed Metal-Organic Framework Heterojunction for Switchable Oxygen Evolution Reaction. *Angew. Chem., Int. Ed.* **2022**, *61*, e202214794.
(128) Chen, R. R.; Chen, G.; Ren, X.; Ge, J.; Ong, S. J. H.; Xi, S.; Wang, X.; Xu, Z. J. $SmCo_5$ with a Reconstructed Oxyhydroxide Surface for Spin-Selective Water Oxidation at Elevated Temperature. *Angew. Chem., Int. Ed.* **2021**, *60*, 25884−25890.
(129) An, L.; Zhang, H.; Zhu, J.; Xi, S.; Huang, B.; Sun, M.; Peng, Y.; Xi, P.; Yan, C. H. Balancing Activity and Stability in Spinel Cobalt Oxides through Geometrical Sites Occupation towards Efficient Electrocatalytic Oxygen Evolution. *Angew. Chem., Int. Ed.* **2023**, *62*, e202214600.
(130) Cai, Z.; Wang, P.; Zhang, J.; Chen, A.; Zhang, J.; Yan, Y.; Wang, X. Reinforced Layered Double Hydroxide Oxygen-Evolution Electrocatalysts: A Polyoxometallic Acid Wet-Etching Approach and Synergistic Mechanism. *Adv. Mater.* **2022**, *34*, 2110696.
(131) Liu, Y.; Li, X.; Zhang, S.; Wang, Z.; Wang, Q.; He, Y.; Huang, W. H.; Sun, Q.; Zhong, X.; Hu, J.; Guo, X.; Lin, Q.; Li, Z.; Zhu, Y.; Chueh, C.-C.; Chen, C.-L.; Xu, Z.; Zhu, Z. Molecular Engineering of Metal-Organic Frameworks as Efficient Electrochemical Catalysts for Water Oxidation. *Adv. Mater.* **2023**, *35*, 2300945.
(132) Chang, G.; Zhou, Y.; Wang, J.; Zhang, H.; Yan, P.; Wu, H. B.; Yu, X. Y. Dynamic Reconstructed RuO_2/NiFeOOH with Coherent Interface for Efficient Seawater Oxidation. *Small* **2023**, *19*, 2206768.
(133) Zeng, Y.; Zhao, M.; Huang, Z.; Zhu, W.; Zheng, J.; Jiang, Q.; Wang, Z.; Liang, H. Surface Reconstruction of Water Splitting Electrocatalysts. *Adv. Energy Mater.* **2022**, *12*, 2201713.
(134) Yang, Y.; Luo, M.; Zhang, W.; Sun, Y.; Chen, X.; Guo, S. Metal Surface and Interface Energy Electrocatalysis: Fundamentals, Performance Engineering, and Opportunities. *Chem.* **2018**, *4*, 2054−2083.
(135) Sun, Y.; Wang, J.; Xi, S.; Shen, J.; Luo, S.; Ge, J.; Sun, S.; Chen, Y.; Hanna, J. V.; Li, S.; Wang, X.; Xu, Z. J. Navigating Surface Reconstruction of Spinel Oxides for Electrochemical Water Oxidation. *Nat. Commun.* **2023**, *14*, 2467.
(136) Zhai, W.; Chen, Y.; Liu, Y.; Sakthivel, T.; Ma, Y.; Guo, S.; Qu, Y.; Dai, Z. Bimetal-Incorporated Black Phosphorene with Surface Electron Deficiency for Efficient Anti-Reconstruction Water Electrolysis. *Adv. Funct. Mater.* **2023**, *33*, 2301565.
(137) Sun, H.; Tung, C. W.; Qiu, Y.; Zhang, W.; Wang, Q.; Li, Z.; Tang, J.; Chen, H. C.; Wang, C.; Chen, H. M. Atomic Metal-Support Interaction Enables Reconstruction-Free Dual-Site Electrocatalyst. *J. Am. Chem. Soc.* **2022**, *144*, 1174−1186.
(138) Du, W.; Shi, Y.; Zhou, W.; Yu, Y.; Zhang, B. Unveiling the In Situ Dissolution and Polymerization of Mo in Ni_4Mo Alloy for Promoting the Hydrogen Evolution Reaction. *Angew. Chem., Int. Ed.* **2021**, *60*, 7051−7055.
(139) Enkhtuvshin, E.; Yeo, S.; Choi, H.; Kim, K. M.; An, B. S.; Biswas, S.; Lee, Y.; Nayak, A. K.; Jang, J. U.; Na, K.-H.; Choi, W.-Y.; Ali, G.; Chae, K. H.; Akbar, M.; Chung, K. Y.; Yoo, K.; Chung, Y.-C.; Shin, T. H.; Kim, H.; Chung, C.-Y.; Han, H. Surface Reconstruction of Ni−Fe Layered Double Hydroxide Inducing Chloride Ion Blocking Materials for Outstanding Overall Seawater Splitting. *Adv. Funct. Mater.* **2023**, *33*, 2214069.
(140) Jin, J.; Yin, J.; Liu, H.; Huang, B.; Hu, Y.; Zhang, H.; Sun, M.; Peng, Y.; Xi, P.; Yan, C.-H. Atomic Sulfur Filling Oxygen Vacancies Optimizes H Absorption and Boosts the Hydrogen Evolution Reaction in Alkaline Media. *Angew. Chem., Int. Ed.* **2021**, *60*, 14117−14123.
(141) Lin, G.; Zhang, Z.; Ju, Q.; Wu, T.; Segre, C. U.; Chen, W.; Peng, H.; Zhang, H.; Liu, Q.; Liu, Z.; Zhang, Y.; Kong, S.; Mao, Y.; Zhao, W.; Suenaga, K.; Huang, F.; Wang, J. Bottom-Up Evolution of Perovskite Clusters into High-Activity Rhodium Nanoparticles toward Alkaline Hydrogen Evolution. *Nat. Commun.* **2023**, *14*, 280.
(142) Liu, J.; Qiao, W.; Zhu, Z.; Hu, J.; Xu, X. Chameleon-Like Reconstruction on Redox Catalysts Adaptive to Alkali Water Electrolysis. *Small* **2022**, *18*, 2202434.
(143) Sun, Y.; Wu, J.; Zhang, Z.; Liao, Q.; Zhang, S.; Wang, X.; Xie, Y.; Ma, K.; Kang, Z.; Zhang, Y. Phase Reconfiguration of Multivalent Nickel Sulfides in Hydrogen Evolution. *Energy Environ. Sci.* **2022**, *15*, 633−644.
(144) Yin, Z.-H.; Huang, Y.; Jiang, L.-W.; Meng, C.; Wu, Y.-Z.; Liu, H.; Wang, J.-J. Revealing the In Situ Evolution of Tetrahedral $NiMoO_4$ Micropillar Array for Energy-Efficient Alkaline Hydrogen Production Assisted by Urea Electrolysis. *Small Struct.* **2023**, *4*, 2300028.
(145) Yang, C.; Zhong, W.; Shen, K.; Zhang, Q.; Zhao, R.; Xiang, H.; Wu, J.; Li, X.; Yang, N. Electrochemically Reconstructed Cu-FeOOH/Fe_3O_4 Catalyst for Efficient Hydrogen Evolution in Alkaline Media. *Adv. Energy Mater.* **2022**, *12*, 2200077.
(146) Luo, X.; Ji, P.; Wang, P.; Tan, X.; Chen, L.; Mu, S. Spherical Ni_3S_2/Fe-NiP_x Magic Cube with Ultrahigh Water/Seawater Oxidation Efficiency. *Adv. Sci.* **2022**, *9*, 2104846.
(147) Zhao, Y.; Dongfang, N.; Triana, C. A.; Huang, C.; Erni, R.; Wan, W.; Li, J.; Stoian, D.; Pan, L.; Zhang, P.; Lan, J.; Iannuzzi, M.; Patzke, G. R. Dynamics and Control of Active Sites in Hierarchically Nanostructured Cobalt Phosphide/Chalcogenide-Based Electrocatalysts for Water Splitting. *Energy Environ. Sci.* **2022**, *15*, 727−739.
(148) Ji, P.; Yu, R.; Wang, P.; Pan, X.; Jin, H.; Zheng, D.; Chen, D.; Zhu, J.; Pu, Z.; Wu, J.; Mu, S. Ultra-Fast and In-Depth Reconstruction of Transition Metal Fluorides in Electrocatalytic Hydrogen Evolution Processes. *Adv. Sci.* **2022**, *9*, e2103567.
(149) Banerjee, S.; Kakekhani, A.; Wexler, R. B.; Rappe, A. M. Relationship Between the Surface Reconstruction of Nickel Phosphides and Their Activity toward the Hydrogen Evolution Reaction. *ACS Catal.* **2023**, *13*, 4611−4621.
(150) Zhou, D.; Li, F.; Zhao, Y.; Wang, L.; Zou, H.; Shan, Y.; Fu, J.; Ding, Y.; Duan, L.; Liu, M.; Sun, L.; Fan, K. Mechanistic Regulation by Oxygen Vacancies in Structural Evolution Promoting Electrocatalytic Water Oxidation. *ACS Catal.* **2023**, *13*, 4398−4408.
(151) Hu, Y.; Zheng, Y.; Jin, J.; Wang, Y.; Peng, Y.; Yin, J.; Shen, W.; Hou, Y.; Zhu, L.; An, L.; Lu, M.; Xi, P.; Yan, C.-H. Understanding the Sulphur-Oxygen Exchange Process of Metal Sulphides Prior to Oxygen Evolution Reaction. *Nat. Commun.* **2023**, *14*, 1949.
(152) Liu, C.; Shi, X. R.; Yue, K.; Wang, P.; Zhan, K.; Wang, X.; Xia, B. Y.; Yan, Y. S-Species-Evoked High-Valence $Ni^{2+\delta}$ of the Evolved Beta-$Ni(OH)_2$ Electrode for Selective Oxidation of 5-Hydroxymethylfurfural. *Adv. Mater.* **2023**, *35*, 2211177.
(153) Liu, H.; Xie, R.; Wang, Q.; Han, J.; Han, Y.; Wang, J.; Fang, H.; Qi, J.; Ding, M.; Ji, W.; He, B.; Lü, W. Enhanced OER Performance and Dynamic Transition of Surface Reconstruction in $LaNiO_3$ Thin Films with Nanoparticles Decoration. *Adv. Sci.* **2023**, *10*, 2207128.
(154) Reith, L.; Hausmann, J. N.; Mebs, S.; Mondal, I.; Dau, H.; Driess, M.; Menezes, P. W. In Situ Detection of Iron in Oxidation States ≥ IV in Cobalt-Iron Oxyhydroxide Reconstructed during Oxygen Evolution Reaction. *Adv. Energy Mater.* **2023**, *13*, 2203886.
(155) Tajuddin, A. A. H.; Wakisaka, M.; Ohto, T.; Yu, Y.; Fukushima, H.; Tanimoto, H.; Li, X.; Misu, Y.; Jeong, S.; Fujita, J. I.; Tada, H.; Fujita, T.; Takeguchi, M.; Takano, K.; Matsuoka, K.; Sato, Y.; Ito, Y. Corrosion-Resistant and High-Entropic Non-Noble-

https://doi.org/10.1021/acs.chemrev.3c00332
Chem. Rev. 2024, 124, 3694−3812

Metal Electrodes for Oxygen Evolution in Acidic Media. *Adv. Mater.* **2023**, *35*, 2207466.
(156) Wang, C.; Zhai, P.; Xia, M.; Liu, W.; Gao, J.; Sun, L.; Hou, J. Identification of the Origin for Reconstructed Active Sites on Oxyhydroxide for Oxygen Evolution Reaction. *Adv. Mater.* **2023**, *35*, 2209307.
(157) Wu, T.; Sun, Y.; Ren, X.; Wang, J.; Song, J.; Pan, Y.; Mu, Y.; Zhang, J.; Cheng, Q.; Xian, G.; Xi, S.; Shen, C.; Gao, H.-J.; Fisher, A. C.; Sherburne, M. P.; Du, Y.; Ager, J. W.; Gracia, J.; Yang, H.; Zeng, L.; Xu, Z. J. Reconstruction of Thiospinel to Active Sites and Spin Channels for Water Oxidation. *Adv. Mater.* **2023**, *35*, 2207041.
(158) Zhang, R.; Pan, L.; Guo, B.; Huang, Z. F.; Chen, Z.; Wang, L.; Zhang, X.; Guo, Z.; Xu, W.; Loh, K. P.; Zou, J. J. Tracking the Role of Defect Types in Co_3O_4 Structural Evolution and Active Motifs during Oxygen Evolution Reaction. *J. Am. Chem. Soc.* **2023**, *145*, 2271−2281.
(159) Zhao, C.-X.; Liu, J.-N.; Wang, C.; Wang, J.; Song, L.; Li, B.-Q.; Zhang, Q. An Anionic Regulation Mechanism for the Structural Reconstruction of Sulfide Electrocatalysts under Oxygen Evolution Conditions. *Energy Environ. Sci.* **2022**, *15*, 3257−3264.
(160) Kuai, C.; Xi, C.; Hu, A.; Zhang, Y.; Xu, Z.; Nordlund, D.; Sun, C. J.; Cadigan, C. A.; Richards, R. M.; Li, L.; Dong, C.-K.; Du, X.-W.; Lin, F. Revealing the Dynamics and Roles of Iron Incorporation in Nickel Hydroxide Water Oxidation Catalysts. *J. Am. Chem. Soc.* **2021**, *143*, 18519−18526.
(161) Tesch, M. F.; Bonke, S. A.; Jones, T. E.; Shaker, M. N.; Xiao, J.; Skorupska, K.; Mom, R.; Melder, J.; Kurz, P.; Knop-Gericke, A.; Schlögl, R.; Hocking, R. K.; Simonov, A. N. Evolution of Oxygen-Metal Electron Transfer and Metal Electronic States during Manganese Oxide Catalyzed Water Oxidation Revealed with In Situ Soft X-Ray Spectroscopy. *Angew. Chem., Int. Ed.* **2019**, *58*, 3426−3432.
(162) Jin, Z.; Bard, A. J. Surface Interrogation of Electrodeposited MnO_x and $CaMnO_3$ Perovskites by Scanning Electrochemical Microscopy: Probing Active Sites and Kinetics for the Oxygen Evolution Reaction. *Angew. Chem., Int. Ed.* **2021**, *60*, 794−799.
(163) Mefford, J. T.; Akbashev, A. R.; Kang, M.; Bentley, C. L.; Gent, W. E.; Deng, H. D.; Alsem, D. H.; Yu, Y. S.; Salmon, N. J.; Shapiro, D. A.; Unwin, P. R.; Chueh, W. C. Correlative Operando Microscopy of Oxygen Evolution Electrocatalysts. *Nature* **2021**, *593*, 67−73.
(164) Sun, Y.; Li, X.; Zhang, T.; Xu, K.; Yang, Y.; Chen, G.; Li, C.; Xie, Y. Nitrogen-Doped Cobalt Diselenide with Cubic Phase Maintained for Enhanced Alkaline Hydrogen Evolution. *Angew. Chem., Int. Ed.* **2021**, *60*, 21575−2152.
(165) Jiang, H.; He, Q.; Zhang, Y.; Song, L. Structural Self-Reconstruction of Catalysts in Electrocatalysis. *Acc. Chem. Res.* **2018**, *51*, 2968−2977.
(166) Hao, J.; Luo, W.; Wang, S.; Zhao, K.; Hou, J.; Li, L.; Ge, B.; Yang, W.; Shi, W. Discharge-Induced Enhancement of the Oxygen Evolution Reaction. *Angew. Chem., Int. Ed.* **2021**, *60*, 20042−20048.
(167) Villalobos, J.; González-Flores, D.; Urcuyo, R.; Montero, M. L.; Schuck, G.; Beyer, P.; Risch, M. Requirements for Beneficial Electrochemical Restructuring: A Model Study on a Cobalt Oxide in Selected Electrolytes. *Adv. Energy Mater.* **2021**, *11*, 2101737.
(168) Wang, Q.; Cheng, Y.; Tao, H. B.; Liu, Y.; Ma, X.; Li, D. S.; Yang, H. B.; Liu, B. Long-Term Stability Challenges and Opportunities in Acidic Oxygen Evolution Electrocatalysis. *Angew. Chem., Int. Ed.* **2023**, *62*, e202216645.
(169) Clament Sagaya Selvam, N.; Kwak, S. J.; Choi, G. H.; Oh, M. J.; Kim, H.; Yoon, W.-S.; Lee, W. B.; Yoo, P. J. Unveiling the Impact of Fe Incorporation on Intrinsic Performance of Reconstructed Water Oxidation Electrocatalyst. *ACS Energy Lett.* **2021**, *6*, 4345−4354.
(170) Peng, C. K.; Lin, Y. C.; Chiang, C. L.; Qian, Z.; Huang, Y. C.; Dong, C. L.; Li, J. F.; Chen, C. T.; Hu, Z.; Chen, S. Y.; Lin, Y.-G. Zhang-Rice Singlets State Formed by Two-Step Oxidation for Triggering Water Oxidation under Operando Conditions. *Nat. Commun.* **2023**, *14*, 529.
(171) Ye, C.; Liu, J.; Zhang, Q.; Jin, X.; Zhao, Y.; Pan, Z.; Chen, G.; Qiu, Y.; Ye, D.; Gu, L.; Waterhouse, G. I. N.; Guo, L.; Yang, S. Activating Metal Oxides Nanocatalysts for Electrocatalytic Water Oxidation by Quenching-Induced Near-Surface Metal Atom Functionality. *J. Am. Chem. Soc.* **2021**, *143*, 14169−14177.
(172) Lin, X.; Huang, Y. C.; Hu, Z.; Li, L.; Zhou, J.; Zhao, Q.; Huang, H.; Sun, J.; Pao, C. W.; Chang, Y.-C.; Lin, H.-J.; Chen, C.-T.; Dong, C.-L.; Wang, J.-Q.; Zhang, L. 5f Covalency Synergistically Boosting Oxygen Evolution of $UCoO_4$ Catalyst. *J. Am. Chem. Soc.* **2022**, *144*, 416−423.
(173) Hunter, B. M.; Gray, H. B.; Muller, A. M. Earth-Abundant Heterogeneous Water Oxidation Catalysts. *Chem. Rev.* **2016**, *116*, 14120−14136.
(174) Kuznetsov, D. A.; Han, B.; Yu, Y.; Rao, R. R.; Hwang, J.; Roman-Leshkov, Y.; Shao-Horn, Y. Tuning Redox Transitions via Inductive Effect in Metal Oxides and Complexes, and Implications in Oxygen Electrocatalysis. *Joule* **2018**, *2*, 225−244.
(175) Gao, L.; Cui, X.; Sewell, C. D.; Li, J.; Lin, Z. Recent Advances in Activating Surface Reconstruction for the High-Efficiency Oxygen Evolution Reaction. *Chem. Soc. Rev.* **2021**, *50*, 8428−8469.
(176) Sun, Y.; Li, R.; Chen, X.; Wu, J.; Xie, Y.; Wang, X.; Ma, K.; Wang, L.; Zhang, Z.; Liao, Q.; Kang, Z.; Zhang, Y. A-Site Management Prompts the Dynamic Reconstructed Active Phase of Perovskite Oxide OER Catalysts. *Adv. Energy Mater.* **2021**, *11*, 2003755.
(177) Lei, H.; Ma, L.; Wan, Q.; Tan, S.; Yang, B.; Wang, Z.; Mai, W.; Fan, H. J. Promoting Surface Reconstruction of NiFe Layered Double Hydroxide for Enhanced Oxygen Evolution. *Adv. Energy Mater.* **2022**, *12*, 2202522.
(178) Bai, J.; Mei, J.; Liao, T.; Sun, Q.; Chen, Z. G.; Sun, Z. Molybdenum-Promoted Surface Reconstruction in Polymorphic Cobalt for Initiating Rapid Oxygen Evolution. *Adv. Energy Mater.* **2022**, *12*, 2103247.
(179) Abdelhafiz, A.; Wang, B.; Harutyunyan, A. R.; Li, J. Carbothermal Shock Synthesis of High Entropy Oxide Catalysts: Dynamic Structural and Chemical Reconstruction Boosting the Catalytic Activity and Stability toward Oxygen Evolution Reaction. *Adv. Energy Mater.* **2022**, *12*, 2200742.
(180) Xu, X.; Pan, Y.; Zhong, Y.; Shi, C.; Guan, D.; Ge, L.; Hu, Z.; Chin, Y. Y.; Lin, H. J.; Chen, C.-T.; Wang, H.; Jiang, S. P.; Shao, Z. New Undisputed Evidence and Strategy for Enhanced Lattice-Oxygen Participation of Perovskite Electrocatalyst through Cation Deficiency Manipulation. *Adv. Sci.* **2022**, *9*, 2200530.
(181) Zegeye, T. A.; Chen, W.-T.; Hsu, C.-C.; Valinton, J. A. A.; Chen, C.-H. Activation Energy Assessing Potential-Dependent Activities and Site Reconstruction for Oxygen Evolution. *ACS Energy Lett.* **2022**, *7*, 2236−2243.
(182) Weng, Z.; Huang, H.; Li, X.; Zhang, Y.; Shao, R.; Yi, Y.; Lu, Y.; Zeng, X.; Zou, J.; Chen, L.; Li, W.; Meng, Y.; Asefa, T.; Huang, C. Coordination Tailoring of Epitaxial Perovskite-Derived Iron Oxide Films for Efficient Water Oxidation Electrocatalysis. *ACS Catal.* **2023**, *13*, 2751−2760.
(183) He, Q.; Wan, Y.; Jiang, H.; Pan, Z.; Wu, C.; Wang, M.; Wu, X.; Ye, B.; Ajayan, P. M.; Song, L. Nickel Vacancies Boost Reconstruction in Nickel Hydroxide Electrocatalyst. *ACS Energy Lett.* **2018**, *3*, 1373−1380.
(184) Wang, J.; Kim, S.-J.; Liu, J.; Gao, Y.; Choi, S.; Han, J.; Shin, H.; Jo, S.; Kim, J.; Ciucci, F.; Kim, H.; Li, Q.; Yang, W.; Long, X.; Yang, S.; Cho, S.-P.; Chae, K. H.; Kim, M. G.; Kim, H.; Lim, J. Redirecting Dynamic Surface Restructuring of a Layered Transition Metal Oxide Catalyst for Superior Water Oxidation. *Nat. Catal.* **2021**, *4*, 212−222.
(185) Selvam, N. C. S.; Du, L.; Xia, B. Y.; Yoo, P. J.; You, B. Reconstructed Water Oxidation Electrocatalysts: The Impact of Surface Dynamics on Intrinsic Activities. *Adv. Funct. Mater.* **2021**, *31*, 2008190.
(186) Chen, Y.; Sun, Y.; Wang, M.; Wang, J.; Li, H.; Xi, H.; Wei, C.; Xi, P.; Sterbinsky, G. E.; Freelandet, J. W.; Fisher, A. C.; Ager, J. W., III; Feng, Z.; Xu, Z. J. Lattice Site−Dependent Metal Leaching in Perovskites toward a Honeycomb-Like Water Oxidation Catalyst. *Sci. Adv.* **2021**, *7*, eabk1788.

https://doi.org/10.1021/acs.chemrev.3c00332
Chem. Rev. 2024, 124, 3694−3812

(187) Lu, M.; Zheng, Y.; Hu, Y.; Huang, B.; Ji, D.; Sun, M.; Li, J.; Peng, Y.; Si, R.; Xi, P.; Yan, C.-H. Artificially Steering Electrocatalytic Oxygen Evolution Reaction Mechanism by Regulating Oxygen Defect Contents in Perovskites. *Sci. Adv.* **2022**, *8*, eabq3563.
(188) Wu, T.; Sun, S.; Song, J.; Xi, S.; Du, Y.; Chen, B.; Sasangka, W. A.; Liao, H.; Gan, C. L.; Scherer, G. G.; Zeng, L.; Wang, H.; Li, H.; Grimaud, A.; Xu, Z. J. Iron-Facilitated Dynamic Active-Site Generation on Spinel $CoAl_2O_4$ with Self-Termination of Surface Reconstruction for Water Oxidation. *Nat. Catal.* **2019**, *2*, 763−772.
(189) Shen, T. H.; Spillane, L.; Peng, J.; Shao-Horn, Y.; Tileli, V. Switchable Wetting of Oxygen-Evolving Oxide Catalysts. *Nat. Catal.* **2022**, *5*, 30−36.
(190) Lopes, P. P.; Chung, D. Y.; Rui, X.; Zheng, H.; He, H.; Farinazzo Bergamo Dias Martins, P.; Strmcnik, D.; Stamenkovic, V. R.; Zapol, P.; Mitchell, J. F.; Klie, F.; Markovic, N. M. Dynamically Stable Active Sites from Surface Evolution of Perovskite Materials during the Oxygen Evolution Reaction. *J. Am. Chem. Soc.* **2021**, *143*, 2741−2750.
(191) Zhao, J.-W.; Zhang, H.; Li, C.-F.; Zhou, X.; Wu, J.-Q.; Zeng, F.; Zhang, J.; Li, G.-R. Key Roles of Surface Fe Sites and Sr Vacancies in the Perovskite for an Efficient Oxygen Evolution Reaction via Lattice Oxygen Oxidation. *Energy Environ. Sci.* **2022**, *15*, 3912−3922.
(192) Xiao, K.; Wang, Y.; Wu, P.; Hou, L.; Liu, Z. Q. Activating Lattice Oxygen in Spinel $ZnCo_2O_4$ through Filling Oxygen Vacancies with Fluorine for Electrocatalytic Oxygen Evolution. *Angew. Chem., Int. Ed.* **2023**, *62*, e202301408.
(193) Duan, Y.; Lee, J. Y.; Xi, S.; Sun, Y.; Ge, J.; Ong, S. J. H.; Chen, Y.; Dou, S.; Meng, F.; Diao, C.; Fisher, A. C.; Wang, X.; Scherer, G. G.; Grimaud, A.; Xu, Z. J. Anodic Oxidation Enabled Cation Leaching for Promoting Surface Reconstruction in Water Oxidation. *Angew. Chem., Int. Ed.* **2021**, *60*, 7418−7425.
(194) Sun, Y.; Wu, J.; Xie, Y.; Wang, X.; Ma, K.; Tian, Z.; Zhang, Z.; Liao, Q.; Zheng, W.; Kang, Z.; Zhang, Y. Dynamics of Both Active Phase and Catalysis Pathway for Spinel Water-Oxidation Catalysts. *Adv. Funct. Mater.* **2022**, *32*, 2207116.
(195) Rasmussen, F. A.; Thygesen, K. S. Computational 2D Materials Database: Electronic Structure of Transition-Metal Dichalcogenides and Oxides. *J. Phys. Chem. C* **2015**, *119*, 13169−13183.
(196) Mei, J.; Shang, J.; He, T.; Qi, D.; Kou, L.; Liao, T.; Du, A.; Sun, Z. 2D/2D Black Phosphorus/Nickel Hydroxide Heterostructures for Promoting Oxygen Evolution via Electronic Structure Modulation and Surface Reconstruction. *Adv. Energy Mater.* **2022**, *12*, 2201141.
(197) Li, S.; Ma, R.; H, J.; Li, Z.; Liu, L.; Wang, X.; Lu, Y.; Sterbinsky, G. E.; Liu, S.; Zheng, L.; Liu, D.; Wang, J.; et al. Coordination Environment Tuning of Nickel Sites by Oxyanions to Optimize Methanol Electro-Oxidation Activity. *Nat. Commun.* **2022**, *13*, 2916.
(198) Zhang, H.; Geng, S.; Ouyang, M.; Yadegari, H.; Xie, F.; Riley, D. J. A Self-Reconstructed Bifunctional Electrocatalyst of Pseudo-Amorphous Nickel Carbide@Iron Oxide Network for Seawater Splitting. *Adv. Sci.* **2022**, *9*, 2200146.
(199) Sun, Y.; Wang, J.; Qi, Y.; Li, W.; Wang, C. Efficient Electrooxidation of 5-Hydroxymethylfurfural Using Co-Doped Ni_3S_2 Catalyst: Promising for H_2 Production under Industrial-Level Current Density. *Adv. Sci.* **2022**, *9*, 2200957.
(200) Zhang, L.; Cai, W.; Bao, N.; Yang, H. Implanting an Electron Donor to Enlarge The D-P Hybridization of High-Entropy (Oxy)-Hydroxide: A Novel Design to Boost Oxygen Evolution. *Adv. Mater.* **2022**, *34*, 2110511.
(201) Zhang, L.; Cai, W.; Bao, N. Top-Level Design Strategy to Construct an Advanced High-Entropy Co-Cu-Fe-Mo (Oxy)-Hydroxide Electrocatalyst for the Oxygen Evolution Reaction. *Adv. Mater.* **2021**, *33*, 2100745.
(202) Chen, R.; Zhang, Z.; Wang, Z.; Wu, W.; Du, S.; Zhu, W.; Lv, H.; Cheng, N. Constructing Air-Stable and Reconstruction-Inhibited Transition Metal Sulfide Catalysts via Tailoring Electron-Deficient Distribution for Water Oxidation. *ACS Catal.* **2022**, *12*, 13234−13246.
(203) Liu, J.; Du, W.; Guo, S.; Pan, J.; Hu, J.; Xu, X. Iron-Locked Hydr(Oxy)Oxide Catalysts via Ion-Compensatory Reconstruction Boost Large-Current-Density Water Oxidation. *Adv. Sci.* **2023**, *10*, 2300717.
(204) Bergmann, A.; Martinez-Moreno, E.; Teschner, D.; Chernev, P.; Gliech, M.; De Araujo, J. F.; Reier, T.; Dau, H.; Strasser, P. Reversible Amorphization and the Catalytically Active State of Crystalline Co_3O_4 during Oxygen Evolution. *Nat. Commun.* **2015**, *6*, 8625.
(205) Su, H.; Zhou, W.; Zhou, W.; Li, Y.; Zheng, L.; Zhang, H.; Liu, M.; Zhang, X.; Sun, X.; Xu, Y.; Hu, F.; Zhang, J.; Hu, T.; Liu, Q.; Wei, S. In-Situ Spectroscopic Observation of Dynamic-Coupling Oxygen on Atomically Dispersed Iridium Electrocatalyst for Acidic Water Oxidation. *Nat. Commun.* **2021**, *12*, 6118.
(206) Ning, M.; Zhang, F.; Wu, L.; Xing, X.; Wang, D.; Song, S.; Zhou, Q.; Yu, L.; Bao, J.; Chen, S.; Ren, Z. Boosting Efficient Alkaline Fresh Water and Seawater Electrolysis via Electrochemical Reconstruction. *Energy Environ. Sci.* **2022**, *15*, 3945−3957.
(207) Lin, R.; Kang, L.; Zhao, T.; Feng, J.; Celorrio, V.; Zhang, G.; Cibin, G.; Kucernak, A.; Brett, D. J. L.; Corà, F.; Parkin, I. P.; He, G. Identification and Manipulation of Dynamic Active Site Deficiency-Induced Competing Reactions in Electrocatalytic Oxidation Processes. *Energy Environ. Sci.* **2022**, *15*, 2386−2396.
(208) Zeng, L.; Chen, Y.; Sun, M.; Huang, Q.; Sun, K.; Ma, J.; Li, J.; Tan, H.; Li, M.; Pan, Y.; Liu, Y.; Luo, M.; Huang, B.; Guo, S. Cooperative Rh-O_5/Ni(Fe) Site for Efficient Biomass Upgrading Coupled with H_2 Production. *J. Am. Chem. Soc.* **2023**, *145*, 17577−17587.
(209) Sun, J.; Xue, H.; Guo, N.; Song, T.; Hao, Y. R.; Sun, J.; Zhang, J.; Wang, Q. Synergetic Metal Defect and Surface Chemical Reconstruction into $NiCo_2S_4$/ZnS Heterojunction to Achieve Outstanding Oxygen Evolution Performance. *Angew. Chem., Int. Ed.* **2021**, *60*, 19435−19441.
(210) Marelli, E.; Gazquez, J.; Poghosyan, E.; Muller, E.; Gawryluk, D. J.; Pomjakushina, E.; Sheptyakov, D.; Piamonteze, C.; Aegerter, D.; Schmidt, T. J.; Medarde, M.; Fabbri, E. Correlation between Oxygen Vacancies and Oxygen Evolution Reaction Activity for a Model Electrode: $PrBaCo_2O_{5+\delta}$. *Angew. Chem., Int. Ed.* **2021**, *60*, 14609−14619.
(211) Chong, X.; Liu, C.; Wang, C.; Yang, R.; Zhang, B. Integrating Hydrogen Production and Transfer Hydrogenation with Selenite Promoted Electrooxidation of α-Nitrotoluenes to *E*-Nitroethenes. *Angew. Chem., Int. Ed.* **2021**, *60*, 22010−22016.
(212) Zhuang, L.; Li, J.; Wang, K.; Li, Z.; Zhu, M.; Xu, Z. Structural Buffer Engineering on Metal Oxide for Long-Term Stable Seawater Splitting. *Adv. Funct. Mater.* **2022**, *32*, 2201127.
(213) Liu, X.; Xia, F.; Guo, R.; Huang, M.; Meng, J.; Wu, J.; Mai, L. Ligand and Anion Co-Leaching Induced Complete Reconstruction of Polyoxomolybdate-Organic Complex Oxygen-Evolving Pre-Catalysts. *Adv. Funct. Mater.* **2021**, *31*, 2101792.
(214) Liao, H.; Luo, T.; Tan, P.; Chen, K.; Lu, L.; Liu, Y.; Liu, M.; Pan, J. Unveiling Role of Sulfate Ion in Nickel-Iron (Oxy)Hydroxide with Enhanced Oxygen-Evolving Performance. *Adv. Funct. Mater.* **2021**, *31*, 2102772.
(215) Hu, C.; Dong, H.; Li, Y.; Sinha, S.; Wang, C.; Xu, W.; Song, L.; Suenaga, K.; Geng, H.; Wang, J.; Huang, Q.; Tan, Y.; Huang, X. Self-Reconstruction of Single-Atom-Thick A Layers in Nanolaminated MAX Phases for Enhanced Oxygen Evolution. *Adv. Funct. Mater.* **2023**, *33*, 2211530.
(216) Zhao, Y.; Wen, Q.; Huang, D.; Jiao, C.; Liu, Y.; Liu, Y.; Fang, J.; Sun, M.; Yu, L. Operando Reconstruction toward Dual-Cation-Defects Co-Containing NiFe Oxyhydroxide for Ultralow Energy Consumption Industrial Water Splitting Electrolyzer. *Adv. Energy Mater.* **2023**, *13*, 2203595.
(217) Solomon, G.; Landström, A.; Mazzaro, R.; Jugovac, M.; Moras, P.; Cattaruzza, E.; Morandi, V.; Concina, I.; Vomiero, A. $NiMoO_4$@Co_3O_4 Core−Shell Nanorods: In Situ Catalyst Recon-

https://doi.org/10.1021/acs.chemrev.3c00332
Chem. Rev. 2024, 124, 3694−3812

struction toward High Efficiency Oxygen Evolution Reaction. *Adv. Energy Mater.* **2021**, *11*, 2101324.
(218) Zhang, Y.; Fu, Q.; Song, B.; Xu, P. Regulation Strategy of Transition Metal Oxide-Based Electrocatalysts for Enhanced Oxygen Evolution Reaction. *Acc. Mater. Res.* **2022**, *3*, 1088−1100.
(219) Zhang, T.; Liu, Y.; Tong, L.; Yu, J.; Lin, S.; Li, Y.; Fan, H. J. Oxidation State Engineering in Octahedral Ni by Anchored Sulfate to Boost Intrinsic Oxygen Evolution Activity. *ACS Nano* **2023**, *17*, 6770−6780.
(220) Wu, T.; Ren, X.; Sun, Y.; Sun, S.; Xian, G.; Scherer, G. G.; Fisher, A. C.; Mandler, D.; Ager, J. W.; Grimaud, A.; Wang, J.; Shen, C.; Yang, H.; Gracia, J.; Gao, H.-J.; Xu, Z. J. Spin Pinning Effect to Reconstructed Oxyhydroxide Layer on Ferromagnetic Oxides for Enhanced Water Oxidation. *Nat. Commun.* **2021**, *12*, 3634.
(221) Yao, N.; Wang, G.; Jia, H.; Yin, J.; Cong, H.; Chen, S.; Luo, W. Intermolecular Energy Gap-Induced Formation of High-Valent Cobalt Species in CoOOH Surface Layer on Cobalt Sulfides for Efficient Water Oxidation. *Angew. Chem., Int. Ed.* **2022**, *61*, e202117178.
(222) An, L.; Yang, F.; Fu, C.; Cai, X.; Shen, S.; Xia, G.; Li, J.; Du, Y.; Luo, L.; Zhang, J. A Functionally Stable RuMn Electrocatalyst for Oxygen Evolution Reaction in Acid. *Adv. Funct. Mater.* **2022**, *32*, 2200131.
(223) You, B.; Sun, Y. Hierarchically Porous Nickel Sulfide Multifunctional Superstructures. *Adv. Energy Mater.* **2016**, *6*, 1502333.
(224) Miao, M.; Hou, R.; Qi, R.; Yan, Y.; Gong, L. Q.; Qi, K.; Liu, H.; Xia, B. Y. Surface Evolution and Reconstruction of Oxygen-Abundant FePi/NiFeP Synergy in NiFe Phosphides For Efficient Water Oxidation. *J. Mater. Chem. A* **2019**, *7*, 18925−18931.
(225) Jiang, H.; He, Q.; Li, X.; Su, X.; Zhang, Y.; Chen, S.; Zhang, S.; Zhang, G.; Jiang, J.; Luo, Y.; Ajayan, P. M.; Song, L. Tracking Structural Self-Reconstruction and Identifying True Active Sites toward Cobalt Oxychloride Precatalyst of Oxygen Evolution Reaction. *Adv. Mater.* **2019**, *31*, 1805127.
(226) Wang, B.; Zhao, K.; Yu, Z.; Sun, C.; Wang, Z.; Feng, N.; Mai, L.; Wang, Y.; Xia, Y. In Situ Structural Evolution of the Multi-Site Alloy Electrocatalyst to Manipulate the Intermediate for Enhanced Water Oxidation Reaction. *Energy Environ. Sci.* **2020**, *13*, 2200−2208.
(227) You, B.; Jiang, N.; Sheng, M.; Bhushan, M. W.; Sun, Y. Hierarchically Porous Urchin-Like Ni_2P Superstructures Supported on Nickel Foam as Efficient Bifunctional Electrocatalysts for Overall Water Splitting. *ACS Catal.* **2016**, *6*, 714−721.
(228) Xiao, Z.; Huang, Y. C.; Dong, C. L.; Xie, C.; Liu, Z.; Du, S.; Chen, W.; Yan, D.; Tao, L.; Shu, Z.; Zhang, G.; Duan, H.; Wang, Y.; Zou, Y.; Chen, R.; Wang, S. Operando Identification of the Dynamic Behavior of Oxygen Vacancy-Rich Co_3O_4 for Oxygen Evolution Reaction. *J. Am. Chem. Soc.* **2020**, *142*, 12087−12095.
(229) Escudero-Escribano, M.; Verdaguer-Casadevall, A.; Malacrida, P.; Gronbjerg, U.; Knudsen, B. P.; Jepsen, A. K.; Rossmeisl, J.; Stephens, I. E.; Chorkendorff, I. Pt_5Gd as a Highly Active and Stable Catalyst for Oxygen Electroreduction. *J. Am. Chem. Soc.* **2012**, *134*, 16476−16479.
(230) Green, C. L.; Kucernak, A. Determination of The Platinum and Ruthenium Surface Areas in Platinum-Ruthenium Alloy Electrocatalysts by Underpotential Deposition of Copper. I. Unsupported Catalysts. *J. Phys. Chem. B* **2002**, *106*, 1036−1047.
(231) Schmidt, T. J.; Gasteiger, H. A.; Stäb, G. D.; Urban, P. M.; Koib, D. M.; Behm, R. J. Characterization of High-Surface-Area Electrocatalysts Using a Rotating Disk Electrode Configuration. *J. Electrochem. Soc.* **1998**, *145*, 2354.
(232) Mathankumar, M.; Anantharaj, S.; Nandakumar, A. K.; Kundu, S.; Subramanian, B. Potentiostatic Phase Formation of β-CoOOH on Pulsed Laser Deposited Biphasic Cobalt Oxide Thin Film for Enhanced Oxygen Evolution. *J. Mater. Chem. A* **2017**, *5*, 23053−23066.
(233) Zhao, T.; Shen, X.; Wang, Y.; Hocking, R. K.; Li, Y.; Rong, C.; Dastafkan, K.; Su, Z.; Zhao, C. In Situ Reconstruction of V-Doped Ni_2P Pre-Catalysts with Tunable Electronic Structures for Water Oxidation. *Adv. Funct. Mater.* **2021**, *31*, 2100614.
(234) Wei, C.; Sun, S.; Mandler, D.; Wang, X.; Qiao, S. Z.; Xu, Z. J. Approaches for Measuring the Surface Areas of Metal Oxide Electrocatalysts for Determining Their Intrinsic Electrocatalytic Activity. *Chem. Soc. Rev.* **2019**, *48*, 2518−2534.
(235) Anderson, R. M.; Yancey, D. F.; Zhang, L.; Chill, S. T.; Henkelman, G.; Crooks, R. M. A Theoretical and Experimental Approach for Correlating Nanoparticle Structure and Electrocatalytic Activity. *Acc. Chem. Res.* **2015**, *48*, 1351−1357.
(236) Liu, X.; Wang, K.; Zhou, L.; Pu, H.; Zhang, T.; Jia, J.; Deng, Y. Shape-Controlled Synthesis of Concave Pt and Willow-Like Pt Nanocatalysts via Electrodeposition With Hydrogen Adsorption/Desorption and Investigation of Their Electrocatalytic Performances toward Ethanol Oxidation Reaction. *ACS Sustainable Chem. Eng.* **2020**, *8*, 6449−6457.
(237) Kuczyński, M.; Łuba, M.; Mikołajczyk, T.; Pierożyński, B. The Influence of Resorcinol on the Kinetics of Underpotentially Deposited Hydrogen, Cathodic Hydrogen and Anodic Oxygen Evolution Reactions, Examined at Polycrystalline Pt Electrode in 0.1 M NaOH Solution. *Int. J. Hydrog. Energy* **2023**, *48*, 10755−10764.
(238) Alia, S. M.; Shulda, S.; Ngo, C.; Pylypenko, S.; Pivovar, B. S. Iridium-Based Nanowires as Highly Active, Oxygen Evolution Reaction Electrocatalysts. *ACS Catal.* **2018**, *8*, 2111−2120.
(239) Fayette, M.; Nelson, A.; Robinson, R. D. Electrophoretic Deposition Improves Catalytic Performance of Co_3O_4 Nanoparticles for Oxygen Reduction/Oxygen Evolution Reactions. *J. Mater. Chem. A* **2015**, *3*, 4274−4283.
(240) Imada, T.; Chiku, M.; Higuchi, E.; Inoue, H. Effect of Rhodium Modification on Activity of Platinum Nanoparticle-Loaded Carbon Catalysts for Electrochemical Toluene Hydrogenation. *ACS Catal.* **2020**, *10*, 13718−13728.
(241) Shen, T.; Gong, M.; Zhao, T.; Hu, Y.; Wang, D.; et al. Optimizing Formic Acid Electro-oxidation Performance by Restricting the Continuous Pd Sites in Pd−Sn Nanocatalysts. *ACS Sustainable Chem. Eng.* **2020**, *8*, 12239−12247.
(242) Permyakova, A. A.; Han, B.; Jensen, J. O.; Bjerrum, N. J.; Shao-Horn, Y. Pt−Si Bifunctional Surfaces for CO and Methanol Electro-Oxidation. *J. Phys. Chem. C* **2015**, *119*, 8023−8031.
(243) Girod, R.; Lazaridis, T.; Gasteiger, H. A.; Tileli, V. Three-Dimensional Nanoimaging of Fuel Cell Catalyst Layers. *Nat. Catal.* **2023**, *6*, 383−391.
(244) Ye, J.-Y.; Jiang, Y.-X.; Sheng, T.; Sun, S.-G. In-Situ FTIR Spectroscopic Studies of Electrocatalytic Reactions and Processes. *Nano Energy* **2016**, *29*, 414−427.
(245) Fan, K.; Zou, H.; Lu, Y.; Chen, H.; Li, F.; Liu, J.; Sun, L.; Tong, L.; Toney, M. F.; Sui, M.; Yu, J. Direct Observation of Structural Evolution of Metal Chalcogenide in Electrocatalytic Water Oxidation. *ACS Nano* **2018**, *12*, 12369−12379.
(246) Yao, Y.; Hu, S.; Chen, W.; Huang, Z.-Q.; Wei, W.; Yao, T.; Liu, R.; Zang, K.; Wang, X.; Wu, G.; et al. Engineering the Electronic Structure of Single Atom Ru Sites via Compressive Strain Boosts Acidic Water Oxidation Electrocatalysis. *Nat. Catal.* **2019**, *2*, 304−313.
(247) Cao, L.; Luo, Q.; Chen, J.; Wang, L.; Lin, Y.; Wang, H.; Liu, X.; Shen, X.; Zhang, W.; Liu, W.; Qi, Z.; Jiang, Z.; Yang, J.; Yao, T. Dynamic Oxygen Adsorption on Single-Atomic Ruthenium Catalyst with High Performance for Acidic Oxygen Evolution Reaction. *Nat. Commun.* **2019**, *10*, 4849.
(248) Huang, J.; Li, Y.; Zhang, Y.; Rao, G.; Wu, C.; Hu, Y.; Wang, X.; Lu, R.; Li, Y.; Xiong, J. Identification of Key Reversible Intermediates in Self-Reconstructed Nickel-Based Hybrid Electrocatalysts for Oxygen Evolution. *Angew. Chem., Int. Ed.* **2019**, *58*, 17458−17464.
(249) Chen, X.; Cheng, Y.; Wen, Y.; Wang, Y.; Yan, X.; Wei, J.; He, S.; Zhou, J. CoP/Fe-Co_9S_8 for Highly Efficient Overall Water Splitting with Surface Reconstruction and Self-Termination. *Adv. Sci.* **2022**, *9*, 2204742.
(250) Zhang, J.; Ye, Y.; Wang, Z.; Xu, Y.; Gui, L.; He, B.; Zhao, L. Probing Dynamic Self-Reconstruction on Perovskite Fluorides toward Ultrafast Oxygen Evolution. *Adv. Sci.* **2022**, *9*, 2201916.

https://doi.org/10.1021/acs.chemrev.3c00332
Chem. Rev. 2024, 124, 3694−3812

(251) Jing, C.; Yuan, T.; Li, L.; Li, J.; Qian, Z.; Zhou, J.; Wang, Y.; Xi, S.; Zhang, N.; Lin, H.-J.; Chen, C.-T.; Hu, Z.; Li, D.-W.; Zhang, L.; Wang, J.-Q. Electrocatalyst with Dynamic Formation of the Dual-Active Site from the Dual Pathway Observed by In Situ Raman Spectroscopy. *ACS Catal.* **2022**, *12*, 10276−10284.
(252) Huang, Z.; Liao, X.; Zhang, W.; Hu, J.; Gao, Q. Ceria-Promoted Reconstruction of Ni-Based Electrocatalysts toward Efficient Oxygen Evolution. *ACS Catal.* **2022**, *12*, 13951−13960.
(253) Chen, Z.; Yang, H.; Mebs, S.; Dau, H.; Driess, M.; Wang, Z.; Kang, Z.; Menezes, P. W. Reviving Oxygen Evolution Electrocatalysis of Bulk La-Ni Intermetallics via Gaseous Hydrogen Engineering. *Adv. Mater.* **2023**, *35*, 2208337.
(254) Lee, W. H.; Han, M. H.; Ko, Y. J.; Min, B. K.; Chae, K. H.; Oh, H. S. Electrode Reconstruction Strategy for Oxygen Evolution Reaction: Maintaining Fe-CoOOH Phase with Intermediate-Spin State During Electrolysis. *Nat. Commun.* **2022**, *13*, 605.
(255) Moysiadou, A.; Lee, S.; Hsu, C. S.; Chen, H. M.; Hu, X. Mechanism of Oxygen Evolution Catalyzed by Cobalt Oxyhydroxide: Cobalt Superoxide Species as a Key Intermediate and Dioxygen Release as a Rate-Determining Step. *J. Am. Chem. Soc.* **2020**, *142*, 11901−11914.
(256) Görlin, M.; de Araújo, J. F.; Schmies, H.; Bernsmeier, D.; Dresp, S.; Gliech, M.; Jusys, Z.; Chernev, P.; Kraehnert, R.; Dau, H.; Strasser, P. Tracking Catalyst Redox States and Reaction Dynamics in Ni-Fe Oxyhydroxide Oxygen Evolution Reaction Electrocatalysts: The Role of Catalyst Support and Electrolyte pH. *J. Am. Chem. Soc.* **2017**, *139*, 2070−2082.
(257) Lee, S.; Moysiadou, A.; Chu, Y.-C.; Chen, H. M.; Hu, X. Tracking High-Valent Surface Iron Species in the Oxygen Evolution Reaction on Cobalt Iron (Oxy)Hydroxides. *Energy Environ. Sci.* **2022**, *15*, 206−214.
(258) Zhao, L.; Sun, Q.; Li, M.; Zhong, Y.; Shen, P.; Lin, Y.; Xu, K. Antiperovskite Nitride Cu_3N Nanosheets for Efficient Electrochemical Oxidation of Methanol to Formate. *Sci. China Mater.* **2023**, *66*, 1820−1828.
(259) Xu, D.; Liu, S.; Zhang, M.; Xu, L.; Gao, H.; Yao, J. Manipulating the Dynamic Self-Reconstruction of CoP Electrocatalyst Driven by Charge Transport and Ion Leaching. *Small* **2023**, *19*, 2300201.
(260) Ji, P.; Zheng, D.; Jin, H.; Chen, D.; Luo, X.; Yang, J.; Wang, Z.; Mu, S. Ultra-Fast in Situ Reconstructed Nickel (Oxy)Hydroxide Nanoparticle Crosslinked Structure for Super-Efficient Alkaline Water Electrolysis by Sacrificing Template Strategy. *Small Struct.* **2023**, *4*, 2300013.
(261) Hung, S.-F.; Zhu, Y.; Tzeng, G.-Q.; Chen, H.-C.; Hsu, C.-S.; Liao, Y.-F.; Ishii, H.; Hiraoka, N.; Chen, H. M. In Situ Spatially Coherent Identification of Phosphide-Based Catalysts: Crystallographic Latching for Highly Efficient Overall Water Electrolysis. *ACS Energy Lett.* **2019**, *4*, 2813−2820.
(262) Reikowski, F.; Maroun, F.; Pacheco, I.; Wiegmann, T.; Allongue, P.; Stettner, J.; Magnussen, O. M. Operando Surface X-Ray Diffraction Studies of Structurally Defined Co_3O_4 and CoOOH Thin Films During Oxygen Evolution. *ACS Catal.* **2019**, *9*, 3811−3821.
(263) Tung, C. W.; Hsu, Y. Y.; Shen, Y. P.; Zheng, Y.; Chan, T. S.; Sheu, H. S.; Cheng, Y. C.; Chen, H. M. Reversible Adapting Layer Produces Robust Single-Crystal Electrocatalyst for Oxygen Evolution. *Nat. Commun.* **2015**, *6*, 8106.
(264) Yan, Z.; Sun, H.; Chen, X.; Liu, H.; Zhao, Y.; Li, H.; Xie, W.; Cheng, F.; Chen, J. Anion Insertion Enhanced Electrodeposition of Robust Metal Hydroxide/Oxide Electrodes for Oxygen Evolution. *Nat. Commun.* **2018**, *9*, 2373.
(265) Isaacs, M. A.; Davies-Jones, J.; Davies, P. R.; Guan, S.; Lee, R.; Morgan, D. J.; Palgrave, R. Advanced XPS Characterization: XPS-Based Multi-Technique Analyses for Comprehensive Understanding of Functional Materials. *Mater. Chem. Front.* **2021**, *5*, 7931−7963.
(266) Jiang, N.; You, B.; Sheng, M.; Sun, Y. Electrodeposited Cobalt-Phosphorous-Derived Films as Competent Bifunctional Catalysts for Overall Water Splitting. *Angew. Chem., Int. Ed.* **2015**, *54*, 6251−6254.
(267) Zhao, Y.; Adiyeri Saseendran, D. P.; Huang, C.; Triana, C. A.; Marks, W. R.; Chen, H.; Zhao, H.; Patzke, G. R. Oxygen Evolution/Reduction Reaction Catalysts: From In Situ Monitoring and Reaction Mechanisms to Rational Design. *Chem. Rev.* **2023**, *123*, 6257−6358.
(268) Dai, T.; Zhang, X.; Sun, M.; Huang, B.; Zhang, N.; Da, P.; Yang, R.; He, Z.; Wang, W.; Xi, P.; Yan, C.-H. Uncovering the Promotion of $CeO_2/CoS_{1.97}$ Heterostructure with Specific Spatial Architectures on Oxygen Evolution Reaction. *Adv. Mater.* **2021**, *33*, 2102593.
(269) Favaro, M.; Yang, J.; Nappini, S.; Magnano, E.; Toma, F. M.; Crumlin, E. J.; Yano, J.; Sharp, I. D. Understanding the Oxygen Evolution Reaction Mechanism on CoO_x using Operando Ambient-Pressure X-Ray Photoelectron Spectroscopy. *J. Am. Chem. Soc.* **2017**, *139*, 8960−8970.
(270) Timoshenko, J.; Guenya, B. R. In Situ/Operando Electrocatalyst characterization by X-Ray Absorption Spectroscopy. *Chem. Rev.* **2021**, *121*, 882−961.
(271) Zhu, Y.; Kuo, T.-R.; Li, Y.-H.; Qi, M.-Y.; Chen, G.; Wang, J.; Xu, Y.-J.; Chen, H. M. Emerging Dynamic Structure of Electrocatalysts Unveiled by In Situ X-Ray Diffraction/Absorption Spectroscopy. *Energy Environ. Sci.* **2021**, *14*, 1928−1958.
(272) Cao, D.; Liu, D.; Chen, S.; Moses, O. A.; Chen, X.; Xu, W.; Wu, C.; Zheng, L.; Chu, S.; Jiang, H.; Wang, C.; Ge, B.; Wu, X.; Zhang, J.; Song, L. Operando X-Ray Spectroscopy Visualizing the Chameleon-Like Structural Reconstruction on an Oxygen Evolution Electrocatalyst. *Energy Environ. Sci.* **2021**, *14*, 906−915.
(273) Peng, W.; Deshmukh, A.; Chen, N.; Lv, Z.; Zhao, S.; Li, J.; Yan, B.; Gao, X.; Shang, L.; Gong, Y.; Wu, L.; Chen, M.; Zhang, T.; Gou, H. Deciphering The Dynamic Structure Evolution of Fe- and Ni-Codoped CoS_2 for Enhanced Water Oxidation. *ACS Catal.* **2022**, *12*, 3743−3751.
(274) Ji, Q.; Kong, Y.; Tan, H.; Duan, H.; Li, N.; Tang, B.; Wang, Y.; Feng, S.; Lv, L.; Wang, C.; Hu, F.; Zhang, W.; Cai, L.; Yan, W. Operando Identification of Active Species and Intermediates on Sulfide Interfaced by Fe_3O_4 for Ultrastable Alkaline Oxygen Evolution at Large Current Density. *ACS Catal.* **2022**, *12*, 4318−4326.
(275) Zheng, X.; Zhang, B.; De Luna, P.; Liang, Y.; Comin, R.; Voznyy, O.; Han, L.; Garcia De Arquer, F. P.; Liu, M.; Dinh, C. T.; et al. Theory-Driven Design of High-Valence Metal Sites for Water Oxidation Confirmed using In Situ Soft X-Ray Absorption. *Nat. Chem.* **2018**, *10*, 149−154.
(276) Zhao, S.; Tan, C.; He, C.-T.; An, P.; Xie, F.; Jiang, S.; Zhu, Y.; Wu, K.-H.; Zhang, B.; Li, H.; et al. Structural Transformation of Highly Active Metal−Organic Framework Electrocatalysts during the Oxygen Evolution Reaction. *Nat. Energy* **2020**, *5*, 881−890.
(277) Cutsail, G. E., Iii; Debeer, S. Challenges and Opportunities for Applications of Advanced X-Ray Spectroscopy in Catalysis Research. *ACS Catal.* **2022**, *12*, 5864−5886.
(278) Gul, S.; Ng, J. W.; Alonso-Mori, R.; Kern, J.; Sokaras, D.; Anzenberg, E.; Lassalle-Kaiser, B.; Gorlin, Y.; Weng, T. C.; Zwart, P. H.; Zhang, J. Z.; Bergmann, U.; Yachandra, V. K.; Jaramillo, T. F.; Yano, J. Simultaneous Detection of Electronic Structure Changes from Two Elements of a Bifunctional Catalyst using Wavelength-Dispersive X-Ray Emission Spectroscopy and In Situ Electrochemistry. *Phys. Chem. Chem. Phys.* **2015**, *17*, 8901−8912.
(279) Hadt, R. G.; Hayes, D.; Brodsky, C. N.; Ullman, A. M.; Casa, D. M.; Upton, M. H.; Nocera, D. G.; Chen, L. X. X-Ray Spectroscopic Characterization of Co(IV) and Metal-Metal Interactions in Co_4O_4: Electronic Structure Contributions to the Formation of High-Valent States Relevant to the Oxygen Evolution Reaction. *J. Am. Chem. Soc.* **2016**, *138*, 11017−11030.
(280) Kuai, C.; Xu, Z.; Xi, C.; Hu, A.; Yang, Z.; Zhang, Y.; Sun, C.-J.; Li, L.; Sokaras, D.; Dong, C.; Qiao, S.-Z.; Du, X.-W.; Lin, F. Phase Segregation Reversibility in Mixed-Metal Hydroxide Water Oxidation Catalysts. *Nat. Catal.* **2020**, *3*, 743−753.
(281) Huang, K.; Xia, J.; Lu, Y.; Zhang, B.; Shi, W.; Cao, X.; Zhang, X.; Woods, L. M.; Han, C.; Chen, C.; Wang, T.; Wu, J.; Huang, Y. Self-Reconstructed Spinel Surface Structure Enabling the Long-Term Stable Hydrogen Evolution Reaction/Oxygen Evolution Reaction

https://doi.org/10.1021/acs.chemrev.3c00332
Chem. Rev. 2024, 124, 3694−3812

Efficiency of FeCoNiRu High-Entropy Alloyed Electrocatalyst. *Adv. Sci.* **2023**, *10*, 2300094.
(282) Stern, L.-A.; Feng, L.; Song, F.; Hu, X. Ni_2P as a Janus Catalyst for Water Splitting: The Oxygen Evolution Activity of Ni_2P Nanoparticles. *Energy Environ. Sci.* **2015**, *8*, 2347−2351.
(283) Yin, Z. W.; Zhao, W.; Li, J.; Peng, X. X.; Lin, C.; Zhang, M.; Zeng, Z.; Liao, H. G.; Chen, H.; Lin, H.; Pan, F. Advanced Electron Energy Loss Spectroscopy for Battery Studies. *Adv. Funct. Mater.* **2022**, *32*, 2107190.
(284) Wang, Y.; Skaanvik, S. A.; Xiong, X.; Wang, S.; Dong, M. Scanning Probe Microscopy for Electrocatalysis. *Matter* **2021**, *4*, 3483−3514.
(285) Santana Santos, C.; Jaato, B. N.; Sanjuan, I.; Schuhmann, W.; Andronescu, C. Operando Scanning Electrochemical Probe Microscopy during Electrocatalysis. *Chem. Rev.* **2023**, *123*, 4972−5019.
(286) Liu, D.-Q.; Zhang, B.; Zhao, G.; Chen, J.; Pan, H.; Sun, W. Advanced In-Situ Electrochemical Scanning Probe Microscopies in Electrocatalysis. *Chin. J. Catal.* **2023**, *47*, 93−120.
(287) Stumm, C.; Bertram, M.; Kastenmeier, M.; Speck, F. D.; Sun, Z.; Rodríguez-Fernández, J.; Lauritsen, J. V.; Mayrhofer, K. J. J.; Cherevko, S.; Brummel, O.; Libuda, J. Structural Dynamics of Ultrathin Cobalt Oxide Nanoislands under Potential Control. *Adv. Funct. Mater.* **2021**, *31*, 2009923.
(288) Sun, Y.; Wu, C.-R.; Ding, T.-Y.; Gu, J.; Yan, J.-W.; Cheng, J.; Zhang, K. H. L. Direct Observation of the Dynamic Reconstructed Active Phase of Perovskite $LaNiO_3$ for the Oxygen-Evolution Reaction. *Chem. Sci.* **2023**, *14*, 5906−5911.
(289) Giessibl, F. J. Advances in Atomic Force Microscopy. *Rev. Mod. Phys.* **2003**, *75*, 949−983.
(290) Deng, J.; Nellist, M. R.; Stevens, M. B.; Dette, C.; Wang, Y.; Boettcher, S. W. Morphology Dynamics of Single-Layered $Ni(OH)_2$/NiOOH Nanosheets and Subsequent Fe Incorporation Studied by In Situ Electrochemical Atomic Force Microscopy. *Nano Lett.* **2017**, *17*, 6922−6926.
(291) Nellist, M. R.; Laskowski, F. A. L.; Qiu, J.; Hajibabaei, H.; Sivula, K.; Hamann, T. W.; Boettcher, S. W. Potential-Sensing Electrochemical Atomic Force Microscopy for in Operando Analysis of Water-Splitting Catalysts and Interfaces. *Nat. Energy* **2018**, *3*, 46−52.
(292) Gao, X.; Chen, Y.; Sun, T.; Huang, J.; Zhang, W.; Wang, Q.; Cao, R. Karst Landform-Featured Monolithic Electrode for Water Electrolysis in Neutral Media. *Energy Environ. Sci.* **2020**, *13*, 174−182.
(293) Sun, T.; Wang, D.; Mirkin, M. V.; Cheng, H.; Zheng, J.-C.; Richards, R. M.; Lin, F. X.; H, L. Direct High-Resolution Mapping of Electrocatalytic Activity of Semi-Two-Dimensional Catalysts with Single-Edge Sensitivity. *Proc. Natl. Acad. Sci. U. S. A.* **2019**, *116*, 11618−11623.
(294) Ahn, H. S.; Bard, A. J. Surface Interrogation Scanning Electrochemical Microscopy of $Ni_{1-X}Fe_XOOH$ ($0 < X < 0.27$) Oxygen Evolving Catalyst: Kinetics of the "Fast" Iron Sites. *J. Am. Chem. Soc.* **2016**, *138*, 313−318.
(295) Tarnev, T.; Aiyappa, H. B.; Botz, A.; Erichsen, T.; Ernst, A.; Andronescu, C.; Schuhmann, W. Scanning Electrochemical Cell Microscopy Investigation of Single ZIF-Derived Nanocomposite Particles as Electrocatalysts for Oxygen Evolution in Alkaline Media. *Angew. Chem., Int. Ed.* **2019**, *58*, 14265−14269.
(296) Luan, C.; Angona, J.; Bala Krishnan, A.; Corva, M.; Hosseini, P.; Heidelmann, M.; Hagemann, U.; Batsa Tetteh, E.; Schuhmann, W.; Tschulik, K.; Li, T. Linking Composition, Structure and Thickness of CoOOH Layers to Oxygen Evolution Reaction Activity by Correlative Microscopy. *Angew. Chem., Int. Ed.* **2023**, *62*, e202305982.
(297) Zhang, L.; Yuan, H.; Wang, L.; Zhang, H.; Zang, Y.; Tian, Y.; Wen, Y.; Ni, F.; Song, H.; Wang, H.; Zhang, B.; Peng, H. The Critical Role of Electrochemically Activated Adsorbates in Neutral OER. *Sci. China Mater.* **2020**, *63*, 2509−2516.
(298) Balakrishnan, A.; Blanc, N.; Hagemann, U.; Gemagami, P.; Wonner, K.; Tschulik, K.; Li, T. Direct Detection of Surface Species Formed on Iridium Electrocatalysts during the Oxygen Evolution Reaction. *Angew. Chem., Int. Ed.* **2021**, *60*, 21396−21403.
(299) Kramm, U. I.; Ni, L.; Wagner, S. ^{57}Fe Mössbauer Spectroscopy Characterization of Electrocatalysts. *Adv. Mater.* **2019**, *31*, 1805623.
(300) Li, N.; Hadt, R. G.; Hayes, D.; Chen, L. X.; Nocera, D. G. Detection of High-Valent Iron Species in Alloyed Oxidic Cobaltates for Catalysing the Oxygen Evolution Reaction. *Nat. Commun.* **2021**, *12*, 4218.
(301) Chen, J. Y.; Dang, L.; Liang, H.; Bi, W.; Gerken, J. B.; Jin, S.; Alp, E. E.; Stahl, S. S. Operando Analysis of NiFe and Fe Oxyhydroxide Electrocatalysts for Water Oxidation: Detection of Fe^{4+} by Mössbauer Spectroscopy. *J. Am. Chem. Soc.* **2015**, *137*, 15090−15093.
(302) He, Z.; Zhang, J.; Gong, Z.; Lei, H.; Zhou, D.; Zhang, N.; Mai, W.; Zhao, S.; Chen, Y. Activating Lattice Oxygen in NiFe-Based (Oxy)Hydroxide for Water Electrolysis. *Nat. Commun.* **2022**, *13*, 2191.
(303) Shi, Z.; Wang, Y.; Li, J.; Wang, X.; Wang, Y.; Li, Y.; Xu, W.; Jiang, Z.; Liu, C.; Xing, W.; Ge, J. Confined Ir Single Sites with Triggered Lattice Oxygen Redox: Toward Boosted and Sustained Water Oxidation Catalysis. *Joule* **2021**, *5*, 2164−2176.
(304) Guan, D.; Zhang, K.; Hu, Z.; Wu, X.; Chen, J. L.; Pao, C. W.; Guo, Y.; Zhou, W.; Shao, Z. Exceptionally Robust Face-Sharing Motifs Enable Efficient and Durable Water Oxidation. *Adv. Mater.* **2021**, *33*, 2103392.
(305) Huang, J.; Scott, S. B.; Chorkendorff, I.; Wen, Z. Online Electrochemistry−Mass Spectrometry Evaluation of the Acidic Oxygen Evolution Reaction at Supported Catalysts. *ACS Catal.* **2021**, *11*, 12745−12753.
(306) Guo, H.; Yang, Y.; Yang, G.; Cao, X.; Yan, N.; Li, Z.; Chen, E.; Tang, L.; Peng, M.; Shi, L.; Xie, S.; Tao, H.; Xu, C.; Zhu, Y.; Fu, X.; Pan, Y.; Chen, N.; Lin, J.; Tu, X.; Shao, Z.; Sun, Y. Ex Situ Reconstruction-Shaped Ir/CoO/Perovskite Heterojunction for Boosted Water Oxidation Reaction. *ACS Catal.* **2023**, *13*, 5007−5019.
(307) Lin, C.; Li, J.-L.; Li, X.; Yang, S.; Luo, W.; Zhang, Y.; Kim, S.-H.; Kim, D.-H.; Shinde, S. S.; Li, Y.-F.; Liu, Z.-P.; Jiang, Z.; Lee, J.-H. In-Situ Reconstructed Ru Atom Array on α-MnO_2 with Enhanced Performance for Acidic Water Oxidation. *Nat. Catal.* **2021**, *4*, 1012−1023.
(308) Yang, M.-Q.; Wang, J.; Wu, H.; Ho, G. W. Noble Metal-Free Nanocatalysts with Vacancies for Electrochemical Water Splitting. *Small* **2018**, *14*, 1703323.
(309) Anantharaj, S.; Ede, S. R.; Sakthikumar, K.; Karthick, K.; Mishra, S.; Kundu, S. Recent Trends and Perspectives in Electrochemical Water Splitting with an Emphasis on Sulfide, Selenide, and Phosphide Catalysts of Fe, Co, and Ni: A Review. *ACS Catal.* **2016**, *6*, 8069−8097.
(310) Audichon, T.; Napporn, T. W.; Canaff, C.; Morais, C.; Comminges, C.; Kokoh, K. B. IrO_2 Coated on RuO_2 as Efficient and Stable Electroactive Nanocatalysts for Electrochemical Water Splitting. *J. Phys. Chem. C* **2016**, *120*, 2562−2573.
(311) Koper, M. T. M. A Basic Solution. *Nat. Chem.* **2013**, *5*, 255−256.
(312) Wu, H. B.; Xia, B. Y.; Yu, L.; Yu, X.-Y.; Lou, X. W. Porous Molybdenum Carbide Nano-Octahedrons Synthesized via Confined Carburization in Metal-Organic Frameworks for Efficient Hydrogen Production. *Nat. Commun.* **2015**, *6*, 6512.
(313) Sheng, W.; Myint, M.; Chen, J. G.; Yan, Y. Correlating the Hydrogen Evolution Reaction Activity in Alkaline Electrolytes with the Hydrogen Binding Energy on Monometallic Surfaces. *Energy Environ. Sci.* **2013**, *6*, 1509−1512.
(314) Yang, Y.; Yao, H.; Yu, Z.; Islam, S. M.; He, H.; Yuan, M.; Yue, Y.; Xu, K.; Hao, W.; Sun, G.; et al. Hierarchical Nanoassembly of $MoS_2/Co_9S_8/Ni_3S_2$/Ni as a Highly Efficient Electrocatalyst for Overall Water Splitting in a Wide pH Range. *J. Am. Chem. Soc.* **2019**, *141*, 10417−10430.
(315) You, B.; Sun, Y. Innovative Strategies for Electrocatalytic Water Splitting. *Acc. Chem. Res.* **2018**, *51*, 1571−1580.

https://doi.org/10.1021/acs.chemrev.3c00332
Chem. Rev. 2024, 124, 3694−3812

(316) Zhang, T.; Jin, J.; Chen, J.; Fang, Y.; Han, X.; Chen, J.; Li, Y.; Wang, Y.; Liu, J.; Wang, L. Pinpointing the Axial Ligand Effect on Platinum Single-Atom-Catalyst towards Efficient Alkaline Hydrogen Evolution Reaction. *Nat. Commun.* **2022**, *13*, 6875.
(317) Chen, Z.; Xu, Y.; Ding, D.; Song, G.; Gan, X.; Li, H.; Wei, W.; Chen, J.; Li, Z.; Gong, Z.; et al. Thermal Migration towards Constructing W-W Dual-Sites for Boosted Alkaline Hydrogen Evolution Reaction. *Nat. Commun.* **2022**, *13*, 763.
(318) Wu, J.; Fan, J.; Zhao, X.; Wang, Y.; Wang, D.; Liu, H.; Gu, L.; Zhang, Q.; Zheng, L.; Singh, D. J.; et al. Atomically Dispersed MoO_x on Rhodium Metallene Boosts Electrocatalyzed Alkaline Hydrogen Evolution. *Angew. Chem., Int. Ed.* **2022**, *61*, e202207512.
(319) An, L.; Wei, C.; Lu, M.; Liu, H.; Chen, Y.; Scherer, G. G.; Fisher, A. C.; Xi, P.; Xu, Z. J.; Yan, C.-H. Recent Development of Oxygen Evolution Electrocatalysts in Acidic Environment. *Adv. Mater.* **2021**, *33*, 2006328.
(320) Rong, C.; Shen, X.; Wang, Y.; Thomsen, L.; Zhao, T.; Li, Y.; Lu, X.; Amal, R.; Zhao, C. Electronic Structure Engineering of Single-Atom Ru Sites via Co-N_4 Sites for Bifunctional pH-Universal Water Splitting. *Adv. Mater.* **2022**, *34*, 2110103.
(321) Chen, Z.; Duan, X.; Wei, W.; Wang, S.; Ni, B.-J. Electrocatalysts for Acidic Oxygen Evolution Reaction: Achievements and Perspectives. *Nano Energy* **2020**, *78*, 105392.
(322) Wu, J.; Liu, M.; Chatterjee, K.; Hackenberg, K. P.; Shen, J.; Zou, X.; Yan, Y.; Gu, J.; Yang, Y.; Lou, J.; et al. Exfoliated 2D Transition Metal Disulfides for Enhanced Electrocatalysis of Oxygen Evolution Reaction in Acidic Medium. *Adv. Mater. Interfaces* **2016**, *3*, 1500669.
(323) Reier, T.; Oezaslan, M.; Strasser, P. Electrocatalytic Oxygen Evolution Reaction (OER) on Ru, Ir, and Pt Catalysts: A Comparative Study of Nanoparticles and Bulk Materials. *ACS Catal.* **2012**, *2*, 1765−1772.
(324) Chen, D.; Pu, Z.; Lu, R.; Ji, P.; Wang, P.; Zhu, J.; Lin, C.; Li, H.-W.; Zhou, X.; Hu, Z.; et al. Ultralow Ru Loading Transition Metal Phosphides as High-Efficient Bifunctional Electrocatalyst for a Solar-to-Hydrogen Generation System. *Adv. Energy Mater.* **2020**, *10*, 2000814.
(325) Shah, K.; Dai, R.; Mateen, M.; Hassan, Z.; Zhuang, Z.; Liu, C.; Israr, M.; Cheong, W.-C.; Hu, B.; Tu, R.; et al. Cobalt Single Atom Incorporated in Ruthenium Oxide Sphere: A Robust Bifunctional Electrocatalyst for HER and OER. *Angew. Chem., Int. Ed.* **2022**, *61*, e202114951.
(326) Yu, J.; He, Q.; Yang, G.; Zhou, W.; Shao, Z.; Ni, M. Recent Advances and Prospective in Ruthenium-Based Materials for Electrochemical Water Splitting. *ACS Catal.* **2019**, *9*, 9973−10011.
(327) Shan, J.; Guo, C.; Zhu, Y.; Chen, S.; Song, L.; Jaroniec, M.; Zheng, Y.; Qiao, S.-Z. Charge-Redistribution-Enhanced Nanocrystalline Ru@IrO_x Electrocatalysts for Oxygen Evolution in Acidic Media. *Chem.* **2019**, *5*, 445−459.
(328) Ai, X.; Zou, X.; Chen, H.; Su, Y.; Feng, X.; Li, Q.; Liu, Y.; Zhang, Y.; Zou, X. Transition-Metal-Boron Intermetallics with Strong Interatomic d-sp Orbital Hybridization for High-Performance Electrocatalysis. *Angew. Chem., Int. Ed.* **2020**, *59*, 3961−3965.
(329) Gao, G.; Sun, Z.; Chen, X.; Zhu, G.; Sun, B.; Yamauchi, Y.; Liu, S. Recent Advances in Ru/Ir-Based Electrocatalysts for Acidic Oxygen Evolution Reaction. *Appl. Catal., B* **2024**, *343*, 123584.
(330) Li, Y.; Wang, W.; Cheng, M.; Feng, Y.; Han, X.; Qian, Q.; Zhu, Y.; Zhang, G. Arming Ru with Oxygen-Vacancy-Enriched RuO_2 Sub-Nanometer Skin Activates Superior Bifunctionality for pH-Universal Overall Water Splitting. *Adv. Mater.* **2023**, *35*, 2206351.
(331) Peng, X.; Zhao, S.; Mi, Y.; Han, L.; Liu, X.; Qi, D.; Sun, J.; Liu, Y.; Bao, H.; Zhuo, L.; et al. Trifunctional Single-Atomic Ru Sites Enable Efficient Overall Water Splitting and Oxygen Reduction in Acidic Media. *Small* **2020**, *16*, 2002888.
(332) Zhu, J.; Guo, Y.; Liu, F.; Xu, H.; Gong, L.; Shi, W.; Chen, D.; Wang, P.; Yang, Y.; Zhang, C.; et al. Regulative Electronic States around Ruthenium/Ruthenium Disulphide Heterointerfaces for Efficient Water Splitting in Acidic Media. *Angew. Chem., Int. Ed.* **2021**, *60*, 12328−12334.
(333) Wang, J.; Han, L.; Huang, B.; Shao, Q.; Xin, H. L.; Huang, X. Amorphization Activated Ruthenium-Tellurium Nanorods for Efficient Water Splitting. *Nat. Commun.* **2019**, *10*, 5692.
(334) Wen, Y.; Chen, P.; Wang, L.; Li, S.; Wang, Z.; Abed, J.; Mao, X.; Min, Y.; Dinh, C. T.; De Luna, P.; et al. Stabilizing Highly Active Ru Sites by Suppressing Lattice Oxygen Participation in Acidic Water Oxidation. *J. Am. Chem. Soc.* **2021**, *143*, 6482−6490.
(335) Zheng, Y.-R.; Vernieres, J.; Wang, Z.; Zhang, K.; Hochfilzer, D.; Krempl, K.; Liao, T.-W.; Presel, F.; Altantzis, T.; Fatermans, J.; et al. Monitoring Oxygen Production on Mass-Selected Iridium-Tantalum Oxide Electrocatalysts. *Nat. Energy* **2022**, *7*, 55−64.
(336) Retuerto, M.; Pascual, L.; Torrero, J.; Salam, M. A.; Tolosana-Moranchel, A.; Gianolio, D.; Ferrer, P.; Kayser, P.; Wilke, V.; Stiber, S.; et al. Highly Active and Stable OER Electrocatalysts Derived from Sr_2MIrO_6 for Proton Exchange Membrane Water Electrolyzers. *Nat. Commun.* **2022**, *13*, 7935.
(337) Cherevko, S.; Geiger, S.; Kasian, O.; Kulyk, N.; Grote, J.-P.; Savan, A.; Shrestha, B. R.; Merzlikin, S.; Breitbach, B.; Ludwig, A.; Mayrhofer, K. J. J. Oxygen and Hydrogen Evolution Reactions on Ru, RuO_2, Ir, and IrO_2 Thin Film Electrodes in Acidic and Alkaline Electrolytes: A Comparative Study on Activity and Stability. *Catal. Today* **2016**, *262*, 170−180.
(338) Kasian, O.; Grote, J.-P.; Geiger, S.; Cherevko, S.; Mayrhofer, K. J. J. The Common Intermediates of Oxygen Evolution and Dissolution Reactions during Water Electrolysis on Iridium. *Angew. Chem., Int. Ed.* **2018**, *57*, 2488−2491.
(339) Zhang, R.; Dubouis, N.; Ben Osman, M.; Yin, W.; Sougrati, M. T.; Corte, D. A. D.; Giaume, D.; Grimaud, A. A Dissolution/Precipitation Equilibrium on the Surface of Iridium-Based Perovskites Controls Their Activity as Oxygen Evolution Reaction Catalysts in Acidic Media. *Angew. Chem., Int. Ed.* **2019**, *58*, 4571−4575.
(340) Guan, J.; Li, D.; Si, R.; Miao, S.; Zhang, F.; Li, C. Synthesis and Demonstration of Subnanometric Iridium Oxide as Highly Efficient and Robust Water Oxidation Catalyst. *ACS Catal.* **2017**, *7*, 5983−5986.
(341) Geiger, S.; Kasian, O.; Ledendecker, M.; Pizzutilo, E.; Mingers, A. M.; Fu, W. T.; Diaz-Morales, O.; Li, Z.; Oellers, T.; Fruchter, L.; et al. The Stability Number as a Metric for Electrocatalyst Stability Benchmarking. *Nat. Catal.* **2018**, *1*, 508−515.
(342) Chen, Y.; Li, H.; Wang, J.; Du, Y.; Xi, S.; Sun, Y.; Sherburne, M.; Ager, J. W., III; Fisher, A. C.; Xu, Z. J. Exceptionally Active Iridium Evolved from a Pseudo-Cubic Perovskite for Oxygen Evolution in Acid. *Nat. Commun.* **2019**, *10*, 572.
(343) Fu, L.; Yang, F.; Cheng, G.; Luo, W. Ultrathin Ir Nanowires as High-Performance Electrocatalysts for Efficient Water Splitting in Acidic Media. *Nanoscale* **2018**, *10*, 1892−1897.
(344) Zhang, J.; Wang, G.; Liao, Z.; Zhang, P.; Wang, F.; Zhuang, X.; Zschech, E.; Feng, X. Iridium Nanoparticles Anchored on 3D Graphite Foam as a Bifunctional Electrocatalyst for Excellent Overall Water Splitting in Acidic Solution. *Nano Energy* **2017**, *40*, 27−33.
(345) Ding, J.; Yang, H.; Zhang, S.; Liu, Q.; Cao, H.; Luo, J.; Liu, X. Advances in the Electrocatalytic Hydrogen Evolution Reaction by Metal Nanoclusters-Based Materials. *Small* **2022**, *18*, 2204524.
(346) Lu, Y.; Chen, W. Sub-Nanometre Sized Metal Clusters: From Synthetic Challenges to the Unique Property Discoveries. *Chem. Soc. Rev.* **2012**, *41*, 3594−3623.
(347) He, T.; Puente-Santiago, A. R.; Xia, S.; Ahsan, M. A.; Xu, G.; Luque, R. Experimental and Theoretical Advances on Single Atom and Atomic Cluster-Decorated Low-Dimensional Platforms towards Superior Electrocatalysts. *Adv. Energy Mater.* **2022**, *12*, 2200493.
(348) Wang, Q.; Xu, C.-Q.; Liu, W.; Hung, S.-F.; Yang, H. B.; Gao, J.; Cai, W.; Chen, H. M.; Li, J.; Liu, B. Coordination Engineering of Iridium Nanocluster Bifunctional Electrocatalyst for Highly Efficient and pH-Universal Overall Water Splitting. *Nat. Commun.* **2020**, *11*, 4246.
(349) Lu, B.; Guo, L.; Wu, F.; Peng, Y.; Lu, J. E.; Smart, T. J.; Wang, N.; Finfrock, Y. Z.; Morris, D.; Zhang, P.; et al. Ruthenium Atomically Dispersed in Carbon Outperforms Platinum toward Hydrogen Evolution in Alkaline Media. *Nat. Commun.* **2019**, *10*, 631.

https://doi.org/10.1021/acs.chemrev.3c00332
Chem. Rev. 2024, 124, 3694−3812

(350) Cheng, Y.; Zhao, S.; Johannessen, B.; Veder, J.-P.; Saunders, M.; Rowles, M. R.; Cheng, M.; Liu, C.; Chisholm, M. F.; De Marco, R.; et al. Atomically Dispersed Transition Metals on Carbon Nanotubes with Ultrahigh Loading for Selective Electrochemical Carbon Dioxide Reduction. *Adv. Mater.* **2018**, *30*, 1706287.
(351) Zhao, C.; Dai, X.; Yao, T.; Chen, W.; Wang, X.; Wang, J.; Yang, J.; Wei, S.; Wu, Y.; Li, Y. Ionic Exchange of Metal Organic Frameworks to Access Single Nickel Sites for Efficient Electroreduction of CO_2. *J. Am. Chem. Soc.* **2017**, *139*, 8078−8081.
(352) Yang, X.-F.; Wang, A.; Qiao, B.; Li, J.; Liu, J.; Zhang, T. Single-Atom Catalysts: A New Frontier in Heterogeneous Catalysis. *Acc. Chem. Res.* **2013**, *46*, 1740−1748.
(353) Luo, F.; Hu, H.; Zhao, X.; Yang, Z.; Zhang, Q.; Xu, J.; Kaneko, T.; Yoshida, Y.; Zhu, C.; Cai, W. Robust and Stable Acidic Overall Water Splitting on Ir Single Atoms. *Nano Lett.* **2020**, *20*, 2120−2128.
(354) Wang, H.; Chen, Z.-N.; Wu, D.; Cao, M.; Sun, F.; Zhang, H.; You, H.; Zhuang, W.; Cao, R. Significantly Enhanced Overall Water Splitting Performance by Partial Oxidation of Ir through Au Modification in Core-Shell Alloy Structure. *J. Am. Chem. Soc.* **2021**, *143*, 4639−4645.
(355) Lv, F.; Zhang, W.; Yang, W.; Feng, J.; Wang, K.; Zhou, J.; Zhou, P.; Guo, S. Ir-Based Alloy Nanoflowers with Optimized Hydrogen Binding Energy as Bifunctional Electrocatalysts for Overall Water Splitting. *Small Methods* **2020**, *4*, 1900129.
(356) Jin, Z.; Lv, J.; Jia, H.; Liu, W.; Li, H.; Chen, Z.; Lin, X.; Xie, G.; Liu, X.; Sun, S.; Qiu, H.-J. Nanoporous Al-Ni-Co-Ir-Mo High-Entropy Alloy for Record-High Water Splitting Activity in Acidic Environments. *Small* **2019**, *15*, 1904180.
(357) Kundu, M. K.; Mishra, R.; Bhowmik, T.; Kanrar, S.; Barman, S. Three-Dimensional Hierarchically Porous Iridium Oxide-Nitrogen Doped Carbon Hybrid: An Efficient Bifunctional Catalyst for Oxygen Evolution and Hydrogen Evolution Reaction in Acid. *Int. J. Hydrog. Energy* **2020**, *45*, 6036−6046.
(358) Hu, C.; Yue, K.; Han, J.; Liu, X.; Liu, L.; Liu, Q.; Kong, Q.; Pao, C.-W.; Hu, Z.; Suenaga, K.; et al. Misoriented High-Entropy Iridium Ruthenium Oxide for Acidic Water Splitting. *Sci. Adv.* **2023**, *9*, eadf9144.
(359) Chen, Z.; Duan, X.; Wei, W.; Wang, S.; Ni, B.-J. Iridium-Based Nanomaterials for Electrochemical Water Splitting. *Nano Energy* **2020**, *78*, 105270.
(360) Tan, X.; Gou, W.; Liao, L.; Ma, Y.; Qu, Y. $Ir/IrO_x/WO_3$ Electrocatalysts for Water Splitting. *Mater. Chem. Front.* **2023**, *7*, 4984−4992.
(361) Zhang, L.; Jang, H.; Li, Z.; Liu, H.; Kim, M. G.; Liu, X.; Cho, J. $SrIrO_3$ Modified with Laminar Sr_2IrO_4 as a Robust Bifunctional Electrocatalyst for Overall Water Splitting in Acidic Media. *Chem. Eng. J.* **2021**, *419*, 129604.
(362) Wang, Z.; Wang, P.; Zhang, H.; Tian, W.; Xu, Y.; Li, X.; Wang, L.; Wang, H. Construction of Hierarchical IrTe Nanotubes with Assembled Nanosheets for Overall Water Splitting Electrocatalysis. *J. Mater. Chem. A* **2021**, *9*, 18576−18581.
(363) Zheng, T.; Shang, C.; He, Z.; Wang, X.; Cao, C.; Li, H.; Si, R.; Pan, B.; Zhou, S.; Zeng, J. Intercalated Iridium Diselenide Electrocatalysts for Efficient pH-Universal Water Splitting. *Angew. Chem., Int. Ed.* **2019**, *58*, 14764−14769.
(364) Wang, X.; Wang, D.; Yin, W.-J.; Si, Y.; Bu, K.; Wang, S.; Zhao, W.; Huang, F. Modulation of the Electronic Structure of $IrSe_2$ by Filling the Bi Atom as a Bifunctional Electrocatalyst for pH Universal Water Splitting. *Adv. Energy Sustainability Res.* **2021**, *2*, 2000074.
(365) Lee, Y.; Suntivich, J.; May, K. J.; Perry, E. E.; Shao-Horn, Y. Synthesis and Activities of Rutile IrO_2 and RuO_2 Nanoparticles for Oxygen Evolution in Acid and Alkaline Solutions. *J. Phys. Chem. Lett.* **2012**, *3*, 399−404.
(366) Kim, J. Y.; Choi, J.; Kim, H. Y.; Hwang, E.; Kim, H.-J.; Ahn, S. H.; Kim, S.-K. Activity and Stability of the Oxygen Evolution Reaction on Electrodeposited Ru and Its Thermal Oxides. *Appl. Surf. Sci.* **2015**, *359*, 227−235.
(367) Yang, L.; Yu, G.; Ai, X.; Yan, W.; Duan, H.; Chen, W.; Li, X.; Wang, T.; Zhang, C.; Huang, X.; et al. Efficient Oxygen Evolution Electrocatalysis in Acid by a Perovskite with Face-Sharing IrO_6 Octahedral Dimers. *Nat. Commun.* **2018**, *9*, 5236.
(368) Antolini, E. Iridium as Catalyst and Cocatalyst for Oxygen Evolution/Reduction in Acidic Polymer Electrolyte Membrane Electrolyzers and Fuel Cells. *ACS Catal.* **2014**, *4*, 1426−1440.
(369) Seitz, L. C.; Dickens, C. F.; Nishio, K.; Hikita, Y.; Montoya, J.; Doyle, A.; Kirk, C.; Vojvodic, A.; Hwang, H. Y.; Nørskov, J. K.; Jaramillo, T. F. A Highly Active and Stable $IrO_x/SrIrO_3$ Catalyst for the Oxygen Evolution Reaction. *Science* **2016**, *353*, 1011−1014.
(370) Lyons, M. E. G.; Floquet, S. Mechanism of Oxygen Reactions at Porous Oxide Electrodes. Part 2-Oxygen Evolution at RuO_2, IrO_2 and $Ir_xRu_{1-x}O_2$ Electrodes in Aqueous Acid and Alkaline Solution. *Phys. Chem. Chem. Phys.* **2011**, *13*, 5314−5335.
(371) Wu, D.; Kusada, K.; Yoshioka, S.; Yamamoto, T.; Toriyama, T.; Matsumura, S.; Chen, Y.; Seo, O.; Kim, J.; Song, C.; Hiroi, S.; Sakata, O.; Ina, T.; Kawaguchi, S.; Kubota, Y.; Kobayashi, H.; Kitagawa, H. Efficient Overall Water Splitting in Acid with Anisotropic Metal Nanosheets. *Nat. Commun.* **2021**, *12*, 1145.
(372) Jiang, Y.; Mao, Y.; Jiang, Y.; Liu, H.; Shen, W.; Li, M.; He, R. Atomic Equidistribution Enhanced RuIr Electrocatalysts for Overall Water Splitting in the Whole pH Range. *Chem. Eng. J.* **2022**, *450*, 137909.
(373) Shan, J.; Ling, T.; Davey, K.; Zheng, Y.; Qiao, S.-Z. Transition-Metal-Doped RuIr Bifunctional Nanocrystals for Overall Water Splitting in Acidic Environments. *Adv. Mater.* **2019**, *31*, 1900510.
(374) Danilovic, N.; Subbaraman, R.; Chang, K. C.; Chang, S. H.; Kang, Y.; Snyder, J.; Paulikas, A. P.; Strmcnik, D.; Kim, Y. T.; Myers, D.; Stamenkovic, V. R.; Markovic, N. M. Using Surface Segregation to Design Stable Ru-Ir Oxides for the Oxygen Evolution Reaction in Acidic Environments. *Angew. Chem., Int. Ed.* **2014**, *53*, 14016−14021.
(375) Seow, J. Z. Y.; Nguyen, T. D. Electrochemically Assisted Synthesis of Ultra-Small $Ru@IrO_x$ Core-Shell Nanoparticles for Water Splitting Electro-Catalysis. *Electrochim. Acta* **2020**, *341*, 136058.
(376) Zhuang, Z.; Wang, Y.; Xu, C.-Q.; Liu, S.; Chen, C.; Peng, Q.; Zhuang, Z.; Xiao, H.; Pan, Y.; Lu, S.; Yu, R.; Cheong, W.-C.; Cao, X.; Wu, K.; Sun, K.; Wang, Y.; Wang, D.; Li, Y.; et al. Three-Dimensional Open Nano-Netcage Electrocatalysts for Efficient pH-Universal Overall Water Splitting. *Nat. Commun.* **2019**, *10*, 4875.
(377) Liu, M.; Liu, S.; Mao, Q.; Yin, S.; Wang, Z.; Xu, Y.; Li, X.; Wang, L.; Wang, H. Ultrafine Ruthenium-Iridium-Tellurium Nanotubes for Boosting Overall Water Splitting in Acidic Media. *J. Mater. Chem. A* **2022**, *10*, 2021−2026.
(378) Li, A.; Ooka, H.; Bonnet, N.; Hayashi, T.; Sun, Y.; Jiang, Q.; Li, C.; Han, H.; Nakamura, R. Stable Potential Windows for Long-Term Electrocatalysis by Manganese Oxides Under Acidic Conditions. *Angew. Chem., Int. Ed.* **2019**, *58*, 5054−5058.
(379) Sardar, K.; Petrucco, E.; Hiley, C. I.; Sharman, J. D. B.; Wells, P. P.; Russell, A. E.; Kashtiban, R. J.; Sloan, J.; Walton, R. I. Water-Splitting Electrocatalysis in Acid Conditions Using Ruthenate-Iridate Pyrochlores. *Angew. Chem., Int. Ed.* **2014**, *53*, 10960−10964.
(380) Pan, S.; Li, H.; Liu, D.; Huang, R.; Pan, X.; Ren, D.; Li, J.; Shakouri, M.; Zhang, Q.; Wang, M.; et al. Efficient and Stable Noble-Metal-Free Catalyst for Acidic Water Oxidation. *Nat. Commun.* **2022**, *13*, 2294.
(381) Gao, J.; Tao, H.; Liu, B. Progress of Nonprecious-Metal-Based Electrocatalysts for Oxygen Evolution in Acidic Media. *Adv. Mater.* **2021**, *33*, 2003786.
(382) Wu, X.; Zhang, H.; Zhang, J.; Lou, X. W. Recent Advances on Transition Metal Dichalcogenides for Electrochemical Energy Conversion. *Adv. Mater.* **2021**, *33*, 2008376.
(383) Wu, W.; Niu, C.; Wei, C.; Jia, Y.; Li, C.; Xu, Q. Activation of MoS_2 Basal Planes for Hydrogen Evolution by Zinc. *Angew. Chem., Int. Ed.* **2019**, *58*, 2029−2033.
(384) Xie, J.; Zhang, H.; Li, S.; Wang, R.; Sun, X.; Zhou, M.; Zhou, J.; Lou, X. W.; Xie, Y. Defect-Rich MoS_2 Ultrathin Nanosheets with Additional Active Edge Sites for Enhanced Electrocatalytic Hydrogen Evolution. *Adv. Mater.* **2013**, *25*, 5807−5813.

https://doi.org/10.1021/acs.chemrev.3c00332
Chem. Rev. 2024, 124, 3694−3812

(385) Merki, D.; Fierro, S.; Vrubel, H.; Hu, X. Amorphous Molybdenum Sulfide Films as Catalysts for Electrochemical Hydrogen Production in Water. *Chem. Sci.* **2011**, *2*, 1262−1267.
(386) Zhang, J.; Wang, T.; Pohl, D.; Rellinghaus, B.; Dong, R.; Liu, S.; Zhuang, X.; Feng, X. Interface Engineering of MoS_2/Ni_3S_2 Heterostructures for Highly Enhanced Electrochemical Overall-Water-Splitting Activity. *Angew. Chem., Int. Ed.* **2016**, *55*, 6702−6707.
(387) Ran, N.; Song, E.; Wang, Y.; Zhou, Y.; Liu, J. Dynamic Coordination Transformation of Active Sites in Single-Atom MoS_2 Catalysts for Boosted Oxygen Evolution Catalysis. *Energy Environ. Sci.* **2022**, *15*, 2071−2083.
(388) Yuan, S.; Pu, Z.; Zhou, H.; Yu, J.; Amiinu, I. S.; Zhu, J.; Liang, Q.; Yang, J.; He, D.; Hu, Z.; Tendeloo, G. V.; Mu, S. A Universal Synthesis Strategy for Single Atom Dispersed Cobalt/Metal Clusters Heterostructure Boosting Hydrogen Evolution Catalysis At All pH Values. *Nano Energy* **2019**, *59*, 472−480.
(389) Zhang, J.; Xie, Y.; Jiang, Q.; Guo, S.; Huang, J.; Xu, L.; Wang, Y.; Li, G. Facile Synthesis of Cobalt Cluster-CoN_x Composites: Synergistic Effect Boosts Electrochemical Oxygen Reduction. *J. Mater. Chem. A* **2022**, *10*, 16920−16927.
(390) Doan, T. L. L.; Nguyen, D. C.; Prabhakaran, S.; Kim, D. H.; Tran, D. T.; Kim, N. H.; Lee, J. H. Single-Atom Co-Decorated MoS_2 Nanosheets Assembled on Metal Nitride Nanorod Arrays as an Efficient Bifunctional Electrocatalyst for pH-Universal Water Splitting. *Adv. Funct. Mater.* **2021**, *31*, 2100233.
(391) Wei, Q.; Wang, D.; Zhang, L.; Zhao, L.; Zhang, B.; Zhou, G.; Zhao, Y. Fabrication of Co Doped MoS_2 Nanosheets with Enlarged Interlayer Spacing as Efficient and pH-Universal Bifunctional Electrocatalyst for Overall Water Splitting. *Ceram. Int.* **2021**, *47*, 24501−24510.
(392) Cheng, W.; Zhang, H.; Zhao, X.; Su, H.; Tang, F.; Tian, J.; Liu, Q. A Metal-Vacancy-Solid-Solution NiAlP Nanowall Array Bifunctional Electrocatalyst for Exceptional All-pH Overall Water Splitting. *J. Mater. Chem. A* **2018**, *6*, 9420−9427.
(393) Wang, Y.; Jiao, Y.; Yan, H.; Yang, G.; Tian, C.; Wu, A.; Liu, Y.; Fu, H. Vanadium-Incorporated CoP_2 with Lattice Expansion for Highly Efficient Acidic Overall Water Splitting. *Angew. Chem., Int. Ed.* **2022**, *61*, e202116233.
(394) Yu, Y.; Zhou, J.; Sun, Z. Novel 2D Transition-Metal Carbides: Ultrahigh Performance Electrocatalysts for Overall Water Splitting and Oxygen Reduction. *Adv. Funct. Mater.* **2020**, *30*, 2000570.
(395) Yang, C.; Shen, K.; Zhao, R.; Xiang, H.; Wu, J.; Zhong, W.; Zhang, Q.; Li, X.; Yang, N. Balance Effect: A Universal Strategy for Transition Metal Carbides to Enhance Hydrogen Evolution. *Adv. Funct. Mater.* **2022**, *32*, 2108167.
(396) Han, N.; Yang, K. R.; Lu, Z.; Li, Y.; Xu, W.; Gao, T.; Cai, Z.; Zhang, Y.; Batista, V. S.; Liu, W.; Sun, X. Nitrogen-Doped Tungsten Carbide Nanoarray as an Efficient Bifunctional Electrocatalyst for Water Splitting in Acid. *Nat. Commun.* **2018**, *9*, 924.
(397) Chen, Y.; Yu, G.; Chen, W.; Liu, Y.; Li, G.-D.; Zhu, P.; Tao, Q.; Li, Q.; Liu, J.; Shen, X.; et al. Highly Active, Nonprecious Electrocatalyst Comprising Borophene Subunits for the Hydrogen Evolution. *J. Am. Chem. Soc.* **2017**, *139*, 12370−12373.
(398) Nsanzimana, J. M. V.; Dangol, R.; Reddu, V.; Duo, S.; Peng, Y.; Khang Ngoc, D.; Huang, Z.; Yan, Q.; Wang, X. Facile Synthesis of Amorphous Ternary Metal Borides-Reduced Graphene Oxide Hybrid with Superior Oxygen Evolution Activity. *ACS Appl. Mater. Interfaces* **2019**, *11*, 846−855.
(399) Guo, F.; Wu, Y.; Chen, H.; Liu, Y.; Yang, L.; Ai, X.; Zou, X. Co-Ni-B High-Performance Oxygen Evolution Electrocatalysis by Boronized Metal Sheets with Self-Functionalized Surfaces. *Energy Environ. Sci.* **2019**, *12*, 684−692.
(400) Jiang, B.; Liang, K.; Yang, Z.; Guo, K.; Shaik, F.; Zheng, J. FeCoNiB@Boron-Doped Vertically Aligned Graphene Arrays: A Self-Supported Electrocatalyst for Overall Water Splitting in a Wide pH Range. *Electrochim. Acta* **2021**, *386*, 138459.
(401) Liu, D.; Ai, H.; Li, J.; Fang, M.; Chen, M.; Liu, D.; Du, X.; Zhou, P.; Li, F.; Lo, K. H.; Tang, Y.; Chen, S.; Wang, L.; Xing, G.; Pan, H. Surface Reconstruction and Phase Transition on Vanadium-Cobalt-Iron Trimetal Nitrides to Form Active Oxyhydroxide for Enhanced Electrocatalytic Water Oxidation. *Adv. Energy Mater.* **2020**, *10*, 2002464.
(402) Wang, H.; Li, J.; Li, K.; Lin, Y.; Chen, J.; Gao, L.; Nicolosi, V.; Xiao, X.; Lee, J.-M. Transition Metal Nitrides for Electrochemical Energy Applications. *Chem. Soc. Rev.* **2021**, *50*, 1354−1390.
(403) Zhang, D.; Sun, C.; Liu, D.; Song, C.; Wang, D. Space-Confined Ultrafine Co_4N Nanodots within an N-Doped Carbon Framework on Carbon Cloth for Highly Efficient Universal pH Overall Water Splitting. *Sci. China Mater.* **2023**, *66*, 1362−1372.
(404) Cao, L.; Luo, Q.; Chen, J.; Wang, L.; Lin, Y.; Wang, H.; Liu, X.; Shen, X.; Zhang, W.; Liu, W.; Qi, Z.; Jiang, Z.; Yang, J.; Yao, T. Dynamic Oxygen Adsorption on Single-Atomic Ruthenium Catalyst with High Performance for Acidic Oxygen Evolution Reaction. *Nat. Commun.* **2019**, *10*, 4849.
(405) Wu, Z.-Y.; Chen, F.-Y.; Lie, B.; Yu, S.-W.; Finfrock, Y. Z.; Meira, D. M.; Yan, Q.-Q.; Zhu, P.; Chen, M.-X.; Song, T.-W.; Yin, Z.; Liang, H.-W.; Zhang, S.; Wang, G.; Wang, H. Non-Iridium-Based Electrocatalyst for Durable Acidic Oxygen Evolution Reaction in Proton Exchange Membrane Water Electrolysis. *Nat. Mater.* **2023**, *22*, 100−108.
(406) Xue, Z.-H.; Su, H.; Yu, Q.-Y.; Zhang, B.; Wang, H.-H.; Li, X.-H.; Chen, J.-S. Janus Co/CoP Nanoparticles as Efficient Mott-Schottky Electrocatalysts for Overall Water Splitting in Wide pH Range. *Adv. Energy Mater.* **2017**, *7*, 1602355.
(407) Shit, S.; Bolar, S.; Murmu, N. C.; Kuila, T. An Account of the Strategies to Enhance the Water Splitting Efficiency of Noble-Metal-Free Electrocatalysts. *J. Energy Chem.* **2021**, *59*, 160−190.
(408) Paul, R.; Zhai, Q.; Roy, A. K.; Dai, L. Charge Transfer of Carbon Nanomaterials for Efficient Metal-Free Electrocatalysis. *Interdiscip. Mater.* **2022**, *1*, 28−50.
(409) Liu, X.; Dai, L. Carbon-Based Metal-Free Catalysts. *Nat. Rev. Mater.* **2016**, *1*, 16064.
(410) Zhao, X.; He, D.; You, B. Laser Engraving and Punching of Graphene Films as Flexible All-Solid-State Planar Micro-Supercapacitor Electrodes. *Mater. Today Sustain.* **2022**, *17*, 100096.
(411) Gao, R.; Dai, Q.; Du, F.; Yan, D.; Dai, L. C_{60}-Adsorbed Single-Walled Carbon Nanotubes as Metal-Free, pH-Universal, and Multifunctional Catalysts for Oxygen Reduction, Oxygen Evolution, and Hydrogen Evolution. *J. Am. Chem. Soc.* **2019**, *141*, 11658−11666.
(412) Xing, C.; Xue, Y.; Huang, B.; Yu, H.; Hui, L.; Fang, Y.; Liu, Y.; Zhao, Y.; Li, Z.; Li, Y. Fluorographdiyne: A Metal-Free Catalyst for Applications in Water Reduction and Oxidation. *Angew. Chem., Int. Ed.* **2019**, *58*, 13897−13903.
(413) Zheng, Y.; Jiao, Y.; Ge, L.; Jaroniec, M.; Qiao, S. Z. Two-Step Boron and Nitrogen Doping in Graphene for Enhanced Synergistic Catalysis. *Angew. Chem., Int. Ed.* **2013**, *52*, 3110−3116.
(414) Cheng, Y.; Pang, K.; Xu, X.; Yuan, P.; Zhang, Z.; Wu, X.; Zheng, L.; Zhang, J.; Song, R. Borate Crosslinking Synthesis of Structure Tailored Carbon-Based Bifunctional Electrocatalysts Directly from Guar Gum Hydrogels for Efficient Overall Water Splitting. *Carbon* **2020**, *157*, 153−163.
(415) Yao, Q.; Huang, B.; Zhang, N.; Sun, M.; Shao, Q.; Huang, X. Channel-Rich RuCu Nanosheets for pH-Universal Overall Water Splitting Electrocatalysis. *Angew. Chem., Int. Ed.* **2019**, *58*, 13983−13988.
(416) Hou, L.; Li, Z.; Jang, H.; Wang, Y.; Cui, X.; Gu, X.; Kim, M. G.; Feng, L.; Liu, S.; Liu, X. Electronic and Lattice Engineering of Ruthenium Oxide Towards Highly Active and Stable Water Splitting. *Adv. Energy Mater.* **2023**, *13*, 2300177.
(417) Fan, Z.; Jiang, J.; Ai, L.; Shao, Z.; Liu, S. Rational Design of Ruthenium and Cobalt-Based Composites with Rich Metal-Insulator Interfaces for Efficient and Stable Overall Water Splitting in Acidic Electrolyte. *ACS Appl. Mater. Interfaces* **2019**, *11*, 47894−47903.
(418) Peng, Z.; Liu, J.; Hu, B.; Yang, Y.; Guo, Y.; Li, B.; Li, L.; Zhang, Z.; Cui, B.; He, L.; Du, M. Surface Engineering on Nickel-Ruthenium Nanoalloys Attached Defective Carbon Sites as Superior Bifunctional Electrocatalysts for Overall Water Splitting. *ACS Appl. Mater. Interfaces* **2020**, *12*, 13842−13851.

https://doi.org/10.1021/acs.chemrev.3c00332
Chem. Rev. 2024, 124, 3694−3812

(419) Feng, T.; Yu, G.; Tao, S.; Zhu, S.; Ku, R.; Zhang, R.; Zeng, Q.; Yang, M.; Chen, Y.; Chen, W.; Chen, W.; Yang, B. A Highly Efficient Overall Water Splitting Ruthenium-Cobalt Alloy Electrocatalyst Across a Wide pH Range via Electronic Coupling with Carbon Dots. *J. Mater. Chem. A* **2020**, *8*, 9638−9645.
(420) Chen, D.; Liu, T.; Wang, P.; Zhao, J.; Zhang, C.; Cheng, R.; Li, W.; Ji, P.; Pu, Z.; Mu, S. Ionothermal Route to Phase-Pure RuB_2 Catalysts for Efficient Oxygen Evolution and Water Splitting in Acidic Media. *ACS Energy Lett.* **2020**, *5*, 2909−2915.
(421) Oh, A.; Kim, H. Y.; Baik, H.; Kim, B.; Chaudhari, N. K.; Joo, S. H.; Lee, K. Topotactic Transformations in an Icosahedral Nanocrystal to Form Efficient Water-Splitting Catalysts. *Adv. Mater.* **2019**, *31*, 1805546.
(422) Xu, W.; Huang, H.; Wu, X.; Yuan, Y.; Liu, Y.; Wang, Z.; Zhang, D.; Qin, Y.; Lai, J.; Wang, L. Mn-Doped Ru/RuO_2 Nanoclusters@CNT with Strong Metal-Support Interaction for Efficient Water Splitting in Acidic Media. *Composits Part. B* **2022**, *242*, 110013.
(423) Wu, Y.; Yao, R.; Zhao, Q.; Li, J.; Liu, G. La-RuO_2 Nanocrystals with Efficient Electrocatalytic Activity for Overall Water Splitting in Acidic Media: Synergistic Effect of La Doping and Oxygen Vacancy. *Chem. Eng. J.* **2022**, *439*, 135699.
(424) Chen, D.; Yu, R.; Wu, D.; Zhao, H.; Wang, P.; Zhu, J.; Ji, P.; Pu, Z.; Chen, L.; Yu, J.; Mu, S. Anion-Modulated Molybdenum Oxide Enclosed Ruthenium Nano-Capsules with Almost the Same Water Splitting Capability in Acidic and Alkaline Media. *Nano Energy* **2022**, *100*, 107445.
(425) Yan, S.; Liao, W.; Zhong, M.; Li, W.; Wang, C.; Pinna, N.; Chen, W.; Lu, X. Partially Oxidized Ruthenium Aerogel as Highly Active Bifunctional Electrocatalyst for Overall Water Splitting in both Alkaline and Acidic Media. *Appl. Catal., B* **2022**, *307*, 121199.
(426) Yao, Q.; Le, J.; Yang, S.; Cheng, J.; Shao, Q.; Huang, X. A Trace of Pt Can Significantly Boost RuO_2 for Acidic Water Splitting. *Chin. J. Catal.* **2022**, *43*, 1493−1501.
(427) Ai, L.; Wang, Y.; Luo, Y.; Tian, Y.; Yang, S.; Chen, M.; Jiang, J. Robust Interfacial Ru-RuO_2 Heterostructures for Highly Efficient and Ultrastable Oxygen Evolution Reaction and Overall Water Splitting in Acidic Media. *J. Alloys Compd.* **2022**, *902*, 163787.
(428) Liu, Z.; Liu, Y.; He, H.; Shao, H.; Zhang, Y.; Li, J.; Cai, W. Valence Regulation of Ru/Mo_2C Heterojunction for Efficient Acidic Overall Water Splitting. *Electrochim. Acta* **2023**, *443*, 141920.
(429) Yang, C.; Zhang, X.; an, Q.; Liu, M.; Zhou, W.; Li, Y.; Hu, F.; Liu, Q.; Su, H. Dynamically-Evolved Surface Heterojunction in Iridium Nanocrystals Boosting Acidic Oxygen Evolution and Overall Water Splitting. *J. Energy Chem.* **2023**, *78*, 374−380.
(430) Yang, J.; Shen, Y.; Sun, Y.; Xian, J.; Long, Y.; Li, G. Ir Nanoparticles Anchored on Metal-Organic Frameworks for Efficient Overall Water Splitting under pH-Universal Conditions. *Angew. Chem., Int. Ed.* **2023**, *62*, e202302220.
(431) Li, M.; Zhao, Z.; Xia, Z.; Luo, M.; Zhang, Q.; Qin, Y.; Tao, L.; Yin, K.; Chao, Y.; Gu, L.; Yang, W.; Yu, Y.; Lu, G.; Guo, S. Exclusive Strain Effect Boosts Overall Water Splitting in PdCu/Ir Core/Shell Nanocrystals. *Angew. Chem., Int. Ed.* **2021**, *60*, 8243−8250.
(432) Mei, J.; He, T.; Bai, J.; Qi, D.; Du, A.; Liao, T.; Ayoko, G. A.; Yamauchi, Y.; Sun, L.; Sun, Z. Surface-Dependent Intermediate Adsorption Modulation on Iridium-Modified Black Phosphorus Electrocatalysts for Efficient pH-Universal Water Splitting. *Adv. Mater.* **2021**, *33*, 2104638.
(433) Lai, C.; Liu, X.; Wang, Y.; Cao, C.; Yin, Y.; Yang, H.; Qi, X.; Zhong, S.; Hou, X.; Liang, T. Modulating Ternary Mo-Ni-P by Electronic Reconfiguration and Morphology Engineering for Boosting All-pH Electrocatalytic Overall Water Splitting. *Electrochim. Acta* **2020**, *330*, 135294.
(434) Wang, L.; Duan, X.; Liu, X.; Gu, J.; Si, R.; Qiu, Y.; Qiu, Y.; Shi, D.; Chen, F.; Sun, X.; Lin, J.; Sun, J. Atomically Dispersed Mo Supported on Metallic Co_9S_8 Nanoflakes as an Advanced Noble-Metal-Free Bifunctional Water Splitting Catalyst Working in Universal pH Conditions. *Adv. Energy Mater.* **2020**, *10*, 1903137.
(435) Liu, H.; Peng, X.; Liu, X.; Qi, G.; Luo, J. Porous Mn-Doped $FeP/Co_3(PO_4)_2$ Nanosheets as Efficient Electrocatalysts for Overall Water Splitting in a Wide pH Range. *ChemSusChem* **2019**, *12*, 1334−1341.
(436) Wang, A.; Wang, Q.; Dou, Y.; Sudi, M. S.; Zhu, W.; Shang, D.; Li, L. Porphyrin Coordination Polymer Supported Transition-Metal Sulfides as Precious-Metal-Free Electrocatalysts for Efficient Overall Water Splitting. *Dyes Pigm.* **2022**, *206*, 110620.
(437) Liu, M.; Sun, Z.; Li, S.; Nie, X.; Liu, Y.; Wang, E.; Zhao, Z. Hierarchical Superhydrophilic/Superaerophobic $CoMnP/Ni_2P$ Nanosheet-Based Microplate Arrays for Enhanced Overall Water Splitting. *J. Mater. Chem. A* **2021**, *9*, 22129−22139.
(438) Chakraborty, B.; Beltran-Suito, R.; Hausmann, J. N.; Garai, S.; Driess, M.; Menezes, P. W. Enabling Iron-Based Highly Effective Electrochemical Water-Splitting and Selective Oxygenation of Organic Substrates through In Situ Surface Modification of Intermetallic Iron Stannide Precatalyst. *Adv. Energy Mater.* **2020**, *10*, 2001377.
(439) Martindale, B. C. M.; Reisner, E. Bi-Functional Iron-Only Electrodes for Efficient Water Splitting with Enhanced Stability through In Situ Electrochemical Regeneration. *Adv. Energy Mater.* **2016**, *6*, 1502095.
(440) Liu, B.; Wang, Y.; Peng, H.-Q.; Yang, R.; Jiang, Z.; Zhou, X.; Lee, C.-S.; Zhao, H.; Zhang, W. Iron Vacancies Induced Bifunctionality in Ultrathin Feroxyhyte Nanosheets for Overall Water Splitting. *Adv. Mater.* **2018**, *30*, 1803144.
(441) Zou, X.; Wu, Y.; Liu, Y.; Liu, D.; Li, W.; Gu, L.; Liu, H.; Wang, P.; Sun, L.; Zhang, Y. In Situ Generation of Bifunctional, Efficient Fe-Based Catalysts from Mackinawite Iron Sulfide for Water Splitting. *Chem.* **2018**, *4*, 1139−1152.
(442) Wang, Y.; Kong, B.; Zhao, D.; Wang, H.; Selomulya, C. Strategies for Developing Transition Metal Phosphides as Heterogeneous Electrocatalysts for Water Splitting. *Nano Today* **2017**, *15*, 26−55.
(443) Yao, S.; Forstner, V.; Menezes, P. W.; Panda, C.; Mebs, S.; Zolnhofer, E. M.; Miehlich, M. E.; Szilvasi, T.; Kumar, N. A.; Haumann, M.; Meyer, K.; Grutzmacher, H.; Driess, M. From an Fe_2P_3 Complex to FeP Nanoparticles as Efficient Electrocatalysts for Water-Splitting. *Chem. Sci.* **2018**, *9*, 8590−8597.
(444) Lyu, Y.; Wang, R.; Tao, L.; Zou, Y.; Zhou, H.; Liu, T.; Zhou, Y.; Huo, J.; Jiang, S. P.; Zheng, J.; Wang, S. In-Situ Evolution of Active Layers on Commercial Stainless Steel for Stable Water Splitting. *Appl. Catal., B* **2019**, *248*, 277−285.
(445) Pan, Y.; Liu, S.; Sun, K.; Chen, X.; Wang, B.; Wu, K.; Cao, X.; Cheong, W.-C.; Shen, R.; Han, A.; Chen, Z.; Zheng, L.; Luo, J.; Lin, Y.; Liu, Y.; Wang, D.; Peng, Q.; Zhang, Q.; Chen, C.; Li, Y. A Bimetallic Zn/Fe Polyphthalocyanine-Derived Single-Atom $Fe-N_4$ Catalytic Site: A Superior Trifunctional Catalyst for Overall Water Splitting and Zn-Air Batteries. *Angew. Chem., Int. Ed.* **2018**, *57*, 8614−8618.
(446) Artero, V.; Chavarot-Kerlidou, M.; Fontecave, M. Splitting Water with Cobalt. *Angew. Chem., Int. Ed.* **2011**, *50*, 7238−7266.
(447) Jadhav, H. S.; Bandal, H. A.; Ramakrishna, S.; Kim, H. Critical Review, Recent Updates on Zeolitic Imidazolate Framework-67 (ZIF-67) and Its Derivatives for Electrochemical Water Splitting. *Adv. Mater.* **2022**, *34*, 2107072.
(448) Li, C.; Han, X.; Cheng, F.; Hu, Y.; Chen, C.; Chen, J. Phase and Composition Controllable Synthesis of Cobalt Manganese Spinel Nanoparticles towards Efficient Oxygen Electrocatalysis. *Nat. Commun.* **2015**, *6*, 7345.
(449) Xu, W.; Lyu, F.; Bai, Y.; Gao, A.; Feng, J.; Cai, Z.; Yin, Y. Porous Cobalt Oxide Nanoplates Enriched with Oxygen Vacancies for Oxygen Evolution Reaction. *Nano Energy* **2018**, *43*, 110−116.
(450) Gao, M.-R.; Liang, J.-X.; Zheng, Y.-R.; Xu, Y.-F.; Jiang, J.; Gao, Q.; Li, J.; Yu, S.-H. An Efficient Molybdenum Disulfide/Cobalt Diselenide Hybrid Catalyst for Electrochemical Hydrogen Generation. *Nat. Commun.* **2015**, *6*, 5982.
(451) Jin, H.; Wang, J.; Su, D.; Wei, Z.; Pang, Z.; Wang, Y. In Situ Cobalt-Cobalt Oxide/N-Doped Carbon Hybrids as Superior Bifunc-

https://doi.org/10.1021/acs.chemrev.3c00332
Chem. Rev. 2024, 124, 3694−3812

tional Electrocatalysts for Hydrogen and Oxygen Evolution. *J. Am. Chem. Soc.* **2015**, *137*, 2688−2694.
(452) Li, Z.; Zhang, X.; Kang, Y.; Yu, C. C.; Wen, Y.; Hu, M.; Meng, D.; Song, W.; Yang, Y. Interface Engineering of Co-LDH@MOF Heterojunction in Highly Stable and Efficient Oxygen Evolution Reaction. *Adv. Sci.* **2021**, *8*, 2002631.
(453) Wang, L.; Dong, Z. H.; Wang, Z. G.; Zhang, F. X.; Jin, J. Layered α-$Co(OH)_2$ Nanocones as Electrode Materials for Pseudocapacitors: Understanding the Effect of Interlayer Space on Electrochemical Activity. *Adv. Funct. Mater.* **2013**, *23*, 2758−2764.
(454) Guo, P.; Wu, J.; Li, X.-B.; Luo, J.; Lau, W.-M.; Liu, H.; Sun, X.-L.; Liu, L.-M. A Highly Stable Bifunctional Catalyst Based on 3D $Co(OH)_2$@NCNTs@NF towards Overall Water-Splitting. *Nano Energy* **2018**, *47*, 96−104.
(455) Chandrasekaran, S.; Yao, L.; Deng, L.; Bowen, C.; Zhang, Y.; Chen, S.; Lin, Z.; Peng, F.; Zhang, P. Recent Advances in Metal Sulfides: From Controlled Fabrication to Electrocatalytic, Photocatalytic and Photoelectrochemical Water Splitting and Beyond. *Chem. Soc. Rev.* **2019**, *48*, 4178−4280.
(456) Liu, T.; Li, P.; Yao, N.; Kong, T.; Cheng, G.; Chen, S.; Luo, W. Self-Sacrificial Template-Directed Vapor-Phase Growth of MOF Assemblies and Surface Vulcanization for Efficient Water Splitting. *Adv. Mater.* **2019**, *31*, 1806672.
(457) Huang, S.; Meng, Y.; He, S.; Goswami, A.; Wu, Q.; Li, J.; Tong, S.; Asefa, T.; Wu, M. N-, O-, and S-Tridoped Carbon-Encapsulated Co_9S_8 Nanomaterials: Efficient Bifunctional Electrocatalysts for Overall Water Splitting. *Adv. Funct. Mater.* **2017**, *27*, 1606585.
(458) Wang, N.; Li, L.; Zhao, D.; Kang, X.; Tang, Z.; Chen, S. Graphene Composites with Cobalt Sulfide: Efficient Trifunctional Electrocatalysts for Oxygen Reversible Catalysis and Hydrogen Production in the Same Electrolyte. *Small* **2017**, *13*, 1701025.
(459) Wang, J.; Cui, W.; Liu, Q.; Xing, Z.; Asiri, A. M.; Sun, X. Recent Progress in Cobalt-Based Heterogeneous Catalysts for Electrochemical Water Splitting. *Adv. Mater.* **2016**, *28*, 215−230.
(460) Song, H.; Yu, J.; Tang, Z.; Yang, B.; Lu, S. Halogen-Doped Carbon Dots on Amorphous Cobalt Phosphide as Robust Electrocatalysts for Overall Water Splitting. *Adv. Energy Mater.* **2022**, *12*, 2102573.
(461) Zhu, Y.-P.; Liu, Y.-P.; Ren, T.-Z.; Yuan, Z.-Y. Self-Supported Cobalt Phosphide Mesoporous Nanorod Arrays: A Flexible and Bifunctional Electrode for Highly Active Electrocatalytic Water Reduction and Oxidation. *Adv. Funct. Mater.* **2015**, *25*, 7337−7347.
(462) Fang, Z.; Wang, Y.; Liu, C.; Chen, S.; Sang, W.; Wang, C.; Zeng, J. Rational Design of Metal Nanoframes for Catalysis and Plasmonics. *Small* **2015**, *11*, 2593−2605.
(463) You, B.; Jiang, N.; Sheng, M.; Drisdell, W. S.; Yano, J.; Sun, Y. Bimetal-Organic Framework Self-Adjusted Synthesis of Support-Free Nonprecious Electrocatalysts for Efficient Oxygen Reduction. *ACS. Catal.* **2015**, *5*, 7068−7076.
(464) You, B.; Jiang, N.; Sheng, M.; Gul, S.; Yano, J.; Sun, Y. High-Performance Overall Water Splitting Electrocatalysts Derived from Cobalt-Based Metal-Organic Frameworks. *Chem. Mater.* **2015**, *27*, 7636−7642.
(465) Liu, H.; Guan, J.; Yang, S.; Yu, Y.; Shao, R.; Zhang, Z.; Dou, M.; Wang, F.; Xu, Q. Metal-Organic Framework-Derived Co_2P Nanoparticle/Multi-Doped Porous Carbon as a Trifunctional Electrocatalyst. *Adv. Mater.* **2020**, *32*, 2003649.
(466) Ji, L.; Wang, J.; Teng, X.; Meyer, T. J.; Chen, Z. CoP Nanoframes as Bifunctional Electrocatalysts for Efficient Overall Water Splitting. *ACS Catal.* **2020**, *10*, 412−419.
(467) Zhong, Y.; Lu, Y.; Pan, Z.; Yang, J.; Du, G.; Chen, J.; Zhang, Q.; Zhou, H.; Wang, J.; Wang, C.; Li, W. Efficient Water Splitting System Enabled by Multifunctional Platinum-Free Electrocatalysts. *Adv. Funct. Mater.* **2021**, *31*, 2009853.
(468) Chen, Z.; Ha, Y.; Jia, H.; Yan, X.; Chen, M.; Liu, M.; Wu, R. Oriented Transformation of Co-LDH Into 2D/3D ZIF-67 to Achieve Co-N-C Hybrids for Efficient Overall Water Splitting. *Adv. Energy Mater.* **2019**, *9*, 1803918.
(469) Li, Y.; Bao, X.; Chen, D.; Wang, Z.; Dewangan, N.; Li, M.; Xu, Z.; Wang, J.; Kawi, S.; Zhong, Q. A Minireview on Nickel-Based Heterogeneous Electrocatalysts for Water Splitting. *ChemCatChem.* **2019**, *11*, 5913−5928.
(470) Yan, Y.; Xia, B. Y.; Zhao, B.; Wang, X. A Review on Noble-Metal-Free Bifunctional Heterogeneous Catalysts for Overall Electrochemical Water Splitting. *J. Mater. Chem. A* **2016**, *4*, 17587−17603.
(471) Dai, L.; Chen, Z.-N.; Li, L.; Yin, P.; Liu, Z.; Zhang, H. Ultrathin Ni(0)-Embedded $Ni(OH)_2$ Heterostructured Nanosheets with Enhanced Electrochemical Overall Water Splitting. *Adv. Mater.* **2020**, *32*, 1906915.
(472) Li, Q.; Wang, D.; Han, C.; Ma, X.; Lu, Q.; Xing, Z.; Yang, X. Construction of Amorphous Interface in an Interwoven NiS/NiS_2 Structure for Enhanced Overall Water Splitting. *J. Mater. Chem. A* **2018**, *6*, 8233−8237.
(473) Kong, D.; Cha, J. J.; Wang, H.; Lee, H. R.; Cui, Y. First-Row Transition Metal Dichalcogenide Catalysts for Hydrogen Evolution Reaction. *Energy Environ. Sci.* **2013**, *6*, 3553−3558.
(474) Zhang, D.; Mou, H.; Lu, F.; Song, C.; Wang, D. A Novel Strategy for 2D/2D NiS/Graphene Heterostructures as Efficient Bifunctional Electrocatalysts for Overall Water Splitting. *Appl. Catal., B* **2019**, *254*, 471−478.
(475) Chen, G.-F.; Ma, T. Y.; Liu, Z.-Q.; Li, N.; Su, Y.-Z.; Davey, K.; Qiao, S.-Z. Efficient and Stable Bifunctional Electrocatalysts Ni/Ni_xM_y (M = P, S) for Overall Water Splitting. *Adv. Funct. Mater.* **2016**, *26*, 3314−3323.
(476) Wang, X.; Li, W.; Xiong, D.; Petrovykh, D. Y.; Liu, L. Bifunctional Nickel Phosphide Nanocatalysts Supported on Carbon Fiber Paper for Highly Efficient and Stable Overall Water Splitting. *Adv. Funct. Mater.* **2016**, *26*, 4067−4077.
(477) Menezes, P. W.; Indra, A.; Das, C.; Walter, C.; Goebel, C.; Gutkin, V.; Schmeisser, D.; Driess, M. Uncovering the Nature of Active Species of Nickel Phosphide Catalysts in High-Performance Electrochemical Overall Water Splitting. *ACS Catal.* **2017**, *7*, 103−109.
(478) Xu, H.; Fei, B.; Cai, G.; Ha, Y.; Liu, J.; Jia, H.; Zhang, J.; Liu, M.; Wu, R. Boronization-Induced Ultrathin 2D Nanosheets with Abundant Crystalline-Amorphous Phase Boundary Supported on Nickel Foam toward Efficient Water Splitting. *Adv. Energy Mater.* **2020**, *10*, 1902714.
(479) Hu, C.; Paul, R.; Dai, Q.; Dai, L. Carbon-Based Metal-Free Electrocatalysts: From Oxygen Reduction to Multifunctional Electrocatalysis. *Chem. Soc. Rev.* **2021**, *50*, 11785−11843.
(480) Xu, Y.; Tu, W.; Zhang, B.; Yin, S.; Huang, Y.; Kraft, M.; Xu, R. Nickel Nanoparticles Encapsulated in Few-Layer Nitrogen-Doped Graphene Derived from Metal-Organic Frameworks as Efficient Bifunctional Electrocatalysts for Overall Water Splitting. *Adv. Mater.* **2017**, *29*, 1605957.
(481) Yan, L.; Xu, Y.; Chen, P.; Zhang, S.; Jiang, H.; Yang, L.; Wang, Y.; Zhang, L.; Shen, J.; Zhao, X.; Wang, L. A Freestanding 3D Heterostructure Film Stitched by MOF-Derived Carbon Nanotube Microsphere Superstructure and Reduced Graphene Oxide Sheets: A Superior Multifunctional Electrode for Overall Water Splitting and Zn-Air Batteries. *Adv. Mater.* **2020**, *32*, 2003313.
(482) Jin, Y.; Wang, H.; Li, J.; Yue, X.; Han, Y.; Shen, P. K.; Cui, Y. Porous MoO_2 Nanosheets as Non-Noble Bifunctional Electrocatalysts for Overall Water Splitting. *Adv. Mater.* **2016**, *28*, 3785−3790.
(483) Tang, C.; Zhong, L.; Zhang, B.; Wang, H.-F.; Zhang, Q. 3D Mesoporous van der Waals Heterostructures for Trifunctional Energy Electrocatalysis. *Adv. Mater.* **2018**, *30*, 1705110.
(484) Amiinu, I. S.; Pu, Z.; Liu, X.; Owusu, K. A.; Monestel, H. G. R.; Boakye, F. O.; Zhang, H.; Mu, S. Multifunctional Mo-N/C@MoS_2 Electrocatalysts for HER, OER, ORR, and Zn-Air Batteries. *Adv. Funct. Mater.* **2017**, *27*, 1702300.
(485) Jiang, Y.; Lu, Y.; Lin, J.; Wang, X.; Shen, Z. A Hierarchical MoP Nanoflake Array Supported on Ni Foam: A Bifunctional Electrocatalyst for Overall Water Splitting. *Small Methods* **2018**, *2*, 1700369.

https://doi.org/10.1021/acs.chemrev.3c00332
Chem. Rev. 2024, 124, 3694−3812

(486) Wang, H.; Cao, Y.; Sun, C.; Zou, G.; Huang, J.; Kuai, X.; Zhao, J.; Gao, L. Strongly Coupled Molybdenum Carbide on Carbon Sheets as a Bifunctional Electrocatalyst for Overall Water Splitting. *ChemSusChem* **2017**, *10*, 3540−3546.
(487) Seh, Z. W.; Fredrickson, K. D.; Anasori, B.; Kibsgaard, J.; Strickler, A. L.; Lukatskaya, M. R.; Gogotsi, Y.; Jaramillo, T. F.; Vojvodic, A. Two-Dimensional Molybdenum Carbide (Mxene) as an Efficient Electrocatalyst for Hydrogen Evolution. *ACS Energy Lett.* **2016**, *1*, 589−594.
(488) Xiao, P.; Ge, X.; Wang, H.; Liu, Z.; Fisher, A.; Wang, X. Novel Molybdenum Carbide-Tungsten Carbide Composite Nanowires and Their Electrochemical Activation for Efficient and Stable Hydrogen Evolution. *Adv. Funct. Mater.* **2015**, *25*, 1520−1526.
(489) Li, J.-S.; Wang, Y.; Liu, C.-H.; Li, S.-L.; Wang, Y.-G.; Dong, L.-Z.; Dai, Z.-H.; Li, Y.-F.; Lan, Y.-Q. Coupled Molybdenum Carbide and Reduced Graphene Oxide Electrocatalysts for Efficient Hydrogen Evolution. *Nat. Commun.* **2016**, *7*, 11204.
(490) Zhang, X.; Cui, X.; Sun, Y.; Qi, K.; Jin, Z.; Wei, S.; Li, W.; Zhang, L.; Zheng, W. Nanoporous Sulfur-Doped Copper Oxide ($Cu_2O_xS_{1-x}$) for Overall Water Splitting. *ACS Appl. Mater. Interfaces* **2018**, *10*, 745−752.
(491) Chakraborty, B.; Beltran-Suito, R.; Hlukhyy, V.; Schmidt, J.; Menezes, P. W.; Driess, M. Crystalline Copper Selenide as a Reliable Non-Noble Electro(Pre)catalyst for Overall Water Splitting. *ChemSusChem* **2020**, *13*, 3222−3229.
(492) Malavekar, D. B.; Kale, S. B.; Shelke, H. D.; Pathan, H. M.; Lokhande, C. D. Efficient Electrochemical Water Splitting Through Self-Supported Copper Selenide Nanosheets on Cu Foil: Effect of Immersion Time. *Energy Technol.* **2023**, *11*, 221300.
(493) Wei, S.; Qi, K.; Jin, Z.; Cao, J.; Zheng, W.; Chen, H.; Cui, X. One-Step Synthesis of a Self-Supported Copper Phosphide Nanobush for Overall Water Splitting. *ACS Omega* **2016**, *1*, 1367−1373.
(494) Han, A.; Zhang, H.; Yuan, R.; Ji, H.; Du, P. Crystalline Copper Phosphide Nanosheets as an Efficient Janus Catalyst for Overall Water Splitting. *ACS Appl. Mater. Interfaces* **2017**, *9*, 2240−2248.
(495) Guan, C.; Liu, X.; Ren, W.; Li, X.; Cheng, C.; Wang, J. Rational Design of Metal-Organic Framework Derived Hollow $NiCo_2O_4$ Arrays for Flexible Supercapacitor and Electrocatalysis. *Adv. Energy Mater.* **2017**, *7*, 1602391.
(496) Rong, J.; Xu, J.; Qiu, F.; Zhu, Y.; Fang, Y.; Xu, J.; Zhang, T. Sea Urchin-Like MOF-Derived Formation of Porous Cu_3P@C as an Efficient and Stable Electrocatalyst for Oxygen Evolution and Hydrogen Evolution Reactions. *Adv. Mater. Interfaces* **2019**, *6*, 1900502.
(497) Luo, Q.; Lu, C.; Liu, L.; Zhu, M. A Review on the Synthesis of Transition Metal Nitride Nanostructures and Their Energy Related Applications. *Green Energy Environ.* **2023**, *8*, 406−437.
(498) Panda, C.; Menezes, P. W.; Zheng, M.; Orthmann, S.; Driess, M. In Situ Formation of Nanostructured Core-Shell Cu_3N-CuO to Promote Alkaline Water Electrolysis. *ACS Energy Lett.* **2019**, *4*, 747−754.
(499) Huang, L.; Su, Y.-Q; Qi, R.; Dang, D.; Qin, Y.; Xi, S.; Zaman, S.; You, B.; Ding, S.; Xia, B. Y. Boosting Oxygen Reduction via Integrated Construction and Synergistic Catalysis of Porous Platinum Alloy and Defective Graphitic Carbon. *Angew. Chem., Int. Ed.* **2021**, *60*, 25530−25537.
(500) Hu, Y.; Jensen, J. O.; Zhang, W.; Cleemann, L. N.; Xing, W.; Bjerrum, N. J.; Li, Q. Hollow Spheres of Iron Carbide Nanoparticles Encased in Graphitic Layers as Oxygen Reduction Catalysts. *Angew. Chem., Int. Ed.* **2014**, *53*, 3675−3679.
(501) Wang, M.; Su, K.; Zhang, M.; Du, X.; Li, Z. Advanced Trifunctional Electrocatalysis with Cu-, N-, S-Doped Defect-Rich Porous Carbon for Rechargeable Zn-Air Batteries and Self-Driven Water Splitting. *ACS Sustainable Chem. Eng.* **2021**, *9*, 13324−13336.
(502) Sanati, S.; Morsali, A.; Garcia, H. First-Row Transition Metal-Based Materials Derived From Bimetallic Metal-Organic Frameworks as Highly Efficient Electrocatalysts for Electrochemical Water Splitting. *Energy Environ. Sci.* **2022**, *15*, 3119−3151.
(503) Xu, Y.; Fan, K.; Zou, Y.; Fu, H.; Dong, M.; Dou, Y.; Wang, Y.; Chen, S.; Yin, H.; Al-Mamun, M.; Liu, P.; Zhao, H. Rational Design of Metal Oxide Catalysts for Electrocatalytic Water Splitting. *Nanoscale* **2021**, *13*, 20324−20353.
(504) Wang, H.; Lee, H.-W.; Deng, Y.; Lu, Z.; Hsu, P.-C.; Liu, Y.; Lin, D.; Cui, Y. Bifunctional Non-Noble Metal Oxide Nanoparticle Electrocatalysts through Lithium-Induced Conversion for Overall Water Splitting. *Nat. Commun.* **2015**, *6*, 7261.
(505) Gao, X.; Zhang, H.; Li, Q.; Yu, X.; Hong, Z.; Zhang, X.; Liang, C.; Lin, Z. Hierarchical $NiCo_2O_4$ Hollow Microcuboids as Bifunctional Electrocatalysts for Overall Water-Splitting. *Angew. Chem., Int. Ed.* **2016**, *55*, 6290−6294.
(506) Fang, L.; Jiang, Z.; Xu, H.; Liu, L.; Guan, Y.; Gu, X.; Wang, Y. Crystal-Plane Engineering of $NiCo_2O_4$ Electrocatalysts towards Efficient Overall Water Splitting. *J. Catal.* **2018**, *357*, 238−246.
(507) Zhu, Y.; Zhou, W.; Zhong, Y.; Bu, Y.; Chen, X.; Zhong, Q.; Liu, M.; Shao, Z. A Perovskite Nanorod as Bifunctional Electrocatalyst for Overall Water Splitting. *Adv. Energy Mater.* **2017**, *7*, 1602122.
(508) Wang, J.; Gao, Y.; Chen, D.; Liu, J.; Zhang, Z.; Shao, Z.; Ciucci, F. Water Splitting with an Enhanced Bifunctional Double Perovskite. *ACS Catal.* **2018**, *8*, 364−371.
(509) He, Z.; Zhang, J.; Gong, Z.; Lei, H.; Zhou, D.; Zhang, N.; Mai, W.; Zhao, S.; Chen, Y. Activating Lattice Oxygen in NiFe-Based (Oxy)Hydroxide for Water Electrolysis. *Nat. Commun.* **2022**, *13*, 2191.
(510) Luo, J.; Im, J.-H.; Mayer, M. T.; Schreier, M.; Nazeeruddin, M. K.; Park, N.-G.; Tilley, S. D.; Fan, H. J.; Gräetzel, M. Water Photolysis at 12.3% Efficiency via Perovskite Photovoltaics and Earth-Abundant Catalysts. *Science* **2014**, *345*, 1593−1596.
(511) Wang, M.; Zhang, L.; He, Y.; Zhu, H. Recent Advances in Transition-Metal-Sulfide-Based Bifunctional Electrocatalysts for Overall Water Splitting. *J. Mater. Chem. A* **2021**, *9*, 5320−5363.
(512) Hou, J.; Zhang, B.; Li, Z.; Cao, S.; Sun, Y.; Wu, Y.; Gao, Z.; Sun, L. Vertically Aligned Oxygenated-CoS_2-MoS_2 Heteronanosheet Architecture from Polyoxometalate for Efficient and Stable Overall Water Splitting. *ACS Catal.* **2018**, *8*, 4612−4621.
(513) Li, F.; Xu, R.; Li, Y.; Liang, F.; Zhang, D.; Fu, W.-F.; Lv, X.-J. N-Doped Carbon Coated $NiCo_2S_4$ Hollow Nanotube as Bifunctional Electrocatalyst for Overall Water Splitting. *Carbon* **2019**, *145*, 521−528.
(514) Kuang, P.; He, M.; Zou, H.; Yu, J.; Fan, K. 0D/3D MoS_2-NiS_2/N-Doped Graphene Foam Composite for Efficient Overall Water Splitting. *Appl. Catal., B* **2019**, *254*, 15−25.
(515) Xia, X.; Wang, L.; Sui, N.; Colvin, V. L.; Yu, W. W. Recent Progress in Transition Metal Selenide Electrocatalysts for Water Splitting. *Nanoscale* **2020**, *12*, 12249−12262.
(516) Yilmaz, C.; Tan, C. F.; Lim, Y.-F.; Ho, C. W. Pseudomorphic Transformation of Interpenetrated Prussian Blue Analogs into Defective Nickel Iron Selenides for Enhanced Electrochemical and Photo-Electrochemical Water Splitting. *Adv. Energy Mater.* **2019**, *9*, 1802983.
(517) Yang, Y.; Zhang, W.; Xiao, Y.; Shi, Z.; Cao, X.; Tang, Y.; Gao, Q. $CoNiSe_2$ Heteronanorods Decorated with Layered-Double-Hydroxides for Efficient Hydrogen Evolution. *Appl. Catal., B* **2019**, *242*, 132−139.
(518) Cao, L.-M.; Zhang, J.; Ding, L.-W.; Du, Z.-Y.; He, C.-T. Metal-Organic Frameworks Derived Transition Metal Phosphides for Electrocatalytic Water Splitting. *J. Energy Chem.* **2022**, *68*, 494−520.
(519) Shi, J.; Qiu, F.; Yuan, W.; Guo, M.; Lu, Z.-H. Nitrogen-Doped Carbon-Decorated Yolk-Shell CoP@FeCoP Micro-Polyhedra Derived from MOF for Efficient Overall Water Splitting. *Chem. Eng. J.* **2021**, *403*, 126312.
(520) Li, J.; Hu, Y.; Huang, X.; Zhu, Y.; Wang, D. Bimetallic Phosphide Heterostructure Coupled with Ultrathin Carbon Layer Boosting overall Alkaline Water and Seawater Splitting. *Small* **2023**, *19*, 2206533.
(521) Li, A.; Zhang, L.; Wang, F.; Zhang, L.; Li, L.; Chen, H.; Wei, Z. Rational Design of Porous Ni-Co-Fe Ternary Metal Phosphides

https://doi.org/10.1021/acs.chemrev.3c00332
Chem. Rev. 2024, 124, 3694−3812

Nanobricks as Bifunctional Electrocatalysts for Efficient Overall Water Splitting. *Appl. Catal., B* **2022**, *310*, 121353.
(522) Xie, J.; Xie, Y. Transition Metal Nitrides for Electrocatalytic Energy Conversion: Opportunities and Challenges. *Chem. Eur. J.* **2016**, *22*, 3588−3598.
(523) Han, N.; Liu, P.; Jiang, J.; Ai, L.; Shao, Z.; Liu, S. Recent Advances in Nanostructured Metal Nitrides for Water Splitting. *J. Mater. Chem. A* **2018**, *6*, 19912−19933.
(524) Zhu, C.; Yin, Z.; Lai, W.; Sun, Y.; Liu, L.; Zhang, X.; Chen, Y.; Chou, S.-L. Fe-Ni-Mo Nitride Porous Nanotubes for Full Water Splitting and Zn-Air Batteries. *Adv. Energy Mater.* **2018**, *8*, 1802327.
(525) Chen, M.; Liu, D.; Zi, B.; Chen, Y.; Liu, D.; Du, X.; Li, F.; Zhou, P.; Ke, Y.; Li, J.; Lo, H. H.; Kwok, C. T.; Ip, W. F.; Chen, S.; Wang, S.; Liu, Q.; Pan, H. Remarkable Synergistic Effect in Cobalt-Iron Nitride/Alloy Nanosheets for Robust Electrochemical Water Splitting. *J. Energy Chem.* **2022**, *65*, 405−414.
(526) Du, L.; Xiong, H.; Lu, H.; Yang, L.-M.; Liao, R.-Z.; Xia, B. Y.; You, B. Electroshock Synthesis of a Bifunctional Nonprecious Multi-Element Alloy for Alkaline Hydrogen Oxidation and Evolution. *Exploration* **2022**, *2*, 20220024.
(527) Menezes, P. W.; Panda, C.; Garai, S.; Walter, C.; Guiet, A.; Driess, M. Structurally Ordered Intermetallic Cobalt Stannide Nanocrystals for High-Performance Electrocatalytic Overall Water-Splitting. *Angew. Chem., Int. Ed.* **2018**, *57*, 15237−15242.
(528) Hao, J.; Zhuang, Z.; Cao, K.; Gao, G.; Wang, C.; Lai, F.; Lu, S.; Ma, P.; Dong, W.; Liu, T.; Du, M.; Zhu, H. Unraveling the Electronegativity-Dominated Intermediate Adsorption on High-Entropy Alloy Electrocatalysts. *Nat. Commun.* **2022**, *13*, 2662.
(529) Zhu, Y. P.; Ma, T. Y.; Jaroniec, M.; Qiao, S. Z. Self-Templating Synthesis of Hollow Co_3O_4 Microtube Arrays for Highly Efficient Water Electrolysis. *Angew. Chem., Int. Ed.* **2017**, *56*, 1324−1328.
(530) Long, X.; Lin, H.; Zhou, D.; An, Y.; Yang, S. Enhancing Full Water-Splitting Performance of Transition Metal Bifunctional Electrocatalysts in Alkaline Solutions by Tailoring CeO_2-Transition Metal Oxides-Ni Nanointerfaces. *ACS Energy Lett.* **2018**, *3*, 290−296.
(531) Lin, J.; Wang, P.; Wang, H.; Li, C.; Si, X.; Qi, J.; Cao, J.; Zhong, Z.; Fei, W.; Feng, J. Defect-Rich Heterogeneous MoS_2/NiS_2 Nanosheets Electrocatalysts for Efficient Overall Water Splitting. *Adv. Sci.* **2019**, *6*, 1900246.
(532) Zhai, Z.; Li, C.; Zhang, L.; Wu, H.-C.; Zhang, L.; Tang, N.; Wang, W.; Gong, J. Dimensional Construction and Morphological Tuning of Heterogeneous MoS_2/NiS Electrocatalysts for Efficient Overall Water Splitting. *J. Mater. Chem. A* **2018**, *6*, 9833−9838.
(533) Li, W.; Sun, Z.; Ge, R.; Li, J.; Li, Y.; Cairney, J. M.; Zheng, R.; Li, Y.; Li, S.; Li, Q.; Liu, B. Nanoarchitectonics of La-Doped Ni_3S_2/MoS_2 Hetetostructural Electrocatalysts for Water Electrolysis. *Small Struct.* **2023**, *4*, 2300175.
(534) Shan, X.; Liu, J.; Mu, H.; Xiao, Y.; Mei, B.; Liu, W.; Lin, G.; Jiang, Z.; Wen, L.; Jiang, L. An Engineered Superhydrophilic/Superaerophobic Electrocatalyst Composed of the Supported $CoMoS_x$ Chalcogel for Overall Water Splitting. *Angew. Chem., Int. Ed.* **2020**, *59*, 1659−1665.
(535) Zeng, L.; Sun, K.; Wang, X.; Liu, Y.; Pan, Y.; Liu, Z.; Cao, D.; Song, Y.; Liu, S.; Liu, C. Three-Dimensional-Networked Ni_2P/Ni_3S_2 Heteronanoflake Arrays for Highly Enhanced Electrochemical Overall-Water-Splitting Activity. *Nano Energy* **2018**, *51*, 26−36.
(536) Yao, N.; Li, P.; Zhou, Z.; Meng, R.; Cheng, G.; Luo, W. Nitrogen Engineering on 3D Dandelion-Flower-Like CoS_2 for High-Performance Overall Water Splitting. *Small* **2019**, *15*, 1901993.
(537) An, L.; Feng, J.; Zhang, Y.; Wang, R.; Liu, H.; Wang, G.-C.; Cheng, F.; Xi, P. Epitaxial Heterogeneous Interfaces on N-$NiMoO_4$/NiS_2 Nanowires/Nanosheets to Boost Hydrogen and Oxygen Production for Overall Water Splitting. *Adv. Funct. Mater.* **2019**, *29*, 1805298.
(538) Xiong, Y.; Xu, L.; Jin, C.; Sun, Q. Interface-Engineered Atomically Thin Ni_3S_2/MnO_2 Heterogeneous Nanoarrays for Efficient Overall Water Splitting in Alkaline Media. *Appl. Catal., B* **2019**, *254*, 329−338.
(539) Jiang, L.; Yang, N.; Yang, C.; Zhu, X.; Jiang, Y.; Shen, X.; Li, C.; Sun, Q. Surface Wettability Engineering: CoS_x-Ni_3S_2 Nanoarray Electrode for Improving Overall Water Splitting. *Appl. Catal., B* **2020**, *269*, 118780.
(540) Du, F.; Shi, L.; Zhang, Y.; Li, T.; Wang, J.; Wen, G.; Alsaedi, A.; Hayat, T.; Zhou, Y.; Zou, Z. Foam-Like Co_9S_8/Ni_3S_2 Heterostructure Nanowire Arrays for Efficient Bifunctional Overall Water-Splitting. *Appl. Catal., B* **2019**, *253*, 246−252.
(541) Zhu, J.; Sun, M.; Liu, S.; Liu, X.; Hu, K.; Wang, L. Study of Active Sites on Se-MnS/NiS Heterojunctions as Highly Efficient Bifunctional Electrocatalysts for Overall Water Splitting. *J. Mater. Chem. A* **2019**, *7*, 26975−26983.
(542) Tran, D. T.; Hoa, V. H.; Le, H. T.; Kim, N. H.; Lee, J. H. Highly Efficient Overall Water Splitting over a Porous Interconnected Network by Nickel Cobalt Oxysulfide Interfacial Assembled Cu@Cu_2S Nanowires. *J. Mater. Chem. A* **2020**, *8*, 14746−14756.
(543) Ren, C.; Chen, Y.; Du, L.; Wang, Q.; Li, L.; Tian, G. Hierarchical $CuCo_2S_4$ Nanoflake Arrays Grown on Carbon Cloth: A Remarkable Bifunctional Electrocatalyst for Overall Water Splitting. *ChemElectroChem.* **2021**, *8*, 1134−1140.
(544) Lu, X. F.; Zhang, S. L.; Sim, W. L.; Gao, S.; Lou, X. W. Phosphorized $CoNi_2S_4$ Yolk-Shell Spheres for Highly Efficient Hydrogen Production via Water and Urea Electrolysis. *Angew. Chem., Int. Ed.* **2021**, *60*, 22885−22891.
(545) Jin, C.; Zhai, P.; Wei, Y.; Chen, Q.; Wang, X.; Yang, W.; Xiao, J.; He, Q.; Liu, Q.; Gong, Y. $Ni(OH)_2$ Templated Synthesis of Ultrathin Ni_3S_2 Nanosheets as Bifunctional Electrocatalyst for Overall Water Splitting. *Small* **2021**, *17*, 2102097.
(546) Ma, Z.; Meng, H.; Wang, M.; Tang, B.; Li, J.; Wang, X. Porous Ni-Mo-S Nanowire Network Film Electrode as a High-Efficiency Bifunctional Electrocatalyst for Overall Water Splitting. *ChemElectroChem.* **2018**, *5*, 335−342.
(547) Hsieh, C.-T.; Chuah, X.-F.; Huang, C.-L.; Lin, H.-W.; Chen, Y.-A.; Lu, S.-Y. NiFe/$(Ni,Fe)_3S_2$ Core/Shell Nanowire Arrays as Outstanding Catalysts for Electrolytic Water Splitting at High Current Densities. *Small Methods* **2019**, *3*, 1900234.
(548) Li, W.; Gao, X.; Xiong, D.; Wei, F.; Song, W.-G.; Xu, J.; Liu, L. Hydrothermal Synthesis of Monolithic Co_3Se_4 Nanowire Electrodes for Oxygen Evolution and Overall Water Splitting with High Efficiency and Extraordinary Catalytic Stability. *Adv. Energy Mater.* **2017**, *7*, 1602579.
(549) Wan, S.; Jin, W.; Guo, X.; Mao, J.; Zheng, L.; Zhao, J.; Zhang, J.; Liu, H.; Tang, C. Self-Templating Construction of Porous $CoSe_2$ Nanosheet Arrays as Efficient Bifunctional Electrocatalysts for Overall Water Splitting. *ACS Sustainable Chem. Eng.* **2018**, *6*, 15374−15382.
(550) Wang, P.; Pu, Z.; Li, W.; Zhu, J.; Zhang, C.; Zhao, Y.; Mu, S. Coupling $NiSe_2$-Ni_2P Heterostructure Nanowrinkles for Highly Efficient overall Water Splitting. *J. Catal.* **2019**, *377*, 600−608.
(551) Wu, H.; Lu, X.; Zheng, G.; Ho, G. W. Topotactic Engineering of Ultrathin 2D Nonlayered Nickel Selenides for Full Water Electrolysis. *Adv. Energy Mater.* **2018**, *8*, 1702704.
(552) Quan, L.; Li, S.; Zhao, Z.; Liu, J.; Ran, Y.; Cui, J.; Lin, W.; Yu, X.; Wang, L.; Zhang, Y.; Ye, J. Hierarchically Assembling CoFe Prussian Blue Analogue Nanocubes on CoP Nanosheets as Highly Efficient Electrocatalysts for Overall Water Splitting. *Small Struct.* **2021**, *5*, 2100125.
(553) Zhang, W.; Zhang, H.; Luo, R.; Zhang, M.; Yan, X.; Sun, X.; Shen, J.; Han, W.; Wang, L.; Li, J. Prussian Blue Analogues-Derived Bimetallic Iron-Cobalt Selenides for Efficient Overall Water Splitting. *J. Colloid Interface Sci.* **2019**, *548*, 48−55.
(554) Dai, J.; Zhao, D.; Sun, W.; Zhu, X.; Ma, L.-J.; Wu, Z.; Yang, C.; Cui, Z.; Li, L.; Chen, S. Cu(II) Ions Induced Structural Transformation of Cobalt Selenides for Remarkable Enhancement in Oxygen/Hydrogen Electrocatalysis. *ACS Catal.* **2019**, *9*, 10761−10772.
(555) Xiao, K.; Zhou, L.; Shao, M.; Wei, M. Fabrication of $(Ni,Co)_{0.85}Se$ Nanosheet Arrays Derived from Layered Double Hydroxides toward Largely Enhanced Overall Water Splitting. *J. Mater. Chem. A* **2018**, *6*, 7585−7591.

https://doi.org/10.1021/acs.chemrev.3c00332
Chem. Rev. 2024, 124, 3694−3812

(556) Fang, Z.; Peng, L.; Lv, H.; Zhu, Y.; Yan, C.; Wang, S.; Kalyani, P.; Wu, X.; Yu, G. Metallic Transition Metal Selenide Holey Nanosheets for Efficient Oxygen Evolution Electrocatalysis. *ACS Nano* **2017**, *11*, 9550−9557.
(557) Ming, F.; Liang, H.; Shi, H.; Xu, X.; Mei, G.; Wang, Z. MOF-Derived Co-Doped Nickel Selenide/C Electrocatalysts Supported on Ni Foam for Overall Water Splitting. *J. Mater. Chem. A* **2016**, *4*, 15148−15155.
(558) Guo, X.; Li, M.; Qiu, L.; Tian, F.; He, L.; Geng, S.; Liu, Y.; Song, Y.; Yang, W.; Yu, Y. Engineering Electron Redistribution of Bimetallic Phosphates with CeO_2 Enables High-Performance Overall Water Splitting. *Chem. Eng. J.* **2023**, *453*, 139796.
(559) Ledendecker, M.; Calderón, S. K.; Papp, C.; Steinrück, H.-P.; Antonietti, M.; Shalom, M. The Synthesis of Nanostructured Ni_5P_4 Films and their Use as a Non-Noble Bifunctional Electrocatalyst for Full Water Splitting. *Angew. Chem., Int. Ed.* **2015**, *54*, 12361−12365.
(560) Jiang, N.; You, B.; Sheng, M.; Sun, Y. Bifunctionality and Mechanism of Electrodeposited Nickel-Phosphorous Films for Efficient Overall Water Splitting. *ChemCatChem.* **2016**, *8*, 106−112.
(561) Xu, H.; Wei, J.; Zhang, K.; Shiraishi, Y.; Du, Y. Hierarchical NiMo Phosphide Nanosheets Strongly Anchored on Carbon Nanotubes as Robust Electrocatalysts for Overall Water Splitting. *ACS Appl. Mater. Interfaces* **2018**, *10*, 29647−29655.
(562) Li, J.; Yan, M.; Zhou, X.; Huang, Z.-Q.; Xia, Z.; Chang, C.-R.; Ma, Y.; Qu, Y. Mechanistic Insights on Ternary $Ni_{2-x}Co_xP$ for Hydrogen Evolution and Their Hybrids with Graphene as Highly Efficient and Robust Catalysts for Overall Water Splitting. *Adv. Funct. Mater.* **2016**, *26*, 6785−6796.
(563) Guan, C.; Xiao, W.; Wu, H.; Liu, X.; Zang, W.; Zhang, H.; Ding, J.; Feng, Y. P.; Pennycook, S. J.; Wang, J. Hollow Mo-Doped CoP Nanoarrays for Efficient Overall Water Splitting. *Nano Energy* **2018**, *48*, 73−80.
(564) Li, X.; Wang, X.; Zhou, J.; Han, L.; Sun, C.; Wang, Q.; Su, Z. Ternary Hybrids as Efficient Bifunctional Electrocatalysts Derived from Bimetallic Metal-Organic-Frameworks for Overall Water Splitting. *J. Mater. Chem. A* **2018**, *6*, 5789−5796.
(565) Zhou, Z.; Mahmood, N.; Zhang, Y.; Pan, L.; Wang, L.; Zhang, X.; Zou, J.-J. CoP Nanoparticles Embedded in P and N Co-Doped Carbon as Efficient Bifunctional Electrocatalyst for Water Splitting. *J. Energy Chem.* **2017**, *26*, 1223−1230.
(566) Hu, Y.; Li, F.; Long, Y.; Yang, H.; Gao, L.; Long, X.; Hu, H.; Xu, N.; Jin, J.; Ma, J. Ultrafine CoPS Nanoparticles Encapsulated in N, P, and S Tri-Doped Porous Carbon as an Efficient Bifunctional Water Splitting Electrocatalyst in both Acid and Alkaline Solutions. *J. Mater. Chem. A* **2018**, *6*, 10433−10440.
(567) Chen, J.; Zhang, Y.; Ye, H.; Xie, J.-Q.; Li, Y.; Yan, C.; Sun, R.; Wong, C.-P. Metal-Organic Framework-Derived $Co_xFe_{1-x}P$ Nanoparticles Encapsulated in N-Doped Carbon as Efficient Bifunctional Electrocatalysts for Overall Water Splitting. *ACS Appl. Energy Mater.* **2019**, *2*, 2734−2742.
(568) Hao, Y.; Xu, Y.; Liu, W.; Sun, X. Co/CoP Embedded in a Hairy Nitrogen-Doped Carbon Polyhedron as an Advanced Tri-Functional Electrocatalyst. *Mater. Horiz.* **2018**, *5*, 108−115.
(569) Du, Y.; Han, Y.; Huai, X.; Liu, Y.; Wu, C.; Yang, Y.; Wang, L. N-Doped Carbon Coated FeNiP Nanoparticles Based Hollow Microboxes for Overall Water Splitting in Alkaline Medium. *Int. J. Hydrogen Energy* **2018**, *43*, 22226−22234.
(570) Yan, L.; Cao, L.; Dai, P.; Gu, X.; Liu, D.; Li, L.; Wang, Y.; Zhao, X. Metal-Organic Frameworks Derived Nanotube of Nickel-Cobalt Bimetal Phosphides as Highly Efficient Electrocatalysts for Overall Water Splitting. *Adv. Funct. Mater.* **2017**, *27*, 1703455.
(571) Pan, Y.; Sun, K.; Liu, S.; Cao, X.; Wu, K.; Cheong, W.-C.; Chen, Z.; Wang, Y.; Li, Y.; Liu, Y.; Wang, D.; Li, Y.; et al. Core-Shell ZIF-8@ZIF-67-Derived CoP Nanoparticle-Embedded N-Doped Carbon Nanotube Hollow Polyhedron for Efficient Overall Water Splitting. *J. Am. Chem. Soc.* **2018**, *140*, 2610−2618.
(572) Jiao, L.; Zhou, Y.-X.; Jiang, H.-L. Metal-Organic Framework-Based CoP/Reduced Graphene Oxide: High-Performance Bifunctional Electrocatalyst for Overall Water Splitting. *Chem. Sci.* **2016**, *7*, 1690−1695.
(573) Yan, L.; Jiang, H.; Xing, Y.; Wang, Y.; Liu, D.; Gu, X.; Dai, P.; Li, L.; Zhao, X. Nickel Metal-Organic Framework Implanted on Graphene and Incubated to be Ultrasmall Nickel Phosphide Nanocrystals Acts as a Highly Efficient Water Splitting Electrocatalyst. *J. Mater. Chem. A* **2018**, *6*, 1682−1691.
(574) Li, N.; Guan, Y.; Li, Y.; Mi, H.; Deng, L.; Sun, L.; Zhang, Q.; He, C.; Ren, X. Co-Mo-P Carbon Nanospheres Derived from Metal-Organic Frameworks as A High-Performance Electrocatalyst towards Efficient Water Splitting. *J. Mater. Chem. A* **2021**, *9*, 1143−1149.
(575) Yang, D.; Su, Z.; Chen, Y.; Lu, Y.; Yu, B.; Srinivas, K.; Wang, B.; Zhang, W. Double-Shelled Hollow Bimetallic Phosphide Nanospheres Anchored on Nitrogen-Doped Graphene for Boosting Water Electrolysis. *J. Mater. Chem. A* **2020**, *8*, 22222−22229.
(576) Sun, H.; Min, Y.; Yang, W.; Lian, Y.; Lin, L.; Feng, K.; Deng, Z.; Chen, M.; Zhong, J.; Xu, L.; Peng, Y. Morphological and Electronic Tuning of Ni_2P through Iron Doping toward Highly Efficient Water Splitting. *ACS Catal.* **2019**, *9*, 8882−8892.
(577) Ma, G.; Ye, J.; Qin, M.; Sun, T.; Tan, W.; Fan, Z.; Huang, L.; Xin, X. Mn-doped NiCoP Nanopin Arrays as High-Performance Bifunctional Electrocatalysts for Sustainable Hydrogen Production via Overall Water Splitting. *Nano Energy* **2023**, *115*, 108679.
(578) Lin, C.; Wang, P.; Jin, H.; Zhao, J.; Chen, D.; Liu, S.; Zhang, C.; Mu, S. An Iron-Doped Cobalt Phosphide Nano-Electrocatalyst Derived from a Metal-Organic Framework for Efficient Water Splitting. *Dalton Trans.* **2019**, *48*, 16555−16561.
(579) Wang, Q.; Liu, Z.; Zhao, H.; Huang, H.; Jiao, H.; Du, Y. MOF-Derived Porous Ni_2P Nanosheets as Novel Bifunctional Electrocatalysts for the Hydrogen and Oxygen Evolution Reactions. *J. Mater. Chem. A* **2018**, *6*, 18720−18727.
(580) Wu, J.; Wang, D.; Wan, S.; Liu, H.; Wang, C.; Wang, X. An Efficient Cobalt Phosphide Electrocatalyst Derived from Cobalt Phosphonate Complex for All-pH Hydrogen Evolution Reaction and Overall Water Splitting in Alkaline Solution. *Small* **2020**, *16*, 1900550.
(581) Xie, Y.; Chen, M.; Cai, M.; Teng, J.; Huang, H.; Fan, Y.; Barboiu, M.; Wang, D.; Su, C.-Y. Hollow Cobalt Phosphide with N-Doped Carbon Skeleton as Bifunctional Electrocatalyst for Overall Water Splitting. *Inorg. Chem.* **2019**, *58*, 14652−14659.
(582) Anandhababu, G.; Huang, Y.; Babu, D. D.; Wu, M.; Wang, Y. Oriented Growth of ZIF-67 to Derive 2D Porous CoPO Nanosheets for Electrochemical-/Photovoltage-Driven Overall Water Splitting. *Adv. Funct. Mater.* **2018**, *28*, 1706120.
(583) Ahn, S. H.; Manthiram, A. Direct Growth of Ternary Ni-Fe-P Porous Nanorods onto Nickel Foam as a Highly Active, Robust Bi-Functional Electrocatalyst for Overall Water Splitting. *J. Mater. Chem. A* **2017**, *5*, 2496−2503.
(584) Zhu, W.; Zhang, W.; Li, Y.; Yue, Z.; Ren, M.; Zhang, Y.; Saleh, N. M.; Wang, J. Energy-Efficient 1.67 V Single- and 0.90 V Dual-Electrolyte Based Overall Water-Electrolysis Devices Enabled by a ZIF-L Derived Acid-Base Bifunctional Cobalt Phosphide Nanoarray. *J. Mater. Chem. A* **2018**, *6*, 24277−24284.
(585) Dutta, S.; Indra, A.; Feng, Y.; Han, H.; Song, T. Promoting Electrocatalytic Overall Water Splitting with Nanohybrid of Transition Metal Nitride-Oxynitride. *Appl. Catal., B* **2019**, *241*, 521−527.
(586) Zhang, Q.; Wang, Y.; Wang, Y.; Al-Enizi, A. M.; Elzatahry, A. A.; Zheng, G. Myriophyllum-Like Hierarchical TiN@Ni_3N Nanowire Arrays for Bifunctional Water Splitting Catalysts. *J. Mater. Chem. A* **2016**, *4*, 5713−5718.
(587) Gu, Y.; Chen, S.; Ren, J.; Jia, Y. A.; Chen, C.; Komarneni, S.; Yang, D.; Yao, X. Electronic Structure Tuning in Ni_3FeN/R-GO Aerogel toward Bifunctional Electrocatalyst for Overall Water Splitting. *ACS Nano* **2018**, *12*, 245−253.
(588) Jiang, J.; Liu, Q.; Zeng, C.; Ai, L. Cobalt/Molybdenum Carbide@N-Doped Carbon as a Bifunctional Electrocatalyst for Hydrogen and Oxygen Evolution Reactions. *J. Mater. Chem. A* **2017**, *5*, 16929−16935.

https://doi.org/10.1021/acs.chemrev.3c00332
Chem. Rev. 2024, 124, 3694−3812

(589) Liu, W.; Du, K.; Liu, L.; Zhang, J.; Zhu, Z.; Shao, Y.; Li, M. One-Step Electroreductively Deposited Iron-Cobalt Composite Films as Efficient Bifunctional Electrocatalysts for Overall Water Splitting. *Nano Energy* **2017**, *38*, 576−584.
(590) Han, G.; Jin, Y.-H.; Burgess, R. A.; Dickenson, N. E.; Cao, X.-M.; Sun, Y. Visible-Light-Driven Valorization of Biomass Intermediates Integrated with H_2 Production Catalyzed by Ultrathin Ni/Cds Nanosheets. *J. Am. Chem. Soc.* **2017**, *139*, 15584−15587.
(591) Jiang, N.; You, B.; Boonstra, R.; Rodriguez, I. M. T.; Sun, Y. Integrating Electrocatalytic 5-Hydroxymethylfurfural Oxidation and Hydrogen Production via Co-P-Derived Electrocatalysts. *ACS Energy Lett.* **2016**, *1*, 386−390.
(592) Kanan, M. W.; Nocera, D. G. In Situ Formation of an Oxygen-Evolving Catalyst in Neutral Water Containing Phosphate and Co^{2+}. *Science* **2008**, *321*, 1072−1075.
(593) Reece, S. Y.; Hamel, J. A.; Sung, K.; Jarvi, T. D.; Esswein, A. J.; Pijpers, J. J. H.; Nocera, D. G. Wireless Solar Water Splitting Using Silicon-Based Semiconductors and Earth-Abundant Catalysts. *Science* **2011**, *334*, 645−648.
(594) Berger, A.; Segalman, R. A.; Newman, J. Material Requirements for Membrane Separators in a Water-Splitting Photoelectrochemical Cell. *Energy Environ. Sci.* **2014**, *7*, 1468−1476.
(595) Chen, L.; Dong, X.; Wang, Y.; Xia, Y. Separating Hydrogen and Oxygen Evolution in Alkaline Water Electrolysis using Nickel Hydroxide. *Nat. Commun.* **2016**, *7*, 11741.
(596) Landman, A.; Dotan, H.; Shter, G. E.; Wullenkord, M.; Houaijia, A.; Maljusch, A.; Grader, G. S.; Rothschild, A. Photoelectrochemical Water Splitting in Separate Oxygen and Hydrogen Cells. *Nat. Mater.* **2017**, *16*, 646−651.
(597) Li, W.; Jiang, N.; Hu, B.; Liu, X.; Song, F.; Han, G.; Jordan, T. J.; Hanson, T. B.; Liu, T. L.; Sun, Y. Electrolyzer Design for Flexible Decoupled Water Splitting and Organic Upgrading with Electron Reservoirs. *Chem.* **2018**, *4*, 637−649.
(598) Rausch, B.; Symes, M. D.; Chisholm, G.; Cronin, L. Decoupled Catalytic Hydrogen Evolution from a Molecular Metal Oxide Redox Mediator in Water Splitting. *Science* **2014**, *345*, 1326−1330.
(599) Rausch, B.; Symes, M. D.; Cronin, L. A Bio-Inspired, Small Molecule Electron-Coupled-Proton Buffer for Decoupling the Half-Reactions of Electrolytic Water Splitting. *J. Am. Chem. Soc.* **2013**, *135*, 13656−13659.
(600) Symes, M. D.; Cronin, L. Decoupling Hydrogen and Oxygen Evolution During Electrolytic Water Splitting Using an Electron-Coupled-Proton Buffer. *Nat. Chem.* **2013**, *5*, 403−409.
(601) Carmo, M.; Fritz, D. L.; Merge, J.; Stolten, D. A Comprehensive Review on PEM Water Electrolysis. *Int. J. Hydrogen Energy* **2013**, *38*, 4901−4934.
(602) Cha, H. G.; Choi, K.-S. Combined Biomass Valorization and Hydrogen Production in a Photoelectrochemical Cell. *Nat. Chem.* **2015**, *7*, 328−333.
(603) Geng, S.-K.; Zheng, Y.; Li, S.-Q.; Su, H.; Zhao, X.; Hu, J.; Shu, H.-B.; Jaroniec, M.; Chen, P.; Liu, Q.-H.; Qiao, S.-Z. Nickel Ferrocyanide as a High-Performance Urea Oxidation Electrocatalyst. *Nat. Energy* **2021**, *6*, 904−912.
(604) Jin, H.; Wang, X.; Tang, C.; Vasileff, A.; Li, L.; Slattery, A.; Qiao, S.-Z. Stable and Highly Efficient Hydrogen Evolution from Seawater Enabled by an Unsaturated Nickel Surface Nitride. *Adv. Mater.* **2021**, *33*, 2007508.
(605) Kuang, Y.; Feng, G.; Li, P.; Bi, Y.; Li, Y.; Sun, X. Single-Crystalline Ultrathin Nickel Nanosheets Array from In Situ Topotactic Reduction for Active and Stable Electrocatalysis. *Angew. Chem., Int. Ed.* **2016**, *55*, 693−697.
(606) Zhang, H.; Feng, Z.; Wang, L.; Li, D.; Xing, P. Bifunctional Nanoporous Ni-Zn Electrocatalysts with Super-Aerophobic Surface for High-Performance Hydrazine-Assisted Hydrogen Production. *Nanotechnology* **2020**, *31*, 365701.
(607) Shi, Y.; Schimmenti, R.; Zhu, S.; Venkatraman, K.; Chen, R.; Chi, M.; Shao, M.; Mavrikakis, M.; Xia, Y. Solution-Phase Synthesis of $PdH_{0.706}$ Nanocubes with Enhanced Stability and Activity toward Formic Acid Oxidation. *J. Am. Chem. Soc.* **2022**, *144*, 2556−2568.
(608) Sun, W.; Li, J.; Gao, W.; Kang, L.; Lei, F.; Xie, J. Recent Advances in the Pre-Oxidation Process in Electrocatalytic Urea Oxidation Reactions. *Chem. Commun.* **2022**, *58*, 2430−2442.
(609) Tang, C.; Zhang, R.; Lu, W.; Wang, Z.; Liu, D.; Hao, S.; Du, G.; Asiri, A. M.; Sun, X. Energy-Saving Electrolytic Hydrogen Generation: Ni_2P Nanoarray as a High-Performance Non-Noble-Metal Electrocatalyst. *Angew. Chem., Int. Ed.* **2017**, *56*, 842−846.
(610) Tong, Y.; Chen, P.; Zhang, M.; Zhou, T.; Zhang, L.; Chu, W.; Wu, C.; Xie, Y. Oxygen Vacancies Confined in Nickel Molybdenum Oxide Porous Nanosheets for Promoted Electrocatalytic Urea Oxidation. *ACS Catal.* **2018**, *8*, 1−7.
(611) Wang, Z.; Xu, L.; Huang, F.; Qu, L.; Li, J.; Owusu, K. A.; Liu, Z.; Lin, Z.; Xiang, B.; Liu, X.; Zhao, K.; Liao, X.; Yang, W.; Cheng, Y.-B.; Mai, L. Copper-Nickel Nitride Nanosheets as Efficient Bifunctional Catalysts for Hydrazine-Assisted Electrolytic Hydrogen Production. *Adv. Energy Mater.* **2019**, *9*, 1900390.
(612) Zhu, B.; Liang, Z.; Zou, R. Designing Advanced Catalysts for Energy Conversion Based on Urea Oxidation Reaction. *Small* **2020**, *16*, 1906133.
(613) Chen, G.-F.; Luo, Y.; Ding, L.-X.; Wang, H. Low-Voltage Electrolytic Hydrogen Production Derived from Efficient Water and Ethanol Oxidation on Fluorine-Modified FeOOH Anode. *ACS Catal.* **2018**, *8*, 526−530.
(614) Chen, S.; Duan, J.; Vasileff, A.; Qiao, S. Z. Size Fractionation of Two-Dimensional Sub-Nanometer Thin Manganese Dioxide Crystals towards Superior Urea Electrocatalytic Conversion. *Angew. Chem., Int. Ed.* **2016**, *55*, 3804−3808.
(615) Huang, Y.; Chong, X.; Liu, C.; Liang, Y.; Zhang, B. Boosting Hydrogen Production by Anodic Oxidation of Primary Amines over a NiSe Nanorod Electrode. *Angew. Chem., Int. Ed.* **2018**, *57*, 13163−13166.
(616) Liu, X.; He, J.; Zhao, S.; Liu, Y.; Zhao, Z.; Luo, J.; Hu, G.; Sun, X.; Ding, Y. Self-Powered H_2 Production with Bifunctional Hydrazine as Sole Consumable. *Nat. Commun.* **2018**, *9*, 4365.
(617) Xiang, K.; Wu, D.; Deng, X.; Li, M.; Chen, S.; Hao, P.; Guo, X.; Luo, J.-L.; Fu, X.-Z. Boosting H_2 Generation Coupled with Selective Oxidation of Methanol into Value-Added Chemical over Cobalt Hydroxide@Hydroxysulfide Nanosheets Electrocatalysts. *Adv. Funct. Mater.* **2020**, *30*, 1909610.
(618) Yu, Z.-Y.; Lang, C.-C.; Gao, M.-R.; Chen, Y.; Fu, Q.-Q.; Duan, Y.; Yu, S.-H. Ni-Mo-O Nanorod-Derived Composite Catalysts for Efficient Alkaline Water-to-Hydrogen Conversion via Urea Electrolysis. *Energy Environ. Sci.* **2018**, *11*, 1890−1897.
(619) Zhang, J.-Y.; Wang, H.; Tian, Y.; Yan, Y.; Xue, Q.; He, T.; Liu, H.; Wang, C.; Chen, Y.; Xia, B. Y. Anodic Hydrazine Oxidation Assists Energy-Efficient Hydrogen Evolution over a Bifunctional Cobalt Perselenide Nanosheet Electrode. *Angew. Chem., Int. Ed.* **2018**, *57*, 7649−7653.
(620) Yang, G.; Jiao, Y.; Yan, H.; Xie, Y.; Wu, A.; Dong, X.; Guo, D.; Tian, C.; Fu, H. Interfacial Engineering of MoO_2-FeP Heterojunction for Highly Efficient Hydrogen Evolution Coupled with Biomass Electrooxidation. *Adv. Mater.* **2020**, *32*, 2000455.
(621) Sun, F.; Qin, J.; Wang, Z.; Yu, M.; Wu, X.; Sun, X.; Qiu, J. Energy-Saving Hydrogen Production By Chlorine-Free Hybrid Seawater Splitting Coupling Hydrazine Degradation. *Nat. Commun.* **2021**, *12*, 4182.
(622) Zhang, M.; Wang, Z.; Duan, Z.; Wang, S.; Xu, Y.; Li, X.; Wang, L.; Wang, H. Anodic Hydrazine Oxidation Assisted Hydrogen Evolution over Bimetallic RhIr Mesoporous Nanospheres. *J. Mater. Chem. A* **2021**, *9*, 18323−18328.
(623) Goshome, K.; Yamada, T.; Miyaoka, H.; Ichikawa, T.; Kojima, Y. High Compressed Hydrogen Production via Direct Electrolysis of Liquid Ammonia. *Int. J. Hydrogen Energy* **2016**, *41*, 14529−14534.
(624) Gwak, J.; Choun, M.; Lee, J. Alkaline Ammonia Electrolysis on Electrodeposited Platinum for Controllable Hydrogen Production. *ChemSusChem* **2016**, *9*, 403−408.

https://doi.org/10.1021/acs.chemrev.3c00332
Chem. Rev. 2024, 124, 3694−3812

(625) Wang, L.; Zhu, Y.; Wen, Y.; Li, S.; Cui, C.; Ni, F.; Liu, Y.; Lin, H.; Li, Y.; Peng, H.; Zhang, B. Regulating the Local Charge Distribution of Ni Active Sites for the Urea Oxidation Reaction. *Angew. Chem., Int. Ed.* **2021**, *60*, 10577−10582.
(626) Jiang, Y.; Gao, S.; Xu, G.; Song, X. Porous and Amorphous Cobalt Hydroxysulfide Core-Shell Nanoneedles on Ti-Mesh as a Bifunctional Electrocatalyst for Energy-Efficient Hydrogen Production via Urea Electrolysis. *J. Mater. Chem. A* **2021**, *9*, 5664−5674.
(627) Li, P.; Zhuang, Z.; Du, C.; Xiang, D.; Zheng, F.; Zhang, Z.; Fang, Z.; Guo, J.; Zhu, S.; Chen, W. Insights into The Mo-Doping Effect on the Electrocatalytic Performance of Hierarchical Co_xMo_yS Nanosheet Arrays for Hydrogen Generation and Urea Oxidation. *ACS Appl. Mater. Interfaces* **2020**, *12*, 40194−40203.
(628) Wang, Y.; Chen, Z.; Wu, H.; Xiao, F.; Cao, E.; Du, S.; Wu, Y.; Ren, Z. Self-Assembly-Induced Mosslike Fe_2O_3 and FeP on Electro-Oxidized Carbon Paper for Low-Voltage-Driven Hydrogen Production Plus Hydrazine Degradation. *ACS Sustainable Chem. Eng.* **2018**, *6*, 15727−15736.
(629) Feng, Y.; Shi, Q.; Lin, J.; Chai, E.; Zhang, X.; Liu, Z.; Jiao, L.; Wang, Y. Decoupled Electrochemical Hydrazine "Splitting" via a Rechargeable Zn-Hydrazine Battery. *Adv. Mater.* **2022**, *34*, 2207747.
(630) Fragal, V. H.; Fragal, E. H.; Zhang, T.; Huang, X.; Cellet, T. S. P.; Pereira, G. M.; Jitianu, A.; Rubira, A. F.; Silva, R.; Asefa, T. Deriving Efficient Porous Heteroatom-Doped Carbon Electrocatalysts for Hydrazine Oxidation from Transition Metal Ions-Coordinated Casein. *Adv. Funct. Mater.* **2019**, *29*, 1808486.
(631) Wang, T.; Wang, Q.; Wang, Y.; Da, Y.; Zhou, W.; Shao, Y.; Li, D.; Zhan, S.; Yuan, J.; Wang, H. Atomically Dispersed Semi-Metallic Selenium on Porous Carbon Membrane as An Electrode for Hydrazine Fuel Cells. *Angew. Chem., Int. Ed.* **2019**, *58*, 13466−13471.
(632) Zhang, T.; Asefa, T. Heteroatom-Doped Carbon Materials for Hydrazine Oxidation. *Adv. Mater.* **2019**, *31*, 1804394.
(633) Zhou, S.; Zhao, Y.; Shi, R.; Wang, Y.; Ashok, A.; Heraly, F.; Zhang, T.; Yuan, J. Vacancy-Rich Mxene-Immobilized Ni Single Atoms as a High-Performance Electrocatalyst for the Hydrazine Oxidation Reaction. *Adv. Mater.* **2022**, *34*, 2204388.
(634) Zhu, L.; Huang, J.; Meng, G.; Wu, T.; Chen, C.; Tian, H.; Chen, Y.; Kong, F.; Chang, Z.; Cui, X.; Shi, J. Active Site Recovery and N-N Bond Breakage During Hydrazine Oxidation Boosting the Electrochemical Hydrogen Production. *Nat. Commun.* **2023**, *14*, 1997.
(635) Qian, Q.; Zhang, J.; Li, J.; Li, Y.; Jin, X.; Zhu, Y.; Liu, Y.; Li, Z.; El-Harairy, A.; Xiao, C.; Zhang, G.; Xie, Y. Artificial Heterointerfaces Achieve Delicate Reaction Kinetics towards Hydrogen Evolution and Hydrazine Oxidation Catalysis. *Angew. Chem., Int. Ed.* **2021**, *60*, 5984−5993.
(636) Zhu, Y.; Zhang, J.; Qian, Q.; Li, Y.; Li, Z.; Liu, Y.; Xiao, C.; Zhang, G.; Xie, Y. Dual Nanoislands on Ni/C Hybrid Nanosheet Activate Superior Hydrazine Oxidation-Assisted High-Efficiency H_2 Production. *Angew. Chem., Int. Ed.* **2022**, *61*, e202113082.
(637) Li, J.; Li, Y.; Wang, J.; Zhang, C.; Ma, H.; Zhu, C.; Fan, D.; Guo, Z.; Xu, M.; Wang, Y.; Ma, H. Elucidating the Critical Role of Ruthenium Single Atom Sites in Water Dissociation and Dehydrogenation Behaviors for Robust Hydrazine Oxidation-Boosted Alkaline Hydrogen Evolution. *Adv. Funct. Mater.* **2022**, *32*, 2109439.
(638) Liu, Y.; Zhang, J.; Li, Y.; Qian, Q.; Li, Z.; Zhang, G. Realizing the Synergy of Interface Engineering and Chemical Substitution For Ni_3N Enables its Bifunctionality toward Hydrazine Oxidation Assisted Energy-Saving Hydrogen Production. *Adv. Funct. Mater.* **2021**, *31*, 2103673.
(639) Liu, Y.; Zhang, J.; Li, Y.; Qian, Q.; Li, Z.; Zhu, Y.; Zhang, G. Manipulating Dehydrogenation Kinetics Through Dual-Doping Co_3N Electrode Enables Highly Efficient Hydrazine Oxidation Assisting Self-Powered H_2 Production. *Nat. Commun.* **2020**, *11*, 1853.
(640) Liu, M.; Zhang, S.; Zhang, Z.; Liu, Z.; Liu, K.; Gao, C. Sulfite Modification of Platinum Nanoparticles Modulates Electrocatalytic Formic Acid Oxidation Activity. *Green Chem.* **2020**, *22*, 5838−5844.
(641) Finkelstein, D. A.; Imbeault, R.; Garbarino, S.; Roué, L.; Guay, D. Trends in Catalysis and Catalyst Cost Effectiveness for N_2H_4 Fuel Cells and Sensors: a Rotating Disk Electrode (RDE) Study. *J. Phys. Chem. C* **2016**, *120*, 4717−4738.
(642) Fu, X.; Cheng, D.; Wan, C.; Kumari, S.; Zhang, H.; Zhang, A.; Huyan, H.; Zhou, J.; Ren, H.; Wang, S.; Zhao, Z.; Zhao, X.; Chen, J.; Pan, X.; Sautet, P.; Huang, Y.; Duan, X. Bifunctional Ultrathin $RhRu_{0.5}$-Alloy Nanowire Electrocatalysts for Hydrazine-Assisted Water Splitting. *Adv. Mater.* **2023**, *35*, 2301533.
(643) Li, Y.; Li, J.; Qian, Q.; Jin, X.; Liu, Y.; Li, Z.; Zhu, Y.; Guo, Y.; Zhang, G. Superhydrophilic Ni-Based Multicomponent Nanorod-Confined-Nanoflake Array Electrode Achieves Waste-Battery-Driven Hydrogen Evolution and Hydrazine Oxidation. *Small* **2021**, *17*, 2008148.
(644) Li, Y.; Yu, X.; Gao, J.; Ma, Y. Hierarchical Ni_2P/Zn-Ni-P Nanosheet Array for Efficient Energy-Saving Hydrogen Evolution and Hydrazine Oxidation. *J. Mater. Chem. A* **2023**, *11*, 2191−2202.
(645) Qian, Q.; Li, Y.; Liu, Y.; Guo, Y.; Li, Z.; Zhu, Y.; Zhang, G. Hierarchical Multi-Component Nanosheet Array Electrode with Abundant NiCo/$MoNi_4$ Heterostructure Interfaces Enables Superior Bifunctionality towards Hydrazine Oxidation Assisted Energy-Saving Hydrogen Generation. *Chem. Eng. J.* **2021**, *414*, 128818.
(646) Liu, M.; Zhang, R.; Zhang, L.; Liu, D.; Hao, S.; Du, G.; Asiri, A. M.; Kong, R.; Sun, X. Energy-Efficient Electrolytic Hydrogen Generation Using a Cu_3P Nanoarray as a Bifunctional Catalyst for Hydrazine Oxidation and Water Reduction. *Inorg. Chem. Front.* **2017**, *4*, 420−423.
(647) Peng, X.; Hou, J.; Mi, Y.; Sun, J.; Qi, G.; Qin, Y.; Zhang, S.; Qiu, Y.; Luo, J.; Liu, X. Bifunctional Single-Atomic Mn Sites for Energy-Efficient Hydrogen Production. *Nanoscale* **2021**, *13*, 4767−4773.
(648) Sun, Q.; Wang, L.; Shen, Y.; Zhou, M.; Ma, Y.; Wang, Z.; Zhao, C. Bifunctional Copper-Doped Nickel Catalysts Enable Energy-Efficient Hydrogen Production via Hydrazine Oxidation and Hydrogen Evolution Reduction. *ACS Sustainable Chem. Eng.* **2018**, *6*, 12746−12754.
(649) Yang, J.; Xu, L.; Zhu, W.; Xie, M.; Liao, F.; Cheng, T.; Kang, Z.; Shao, M. Rh/RhO_x Nanosheets as pH-Universal Bifunctional Catalysts for Hydrazine Oxidation and Hydrogen Evolution Reactions. *J. Mater. Chem. A* **2022**, *10*, 1891−1898.
(650) Jia, N.; Liu, Y.; Wang, L.; Chen, P.; Chen, X.; an, Z.; Chen, Y. 0.2 V Electrolysis Voltage-Driven Alkaline Hydrogen Production with Nitrogen-Doped Carbon Nanobowl-Supported Ultrafine Rh Nanoparticles of 1.4 nm. *ACS Appl. Mater. Interfaces* **2019**, *11*, 35039−35049.
(651) Xue, Q.; Huang, H.; Zhu, J.-Y.; Zhao, Y.; Li, F.-M.; Chen, P.; Chen, Y. Au@Rh Core-Shell Nanowires for Hydrazine Electrooxidation. *Appl. Catal., B* **2020**, *278*, 119269.
(652) Li, Y.; Zhang, J.; Liu, Y.; Qian, Q.; Li, Z.; Zhu, Y.; Zhang, G. Partially Exposed RuP_2 Surface in Hybrid Structure Endows its Bifunctionality for Hydrazine Oxidation and Hydrogen Evolution Catalysis. *Sci. Adv.* **2020**, *6*, eabb4197.
(653) Zhou, L.; Cheng, Y. F. Catalytic Electrolysis of Ammonia on Platinum in Alkaline Solution for Hydrogen Generation. *Int. J. Hydrogen Energy* **2008**, *33*, 5897−5904.
(654) Li, Y.; Wang, H.; Priest, C.; Li, S.; Xu, P.; Wu, G. Advanced Electrocatalysis for Energy and Environmental Sustainability via Water and Nitrogen Reactions. *Adv. Mater.* **2021**, *33*, 2000381.
(655) Sun, H.-Y.; Xu, G.-R.; Li, F.-M.; Hong, Q.-L.; Jin, P.-J.; Chen, P.; Chen, Y. Hydrogen Generation from Ammonia Electrolysis on Bifunctional Platinum Nanocubes Electrocatalysts. *J. Energy Chem.* **2020**, *47*, 234−240.
(656) Xue, Q.; Zhao, Y.; Zhu, J.; Ding, Y.; Wang, T.; Sun, H.; Li, F.; Chen, P.; Jin, P.; Yin, S.; Chen, Y. PtRu Nanocubes as Bifunctional Electrocatalysts for Ammonia Electrolysis. *J. Mater. Chem. A* **2021**, *9*, 8444−8451.
(657) Hu, S.; Tan, Y.; Feng, C.; Wu, H.; Zhang, J.; Mei, H. Synthesis of N Doped NiZnCu-Layered Double Hydroxides with Reduced Graphene Oxide on Nickel Foam as Versatile Electrocatalysts for Hydrogen Production in Hybrid-Water Electrolysis. *J. Power Sources* **2020**, *453*, 227872.

https://doi.org/10.1021/acs.chemrev.3c00332
Chem. Rev. 2024, 124, 3694−3812

(658) Zhang, M.; Li, H.; Duan, X.; Zou, P.; Jeerh, G.; Sun, B.; Chen, S.; Humphreys, J.; Walker, M.; Xie, K.; Tao, S. An Efficient Symmetric Electrolyzer Based on Bifunctional Perovskite Catalyst for Ammonia Electrolysis. *Adv. Sci.* **2021**, *8*, 2101299.
(659) Jiang, K.; Li, K.; Liu, Y.-Q.; Lin, S.; Wang, Z.; Wang, D.; Ye, Y. Nickel-Cobalt Nitride Nanoneedle Supported on Nickel Foam as an Efficient Electrocatalyst for Hydrogen Generation from Ammonia Electrolysis. *Electrochim. Acta* **2022**, *403*, 139700.
(660) Wu, M.; Du, J.; Tao, C.; Liu, Z.; Li, Y. A Tri-Functionalised Pt-SnO_x-Based Electrocatalyst for Hydrogen Generation via Ammonia Decomposition under Native pH Conditions. *J. Colloid Interface Sci.* **2019**, *542*, 451−459.
(661) Xu, Q.; Yu, T.; Chen, J.; Qian, G.; Song, H.; Luo, L.; Chen, Y.; Liu, T.; Wang, Y.; Yin, S. Coupling Interface Constructions of $FeNi_3$-MoO_2 Heterostructures for Efficient Urea Oxidation and Hydrogen Evolution Reaction. *ACS Appl. Mater. Interfaces* **2021**, *13*, 16355−16363.
(662) Wang, Z.; Liu, W.; Hu, Y.; Guan, M.; Xu, L.; Li, H.; Bao, J.; Li, H. Cr-Doped CoFe Layered Double Hydroxides: Highly Efficient and Robust Bifunctional Electrocatalyst for the Oxidation of Water and Urea. *Appl. Catal., B* **2020**, *272*, 118959.
(663) Zhang, Q.; Kazim, F. M. D.; Ma, S.; Qu, K.; Li, M.; Wang, Y.; Hu, H.; Cai, W.; Yang, Z. Nitrogen Dopants in Nickel Nanoparticles Embedded Carbon Nanotubes Promote Overall Urea Oxidation. *Appl. Catal., B* **2021**, *280*, 119436.
(664) Zhang, Q.; Sun, M.; Zhu, J.; Yang, S.; Chen, L.; Yang, X.; Wang, P.; Li, K.; Xue, F.; Lu, Y.; Zhang, J.; Zhao, P. New Strategy to Synthesize Oxygen Vacancy-Rich CoFe Nanoneedles for Overall Water Splitting and Urea Electrolysis. *Chem. Eng. J.* **2022**, *432*, 134275.
(665) Zhu, X.; Dou, X.; Dai, J.; An, X.; Guo, Y.; Zhang, L.; Tao, S.; Zhao, J.; Chu, W.; Zeng, X. C.; Wu, C.; Xie, Y. Metallic Nickel Hydroxide Nanosheets Give Superior Electrocatalytic Oxidation of Urea for Fuel Cells. *Angew. Chem., Int. Ed.* **2016**, *55*, 12465−12469.
(666) Feng, S.; Luo, J.; Li, J.; Yu, Y.; Kang, Z.; Huang, W.; Chen, Q.; Deng, P.; Shen, Y.; Tian, X. Heterogeneous Structured Ni_3Se_2/MoO_2@$Ni_{12}P_5$ Catalyst for Durable Urea Oxidation Reaction. *Mater. Today Phys.* **2022**, *23*, 100646.
(667) Ni, S.; Qu, H.; Xu, Z.; Zhu, X.; Xing, H.; Wang, L.; Yu, J.; Liu, H.; Chen, C.; Yang, L. Interfacial Engineering of the $NiSe_2$/$FeSe_2$ p-p Heterojunction for Promoting Oxygen Evolution Reaction and Electrocatalytic Urea Oxidation. *Appl. Catal., B* **2021**, *299*, 120638.
(668) Sha, L.; Ye, K.; Yin, J.; Zhu, K.; Cheng, K.; Yan, J.; Wang, G.; Cao, D. In Situ Grown 3D Hierarchical $MnCo_2O_4$. 5@Ni(OH)2 Nanosheet Arrays on Ni Foam for Efficient Electrocatalytic Urea Oxidation. *Chem. Eng. J.* **2020**, *381*, 122603.
(669) Liu, D.; Liu, T.; Zhang, L.; Qu, F.; Du, G.; Asiri, A. M.; Sun, X. High-Performance Urea Electrolysis Towards Less Energy-Intensive Electrochemical Hydrogen Production Using a Bifunctional Catalyst Electrode. *J. Mater. Chem. A* **2017**, *5*, 3208−3213.
(670) Jiang, H.; Sun, M.; Wu, S.; Huang, B.; Lee, C.-S.; Zhang, W. Oxygen-Incorporated NiMoP Nanotube Arrays as Efficient Bifunctional Electrocatalysts for Urea-Assisted Energy-Saving Hydrogen Production in Alkaline Electrolyte. *Adv. Funct. Mater.* **2021**, *31*, 2104951.
(671) Khalafallah, D.; Zou, Q.; Zhi, M.; Hong, Z. Tailoring Hierarchical Yolk-Shelled Nickel Cobalt Sulfide Hollow Cages with Carbon Tuning for Asymmetric Supercapacitors and Efficient Urea Electrocatalysis. *Electrochim. Acta* **2020**, *350*, 136399.
(672) Xu, X.; Ullah, H.; Humayun, M.; Li, L.; Zhang, X.; Bououdina, M.; Debecke, D. P.; Huo, K.; Wang, D.; Wang, C. Fluorinated Ni-O-C Heterogeneous Catalyst for Efficient Urea-Assisted Hydrogen Production. *Adv. Funct. Mater.* **2023**, *33*, 2303986.
(673) Dutta, B.; Wu, Y.; Chen, J.; Wang, J.; He, J.; Sharafeldin, M.; Kerns, P.; Jin, L.; Dongare, A. M.; Rusling, J.; Suib, S. Partial Surface Selenization of Cobalt Sulfide Microspheres for Enhancing the Hydrogen Evolution Reaction. *ACS Catal.* **2019**, *9*, 456−465.
(674) Gong, Q.; Cheng, L.; Liu, C.; Zhang, M.; Feng, Q.; Ye, H.; Zeng, M.; Xie, L.; Liu, Z.; Li, Y. Ultrathin $MoS_{2(1-X)}Se_{2x}$ Alloy Nanoflakes for Electrocatalytic Hydrogen Evolution Reaction. *ACS Catal.* **2015**, *5*, 2213−2219.
(675) Zhou, H.; Yu, F.; Sun, J.; Zhu, H.; Mishra, I. K.; Chen, S.; Ren, Z. Highly Efficient Hydrogen Evolution from Edge-Oriented $WS_{2(1-X)}Se_{2x}$ Particles on Three-Dimensional Porous $NiSe_2$ Foam. *Nano Lett.* **2016**, *16*, 7604−7609.
(676) Du, X.; Ma, G.; Zhang, X. Boosting Alkaline Water Splitting and the Urea Electrolysis Kinetic Process of a Co_3O_4 Nanosheet by Electronic Structure Modulation of F. *P Co-Doping. Dalton Trans.* **2022**, *51*, 4909−4918.
(677) Chen, N.; Du, Y.-X.; Zhang, G.; Lu, W.-T.; Cao, F.-F. Amorphous Nickel Sulfoselenide for Efficient Electrochemical Urea-Assisted Hydrogen Production in Alkaline Media. *Nano Energy* **2021**, *81*, 105605.
(678) Zhang, J.-Y.; He, T.; Wang, M.; Qi, R.; Yan, Y.; Dong, Z.; Liu, H.; Wang, H.; Xia, B. Y. Energy-Saving Hydrogen Production Coupling Urea Oxidation over a Bifunctional Nickel-Molybdenum Nanotube Array. *Nano Energy* **2019**, *60*, 894−902.
(679) Wang, C.; Lu, H.; Mao, Z.; Yan, C.; Shen, G.; Wang, X. Bimetal Schottky Heterojunction Boosting Energy-Saving Hydrogen Production from Alkaline Water via Urea Electrocatalysis. *Adv. Funct. Mater.* **2020**, *30*, 2000556.
(680) Ligani Fereja, S.; Li, P.; Zhang, Z.; Guo, J.; Fang, Z.; Li, Z.; He, S.; Chen, W. W-Doping Induced Abundant Active Sites in a 3D NiS_2/MoO_2 Heterostructure as an Efficient Electrocatalyst for Urea Oxidation and Hydrogen Evolution Reaction. *Chem. Eng. J.* **2022**, *432*, 134274.
(681) He, M.; Feng, C.; Liao, T.; Hu, S.; Wu, H.; Sun, Z. Low-Cost Ni_2P/$Ni_{0.96}S$ Heterostructured Bifunctional Electrocatalyst Toward Highly Efficient Overall Urea-Water Electrolysis. *ACS Appl. Mater. Interfaces* **2020**, *12*, 2225−2233.
(682) Wang, K.; Huang, W.; Cao, Q.; Zhao, Y.; Sun, X.; Ding, R.; Lin, W.; Liu, E.; Gao, P. Engineering NiF_3/Ni_2P Heterojunction as Efficient Electrocatalysts for Urea Oxidation and Splitting. *Chem. Eng. J.* **2022**, *427*, 130865.
(683) Liao, L.; Zhao, Y.; Zhou, H.; Li, D.; Qi, Y.; Zhang, Y.; Sun, Y.; Zhou, Q.; Yu, F. Edge-Oriented N-Doped WS_2 Nanoparticles on Porous Co_3N Nanosheets for Efficient Alkaline Hydrogen Evolution and Nitrogenous Nucleophile Electrooxidation. *Small* **2022**, *18*, 2203171.
(684) Xie, H.; Feng, Y.; He, X.; Zhu, Y.; Li, Z.; Liu, H.; Zeng, S.; Qian, Q.; Zhang, G. Construction of Nitrogen-Doped Biphasic Transition-Metal Sulfide Nanosheet Electrode for Energy-Efficient Hydrogen Production via Urea Electrolysis. *Small* **2023**, *19*, 2207425.
(685) Xu, C.; Yang, X.; Feng, K.; Zhang, M.; Yang, L.; Yin, S. Carbon-Encapsulated Multimetallic Hybrid Electrocatalyst for Overall Water Splitting and Urea Oxidation. *ACS Appl. Energy Mater.* **2023**, *6*, 1404−1412.
(686) Zhang, M.; Duan, Z.; Cui, L.; Yu, H.; Wang, Z.; Xu, Y.; Li, X.; Wang, L.; Wang, H. A Phosphorus Modified Mesoporous AuRh Film as an Efficient Bifunctional Electrocatalyst for Urea-Assisted Energy-Saving Hydrogen Production. *J. Mater. Chem. A* **2022**, *10*, 3086−3092.
(687) Xu, H.; Ye, K.; Zhu, K.; Yin, J.; Yan, J.; Wang, G.; Cao, D. Template-Directed Assembly of Urchin-Like CoS_x/Co-MOF as an Efficient Bifunctional Electrocatalyst for Overall Water and Urea Electrolysis. *Inorg. Chem. Front.* **2020**, *7*, 2602−2610.
(688) Zhang, Y.; Zhang, Z.; Addad, A.; Wang, Q.; Roussel, P.; Amin, M. A.; Szunerits, S.; Boukherroub, R. 0D/2D Co_3O_4/Ti_3C_2 Mxene Composite: A Dual-Functional Electrocatalyst for Energy-Saving Hydrogen Production and Urea Oxidation. *ACS Appl. Energy Mater.* **2022**, *5*, 15471−15482.
(689) Wang, T.; Miao, L.; Zheng, S.; Qin, H.; Cao, X.; Yang, L.; Jiao, L. Interfacial Engineering of Ni_3N/Mo_2N Heterojunctions for Urea-Assisted Hydrogen Evolution Reaction. *ACS Catal.* **2023**, *13*, 4091−4100.
(690) Liu, T.; Liu, D.; Qu, F.; Wang, D.; Zhang, L.; Ge, R.; Hao, S.; Ma, Y.; Du, G.; Asiri, A. M.; Chen, L.; Sun, X. Enhanced Electrocatalysis for Energy-Efficient Hydrogen Production over CoP

https://doi.org/10.1021/acs.chemrev.3c00332
Chem. Rev. 2024, 124, 3694−3812

Catalyst with Nonelectroactive Zn as a Promoter. *Adv. Energy Mater.* **2017**, *7*, 1700020.
(691) Dong, Z.; Lin, F.; Yao, Y.; Jiao, L. Crystalline $Ni(OH)_2$/Amorphous $NiMoO_x$ Mixed-Catalyst with Pt-Like Performance for Hydrogen Production. *Adv. Energy Mater.* **2019**, *9*, 1902703.
(692) Li, D.; Wan, W.; Wang, Z.; Wu, H.; Wu, S.; Jiang, T.; Cai, G.; Jiang, C.; Ren, F. Self-Derivation and Surface Reconstruction of Fe-Doped Ni_3S_2 Electrode Realizing High-Efficient and Stable Overall Water and Urea Electrolysis. *Adv. Energy Mater.* **2022**, *12*, 2201913.
(693) Chen, C. C.; Jin, L. J.; Hu, L.; Zhang, T. Y.; He, J. H.; Gu, P. Y.; Xu, Q. F.; Lu, J. M. Urea-Oxidation-Assisted Electrochemical Water Splitting for Hydrogen Production on a Bifunctional Heterostructure Transition Metal Phosphides Combining Metal-Organic Frameworks. *J. Colloid Interface Sci.* **2022**, *628*, 1008−1018.
(694) Wei, D.; Tang, W.; Wang, Y. Hairy Sphere-Like Ni_9S_8/CuS/Cu_2O Composites Grown on Nickel Foam as Bifunctional Electrocatalysts for Hydrogen Evolution and Urea Electrooxidation. *Int. J. Hydrogen Energy* **2021**, *46*, 20950−20960.
(695) Lv, L.; Li, Z.; Wan, H.; Wang, C. Achieving Low-Energy Consumption Water-to-Hydrogen Conversion via Urea Electrolysis over a Bifunctional Electrode of Hierarchical Cuprous Sulfide@Nickel Selenide Nanoarrays. *J. Colloid Interface Sci.* **2021**, *592*, 13−21.
(696) Wang, J.; Sun, Y.; Qi, Y.; Wang, C. Vanadium-Doping and Interface Engineering for Synergistically Enhanced Electrochemical Overall Water Splitting and Urea Electrolysis. *ACS Appl. Mater. Interfaces* **2021**, *13*, 57392−57402.
(697) Wu, Z.; Guo, X.; Zhang, Z.; Song, M.; Jiao, T.; Zhu, Y.; Wang, J.; Liu, X. Interface Engineering of MoS_2 for Electrocatalytic Performance Optimization for Hydrogen Generation via Urea Electrolysis. *ACS Sustainable Chem. Eng.* **2019**, *7*, 16577−16584.
(698) Jiang, Y.; Gao, S.; Liu, J.; Xu, G.; Jia, Q.; Chen, F.; Song, X. Ti-Mesh Supported Porous CoS_2 Nanosheet Self-Interconnected Networks with High Oxidation States for Efficient Hydrogen Production via Urea Electrolysis. *Nanoscale* **2020**, *12*, 11573−11581.
(699) Kim, B.; Das, G.; Kim, J.; Yoon, H. H.; Lee, D. H. Ni-Co-B Nanoparticle Decorated Carbon Felt by Electroless Plating as a Bi-Functional Catalyst for Urea Electrolysis. *J. Colloid Interface Sci.* **2021**, *601*, 317−325.
(700) Sun, C. B.; Guo, M. W.; Siwal, S. S.; Zhang, Q. B. Efficient Hydrogen Production via Urea Electrolysis with Cobalt Doped Nickel Hydroxide-Riched Hybrid Films: Cobalt Doping Effect and Mechanism Aspect. *J. Catal.* **2020**, *381*, 454−461.
(701) Song, W.; Xu, M.; Teng, X.; Niu, Y.; Gong, S.; Liu, X.; He, X.; Chen, Z. Construction of Self-Supporting, Hierarchically Structured Caterpillar-Like $NiCo_2S_4$ Arrays as an Efficient Trifunctional Electrocatalyst for Water and Urea Electrolysis. *Nanoscale* **2021**, *13*, 1680−1688.
(702) Liu, H.; Liu, Z.; Wang, F.; Feng, L. Efficient Catalysis of N Doped NiS/NiS_2 Heterogeneous Structure. *Chem. Eng. J.* **2020**, *397*, 125507.
(703) Liu, Z.; Zhang, C.; Liu, H.; Feng, L. Efficient Synergism of $NiSe_2$ Nanoparticle/NiO Nanosheet for Energy-Relevant Water and Urea Electrocatalysis. *Appl. Catal., B* **2020**, *276*, 119165.
(704) Wang, F.; Zhao, D.; Zhang, L.; Fan, L.; Zhang, X.; Hu, S. Nanostructured Nickel Nitride with Reduced Graphene Oxide Composite Bifunctional Electrocatalysts for an Efficient Water-Urea Splitting. *Nanomaterials* **2019**, *9*, 1583.
(705) Liu, Q.; Xie, L.; Qu, F.; Liu, Z.; Du, G.; Asiri, A. M.; Sun, X. A Porous Ni_3N Nanosheet Array as a High-Performance Non-Noble-Metal Catalyst for Urea-Assisted Electrochemical Hydrogen Production. *Inorg. Chem. Front.* **2017**, *4*, 1120−1124.
(706) Wilkinson, J. L.; Boxall, A. B. A.; Kolpin, D. W.; Leung, K. M. Y.; Lai, R. W. S.; Galbán-Malagón, C.; Adell, A. D.; Mondon, J.; Metian, M.; Marchant, R. A.; et al. Pharmaceutical Pollution of the World's Rivers. *Proc. Natl. Acad. Sci. U.S.A.* **2022**, *119*, e2113947119.
(707) Li, M.-F.; Liu, Y.-G.; Zeng, G.-M.; Liu, N.; Liu, S.-b. Graphene and Graphene-Based Nanocomposites Used for Antibiotics Removal in Water Treatment: A Review. *Chemosphere* **2019**, *226*, 360−380.
(708) Safardoust-Hojaghan, H.; Salavati-Niasari, M. Degradation of Methylene Blue as a Pollutant with N-Doped Graphene Quantum Dot/Titanium Dioxide Nanocomposite. *J. Cleaner Prod.* **2017**, *148*, 31−36.
(709) Uheida, A.; Mejia, H. G.; Abdel-Rehim, M.; Hamd, W.; Dutta, J. Visible Light Photocatalytic Degradation of Polypropylene Microplastics in a Continuous Water Flow System. *J. Hazard. Mater.* **2021**, *406*, 124299.
(710) Nidheesh, P. V.; Zhou, M.; Oturan, M. A. An Overview on the Removal of Synthetic Dyes from Water by Electrochemical Advanced Oxidation Processes. *Chemosphere* **2018**, *197*, 210−227.
(711) Sires, I.; Brillas, E. Remediation of Water Pollution Caused by Pharmaceutical Residues Based on Electrochemical Separation and Degradation Technologies: A Review. *Environ. Int.* **2012**, *40*, 212−229.
(712) Wang, Y.; Shen, C.; Zhang, M.; Zhang, B.-T.; Yu, Y.-G. The Electrochemical Degradation of Ciprofloxacin Using a SnO_2-Sb/Ti Anode: Influencing Factors, Reaction Pathways and Energy Demand. *Chem. Eng. J.* **2016**, *296*, 79−89.
(713) Zhang, X.; Wang, Y.; Liu, C.; Yu, Y.; Lu, S.; Zhang, B. Recent Advances in Non-Noble Metal Electrocatalysts for Nitrate Reduction. *Chem. Eng. J.* **2021**, *403*, 126269.
(714) Li, Z.; Xu, Q. Metal-Nanoparticle-Catalyzed Hydrogen Generation from Formic Acid. *Acc. Chem. Res.* **2017**, *50*, 1449−1458.
(715) Wang, Q.; Chen, F.; Tang, Q.; Guo, L.; Gebremariam, T. T.; Jin, T.; Liu, H.; Kou, B.; Li, Z.; Bian, W. Transition from Core-Shell to Janus Segregation Pattern in AgPd Nanoalloy by Ni Doping for the Formate Oxidation. *Appl. Catal., B* **2020**, *270*, 118861.
(716) Kang, Y. S.; Choi, D.; Cho, J.; Park, H.-Y.; Lee, K.-S.; Ahn, M.; Jang, I.; Park, T.; Ham, H. C.; Yoo, S. J. Highly Active and Durable Ordered Intermetallic PdFe Electrocatalyst for Formic Acid Electrooxidation Reaction. *ACS Appl. Energy Mater.* **2020**, *3*, 4226−4237.
(717) Mondal, S.; Raj, C. R. Electrochemical Dealloying-Assisted Surface-Engineered Pd-Based Bifunctional Electrocatalyst for Formic Acid Oxidation and Oxygen Reduction. *ACS Appl. Mater. Interfaces* **2019**, *11*, 14110−14119.
(718) Rettenmaier, C.; Arán-Ais, R. M.; Timoshenko, J.; Rizo, R.; Jeon, H. S.; Kühl, S.; Chee, S. W.; Bergmann, A.; Cuenya, B. R. Enhanced Formic Acid Oxidation over SnO_2-Decorated Pd Nanocubes. *ACS Catal.* **2020**, *10*, 14540−14551.
(719) Shen, T.; Lu, Y.; Gong, M.; Zhao, T.; Hu, Y.; Wang, D. Optimizing Formic Acid Electro-Oxidation Performance by Restricting the Continuous Pd Sites in Pd-Sn Nanocatalysts. *ACS Sustainable Chem. Eng.* **2020**, *8*, 12239−12247.
(720) Li, J.; Liang, X.; Cai, L.; Huang, S.; Zhao, C. Modification of Palladium Nanocrystals with Single Atom Platinum via an Electrochemical Self-Catalysis Strategy for Efficient Formic Acid Electrooxidation. *ACS Appl. Mater. Interfaces* **2022**, *14*, 8001−8009.
(721) Yang, L.; Li, G.; Chang, J.; Ge, J.; Liu, C.; Vladimir, F.; Wang, G.; Jin, Z.; Xing, W. Sea Urchin-Like Au_{Core}@Pd_{Shell} Electrocatalysts with High FAOR Performance: Coefficient of Lattice Strain and Electrochemical Surface Area. *Appl. Catal., B* **2020**, *260*, 118200.
(722) Li, C.; Chen, Z.; Yi, H.; Cao, Y.; Du, L.; Hu, Y.; Kong, F.; Campen, R. K.; Gao, Y.; Du, C.; Yin, G.; Zhang, I. Y.; Tong, Y. Polyvinylpyrrolidone-Coordinated Single-Site Platinum Catalyst Exhibits High Activity for Hydrogen Evolution Reaction. *Angew. Chem., Int. Ed.* **2020**, *59*, 15902−15907.
(723) Rajala, T.; Kronberg, R.; Backhouse, R.; Buan, M. E. M.; Tripathi, M.; Zitolo, A.; Jiang, H.; Laasonen, K.; Susi, T.; Jaouen, F.; Kallio, T. A Platinum Nanowire Electrocatalyst on Single-Walled Carbon Nanotubes to Drive Hydrogen Evolution. *Appl. Catal., B* **2020**, *265*, 118582.
(724) Xue, S.; Haid, R. W.; Kluge, R. M.; Ding, X.; Garlyyev, B.; Fichtner, J.; Watzele, S.; Hou, S.; Bandarenka, A. S. Enhancing the Hydrogen Evolution Reaction Activity of Platinum Electrodes in Alkaline Media Using Nickel-Iron Clusters. *Angew. Chem., Int. Ed.* **2020**, *59*, 10934−10938.
(725) Bhalothia, D.; Huang, T.-H.; Chang, C.-W.; Lin, T.-H.; Wu, S.-C.; Wang, K.-W.; Chen, T.-Y. High-Performance and Stable

https://doi.org/10.1021/acs.chemrev.3c00332
Chem. Rev. 2024, 124, 3694−3812

Hydrogen Evolution Reaction Achieved by Pt Trimer Decoration on Ultralow-Metal Loading Bimetallic PtPd Nanocatalysts. *ACS Appl. Energy Mater.* **2020**, *3*, 11142−11152.
(726) Shi, Y.; Ma, Z.-R.; Xiao, Y.-Y.; Yin, Y.-C.; Huang, W.-M.; Huang, Z.-C.; Zheng, Y.-Z.; Mu, F.-Y.; Huang, R.; Shi, G.-Y.; Sun, Y.-Y.; Xia, X.-H.; Chen, W. Electronic metal-support interaction modulates single-atom platinum catalysis for hydrogen evolution reaction. *Nat. Commun.* **2021**, *12*, 3021−3031.
(727) Liu, D.; Li, X.; Chen, S.; Yang, H.; Wang, C.; Wu, C.; Haleem, Y. A.; Duan, S.; Lu, J.; Ge, B.; Ajayan, P.; Luo, Y.; Jiang, J.; Song, L. Atomically dispersed platinum supported on curved carbon supports for efficient electrocatalytic hydrogen evolution. *Nat. Energy* **2019**, *4*, 512−518.
(728) Zhu, Z.; Chen, X.; Liu, J.; Fan, S.; You, B. Negatively Charging Nonprecious Metal Phosphides/Selenides via General Polyaniline Coating for Improved Alkaline H_2 Evolution. *Energy Fuels* **2023**, *37*, 18038−18045.
(729) Xue, Q.; Bai, X.-Y.; Zhao, Y.; Li, Y.-N.; Wang, T.-J.; Sun, H.-Y.; Li, F.-M.; Chen, P.; Jin, P.; Yin, S.-B.; Chen, Y. Au Core-PtAu Alloy Shell Nanowires for Formic Acid Electrolysis. *J. Energy Chem.* **2022**, *65*, 94−102.
(730) Ge, Z.-X.; Ding, Y.; Wang, T.-J.; Shi, F.; Jin, P.-J.; Chen, P.; He, B.; Yin, S.-B.; Chen, Y. Interfacial Engineering of Holey Platinum Nanotubes for Formic Acid Electrooxidation Boosted Water Splitting. *J. Energy Chem.* **2023**, *77*, 209−216.
(731) Liu, X.; Ji, Y.; Chen, G.; Peng, X.; Yi, L.; Chen, J.; Feng, X.; Wen, Z. High-Performance Bifunctional Electrocatalysts of Palladium Decoration on Carbon Nanoarchitectures for Indirect Releasing of H_2 Stored in Formate. *Small Struct.* **2021**, *2*, 2100121.
(732) Wang, H.; Wang, W.; Mao, Q.; Yu, H.; Deng, K.; Xu, Y.; Li, X.; Wang, Z.; Wang, L. Tensile Strained PdNi Bimetallene for Energy-Efficient Hydrogen Production Integrated with Formate Oxidation. *Chem. Eng. J.* **2022**, *450*, 137995.
(733) Carvalho, R. H.; Lemos, M. A. N. D. A.; Lemos, F.; Cabral, J. M. S.; Ribeiro, F. R. Electro-Oxidation of Phenol on Zeolite/Graphite Composite Electrodes Part 3. Influence of the Electrolyte and of Nonelectroactive Cations. *Cataly. Today* **2008**, *133*, 855−862.
(734) Qin, H.; Wei, X.; Ye, Z.; Liu, X.; Mao, S. Promotion of Phenol Electro-Oxidation by Oxygen Evolution Reaction on an Active Electrode for Efficient Pollution Control and Hydrogen Evolution. *Environ. Sci. Technol.* **2022**, *56*, 5753−5762.
(735) Busca, G.; Berardinelli, S.; Resini, C.; Arrighi, L. Technologies for the Removal of Phenol from Fluid Streams: a Short Review of Recent Developments. *J. Hazard. Mater.* **2008**, *160*, 265−288.
(736) Chand, R.; Ince, N. H.; Gogate, P. R.; Bremner, D. H. Phenol Degradation Using 20, 300 and 520 Khz Ultrasonic Reactors with Hydrogen Peroxide, Ozone and Zero Valent Metals. *Sep. Purif. Technol.* **2009**, *67*, 103−109.
(737) Alshabib, M.; Onaizi, S. A. A Review on Phenolic Wastewater Remediation Using Homogeneous and Heterogeneous Enzymatic Processes: Current Status and Potential Challenges. *Sep. Purif. Technol.* **2019**, *219*, 186−207.
(738) Zhang, H.; Zhang, R.; Ling, Z.; Li, W.; Yan, Y.; Gong, M.; Ma, J. Partial Oxidation of Phenolic Wastewater Using Naoh and Ni Addition for Hydrogen Production and Phenolics Degradation in Supercritical Water. *Sep. Purif. Technol.* **2021**, *268*, 118685.
(739) Qin, H.; Ye, Z.; Wei, X.; Liu, X.; Liu, X.; Fan, J.; Wen, Z.; Mao, S. Bifunctional Electrolyzation for Simultaneous Organic Pollutant Degradation and Hydrogen Generation. *ACS EST Engg.* **2021**, *1*, 1360−1368.
(740) Zheng, Y.; Xu, X. Surface Atom Regulation on Polyoxometalate Electrocatalyst for Simultaneous Low-Voltage H_2 Production and Phenol Degradation. *ACS Appl. Mater. Interfaces* **2020**, *12*, 53739−53748.
(741) Bolzan, A. E.; Schilardi, P. L.; Piatti, R. C. V.; Iwasita, T.; Cuesta, A.; Gutierrez, C.; Arvia, A. J. Comparative voltammetric and FTIRRAS study on the electro-oxidation of Thiourea and Methyl-Thioureas on Platinum in Aqueous Acid Solutions. *J. Electroanal. Chem.* **2004**, *571*, 59−72.
(742) Bolzán, A. E.; Wakenge, I. B.; Salvarezza, R. C.; Arvia, A. J. Electrochemical Response of Thiourea and Formamidine Disulphide on Polycrystalline Platinum in Aqueous 0.5 M Sulphuric Acid. *J. Electroanal. Chem.* **1999**, *475*, 181−189.
(743) Qu, J.; Xu, Y.; Zhang, X.; Sun, M.; Tao, Y.; Zhang, X.; Zhang, G.; Ge, C.; Zhang, Y. Ball Milling-Assisted Preparation of N-Doped Biochar Loaded with Ferrous Sulfide as Persulfate Activator for Phenol Degradation: Multiple Active Sites-Triggered Radical/Non-Radical Mechanism. *Appl. Catal., B* **2022**, *316*, 121639.
(744) Sun, J.; Mu, Q.; Kimura, H.; Murugadoss, V.; He, M.; Du, W.; Hou, C. Oxidative Degradation of Phenols and Substituted Phenols in the Water and Atmosphere: A Review. *Adv. Compos. Hybrid Mater.* **2022**, *5*, 627−640.
(745) Wang, S.; Gao, Q.; Wang, J. Thermodynamic Analysis of Decomposition of Thiourea and Thiourea Oxides. *J. Phys. Chem. B* **2005**, *109*, 17281−17289.
(746) Hung, C.-H.; Pavlostathis, S. G. Aerobic Biodegradation of Thiocyanate. *Water Res.* **1997**, *31*, 2761−2770.
(747) Pan, J.; Ma, J.; Wu, H.; Ren, Y.; Fu, B.; He, M.; Zhu, S.; Wei, C. Simultaneous Removal of Thiocyanate and Nitrogen from Wastewater by Autotrophic Denitritation Process. *Bioresour. Technol.* **2018**, *267*, 30−37.
(748) Deng, J.; Chen, S.; Yao, N.; Wang, Q.; Li, J.; Wei, Z. Integrating H_2 Generation with Sewage Disposal by an Efficient Anti-Poisoning Bifunctional Electrocatalyst. *Appl. Catal., B* **2020**, *277*, 119175.
(749) Pieplu, A.; Saur, O.; Lavalley, J. C.; Legendre, O.; Nedez, C. Claus Catalysis and H_2S Selective Oxidation. *Catal. Rev.* **1998**, *40*, 409−450.
(750) Yang, K.; Zhang, N.; Yang, J.; Xu, Z.; Yan, J.; Li, D.; Liu, S. Synergistic Marriage of CO_2 Reduction and Sulfide Oxidation towards a Sustainable Co-Electrolysis Process. *Appl. Catal., B* **2023**, *332*, 122718.
(751) Zhang, X.; Qi, R.; Wu, A.; Sheng, K.; Lin, H. Effective Anodic Sulfide Removal Catalyzed by Single Nickel Atoms on Nitrogen-Doped Graphene with Stainless Steel Substrate. *Chem. Eng. J.* **2022**, *427*, 130963.
(752) Zhou, Q.; Shen, Z.; Zhu, C.; Li, J.; Ding, Z.; Wang, P.; Pan, F.; Zhang, Z.; Ma, H.; Wang, S.; Zhang, H. Nitrogen-Doped CoP Electrocatalysts for Coupled Hydrogen Evolution and Sulfur Generation with Low Energy Consumption. *Adv. Mater.* **2018**, *30*, 1800140.
(753) Chen, T.; Zhang, Z.; Cheng, B.; Chen, R.; Hu, Y.; Ma, L.; Zhu, G.; Liu, J.; Jin, Z. Self-Templated Formation of Interlaced Carbon Nanotubes Threaded Hollow Co_3S_4 Nanoboxes for High-Rate and Heat-Resistant Lithium-Sulfur Batteries. *J. Am. Chem. Soc.* **2017**, *139*, 12710−12715.
(754) Xu, J.; Yang, L.; Cao, S.; Wang, J.; Ma, Y.; Zhang, J.; Lu, X. Sandwiched Cathodes Assembled from CoS_2-Modified Carbon Clothes for High-Performance Lithium-Sulfur Batteries. *Adv. Sci.* **2021**, *8*, 2101019.
(755) Zhang, H.; Zou, M.; Zhao, W.; Wang, Y.; Chen, Y.; Wu, Y.; Dai, L.; Cao, A. Highly Dispersed Catalytic Co_3S_4 among a Hierarchical Carbon Nanostructure for High-Rate and Long-Life Lithium-Sulfur Batteries. *ACS Nano* **2019**, *13*, 3982−3991.
(756) Xiao, Z.; Lu, C.; Wang, J.; Qian, Y.; Wang, B.; Zhang, Q.; Tang, A.; Yang, H. Bifunctional Co_3S_4 Nanowires for Robust Sulfion Oxidation and Hydrogen Generation with Low Power Consumption. *Adv. Funct. Mater.* **2023**, *33*, 2212183.
(757) Pei, Y.; Cheng, J.; Zhong, H.; Pi, Z.; Zhao, Y.; Jin, F. Sulfide-Oxidation-Assisted Electrochemical Water Splitting for H_2 Production on a Bifunctional Cu_2S/Nickel Foam Catalyst. *Green Chem.* **2021**, *23*, 6975−6983.
(758) De Gouw, J. A.; Parrish, D. D.; Frost, G. J.; Trainer, M. Reduced Emissions of CO2, NOx, and SO2 from U.S. Power Plants Owing to Switch from Coal to Natural Gas with Combined Cycle Technology. *Earth's Future* **2014**, *2*, 75−82.
(759) Park, J.; Yoon, H.; Lee, D.-Y.; Ji, S. G.; Yang, W.; David Tilley, S.; Sung, M.-C.; Park, I. J.; Tan, J.; Lee, H.; Kim, J. Y.; Kim, D.-W.;

https://doi.org/10.1021/acs.chemrev.3c00332
Chem. Rev. 2024, 124, 3694−3812

Moon, J. Photovoltaic Powered Solar Hydrogen Production Coupled with Waste SO_2 Valorization Enabled by MoP Electrocatalysts. *Appl. Catal., B* **2022**, *305*, 121045.
(760) Ruan, W.; Liang, S.; Yuan, C.; Hao, W.; Lu, Z.; Wang, D.; Cheng, G.; Wang, Q.; Jiang, W.; Ibhadon, A. O.; Teng, F. Boosted Electrocatalytic Hydrogen Production by Methylene Blue and Urea and Synergistic Electrooxidation Degradation. *Mater. Today Energy* **2021**, *22*, 100880.
(761) Goren, A. Y.; Recepoğlu, Y. K.; Edebali, O.; Sahin, C.; Genisoglu, M.; Okten, H. E. Electrochemical Degradation of Methylene Blue by a Flexible Graphite Electrode: Techno-Economic Evaluation. *ACS Omega* **2022**, *7*, 32640−32652.
(762) Pahra, S.; Sangabathula, O.; Sharma, C. S.; Devi, P. A Noble Metal-Free Candle Soot Derived Carbon Electrocatalyst for Simultaneous H_2 Generation and Wastewater Treatment. *J. Phys. Chem. Solids* **2023**, *173*, 111106.
(763) Han, G.; Li, M.; Liu, H.; Zhang, W.; He, L.; Tian, F.; Liu, Y.; Yu, Y.; Yang, W.; Guo, S. Short-Range Diffusion Enables General Synthesis of Medium-Entropy Alloy Aerogels. *Adv. Mater.* **2022**, *34*, 2202943.
(764) Cloutier, C. R.; Wilkinson, D. P. Electrolytic Production of Hydrogen from Aqueous Acidic Methanol Solutions. *Int. J. Hydrogen Energy* **2010**, *35*, 3967−3984.
(765) Chu, Y.-Y.; Wang, Z.-B.; Jiang, Z.-Z.; Gu, D.-M.; Yin, G.-P. A Novel Structural Design of a Pt/C-CeO_2 Catalyst with Improved Performance for Methanol Electro-Oxidation by β-Cyclodextrin Carbonization. *Adv. Mater.* **2011**, *23*, 3100−3104.
(766) Li, S.; Ma, R.; Hu, J.; Li, Z.; Liu, L.; Wang, X.; Lu, Y.; Sterbinsky, G. E.; Liu, S.; Zheng, L.; Liu, J.; Liu, D.; Wang, J. Coordination Environment Tuning of Nickel Sites by Oxyanions to Optimize Methanol Electro-Oxidation Activity. *Nat. Commun.* **2022**, *13*, 2916.
(767) Zhu, B.; Dong, B.; Wang, F.; Yang, Q.; He, Y.; Zhang, C.; Jin, P.; Feng, L. Unraveling a Bifunctional Mechanism for Methanol-to-Formate Electro-Oxidation on Nickel-Based Hydroxides. *Nat. Commun.* **2023**, *14*, 1686.
(768) Kumar Katiyar, N.; Biswas, K.; Yeh, J.-W.; Sharma, S.; Sekhar Tiwary, C. A Perspective on the Catalysis Using the High Entropy Alloys. *Nano Energy* **2021**, *88*, 106261.
(769) Wang, S.; Mao, Q.; Ren, H.; Wang, W.; Wang, Z.; Xu, Y.; Li, X.; Wang, L.; Wang, H. Liquid Metal Interfacial Growth and Exfoliation to Form Mesoporous Metallic Nanosheets for Alkaline Methanol Electroreforming. *ACS Nano* **2022**, *16*, 2978−2987.
(770) Sheng, J.; Kang, J.; Ye, H.; Xie, J.; Zhao, B.; Fu, X.-Z.; Yu, Y.; Sun, R.; Wong, C.-P. Porous Octahedral PdCu Nanocages as Highly Efficient Electrocatalysts for the Methanol Oxidation Reaction. *J. Mater. Chem. A* **2018**, *6*, 3906−3912.
(771) Wang, Z.; Ren, X.; Luo, Y.; Wang, L.; Cui, G.; Xie, F.; Wang, H.; Xie, Y.; Sun, X. An Ultrafine Platinum-Cobalt Alloy Decorated Cobalt Nanowire Array with Superb Activity toward Alkaline Hydrogen Evolution. *Nanoscale* **2018**, *10*, 12302−12307.
(772) Xu, W.; Chang, J.; Cheng, Y.; Liu, H.; Li, J.; Ai, Y.; Hu, Z.; Zhang, X.; Wang, Y.; Liang, Q.; et al. A Multi-Step Induced Strategy to Fabricate Core-Shell Pt-Ni Alloy as Symmetric Electrocatalysts for Overall Water Splitting. *Nano Res.* **2022**, *15*, 965−971.
(773) Guo, Y.; Yang, X.; Liu, X.; Tong, X.; Yang, N. Coupling Methanol Oxidation with Hydrogen Evolution on Bifunctional Co-Doped Rh Electrocatalyst for Efficient Hydrogen Generation. *Adv. Funct. Mater.* **2023**, *33*, 2209134.
(774) Yang, Q.; Zhang, C.; Dong, B.; Cui, Y.; Wang, F.; Cai, J.; Jin, P.; Feng, L. Synergistic Modulation of Nanostructure and Active Sites: Ternary Ru&Fe-WO_x Electrocatalyst for Boosting Concurrent Generations of Hydrogen and Formate over 500 mA cm^{-2}. *Appl. Catal., B* **2021**, *296*, 120359.
(775) Xu, Y.; Liu, M.; Wang, M.; Ren, T.; Ren, K.; Wang, Z.; Li, X.; Wang, L.; Wang, H. Methanol Electroreforming Coupled to Green Hydrogen Production over Bifunctional NiIr-Based Metal-Organic Framework Nanosheet Arrays. *Appl. Catal., B* **2022**, *300*, 120753.
(776) Li, M.; Deng, X.; Xiang, K.; Liang, Y.; Zhao, B.; Hao, J.; Luo, J.-L.; Fu, X.-Z. Value-Added Formate Production from Selective Methanol Oxidation as Anodic Reaction to Enhance Electrochemical Hydrogen Cogeneration. *ChemSusChem* **2020**, *13*, 914−921.
(777) Wu, X.; Zhang, Y.; Yang, Y.; Fu, G.; Si, F.; Chen, J.; Ahmad, M.; Zhang, Z.; Ye, C.; Zhang, J.; et al. Ni_2P with Phosphorus Vacancy Supported Pt Clusters for Efficiently Electrocatalytic Co-Production of Hydrogen and Value-Added Chemicals from Methanol-Water at Low Potential. *Chem. Eng. J.* **2023**, *452*, 139057.
(778) Wang, T.; Cao, X.; Qin, H.; Chen, X.; Li, J.; Jiao, L. Integrating Energy-Saving Hydrogen Production with Methanol Electrooxidation over Mo Modified Co_4N Nanoarrays. *J. Mater. Chem. A* **2021**, *9*, 21094−21100.
(779) Zhao, B.; Liu, J.-W.; Yin, Y.-R.; Wu, D.; Luo, J.-L.; Fu, X.-Z. Carbon Nanofibers@NiSe Core/Sheath Nanostructures as Efficient Electrocatalysts for Integrating Highly Selective Methanol Conversion and Less-Energy Intensive Hydrogen Production. *J. Mater. Chem. A* **2019**, *7*, 25878−25886.
(780) Wang, H.; Cui, L.; Yin, S.; Yu, H.; Deng, K.; Xu, Y.; Wang, X.; Wang, Z.; Wang, L. Methanol-Assisted Energy-Efficient Water Splitting over Rambutan-Like Au@PdRu Core-Shell Nanocatalysts. *J. Mater. Chem. A* **2022**, *10*, 18889−18894.
(781) Zhou, Y.; Kuang, Y.; Hu, G.; Wang, X.; Feng, L. An Effective Pt-CoTe/NC Catalyst of Bifunctional Methanol Electrolysis for Hydrogen Generation. *Mater. Today Phys.* **2022**, *27*, 100831.
(782) Zhang, Y.; Wu, X.; Fu, G.; Si, F.; Fu, X.-Z.; Luo, J.-L. $NiFe_xP$@NiCo-LDH Nanoarray Bifunctional Electrocatalysts for Coupling of Methanol Oxidation and Hydrogen Production. *Int. J. Hydrogen Energy* **2022**, *47*, 17150−17160.
(783) Zhou, Y.; Wang, Q.; Tian, X.; Feng, L. Efficient Bifunctional Catalysts of CoSe/N-Doped Carbon Nanospheres Supported Pt Nanoparticles for Methanol Electrolysis of Hydrogen Generation. *Nano Res.* **2022**, *15*, 8936−8945.
(784) Li, L.; Zhang, L.; Gou, L.; Wei, S.; Hou, X.; Wu, L. High-Performance Methanol Electrolysis towards Energy-Saving Hydrogen Production: Using Cu_2O-Cu Decorated Ni_2P Nanoarray as Bifunctional Monolithic Catalyst. *Chem. Eng. J.* **2023**, *454*, 140292.
(785) Li, M.; Deng, X.; Liang, Y.; Xiang, K.; Wu, D.; Zhao, B.; Yang, H.; Luo, J.-L.; Fu, X.-Z. Co_xP@NiCo-LDH Heteronanosheet Arrays as Efficient Bifunctional Electrocatalysts for Co-Generation of Value-Added Formate and Hydrogen with Less-Energy Consumption. *J. Energy Chem.* **2020**, *50*, 314−323.
(786) Peng, X.; Xie, S.; Wang, X.; Pi, C.; Liu, Z.; Gao, B.; Hu, L.; Xiao, W.; Chu, P. K. Energy-Saving Hydrogen Production by the Methanol Oxidation Reaction Coupled with the Hydrogen Evolution Reaction Co-Catalyzed by a Phase Separation Induced Heterostructure. *J. Mater. Chem. A* **2020**, *10*, 20761−20769.
(787) Mao, Q.; Wang, P.; Wang, Z.; Xu, Y.; Li, X.; Wang, L.; Wang, H. PdRh Bimetallene for Energy-Saving Hydrogen Production via Methanol Electroreforming. *Appl. Mater. Today* **2022**, *26*, 101400.
(788) Du, X.; Tan, M.; Wei, T.; Kobayashi, H.; Song, J.; Peng, Z.; Zhu, H.; Jin, Z.; Li, R.; Liu, W. Highly Efficient and Robust Nickel-Iron Bifunctional Catalyst Coupling Selective Methanol Oxidation and Freshwater/Seawater Hydrogen Evolution via CO-Free Pathway. *Chem. Eng. J.* **2023**, *452*, 139404.
(789) Arshad, F.; Ul Haq, T.; Khan, A.; Haik, Y.; Hussain, I.; Sher, F. Multifunctional Porous NiCo Bimetallic Foams Toward Water Splitting and Methanol Oxidation-Assisted Hydrogen Production. *Energy Convers. Manag.* **2022**, *254*, 115262.
(790) Arshad, F.; Tahir, A.; Haq, T.; Duran, H.; Hussain, I.; Sher, F. Fabrication of NiCu Interconnected Porous Nanostructures for Highly Selective Methanol Oxidation Coupled with Hydrogen Evolution Reaction. *Int. J. Hydrogen Energy* **2022**, *47*, 36118−36128.
(791) Dai, L.; Qin, Q.; Zhao, X.; Xu, C.; Hu, C.; Mo, S.; Wang, Y. O.; Lin, S.; Tang, Z.; Zheng, N. Electrochemical Partial Reforming of Ethanol into Ethyl Acetate Using Ultrathin Co_3O_4 Nanosheets as a Highly Selective Anode Catalyst. *ACS Cent. Sci.* **2016**, *2*, 538−544.
(792) Sheng, S.; Ye, K.; Sha, L.; Zhu, K.; Gao, Y.; Yan, J.; Wang, G.; Cao, D. Rational Design of Co-S-P Nanosheet Arrays as Bifunctional

https://doi.org/10.1021/acs.chemrev.3c00332
Chem. Rev. 2024, 124, 3694−3812

Electrocatalysts for both Ethanol Oxidation Reaction and Hydrogen Evolution Reaction. *Inorg. Chem. Front.* **2020**, *7*, 4498−4506.
(793) Kim, T.; Roy, S. B.; Moon, S.; Yoo, S.; Choi, H.; Parale, V. G.; Kim, Y.; Lee, J.; Jun, S. C.; Kang, K.; Chun, S.-H.; Kanamori, K.; Park, H.-H. Highly Dispersed Pt Clusters on F-Doped Tin(IV) Oxide Aerogel Matrix: An Ultra-Robust Hybrid Catalyst for Enhanced Hydrogen Evolution. *ACS Nano* **2022**, *16*, 1625−1638.
(794) Li, M.; Duanmu, K.; Wan, C.; Cheng, T.; Zhang, L.; Dai, S.; Chen, W.; Zhao, Z.; Li, P.; Fei, H.; Zhu, Y.; Yu, R.; Luo, J.; Zhang, K.; Lin, Z.; Ding, M.; Huang, J.; Sun, H.; Guo, J.; Pan, X.; Goddard, W.; Sautet, P.; Huang, Y.; Duan, X. Single-Atom Tailoring of Platinum Nanocatalysts for High-Performance Multifunctional Electrocatalysis. *Nat. Catal.* **2019**, *2*, 495−503.
(795) Dai, C.; Yang, Y.; Zhao, Z.; Fisher, A.; Liu, Z.; Cheng, D. From Mixed to Three-Layer Core/Shell PtCu Nanoparticles: Ligand-Induced Surface Segregation to Enhance Electrocatalytic Activity. *Nanoscale* **2017**, *9*, 8945−8951.
(796) Fu, H.; Zhang, N.; Lai, F.; Zhang, L.; Chen, S.; Li, H.; Jiang, K.; Zhu, T.; Xu, F.; Liu, T. Surface-Regulated Platinum-Copper Nanoframes in Electrochemical Reforming of Ethanol for Efficient Hydrogen Production. *ACS Catal.* **2022**, *12*, 11402−11411.
(797) Zhao, X.; Dai, L.; Qin, Q.; Pei, F.; Hu, C.; Zheng, N. Self-Supported 3D PdCu Alloy Nanosheets as a Bifunctional Catalyst for Electrochemical Reforming of Ethanol. *Small* **2017**, *13*, 1602970.
(798) Wang, H.; Guo, Y.; Mao, Q.; Yu, H.; Deng, K.; Wang, Z.; Li, X.; Xu, Y.; Wang, L. Sulfur and Phosphorus Co-Doping Optimized Electronic Structure and Modulated Intermediate Affinity on PdSP Metallene for Ethanol-Assisted Energy-Saving H_2 Production. *Nanoscale* **2023**, *15*, 7765−7771.
(799) Begum, H.; Ahmed, M. S.; Jeon, S. Highly Efficient Dual Active Palladium Nanonetwork Electrocatalyst for Ethanol Oxidation and Hydrogen Evolution. *ACS Appl. Mater. Interfaces* **2017**, *9*, 39303−39311.
(800) Yin, K.; Chao, Y.; Lv, F.; Tao, L.; Zhang, W.; Lu, S.; Li, M.; Zhang, Q.; Gu, L.; Li, H.; Guo, S. One Nanometer PtIr Nanowires as High-Efficiency Bifunctional Catalysts for Electrosynthesis of Ethanol into High Value-Added Multicarbon Compound Coupled with Hydrogen Production. *J. Am. Chem. Soc.* **2021**, *143*, 10822−10827.
(801) Li, J.-Y.; Li, Y.-H.; Zhang, F.; Tang, Z.-R.; Xu, Y.-J. Visible-Light-Driven Integrated Organic Synthesis and Hydrogen Evolution over 1D/2D CdS-$Ti_3C_2T_x$ Mxene Composites. *Appl. Catal., B* **2020**, *269*, 118783.
(802) Zheng, J.; Chen, X.; Zhong, X.; Li, S.; Liu, T.; Zhuang, G.; Li, X.; Deng, S.; Mei, D.; Wang, J.-G. Hierarchical Porous NC@CuCo Nitride Nanosheet Networks: Highly Efficient Bifunctional Electrocatalyst for Overall Water Splitting and Selective Electrooxidation of Benzyl Alcohol. *Adv. Funct. Mater.* **2017**, *27*, 1704169.
(803) Zhou, H.; Ren, Y.; Li, Z.; Xu, M.; Wang, Y.; Ge, R.; Kong, X.; Zheng, L.; Duan, H. Electrocatalytic Upcycling of Polyethylene Terephthalate to Commodity Chemicals and H_2 Fuel. *Nat. Commun.* **2021**, *12*, 4679.
(804) Si, D.; Xiong, B.; Chen, L.; Shi, J. Highly Selective and Efficient Electrocatalytic Synthesis of Glycolic Acid in Coupling with Hydrogen Evolution. *Chem. Catal.* **2021**, *1*, 941−955.
(805) Mao, Q.; Deng, K.; Yu, H.; Xu, Y.; Wang, Z.; Li, X.; Wang, L.; Wang, H. In Situ Reconstruction of Partially Hydroxylated Porous Rh Metallene for Ethylene Glycol-Assisted Seawater Splitting. *Adv. Funct. Mater.* **2022**, *32*, 2201081.
(806) Fan, J.; Wu, J.; Cui, X.; Gu, L.; Zhang, Q.; Meng, F.; Lei, B.-H.; Singh, D. J.; Zheng, W. Hydrogen Stabilized RhPdH 2D Bimetallene Nanosheets for Efficient Alkaline Hydrogen Evolution. *J. Am. Chem. Soc.* **2020**, *142*, 3645−3651.
(807) Luo, M.; Zhao, Z.; Zhang, Y.; Sun, Y.; Xing, Y.; Lv, F.; Yang, Y.; Zhang, X.; Hwang, S.; Qin, Y.; Ma, J.-Y.; Lin, F.; Su, D.; Lu, G.; Guo, S. PdMo Bimetallene for Oxygen Reduction Catalysis. *Nature* **2019**, *574*, 81−85.
(808) Prabhu, P.; Lee, J.-M. Metallenes as Functional Materials in Electrocatalysis. *Chem. Soc. Rev.* **2021**, *50*, 6700−6719.
(809) Yu, H.; Zhou, T.; Wang, Z.; Xu, Y.; Li, X.; Wang, L.; Wang, H. Defect-Rich Porous Palladium Metallene for Enhanced Alkaline Oxygen Reduction Electrocatalysis. *Angew. Chem., Int. Ed.* **2021**, *60*, 12027−12031.
(810) Jiang, X.; Dong, Z.; Zhang, Q.; Xu, G.-R.; Lai, J.; Li, Z.; Wang, L. Decoupled Hydrogen Evolution from Water/Seawater Splitting by Integrating Ethylene Glycol Oxidation on $PtRh_{0.02}$@Rh Nanowires with Rh Atom Modification. *J. Mater. Chem. A* **2022**, *10*, 20571−20579.
(811) Selembo, P. A.; Perez, J. M.; Lloyd, W. A.; Logan, B. E. High Hydrogen Production from Glycerol or Glucose by Electrohydrogenesis Using Microbial Electrolysis Cells. *Int. J. Hydrogen Energy* **2009**, *34*, 5373−5381.
(812) Li, T.; Harrington, D. A. An Overviewof Glycerol Electrooxidation Mechanisms on Pt, Pd and Au. *ChemSusChem* **2021**, *14*, 1472−1495.
(813) Li, Y.; Wei, X.; Chen, L.; Shi, J.; He, M. Nickel-Molybdenum Nitride Nanoplate Electrocatalysts for Concurrent Electrolytic Hydrogen and Formate Productions. *Nat. Commun.* **2019**, *10*, 5335.
(814) Zhou, P.; Lv, X.; Tao, S.; Wu, J.; Wang, H.; Wei, X.; Wang, T.; Zhou, B.; Lu, Y.; Frauenheim, T.; Fu, X.; Wang, S.; Zou, Y. Heterogeneous-Interface-Enhanced Adsorption of Organic and Hydroxyl for Biomass Electrooxidation. *Adv. Mater.* **2022**, *34*, 2204089.
(815) Qian, Q.; He, X.; Li, Z.; Chen, Y.; Feng, Y.; Cheng, M.; Zhang, H.; Wang, W.; Xiao, C.; Zhang, G.; Xie, Y. Electrochemical Biomass Upgrading Coupled with Hydrogen Production under Industrial-Level Current Density. *Adv. Mater.* **2023**, *35*, 2300935.
(816) Yu, X.; dos Santos, E. C.; White, J.; Salazar-Alvarez, G.; Pettersson, L. G. M.; Cornell, A.; Johnsson, M. Electrocatalytic Glycerol Oxidation with Concurrent Hydrogen Evolution Utilizing an Efficient MoO_x/Pt Catalyst. *Small* **2021**, *17*, 2104288.
(817) Li, G.; Han, G.; Wang, L.; Cui, X.; Moehring, N. K.; Kidambi, P. R.; Jiang, D.-e.; Sun, Y. Dual Hydrogen Production from Electrocatalytic Water Reduction Coupled with Formaldehyde Oxidation via a Copper-Silver Electrocatalyst. *Nat. Commun.* **2023**, *14*, 525.
(818) Han, G.; Li, G.; Sun, Y. Electrocatalytic Dual Hydrogenation of Organic Substrates with a Faradaic Efficiency Approaching 200%. *Nat. Catal.* **2023**, *6*, 224−233.
(819) Preti, D.; Squarcialupi, S.; Fachinetti, G. Aerobic, Copper-Mediated Oxidation of Alkaline Formaldehyde to Fuel-Cell Grade Hydrogen and Formate: Mechanism and Applications. *Angew. Chem., Int. Ed.* **2009**, *48*, 4763−4766.
(820) Wang, T.; Tao, L.; Zhu, X.; Chen, C.; Chen, W.; Du, S.; Zhou, Y.; Zhou, B.; Wang, D.; Xie, C.; Long, P.; Li, W.; Wang, Y.; Chen, R.; Zou, Y.; Fu, X.-Z.; Li, Y.; Duan, X.; Wang, S. Combined Anodic and Cathodic Hydrogen Production from Aldehyde Oxidation and Hydrogen Evolution Reaction. *Nat. Catal.* **2022**, *5*, 66−73.
(821) Sharpe, H. R.; Geer, A. M.; Taylor, L. J.; Gridley, B. M.; Blundell, T. J.; Blake, A. J.; Davies, E. S.; Lewis, W.; Mcmaster, J.; Robinson, D.; Kays, D. L. Selective Reduction and Homologation of Carbon Monoxide by Organometallic Iron Complexes. *Nat. Commun.* **2018**, *9*, 3757.
(822) Qin, M.; Fan, S.; Li, X.; Yin, Z.; Wang, L.; Chen, A. Double Active Sites in Co-N_x-C@Co Electrocatalysts for Simultaneous Production of Hydrogen and Carbon Monoxide. *ACS Appl. Mater. Interfaces* **2021**, *13*, 38256−38265.
(823) Zhou, Z.; Zeng, L.; Xiong, G.; Yang, L.; Yuan, H.; Yu, J.; Xu, S.; Wang, D.; Zhang, X.; Liu, H.; Zhou, W. Multifunctional Electrocatalyst of NiCo-NiCoP Nanoparticles Embedded into P-Doped Carbon Nanotubes for Energy-Saving Hydrogen Production and Upgraded Conversion of Formaldehyde. *Chem. Eng. J.* **2021**, *426*, 129214.
(824) Jagadeesh, R. V.; Junge, H.; Beller, M. "Nanorust"-Catalyzed Benign Oxidation of Amines for Selective Synthesis of Nitriles. *ChemSusChem* **2015**, *8*, 92−96.
(825) Kim, J.; Golime, G.; Kim, H. Y.; Oh, K. Copper(II)-Catalyzed Aerobic Oxidation of Amines: Divergent Reaction Pathways by

https://doi.org/10.1021/acs.chemrev.3c00332
Chem. Rev. 2024, 124, 3694−3812

Solvent Control to Imines and Nitriles. *Asian J. Org. Chem.* **2019**, *8*, 1674−1679.
(826) Xu, B.; Hartigan, E. M.; Feula, G.; Huang, Z.; Lumb, J.-P.; Arndtsen, B. A. Simple Copper Catalysts for the Aerobic Oxidation of Amines: Selectivity Control by the Counterion. *Angew. Chem., Int. Ed.* **2016**, *55*, 15802−15806.
(827) Yamaguchi, K.; Mizuno, N. Efficient Heterogeneous Aerobic Oxidation of Amines by a Supported Ruthenium Catalyst. *Angew. Chem., Int. Ed.* **2003**, *42*, 1480−1483.
(828) Chaumontet, M.; Piccardi, R.; Baudoin, O. Synthesis of 3,4-Dihydroisoquinolines by a C(sp^3)-H Activation/Electrocyclization Strategy: Total Synthesis of Coralydine. *Angew. Chem., Int. Ed.* **2009**, *48*, 179−182.
(829) Zheng, B.; Trieu, T. H.; Li, F.-L.; Zhu, X.-L.; He, Y.-G.; Fan, Q.-Q.; Shi, X.-X. Copper-Catalyzed Benign and Efficient Oxidation of Tetrahydroisoquinolines and Dihydroisoquinolines Using Air as a Clean Oxidant. *ACS Omega* **2018**, *3*, 8243−8252.
(830) Galli, C. Radical Reactions of Arenediazonium Ions: An Easy Entry into the Chemistry of the Aryl Radical. *Chem. Rev.* **1988**, *88*, 765−792.
(831) Ding, Y.; Miao, B.-Q.; Li, S.-N.; Jiang, Y.-C.; Liu, Y.-Y.; Yao, H.-C.; Chen, Y. Benzylamine Oxidation Boosted Electrochemical Water-Splitting: Hydrogen and Benzonitrile Co-Production at Ultra-Thin Ni_2P Nanomeshes Grown on Nickel Foam. *Appl. Catal., B* **2020**, *268*, 118393.
(832) Luterbacher, J. S.; Rand, J. M.; Alonso, D. M.; Han, J.; Youngquist, J. T.; Maravelias, C. T.; Pfleger, B. F.; Dumesic, J. A. Nonenzymatic Sugar Production from Biomass Using Biomass-Derived Gamma-Valerolactone. *Science* **2014**, *343*, 277−280.
(833) Xia, Q.; Chen, Z.; Shao, Y.; Gong, X.; Wang, H.; Liu, X.; Parker, S. F.; Han, X.; Yang, S.; Wang, Y. Direct Hydrodeoxygenation of Raw Woody Biomass into Liquid Alkanes. *Nat. Commun.* **2016**, *7*, 11162.
(834) Zhang, Z.; Deng, K. Recent Advances in the Catalytic Synthesis of 2,5-Furandicarboxylic Acid and its Derivatives. *ACS Catal.* **2015**, *5*, 6529−6544.
(835) Zhao, H.; Lu, D.; Wang, J.; Tu, W.; Wu, D.; Koh, S. W.; Gao, P.; Xu, Z. J.; Deng, S.; Zhou, Y.; You, B.; Li, H. Raw Biomass Electroreforming Coupled to Green Hydrogen Generation. *Nat. Commun.* **2021**, *12*, 2008.
(836) Hutchings, G. J. Selective Oxidation Using Supported Gold Bimetallic and Trimetallic Nanoparticles. *Catal. Today* **2014**, *238*, 69−73.
(837) Lv, G.; Wang, H.; Yang, Y.; Deng, T.; Chen, C.; Zhu, Y.; Hou, X. Graphene Oxide: A Convenient Metal-Free Carbocatalyst for Facilitating Aerobic Oxidation of 5-Hydroxymethylfurfural into 2, 5-Diformylfuran. *ACS Catal.* **2015**, *5*, 5636−5646.
(838) Wang, T.; Nolte, M. W.; Shanks, B. H. Catalytic Dehydration of C_6 Carbohydrates for the Production of Hydroxymethylfurfural (HMF) as a Versatile Platform Chemical. *Green Chem.* **2014**, *16*, 548−572.
(839) van Putten, R.-J.; van der Waal, J. C.; de Jong, E.; Rasrendra, C. B.; Heeres, H. J.; de Vries, J. G. Hydroxymethylfurfural, A Versatile Platform Chemical Made from Renewable Resources. *Chem. Rev.* **2013**, *113*, 1499−1597.
(840) Nam, D.-H.; Taitt, B. J.; Choi, K.-S. Copper-Based Catalytic Anodes to Produce 2,5-Furandicarboxylic Acid, a Biomass-Derived Alternative to Terephthalic Acid. *ACS Catal.* **2018**, *8*, 1197−1206.
(841) Zhang, N.; Zou, Y.; Tao, L.; Chen, W.; Zhou, L.; Liu, Z.; Zhou, B.; Huang, G.; Lin, H.; Wang, S. Electrochemical Oxidationof 5-Hydroxymethylfurfural on Nickel Nitride/Carbon Nanosheets: Reaction Pathway Determined by In Situ Sum Frequency Generation Vibrational Spectroscopy. *Angew. Chem., Int. Ed.* **2019**, *58*, 15895−15903.
(842) Zhou, Z.; Chen, C.; Gao, M.; Xia, B.; Zhang, J. *In Situ* Anchoring of a Co_3O_4 Nanowire on Nickel Foam: An Outstanding Bifunctional Catalyst for Energy-Saving Simutaneous Reactions. *Green Chem.* **2019**, *21*, 6699−6706.
(843) Wang, L.; Cao, J.; Lei, C.; Dai, Q.; Yang, B.; Li, Z.; Zhang, X.; Yuan, C.; Lei, L.; Hou, Y. Strongly Coupled 3D N-Doped MoO_2/Ni_3S_2 Hybrid for High Current Density Hydrogen Evolution Electrocatalysis and Biomass Upgrading. *ACS Appl. Mater. Interfaces* **2019**, *11*, 27743−27750.
(844) Gao, L.; Liu, Z.; Ma, J.; Zhong, L.; Song, Z.; Xu, J.; Gan, S.; Han, D.; Niu, L. NiSe@NiO_x Core-Shell Nanowires as a Non-Precious Electrocatalyst for Upgrading 5-Hydroxymethylfurfural into 2,5-Furandicarboxylic Acid. *Appl. Catal., B* **2020**, *261*, 118235.
(845) Du, P.; Zhang, J.; Liu, Y.; Huang, M. Hydrogen Generation from Catalytic Glucose Oxidation by Fe-Based Electrocatalysts. *Electrochem. Commun.* **2017**, *83*, 11−15.
(846) Liu, W.-J; Xu, Z.; Zhao, D.; Pan, X.-Q.; Li, H.-C.; Hu, X.; Fan, Z.-Y.; Wang, W.-K.; Zhao, G.-H.; Jin, S.; Huber, G. W.; Yu, H.-Q. Efficient Electrochemical Production of Glucaric Acid and H_2 via Glucose Electrolysis. *Nat. Commun.* **2020**, *11*, 265.
(847) Zheng, D.; Li, J.; Ci, S.; Cai, P.; Ding, Y.; Zhang, M.; Wen, Z. Three-Birds-with-One-Stone Electrolysis for Energy-Efficiency Production of Gluconate and Hydrogen. *Appl. Catal., B* **2020**, *277*, 119178.
(848) Sun, F.; Zhou, Y.; You, Z.; Xia, H.; Tuo, Y.; Wang, S.; Jia, C.; Zhang, J. Bi-Functional Fe_3O_4/Au/CoFe-LDH Sandwich-Structured Electrocatalyst for Asymmetrical Electrolyzer with Low Operation Voltage. *Small* **2021**, *17*, 2103307.
(849) Liu, H.; Zhang, R.; Chen, L.; Wang, L.; Guo, Y.; Yang, Y. Synergistic Coupling of Nickel Boride with Ru Cluster as a Highly Active Multifunctional Electrocatalyst for Overall Water Splitting and Glucose Electrolysis. *Adv. Sustainable Syst.* **2021**, *5*, 2000184.
(850) Geyer, R.; Jambeck, J. R.; Law, K. L. Production, Use, and Fate of All Plastics Ever Made. *Sci. Adv.* **2017**, *3*, e1700782.
(851) Kane, I. A.; Clare, M. A.; Miramontes, E.; Wogelius, R.; Rothwell, J. J.; Garreau, P.; Pohl, F. Seafloor Microplastic Hotspots Controlled by Deep-Sea Circulation. *Science* **2020**, *368*, 1140−1145.
(852) Li, L.; Luo, Y.; Li, R.; Zhou, Q.; Peijnenburg, W. J. G. M.; Yin, N.; Yang, J.; Tu, C.; Zhang, Y. Effective Uptake of Submicrometre Plastics by Crop Plants via a Crack-Entry Mode. *Nat. Sustain.* **2020**, *3*, 929−937.
(853) Uekert, T.; Kasap, H.; Reisner, E. Photoreforming of Nonrecyclable Plastic Waste over a Carbon Nitride/Nickel Phosphide Catalyst. *J. Am. Chem. Soc.* **2019**, *141*, 15201−15210.
(854) Salvatore, D. A.; Gabardo, C. M.; Reyes, A.; O'Brien, C. P.; Holdcroft, S.; Pintauro, P.; Bahar, B.; Hickner, M.; Bae, C.; Sinton, D.; Sargent, E. H.; Berlinguette, C. P. Designing Anion Exchange Membranes for CO_2 Electrolysers. *Nat. Energy* **2021**, *6*, 339−348.
(855) Wei, C.; Rao, R. R.; Peng, J.; Huang, B.; Stephens, I. E. L.; Risch, M.; Xu, Z. J.; Shao-Horn, Y. Recommended Practices and Benchmark Activity for Hydrogen and Oxygen Electrocatalysis in Water Splitting and Fuel Cells. *Adv. Mater.* **2019**, *31*, 1806296.
(856) Wang, N.; Li, X.; Hu, M.-K.; Wei, W.; Zhou, S.-H.; Wu, X.-T.; Zhu, Q.-L. Ordered Macroporous Superstructure of Bifunctional Cobalt Phosphide with Heteroatomic Modification for Paired Hydrogen Production and Polyethylene Terephthalate Plastic Recycling. *Appl. Catal., B* **2022**, *316*, 121667.
(857) Ma, F.; Wang, S.; Gong, X.; Liu, X.; Wang, Z.; Wang, P.; Liu, Y.; Cheng, H.; Dai, Y.; Zheng, Z.; Huang, B. Highly Efficient Electrocatalytic Hydrogen Evolution Coupled with Upcycling of Microplastics in Seawater Enabled via Ni_3N/W_5N_4 Janus Nanostructures. *Appl. Catal., B* **2022**, *307*, 121198.
(858) Li, Y.; Zhao, Y.; Zhao, H.; Wang, Z.; Li, H.; Gao, P. A Bifunctional Catalyst of Ultrathin Cobalt Selenide Nanosheets for Plastic-Electroreforming-Assisted Green Hydrogen Generation. *J. Mater. Chem. A* **2022**, *10*, 20646−20646.

https://doi.org/10.1021/acs.chemrev.3c00332
Chem. Rev. 2024, 124, 3694−3812